

UC Berkeley

UC Berkeley Electronic Theses and Dissertations

Title

Evaluation of the State of Practice Regarding Nonlinear Seismic Deformation Analyses of Embankment Dams Subject to Soil Liquefaction Based on Case Histories

Permalink

<https://escholarship.org/uc/item/4515d2j1>

Author

Chowdhury, Khaled Hossain

Publication Date

2018

Peer reviewed|Thesis/dissertation

Evaluation of the State of Practice Regarding Nonlinear
Seismic Deformation Analyses of Embankment Dams
Subject to Soil Liquefaction Based on Case Histories

By

Khaled Hossain Chowdhury

A dissertation submitted in partial satisfaction of the
requirements for the degree of
Doctor of Philosophy
in
Engineering – Civil and Environmental Engineering
in the
Graduate Division
of the
University of California, Berkeley

Committee in charge:

Professor Raymond B. Seed, Chair
Professor Nicholas Sitar
Professor Douglas S. Dreger

Spring 2019

Evaluation of the State of Practice Regarding Nonlinear
Seismic Deformation Analyses of Embankment Dams
Subject to Soil Liquefaction Based on Case Histories

Copyright © 2019

By

Khaled Hossain Chowdhury

Abstract

Evaluation of the State of Practice Regarding Nonlinear Seismic Deformation Analyses of Embankment Dams Subject to Soil Liquefaction Based on Case Histories

By

Khaled Hossain Chowdhury

Doctor of Philosophy – Civil and Environmental Engineering

University of California, Berkeley

Professor Raymond B. Seed, Chair

Nonlinear seismic deformation analysis (NDA) is an important analytical tool used to (1) evaluate seismic safety of existing dams, (2) to design seismic mitigation of dams, (3) to evaluate and implement reservoir restrictions and other interim safety measures while seismic mitigation design and implementation are pending, and (4) for design of new embankment dams to ensure the seismic safety of dams that serve important purposes such as flood control, water supply, power generation, and tailings impoundments, especially with regard to risk exposures of downstream populations and facilities.

Nonlinear seismic deformation analyses of embankment dams are complex. They require (1) proper site characterization, (2) development of ground motions considering the recent State of Knowledge protocols, (3) liquefaction triggering relationships, (4) post-liquefaction strength relationships, (4) modeling of behaviors of non-liquefiable soils, (5) constitutive models, (6) accounting for volumetric recompression settlement, and (7) engineering evaluation of analysis results. These inter-dependent aspects of seismic deformation analyses, when applied through nonlinear analytical tools such as FLAC, may not always provide correct predictive answers if the concepts, relationships, and models are not implemented properly.

Evaluation of different aspects of the current State of Practice in seismic deformation analyses was performed in these current studies. The approach taken was to apply suites of combinations of (1) four different analytical or constitutive models, (2) three liquefaction triggering relationships, (3) three post-liquefaction residual strength (S_r) relationships, and (4) various additional analysis protocols to back-analyses of a series of three well-documented seismic performance field case histories.

The three field performance case histories were (1) seismic site response and performance of the Port Island vertical strong motion array in the 1995 Kobe, Japan earthquake, (2) the performance of the Lower San Fernando Dam during the 1971 San Fernando earthquake (a large deformations or flow failure case history), and (3) the performance of the Upper San Fernando dam (a moderate deformations case history) during the 1971 San Fernando earthquake.

Approaches and implementation protocols for the current studies included (1) evaluating different modeling schemes, (2) performing seismic deformation analyses with different numerical modeling schemes, (3) identifying the accuracy and reliability of different modeling schemes, and their advantages and limitations, based on three well documented case histories, (4) identifying advantages and limitations of continuum-based numerical modeling schemes in predicting deformations in embankment dams, and (5) developing improved analytical approaches to improve performance of seismic deformation modeling for forward analyses.

The lessons learned from the NDA are important. A careful implementation of the different concepts, relationships, and models successfully predicted the performance of both the moderate deformations observed in the Upper San Fernando Dam, and the large deformations or flow failure observed in the Lower San Fernando Dam in the 1971 San Fernando earthquake. Six out of nine NDA performed for the USFD successfully predicted magnitudes and principal mechanisms of this moderate deformations case history. Four out of six NDA performed for the LSFD successfully predicted magnitudes and mechanisms of this large deformations or flow failure case history.

Lessons learned from evaluation of the current State of Practice regarding seismic deformation analyses of embankment dams subject to liquefaction are important. These lessons were developed based on insights from different NDA performed in the current studies and also considering the current State of Practice guidance and protocols.

The back-analyses in the current studies demonstrated an ability to produce very good engineering “predictions” of both observed mechanisms of displacements and distress, as well as magnitudes of deformations and displacements.

Accomplishing this appears to require the following:

1. Suitable analytical or constitutive models.
2. Calibration of these models with respect to cyclic (seismic) pore pressure generation with suitable liquefaction triggering relationships, including both K_α and K_σ relationships.
3. Use of suitable post-liquefaction residual strength (S_r) relationships.

4. Suitable procedures and protocols for transition to S_r behaviors in potentially liquefiable soils.
5. Suitable treatment of potential cyclic softening, and strain softening, behaviors in sensitive clayey soils.
6. Suitable characterization of geometry and stratigraphy, and suitable evaluation of material properties and behaviors.
7. Suitable development and application of appropriate seismic “input” motions.
8. Appropriate evaluation and interpretation of the analysis results, with an understanding of the models and relationships employed, and also the intrinsic limitations of the continuum analysis methods employed with regard to accurate analyses of very large deformations and displacements.
9. And engineering judgment.

To my wife, Lubna Chowdhury,
without your support and inspiration,
this accomplishment would not happen.

Table of Contents

Acknowledgements	vii
Chapter 1: Introduction and Overview	1
Chapter 2: Concepts, Analytical Models, and Engineering Relationships	5
2.1 BRIEF DISCUSSION OF KEY SOIL LIQUEFACTION AND POST-LIQUEFACTION CONCEPTS AND BEHAVIORS	5
2.2 BRIEF DISCUSSION OF THE FOUR ANALYTICAL AND/OR CONSTITUTIVE MODELS USED IN THESE CURRENT STUDIES	10
2.2.1 The Roth Model	10
2.2.2 The UBCSAND Model	13
2.2.3 The PM4Sand Model	17
2.2.4 The Wang2D Model	22
2.3 LIQUEFACTION TRIGGERING RELATIONSHIPS	24
2.3.1 Introduction and Overview	24
2.3.2 The Three Triggering Relationships Employed in These Current Studies	26
2.3.2.1 Youd et al. (2001)	29
2.3.2.2 Boulanger and Idriss (2014)	34
2.3.2.3 Cetin et al. (2018)	38
2.3.2.4 Magnitude-Related Duration Weighting Factors and Fines Corrections	38
2.4 POST-LIQUEFACTION RESIDUAL STRENGTH (S_r) RELATIONSHIPS	39
Chapter 3: The Port Island Vertical Array Site Seismic Performance Case History During the 1995 Kobe Earthquake	46
3.1 INTRODUCTION	46
3.2 GEOLOGY AND CONSTRUCTION OF PORT ISLAND	47
3.3 OBSERVED PERFORMANCE OF PORT ISLAND DURING THE 1995 KOBE EARTHQUAKE	49
3.4 GEOTECHNICAL/GEOLOGICAL CROSS-SECTION AND BACK ANALYSIS	51
3.5 GEOTECHNICAL PARAMETERS FOR SITE RESPONSE ANALYSES	56
3.5.1 Fines contents for Masado fill	56
3.5.2 Shear wave (S-wave) velocity and compression wave (P-wave) velocity	56
3.5.3 SPT blow counts (N_{78} , $N_{1,60}$, $N_{1,60,CS}$)	59
3.5.4 Soil Strength and Consolidation Parameters	62

3.6 GROUND MOTION TIME HISTORIES FOR SITE RESPONSE ANALYSES	65
3.6.1 Fault Mechanism of Kobe Earthquake	65
3.6.2 Ground Motions at the Port Island Vertical Array Site	66
3.6.3 Ground Motion Processing for the Current Study	70
3.7 PREVIOUS STUDIES OF PORT ISLAND	75
3.7.1 Wang et al. (2001)	75
3.7.2 Gingery (2014)	77
3.7.3 Ziotopoulou (2010) and Ziotopoulou et al. (2012)	77
3.8 RESULTS OF PORT ISLAND VERTICAL ARRAY SITE RESPONSE ANALYSES PERFORMED AS PART OF THESE CURRENT STUDIES.....	85
3.9 SUMMARY AND CONCLUSIONS	90
Chapter 4: The Lower San Fernando Dam (LSFD) Seismic Performance Case	
History During the 1971 San Fernando Earthquake	91
4.1 INTRODUCTION	91
4.2 DAM PERFORMANCE DURING THE 1971 SAN FERNANDO EARTHQUAKE	92
4.3 CONSTRUCTION OF THE LOWER SAN FERNANDO DAM	96
4.4 GEOLOGICAL/GEOTECHNICAL ANALYSIS CROSS-SECTION AND ANALYSIS PLAN	100
4.4.1 Analysis Cross-Section	100
4.4.2 Analysis Plan	101
4.5 GEOLOGICAL PARAMETERS FOR NONLINEAR SEISMIC DEFORMATION ANALYSES.....	104
4.5.1 Brief Summary of Available Data	104
4.5.2 SPT Blow Counts for Potentially Liquefiable Materials.....	106
4.5.3 Cross-Checks on $N_{1,60,CS}$ Values Developed	114
4.5.3.1 Cross-Comparisons of $N_{1,60,CS}$ Values with Previous Studies	114
4.5.3.2 Relative Density	117
4.5.4 Shear Strengths and Strength Behaviors for Non-Liquefiable Soils	121
4.5.5 Hydraulic Conductivity and Pre-Earthquake Phreatic Surface for LSFD Analyses.....	123
4.5.6 Strength and Stiffness Parameters	124
4.6 DEVELOPMENT OF INPUT GROUND MOTION TIME HISTORIES FOR LSFD AND USFD NONLINEAR SEISMIC DEFORMATION ANALYSES	126

4.6.1 Overview of Input Ground Motion Time Histories for These Two Case Histories.....	126
4.6.2 Development of the Input Strong Motion Time Histories Used in Most Previous Back-Analyses of the USFD and the LSFD.....	127
4.6.3 Approaches for Development of Input Acceleration Time Histories for These Current Studies	137
4.6.3.1 Fault Mechanisms for the 1971 San Fernando Earthquake.....	138
4.6.3.2 Development of Scaling Factors for Development of Input Motions for Back Analyses of the LSFD and USFD	143
4.6.4 Ground Motion Processing with Different Filtering Bands	155
4.6.5 Ground Motion Processing with Estimated Permanent Displacement.....	163
4.6.6 Simulated Ground Motions for Use as Input Motions for Back-Analyses of the USFD and LSFD Case Histories (Approach 2)	169
4.6.6.1 SCEC Broadband Platform Simulation Approach for the Current Study	169
4.6.6.2 Slip Models for SCEC-BPP Simulations of the 1971 San Fernando Earthquake in These Current Studies.....	173
4.7 NONLINEAR SEISMIC DEFORMATION ANALYSES OF THE LOWER SAN FERNANDO DAM	181
4.7.1 Model Construction and Static Analyses	181
4.7.2 Dynamic or Earthquake Shaking Analyses	184
4.7.3 Transitioning to S_r , and Post-Shaking Analyses.....	188
4.8 RESULTS OF LOWER SAN FERNANDO DAM NONLINEAR SEISMIC DEFORMATION ANALYSES	194
4.8.1 LSFD Analysis 1: Roth Model, with the Cetin et al. (2018) Liquefaction Triggering Relationship, Youd et al. (2001) $K\sigma$, and the Weber et al. (2015) S_r Relationship	196
4.8.2 LSFD Analysis 2: UBCSAND Model, with the Youd et al. (2001) Liquefaction Triggering Relationship and the Seed and Harder (1990) S_r Relationship.....	204
4.8.3 LSFD Analysis 3: UBCSAND Model, with the Youd et al. (2001) Soil Liquefaction Triggering Relationship, and the Weber et al. (2015) Post-Liquefaction S_r Relationship.....	211
4.8.4 LSFD Analysis 4: PM4Sand Model, with Boulanger and Idriss (2014) Liquefaction Triggering Relationship, and the Idriss and Boulanger (2015) S_r Relationship.....	213

4.8.5 LSFDA Analysis 5: PM4Sand Model, with the Cetin et al. (2018) Liquefaction Triggering Relationship, the Youd et al. (2001) K_σ relationship, and the Weber et al. (2015) S_r Relationship.....	219
4.8.6 LSFDA Analysis 6: Wang2D Model, with the Cetin et al. (2018) Liquefaction Triggering Relationship, and the Weber et al. (2015) S_r Relationship	226
4.9 SUMMARY AND CONCLUSION	233
Chapter 5: The Upper San Fernando Dam Seismic Performance Case History	
During the 1971 San Fernando Earthquake	238
5.1 INTRODUCTION	238
5.2 CONSTRUCTION OF THE UPPER SAN FERNANDO DAM	239
5.3 OBSERVED PERFORMANCE OF THE UPPER SAN FERNANDO DAM DURING THE 1971 SAN FERNANDO EARTHQUAKE	240
5.3.1 Observed Performance	240
5.3.2 Principal Distress Mechanisms of the USFD; Deep Seated Basal Shear Surface Due to Liquefaction and Strain Softening of Soils, and Strong Influence of Near-Source Seismic Ground Motions	246
5.4 GEOLOGICAL/GEOTECHNICAL CROSS-SECTION AND BACK-ANALYSIS PLAN	247
5.5 GEOTECHNICAL PARAMETERS FOR DEFORMATION ANALYSES	251
5.5.1 SPT Blow Counts.....	251
5.5.2 Shear Strengths and Strength Behaviors for Non-Liquefiable Soils	255
5.5.3 Hydraulic Conductivity and Pre-Earthquake Phreatic Surface	257
5.5.4 Strength and Stiffness Parameters	258
5.6 INPUT GROUND MOTION TIME HISTORY FOR THE UPPER SAN FERNANDO DAM (USFD) SEISMIC DEFORMATION ANALYSES.....	259
5.7 FLAC MODEL DEVELOPMENT FOR USFD SEISMIC DEFORMATION ANALYSES	262
5.8 RESULTS OF UPPER SAN FERNANDO DAM NONLINEAR SEISMIC DEFORMATION ANALYSES	262
5.8.1 USFD Analysis 1: Roth Model, with the Youd et al. (2001) Liquefaction Triggering Relationship, and the Seed and Harder (1990) S_r Relationship.....	264
5.8.2 USFD Analysis 2: Roth Model, with the Boulanger and Idriss (2014) Liquefaction Triggering Relationship, and the Idriss and Boulanger (2015) S_r Relationship	271

5.8.3 USFD Analysis 3: Roth Model, with the Cetin et al. (2018) Liquefaction Triggering Relationship, Youd et al. (2001) K_s Relationship, and the Weber et al. (2015) S_r Relationship.....	276
5.8.4 USFD Analysis 4: UBCSAND Model, with the Youd et al. (2001) Liquefaction Triggering Relationship and the Seed and Harder (1990) S_r Relationship.....	281
5.8.5 USFD Analysis 5: UBCSAND Model with Youd et al. (2001) Liquefaction Triggering and Idriss and Boulanger (2015) S_r Relationship.....	288
5.8.6 USFD Analysis 6: UBCSAND Model with the Youd et al. (2001) Liquefaction Triggering Relationship, and the Weber et al. (2015) S_r Relationship.....	294
5.8.7 USFD Analysis 7: PM4Sand Model, with the Boulanger and Idriss (2014) Liquefaction Triggering Relationship, and the Idriss and Boulanger (2015) S_r Relationship.....	300
5.8.8 USFD Analysis 8: PM4Sand Model, with the Cetin et al. (2018) Liquefaction Triggering Relationship, the Youd et al. (2001) K_σ Relationship, and the Weber et al. (2015) S_r Relationship	306
5.8.9 USFD Analysis 9: Wang2D Model, with the Cetin et al. (2018) Liquefaction Triggering Relationship, and the Weber et al. (2015) S_r Relationship.....	314
5.9 SENSITIVITY ANALYSIS WITH GROUND MOTIONS WITH STATIC OFFSET	322
5.10 SUMMARY AND CONCLUSIONS	325
Chapter 6: Summary Findings and Conclusions.....	333
6.1 INTRODUCTION	333
6.2 LESSONS LEARNED FROM BACK-ANALYSES OF THE PORT ISLAND VERTICAL ARRAY DURING THE 1995 KOBE $M_w = 6.9$ EARTHQUAKE	333
6.3 LESSONS LEARNED FROM BACK-ANALYSES OF THE LOWER SAN FERNANDO DAM DURING THE 1971 SAN FERNANDO $M_w=6.61$ EARTHQUAKE	335
6.3.1 Overview.....	335
6.3.2 Lessons Learned.....	335
6.4 LESSONS LEARNED FROM BACK-ANALYSES OF THE UPPER SAN FERNANDO DAM DURING THE 1971 SAN FERNANDO EARTHQUAKE.....	352
6.4.1 Overview and Lessons Learned.....	352
6.5 ADDITIONAL LESSONS LEARNED FROM BACK-ANALYSES OF BOTH THE LSFD AND USFD DURING THE 1971 SAN FERNANDO EARTHQUAKE.....	361
6.5.1 Overview and Lessons Learned.....	361
References	365

ACKNOWLEDGEMENTS

It was a journey! I am happy to be here!

I consider myself blessed for having Professor Raymond B. Seed as my supervisor. In my 27 years as a student and a practitioner, I have not seen anyone more passionate, intelligent, and honest in advancing the State of Practice in geotechnical engineering that affects the policy and engineering. The last six years of my life was simply the most intellectually challenging and enriching experience, mostly due to the guidance I have received from Professor Seed as his last PhD student. I am grateful to Mary Seed and the family for the support, sometimes when there were competing needs for time.

When I got my admission at the University of California, Berkeley, Professor Seed told me “you should buy flowers and tell your wife, Honey, we have got admissions, as for the next several years you will have all the fun in the world while she suffers”. Sadly, his words came true. This PhD would not happen without the sacrifice that my wife, Lubna Chowdhury made. I am thankful for the inspiration that Lubna has given me in the last six years.

I am thankful to my mother, Salma Akhter, for still treating us like birds in a nest. I am thankful to my eight years old son, Zahi Hossain, and three years old daughter, Kashfya Hossain (may be for not realizing that dads usually spend way more time, if not busy with PhD along with a full-time job). My gratitude to my sister Rehnuma Akhter, brother Tarek Chowdhury, sister-in law Nazreena Latif and their families, my aunt Khurshid Hossain, and cousins Syeda Sanjana and Adnan Jamil for encouragements throughout the last six years.

Then comes my mentor and friend, Dr. Vlad Perlea. FLAC is a complex modeling tool, and not many people know the intricacies better than Dr. Vlad Perlea. Vlad selflessly helped me to learn this tool with attention to minor details, answered every silly question, and every time I had a FLAC issue, I had Vlad to guide me. And I am thankful to Mary Perlea for letting me steal Vlad’s time!

Professor Douglas Dreger just did not teach me seismology, he was an important contributor to this research effort. I have learned SCEC BBP modeling techniques from Professor Dreger, who was also the task lead for validation of SCEC BBP.

Professor Norm Abrahamson is a busy person. However, he graciously found time for us. Professor Abrahamson helped us with many details in ground motion processing, which were instrumental in the current studies.

When it comes to FLAC modeling, Dr. Ethan Dawson conveys complex thoughts in the simplest and transparent ways. It was immensely valuable to get guidance from Ethan regarding Roth model and other aspects of the numerical modeling.

Dr. Zhi-Liang Wang and Dr. Fenggang Ma helped us to understand the Wang2D protocols. They implemented several improvisations to their models during the process,

which show their interest to advance the Wang2D modeling capabilities. I am thankful to Dr. Faiz Makdisi for introducing me to Drs. Wang and Ma.

Dr. Mike Beaty gave us the initial guidance and encouragement in taking this apparently complex and over-arching research effort, which was important. The in-person meetings with Mike in Portland and Sacramento happened at the right junctures to give confidence to continue and advance the work.

Having George Hu as a co-worker at USACE was another good thing that happened to me during the research. Dr. Zia Zafir helped us to understand the needs of geotechnical engineering community, and the current State of Practice.

I learned a lot by being part of the research efforts by Weber et al. (2015) and Cetin et al. (2018). I am thankful to Professor Seed, Professor Joe Weber, and Professor Onder Cetin for the opportunities to be part of these recent research efforts. I am thankful to Dr. Jerry Wu for sharing his laboratory test data.

I would also like to thank David Gillette, Navead Jensen, and Dennis Hanneman of USBR for their interest and discussions during this research.

I have driven a total three to five hours a day in my commute to Berkeley from Rancho Cordova, when I was taking courses in the campus. However, I have never felt tired or discouraged. The reason is simple. I took classes from Professors Juan Pestana, Nicholas Sitar, Jonathan Bray, Norm Abrahamson, Douglas Dreger, William Dietrich, and James Rector. These classes were essential not only for our research, every day I get the benefits in my work. We are thankful to Professor Kenichi Soga and his students for their interest in our research.

Interactions with the fellow graduate students were motivational and those discussions helped me to feel encouraged. I am grateful for all the discussions with Nathaniel Wagner, Joe Weber, Justin Hollenback, John Murphy, Francesco Tetone, Mike Gardner, Robert Lanzafame, Ebuka Chukwuebuka, Julien Waeber, Christie Hale, Christie Beyzaie, Makbule Illgac, Nella Pierre-Louis, Jorge Macedo, Estefan Thibode, Mike George, Roberto Luque, Ezra Satiasabda, Amr Ewais, Daniel Hutabarat, and all those who I missed.

I am grateful to my co-workers at USACE (current employer since May, 2016) and URS (former employer) for their support during the last six years. Their considerations for my schedule were instrumental in my ability to handle both work and studies/research at the same time. I would like to thank Derek Morley, who has been an inspiration to me with his work ethics, team building skills, and passion to get things right. I have got many insights from discussions with Derek and other USACE DSPC and URS employees that were helpful in this research effort.

I am thankful to Syed Sajidul Haq, Mynul Chowdhury, Javed Faruque and all my friends for their support during the last six years. At last, I am simply grateful to Shelley Okimoto of UC Berkeley CE graduate office to help me to navigate the procedural steps.

Chapter 1

Introduction and Overview

Nonlinear seismic deformation analysis (NDA) is an important analytical tool used (1) to evaluate seismic safety of existing dams, (2) to design seismic mitigation of dams, (3) to evaluate and implement reservoir restrictions and other interim safety measures while seismic mitigation design and implementation are pending, and (4) for design of new embankment dams to ensure the seismic safety of dams that serve important purposes such as flood control, water supply, power generation, and tailings impoundments, especially with regard to risk exposures of downstream populations and facilities.

These current studies will focus primarily on the application of this approach to analyses of dams with soils, either in the embankment and/or in the foundation, that are potentially susceptible to seismically-induced soil liquefaction.

Seismic deformation analyses can be performed in either a two-dimensional framework, or a three-dimensional framework. As the two-dimensional approach is currently the most common application, this study will primarily evaluate the two-dimensional approach. It should be noted, however, that many of the resulting lessons learned will be similarly applicable to three-dimensional seismic deformation analyses.

Nonlinear seismic deformation analyses have gained increasing importance and popularity in recent years due to (1) advancements in computing capabilities, and (2) increasing development and improvement of different engineering relationships and constitutive models for characterization and modeling of the types of soil behaviors that must be analyzed in these applications. A successful implementation of a seismic deformation analysis depends on many factors such as site characterization, material parameter development, development of suitable seismic input seismic ground motions, modeling the behaviors of non-liquefiable soil units, soil liquefaction triggering relationships, evaluation and implementation of post-liquefaction strengths, and the constitutive and/or analytical models employed. These are complex analyses involving combinations of many sub-elements. Even though the importance of seismic deformation analyses in assessing and mitigating risks for dams is both large, and growing, the implementation of this approach varies considerably in current engineering practice.

The objective of these current studies is to evaluate the accuracy, reliability, and usefulness of nonlinear seismic deformation analyses by means of back-analyses of three well-documented seismic field performance case histories. The approach taken is to perform seismic deformation analyses of the three case histories using several sets of (1) analytical models or constitutive relationships, (2) seismic soil liquefaction triggering

relationships used to calibrate the analytical models with regard to the seismic pore pressure generation behaviors of potentially liquefiable soils, (3) post-liquefaction residual strength (S_r) relationships and associated analysis protocols used to implement post-liquefaction behavior modeling in each of the analytical models/frameworks employed, and (4) different analysis protocols with regard to other details of overall analysis implementation.

The four analytical models/frameworks employed in these back-analyses range from (1) a relatively simple cycle-counting and damage accumulation model, through (2) a mid-level complexity hyperbolic/plasticity model, and (3,4) two bounding surface plasticity models. The models employed are (1) the Roth Model (Dawson and Mejia, 2012), (2) UBCSAND (Beaty and Byrne, 2011), (3) PM4Sand (Boulanger and Ziotopoulou, 2015) and (4) Wang2D (Wang and Ma, 2018).

The three sets of soil liquefaction triggering relationships employed are (1) Youd et al. (2001), (2) Boulanger and Idriss (2014) and (3) Cetin et al. (2018).

The three post-liquefaction residual strength (S_r) relationships employed are (1) Seed and Harder (1990), (2) Idriss and Boulanger (2015), and (3) Weber et al. (2015).

The three case histories back-analyzed are (1) the observed response at the Port Island vertical array site during the 1995 Kobe Earthquake (or Great Hanshin Earthquake), (2) the observed performance of the Lower San Fernando Dam (LSFD) which experienced an upstream liquefaction-induced flow failure during the 1971 San Fernando Earthquake, and (3) the observed performance of the nearby Upper San Fernando Dam (USFD) which experienced only moderate liquefaction-induced and inertially-induced seismic deformations during the 1971 San Fernando Earthquake.

The Port Island array site case history was selected because (1) it is an unusually well-instrumented vertical accelerometer array site that was subjected to very strong shaking, (2) significant and widespread liquefaction occurred during the earthquake, (3) observed performance was well documented, and (4) a considerable amount of both geotechnical and geological data is available to facilitate site characterization and modeling. This represents an unusually well-defined one-dimensional site response case history with both (1) suitable available geotechnical data, and (2) available seismic “input” strong ground motion recordings at the actual site.

The unusually well-documented field performance case histories of the Upper and Lower San Fernando Dams during the 1971 San Fernando Earthquake have been foundational to the development of the field of modern seismic dam engineering, and to the inception of the U.S. national seismic dam safety programs ongoing today. It is important to periodically re-assess the strengths of reliability of analytical models and approaches employed in engineering analyses of these types of critical structures. These two performance case histories of the Upper and Lower San Fernando Dams are a particularly

important pair of case histories because, despite some significant common features and characteristics, they each experienced very different, and important, types of observed performance. The Lower San Fernando Dam (LSFD) experienced a liquefaction-induced upstream side flow failure that carried away the crest of the dam, leaving in place only the top of the upstream slide heel scarp to retain the reservoir. The nearby Upper San Fernando Dam (USFD) was built at the same time, as part of the same project, and with similar methods and materials. It also suffered significant seismically induced soil liquefaction, but experienced only limited to moderate deformations and displacements. Successful analytical schemes (combinations of models, relationships, and implementation protocols) would be those which can reasonably accurately and reliably “predict” these two very different sets of behaviors (massive flow failure on the upstream side of the Lower San Fernando Dam, and only moderate deformations and no flow failure for the Upper San Fernando Dam).

These current studies look more closely at comparisons of “predicted” and observed performance than just these two differing types of “macro” behaviors, however, and also examine the accuracy and reliability of the various analyses with regard to finer details such as (1) overall deformation mechanisms for the LSFD, (2) the heel scarp location for the upstream flow failure (slide) of the LSFD (the heel scarp, with allowance for transverse cracking, defined the nearly marginal post-earthquake freeboard available to prevent catastrophic reservoir release immediately after the event), (3) the downstream side deformations and displacements for the LSFD, (4) overall deformation mechanisms for the USFD, and (5) horizontal and vertical deformations at the crest, upper upstream face, downstream face, and downstream toe of the USFD, etc. The over-arching objective of these studies is to examine the capability, accuracy and reliability of the various analysis combinations with regard to predicting all of these types of behaviors and details.

The main objectives of this study included

- Evaluating current State of Practice modeling schemes in seismic deformation analyses of embankment dams, including site characterization, ground motions, liquefaction triggering relationships, post-liquefaction strength relationships, non-liquefiable soil behaviors, constitutive models, volumetric recompression relationships, etc.
- Performing seismic deformation analyses using the finite difference method (FD)-based software FLAC to evaluate performance of different numerical modeling schemes employing different combinations of soil liquefaction triggering relationships, post-liquefaction strength relationships, analytical and constitutive models, and analytical protocols and procedures.
- Identifying the accuracy and reliability of different numerical modeling schemes, and their advantages and limitations, based on comparison of analysis results with the well documented case histories of the Port Island vertical array site in the 1995

Kobe earthquake, and the Upper and Lower San Fernando Dams in the 1971 San Fernando Earthquake.

- Identifying advantages and limitations of continuum-based numerical modeling schemes (Finite Difference Method) in predicting deformations in embankment dams.
- Developing improved analytical approaches to improve performance of numerical modeling schemes for seismic deformation analyses for forward analyses.

A significant number of top experts in the fields of both engineering seismology as well as geotechnical earthquake engineering have assisted and collaborated with these current studies, including developers of a number of the models and relationships employed in some of the analyses performed. This has been an unprecedented effort, with regard to the scope of models and relationships examined, and the breadth and caliber of expertise graciously provided by experts who have contributed their time and insights.

Two different general approaches can be taken in performing the back-analyses of field performance case histories. One approach is to employ existing analysis tools, models, procedures and protocols, as a check, or “test”, of the accuracy and reliability of the analysis schemes employed. An alternate approach is to modify elements of the analysis scheme and/or protocols, either (1) to assess sensitivities to analysis and modeling choices available to the analyst, or (2) to develop improved schemes and protocols for subsequent use in forward applications of seismic deformation analyses.

Both approaches are taken in these current studies.

Lessons learned from back-analyses employing largely “existing” analysis schemes and protocols are used to assess the accuracy and reliability of these existing approaches, and by extension to examine the likely accuracy and reliability of various analyses that have been performed in recent years. That has ramifications with regard to the potential need to re-evaluate a number of existing dams.

Lessons learned are also applied to the development and implementation of improved analysis combinations, schemes and protocols, and these are then tested by means of application to the two dam performance case histories to assess the accuracy and reliability of these modified analysis details and protocols. That has the potential to improve the accuracy and reliability of these types of analyses going forward.

Chapter 2

Concepts, Analytical Models, and Engineering Relationships

2.1 BRIEF DISCUSSION OF KEY SOIL LIQUEFACTION AND POST-LIQUEFACTION CONCEPTS AND BEHAVIORS

Soil liquefaction, and the only slightly narrower topic of seismically-induced soil liquefaction, have been studied by innumerable researchers, and addressed by innumerable engineers in practice. We will not attempt to execute a comprehensive review of previous works on this topic. Instead, Section 2.1 will present a brief set of descriptions and discussions of selected key concepts and principles associated with soil liquefaction.

Sections 2.2 through 2.4 will then present brief descriptions and discussions of: (1) the four analytical and/or constitutive models that will be used for back-analyses of the three performance case histories in these current studies, (2) the three liquefaction triggering relationships that will be used in these current studies to calibrate the four different analytical or constitutive models, and (3) the three post-liquefaction strength relationships that will be used to implement post-liquefaction strengths (S_r) in the back-analyses performed.

Discussions of various analytical approaches and protocols involved in the back-analyses performed as part of these current studies, as well as modeling details, etc., will be discussed in Chapters 3 through 5, as the need arises.

Soil liquefaction will be defined in these current studies as significant reduction of both the strength and stiffness of saturated (and primarily cohesionless) soils due to increases in pore pressures, and resulting diminishment of effective confining stresses.

The engineering analyses performed in these current studies will mainly be concerned with cyclic simple shear types of loading, and so this brief opening discussion will begin with a discussion of liquefaction-related behaviors observed in cyclic simple shear laboratory testing.

Figures 2-1 and 2-2 present laboratory test results of two samples of the same clean sand subjected to cyclic simple shear loading under undrained conditions. Both of these figures are from the cyclic simple shear testing database of Kammerer and Wu (Wu et al., 2003).

Figure 2-1 shows a cyclic simple shear test on a “relatively loose” sample ($D_R \approx 54\%$) with an initial effective vertical stress of $\sigma'_{v,i} = 95\text{kPa}$. This sample was subjected to one-directional (back-and forth in a single lateral direction) cyclic simple shear loading, under undrained conditions, with uniform cyclic loads of $\text{CSR} = 0.20$, where CSR in simple shear is

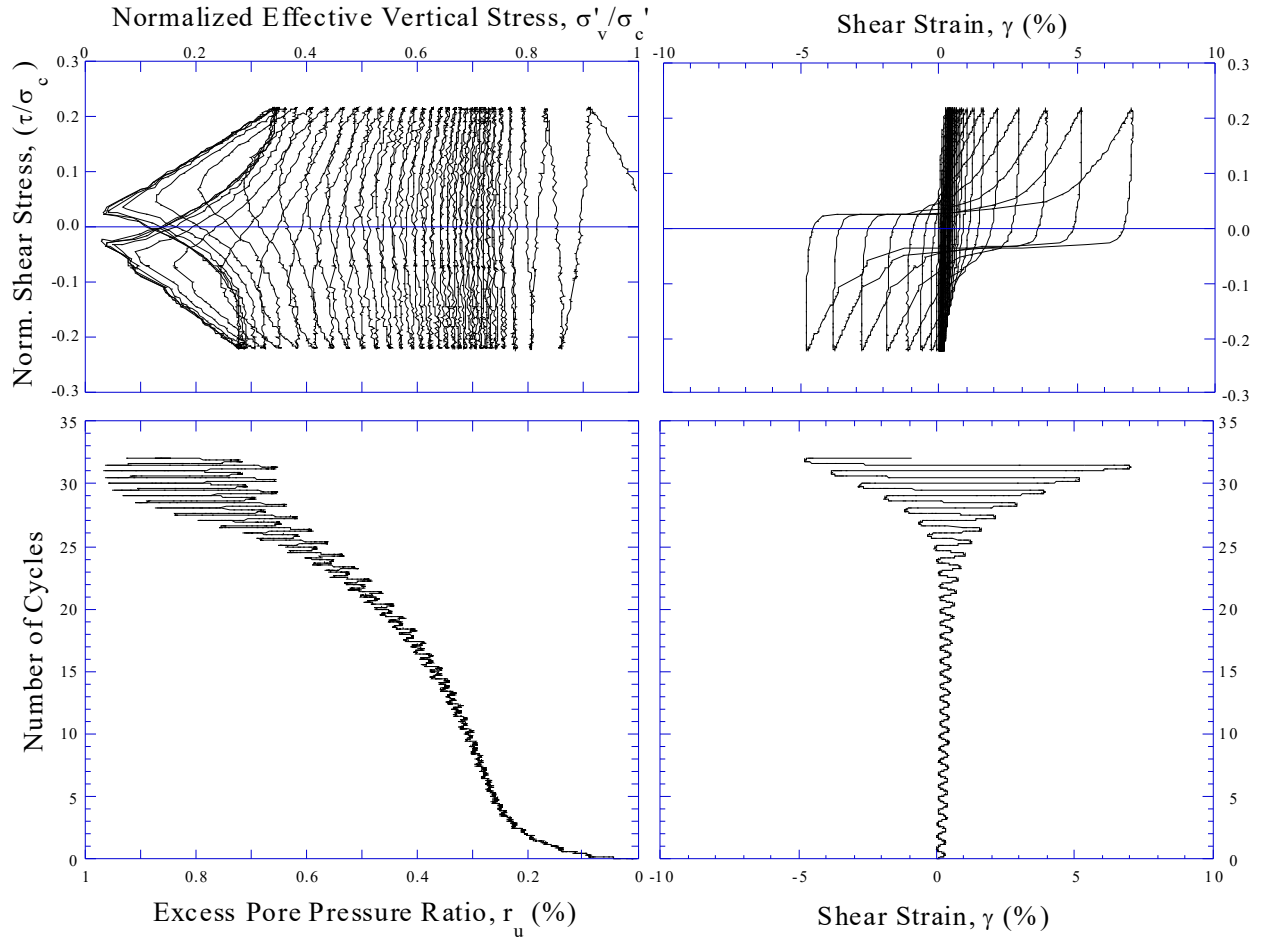


Figure 2-1: Results of a 1-Directional Cyclic Simple Shear Test (#Ms15j) on a sample of a clean sand with $D_r=54\%$, $\sigma'_{v,i}=95\text{kPa}$, and a uniform applied cyclic shear stress ratio of $\text{CSR}=0.20$ (Wu et al., 2003)

defined as

$$\text{CSR (Cyclic Stress Ratio)} = \tau_{\text{hv,cyclic}} / \sigma'_{v,i} \quad \text{Equation 2-1}$$

Each of the four sub-figures shown in Figure 2-1 “maps” onto the two adjacent figures located clockwise and counter-clockwise from themselves, as these adjacent pairs of sub-figures share a common axis.

The bottom left sub-figure shows a plot of seismically-induced cyclic pore pressure generation ($R_{u,\text{seis}}$) which is the ratio of cyclic pore pressure increase divided by the pore pressure increase that would reduce the effective confining stress fully to zero, as

$$R_{u,\text{seis}} = \Delta u_{\text{cyclic}} / \sigma'_{v,i} \quad \text{Equation 2-2}$$

As shown in this sub-figure, pore pressures cyclically increase and decrease during each simple shear loading cycle, but they tend to increase overall as cyclic loading progresses with increasing numbers of cycles.

The sub-figure in the bottom right corner is a plot of cyclic shear strain vs. number of cycles of loading. As shown in this figure, cyclic shear strains increase with additional loading cycles as the pore pressures in the bottom left sub-figure progressively increase (progressively reducing the effective confining stresses, and thus decreasing both strength and stiffness).

The figure in the top left corner sub-figure shows a stress path “type” of plot showing (1) instantaneous vertical effective stress divided by the initial applied effective vertical consolidation stress vs. (2) normalized applied cyclic shear stress on the horizontal plane ($\tau_{hv} / \sigma'_{v,i}$). As shown in this figure, the stress path generally moves towards the origin (zero effective stress), but it does so in a pattern of increase, and then decrease, in pore pressure during each half cycle. Pore pressures decrease during dilation (attempted volumetric expansion of the soil) as particles attempt to move apart in order to move past each other during periods of relatively sustained shear loading, and pore pressures increase mainly immediately after shear stress reversals as densification attempts to occur in the saturated and undrained sample; squeezing the pore fluid. In this sub-figure, pore pressure increases move the stress path towards the left (reducing effective stress), and pore pressure decreases (undrained dilation) move the stress path to the right.

The figure in the top right presents conventional stress-strain plots of (1) applied shear stress vs. resulting current shear strain. Initially the cyclic simple shear loading produces very steep stress-strain behaviors (which are actually very tall and thin “oblate loops”; like tall, skinny and slightly inclined American footballs), but as loading progresses, and the progressive increases in pore pressures both soften and weaken the sample, these change shape and begin to produce shapes sometimes referred to as “banana loops”. In these loops, the sample begins to dilate under sustained simple shear loading shortly after it recrosses the zero strain axis and then it increases in both strength and stiffness as dilation reduces the internal pore pressures. When the shear loading then reverses, the initial behavior is a steep and nearly vertical stress-strain behavior (unloading), with contractive behavior again producing significant pore pressure increases, until the zero shear strain axis is again crossed and then positive sustained simple shear stress loading begins to occur and dilation again occurs; reducing pore pressure and producing associated gains in strength and stiffness. And then the simple shear loading again reverses, and the cycle repeats. Shear stress reversals tend to produce contractive behavior and to cause the most significant increases in pore pressure, and sustained shear loading in a given direction tends to produce dilatant behavior, and to cause pore pressure reduction. Changes in strength and stiffness are the result of pore pressure changes (which produce equal and opposite changes in effective confining stresses).

For this relatively loose sample it is relatively easy to select an approximate point at which “liquefaction” might be judged to have occurred. For conditions with no permanent

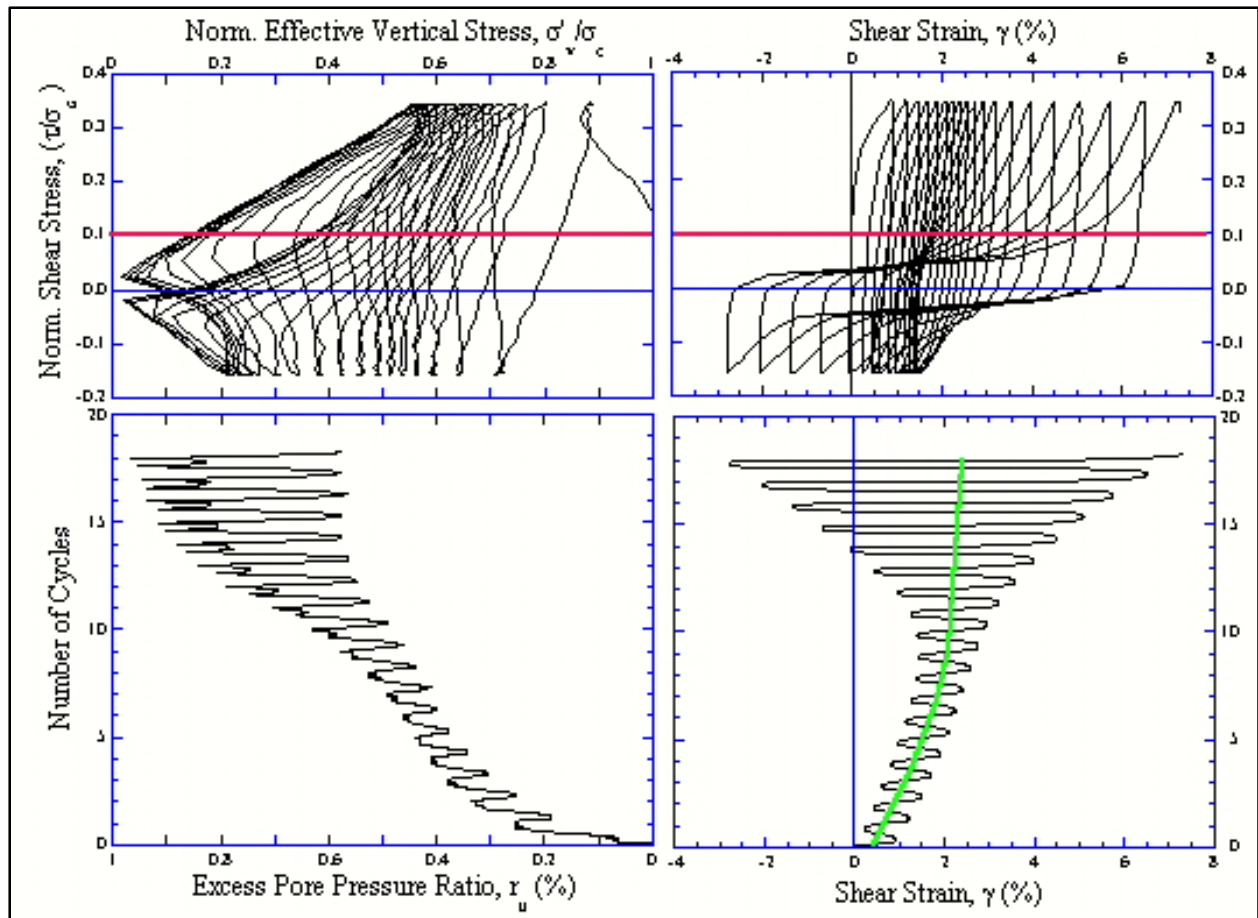


Figure 2-2: Results of a 1-Directional Cyclic Simple Shear Test on a sample of a clean sand with $D_r = 65\%$, $\sigma'_{v,i} = 40$ kPa, $CRR = 0.25$, and $\alpha = 0.10$ (Wu et al., 2003)

initial shear stress bias, this is commonly taken either as the achievement of $R_{u,seis} \approx 1.0$, or the occurrence of $\pm 3.5\%$ double amplitude cyclic simple shear strains, or $\pm 5\%$ double amplitude cyclic shear strains, or similar measures. By either of these strain measures, “liquefaction” would be judged to have occurred at approximately 29 to 30 cycles, but $R_{u,seis}$ fully equal to 1.0 would never quite have been achieved in this soil sample of relatively loose to medium density.

Figure 2-2 shows a similar uni-directional uniform cyclic simple shear test, but this time on a slightly denser sample of the same sand. In this test, there is an initial static stress “bias” (a non-zero driving shear stress that remains in place, as with sloping ground conditions, or an applied foundation load). The red line in the upper two figures indicates this initial (and constant) applied static stress bias, and the uniform cyclic simple shear stresses cycle symmetrically about this initial shear stress. The permanent shear stress bias produces a tendency for the shear stress-strain plot to “walk” in the downslope direction as cyclic loading progresses. This affects all four of the sub-figures in Figure 2-2, but the general principles and characteristic of the behavior shown previously in Figure 2-1 continue to be discernable.

Cyclic simple shear loading with an initial (and permanent) shear stress bias is more complicated to deal with in both simplified engineering analyses, as well as in more complex nonlinear seismic deformation analyses using relatively complex constitutive models that can capture many or even most of the behavioral characteristic illustrated in these two cyclic simple shear tests.

And it is cyclic simple shear loading with initial static stress bias that it of principal engineering interest and concern. A level site (with no slope, and no applied building loads, etc.) has no initial and permanent shear stress bias (no “driving shear stress”), and such cases are not usually of much engineering concern. Instead engineers tend to be concerned with slopes, dams, levees, building foundations, etc. All of these involve a gravity-driven initial static stress “push”, or stress bias.

In addition, earthquakes do not tend to produce uniform cyclic loading. Instead loading cycles during an earthquake are highly variable and irregular. As a result, (1) “simplified” analytical methods must make suitable approximations in order to simplify this chaotic loading, and (2) more complex and advanced analytical models for fully nonlinear seismic deformation analyses must suitably model a sufficient amount of this overall complexity as to achieve a useful and suitably reliable engineering result.

All of the cyclic loading behaviors discussed above conform to the principles of Critical State Soil Mechanics, and engineers engaging in liquefaction-related works should be suitably well versed in these fundamental principles of soil mechanics.

It is often traditional at this juncture to enter into a long discussion and exposition of either the history and/or selected details of soil liquefaction behaviors. But such discussions are necessarily incomplete, and readers who have arrived here should already be reasonably well versed in these issues, behaviors, and their underlying principles and causes; including critical state soil mechanics.

Some useful primers here would include Kramer (1996), Ishihara (1996), Schofield and Wroth (1968), etc.

Engineers and/or researchers engaging in works targeting seismically-induced soil liquefaction issues and effects should also have a useful background in (1) earthquakes and seismology, as earthquakes are an important element of the overall problem, and (2) in soil dynamics, as evaluation of dynamic response to (cyclic and irregular) seismic loading is important.

And they should also have a good and well-rounded background in soil mechanics. There can be a tendency to overly focus on cyclic behaviors of potentially liquefiable (and generally cohesionless) soils. But it is important to also understand and to deal suitably with the behaviors of other geo-materials. In these case-history based studies, for example, the behaviors of cohesive, clayey soils are important, and so is suitable treatment of (1) cyclic softening, and (2) strain softening, of moderately sensitive clays. Geology, seepage and flow, and fundamentals of hydraulics and physics also matter.

2.2 BRIEF DISCUSSION OF THE FOUR ANALYTICAL AND/OR CONSTITUTIVE MODELS USED IN THESE CURRENT STUDIES

The four analytical and/or constitutive models that will be used in the nonlinear seismic deformation analyses (back-analyses) performed in these current studies are (1) the Roth model, (2) the UBCSAND model, (3) the PM4Sand model, and (4) the Wang2D model. There are a large number of analytical and/or constitutive models available that can be used for nonlinear seismic deformation analyses for problems involving potentially liquefiable soils, and these four were selected (1) to provide a wide range of complexity levels and characteristics, and (2) based on their history of relatively widespread use in seismic analyses of dams. Some of these models have significant histories of engineering usage, especially with regard to seismic dam engineering, and some of them have evolved over a number of years to their current forms. Some of them have been through name changes and/or changes in how they are referenced over their years of engineering application.

2.2.1 The Roth Model

The Roth model (also known as the Dames and Moore/URS model) is a practice-oriented model initially developed by Wolfgang Roth at Dames and Moore in 1980's. It was developed for dynamic analyses of Pleasant Valley Dam in California for the Los Angeles Department of Water and Power (Dames and Moore, 1985; Roth et al. 1991). Ethan Dawson and Wolfgang Roth summarized model approaches in the second international FLAC symposium in 1999 (Dawson et al., 2001). The Roth model was later modified by Ethan Dawson and Lelio Mejia in 2012 (Dawson and Mejia, 2012). This model is known as a practice-oriented pore water pressure generation model, or practice-oriented liquefaction model, because it incorporates empirical cyclic pore water pressure generation, liquefaction triggering, and post-liquefaction strength relationships in a simple sequential manner. The Roth model has been utilized in nonlinear dynamic deformation analyses of a significant number of dams (e.g. Inel et al. 1993, Bureau et al. 1996, Dawson et al. 2001, etc).

The Roth model is the oldest, and the simplest, of the four analytical models used in these current studies. Each of the four models has their own sets of advantages relative to the other three. For the Roth model, these include (1) it is the simplest model, and it is easy to parameterize, (2) it is the only one of the four models that can be parameterized to exactly match (a) a selected liquefaction triggering relationship, (b) a selected K_σ relationship, and (c) a K_α relationship, and (3) it is the only one of the four models that currently transitions to post-liquefaction strength (S_r) incrementally, element by element, as any given element achieves either of two criteria for transition to S_r during shaking. The other three models currently transition to S_r only after stoppage of the analysis (usually at the end of strong shaking) and then assignment of S_r to elements judged to meet the user's selected criteria.

The Roth model is a Mohr-Coulomb (linearly elastic and perfectly plastic) soil model coupled with an empirical pore pressure generation scheme. The basic approach of the Roth model has been summarized in the available FLAC FISH function as below:

This model is built around the standard FLAC Mohr-Coulomb model. The model counts shear stress cycles by tracking the shear stress acting on horizontal planes (σ_{xy}) and looking for stress reversals. The cyclic stress ratio (CSR) of each cycle is measured and this is used to compute the incremental “damage” which is translated into an increment of excess pore pressure.

Based on Dawson et al. (2001) and Dawson and Mejia (2012), the Roth model analytical steps can be summarized as below:

(a) The Cyclic Stress Approach and Pore Pressure Generation Model

The Roth model uses a simplified cyclic stress approach, originally developed by Seed and Idriss (1971) for use in developing liquefaction triggering relationships. This is illustrated schematically in Figure 2-3.

In this cyclic-stress approach, the cyclic pore pressure generation within a soil element is a function of the number and amplitude of shear stress cycles experienced during shaking. Shear stress cycles are measured in terms of the cyclic stress ratio (CSR), which is the ratio of cyclic shear stress on a horizontal plane (τ_{cy}) to initial vertical effective stress, $\sigma'_{v,i}$ as

$$CSR = \tau_{hv,cy} / \sigma'_{v,i} \quad (= \tau_{cy} / \sigma'_v \text{ in Figure 2-3}) \quad [\text{Equation 2-3}]$$

The shear stress time history of each element is monitored in each potentially liquefiable element, and shear stress cycles are counted in “half cycles”. Each half cycle varies in size at any point of earthquake loading because seismic loading pulses vary randomly and chaotically. The size of a half cycle is determined at the end of the half cycle, and the end of a half cycle is defined when a reversal of the direction of cyclic (not initial or permanent) shear stress loading on a horizontal plane reverses direction. The model monitors the shear stress on horizontal planes, σ_{xy} rather than a shear stress invariant. As soon as the end of a half of a stress cycle is detected, the excess pore pressure is incremented by an amount dependent on the cyclic stress ratio amplitude of that half cycle (see Figure 2-3). The generated increment of excess pore pressure, u_e is described in terms of the increase in the seismic (cyclic) pore pressure ratio ($r_{u,seis}$) that would be required to reduce effective confining stress fully to zero as

$$r_{u,seis} = u_e / \sigma'_{v,i} \quad [\text{Equation 2-4}]$$

The liquefaction resistance of a soil is described by a cyclic strength curve, which is developed as a function of the number of (full) uniform cycles required for liquefaction to occur at a specific uniform cyclic stress ratio. Seed et al. (1975) developed this uniform cycle approach. The cyclic strength curves in the Roth model use the following functional form:

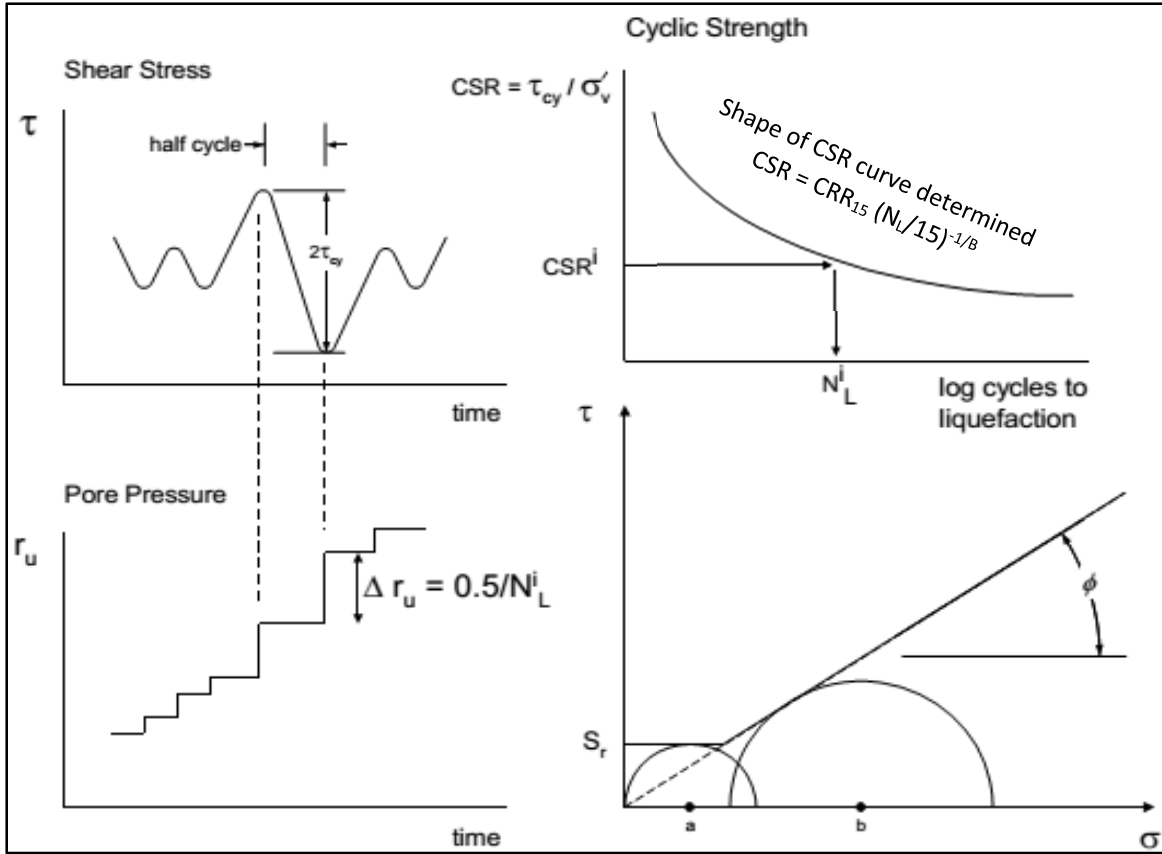


Figure 2-3: Pore pressure generation procedure, cyclic strength curve, and shear strength for the Roth Model (weighted half cycle)
(Dawson and Mejia, 2012)

$$CSR = CRR_{15} (N_L/15)^{-1/b} \quad [\text{Equation 2-5}]$$

where CRR_{15} is the cyclic stress ratio required to just produce liquefaction in 15 cycles (corresponding to an earthquake magnitude of $M_w = 7.5$). The parameter $B (=1/b)$ is a constant controlling the overall shape of the cyclic strength curve. CRR_{15} values in this study were developed using each of the three different liquefaction triggering relationships: Youd et al. (2001), Boulanger and Idriss (2014), and Cetin et al. (2018). The corresponding B values are developed using the correction factor for magnitude duration, K_{Mw} , also known as the magnitude (or magnitude-correlated duration) scaling factor. The Roth model also allows for directly employing correction factors for overburden stress, K_σ (for initial effective stress greater than 1 atmosphere) and for initial static shear stress bias (K_α), as per user-employed relationships.

From the cyclic strength curve, if N_L^i uniform cycles are required for complete liquefaction triggering ($r_u = 1.0$ or 0.98) at a cyclic stress ratio, CSR^i , then the increment in pore pressure Δr_u^i for a half cycle is

$$\Delta r_u^i = 0.5 / N_L^i \quad [\text{Equation 2-6}]$$

and the increment in pore pressure, Δu_e is then

$$\Delta u_e^i = \Delta r_u^i \sigma'_v \quad [\text{Equation 2-7}]$$

The effect of increasing the pore pressure is to decrease the effective stress, and thus, to decrease the shear strength. As an optional feature in the Roth model, the elastic shear modulus can be reduced as pore pressure increases, as per

$$G = G_{initial} \sqrt{(1 - r_u)} \quad [\text{Equation 2-8}]$$

However, even if the shear modulus is not reduced, decreasing the effective shear strength changes the resulting secant modulus and damping ratio for plastic stress-strain loops.

(b) Post-Liquefaction Residual Strength

The Roth model incorporates a two-segment failure envelope (Figure 2-3) consisting of (1) a Mohr-Coulomb strength envelope to be used for initial stress condition up to liquefaction triggering state and (2) a post-liquefaction strength envelope to be used from onset of liquefaction to end of seismic shaking. The post-liquefaction strength envelopes for this study have been developed using each of the three different post-liquefaction (S_r) relationships employed in these current studies.

The advantages of Roth model include (1) simplicity of the modeling scheme, (2) flexibility to use any liquefaction triggering and post-liquefaction strength relationships, (3) direct implementation of K_σ and K_α relationships, and with perfect precision, rather than by validating through approximate calibration, (4) much faster computational speed than the other three nonlinear models, and (5) an ability to transition to S_r during shaking based on user-specified criteria for S_r transition. Disadvantages include (1) this method does not model dilation behavior directly, as the pore pressure development follows a simplified relationship, and as a result pore pressure development rate is tends to be a bit faster than the other analytical models, and (2) the current model appears to slightly conservatively over-predict crest loss, which is generally taken as compensating for a current lack of well-vetted approaches for computation of post-earthquake volumetric recompression settlements.

2.2.2 The UBCSAND Model

The UBCSAND model (Beaty, 2001, Beaty and Byrne, 2011) is a widely used soil constitutive model for dynamic analyses of liquefiable soils, and it has been applied to a significant number of seismic deformation analyses for dams. The most recent version of UBCSAND is 904aR, which was developed by modifying the original version (904a) during work on Success Dam for the USACE in California (Beaty and Byrne, 2011). During the

Success Dam work, the performance of UBCSAND was compared with the results from the Roth model, and the overall behavior of the UBCSAND model was examined and reviewed by the USACE Sacramento District, including Dr. Vlad Perlea. It is this most recent version that was used in these current studies. The backup documentation for UBCSAND is one of the best documents among the four constitutive models that have been evaluated during this current study, and the interactive reviews by the USACE led to good verification of the suitability of the modeling of the Youd et al. (2001) liquefaction triggering relationship and K_σ relationship, as well as the Idriss and Boulanger (2001) K_α relationship. Beaty and Byrne (2011) provided details of changes made to the updates from a previous version of UBCSAND (version 904a), and provided calibration results to show effects of modeling schemes on parameters such as CSR, K_σ , K_α , etc. They also discussed approaches for use of post-liquefaction strength, and validated the updated model by using an appropriate case history (the Upper San Fernando Dam).

UBCSAND is a two-dimensional effective stress plasticity model for use in analyzing geotechnical structures such as earthen dams. The following is a summary of the UBCSAND model based on Beaty and Byrne (2011).

The elastic component of response is assumed to be isotropic and specified by a shear modulus, G^e , and bulk modulus, B^e , as follows:

$$K^e = K_G^e P_a \left(\frac{\sigma'}{P_a} \right)^{ne} \quad [\text{Equation 2-9}]$$

and $B^e = \alpha G^e \quad [\text{Equation 2-10}]$

where,

- K_G^e is a shear modulus number that depends on the relative density and varies from about 500 for loose sand to 2000 for dense sand.
- P_a is atmospheric pressure in chosen units
- σ' is the mean stress in the plane of loading equal to $(\sigma'_x + \sigma'_y)/2$
- ne varies between 0.4 and 0.6, or approximately 0.5
- α depends on the elastic Poisson's ratio, which is generally in the range of approximately 0.0 to 0.2 (Hardin, 1978), with the result that α varies between 2/3 and 4/3, or is taken as approximately unity.

Plastic strains are controlled by the yield surface and flow rule. The yield surface is represented by a radial line from the origin in stress space, as shown on Figure 2-4. For the first time shear loading, the yield surface is controlled by the current stress state (Point A in Figure 2-4). As the shear increases, the shear stress ratio $\eta (= \tau/\sigma')$ increases and causes the stress point to move to Point B. τ and σ' are the shear and normal effective stresses on the plane of maximum shear stress. The yield surface is dragged to the new location passing through Point B and the origin. This results in plastic strains, both shear and volumetric. The plastic strain increment, $d\gamma^p$, is related to the change in shear stress ratio, $d\eta$, in a

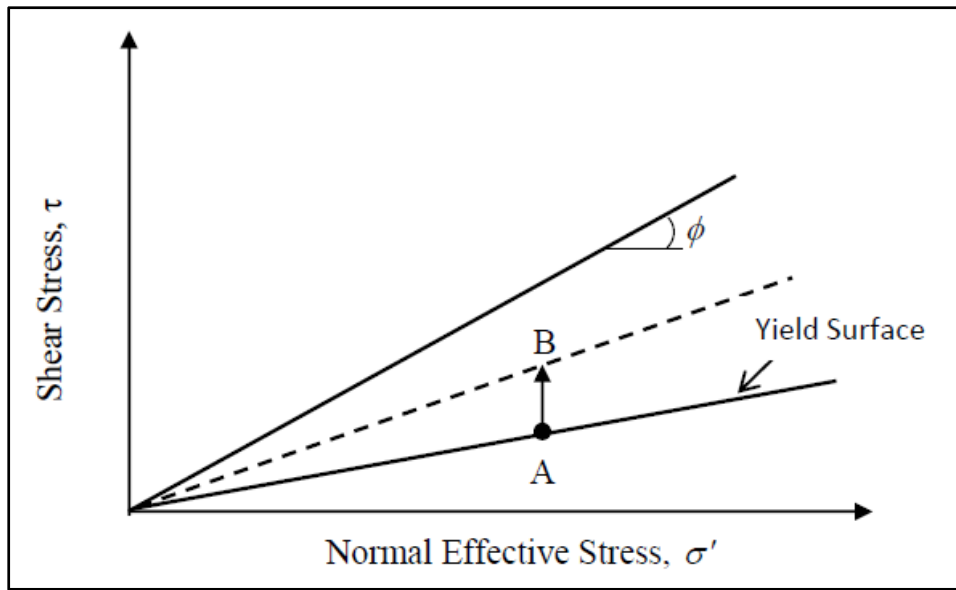


Figure 2-4: Yield surface in UBCSAND (Beatty and Byrne, 2011)

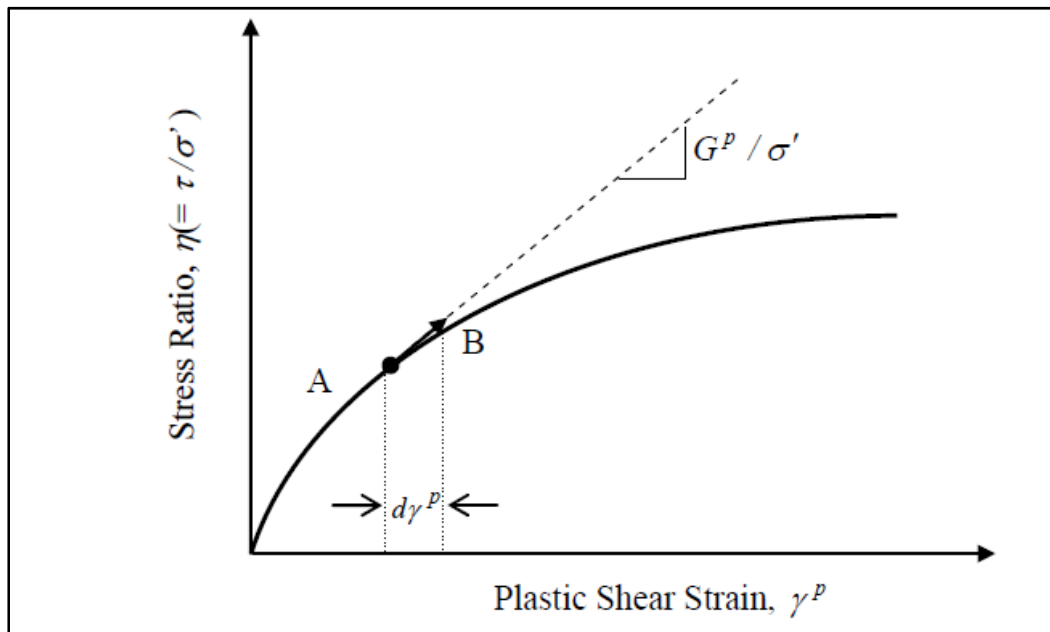


Figure 2-5: Plastic strain increment and plastic modulus in UBCSAND (Beatty and Byrne, 2011)

hyperbolic form (similar to Duncan and Chang, 1970), as shown in Figure 2-5 and can be expressed as

$$d\gamma^p = \frac{1}{G^p/\sigma'} d\eta \quad [\text{Equation 2-11}]$$

where G^p is the plastic shear modulus, and this can be obtained by

$$G^p = G_i^p \left(1 - \frac{n}{n_f} R_f\right)^2 \quad [\text{Equation 2-12}]$$

where

- G_i^p is the plastic modulus at a low level of stress ratio ($\eta = 0$)
- n_f is the stress ratio at failure and equals $\sin\phi_f$
- ϕ_f is the peak friction angle
- R_f is the failure ration used to truncate the best fit hyperbolic relationship and prevent the overprediction of strength at failure. R_f generally varies between 0.7 and 0.98 and decreases with increasing relative density

The associated increment of plastic volumetric strain, ε_v^p , is related to the increment of plastic shear strain, $d\gamma^p$, through the flow rule

$$d\varepsilon_v^p = \left(\sin\phi_{cv} - \frac{\tau}{\sigma'}\right) d\gamma^p \quad [\text{Equation 2-13}]$$

where ϕ_{cv} is the constant volume friction angle or phase transformation angle. This flow rule can be derived from energy considerations and is similar to stress dilation theory (Rowe 1962, Matsuoka and Nakai, 1977).

Yield loci and the corresponding direction of the plastic shear strains resulting from the flow rule are shown in Figure 2-5. Significant shear-induced plastic compaction occurs at low stress ratios, while no compaction is predicted at stress ratios corresponding to ϕ_{cv} . At stress ratios greater than ϕ_{cv} , shear induced plastic expansion or dilation is predicted. This simple flow rule is in good agreement with the characteristic behavior of sand observed in laboratory element testing.

Table 2-1 presents default parameters and equations that are utilized in this current study when UBCSAND is employed to model behavior of potentially liquefiable soils.

Table 2-1: Default parameters and equations used in UBCSAND analyses

Parameter	Equations and Generic Values in UBCSAND (adopted for this study also)
Elastic Shear Modulus	$G_{tangent} = K_{ge} P_{atm} \left(\frac{\sigma'_m}{P_{atm}} \right)^{n_e} \left(1 - R_f \frac{\tau}{\tau_{failure}} \right)$ $n_e = 0.5$ $K_{ge} = 21.7 * K_{2max}$ $K_{2max} = 20 * N_{1,60,CS}^{0.33}$ $R_f = 1.1 (N_{1,60,CS})^{-0.15}$
Elastic Bulk Modulus	$B = K_b * P_{atm} * \left(\frac{\sigma'_m}{P_a} \right)^{m_e}$ $K_b = 0.7 * K_{ge}$
Friction Angle	<p>Constant Volume Friction Angle</p> $\phi_{cv} = 33^\circ$ $\phi' = \phi_{cv} + \left(N_{1,60,CS} / 10 \right)$ <p>Peak Friction Angle</p> $\phi_f = \phi' + \max[0, (N_{1,60,CS} - 15) / 15]$
Plastic Shear Modulus Number	$K_{gp} = K_{ge} * (N_{1,60,CS})^2 * 0.003 + 100$

The model predicts the shear stress-strain behavior of the soil using an assumed hyperbolic relationship, and estimates the associated volumetric response (and pore pressure response) of the soil skeleton using a flow rule that is a function of the current stress ratio, η . The model can be used in a fully coupled fashion where the mechanical and groundwater flow calculations can be performed simultaneously.

In UBCSAND 904aR documentation (Beatty and Byrne, 2011), a set of input parameters have been developed to represent the response of a hypothetical generic sand. These parameters provide reasonable estimates of stiffness and capture the liquefaction response in terms of the cyclic resistance ratio (CRR) as per the liquefaction triggering relationship of Youd et al. (2001), the effect of overburden stress on liquefaction as captured by the K_σ factor of Youd et al. (2001), and interpretation of the effects of initial static shear stress bias (K_α) as per Idriss and Boulanger (2003).

2.2.3 The PM4Sand Model

PM4Sand (version 3) (Boulanger and Ziotopolou, 2015) is another of the plasticity models that was utilized in this study. The user manual of PM4Sand (Boulanger and Ziotopolou, 2015) describes that the model follows the basic framework of the stress-ratio

controlled, critical state compatible, bounding surface plasticity model for sand initially presented by Manzari and Dafalias (1997) and later extended by Dafalias and Manzari (2004). PM4Sand represents an update and re-parameterization of that model.

PM4Sand uses a critical state line developed using Bolton's (1986) dilatancy relationship with $Q=10$ and $R=1$ (values suggested by Bolton for quartz sand). The critical state concept in PM4Sand utilizes the relative state parameter index (ξ_R), as presented by Boulanger (2003). Boulanger and Ziotopolou suggest that the relative state parameter "index" is the relative state parameter defined using an empirical relationship for the critical state line. The critical state line in PM4Sand is a constant line, and is not varied for different coarse-grained (cohesionless) soils. The initial state of the soil with respect to the critical state line is determined using the relative state parameter index (ξ_R). Figure 2-6 shows the definition of the relative state parameter index (ξ_R) in relation with critical state line based on Bolton's (1986) I_{RD} relationship for $Q=10$ and $R=1$. Boulanger and Ziotopolou (2015) utilizes $C_d = 46$ as a default value to compute relative density as $[D_r = \sqrt{N_{1,60,CS}/C_d}]$, a value consistent with the liquefaction triggering relationship of Boulanger and Idriss (2014). Chapter 4 of this dissertation includes a discussion of details regarding C_d values for different soil types.

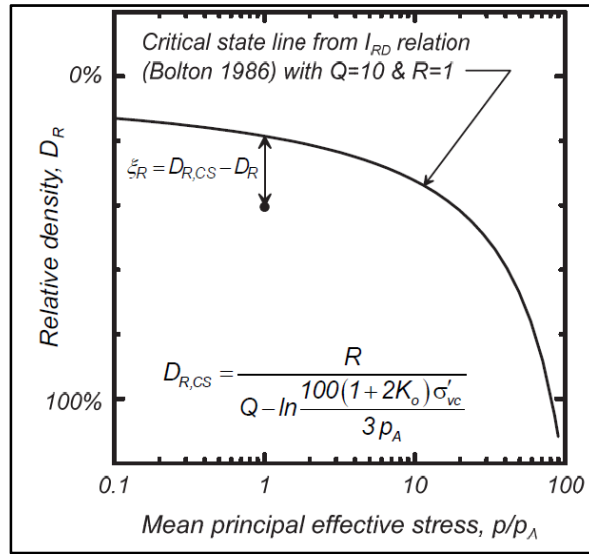


Figure 2-6: Definition of the relative state parameter index, (ξ_R) (Boulanger, 2003) in relation to the critical state line from Bolton (1986) I_{RD} relation with $Q=10$ and $R=1$.

The PM4Sand model incorporates bounding, dilatancy, and critical state surfaces following the form of Dafalias and Manzari (2004). A schematic of the yield, critical, dilatancy, and bounding lines in q - p space, as per Dafalias and Manzari (2004) is shown in Figure 2-7. The bounding, critical, and dilatancy ratios are determined using the following relationships:

$$M^b = M \exp(-n^b \xi_R) \quad [\text{Equation 2-14}]$$

$$M = 2 \sin(\Phi_{cv}) \quad [\text{Equation 2-15}]$$

$$M^d = M \exp(-n^d \xi_R) \quad [\text{Equation 2-16}]$$

PM4Sand utilizes default values of $n^b = 0.5$ (for loose or critical state, $n^b/4$), $n^d = 0.1$ (for loose or critical state, $4n^d$), and $\Phi_{cv} = 33^\circ$. Li and Dafalias (2000) and Dafalias and Manzari (2004) used $n^b = 1.1$ and $n^d = 3.5$ for calibration of their plasticity models to simulate drained and undrained behaviors of Toyoura sand, as tested by Verdugo (1992) and Verdugo and Ishihara (1996).

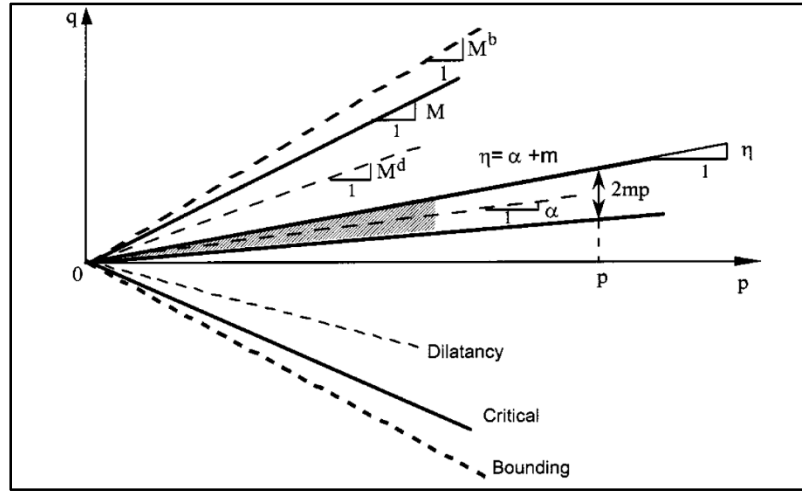


Figure 2-7: Schematic of the yield, critical, dilatancy, and bounding lines in q-p space (Dafalias and Manzari, 2004)

PM4Sand incorporates five primary parameters and eighteen secondary parameters. The PM4Sand developers encourage that the user input should be on primary parameters, and that the default secondary parameters should be considered for design projects, unless site specific data are available. The primary parameters include relative density (D_r), shear modulus coefficient (G_0), contraction rate parameters (h_{po}), and atmospheric pressure (P_a). The contraction rate parameter is developed using a single element direct simple shear (DSS) simulation (Boulanger and Ziotopolou, 2015), which utilizes D_r , $N_{1,60,cs}$, G_0 , and CRR to simulate liquefaction triggering at different criteria (e.g. 98% excess pore pressure ratio, or 3% shear strain, or other criteria at the user's discretion).

PM4Sand Version 3 introduced a new option to estimate post-shaking reconsolidation, commonly known as volumetric strain. This sub-routine reportedly estimates post-shaking reconsolidation strains that match well with values estimated by Ishihara and Yoshimine (1992) (Boulanger and Ziotopolou, 2015). In this current dissertation, no post-earthquake volumetric reconsolidation analyses are performed. The volumetric strain computation should be considered after application of the post-liquefaction strength in the liquefied elements in the post-earthquake stage.

Figures 2-8 through 2-10 show examples of undrained cyclic loading response in the PM4Sand model for loose to dense sands ($D_r = 35, 55, \text{ and } 75$ percent respectively) with initial vertical effective consolidation stress of 1 atmosphere, and with initial static stress ratios of $\alpha = 0, 0.1, \text{ and } 0.2$. The cyclic stress ratio analytically applied is 0.1 in Figure 2-8, 0.15 in Figure 2-9 and 0.3 in Figure 2-10.

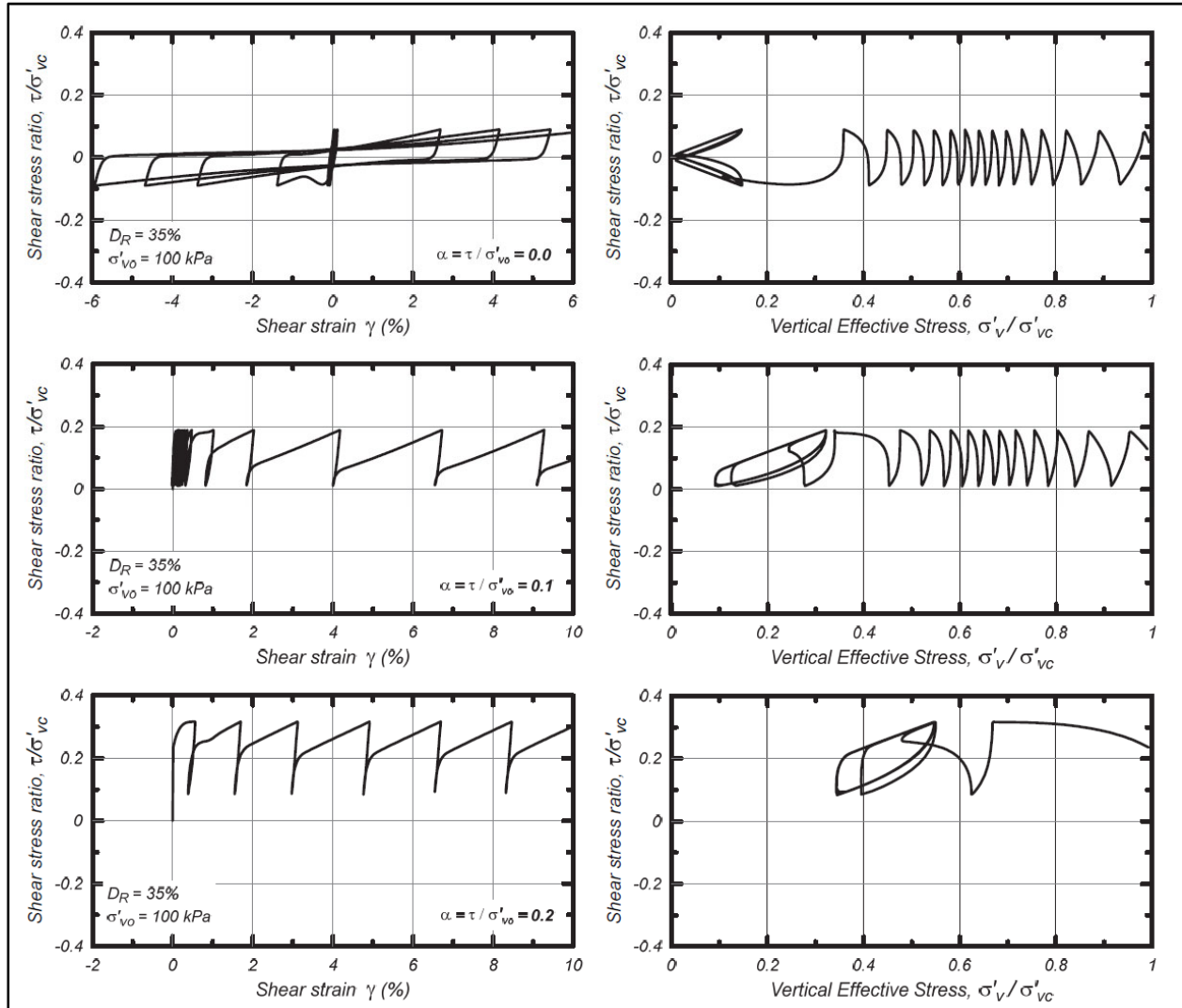


Figure 2-8: Undrained cyclic DSS loading response in PM4Sand for $D_r = 35\%$ with vertical effective consolidation stress of 1 atmosphere and with initial static shear stress ratios of 0.0, 0.1, and 0.2 (Boulanger and Ziotopolou, 2015).

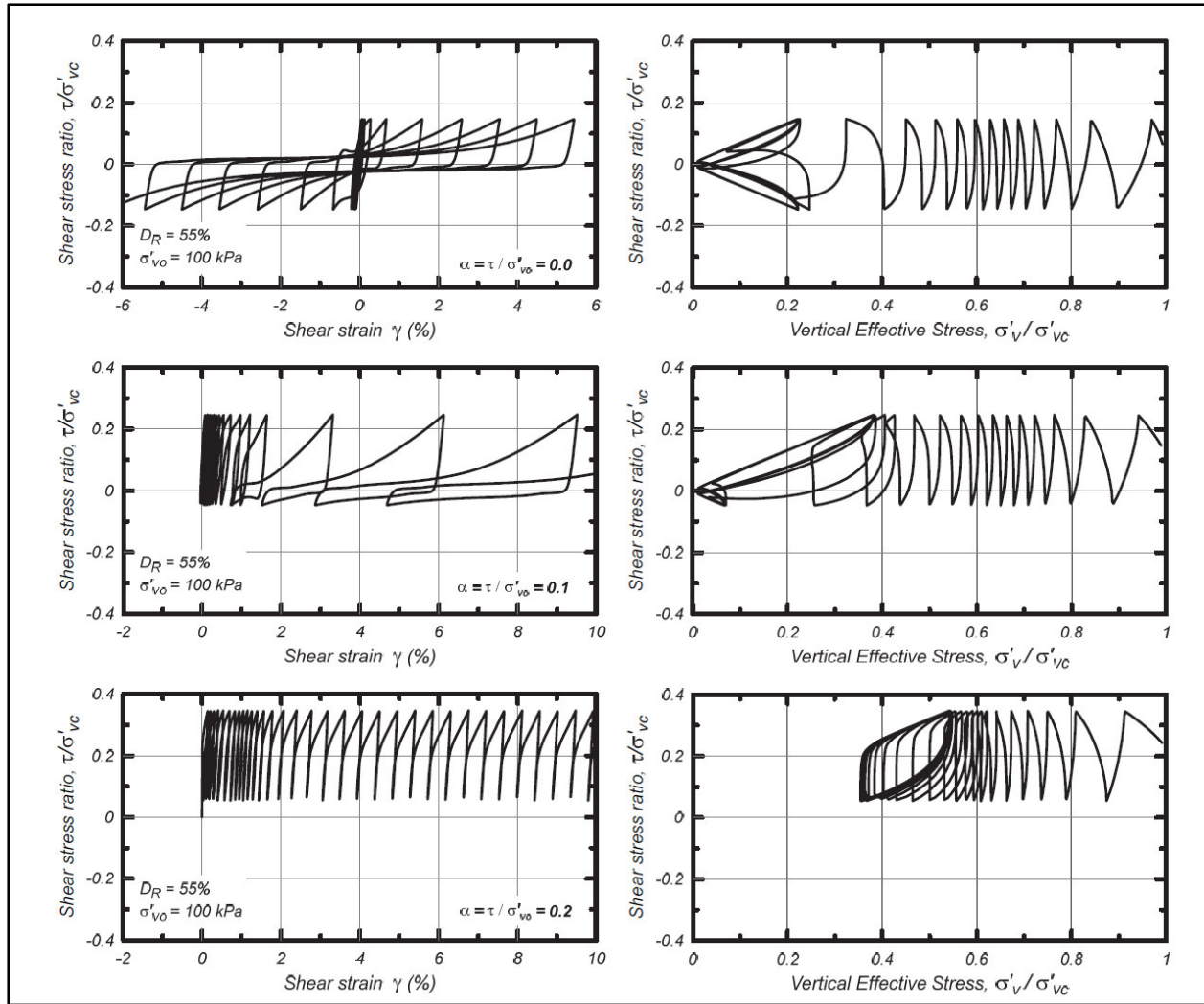


Figure 2-9: Undrained cyclic DSS loading response in PM4Sand for $D_r=55\%$ with vertical effective initial consolidation stress of 1 atmosphere and with initial static shear stress ratios of 0.0, 0.1, and 0.2 (Boulanger and Ziotopolou, 2015).

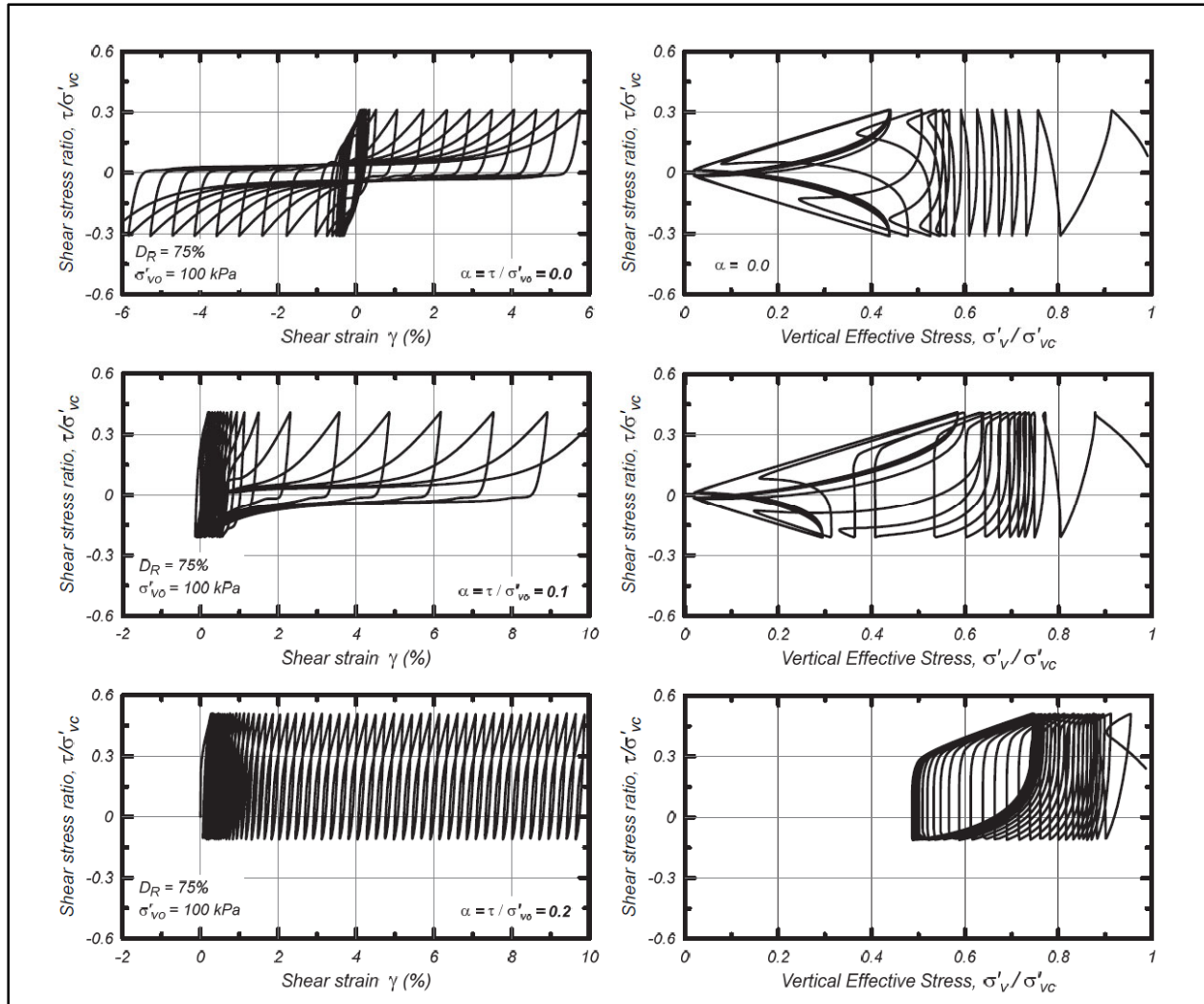


Figure 2-10: Undrained cyclic DSS loading response in PM4Sand for $D_r=75\%$ with vertical effective consolidation stress of 1 atmosphere and with initial static shear stress ratios of 0.0, 0.1, and 0.2 (Boulanger and Ziotopolou, 2015).

2.2.4 The Wang2D Model

Wang (1990) developed a fully three-dimensional bounding surface hypoplasticity model for modeling cyclic liquefaction behaviors of cohesionless soils under the supervision of Professor Dafalias at the University of California, Davis. Wang (1990) and Wang et al. (2002) suggest that one of the distinctive features of this model is the dependence of the loading and plastic strain rate directions on the stress rate direction. The model can simulate different features of sand behavior under different loading conditions, which range from simple monotonic to complex cyclic loadings at different amplitudes and directions. The ability to successfully model response under “rotational shear” is another of the distinctive properties of the model, and this is mainly due to its hypoplastic character. This model is particularly useful in predicting liquefaction, which may occur under complex cyclic

loading conditions, entailing cyclic changes of both principal stress values and principal stress directions.

This fully three-dimensional model performed impressively in performing 3-D back-analyses of the (well-recorded) site response of the Port Island vertical strong motion array site in the 1995 Kobe earthquake, producing some of the best matches achieved to date (of the many back-analyses performed) with the recorded strong motion records obtained during that event in which significant liquefaction occurred in the upper fill soils (Wang et al., 2001).

The Wang2D model is a two-dimensional version of the original three-dimensional model. Wang et al. (2000) updated the model to incorporate a dependency on the state pressure index (I_p), and to establish conformity with the critical-state concept. The modifications included (1) the constant phase transformation stress ratio in the stress space was modified to be a function of the state pressure index, and (2) the constant failure ratio in the stress space was changed to a variable virtual peak stress ratio, which also is a function of the state pressure index. Wang et al. (2000) performed numerical simulations to compare the results with undrained and drained triaxial tests performed by Verdugo (1992) and Verdugo and Ishihara (1996).

Wang and Ma (2018) updated the Wang (2002) model by further calibrating the model to match the large cyclic simple shear laboratory testing database developed by Kammerer and Wu (Wu et al., 2003).

The updated version of the Wang (2000) model, as developed by Wang and Ma (2018) is available in the Itasca-UDM site. In this current study, this updated Wang model is used and identified as the Wang2D model.

Both the PM4Sand and Wang2D models share a number of common attributes and capabilities, which is not surprising as both are from the family of analytical models developed by students of Prof. Yannis Dafalias. There are some differences, but both models appear to be able to provide good modeling capabilities for undrained cyclic loading (seismic loading) of potentially liquefiable cohesionless soils. The Wang2D model has an arguable slight advantage with regard to the treatment of the out of plane normal stress, owing to its fully three-dimensional background, but this can be largely equaled out by proper calibration against laboratory test data. The Wang2D model also benefits from calibration against the laboratory data sets of Kammerer and Wu (Wu et al., 2003). As a result, Wang and Ma (2018) correctly note some advantages with regard to details of the modeling of pore pressure development upon shear stress reversal. In the end, however, both models have good “bones”; they have good forms, good basis in mechanics, and good ability to be calibrated to the types of liquefaction behaviors of engineering interest with respect to seismic analyses of dams. However, Wang2D provides more flexibility to users regarding use of liquefaction triggering and other input parameters. In the end, assessment of the usefulness and reliability of these two models as engineering tools is best based on back-analyses of well-documented and meaningful case histories.

2.3 LIQUEFACTION TRIGGERING RELATIONSHIPS

2.3.1 Introduction and Overview

Each of the four analytical or constitutive models discussed in the previous section must be calibrated to match expected behaviors with regard to cyclic pore pressure generation under non-uniform (irregular) seismic loadings. The basis for this calibration is the use of empirical soil liquefaction triggering relationships.

There have been excellent advances in laboratory testing capabilities over the past several decades with regard to cyclic triaxial, cyclic simple shear and cyclic torsional shear testing, and the data produced serves usefully to inform and calibrate development of analytical and/or constitutive models such as the four models discussed in Section 2.2.

But project-specific parameterization of these types of analytical models is currently best based on empirical liquefaction triggering relationships developed by field forensic investigations of sites that did, and did not, liquefy during earthquakes. These types of liquefaction triggering evaluations for purposes of development of liquefaction triggering relationships are generally performed for level sites with no static driving shear stress bias ($K_\alpha = 0$ conditions).

In situ tests are generally used to evaluate the ground conditions in the forensic back-analyses for development, and it is assumed that the same types of in situ tests will be used to calibrate and parameterize forward engineering analyses.

There are five principal factors that significantly affect the liquefaction triggering resistance of a saturated cohesionless soil, and these are listed in Table 2-2 (Seed et al., 2003). As indicated in the table, the most important of these is relative density, or density relative to critical state. But each of the other four factors can also have a potentially non-negligible effect on soil liquefaction resistance. The more “violence” a soil deposit (or engineered fill), the greater its liquefaction resistance will be at the same relative density. As overconsolidation (or overconsolidation ratio, OCR) increases the lateral earth pressure coefficient (K_0) increases, increasing the mean effective confining stress, and the soil becomes somewhat stiffer (at the same given relative density; and so cyclic shear strains and associated cyclic pore pressure generation behaviors are slightly to somewhat diminished). As soils age in place under overburden pressures, resistance to soil liquefaction improves. The mechanism for this is still somewhat under debate, but it is thought to be due to (1) micro-cementation or particle contact bonding, or (2) micro-creep rearrangement of particles seeking a slightly more stable configuration without noticeable overall volume reduction. Prior cyclic history, or “a history of violence”, can also measurably increase resistance to subsequent cyclic pore pressure generation; so long as the soil suffers cyclic pore pressure increases of less $R_{u,seis}$ less than about 0.7 or so. If full liquefaction occurs, the soils may be fully disturbed, and all beneficial effects of factors 1 through 5 may be “erased”.

Table 2-2: Five Principal Factors Affecting Liquefaction Resistance

Factor	SPT (N-Value)	CPT (q_c)	V_s	Affected by Sampling, Set-Up, and/or Lab Reconsol.
1. "Density" (\uparrow) (Relative Density, or Density Relative to Critical State)	\uparrow	\uparrow	\uparrow	YES
2. "Soil Fabric" (\uparrow) (Method of Deposition, etc.)	\uparrow	\uparrow	\uparrow	(?)
3. Overconsolidation (\uparrow)	\uparrow	\uparrow	\uparrow	Yes
4. Ageing Effects (\uparrow)	\uparrow	\uparrow	$\uparrow \uparrow$	Yes
5. Prior Cyclic History (\uparrow)	(\uparrow ?)	\uparrow	(?)	Yes

Unfortunately, all five of these factors can be affected by unavoidable sampling disturbance (unless high quality frozen sampling is accomplished, including to have the advancing freezing front push water ahead of itself rather than having expansion of water with freezing separate the soil particles and completely disturb the sample). Frozen sampling and then coring to obtain fully "undisturbed" samples of cohesionless soils is prohibitively expensive for most projects, and it often cannot be successfully accomplished when either (1) silt contents are too high (in which case ice-jacking is likely to occur), or (2) groundwater is relatively warm, and actively moving as seepage, in which case it can be difficult to freeze a zone of water/soil with a propagating freezing front (and encapsulation freezing can also cause ice-jacking). Frozen sampling is usually reserved for very high priority projects, and for research purposes.

More routine field sampling, transport, trimming, mounting, and reconsolidation of samples for laboratory testing disturbs at least four of the five factors in Table 2-2, and as a result laboratory testing of samples from the field can produce misleading results with regard to evaluation of liquefaction resistance.

As a result, most engineering evaluations of liquefaction-related hazard are performed based on the use of in situ test data. The three most common tests here are (1) the Standard Penetration Test (SPT), (2) the cone penetration test (CPT), and (3) shear wave velocity measurements (V_s). Triggering relationships are available employing each of these methods. Other methods are also available, including larger-scale penetrometers such as

BPT and LPT, etc., but the three methods listed in Table 2-2 continue to be the most widely used at this time.

As shown in Table 2-2, the indices measured in all three of these methods also tend to increase with each of the factors. As a result, these in situ tests can be more reliable indicators of basic resistance to cyclic pore pressure generation (or liquefaction “resistance”). Note should be taken that shear wave velocity measurements (V_s) are small strain measurements, and these may be more strongly affected by ageing effects than the other two methods; as a result it is important to consider potential resulting unconservative bias with regard to use of V_s -based triggering relationships in older soils (e.g. non-Holocene deposits) unless the V_s triggering relationship specifically incorporates ageing effects.

Common practice with regard to seismic dam engineering is to use mainly either SPT-based or CPT-based liquefaction triggering relationships. SPT-based relationships will be the primary approach in these current studies.

Three SPT-based liquefaction triggering relationships will be used, and these are (1) the relationship of Youd et al. (2001), (2) the relationship of Boulanger and Idriss (2014), and (3) the relationship of Cetin et al. (2018). These will be discussed in the sections that follow.

All three of the liquefaction triggering relationships used in these current studies are based on forensic studies of sites that liquefied, or did not liquefy, in past earthquake. All three methods are based on the “simplified” procedure developed by Seed and Idriss (1971), and all three are based on Standard Penetration testing.

2.3.2 The Three Triggering Relationships Employed in These Current Studies

To update and enhance criteria that are routinely applied in practice, two workshops were convened in 1996 and 1998 by NCEER and NCEER/NSF, respectively, to gain consensus from 20 experts on updates and augmentations on standard procedures for assessment of liquefaction resistance of soils. Youd et al. (2001) summarized the workshop discussions and reports (NCEER, 1997).

The NCEER Panel adopted the Seed et al. (1984) triggering relationship, with an adjustment at $N_{1,60,CS}$ values of less than about 5 blows/foot, and this has been referenced side as the relationship of Youd et al. (2001). This relationship is shown in the left-hand figure of Figure 2-11.

Figure 2-11 shows all three of the SPT-based triggering relationships used in these current studies, and for the first time all three figures are plotted at the same vertical and horizontal scales to facilitate direct comparisons. The modification made by the NCEER Panel is the dashed line at low $N_{1,60,CS}$ values.

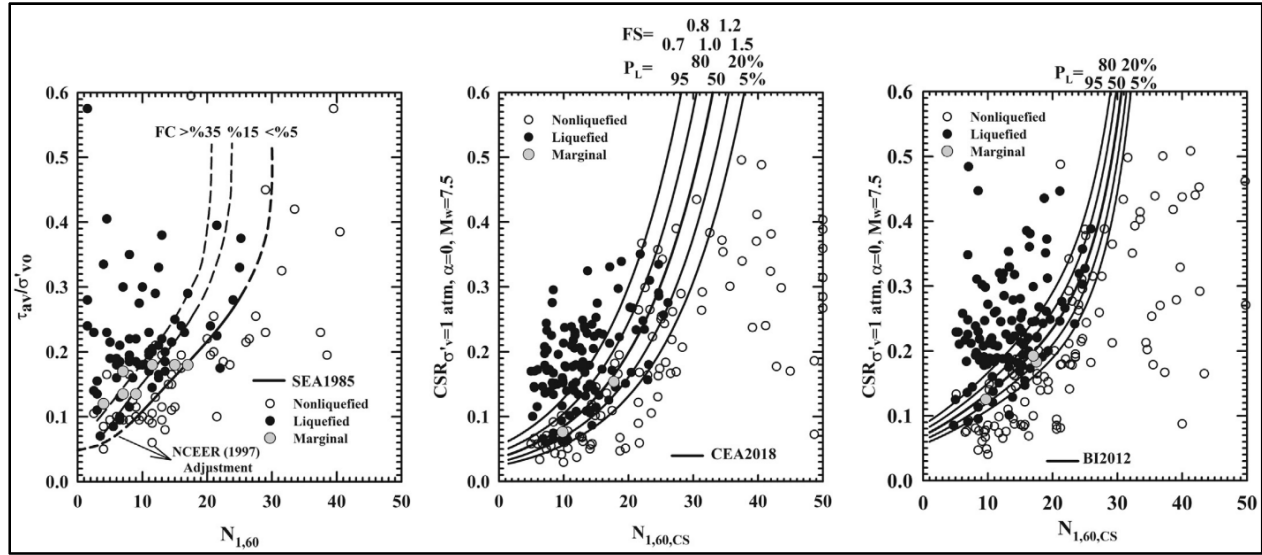


Figure 2-11: The SPT-based liquefaction triggering relationships of (a) Youd et al. (2001), Cetin et al. (2018), Boulanger and Idriss (2012) – Figure by Cetin et al. (2018)

In each of these figures, the vertical axis is the uniform cyclic stress ratio that will cause liquefaction in 15 uniform cycles, for soil with an initial effective vertical stress of 1 atmosphere, and for a number of equivalent cycles typical of the character and duration of an earthquake of $M_w = 7.5$. and for conditions with no initial “driving” shear stress bias ($K_\alpha = 0$).

Cyclic stress ratio is defined as the cyclic shear stress on a horizontal plane divided (normalized) by the initial effective vertical stress as

$$CSR = \tau_{hv,cyclic} / \sigma'_{v,i} \quad [\text{Equation 2-17}]$$

The horizontal axis in these figures represents SPT blow counts ($N_{1,60,CS}$ values) after correction for (1) SPT equipment, energy and procedural effects, (1) effective overburden stress effects, and (3) effects of fines content.

The dots and circles represent the results of back-analyses of field performance case histories from level ground sites. The dots represent sites that liquefied, and the open circles represent sites that did not liquefy.

It will not be possible to present a full discussion of the details involved in the forensic investigations that establish these data points in this dissertation. The data presented were developed by means of post-earthquake forensic field investigations and back-analyses performed over the past five decades by dedicated teams of international researchers. The data (case histories) presented in Figures 2-11(a) through(c) were each selected and vetted by the developers of each of the three triggering relationships shown.

These forensic back-analyses are performed using the simplified methods of Seed and Idriss (1971) to evaluate the peak cyclic stress ratio at any depth as

$$CSR_{peak} = \left(\frac{a_{max}}{g} \right) \left(\frac{\sigma_v}{\sigma'_v} \right) r_d \quad [\text{Equation 2-18}]$$

where, a_{max} = peak horizontal acceleration at the ground surface generated by an earthquake, g = acceleration of gravity, σ_v and σ'_v are total and effective vertical stress, and r_d = the nonlinear shear mass participation factor.

The equivalent uniform cyclic stress ratio is then taken as being equal to 65% of the single, one-time peak cyclic stress ratio, as

$$CSR_{peak} = 0.65 \left(\frac{a_{max}}{g} \right) \left(\frac{\sigma_v}{\sigma'_v} \right) r_d \quad [\text{Equation 2-19}]$$

The shear mass participation factor (r_d) is based on one-dimensional site response analyses, and each of the three triggering relationships developed their own relationships for r_d vs. depth.

When cyclic stress ratio is calculated to evaluate “loading” for forward engineering analyses, it is referred to as CSR. When it is determined based on one of the three triggering relationships, it is more correctly referred to as cyclic resistance ratio (CRR), though in common usage these two terms are often interchanged.

Adjustments/corrections must be made to the CRR values from each of the three liquefaction triggering relationships for (1) initial effective vertical stress effects (K_σ), (2) duration of cyclic loading, or number of equivalent uniform shear stress loading cycles, which is correlated with causative earthquake magnitude and expressed as a duration weighting factor (DWF), and (3) initial static driving shear stress effects (K_α). Each of the three triggering relationships shown has their own underlying K_σ and DWF relationships. Engineers are on their own to select their preferred K_α behavior characterizations, independent of the triggering relationship chosen, as the level ground sites investigated for development of the triggering relationships were selected as having had $K_\alpha = 0$ conditions.

A full discussion of triggering, and their engineering usage, will not be presented in this dissertation. Instead, only a brief discussion of select details will be made. A more complete discussion will be presented in the eventual U.C. Berkeley geotechnical research report that will be produced when these overall studies are completed.

Close examination of the three relationships as shown in Figure 2-11 shows that the “data points” in the left-hand and right-hand figures are a bit higher up in the plot than the middle figure. Also that the three triggering relationships (the “triggering curves”) differ.

There is a significant amount of engineering judgment involved in selection, processing, and analyzing the field data to produce these relationships. In addition, as they

were developed at different times, different amounts of field case history data were available to the development teams. Data availability continues to increase over time as new earthquakes occur, and post-earthquake field investigations are also improving as the profession advances.

2.3.2.1 Youd et al. (2001):

There are three sets of errors or short-comings in the triggering relationship developed by Seed, Tokmatsu, Harder and Chung (1984), which is the basis for Youd et al (2001).

The first of these was a paucity of available data at that early point in time. That has since been remedied as international researchers continue to investigate and process new case histories.

The second was the failure to address K_σ effects. That was understandable at the time, as all of the post-earthquake field performance case histories necessarily involved relatively “shallow” soil strata, because it is not usually possible to determine with full reliability whether or not a deeper soil layer or stratum liquefied. It was simply assumed that the triggering relationship was appropriate for “shallow” applications, as were typical for most early engineering applications at the time (e.g. shallow foundations, etc.) But that changed with the 1971 San Fernando earthquake, when these types of triggering relationships began to be applied to large dams. Most K_σ relationships are developed based on laboratory cyclic testing, and the new K_σ relationships being developed were applied to the triggering relationship of Seed et al. (1984) based on the assumption that the “representative” initial effective vertical stress for that relationship was approximately one atmosphere. It was not until some years later that Cetin et al. (2000, 2004) determined that the representative effective overburden stress for the field data set used was actually approximately 0.7 atmospheres, which makes a significant difference. That was not an error at the time of the original work, but it subsequently became an “error” when deeper soil strata were analyzed. The failure to formally address K_σ in the original work biases the locations of the data points shown in the figure at the left in Figure 2-13. The bias varies from case to case (dot to dot), but on average the data are located about 15% too high up on the figure (Cetin et al, 2018).

The third “error” in the triggering relationship of Seed, Tokimatsu, Harder and Chung (1984) was the continued use of the early r_d relationship developed by Seed and Idriss (1971). Figure 2-12 (Cetin et al., 2018) shows several selected sets of “ r_d curves” or relationships for evaluation of the shear mass participation factor (r_d) vs depth. All four figures are again shown with the same scaled vertical and horizontal axes to facilitate cross-comparisons.

The dotted line in the right-hand figure shows the early r_d relationship of Seed and Idriss (1971) which was the basis for the back-analyses of field performance case histories used in developing the triggering relationship of Seed and Idriss (1971) and also that of Seed et al. (1984) that went on to become Youd et al. (2001). Those back-analyses were one-

dimensional site response analyses performed using the equivalent linear method to approximate nonlinearity of seismic site response. That was revolutionary at the time (1971) as the use of computers to perform dynamic site response analyses was a relatively new idea, and it required significant developments with regard to evaluation and modeling of dynamic behaviors of soils.

At that early juncture, only five idealized sites were back-analyzed to develop the early r_d curves of Seed and Idriss (1971). All five sites consisted of 100 feet of sand, underlain by rock. One site was dense sand, one was medium sand, and one was loose sand. One site had 30 feet of loose sand over 70 feet of dense sand, and one site had 30 feet of medium sand over 70 feet of dense sand; based on the observation that sand density tends to increase with depth, especially in seismically active regions.

In hindsight, it is now understood that these simplified site conditions do not well reflect the large variability or real site conditions, with variable material (silts, clays, sands, gravels, etc.) and with variable stratigraphies, represented by the liquefaction triggering field performance case histories back-analyzed to develop triggering relationships.

A group of Japanese researchers (Imai et al., 1981) recognized this, and performed one dimensional site response analyses on a selected set of actual (real) sites, with real stratigraphies, to produce the r_d curves shown in the second figure from the left in Figure 2-12. They found that variability of site conditions (e.g. layering and stratigraphy, etc.) produced variability of modal shear mass participation (r_d) behaviors.

Golesorkhi (1989) performed one-dimensional site response analyses, and found that additional factors also affected the variability of r_d behaviors, including magnitude of the causative earthquake (or duration of seismic loading). Some of his results, for sites consisting of 100 feet of clean sands (to eliminate stratigraphy as a variable), are shown in the left-hand figure of Figure 2-12.

Cetin and Seed (2004) performed 2,153 site response analyses to better evaluate the effects of (1) variability of site stratigraphy, and (2) variability of seismic “input” motions on

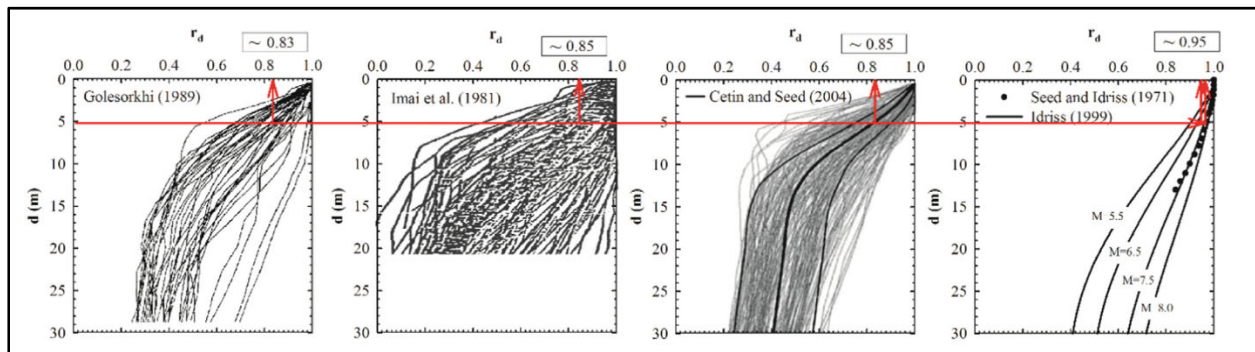


Figure 2-12: Same-scaled side by side comparison between the r_d relationships of (a) Golesorkhi (1989), (b) Imai et al. (1981), (c) Cetin and Seed (2004), and (d) Seed and Idriss (1971)- Dots, and Idriss (1999)-Lines [Cetin et al. 2018]

r_d behaviors. They analyzed 53 actual sites, with real stratigraphy, nearly all of which came from case histories in the field performance dataset used in developing the triggering relationships shown in Figure 2-11. They applied 42 different input ground motions in these analyses, and those input motions were selected to represent a wide range of causative earthquake magnitudes; and within each magnitude range they selected near-field, mid-field, and far-field recorded motions.

They found that the principal factors affecting modal shear mass participation factors were (1) site stiffness, (2) severity of seismic loading, and (3) duration of loading. Simply put, the harder a site is shaken, and the softer a site is, the more nonlinearity occurs; and as a result, the lower the r_d behavior that is observed. Duration of loading, which correlated with causative magnitude, also had an effect. They developed a predictive relationship for r_d as a function of these factors as

Equation 2-20:

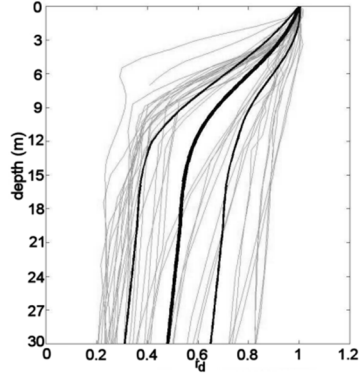
$d < 20$ m (~65 ft):

$$r_d(d, M_w, a_{\max}, V_{s,12m}^*) = \frac{\left[\frac{-23.013 - 2.949 \cdot a_{\max} + 0.999 \cdot M_w + 0.0525 \cdot V_{s,12m}^*}{16.258 + 0.201 \cdot e^{0.341 \cdot (-d + 0.0785 \cdot V_{s,12m}^* + 7.586)}} \right]}{\left[\frac{-23.013 - 2.949 \cdot a_{\max} + 0.999 \cdot M_w + 0.0525 \cdot V_{s,12m}^*}{16.258 + 0.201 \cdot e^{0.341 \cdot (0.0785 \cdot V_{s,12m}^* + 7.586)}} \right]} \pm \sigma_{\varepsilon r_d}$$

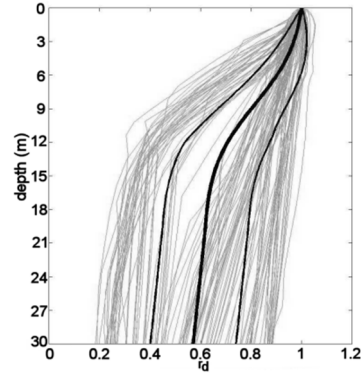
$d \geq 20$ m (~65 ft):

$$r_d(d, M_w, a_{\max}, V_{s,12m}^*) = \frac{\left[\frac{-23.013 - 2.949 \cdot a_{\max} + 0.999 \cdot M_w + 0.0525 \cdot V_{s,12m}^*}{16.258 + 0.201 \cdot e^{0.341 \cdot (-20 + 0.0785 \cdot V_{s,12m}^* + 7.586)}} \right]}{\left[\frac{-23.013 - 2.949 \cdot a_{\max} + 0.999 \cdot M_w + 0.0525 \cdot V_{s,12m}^*}{16.258 + 0.201 \cdot e^{0.341 \cdot (0.0785 \cdot V_{s,12m}^* + 7.586)}} \right]} - 0.0046 \cdot (d - 20) \pm \sigma_{\varepsilon r_d}$$

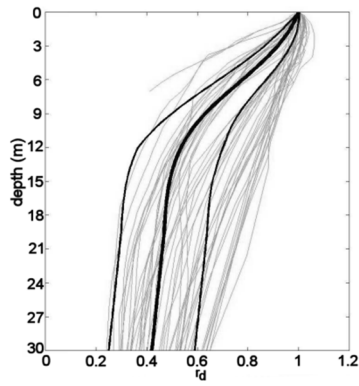
$$\mathbf{d < 12 \text{ m (~40 ft):}} \quad \sigma_{\varepsilon r_d}(d) = d^{0.850} \cdot 0.0198 \quad \mathbf{d \geq 12 \text{ m (~40 ft):}} \quad \sigma_{\varepsilon r_d}(d) = 12^{0.850} \cdot 0.0198$$



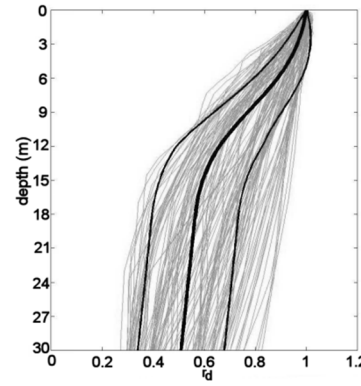
(a) $M_w \geq 6.8$, $a_{\max} \leq 0.12g$, $V^*_{s,12m} \leq 160$ m/s



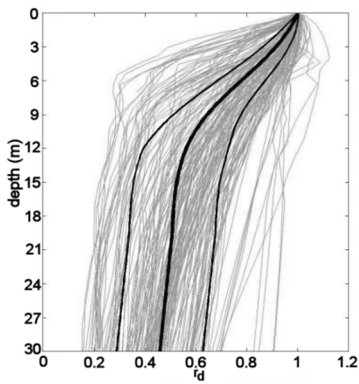
(b) $M_w \geq 6.8$, $a_{\max} \leq 0.12g$, $V^*_{s,12m} > 160$ m/s



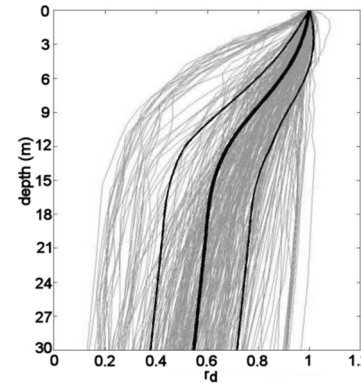
(c) $M_w < 6.8$, $a_{\max} \leq 0.12g$, $V^*_{s,12m} \leq 160$ m/s



(d) $M_w < 6.8$, $a_{\max} \leq 0.12g$, $V^*_{s,12m} > 160$ m/s

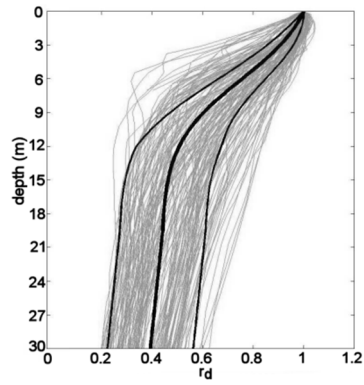


(e) $M_w \geq 6.8$, $0.12g < a_{\max} \leq 0.23g$, $V^*_{s,12m} \leq 160$ m/s

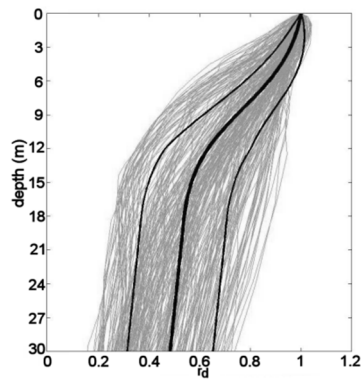


(f) $M_w \geq 6.8$, $0.12g < a_{\max} \leq 0.23g$, $V^*_{s,12m} > 160$ m/s

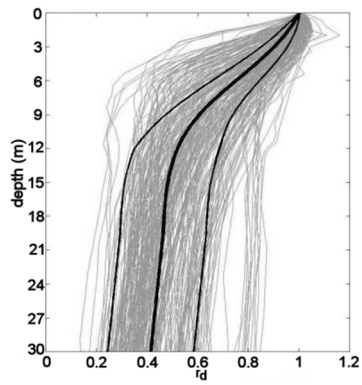
Figure 2-14 (Part 1): Comparison between r_d values calculated by means of site response analyses vs. values predicted by Equation 2-20



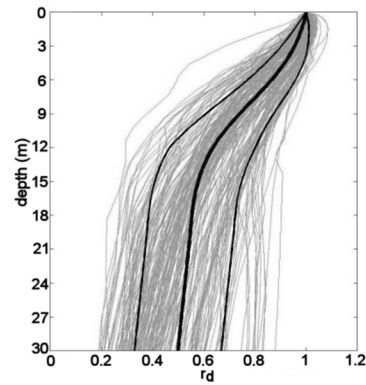
(g) $M_w < 6.8$, $0.12g < a_{\max} \leq 0.23g$, $V^*_{s,12m} \leq 160$ m/s



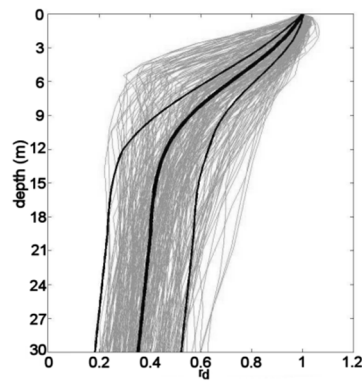
(h) $M_w < 6.8$, $0.12g < a_{\max} \leq 0.23g$, $V^*_{s,12m} > 160$ m/s



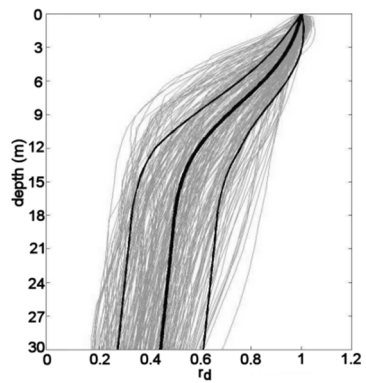
(i) $M_w \geq 6.8$, $0.23g < a_{\max}$, $V^*_{s,12m} \leq 160$ m/s



(j) $M_w \geq 6.8$, $0.23g < a_{\max}$, $V^*_{s,12m} > 160$ m/s



(k) $M_w < 6.8$, $0.23g < a_{\max}$, $V^*_{s,12m} \leq 160$ m/s



(l) $M_w < 6.8$, $0.23g < a_{\max}$, $V^*_{s,12m} > 160$ m/s

Figure 2-14 (Part 2): Comparison between r_d values calculated by means of site response analyses vs. values predicted by Equation 2-20

This equation is a spreadsheet challenge, but once correctly entered it provides excellent predictive results relative to the 2,153 site response analyses performed as shown in Figure 2-13. In this figure, the results of the 2,153 site response analyses are shown with the finer gray lines, and the heavier lines show the mean and +/- one standard deviation values as predicted by Equation 2-20.

The first four sub-figures of Figure 2-13 show results for input motions with $a_{max} < 0.12\text{ g}$, the second four with $0.12\text{ g} \leq a_{max} \leq 0.23\text{ g}$, and the remaining four with $a_{max} > 0.23\text{ g}$. In each sub-group of four, the left-hand figures are softer sites with $V_{s,12m} \leq 160\text{ m/sec}$, and the right-hand figures are stiffer sites with $V_{s,12m} > 160\text{ m/sec}$. In each sub-group of four figures, the uppermost figures are for smaller magnitudes of input motions ($M_w \leq 6.8$), and the lower-most two figures are for higher magnitudes. The trends of r_d with regard to stiffness, severity of shaking, and magnitude-correlated duration can clearly be seen, as can the ability of the predictive relationship to correctly track and predict these. For example, (1) the r_d “curves” move farther to the left as intensity of shaking (a_{max}) increases, and (2) the softer sites have lower r_d values than the stiffer sites.

None of that information was available to Seed, Tokimatsu, Harder and Chung (1984), and so the triggering relationship of Youd et al. (2001) is based on back-analyses of the field performance case histories that employed the r_d relationship of Seed and Idriss (1971). As shown in Figure 2-12 (the large dots in the far right sub-figure), this over-predicts r_d relative to the other relationships (including Cetin and Seed, 2004; second sub-figure from the right).

This over-prediction of r_d causes the data points in the triggering relationship of Youd et al. (2001), in the left sub-figure of Figure 2-13, to be located too high on the page, and by an average of about 12 to 15 percent or so, as illustrated by the comparisons of Figure 2-20, and by the more rigorous analyses and comparisons of Cetin et al. (2018).

On balance, the triggering relationship of Youd et al. (2001), or Seed et al. (1984), is biased unconservatively due to (1) paucity of data, (2) lack of use of K_σ in its derivation, and (3) use of unconservative r_d values in its derivation.

The final element of the Youd et al. (2001) triggering relationship is the effective overburden stress correction (K_σ) relationship. It now turns out that the laboratory-based K_σ relationship recommended by the 20 members of the GEER panel matches very closely with the K_σ relationship now regressed from the field performance liquefaction triggering data set; so this appears to be approximately the correct relationship; so there is no additional apparent bias added here.

2.3.2.2 Boulanger and Idriss (2014)

The liquefaction triggering relationship of Boulanger and Idriss (2014) also has at least three errors in its derivation, and these also produce unconservative bias in the overall relationship. In addition, they also make an unconservative choice with regard to the

selection of a K_σ relationship; both for development of their relationship, and also with regard to use in forward engineering analyses.

The first error is that they again use site response analyses performed on only a limited number of non-representative sites, as a basis for development of the r_d curves used to process the liquefaction triggering field database to develop their relationship. Only six sites are back-analyzed. Five of these are again sites consisting of 100 feet of sand over rock, and they add a sixth site with real stratigraphy. That sixth site is the La Cienega site near the Highway 10 overpass in Los Angeles. The La Cienega site is an instrumented strong motion recording site, so the stratigraphy and site properties are well-established. The site has good, and variable stratigraphy, and there is a V_s profile as well to help to establish baseline dynamic soil properties for site response. Unfortunately, they do not use the measured V_s profile, and instead employ a much stiffer profile; which has the effect of making this sixth site both “stiffer” and more “monolithic” than the other five sites consisting of 100 feet of sand.

Boulanger and Idriss (2014) do employ a wider range of input motions in their site response analyses, much like Cetin et al., and as a result they are able to discern an effect of causative magnitude on r_d behavior despite analyzing stiff, monolithic sites not representative of the liquefaction triggering field performance case history database.

Their resulting r_d relationship is shown in the far right sub-figure of Figure 2-12. The four curves are for $M_w = 5.5, 6.5, 7.5$ and 8.0 , respectively. As shown in this figure, incorporating M_w in their relationship spreads out the r_d curves a bit, but they are still too stiff and too narrowly banded vs. all of the other relationships plotted in Figure 2-12; due to a lack of realistic variability of stratigraphy of the only limited number of site conditions analyzed.

In addition, as shown by the red arrows and lines in Figure 2-12, because all six sites were too stiff and monolithic, their r_d curves are biased to the right; especially at depths of approximately 2.5 to 7 meters, which is the range in which a majority of the triggering field performance case history data occur; due to the need to use data from relatively shallow soil strata because it is difficult to be certain in post-earthquake studies whether or not significantly deeper strata liquefied. The resulting unconservative overall bias introduced into the Idriss and Boulanger triggering relationship (the data points in Figure 2-20 are generally too high) by using overly stiff and non-representative site conditions for development of their r_d curves is approximately equal to that of the Youd et al. (2001) relationship, and for the same reasons (Cetin et al, 2018).

The differences between the r_d curves of Boulanger and Idriss, and those of Cetin et al., have been a contentious issue for the past decade. This was recently at least partially resolved by the work of Laslie, Green, and Rodriguez-Marek (2015), who developed r_d curves based on site response analyses of a large number of U.S. liquefaction triggering performance case history sites, with a large and diverse set of input motions, and then compared the results with six different predictive relationships for r_d . They found (1) that the r_d relationship of Cetin et al. provided the best fit of the relationships available, (2) that the r_d

relationship of Idriss (1999) provided a very poor fit, and (3) they developed a new predictive relationship for r_d .

The second error in the derivation of the Idriss and Boulanger triggering relationship was the performance of an incorrect probabilistic regression (Cetin et al. , 2018). They performed a probabilistic regression to establish their relationship (to “fit” their curves), and the equational form used for their regression is a highly complex polynomial function which produces a bent shape, with a curved transition section, as shown in Figure 2-11(c). Unfortunately, this equation has only one regressable variable, and as a result “curve fitting” can only be achieved by sliding the bent curve (polynomial function) upwards or downwards; the bent curve cannot translate laterally, it cannot change its curvature, and it cannot rotate in order to better fit the data set. Because it cannot do any of these things, especially not translate laterally, it is driven upwards in attempting to fit the large number of unliquefied data points in the range of $N_{1,60,CS} \approx 15$ to 30 blows/foot. As a result, it provides an unconservative fit of the data in the range of $N_{1,60,CS}$ less than or equal to about 18 blows per foot. This can clearly be seen (visually) in Figure 2-11(C), as there are far too many “dots” (liquefied cases) below the lines, and too few “circles” (non-liquefied cases) above the lines.

The third error was the truncation of K_σ at a maximum value of 1.1, which unconservatively biased the corrected CSR values for shallow case history data, which were numerous in the data set. As shown in Figure 2-14, the laboratory data, and the regression of field case history data, both clearly show that K_σ does not “truncate”; instead it continues smoothly upwards at low effective stresses.

On balance, these three errors produced an overall triggering relationship that is more unconservatively biased than that of Youd et al. (2001).

That unconservative bias is then further exacerbated by their choice of a K_σ relationship. K_σ is applied as an adjustment factor to the “baseline” triggering curves, which are established to match conditions at an initial effective vertical stress of 1 atmosphere. K_σ is defined, and applied, as

$$CSR_{liq} = CSR_{latm} \times K_\sigma \quad [Eq. 2-21]$$

Figure 2-14 shows a collection of much of the available laboratory data regarding K_σ , as well as several K_σ relationships. The data shown in this figure includes laboratory data compiled from a number of different researchers by Montgomery et al. (2014), as well as data developed in laboratory testing and presented by Cetin et al. (2018).

As shown in this Figure, the relationship recommended by the NCEER Working Group (Youd et al., 2001) for use with the triggering relationship of Seed et al. (1984) is in close agreement with that of Cetin et al. (2018). These two K_σ relationships were, however, developed very differently. The NCEER recommended K_σ curves (black solid lines and black dashed line, for $Dr = 60\%$ and 40% , respectively) were based on available laboratory data. Cetin et al. (2018), on the other hand, were the first to successfully develop K_σ curves by regression of the very large liquefaction triggering field performance database.

Cetin et al. (2018) were first (and still the only) ones to develop a K_σ relationship based on regression of the liquefaction field performance case history database. This is arguably the best process to develop K_σ relationships at present, because it intrinsically incorporates field effects like multi-directional loading, etc. that cannot yet be fully reliably handled in laboratory cyclic testing; and it has no adverse “laboratory testing” boundary conditions.

This K_σ relationship is valid only down to a depth where the effective overburden stress is approximately 1.6 atmospheres, because the field performance data are from rel-

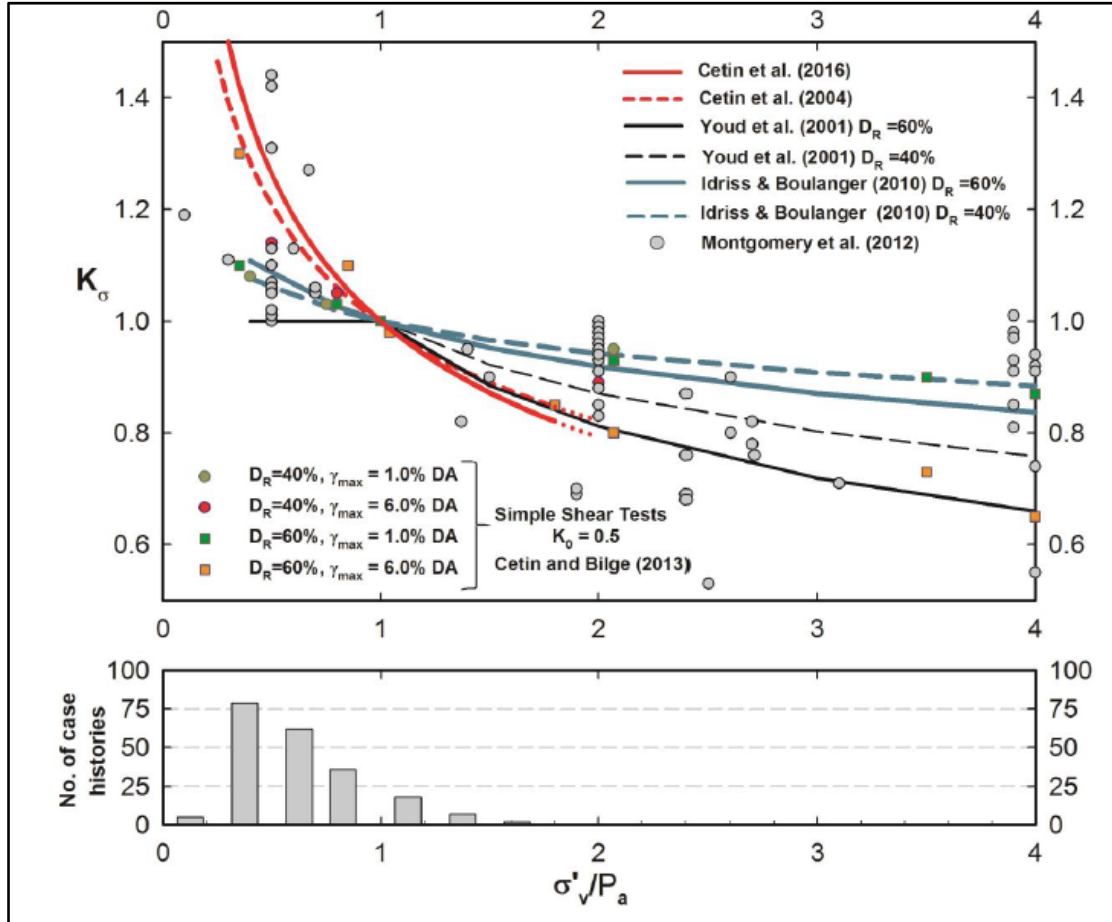


Figure 2-14: The recommended K_σ relationships of (1) Youd et al. (2001), as appended to the triggering relationship of Seed et al. (1985), (2) Boulanger and Idriss (2012), and (3) Cetin et al. (2016)

atively shallow sites so that the field investigators can reliably determine whether or not a specific soil stratum liquefied during the earthquake. Engineers are therefore free to make their own judgments at greater depths; but it is noted that this should not include selecting K_σ relationships that are in strong disagreement with the field data regressed relationship for $\sigma'_{v,i} \leq 1.6$ atmospheres.

As shown in Figure 2-14, the K_σ relationship of Idriss and Boulanger (2014) is unconservative relative to much of the available laboratory data at $\sigma'_{v,i} \geq 1.6$ atmospheres, and it is also in strong contrast to the field data-regressed relationship for $\sigma'_{v,i} \geq 1.6$ atmospheres. That means that the K_σ relationship of Idriss and Boulanger (2008) appears to be significantly unconservative at initial effective vertical stresses of progressively greater than 1 atmosphere; and these are important in large dams. This unconservatism in K_σ is multiplicatively compounded with the unconservatism(s) in the baseline triggering relationship (which is normalized to an initial effective vertical stress equal to 1 atmosphere) of Boulanger and Idriss (2014).

On balance, the triggering relationship of Boulanger and Idriss (2014) has three clear sources of unconservative bias (see Cetin et al, 2018), especially at $\sigma'_{v,i} \geq 1$ atmosphere, and this unconservatism is compounded by the selection and use of an unconservative interpretation of K_σ behavior. As a result, it is the least conservative of the three liquefaction triggering relationships employed in these current studies.

2.3.2.3 Cetin et al. (2018)

Cetin et al. (2018) had the luxury of studying all of the previous efforts that developed liquefaction triggering relationships, which was a significant advantage. This new liquefaction triggering relationship avoids the problems discussed above relative to the other two triggering relationships employed in these current studies. It will certainly be studied by other investigators, but at present there are no known significant causes of bias.

2.3.2.4 Magnitude-Correlated Duration Weighting Factors and Fines Corrections

Two additional factors affecting the accuracy and reliability of these types of liquefaction triggering relationships are (1) magnitude-correlated duration weighting factors (DWF) and (2) fines corrections (ΔN_{fines}).

Fortunately, the magnitude-correlated DWF's of these three liquefaction triggering relationships do not differ nearly as strongly as the issues discussed in the preceding sections, and especially not for an event of $M_w \approx 7.5$.

Fines corrections are specific to each of the three triggering relationships, and each relationship should be employed in conjunction with the (1) fines corrections, (2) the specific SPT energy, equipment, procedural corrections used in the development of each of these relationships.

2.4 POST-LIQUEFACTION RESIDUAL STRENGTH (S_r) RELATIONSHIPS

The final issue to be discussed briefly here is the selection and use of post-liquefaction residual strength, S_r relationships.

Naturally deposited soil layers and artificially placed fill layers are inevitably sub-layered with local variability in hydraulic conductivities due to many factors such as soil types, variability in grain size distributions, varying compaction vs. lift depth, alluvial depositional environments, etc. During an earthquake, this stratification may lead to a soil liquefaction mechanism, known as “Void Redistribution”. The NRC panel (1985) and Seed (1987) discussed the void redistribution mechanism of stratified soil layers wherein a higher permeability sublayer layer or lens of soil is overlain and underlain by lower permeability strata. When this situation presents (as is common in alluvial deposits, aeolian deposits, hydraulic fills, and engineered fills placed in lifts) cyclic pore pressure generation can reduce effective confining stresses, and cause the more granular soil layer or stratum to attempt to densify due to cyclic agitation. If the sub-layer is entrapped between two layers of lower permeability, then globally “undrained” conditions occur, at least over finite intervals of time, as fluids cannot rapidly escape. Solid soil particles may settle a bit, however, and to maintain constant overall volume, fluids may rise upwards to maintain overall constant volume. This is “localized void redistribution”, and it can result in the formation of a loosened layer at the top of the entrapped stratum, and in some cases it can even temporarily produce an entrapped blister of water.

The shear strength of a blister of water is negligibly small but can facilitate very rapid rates of shearing.

The loosened soil zones that can form as part of this process will have post-liquefaction (steady state) strengths that are a function of their density relative to critical state. But these strengths are not a function of their pre-earthquake density relative to critical state; instead they are a function of the density of the loosened top layer of entrapped soil after localized void redistribution, and in some cases likely with some parts of any shear zone also passing preferentially through water-filled lenses that are also the result of void redistribution. Because they represent a new (and looser) material, their steady state strengths can be significantly lower than those of the materials that were present before void redistribution occurred.

This has been observed, and reasonably well-studied in both centrifuge model testing, and in table top scale model testing, and the process is reasonably well understood.

The problem is that overall post-liquefaction (and post-void redistribution) strength will be controlled by a chaotic mix of water lenses and/or “loosened” upper portions of soil strata that now exist at a lower void ratio than was present prior to earthquake shaking; essentially representing a new material with lower steady state strength.

It is not currently possible to investigate a site sufficiently as to identify the likely most critical sub-layer or lens that will have the lowest shear strength after void

redistribution, and failure surfaces may cross diagonally across multiple void redistribution zones. And it is generally not possible to determine the sub-strata thickness at which the most critical void redistribution will occur. So it is not currently possible to reliably sample and test samples in undrained simple shear at that vertical sample thickness scale.

Nature, however, has the ability to unerringly identify and exploit the weakest link in a stratified soil deposit.

As a result, the most useful current methods for prediction of post-liquefaction residual strengths are based on empirical approaches involving back-analyses of large displacement liquefaction failures.

The first predictive relationship of this type was presented in the final journal paper of the late Prof. Harry Seed (1987), and it was based on the results of back-analyses of a number of liquefaction-induced failure case histories to estimate field post-liquefaction strengths in liquefied soils for situations that produced large displacement slides or flow failures, and the relationship predicts S_r as a function of $N_{1,60,CS}$. Prof. Seed died shortly after the paper was approved for publication.

Two of his former students noticed that he had made an error in back-analysis of the post-liquefaction strength of the flow slide of the Lower San Fernando Dam (basing his S_r value on the shear strength required for stability in the un-displaced geometry). If the strength had that value, then the flow slide would not have occurred; the strength must have been lower. Seed and Harder “fixed” the S_r values calculated by Seed (1990) for two of the cases, and added a few additional cases, and published the repaired S_r relationship shown in Figure 2-15 in the H.B Seed memorial symposium proceedings. It took on a life of its own, and is known as the Seed and Harder (1990) S_r relationship.

Stark and Mesri (1992) noted that post-liquefaction strength of liquefiable soils might have some things in common with undrained strengths of clays, and re-formulated the data and relationship of Seed and Harder (1990), adding cases, as a predictive relationship for $S_r/\sigma'_{v,i}$ as a function of $N_{1,60,CS}$. That same approach was taken by Olson and Stark (2002), who developed a similar relationship, but based on more case histories, and with some innovative back-analysis approaches, as shown in Figure 2-16.

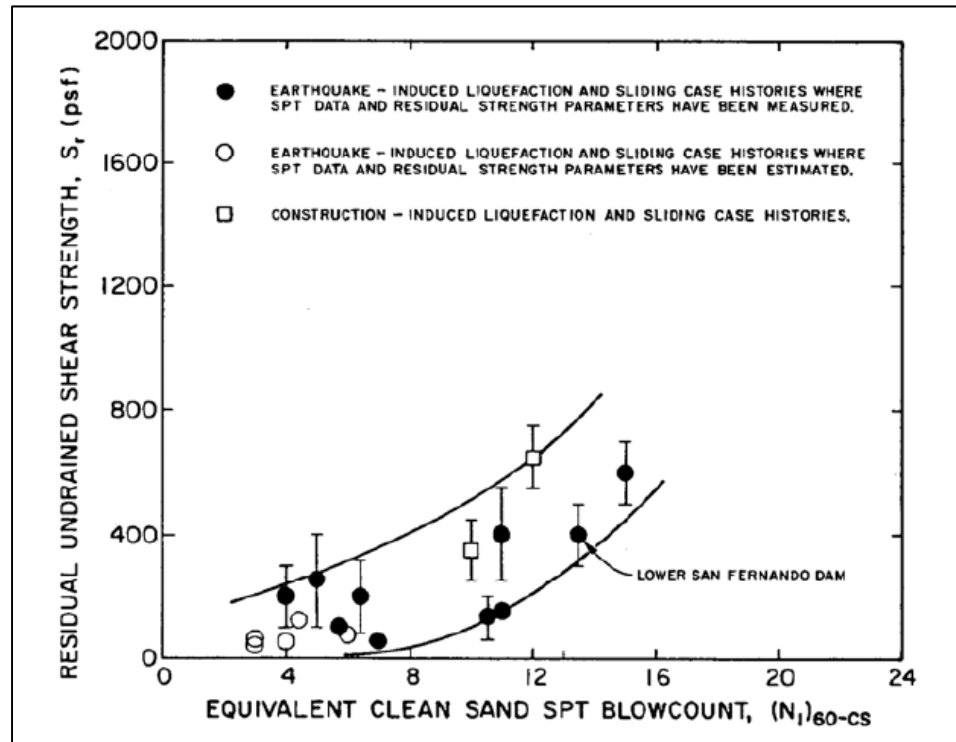


Figure 2-15: Variation of post-liquefaction residual strength S_r as a function of fines adjusted SPT penetration resistance $(N_1)_{60-CS}$ (Seed and Harder, 1990).

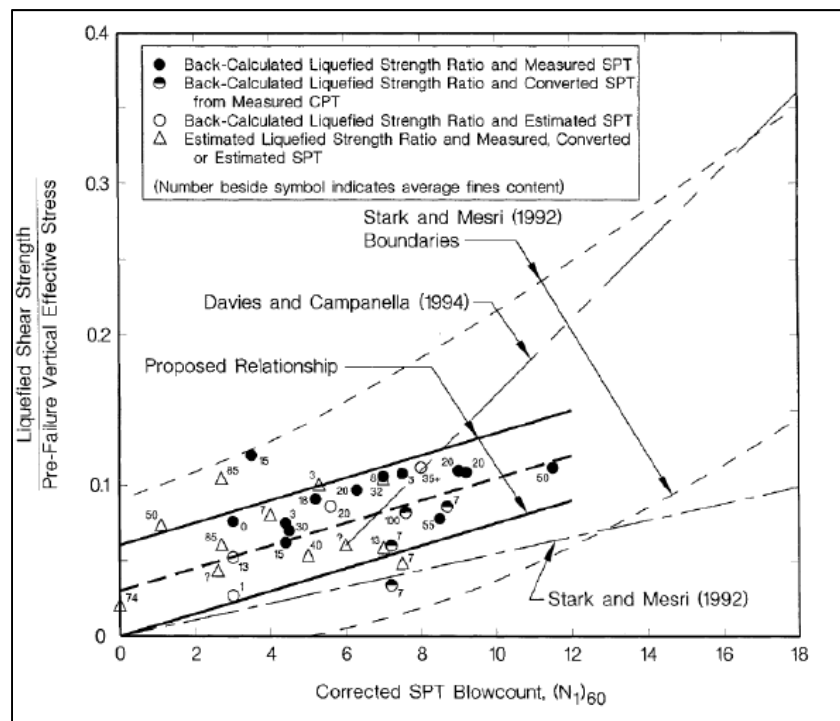


Figure 2-16: Recommended relationship for estimation of normalized residual strength ratio as a function of SPT penetration resistance (Olson and Stark, 2002)

There was never really any question that neither S_r vs $N_{1,60,CS}$, nor $S_r / \sigma'_{v,i}$ vs. $N_{1,60,CS}$, was the optimal approach. Instead it was clear early on that the best relationships would predict both S_r and $S_r / \sigma'_{v,i}$ as a function of both $N_{1,60,CS}$ and $\sigma'_{v,i}$.

In these current studies, three S_r relationships will be used as a basis for evaluation and use of post-liquefaction strengths. These will be the relationships of (1) the S_r vs. $N_{1,60,CS}$ relationship of Seed and Harder (1990), (2) the $S_r / \sigma'_{v,i}$ relationship of Idriss and Boulanger (2015), and (3) the S_r and $S_r / \sigma'_{v,i}$ (predicts both simultaneously) vs. both $N_{1,60,CS}$ and $\sigma'_{v,i}$ relationship of Weber et al. (2015).

All three of these relationships are based on back-analyses of large displacement liquefaction failure case histories. Many of the same sites have been back-analyzed by all three investigation teams. The work of Weber et al. (2015) involved a larger team of experts, and more years of work, and it was a more comprehensive process involving development of (1) understandings of the mechanics of the relationships between S_r and displacements (and runout distances, etc.) , (2) new mechanics-based back-analysis procedures for large displacement liquefaction failures, and (3) two sets of relationships for internal cross-checks of both the individual S_r values determined for each case history, and for cross-checks and understanding of the S_r values determined by other investigation teams for those same cases.

Figure 2-15 shows the S_r vs. $N_{1,60,CS}$ relationship of Seed and Harder (1990). This is very closely similar to the S_r vs. $N_{1,60,CS}$ relationship of Idriss and Boulanger (2015), so the nonlinear seismic deformation analyses performed in these current studies that employ the Seed and Harder (1990) relationship also shed light on the utility and reliability of the Idriss and Boulanger (2015) relationship.

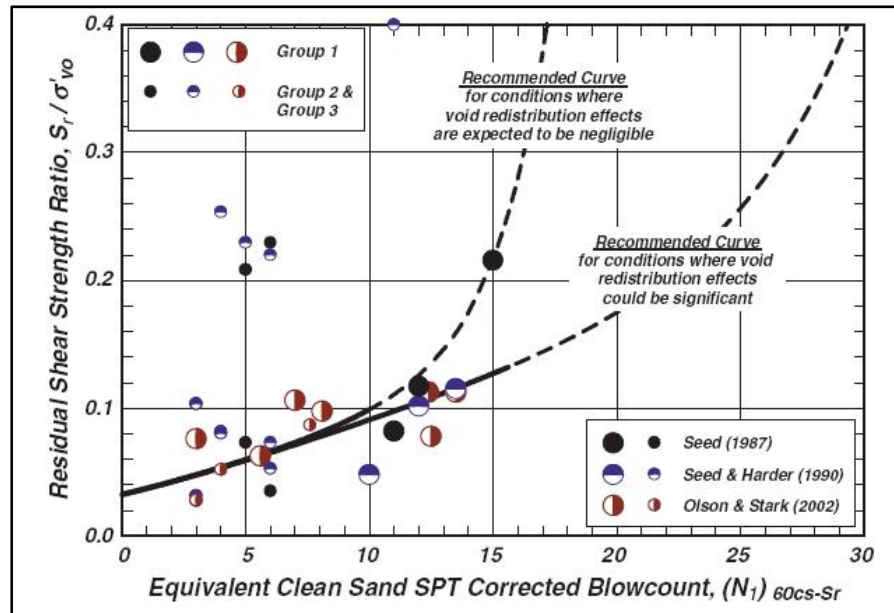


Figure 2-17: Recommended relationship for estimation of normalized residual strength ratio as a function of SPT resistance (Idriss and Boulanger, 2015)

Figure 2-17 shows the $S_r / \sigma'_{v,i}$ relationship of Idriss and Boulanger (2015). The line “with void redistribution” is the one applicable to field conditions. This relationship is very similar the $S_r / \sigma'_{v,i}$ relationship of Olson and Stark (2002), except that it inflects gently upwards at higher $N_{1,60,CS}$ values, so the nonlinear seismic deformation analyses performed in these current studies that employ the Idriss and Boulanger (2015) relationship also shed light on the utility and reliability of the Olson and Stark (2002) relationship.

The S_r relationship of Weber et al. (2015) was developed by means of a multi-dimensional Bayesian regression of the innovative back-analyses of large deformation field case histories. It predicts S_r as a function of both $N_{1,60,CS}$ and $\sigma'_{v,i}$, as shown in Figure 2-18. It can be expressed as either S_r vs. $N_{1,60,CS}$, (as a function of $\sigma'_{v,i}$), or as $S_r / \sigma'_{v,i}$ vs $N_{1,60,CS}$ (again as a function of $\sigma'_{v,i}$) as shown in Figure 2-19.

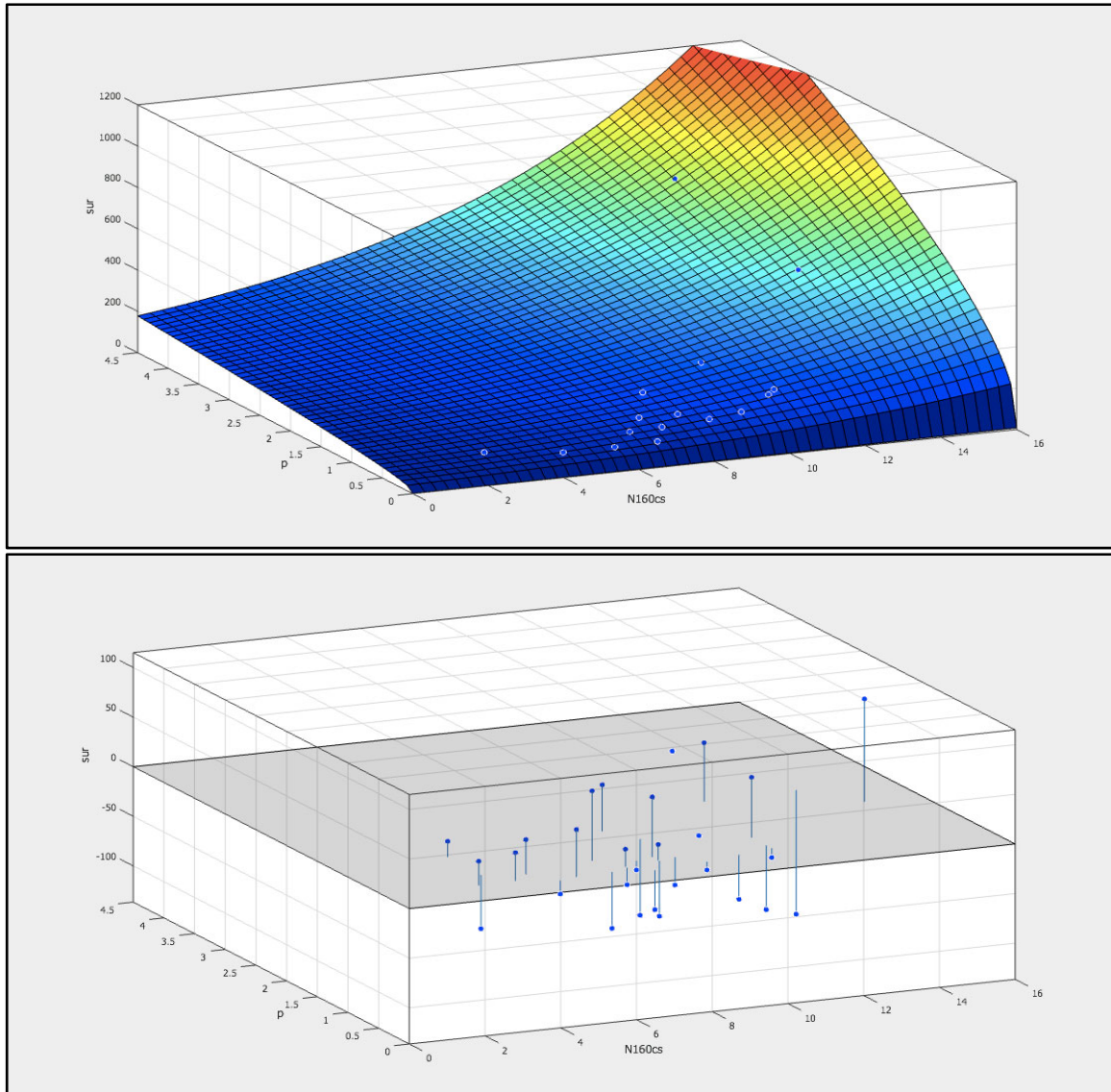


Figure 2-18: Results of probabilistic maximum likelihood regression showing (a) the relationship for post-liquefaction strength (\bar{S}_r) as a function of both $\bar{N}_{1,60,CS}$ and $\bar{\sigma}'_{vo}$, and (b) residuals from the deterministic least squares regression in terms of predicted vs. observed \bar{S}_r for each of the 29 liquefaction field case histories. [Note: Residuals in the lower figure are vertically exaggerated by a factor of 5 for clarity.] [Weber (2015) and Weber et al. (2015)]

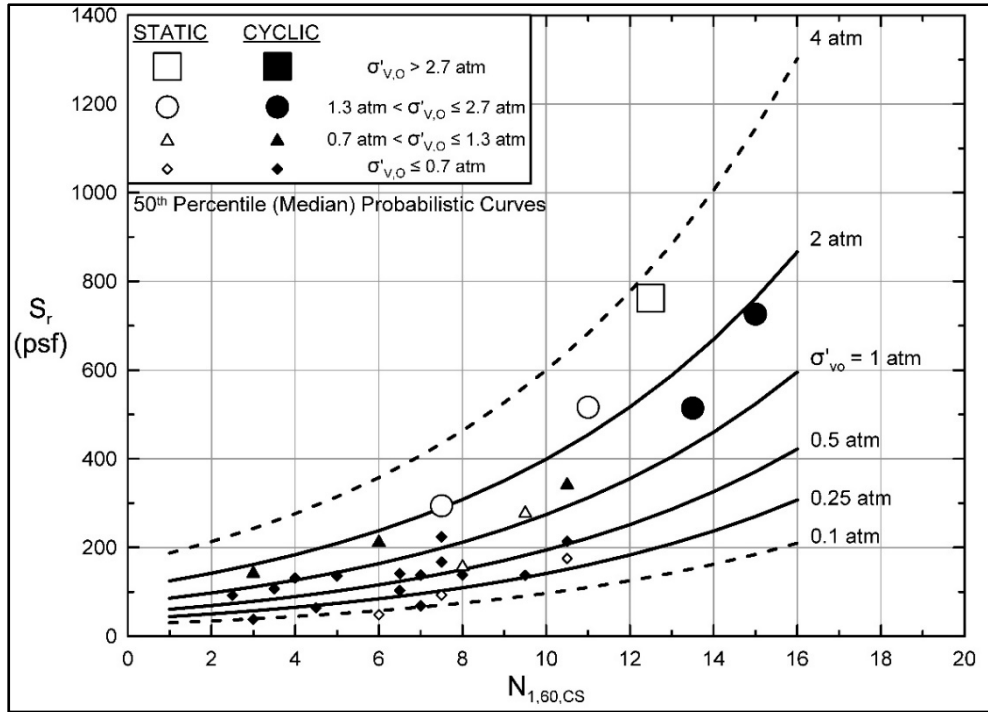


Figure 2-19(a): Results of probabilistic regression showing median values of S_r as a function of both penetration resistance and initial effective vertical stress. [Weber (2015) and Weber et al. (2015)]

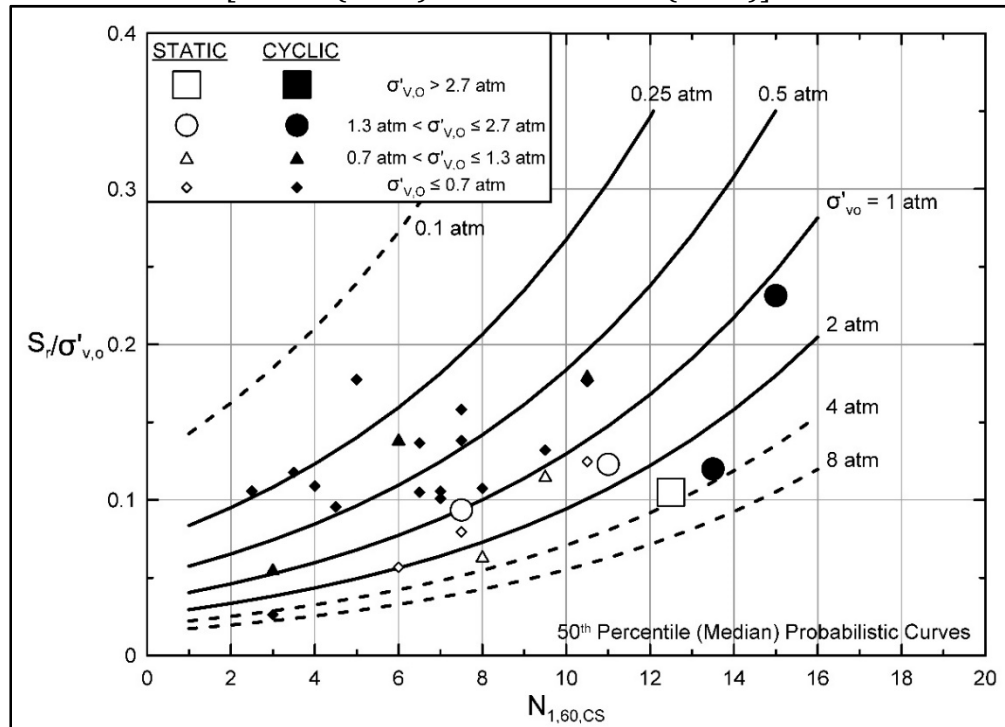


Figure 5-19(b): Results of probabilistic regression showing median values of S_r/P as a function of both penetration resistance and initial effective vertical stress [Weber (2015) and Weber et al. (2015)]

Chapter 3

The Port Island Vertical Array Site Seismic Performance Case History During the 1995 Kobe Earthquake

3.1 INTRODUCTION

The great Hyogoken-Nambu earthquake (also known as the 1995 Kobe earthquake) struck the southern part of Hyogo prefecture in Japan on January 17, 1995 with an M_w of 6.9 (Sitar et al., 1996). The earthquake caused numerous loss of lives and enormous property damage. Liquefaction-induced damages were widespread in this earthquake in coastal regions including man-made islands in Osaka Bay. Figure 3-1 shows a distribution of sites where sand boils were observed (Shibata et al., 1996). An instrumented vertical strong motion array station in Port Island, consisting of four sets of seismometers, provided valuable ground motion records at depths ranging from the ground surface to a depth of 83 meters below the ground surface.

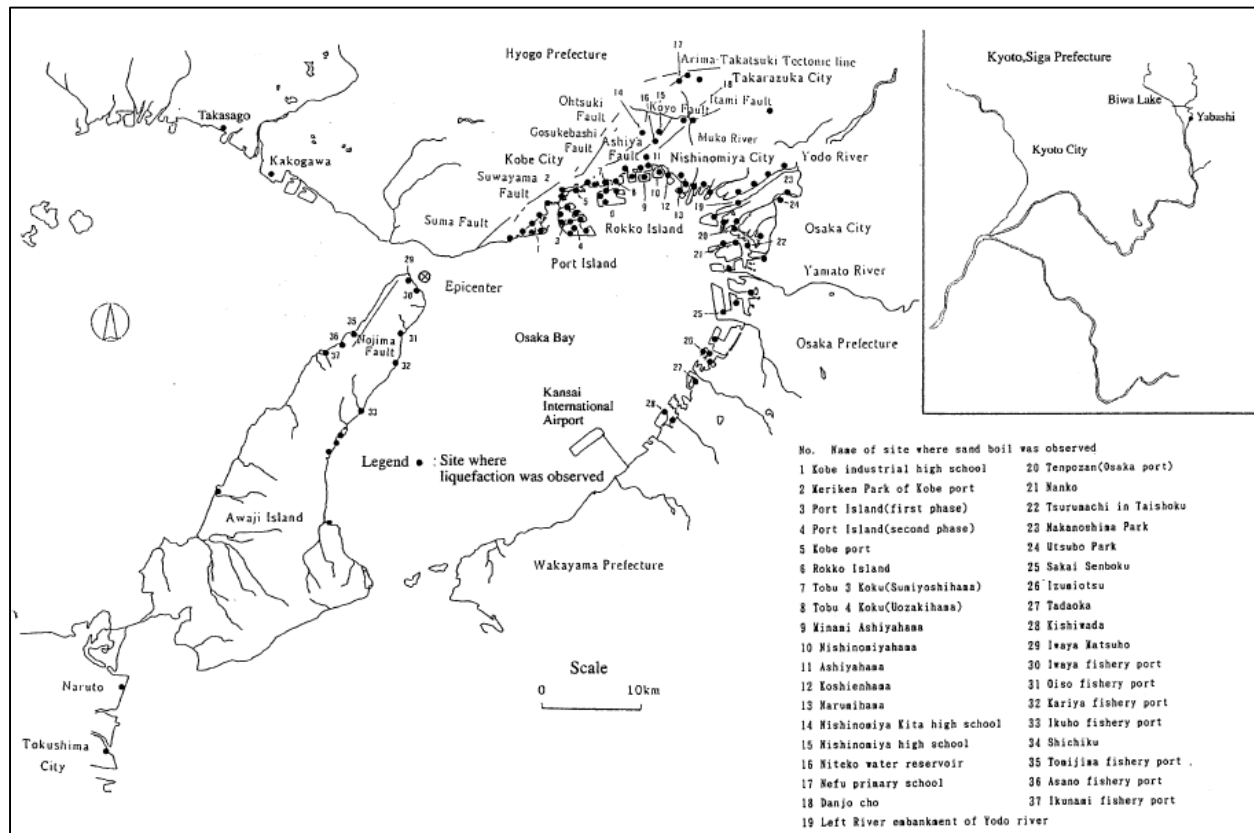


Figure 3-1: Distribution of sites where sand boils were observed during the 1995 Kobe earthquake (Shibata et al., 1996)

Because Port Island experienced widespread liquefaction, including liquefaction at the vertical array site, the ground motion recordings have been the subject of significant interest with regard to understanding the liquefaction behaviors of soils, and the interactions of these behaviors with site response during strong shaking. In these current studies, evaluations and/or back-analyses comparisons of the recorded site response and performance are performed as a test of the various sets of (1) analytical and constitutive models, (2) liquefaction triggering relationships, and (3) post-liquefaction relationships with regard to their abilities to suitably reproduce the observed and recorded site response. These analyses will be performed using the same FLAC analytical platforms that will then next be used for back-analyses of the seismic performances of the Upper and Lower San Fernando Dams in the 1971 San Fernando earthquake, as presented in Chapters 4 and 5.

3.2 GEOLOGY AND CONSTRUCTION OF PORT ISLAND

Port Island is an artificial island located in the north-west part of Osaka Bay. The island was constructed in two phases (Shibata et al., 1996). During the first phase, a total of 436 hectares area was reclaimed between 1966 and 1981. In the second phase, the island was extended southward by reclaiming 319 hectares. The first phase of reclamation was performed using a decomposed granite soil, called “Masado”, and a sedimentary rock debris (sandstone, mudstone, and tuff) was employed in the second phase of reclamation. During the 1995 Kobe earthquake, liquefaction in the first phase of the site was significantly more severe than the second phase. Figure 3-2 is a map of the Port Island first phase area, showing the location of the instrumented strong motion array site. The vertical array site was in the first phase area, about 350 meters from the edge of the island.

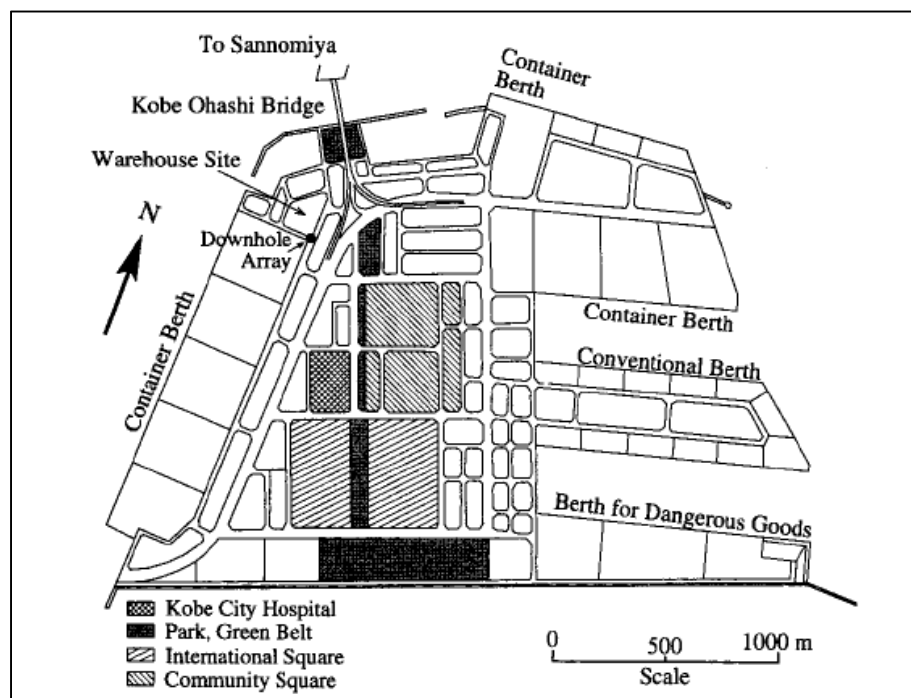


Figure 3-2: Map of Port Island first phase area, showing the vertical array site on the north-western portion of the island (Nakakita and Watanabe, 1981)

Port Island is in the north-western area of Osaka Bay, in southwest Japan. The Rokko mountain regions are located to the north of Osaka Bay. The bedrock in Osaka Bay occurs at a depth of more than 3,000 meters (10,000 feet) at the center of the Bay. Based on Mesri and Funk (2015), the bedrock depth in the Port Island area is between 1,400 and 2,200 meters, as shown in Figure 3-3.

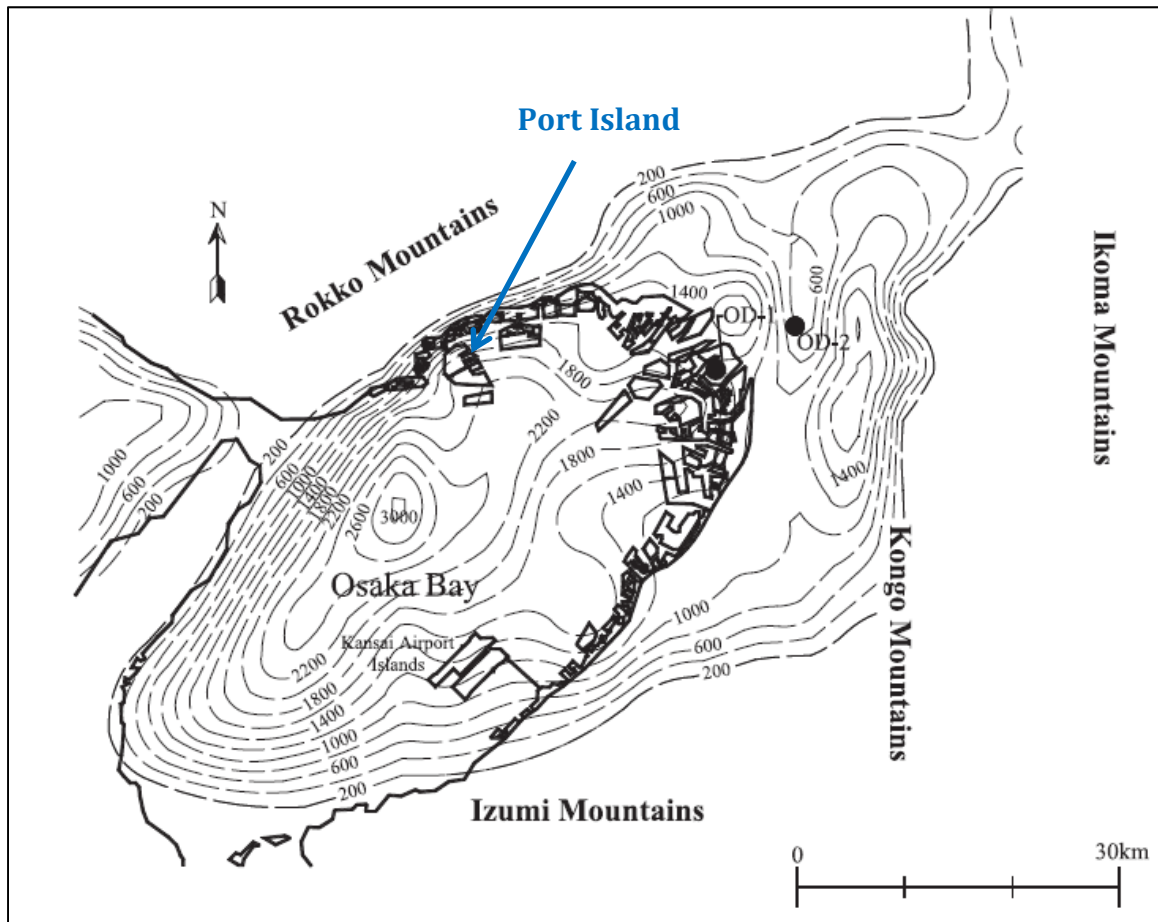


Figure 3-3: Osaka Bay bedrock depth contours (Mesri and Funk, 2015)

Osaka Bay geology includes a sequence of marine clay layers that alternate with sand layers and layers of non-marine clays. Figure 3-4(a) shows a sub-seabed sediment profile for the Kansai International Airport area, which is in the south-east portion of Osaka Bay (Mesri and Funk, 2015). The sediment profile includes Pleistocene marine clay layers Ma0 to Ma12 (Ma0 at the bottom and Ma12 at top) and Holocene marine clay layer Ma13. Marine clay layers alternate with sand layers Ds1 through Ds10 and non-marine clays Doc and NMC (Non Marine Clay), as well as very thin layers of volcanic ash deposits (Mesri and Funk, 2015). Based on the geologic profile of Port Island (Figure 3-6b) vertical array site, the sediment sequencing of Port Island is consistent with the general sediment sequencing of the Kansai Airport area. As shown in Figure 3-4(b), the thickness of man made deposits of Masadso soil fill placed to reclaim the land at the Port Island array site is about 19 meters.

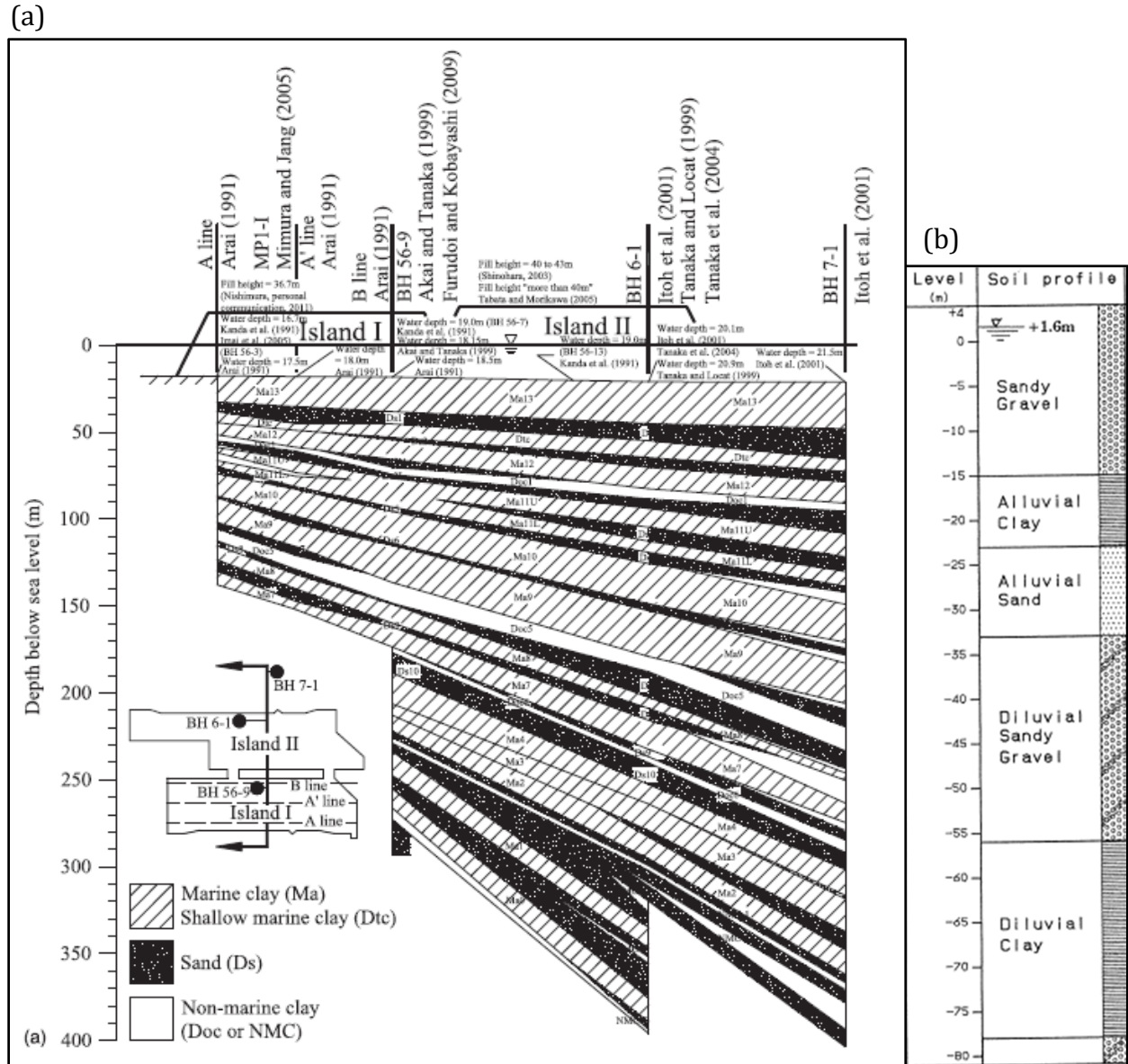


Figure 3-4: (a) Sub-seabed profile of Kansai International Airport site (10:1 vertical to horizontal exaggeration) (Mesri and Funk, 2015); (b) Soil profile at the Port Island vertical borehole array station (Shibata et al. 1998)

3.3 OBSERVED PERFORMANCE OF PORT ISLAND DURING THE 1995 KOBE EARTHQUAKE

Port Island suffered widespread liquefaction during the 1995 earthquake, and damaging liquefaction effects such as sand boils and volumetric recompression settlements in the island, lateral spreading and/or slope instability near the edges of the island, as well

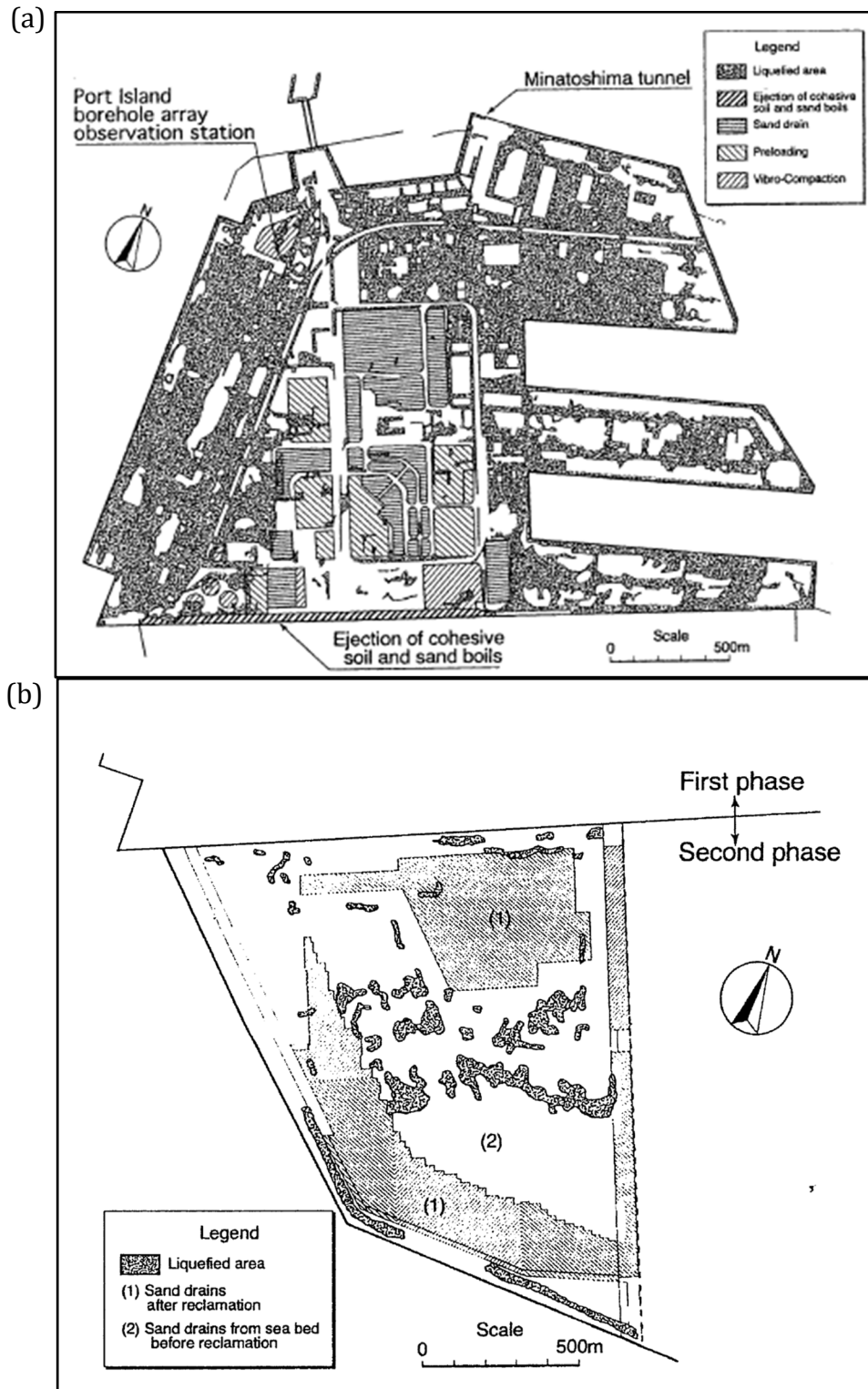


Figure 3-5: Distribution of liquefaction in Port Island and areas where soil improvement techniques were used; (a) first phase, and (b) second phase (Shibata et al. 1996, who reproduced this figure from Geographical Survey Institute, 1995, with modifications)

as damages to harbor quay walls and other built structures and systems during the 1995 earthquake. Figure 3-5 (a) shows the mapped distribution of liquefaction effects in the first phase area of Port Island, and Figure 3-5 (b) shows the mapped distribution of liquefaction in the second phase area of Port Island due to the Kobe earthquake (Shibata et al., 1996).

Figure 3-6 shows results of post-earthquake survey of liquefaction induced settlement in Port Island (Ishihara et al., 1996), showing the approximate statistical distribution of settlements measured in post-earthquake surveys at a number of locations. As shown, these ranged from no settlement to approximately 90 cm (~3 feet) with an average of 50 cm (~1.6 feet), and a median of 45 cm (~1.5 feet).

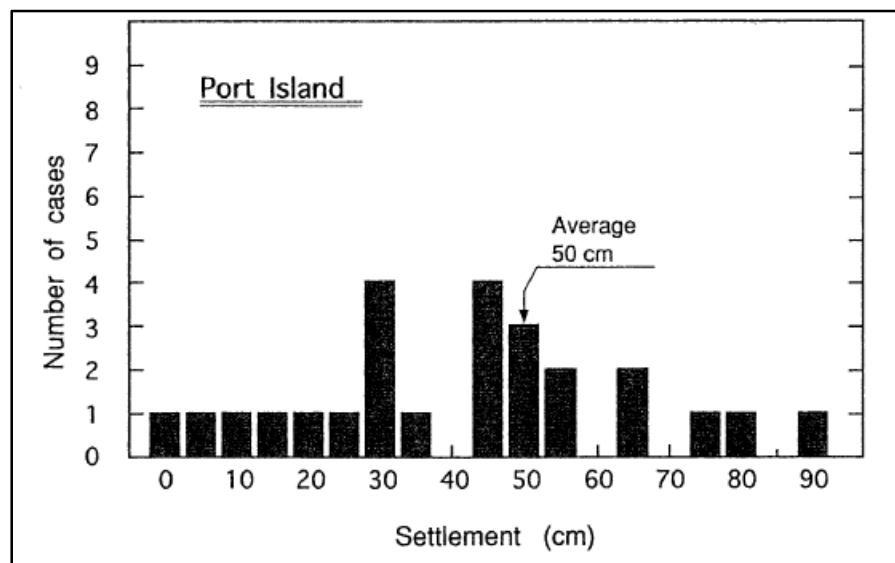


Figure 3-6: Post-earthquake settlements observed at the ground surface on Port Island (Ishihara et al., 1996)

3.4 GEOTECHNICAL/GEOLOGICAL CROSS-SECTION AND BACK ANALYSIS PLAN

Site-specific geotechnical and geophysical data were obtained at the vertical array site prior to the 1995 Kobe earthquake. Figure 3-7 shows a soil profile from Elgamal et al. (1996), which was prepared based on information from Iwasaki (personal communication). Figure 3-8 shows a summary of a soil profile from Shibata et al. (1996), who referenced the Kobe City Development Bureau. Figure 3-9 shows a soil profile from Ishihara et al. (1996), which referenced information sourced from Toki (1995). A close examination of these figures indicates slight differences in soil layering and maximum SPT-N values among the different research teams. It appears that the differences are near transition zones of different soil layers, where a change in shear wave velocity, or compression wave velocity, or SPT-N values were observed. These appear to be differences in engineering interpretations.

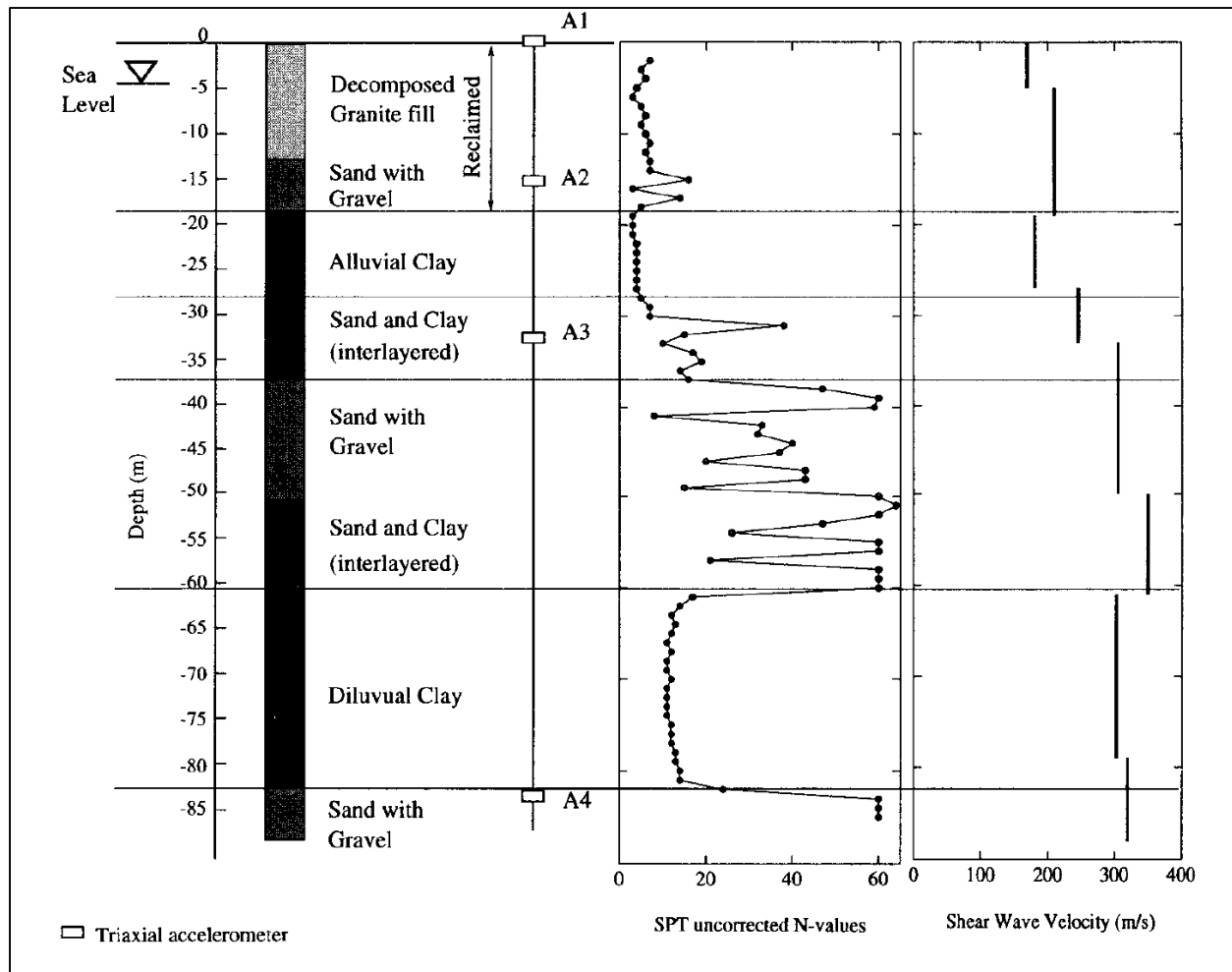


Figure 3-7: Soil profile and instrumentation at Port Island site (Elgamal et al., 1996) (after Iwasaki, personal communication, 1995)

Depth (m)	Soil type	P-velocity (km/sec)	S-velocity (km/sec)	Poisson's ratio	Location of seismometer
0-2.0	Sandy gravel	0.26	0.170	0.127	●GL-0.0 m
2.0-5.0	Sandy gravel	0.33	0.170	0.319	
5.0-12.5	Sandy gravel	0.78	0.210	0.461	
12.6-19.0	Sand with gravel	1.48	0.210	0.490	●GL-16.0 m
19.0-27.0	Alluvial clay	1.18	0.180	0.488	●GL-32.0 m
27.0-33.0	Alluvial sand	1.33	0.245	0.482	
33.0-50.0	Sand with gravel	1.53	0.305	0.479	
50.0-61.0	Diluvial sand	1.61	0.350	0.475	●GL-83.0 m
61.0-79.0	Diluvial clay	1.61	0.303	0.482	
79.0-85.0	Sand with gravel	2.00	0.320	0.487	

Figure 3-8: Soil profile for the Port Island borehole array observation station (Kobe City Development Bureau) (Shibata et al., 1996)

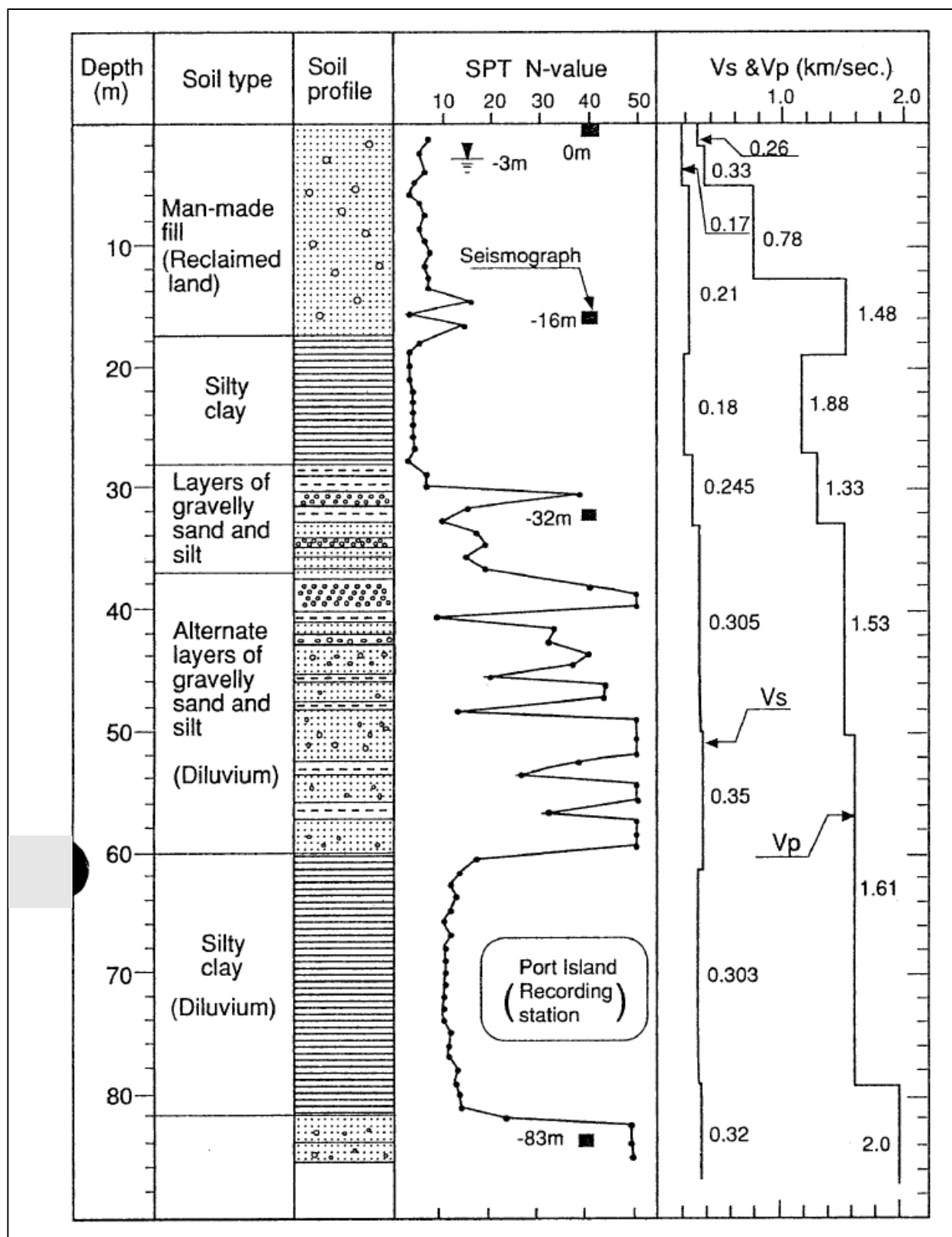


Figure 3-9: Soil profile at the site of vertical array site (Source: Toki, 1995)
(Ishihara et al., 1996)

Table 3-1: Soil profile for site response analyses at the Port Island vertical array site

Geologic Unit	Soil Layer Symbol	Depth range (meter)
Masado Fill (Water Level at ~2.4 m depth during earthquake. Source: Shibata et al., 1996)	PIF-1	0 m – 2.4m
	PIF-2	2.4 m – 5 m
	PIF-3	5 m – 13 m
	PIF-4	13 m – 19 m
Alluvial Clay (Ac)	Ma-13 (4 sub-layers)	19 m – 27 m
Alluvial Sand (As)	As (2 sub-layers)	27 m – 37 m
Diluvial Sand with Gravel (Ds1)	Ds-1A (4 sub-layers)	37 m – 50 m
	Ds-1B (3 sub-layers)	50 m – 61 m
Diluvial Clay (Ma12)	Ma-12 (6 sub-layers)	61 m – 79 m
Diluvial Sand with Gravel (Ds2)	Ds2	79 m – 83 m
Note: The Diluvial Clay (Ma12) and Diluvial Sand with Gravel (Ds2) boundary is based on the increase in S-wave velocity and SPT N-values observed at 79 meters depth.		

Based on an evaluation of available data sources, Table 3-1 was developed for these current studies, comprising six geologic units and twenty-four sub-layers. In developing the soil profile, the characteristics of Diluvial soils were also considered (see Section 3.5.5).

These current studies employ a limited set of selected analytical models, and all of them are applied within a finite difference analysis framework using the code FLAC (Fast Lagrangian Analysis of Continua; Itasca, 2011). The material behavior models employed in these analyses are listed in Table 3-2. Potentially liquefiable soil layers (e.g. the Masado fill) were modeled using Roth, UBCSAND, PM4Sand, and Wang2D constitutive models. Non-liquefiable soils used the FLAC Mohr-Coulomb model.

The principal potentially liquefiable soils were the man-placed Masado fill materials. These were comprised of excavated decomposed granitic material, with variable gradations and fines contents, that were loosely dumped through the water to raise the land surface elevation above sea level to create “reclaimed” land. The material was generally silty and sandy gravel, but the detailed compositions and gradations varied. As shown in Figures 3-7 and 3-9, SPT blow counts were very low in these materials. This, along with the shallow water table, created thick deposits of potentially liquefiable materials.

Table 3-2: Summary of analytical modeling schemes for the Port Island back-analyses to be performed.

Analysis ID	Description
Analysis 1: Roth (C,WEA)	Constitutive model for liquefiable soils – Roth Liquefaction Triggering – Cetin et al. (2018); K_{σ} – Youd et. al. (2001) Post Liquefaction Strength, S_r – Weber et al. (2015) Constitutive model for non-liquefiable soils – Mohr-Coulomb
Analysis 2: UBCSAND (Y)	Constitutive model for liquefiable soils – Roth Liquefaction Triggering and K_{σ} – Youd et al. (2001) Constitutive model for non-liquefiable soils – Mohr-Coulomb
Analysis 3: PM4Sand (I&B)	Constitutive model for liquefiable soils – PM4Sand Liquefaction Triggering and K_{σ} – Boulanger and Idriss (2014) Constitutive model for non-liquefiable soils – Mohr-Coulomb
Analysis 4: Wang2D (C)	Constitutive model for liquefiable soils – WANG2D Liquefaction triggering - Cetin et al. (2018); K_{σ} – Youd et al. (2001) Constitutive model for non-liquefiable soils – Mohr-Coulomb

Analysis 1 (with the Roth analytical model) is the only back-analysis of the Port Island vertical array site that employs a post-liquefaction residual strength relationship (in this case the post-liquefaction S_r relationship of Weber et al., 2015) because the Roth model is the only model in which transition to post-liquefaction strength (S_r) occurs incrementally (element by element, at any given time step) during shaking as seismically-induced pore pressures rise to a level where shear strength in the element drops to S_r (when $S \leq S_r$ in the element).

In the other nonlinear seismic deformation analyses performed in these current studies with the other three analytical/constitutive models (UBCSAND, PM4Sand and Wang2D) the transition to post-liquefaction strengths (S_r) occurs at a stoppage at the end of shaking; at that juncture, S_r is implemented in elements that satisfy specific criteria for transition to S_r , and the analysis is then re-started and continued after the end of strong shaking. This continuation after the end of shaking is an important element of the two-dimensional nonlinear seismic deformation analyses of the Upper and Lower San Fernando Dams presented in Chapters 4 and 5. The Port Island vertical array site is a one-dimensional (level) site response case history, therefore gravity-driven potential instability is not an issue and as a result there is no transition to S_r and no need for continuation of the analyses after the end of shaking until the site either (1) becomes statically stable, or (2) deformations and displacements become so large that re-meshing in order to continue (propagate the analysis forward) become tedious and reduce analytical accuracy, and the analysis has advanced sufficiently for purposes of both engineering evaluation and decision-making.

3.5 GEOTECHNICAL PARAMETERS FOR SITE RESPONSE ANALYSES

As presented in Table 3-1, the main soil layers at the Port Island vertical array site include (from top to bottom): (1) approximately 19 meters of Masado Fill, (2) 8 meters of alluvial clay (Ma13), (3) 10 meters of alluvial sand, and (4) 48 meters of diluvial sand with gravel and interbedded diluvial clay layers. Geotechnical parameters for these current studies were developed based on site specific data that were collected prior to the 1995 Kobe earthquake and from geotechnical and geological studies in the Osaka Bay area. The geotechnical and geophysical parameters that are required for NDA for Port Island are:

- (1) Fines contents of Masado soil,
- (2) Shear wave (S-wave) velocity and compression wave (P-wave) velocity,
- (3) SPT blow counts (N_{78} , N_{60} , $N_{1,60}$, $N_{1,60,CS}$),
- (4) Soil density, bulk modulus, shear modulus, and Poisson's ratio, and
- (5) Soil strength and consolidation parameters (ϕ' , PI, and OCR) and hydraulic conductivity

3.5.1 Fines contents for Masado fill

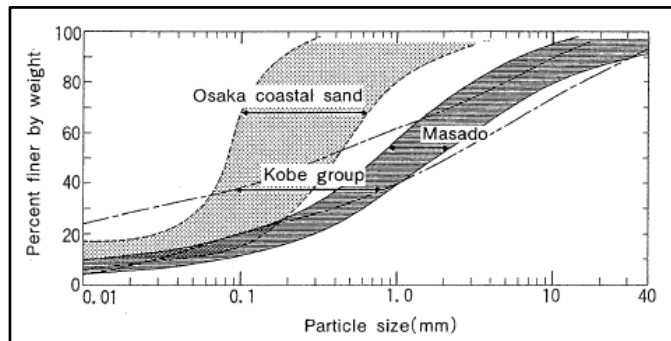
Masado fill is a granitic-origin sandy soil. This material, also known as decomposed granite (DG) soil, consists of variable mixtures of sand, gravel, and silt. Figure 3-10 shows grain size distributions of Masado soil from Shibata et al. (1996), Cubrinovski et al. (2000), and Yasuda et al. (1996). There are some differences between ranges of fines contents, as per these three papers.

Based on these different grain size distributions for Masado soil, a representative fines content of 10 percent was adopted for the current studies. Also, a representative fines content of 12 percent was adopted for the deeper sand and gravel layers.

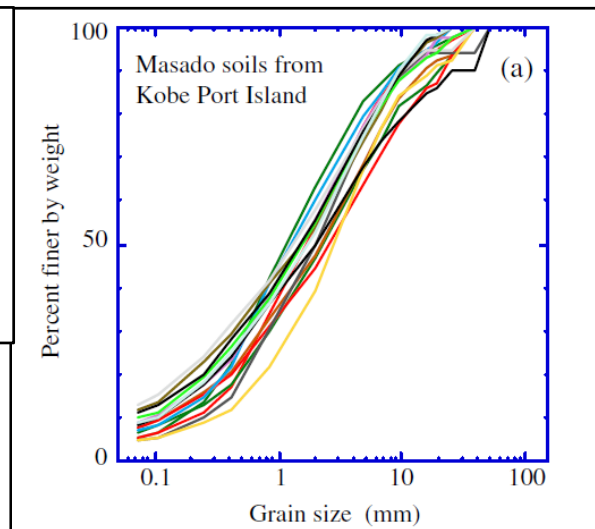
3.5.2 Shear wave (S-wave) velocity and compression wave (P-wave) velocity

S-wave and P-wave velocities at the vertical array site were measured using the downhole PS-logging method in 1991. S-wave and P-wave velocities were again measured at the vertical array site after the 1995 Kobe earthquake using downhole PS and suspension PS methods. Figure 3-11 shows profiles of P-wave and S-wave velocities at the Port Island vertical array site measured both before, and after, the earthquake.

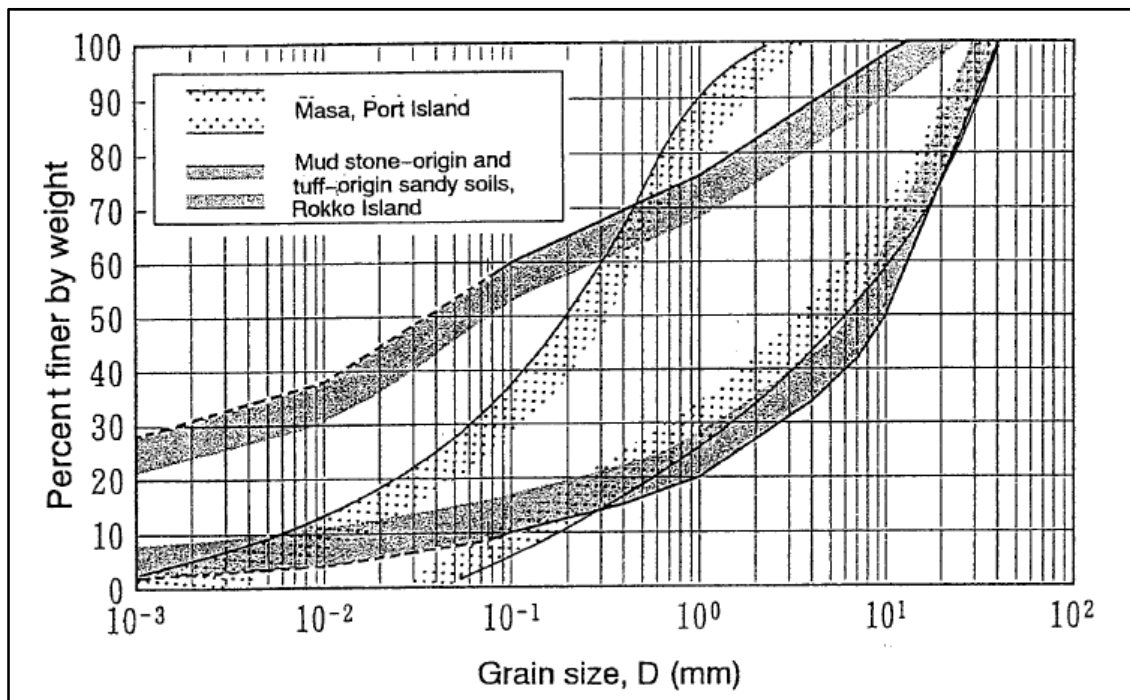
Table 3-3 presents pre-earthquake S-wave and P-wave velocities as modeled in these current studies. S-wave velocities were used in the analyses to determine initial dynamic shear moduli.



a. Grain Size distribution of Masado Soil from Shibata et al. (1996)



b. Grain size distribution of Masado soil from Kubrinovski et al. (2000)



c. Grain size distribution curves for fill soils at Port and Rokko Islands (Yasuda et al., 1996)

Figure 3-10: Grain size distributions for Masado Soil (fill soil at Port Island) from different publications

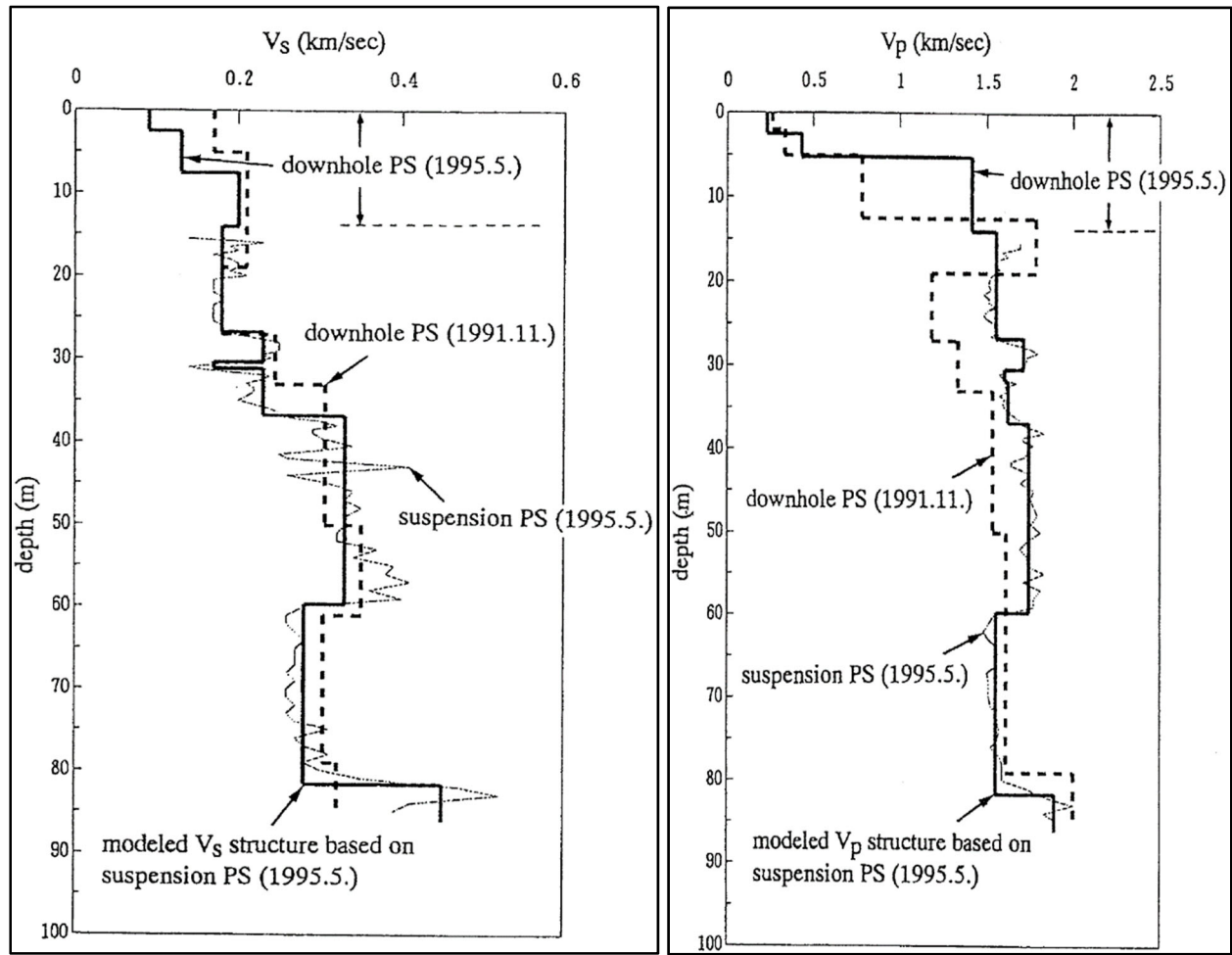


Figure 3-11: Vertical profiles of S-wave and P-wave velocity at the Port Island vertical array site. Dashed lines = pre-Kobe earthquake (1991), and solid lines = post-Kobe earthquake (1995) (Shibata et al. 1996)

Table 3-3: S-wave and P-wave velocities modeled in the different soil layers at the Port Island vertical array station

Geologic Unit	Soil Layer Symbol	Depth range (meters)	S- Wave Velocity, V_s (m/sec)	P- Wave Velocity, V_p (m/sec)	Poissons Ratio, ν
Masado Fill	PIF-1	0 – 2.4	170	260	0.127
	PIF-2	2.4 – 5	170	330	0.319
	PIF-3	5 – 13	210	780	0.461
	PIF-4	13 – 19	210	1480	0.490
Alluvial Clay (Ac)	Ma-13	19 – 27	180	1180	0.488
Alluvial Sand (As)	As-1A	27 – 33	245	1330	0.482
	As-1B	33 – 37	305	1530	0.479
Diluvial Sand with Gravel (Ds1)	Ds-1A	37 – 50	305	1530	0.479
	Ds-1B	50 – 61	350	1610	0.475
Diluvial Clay (Ma12)	Ma-12	61 – 79	303	1610	0.482
Diluvial Sand with Gravel (Ds2)	Ds2	79 – 83	320	2000	0.487

3.5.3 SPT blow counts (N_{78} , $N_{1,60}$, $N_{1,60,CS}$)

Figures 3-7 and 3-9 show distributions of SPT-N values measured at the Port Island vertical array site prior to the 1995 Kobe earthquake. SPT N-values were also measured after the 1995 Kobe earthquake. Figure 3-12 shows SPT N-values prior to and after the 1995 Kobe earthquake. As shown in Figure 3-12, due to the occurrence of liquefaction and the outflow of pore water and resulting re-consolidation, the Masado fill soils were densified somewhat, and consequently the SPT N-values increased (Shibata et al., 1996).

The Japanese SPT-N values were obtained using a higher SPT hammer energy ratio of about 78 percent (a commonly assumed energy ratio used in Japan). In these current studies, SPT N-values were converted to U.S. standard SPT-N values with 60 percent energy ratio, and then converted to $N_{1,60}$ and to $N_{1,60,CS}$ in accordance with the energy, equipment, procedural, and fines content corrections of each of the liquefaction triggering relationships used in these Port Island array back-analyses. Table 3-4 presents measured N_{78} , computed $N_{1,60}$, and the corrected $N_{1,60,CS}$ values developed using the corrections of the (1) Youd et al. (2001), (2) Boulanger and Idriss (2014), and (3) Cetin et al. (2018) liquefaction triggering relationships. Median SPT $N_{1,60,CS}$ values were used for the back-analyses of the Port Island vertical array site in these current studies.

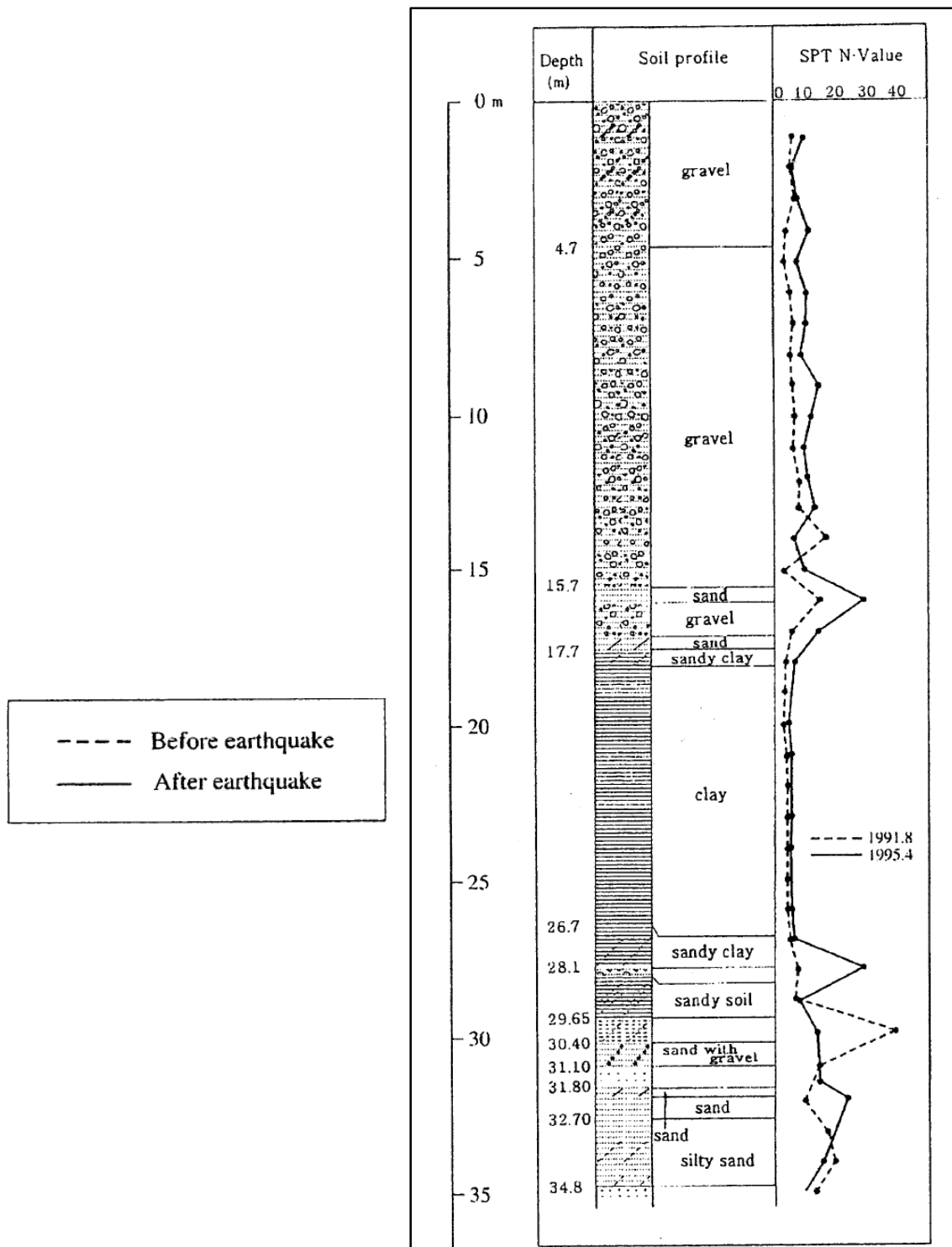


Figure 3-12: Distribution of N-values before and after the 1995 Kobe earthquake (Shibata et., 1996)

Table 3-4: SPT $N_{1,60,CS}$ values developed for use in each of the three different liquefaction triggering relationships employed in these current studies

Soil Layer	Total Unit Weight and Fines Content (%)	Median SPT Blow Counts with 78% Energy Ratio, N_{78}	Youd et al. (2001) Liquefaction Triggering Relationship		Boulanger and Idriss (2014) Liquefaction Triggering Relationship		Cetin et al. (2018) Liquefaction Triggering Relationship	
			$(N_1)_{60}$	$N_{1,60,CS}$	$(N_1)_{60}$	$N_{1,60,CS}$	$(N_1)_{60}$	$N_{1,60,CS}$
PIF-1 (above WT) and PIF-2	10	6.0	9.2	10.3	9.6	10.7	8.9	10.0
PIF-3	10	6.0	7.7	8.7	7.6	8.8	7.7	8.7
PIF-4	10	10.0	10.1	11.1	9.8	11.0	10.1	11.1
Ma13	95	4.0	3.5	9.3	3.2	8.7	3.5	6.9
As	12	14.5	11.3	13.2	10.9	13.0	11.3	12.6
Ds-1A	12	40.0	26.5	28.8	32.7	34.8	26.5	28.1
Ds-1B	12	60.0	34.8	37.5	56.4	58.5	34.8	36.6
Ma12	95	12.0	6.3	12.6	5.2	10.7	6.3	9.8
Ds-2	12	60.0	29.9	32.4	50.3	52.4	29.9	31.6

Table 3-5: Soil unit weight for these current studies

Soil Layer	Unit Weight (kN/m^3)
PIF-1	18.1
PIF-2	18.9
PIF-3	18.9
PIF-4	19.3
Ma13	14.9
As-1A	19.2
As-1B	19.2
Ds-1A	19.5
Ds-1B	19.5
Ma12	15.7
Ds-2	19.5

3.5.4 Soil Strength and Consolidation Parameters

The soil strength parameters (effective friction angle, ϕ') for Masado fill layers were estimated using the Hatanaka and Uchida (1996) relationship based on SPT-N values. The soil strength parameters for the deeper sand and gravel layers were estimated using the effective stress correction factors (Duncan and Wright, 2005 and Wong and Duncan, 1994) to account for high effective overburden stress effects. The following equations were used for estimating effective friction angle, ϕ' for Masado fill and for alluvial and diluvial sand and gravel layers.

$$\phi' = 20^\circ + [15.4(N_1)_{60}]^{0.5} \quad \text{Equation 3-1 (Hatanaka and Uchida, 1996)}$$

$$\phi' = \phi_0 - \Delta\phi \log_{10} \sigma_3' / \text{Pa} \quad \text{Equation 3-2 (Wong and Duncan, 1974)}$$

where: $\phi_0 = \phi'$ at 1 atmosphere confining pressure, and

$\Delta\phi$ = reduction in ϕ' for a ten-fold increase of effective confining pressure, σ_3' [$\sim 6^\circ$ for As and $\sim 8^\circ$ for Ds1 and Ds2]

Two clay soil units are present at the Port Island vertical array site within the depth to the deepest instrument location. These layers are a shallower Alluvial clay (Ma13 or Ac) and a deeper Diluvial clay (Ma12). The Ma13 layer extends from 19 meters to 27 meters depth, and the Ma12 layer extends from 61 meters to 79 meters depth.

Figure 3-13 shows a soil profile of Osaka Bay with water contents and Atterberg limits, void ratio, and yield stress of four clay units (Ma13 or Ac, Ma12, Ma11, and Ma10). These diluvial layers (Ma13 to Ma10) were deposited between 10,000 and 200,000 years ago. The liquid limits of these layers range between 80 and 130 percent, and the plastic limits range between 30 and 45 percent. The water content (w_o) profile in each layer shows a bow-like shape, with higher water contents in the center portions of the layers. Akai et al. (1991) postulated that this variation of water contents is due to the changes of the sea water level in geological time. During the high glacial epoch, the sea water level had been low and coarser-grained clays with low plasticity or sand had been deposited, while in the interglacial epoch, the sea water level had been high and finer-grained clays with high plasticity had been deposited. As a result, Akai et al. (1991) noted that the plasticity tends to change with depth due to the cyclic repetition of the glacial and the interglacial epochs.

Akai et al. (1991) also noted that (1) marine clay layers at greater depths tend to become denser and their water contents tend to become lower on the whole, due to prolonged consolidation and secondary compression under large overburden stresses for a long period of time, but that (2) the water contents of the diluvial clay layers in Osaka Bay vary between 50 percent and 80 percent, and there is no pronounced trend of decreasing water contents with depth when comparing Ac with Ma12, Ma11, and Ma10. The void ratio profile also follows a similar trend. Akai et al. (1991) considered this behavior likely to be caused by cementation bonding. As the mechanical strength of clay increases due to the development of cementation bonding, the diluvial clay layers in Osaka Bay have largely preserved their water contents and prevented significant additional decrease of voids.

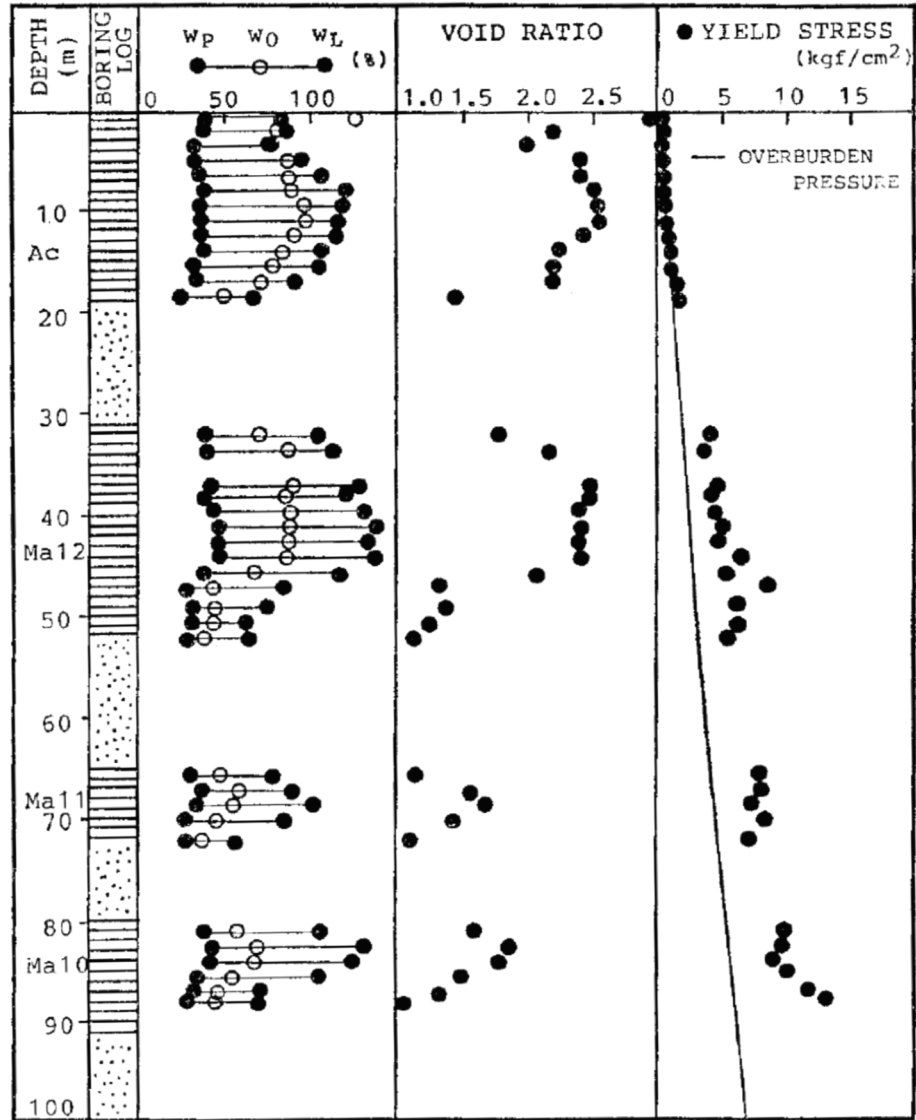


Figure 3-13: Soil profile of Osaka Bay with water contents, Atterberg limits, void ratio, and yield stress (Akai et al., 1991)

Based on the above discussions of Alluvial clay and Diluvial clay characteristics, it can be concluded that near the top and bottom edges of the Ac and Ma12 layers, the strength would be slightly higher than in the center portions of the layers. The consolidation parameters of Ma13 and Ma12 layers were estimated based on an evaluation of characteristics of Osaka Bay clay.

Table 3-6 presents shear strength and consolidation parameters for these current studies. Shear strengths of clayey soils were modeled with 20 percent strength reduction to account for cyclic degradation during strong shaking. Table 3-7 presents hydraulic conductivity and porosity values for these current studies.

Table 3-6: Shear strength and consolidation parameters for these current studies

Soil Layer	Effective Friction Angle, ϕ'	Effective Friction Angle, ϕ' Using Effective Stress Reduction Factor	Plasticity Index, PI	Overconsolidation Ratio, OCR
PIF-1and PIF-2	31.7			
PIF-3	30.9			
PIF-4	32.4			
Ma13			50	19 to 21 meters: OCR=1.6, and $S_u/P = 0.268$ 21 to 25 meters: OCR=1.5, and $S_u/P = 0.255$ 25 to 27 meters: OCR=1.6, and $S_u/P = 0.268$ [Shear strengths by SHANSEP, using 20 percent strength reduction]
As-1A	33.2	30.7		
As-1B	33.2	30.3		
Ds-1A	40.4	Ds1A-1: 36.0 Ds1A-2: 35.7 Ds1A-3: 35.4 Ds1A-4: 35.1		
Ds-1B	43.2	Ds1B-1: 37.8 Ds1B-2: 37.5 Ds1B-3: 37.3		
Ma12			60	61 to 63 meters: OCR=1.6, and $S_u/P = 0.335$ 63 to 77 meters : OCR=1.5, and $S_u/P = 0.318$ 77 to 79 meters: OCR=1.7, and $S_u/P = 0.352$ [Shear strengths by SHANSEP, using 20 percent strength reduction]
Ds-2	41.5	34.9		

Table 3-7: Hydraulic conductivity and porosity for these current studies

Soil Layer	Porosity	Horizontal Hydraulic Conductivity, k_h (cm/sec)	Vertical Hydraulic Conductivity, k_v (cm/sec)	Anisotropy Ratio (k_h/k_v)	Basis or Rationale for Hydraulic Conductivity Value Selection
PIF-1	0.50	1.21E-02	3.03E-03	4	Using Chapuis (2004) Equation for $d_{10}=0.11\text{mm}$
PIF-2	0.45	1.21E-02	3.03E-03	4	
PIF-3	0.45	1.21E-02	3.03E-03	4	
PIF-4	0.45	1.21E-02	3.03E-03	4	
PIF-5	0.42	1.21E-02	3.03E-03	4	
Ma13	0.69	3.38E-06	8.44E-07	4	Mesri and Funk (2015)
As-1A	0.50	2.13E-02	5.32E-03	4	Jang and Mimura (2005) and Mimura and Jang (2004)
As-1B	0.43	2.13E-02	5.32E-03	4	
Ds-1A	0.41	2.13E-02	5.32E-03	4	
Ds-1B	0.41	2.13E-02	5.32E-03	4	
Ma12	0.64	3.5E-07	8.7E-08	4	Mesri and Funk (2015)
Ds-2	0.41	1.00E-04	2.50E-05	4	Mimura et. al. (2003)

3.6 GROUND MOTION TIME HISTORIES FOR SITE RESPONSE ANALYSES

3.6.1 Fault Mechanism of Kobe Earthquake

The fault slip model of the 1995 Kobe earthquake indicates strike-slip movement along Nojima fault plane southwest of the epicenter and on the Suma fault plane northeast of the epicenter. The Kobe earthquake produced a 9 km long surface break with maximum right-lateral slip of 1.9 meters along the Nojima fault on Awaji Island, and no significant observable surface ruptures on the main island, probably because of the thick sedimentary strata overlying bedrock around the Osaka Bay (Li et al., 1998). Li et al. (1998) also suggested that the main shock nucleated on the southwest end of Suma fault with bilateral faulting, and between the two rupture planes there is an offset near the epicenter. Wald (1996) presented a slip model using two planar rupture planes, the southwestern plane (Nojima) is 20 km long and dips 80° to southwest, and the northwestern plane (Suma) is 40 km long and dips 85° to northwest. Port Island is within 5 km of the Suma fault in the transverse direction, and so would likely be subject to near source directivity effects. Figure 3-14 shows faults in the Port Island area with main shock epicenter of the 1995 Kobe earthquake (Li et al. 1998).

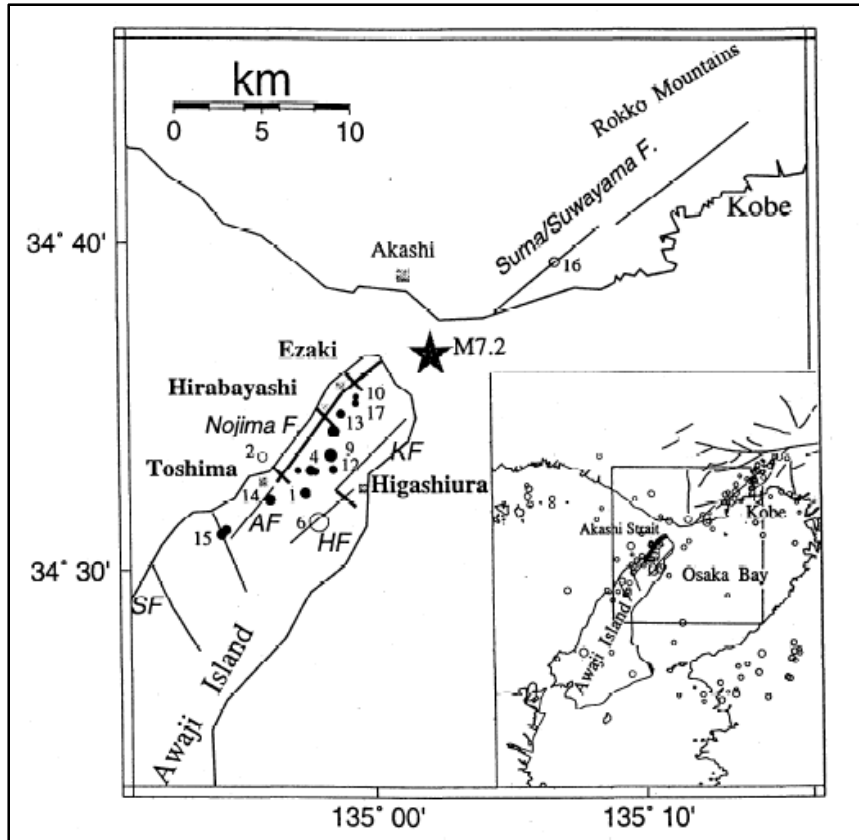


Figure 3-14: Map showing faults in the Port Island area. The star denotes the mainshock epicenter; the Nojima fault is denoted by thick lines, AF=Asano fault, HF=Higashiura fault, KF=Kusumoto fault, and SF=Shichiku fault. (Li et al., 1996)

3.6.2 Ground Motions at the Port Island Vertical Array Site

Ground motions were recorded at the Port Island Vertical Array site during the 1995 Kobe Earthquake. Four sets of seismometers were located at the ground surface, and at depths 16 meters, 32 meters, and 83 meters.

Shibata et al. (1996) corrected an azimuthal orientation error for the record at 83 meters depth. They observed that the main direction (and largest displacement pulse) of the earthquake is about 30 degrees counterclockwise from the north. This direction is largely orthogonal to the main fault which strikes at 51 to 58 degrees clockwise from north direction. Shibata et al. (1996) also suggested that this fact is consistent with the anticipated direction based on the double couple theory of faulting. It indicates a strong fault-normal component perhaps due to rupture directivity. Based on these observations, they concluded that the orientation of the seismometer pair at 83 meters depths was inadvertently rotated 22 degrees clockwise in a horizontal direction from the direction originally reported. Figure

3-15 shows recorded displacement orbits at 4 depths including the corrected (re-oriented) record for the horizontal seismometer pair at 83 meters depth. Figures 3-15(a), (b), (c) and (d) present the displacement orbits as originally reported, and Figure 3-15(e) shows the displacement orbits for the corrected (re-oriented by 22 degrees) instrument pair recording at a depth of 83 meters. It is clear that Shibata et al. (1996) are correct, and that the recordings at 83 meters must be re-oriented by 22 degrees of azimuthal rotation to serve as “input” motions for site response analyses (back-analyses) of the Port Island vertical array.

Figure 3-16 shows acceleration time histories from the 4 pairs of horizontal seismometers (and the 4 co-located vertical seismometers) at the Port Island Array site, processed to produce motions in three orthogonal directions: N-S, E-W, and vertical. The motions at 83 meters depth have been azimuthally rotated by 22 degrees. In these current studies, the ground motion records used were obtained from Professor Laurie Baise of Tufts University, who utilized these records in her dissertation at the University of California, un-

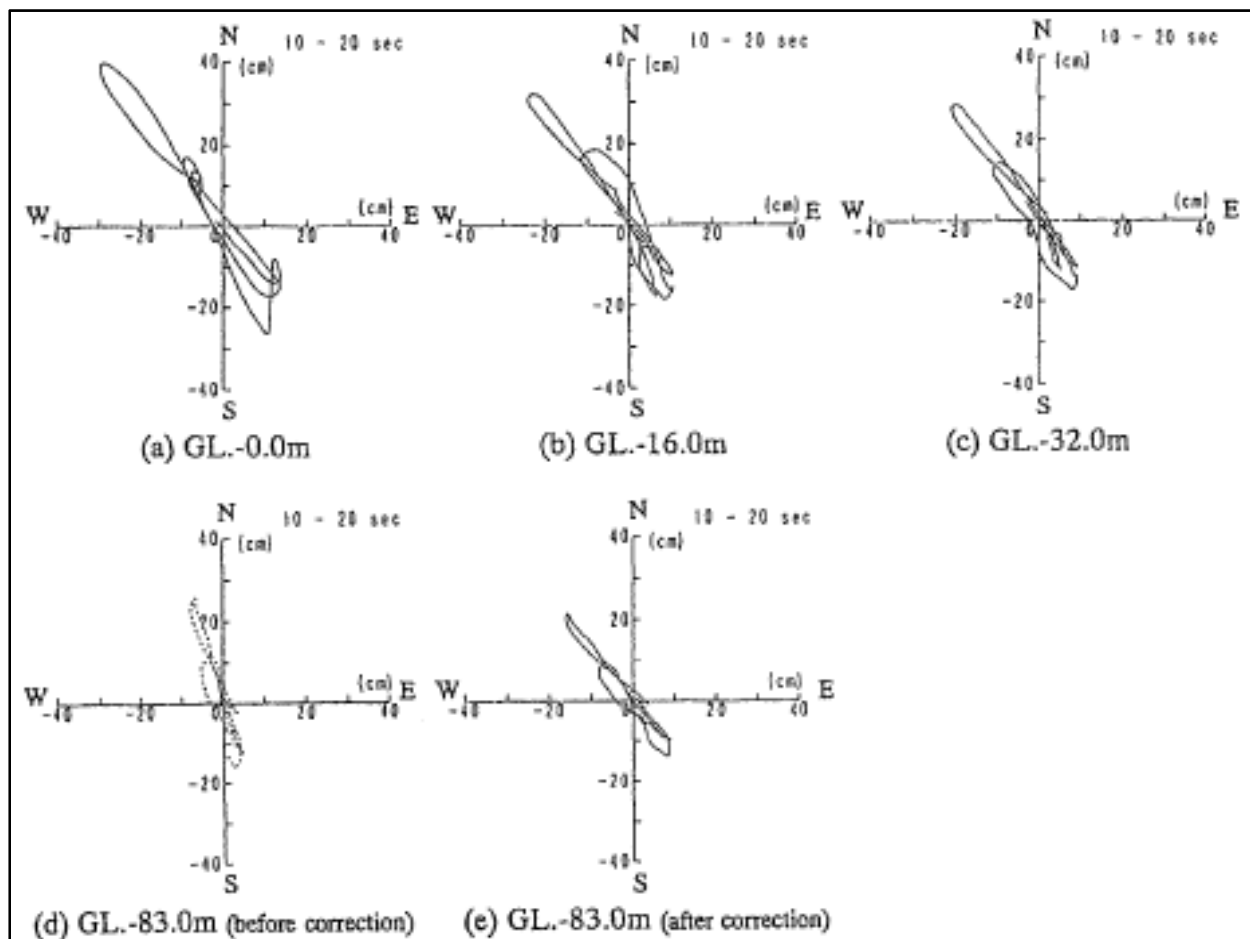


Figure 3-15: Displacement orbits at seismometer pair locations (Shibata et al., 1998)

der the supervision of Professor Steven Glaser (Baise 2000). Professor Baise (2000) obtained the ground motion records from Kobe Development Bureau and the Port and Harbor Research Institute.

Table 3-8 presents a comparison of peak ground acceleration (PGA) values at a depth of 83 meters in (1) the north-south direction, and (2) the east-west directions of processed records employed as “input” motions by Shibata et al. (1996), Ansari et al. (1997), and Baise (2001). Shibata et al. (1996) and Ansari et al. (1997) discussed the rotation of ground motion records at 83 meters depth by 19 to 22 degrees to align the motions in the four sets of motions (at four depths) in the north-south and east-west directions; the same directions of the instrumental motions recorded at (1) the ground surface, (2) at 16 meters depth, and (3) at 32 meters depths. PGA values of the “input” motions at a depth of 83 meters in the north-south direction for these three studies were $a_{\max} = 0.537, 0.572$ and 0.549 , respectively, and PGA values in the east-west direction were $a_{\max} = 0.496, 0.466$ and 0.480 , respectively. The minor differences between the three studies are the result of different details with regard to processing and baseline correction of the original records, etc.

However, it appears that a number of researchers have utilized the un-corrected (un-rotated) motions at 83 meters for analyses, and then incorrectly compared the results with recorded motions in north-south and east-west directions. Table 3-9 presents a comparison of peak ground acceleration (PGA) values at a depth of 83 meters in (1) the north-south direction, and (2) the east-west direction of processed but un-rotated records employed as “input” motions at a depth of 83 meters by Iwasaki and Tai (1996), Sato et al. (1996), and Ziotopoulou et al. (2012). who did not indicate any rotation of recorded ground motions at 83 meters depth to align these motions in the north-south and east-west directions. PGA values of the “input” motions at a depth of 83 meters in the north-south direction for these three studies were $a_{\max} = 0.692, 0.692$ and 0.692 , respectively, and PGA values in the east-west direction were $a_{\max} = 0.309, 0.309$ and 0.309 , respectively.

The six sets of investigation teams listed in Tables 3-8 and 3-9 are not a fully comprehensive list of investigation teams that have back-analyzed the Port Island vertical array site response case history; this case history has been investigated and back-analyzed by a larger number of researchers.

In these current studies, an additional evaluation was performed to determine the direction of maximum PGA, which would likely align reasonably closely with the fault perpendicular direction of the strike-slip fault. The ground motions recorded at each depth (after rotating the deepest motion at 83 meters depth by 22 degrees) in the north-south and east-west directions were utilized to obtain rotated motions at directions of between 51 degrees and 58 degrees measured clockwise from north. This range of directions are approximate directions of the fault normal directions (Shibata et al, 1996). With rotation of ground motions between N51E and N58E, it was determined that the maximum PGA is likely in the direction of approximately N51E. The PGA at N51E (fault normal) is about $0.74g$ and the PGA at N39W (fault parallel) is about $0.33g$. The three liquefaction triggering relation-

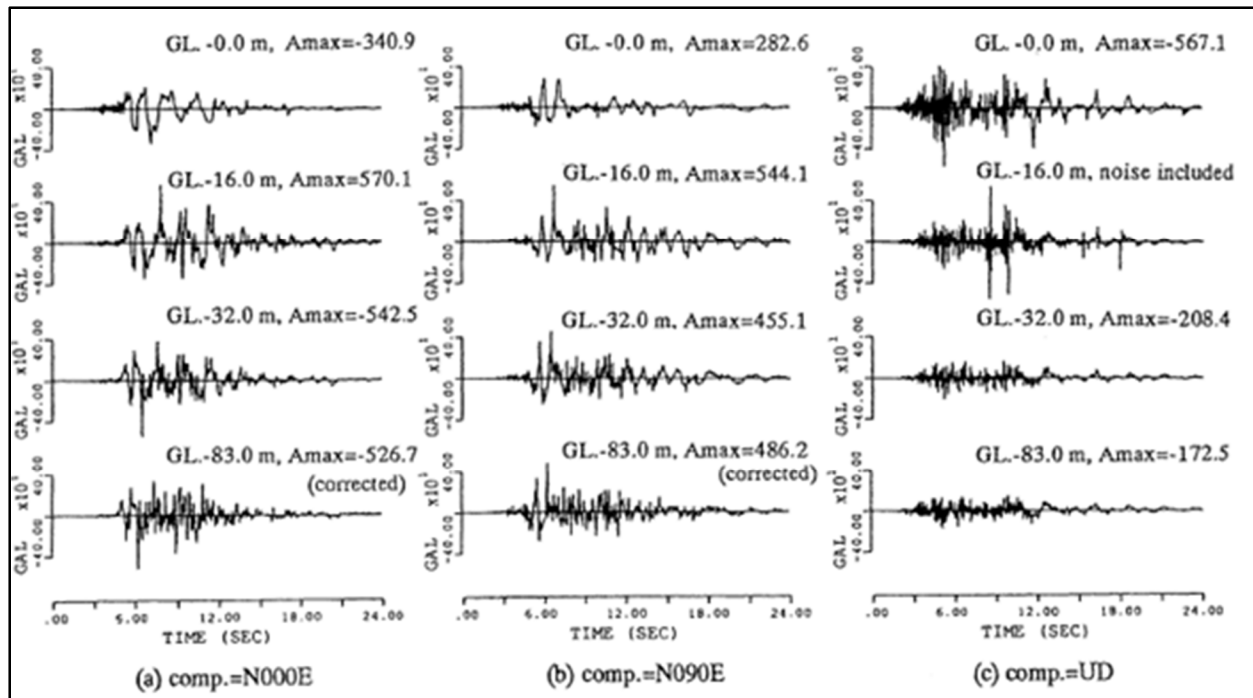


Figure 3-16: Acceleration Time Histories Recorded at the Port Island Vertical Array Site (Shibata et al. 1996)

Table 3-8: Comparison of PGA values from different studies with azimuthal rotations (by 22 degrees) of horizontal ground motions recorded at a depth of 83 m.

	Shibata et al. (1996) (22 degrees rotation of ground motion record at 83 meters)			Ansari et al. (1997) (19 degrees rotation of ground motion record at 83 meters)			Ground Motions Records for this Study (Data from Professor Laurie Baise, personal communication)		
Depth (meters)	North- South	East- West	Up- Down	North- South	East- West	Up- Down	North- South	East- West	Up- Down
83	0.537	0.496	0.176	0.572	0.466	-	0.549	0.480	0.206

Table 3-9: Comparison of PGA values from three different studies without rotations of horizontal ground motions recorded at a depth of 83 m.

	Iwasaki and Tai (1996)			Sato et l. (1996)			Ziotopoulou et al. (2012)		
Depth (meters)	North- South	East- West	Up- Down	North- South	East- West	Up- Down	North- South	East- West	Up- Down
83	0.692	0.309	0.190	0.692	0.309	0.191	0.692	0.309	-

ships employed in these current studies (e.g. Cetin et al. (2018)) all utilize geometric mean of PGA in two orthogonal directions. The geometric mean of the ground motions recorded at 83 meters depth at the Port Island vertical array site is approximately 0.49g.

Noting that (1) the (rotated) recorded ground motions at 83 meters in the north-south direction (0.56g) and east-west direction (0.48g) are both close to geometric mean (0.49g), and (2) the north-south direction has the slightly larger of the two PGA's, the nonlinear seismic “deformation” analyses performed as one-dimensional site response analyses (with seismic pore pressure generation included) for these current studies were performed utilizing the recorded motions at 83 meters depth, rotated to the north-south direction. The analytical results will be compared to the recordings obtained at depths of 0 meters, 16 meters, and 32 meters, also in the north-south direction.

3.6.3 Ground Motion Processing for the Current Study

The ground motion records were processed for these current studies using the software package Seismosignal (Seismosoft, 2018). The approach for ground motion processing was developed based on recommendations by Professor Norman Abrahamson of U.C. Berkeley (personal communication, 2018). The ground motion processing was performed in accordance with the following procedure.

- 1) High Pass Filter: A Fourier Amplitude Spectra (FAS) was developed using the uncorrected N-S ground motion. At low frequencies, the FAS should approach a slope of 2 (on a log-log scale) and any flattening of slope at lower frequencies indicate noise. Based on an evaluation of the FAS at 83 meters depth it was found that the slope approaches about 2 at frequencies between 0.04 Hz and 0.15 Hz. The slope flattens at frequencies lower than about 0.04 Hz, which indicates noise. Considering that a higher frequency for filtering may change the corner frequency (also discussed in Chapter 4), the ground motions at Port Island vertical array site were processed using a high Butterworth-type high pass filter of 0.04Hz.
- 2) The low pass filter (Anti-Aliasing filter) is usually selected at 80 percent of Nyquist frequency. The Nyquist frequency of the ground motion records at Port Island is 50 Hz based on a sample rate of 0.01 seconds (Nyquist frequency = $0.5 \times$ sampling rate frequency). This indicates that the anti-aliasing filter of the ground motion record would be set at 40 Hz. Therefore, no low pass filter was used considering that the records were already low-pass filtered before they were digitized.
- 3) The baseline correction procedure in Seismosignal consists of determining through regression analysis (least squares fit method), the polynomial method that best fits the time acceleration pairs of values, and then subtracting from the actual acceleration values their corresponding counterparts as obtained with the regression-derived equation (Seismosoft, 2018). In this way, spurious baseline trends are removed from displacement time history. It should be noted

that the available ground motion records at Port Island were not suitable for use to try to directly evaluate permanent offset, as the ground motion records had already been processed with a low-pass filter.

Figures 3-17 through Figure 3-20 show ground motion time histories (1) at the ground surface, (2) at 16 meters depth, (3) at 32 meters depth, and (4) at 83 meters depths.

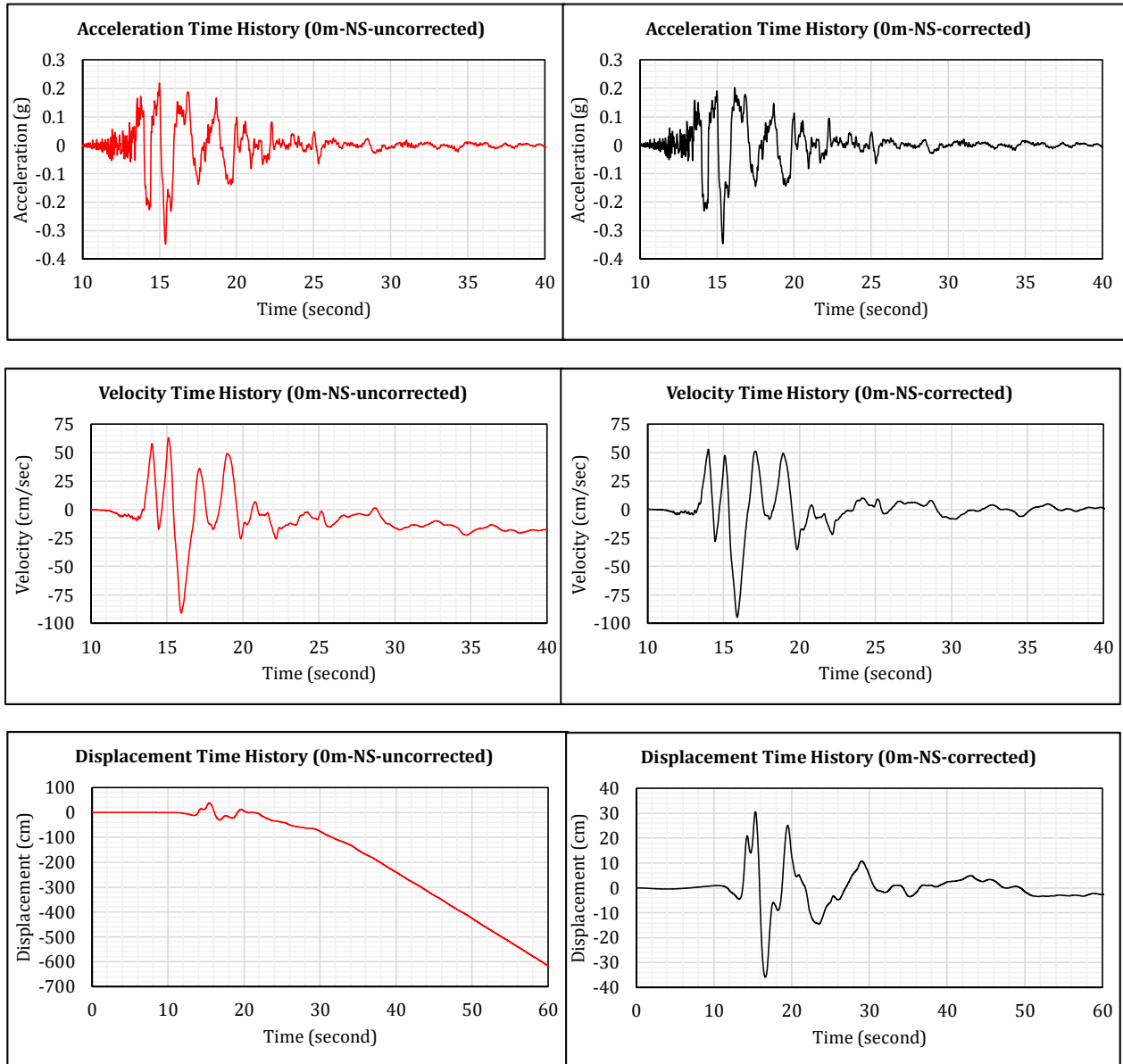


Figure 3-17: Port Island vertical array site ground motion time histories recorded at the ground surface (a) left column – without correction, and (b) right column – with baseline correction and filtering, during the 1995 Kobe earthquake

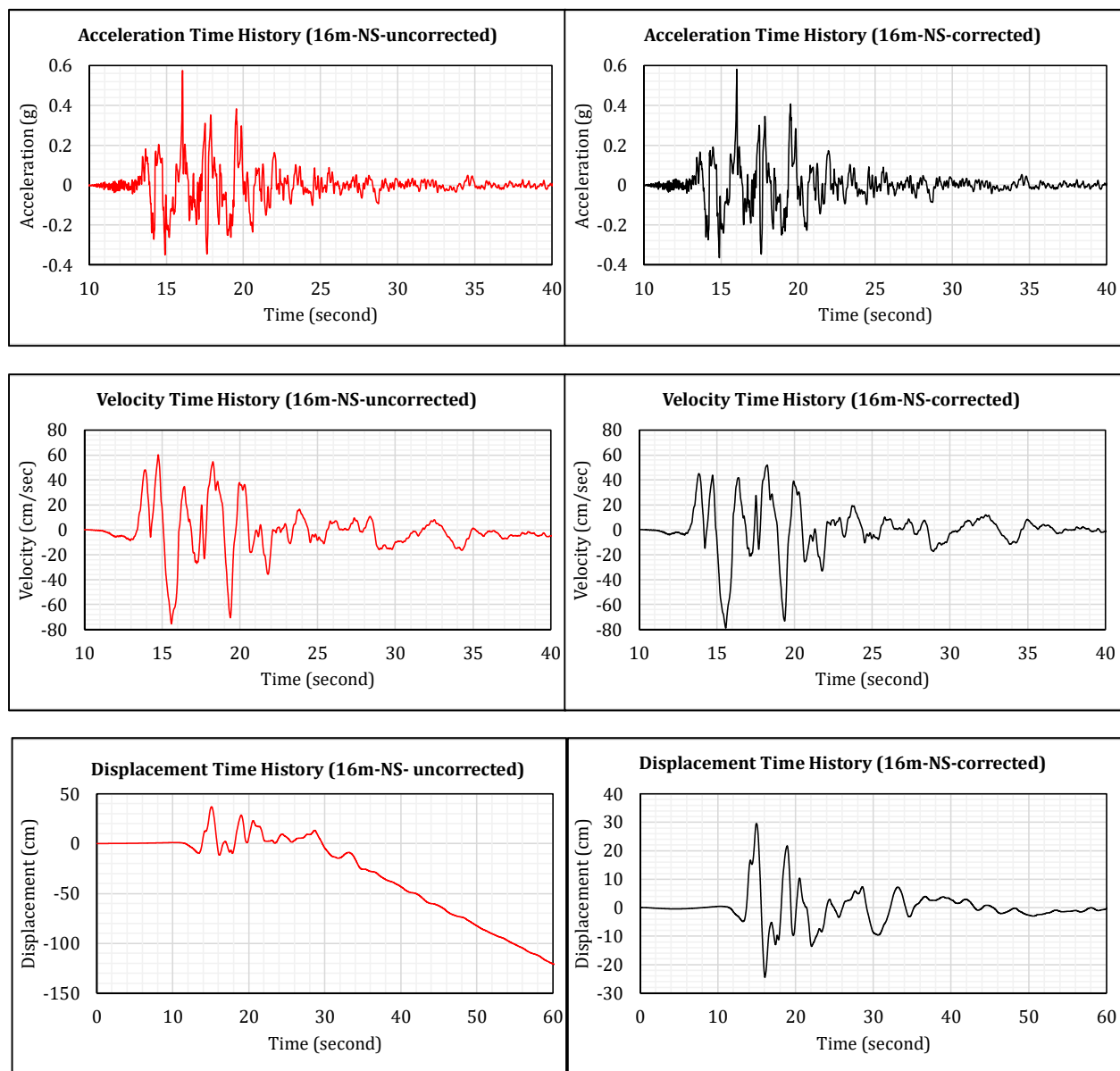


Figure 3-18: Port Island vertical array site ground motion time histories recorded at 16 meter depth (a) left column – without correction, and (b) right column – with baseline correction and filtering, during the 1995 Kobe earthquake

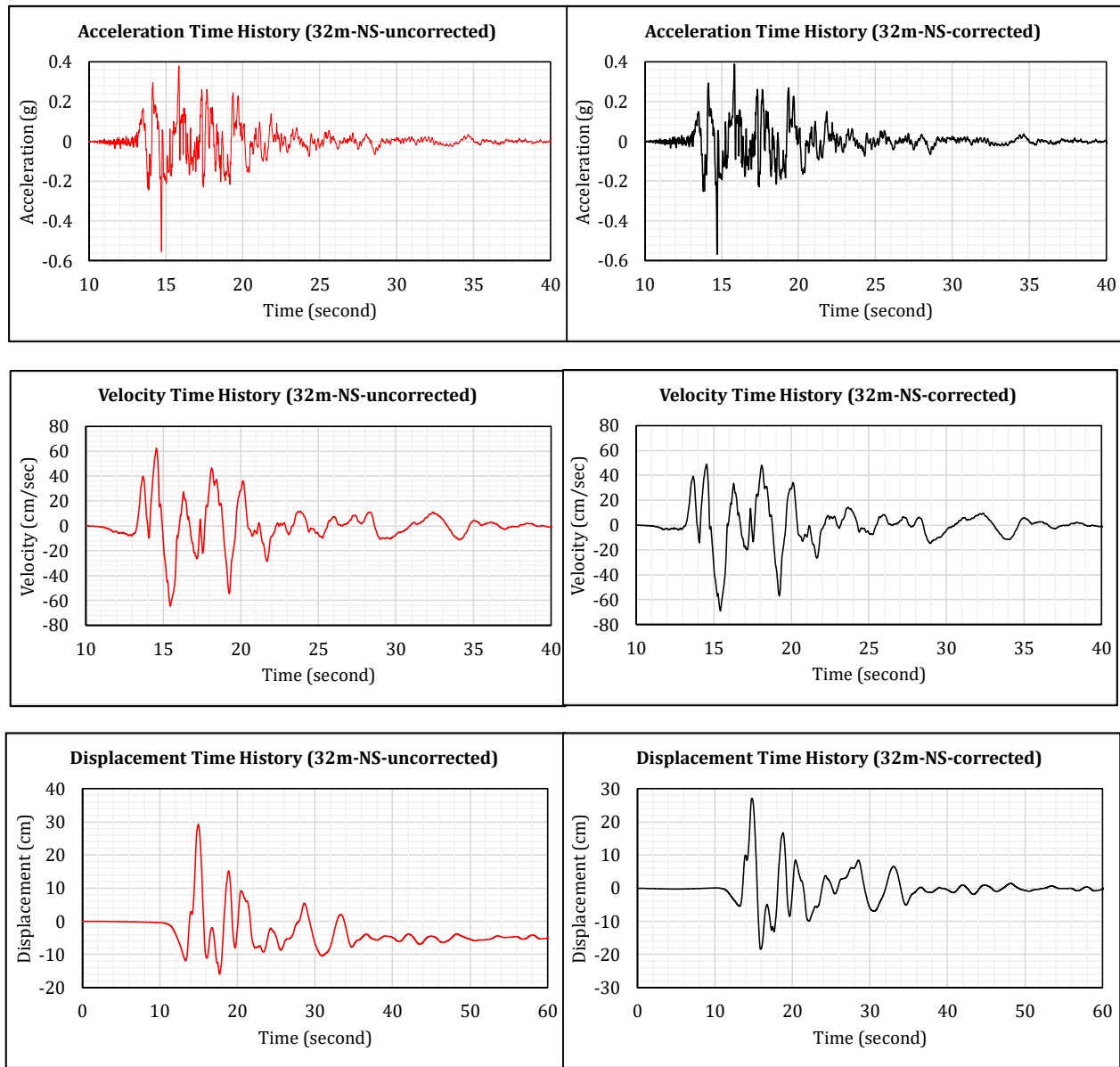


Figure 3-19: Port Island vertical array site ground motion time histories recorded at 32 meters depth (a) left column – without correction, and (b) right column – with baseline correction and filtering, during the 1995 Kobe earthquake

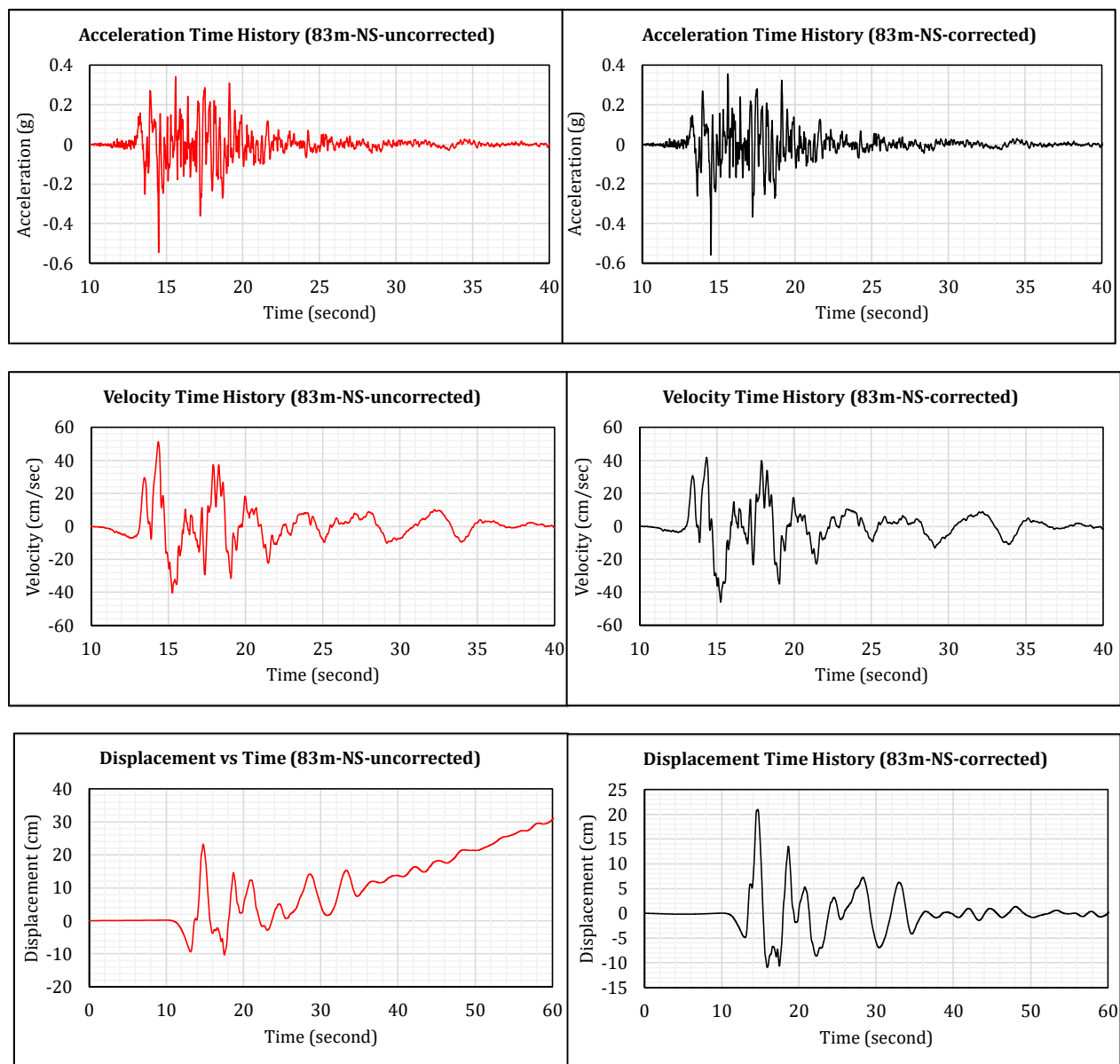


Figure 3-20: Port Island vertical array site ground motion time histories recorded at 83 meters depth (a) left column – without correction, and (b) right column – with baseline correction and filtering, during the 1995 Kobe earthquake

3.7 PREVIOUS STUDIES OF PORT ISLAND

The Port Island vertical array site case history has been analyzed by many researchers. The analyses can be grouped into three main groups based on the stated purposes of the investigations: (1) to understand the liquefaction characteristics phenomena from the recorded ground motions, (2) to evaluate the performance of 1-dimensional site response analysis schemes, and (3) to evaluate the performance of commonly used constitutive models for potentially liquefiable soils in predicting ground motion characteristics, as recorded in the Port Island vertical array site.

The focus of these current studies is in line with the third group of comparative studies. In these current studies, back-analyses of the seismic performance of (1) the Upper San Fernando Dam, and (2) the Lower San Fernando Dam during the 1971 San Fernando earthquake will be performed using different combinations of (1) four different analytical or constitutive models, (2) three different soil liquefaction triggering relationships, and (3) three different post-liquefaction residual strength (S_r) relationships. Before advancing to the more complicated two-dimensional back-analyses of the well-documented performance of these two dams during the 1971 San Fernando earthquake, it is important to also take advantage of the unusual opportunity provided by the Port Island vertical array recordings to evaluate the ability of the four different analytical or constitutive models used in these current studies to suitably back-analyze the recorded behaviors of the Port Island vertical array during the 1995 Kobe earthquake.

Three previous studies have been identified as particularly useful in this regard. These are (1) Wang et al. (2001), (2) Ziotopoulou (2010) and Ziotopoulou, et al. (2012), and (3) Gingery (2014).

3.7.1 Wang et al. (2001)

Wang et al. (2001) used the computer program SUMDES (Li et al., 1992) to perform fully nonlinear 3-dimensional site response analyses for the Port Island vertical array site. Wang et al. (2001) used a slightly older and 3-D version of the Wang2D constitutive model used in these current studies. This is a hypo-plasticity model that operates in 3-dimensional space, and it is an older and three-dimensional version of the Wang2D constitutive model utilized in these current studies.

Wang et al. (2001) obtained a very good match with the recorded ground motions (1) at the ground surface, (2) at a depth of 16 meters, and (3) at a depth of 32 meters. Figures 3-21 and 3-22 show comparisons between recorded and calculated motions at the ground surface in (1) the north-south, and (2) the east-west directions, respectively. Agreement between the analytical results, and the actual recordings is very good. It should be noted, however, that Wang et al. (2001) utilized the recorded ground motions at 83 meters depth as input motions without a 22 degrees counter-clockwise rotation, slightly diminishing the value of this comparison. Nonetheless, this was an impressive match, achieved with a fully three-dimensional analysis and a fully three-dimensional constitutive model.

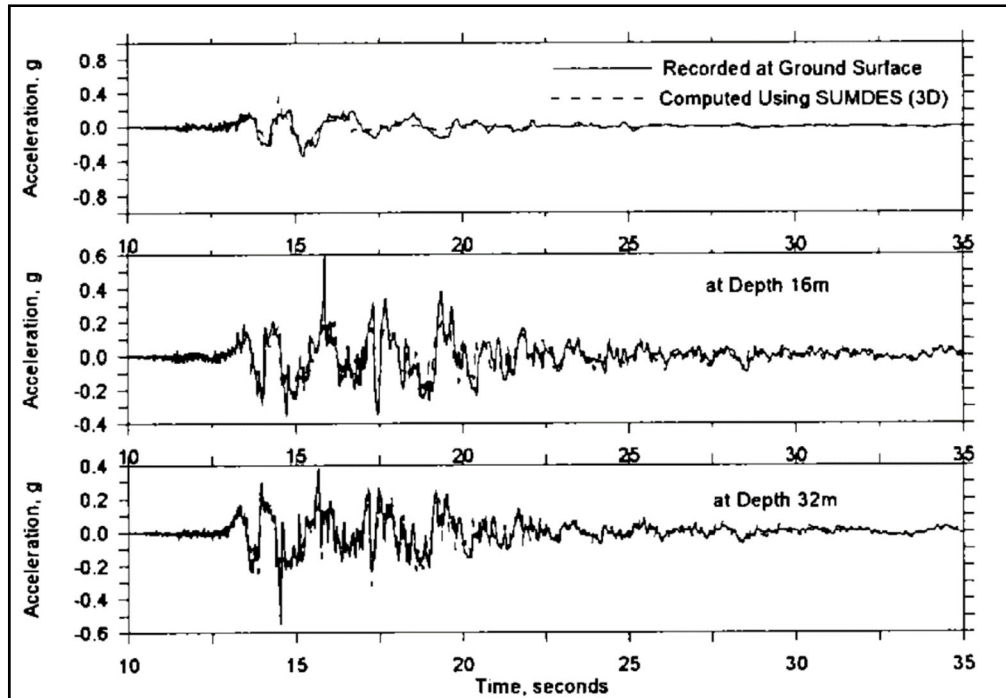


Figure 3-21: Comparison between calculated and recorded motions at the ground surface, and at depths of 16 m and 32 m, at the Port Island vertical array site in the north-south direction (Wang et al., 2001)

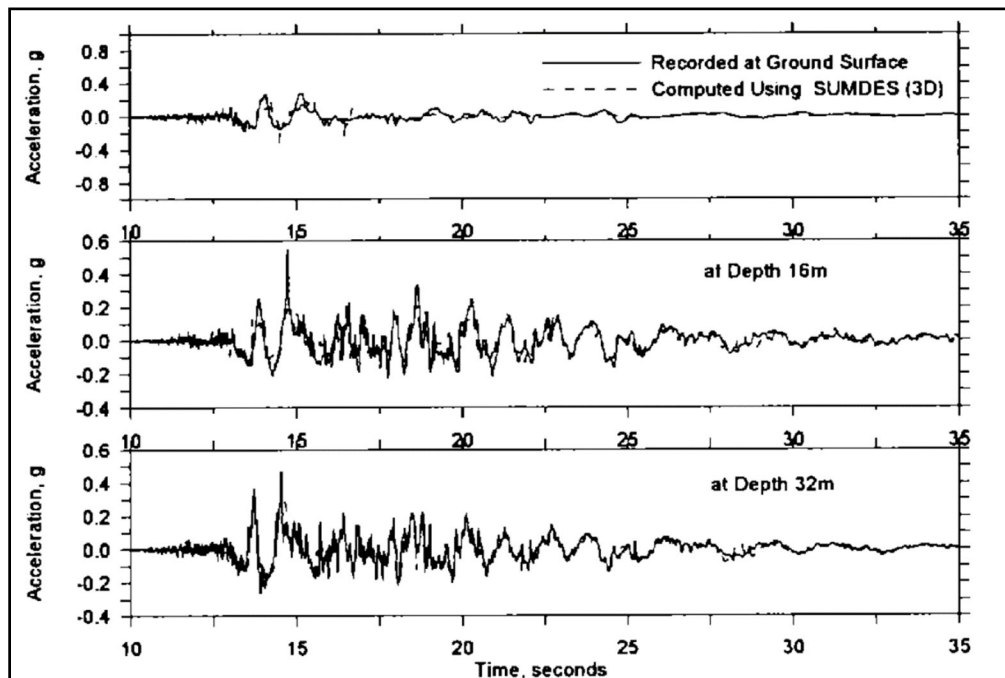


Figure 3-22: Comparison between calculated and recorded motions at the ground surface, and at depths of 16 m and 32 m, at the Port Island vertical array site in the east-west direction (Wang et al., 2001)

This is encouraging, as the Wang2D model employed in these current studies is an updated and two-dimensional version of this three-dimensional model.

3.7.2 Gingery (2014)

Gingery (2014), in his PhD dissertation under the supervision of Professor Ahmed Elgamal, performed one-dimensional site response analyses of the Port Island vertical array site using the liquefaction model UCSD PDMY2 (Pressure Dependent Multi-Yield 02). Site-specific UCSD PDMY02 model parameters were developed based on (1) the Idriss and Boulanger (2008) liquefaction triggering relationship, and (2) more general calibration with the cyclic simple shear database of Wu and Kammerer (Wu et al., 2003). Gingery found good agreement between his site response analyses and the instrumentally recorded motions, as shown in Figures 3-23 and 3-24. Gingery's (2014) approach has two notable differences with the current studies beside the constitutive models employed. He utilized the recorded ground motions at 32 meters depth as the input motions, whereas the current studies utilize the input motion at 83 meters depth as the input motions. Also, the alluvial clay layer (Ma13) has been modeled with $PI = 30$, $OCR=2$, and $S_u/\sigma'_{vi} = 0.4$ in the Gingery (2014) study, which is slightly higher than $S_u/\sigma'_{vi} = 0.255$ to 0.268 ($OCR = 1.5$ to 1.6 , and with 20 percent strength reduction) used in these current studies.

3.7.3 Ziotopoulou (2010) and Ziotopoulou et al. (2012)

Ziotopoulou (2010) in her M.S thesis under the supervision of Professor Ross Boulanger at U.C. Davis performed a comparative evaluation of three of the four constitutive models being used in these current studies by means of back-analyses of the Port Island vertical array data set. These three models were (1) PM4Sand, (2) UBCSAND, and (3) URS (currently known as the Roth model) for Port Island vertical array site as well as a few other sites. As discussed in Section 3.6.2, Ziotopoulou (2010) appears to have utilized the original ground motion recordings without a 22 degree counter-clockwise rotation of the recorded motions at a depth of 83 meters to correctly align the motion with the shallower recordings. Ziotopoulou performed one-dimensional site response analyses in both the north-south and east-west directions, and compared the results with north-south and east-west recorded motions at 32 meters, 16 meters, and at the ground surface.

Figure 3-25 shows comparisons between computed and recorded acceleration response at depths of zero, 16 meters, 32 meters, and the (recorded and processed) "input" motion at 83 meters for the response analysis performed with the UBCSAND model in the north-south direction. This was judged to be a relatively good match (Ziotopoulou et al., 2012), and that it serves to confirm the ability of the UBCSAND model to suitably predict site response for this site in the face of significant occurrence of soil liquefaction.

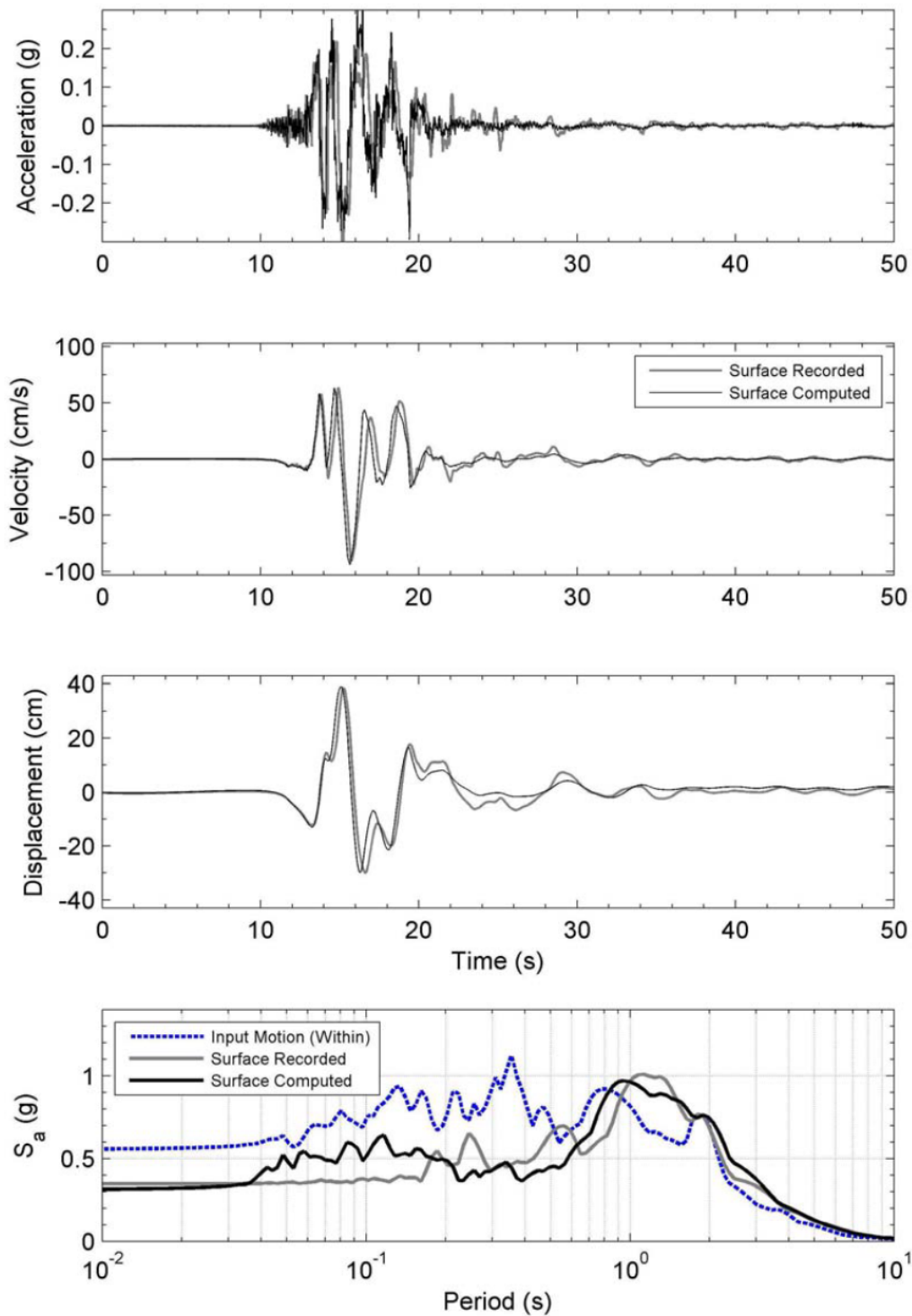


Figure 3-23: Comparison between computed surface response and recorded response at the ground surface of the Port Island vertical array site in the north-south direction (Gingery, 2014)

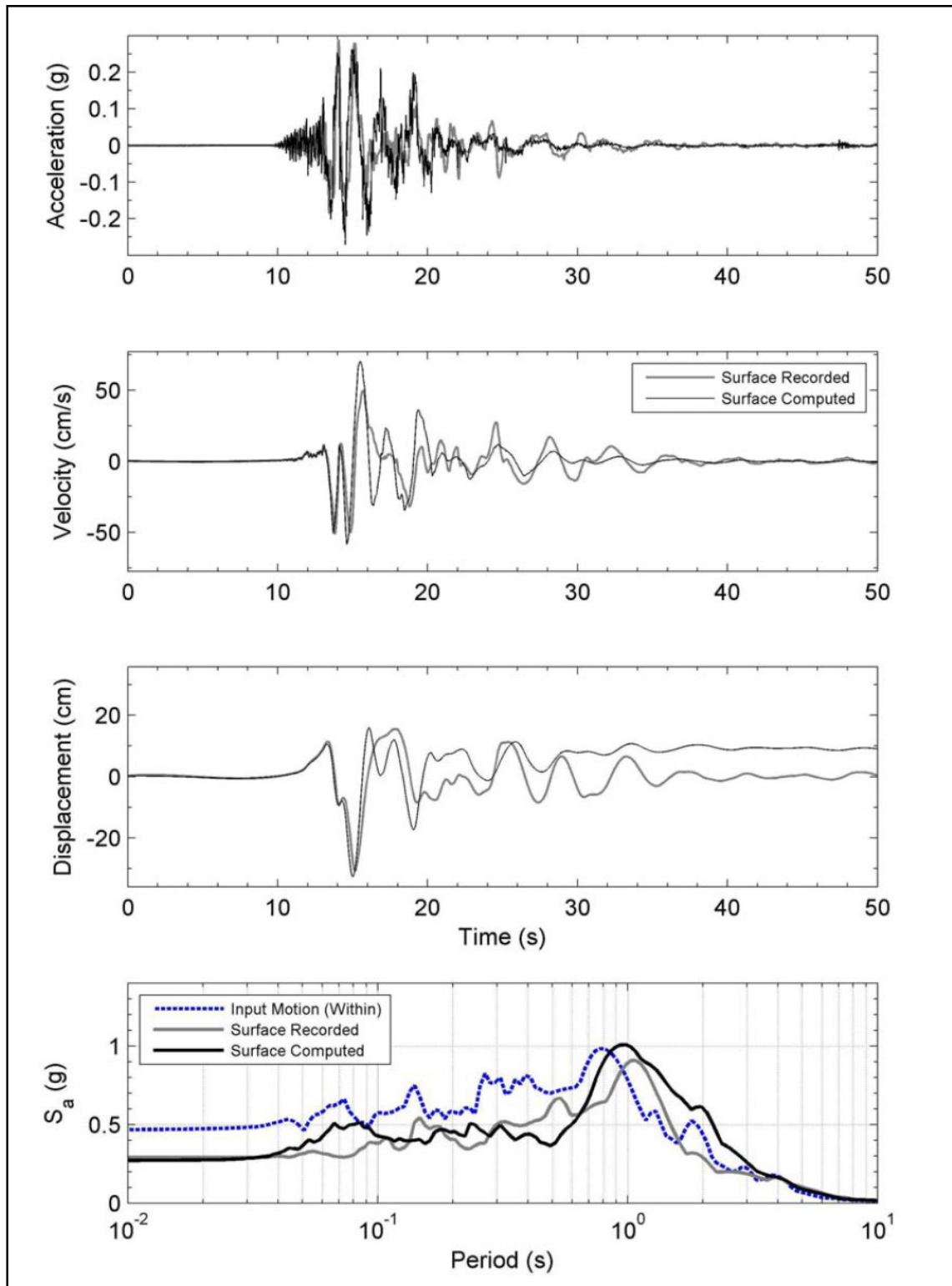


Figure 3-24: Comparison between computed surface response and recorded response at the ground surface of the Port Island vertical array site in the east-west direction (Gingery, 2014)

It is noted here that the match does appear to be relatively good up to about 15 seconds into the record, but that the surface response match degrades somewhat after that point. It continues to be adequate for engineering purposes. Also that the calculated response is not as good at a depth of 16 meters, where the computed response underestimates peak acceleration, and under-predicts several large acceleration spikes in the recorded motion. Also that the “input” recordings at a depth of 83 meters were not properly rotated azimuthally by 22 degrees to correctly align the north-south input motion with the three recorded motions at the shallower depths.

Figure 3-26 shows comparisons between computed and recorded acceleration response at depths of zero, 16 meters, 32 meters, and the (recorded and processed) “input” motion at 83 meters for the response analysis performed with the PM4Sand model in the north-south direction. This was also judged to be a good match (Ziotopoulou et al., 2012), and to confirm the ability of the PM4Sand model to suitably predict site response for this site in the face of significant occurrence of soil liquefaction.

It is noted here that the surface response calculated is not a very good match with the recorded response, as (1) it significantly over-predicts the peak ground surface acceleration, and also over-predicts several other large acceleration spikes, (2) it appears to fail to capture the character of the recorded surface acceleration time history, replacing the longer duration (and lower) acceleration pulses with shorter (higher frequency) “spikes”, and (3) it also over-predicts peak acceleration (and high frequency acceleration spikes) at a depth of 16 meters. This would appear likely to be the result of overly sharp dilation in the PM4Sand constitutive model, relative to the actual site response and the performance/behavior of the potentially liquefiable upper Masado fill soils under undrained cyclic loading.

Figure 3-27 shows comparisons between computed and recorded acceleration response at depths of zero, 16 meters, 32 meters, and the (recorded and processed) “input” motion at 83 meters for the response analysis performed with the URS (Roth) analytical model in the north-south direction. This was judged to be a very poor match (Ziotopoulou et al., 2012).

Figure 3-28 shows maximum calculated relative lateral translation at all depths for three sets of response analyses performed by Ziotopoulou (2012) with (1) the PM4Sand model, (2) the UBCSAND model, and (3) the URS (Roth) model. The “baseline” cases employed best-estimated parameters, and the two “parametric” analyses were performed with either an increase of 20% in CRR required to trigger liquefaction, or an increase of 20% in initial shear wave velocity. As shown in this figure, the “base case” lateral deformations at the ground surface were approximately 61 cm for the PM4Sand analysis, 47 cm for the UBCSAND analysis, and 299 cm for the URS (Roth) analysis.

As shown in this figure, there was an accumulation of approximately 3 meters of lateral displacements in the calculated results (Figure 3-28(c)) for the Roth analysis base case. That, along with the poor match of the acceleration time history at the ground surface, has led to questioning of the adequacy and suitability of the Roth model for performing nonlinear seismic deformation analyses.

Closer inspection and evaluation of the analytical results of Ziotopoulou et al. (2010, 2012), as well as performance of similar response analyses of the Port Island vertical array site in these current studies (see Section 3.8), sheds light on this.

Ziotopolou made two errors in her site response analyses of the Port Island vertical array site. As discussed above, the first of these was the failure to correctly rotate the base input motions (at 83 meters depth) clockwise by 22 degrees to align them with the three shallower recording sets. This was a relatively minor error, and it is not the pivotal issue here.

The second error was in the implementation of the Roth model analysis. Ziotopoulou ran the Roth model with no provision for transition to post-liquefaction residual strength (S_r). As a result, the Roth model dutifully incrementally increased cyclically generated pore pressures until the pore pressure ratio reached a full value of $R_u = 1.0$. At that juncture, and from that point onwards, the upper Masado fill soils had zero effective stress, zero shear strength, and zero stiffness. The seismic response was therefor no longer soil-like, instead the liquefied soils behaved as a slightly heavy fluid (much like water).

This can be seen in Figures 3-27 and 3-28. In Figure 3-27, it can be seen that the surface acceleration response match is generally good up until nearly 15 seconds, after which the computed surface response “dies” as the fully liquefied soils (with zero strength and stiffness) cannot properly transmit shear stresses. This “deadens” the response, and it also leaves no shear strength or shear stiffness in the upper soils to resist the accumulation of lateral drift; resulting in the prediction of excessive permanent lateral displacements at the ground surface. In Figure 3-28, it can be seen that reduction of both strength and stiffness to zero eliminates resistance to lateral deformations and results in over-estimation of same.

As discussed in Chapter 2, Section 2.2.1, the Roth model utilizes a simplified half-cycle counting pore pressure generation scheme, where the shear strength of soil continues to drop until it reaches post-liquefaction residual strength (S_r), at which point the shear strength is kept constant. In these current studies, Roth model analyses transition to post-liquefaction when the shear strength in any potentially liquefiable element drops to a strength of $S = S_r$, at which point a transition to the post-liquefaction residual strength S_r is implemented in that element as the analysis continues.

This response analysis with the Roth model was repeated as part of these current studies (see Section 3.8), and the results of this correct implementation of the Roth model with post-liquefaction strength of $S = S_r$, instead of $S = 0$, are presented in Section 3.8. When this analysis was repeated, with a transition to $S = S_r$ instead of allowing strength to decrease to $S = 0$, the calculation of excessive lateral ground surface displacements that was observed in the site response analyses by Ziotoupolou et al. (2010, 2012) was abated.

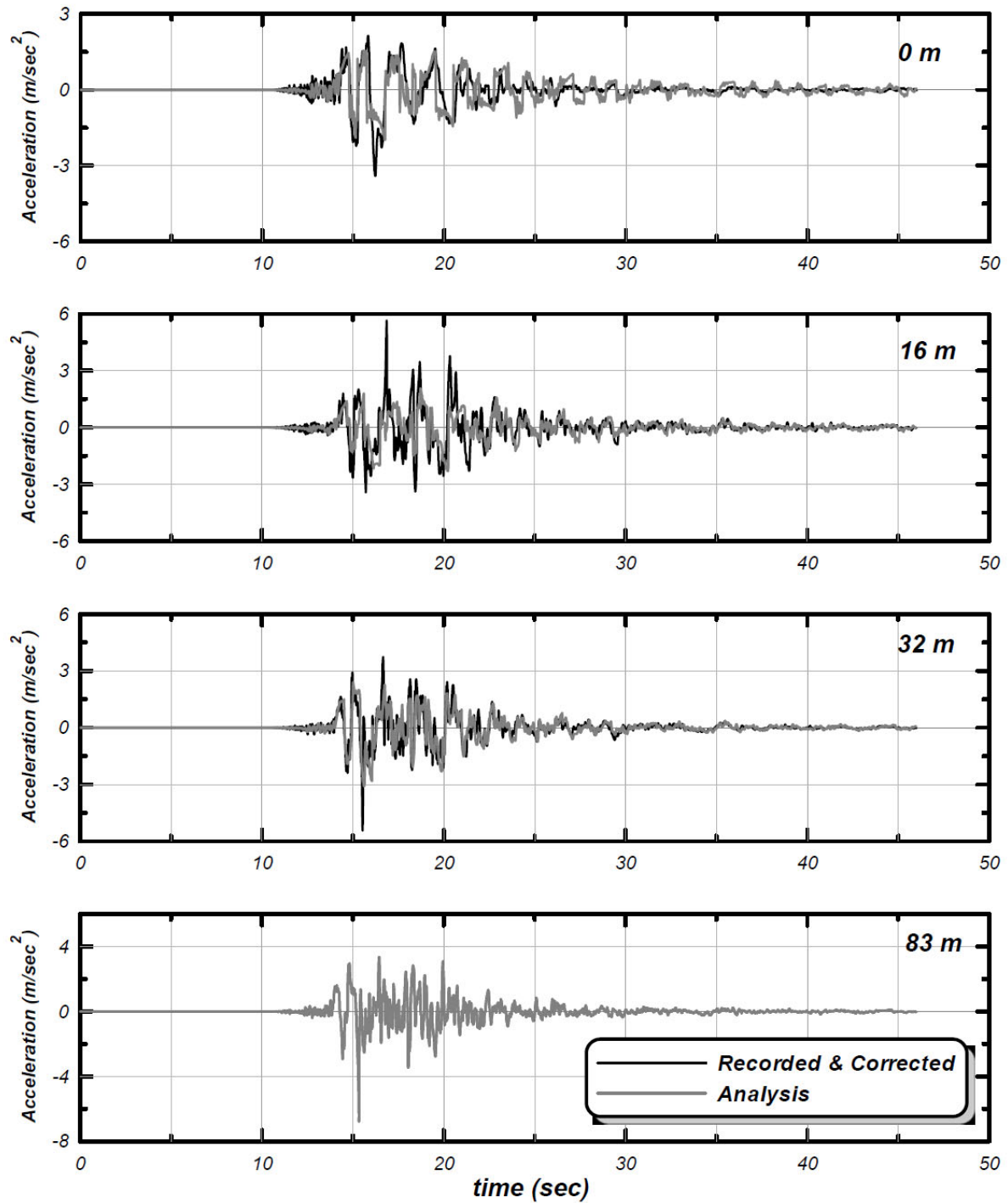


Figure 3-25: Comparison between computed and recorded acceleration response at the Port Island vertical array site using the UBCSAND model (Ziotoupolou, 2010)

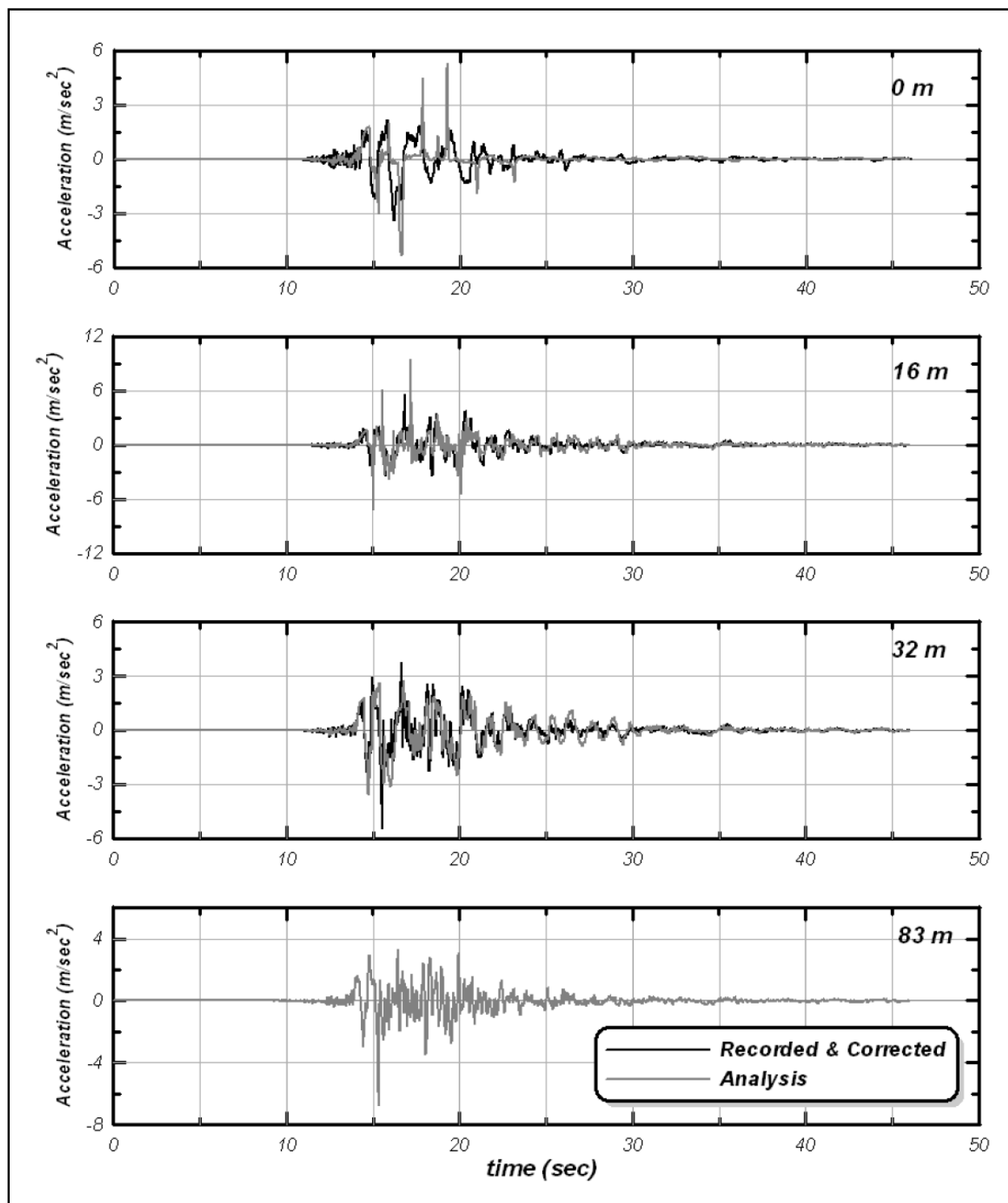


Figure 3-26: Comparison between computed and recorded acceleration response at the Port Island vertical array site using the PM4SAND model (Ziotoupolou, 2010)

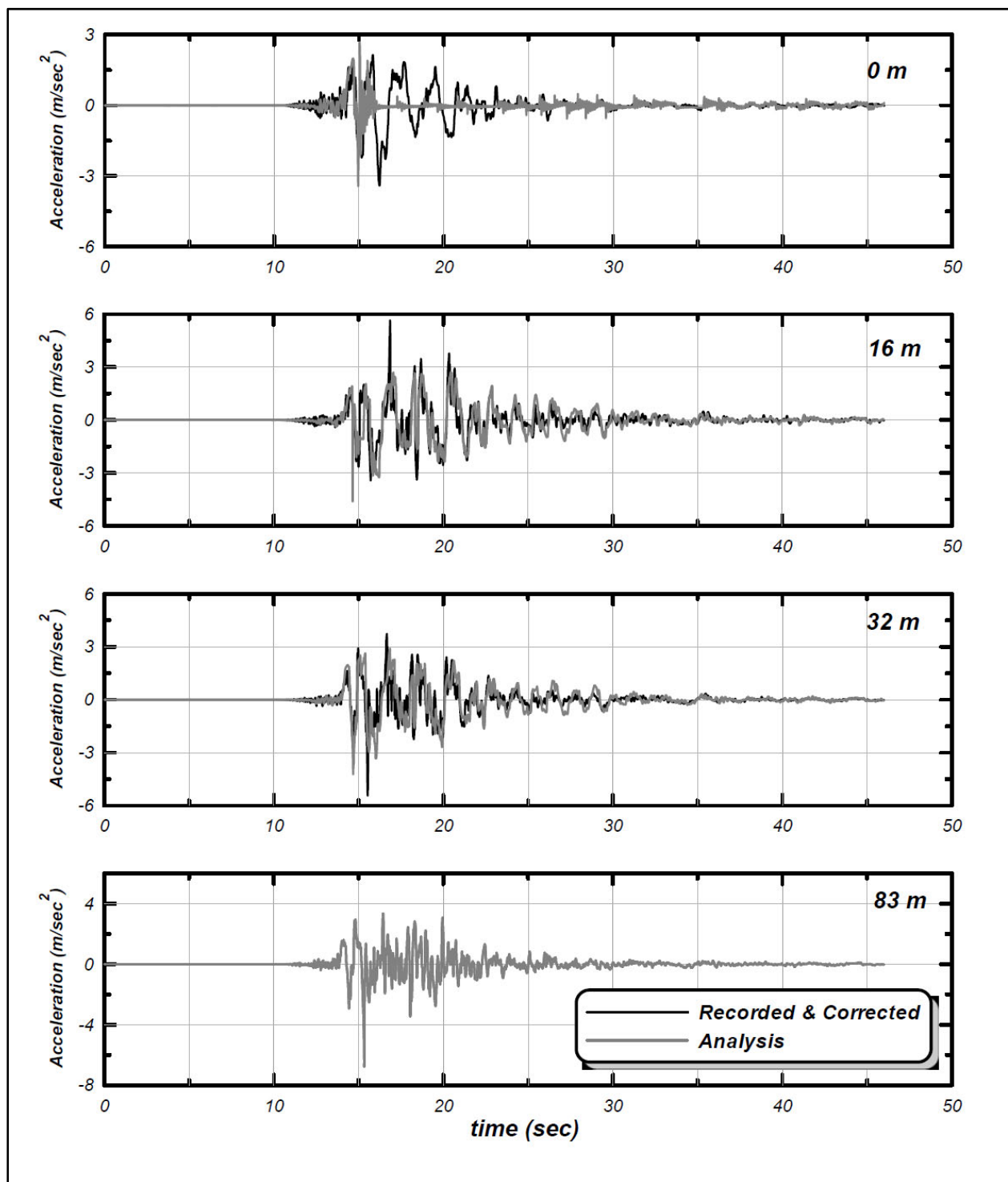


Figure 3-27: Comparison between computed and recorded acceleration response at the Port Island vertical array site using the URS (Roth) model (Ziotopoulou, 2010)

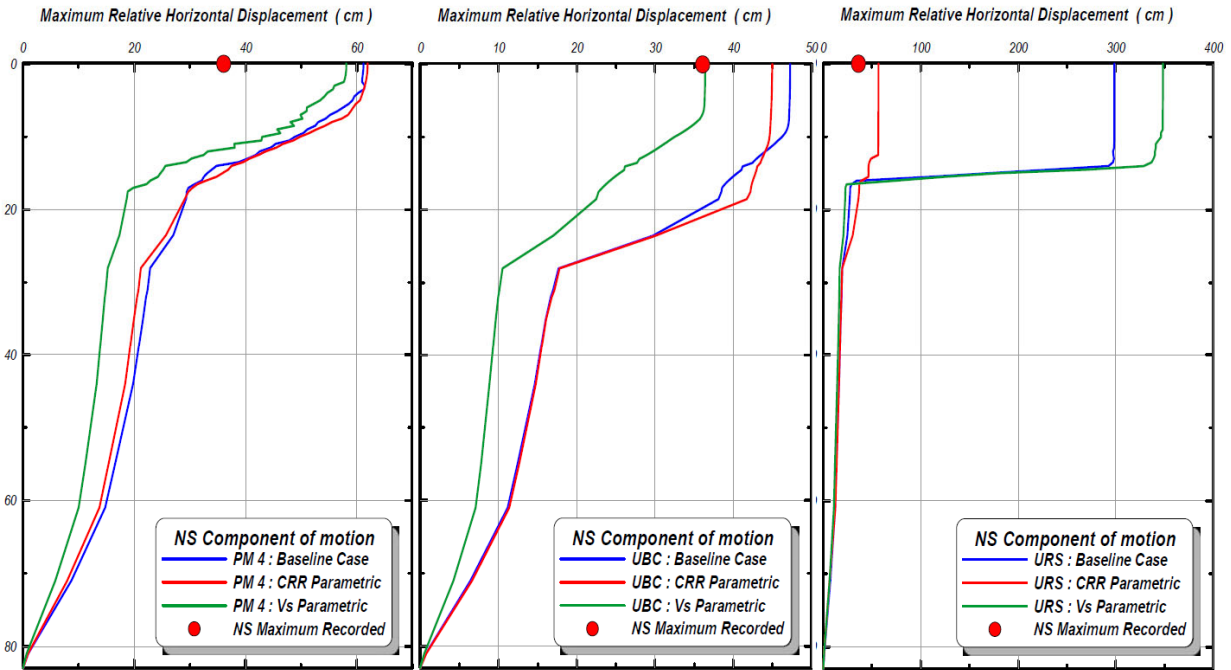


Figure 3-28: Plots of relative horizontal displacement distributions from the three constitutive models (PM4SAND, UBCSAND and URS(Roth)) for (1) the baseline case, (2) CRR (+20%) and (3) Vs (+20%); results shown are for the N-S component of motion (Ziotopoulou, 2010).

3.8 RESULTS OF PORT ISLAND VERTICAL ARRAY SITE RESPONSE ANALYSES PERFORMED AS PART OF THESE CURRENT STUDIES

Based on review of previous back-analyses of the Port Island vertical array site response during the 1995 Kobe earthquake, it appears that informative and/or largely suitable one-dimensional “site response” back-analyses have been performed for three of the four analytical models employed in these current studies.

Wang et al. (2001) presented back-analyses using an older, and fully three-dimensional version of the Wang2D model, and as shown in Figures 3-21 and 3-22, these back-analyses provided a very good engineering match with the recorded site response during the 1995 Kobe earthquake. As a result, the Wang2D model will be carried forward and used for two-dimensional fully nonlinear seismic deformation back-analyses of the Upper and Lower San Fernando Dams.

Ziotopoulou (2010) presented back-analyses performed using the UBCSAND model, and as shown and discussed in Section 3.7.3, the results of these back-analyses represented a good engineering match with the recorded records. This satisfies the objective of examining the general suitability of the UBCSAND model for site response purposes in the face of significant development of seismically-induced soil liquefaction. This model will also be carried forward and used for two-dimensional fully nonlinear seismic deformation back-analyses of the Upper and Lower San Fernando Dams.

Ziotopoulou (2010) also presented back-analyses performed using the PM4Sand model. As shown and discussed in Section 3.7.3, the results of these back-analyses did not represent a very good engineering match with the recorded records. This model is, however, currently widely used for nonlinear seismic deformation analyses of dams, and the site responses matches were not very poor either. The degree of match was more intermediate. Because this model is widely used, and because the back-analysis match with the Port Island vertical array site recorded data was not very poor, this model will also be carried forward and used for two-dimensional fully nonlinear seismic deformation back-analyses of the Upper and Lower San Fernando Dams.

Ziotopoulou (2010) also presented back-analyses performed using the URS (Roth) model. As shown and discussed in Section 3.7.3, the results of these back-analyses showed a very poor engineering match with the recorded records. This appeared to be the result of an incorrect implementation of the Roth model in which the cycle-counting algorithm of the Roth seismic pore pressure generation model was allowed to proceed to the development of $R_{u,seis} = 1.0$, which reduced effective stresses, shear strengths, and stiffnesses fully to zero. As discussed in Section 3.7.3, the correct implementation would have been to transition to post-liquefaction strength when pore pressures in any element increased to a point where the remaining shear strength (S) in the element decreased to $S \leq S_r$, rather than continuing until $S = 0$.

An additional one-dimensional site response analysis is therefore performed here in order to assess the performance of the Roth model for the Port Island case history with this correct implementation.

Sections 3.4 and 3.5 present the site characterizations and the material and model parameterizations for this analysis. The recordings at a depth of 83 meters were rotated counter-clockwise by 22 degrees to develop the input motions, and this analysis was performed in the north-south direction. In this analysis, potentially liquefiable soil elements (saturated elements in the Masado fill) transitioned to S_r when pore pressure increases were sufficient to reduce shear strength (S) to $S \leq S_r$.

The results of this response analysis with the Roth model are shown in Figures 3-29 through 3-31. This one-dimensional site response analysis using FLAC was performed applying (1) the recorded ground motions (horizontal north-south component and vertical component ground motions) at 83 meters through a rigid base (e.g. acceleration time history), (2) single soil column with left-side (aside) attached with right side (bside) nodes, (3) element sizes equal or less than 1 meter, and (4) using Cetin et al. (2018) liquefaction

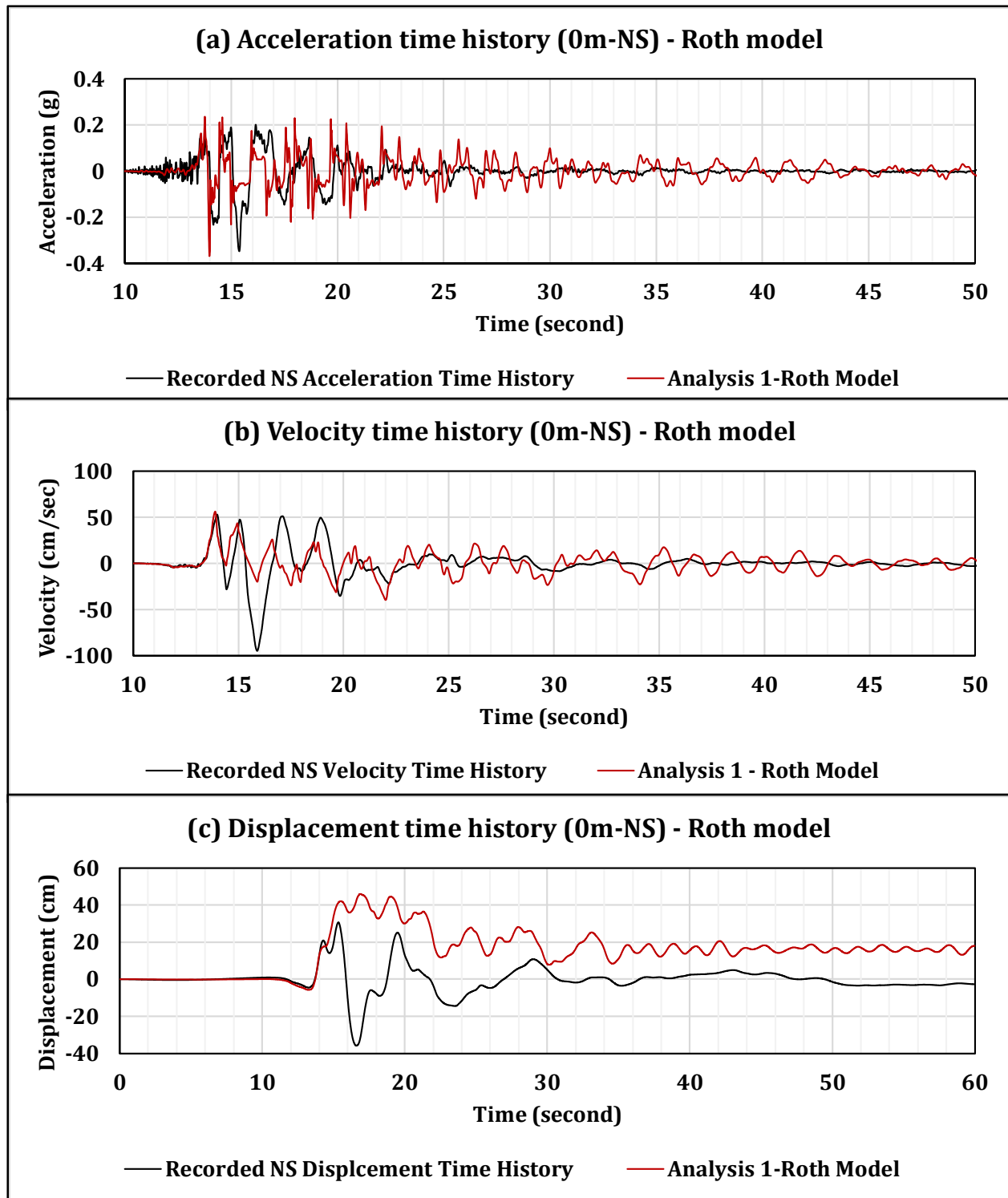


Figure 3-29: Acceleration, velocity, and displacement time Histories at the ground surface for Port Island Analysis 1; using the Roth Model, with Cetin et al. (2018) liquefaction triggering, and Weber et al. (2015) post-liquefaction strength (S_r)

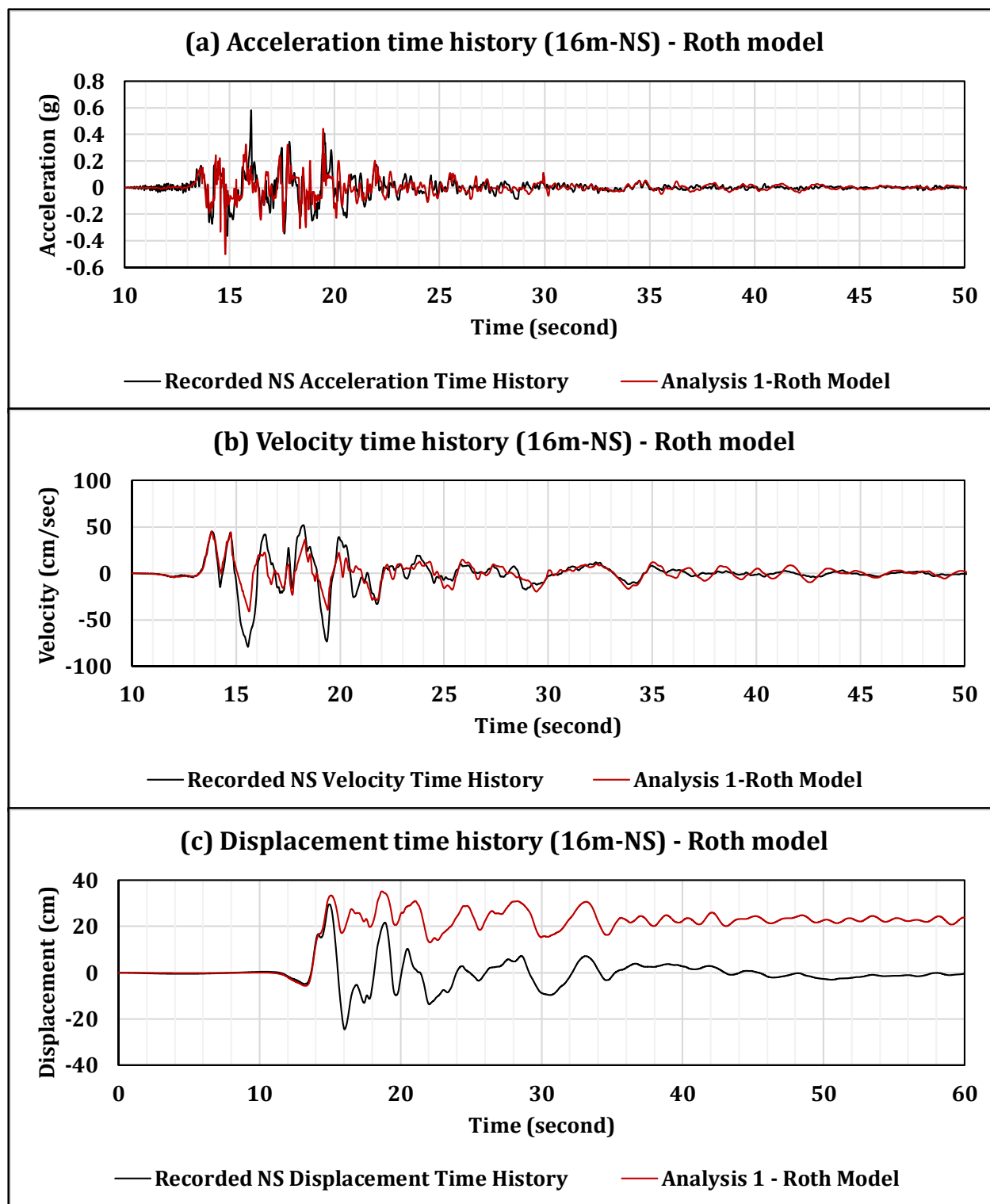


Figure 3-30: Acceleration, velocity, and displacement time Histories at depth = 16 meters for Port Island Analysis 1; using the Roth Model, with Cetin et al. (2018) liquefaction triggering, and Weber et al. (2015) post-liquefaction strength (S_r)

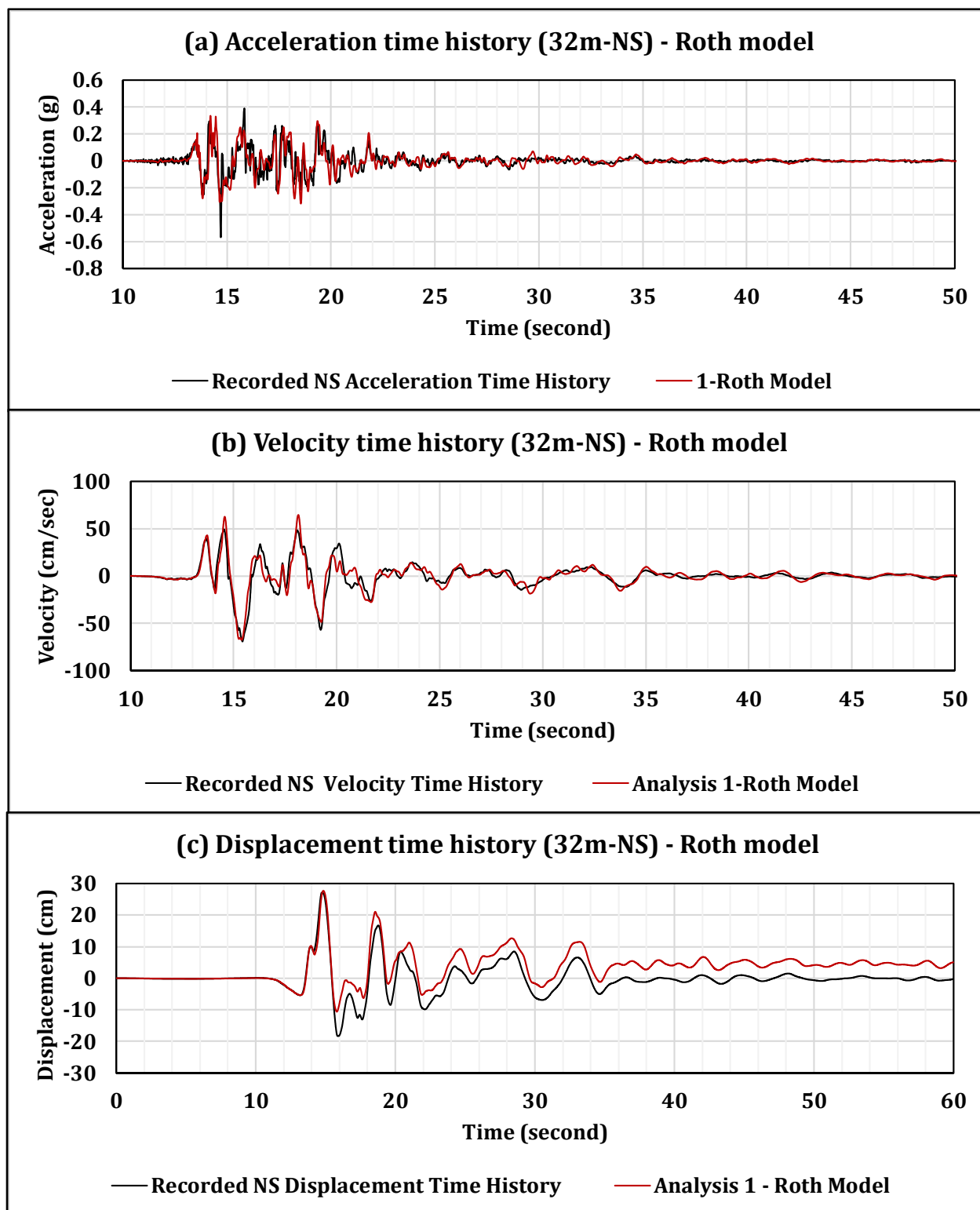


Figure 3-31: Acceleration, velocity, and displacement time Histories at depth = 32 meters for Port Island Analysis 1; using the Roth Model, with Cetin et al. (2018) liquefaction triggering, and Weber et al. (2015) post-liquefaction strength (S_r)

triggering, Youd et al. (2001) K_σ , Idriss and Boulanger (2003) K_α , and Weber et al. (2015) S_r relationships for Masado fill layers (0-19 meters) and Mohr-Coulomb models in the remaining layers.

As shown in Figure 3-29, this response analysis produced very different results from those of the response analysis performed by Ziotopoulou (2010), as presented previously in Figure 3-27. In these new analyses, the surface response does not “die” at approximately 16 seconds; instead surface response continues onwards after 16 seconds, and exhibits response motions that exceed the instrumentally recorded data.

This represents a better level of “match” with the instrumentally recorded motions than was achieved in the back-analysis performed by Ziotopoulou (2010) employing the PM4SAND model (see Figure 3-26), and a similar level of match to the back-analysis performed by Ziotopoulou (2010) employing the UBCSAND model (see Figure 3-25). The back-analysis performed by Wang et al. (2001) (See Figures 3-21 and 3-22) employing the Wand2D model provided the best overall match with the recorded response data.

On balance, this level of match with the recorded response at Port Island achieved with the Roth model appears suitable and adequate, and this model will also be carried forward for use in the two-dimensional nonlinear seismic deformation back-analyses of the Upper and Lower San Fernando Dams in Chapters 4 and 5.

3.9 SUMMARY AND CONCLUSIONS

This review of previous studies and one-dimensional site response analyses (back-analyses) of the Port Island vertical array site response during the 1995 Kobe earthquake lead the current research team to conclude that all four of the analytical/constitutive models (Roth, UBCSAND, PM4Sand, and Wang2D) warrant continued evaluation, and that all four models will be carried forward to the two-dimensional nonlinear seismic deformation back-analyses of the performances of the Upper and Lower San Fernando Dams during the 1971 San Fernando earthquake.

This element of this overall research effort is not fully complete here. After the filing of this dissertation, additional work will continue, and eventually an overarching U.C. Berkeley geotechnical research report will present the full results. One element of further work still to be completed will be the performance of four formal back-analyses of the Port Island vertical array site response during the 1995 Kobe earthquake, employing each of the four analytical/constitutive models used in these current studies. Table 3-2 lists the four analyses to be performed.

Chapter 4

The Lower San Fernando Dam (LSFD) Seismic Performance Case History During the 1971 San Fernando Earthquake

4.1 INTRODUCTION

The Lower San Fernando Dam (LSFD), also known as the Lower Van Norman Dam (as it is part of the Van Norman Dam Complex), experienced liquefaction-induced large deformations and a resulting flow failure on its upstream side during the San Fernando Earthquake of February 9, 1971. The dam was in very close proximity to the fault rupture during the $M_w \approx 6.6$ event, and it was strongly shaken. Soil liquefaction occurred within the hydraulic fill materials on the upstream side of the dam embankment, and the ensuing flow slide carried a large portion of the embankment, including most of the crest and most of the upstream side of the dam, back into the reservoir. The upstream toe of the failure mass travelled approximately 140 feet into the reservoir. The dam had thirty-six feet of freeboard prior to the earthquake, and the nearly catastrophic upstream slide reduced the effective freeboard to only a few feet (~ 5 feet) from overtopping. Approximately 80,000 people were evacuated from the area downstream while the reservoir was safely drawn down over the next four days (Seed et al., 1973).

This well-studied field performance case history has been foundational to the development of the field of modern seismic dam engineering, and to the inception of the U.S. national seismic dam safety programs that continue to be ongoing today.

The performance of the LSFD during the 1971 San Fernando Earthquake is a well-documented seismic performance field case history involving a liquefaction-induced full flow failure of the upstream side of the embankment. Post-earthquake studies of the LSFD have produced significant amounts of both field and laboratory data (e.g.: Seed et al., 1973; Serff, 1976; Seed et al., 1989; Castro et al., 1989; etc.). As a result, this field performance case history is a good candidate for assessing impacts of numerical modeling approaches and details on the results of nonlinear dynamic deformation analyses of dams, and it has repeatedly been used to develop, examine, and calibrate analytical approaches and methods.

In these current studies, a re-evaluation of the LSFD field performance case history was performed to develop an understanding of the principle mechanisms that had influenced the observed field performance, and the abilities of a suite of current analytical frameworks (and models and engineering relationships) to suitably capture those behaviors. A suite of four analytical or constitutive models for potentially liquefiable soils are utilized in these current studies to evaluate effects of (1) model selection, (2) parameter selection details, (3) different liquefaction triggering relationships, (4) different post-liquefaction residual strength evaluation approaches, and (5) analysis protocols and modeling details on the accuracy and reliability of the predictive results of these types of analyses.

4.2 DAM PERFORMANCE DURING THE 1971 SAN FERNANDO EARTHQUAKE

Figure 4-1 is a high angle oblique air photo, taken by Lloyd Cluff from a helicopter in the near-immediate aftermath of the earthquake. This photo shows most of the crest road (and the crest of the dam) to be largely missing, as it slid back into the reservoir atop the large upstream flow slide. Prior to the earthquake, the dam had two essentially matching concrete outlet towers in the reservoir; but only the outlet tower near the right abutment remains in this photograph. The outlet tower near the left abutment had been carried away by the upstream side flow failure. As shown in this photo, remaining crest freeboard is only a few feet, and the lowest part of the upstream slide heel scarp that largely defines the remaining useful freeboard has suffered longitudinal cracking, further reducing likely effective remaining freeboard to an unknown degree. This was a potentially perilous condition, and approximately 80,000 residents downstream were evacuated for four days until the reservoir had been safely lowered.

Figures 4-2 and 4-3 show conditions after drawdown of the reservoir, revealing additional details of the upstream flow slide and of the remaining heel scarp feature.

Extensive field and laboratory investigations were performed in the aftermath of the earthquake. Figure 4-4 shows the locations of the four cross-sections at which the principal initial in-situ field investigations were performed; these investigations included borings, sampling, and in-situ SPT testing (Seed et al., 1973, 1975). They also included the excavation



Figure 4-1: Oblique aerial view of the Lower San Fernando Dam (at the bottom right in this photo) shortly after the earthquake, prior to reservoir drawdown. [Steinbrugge Collection, 1971; NICEE Library, U.C. Berkeley]



Figure 4-2: The Lower San Fernando Dam after the 1971 San Fernando earthquake (looking West) showing conditions after reservoir drawdown.
[Steinbrugge Collection, 1971; NICEE Library, U.C. Berkeley]



Figure 4-3: Lower San Fernando Dam after the 1971 San Fernando earthquake (looking South-East) [Steinbrugge Collection; 1971, NICEE library, U.C. Berkeley]

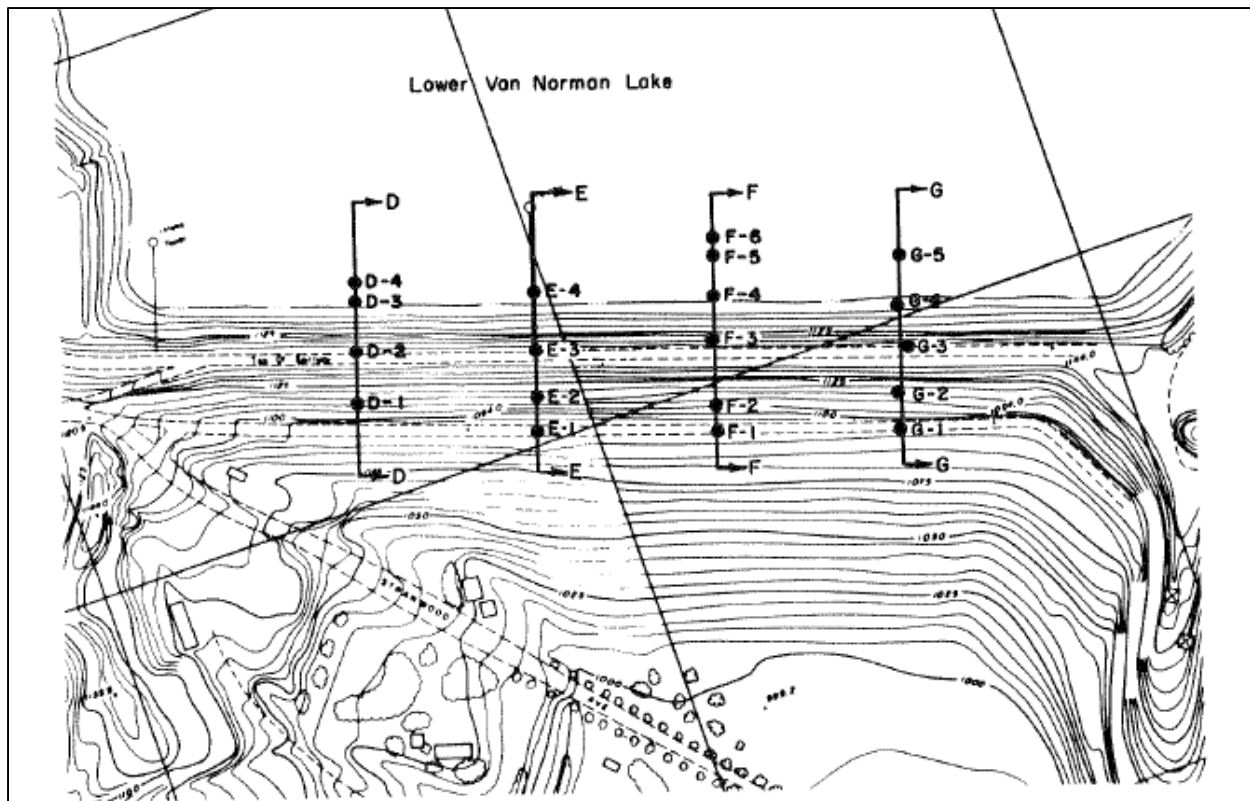
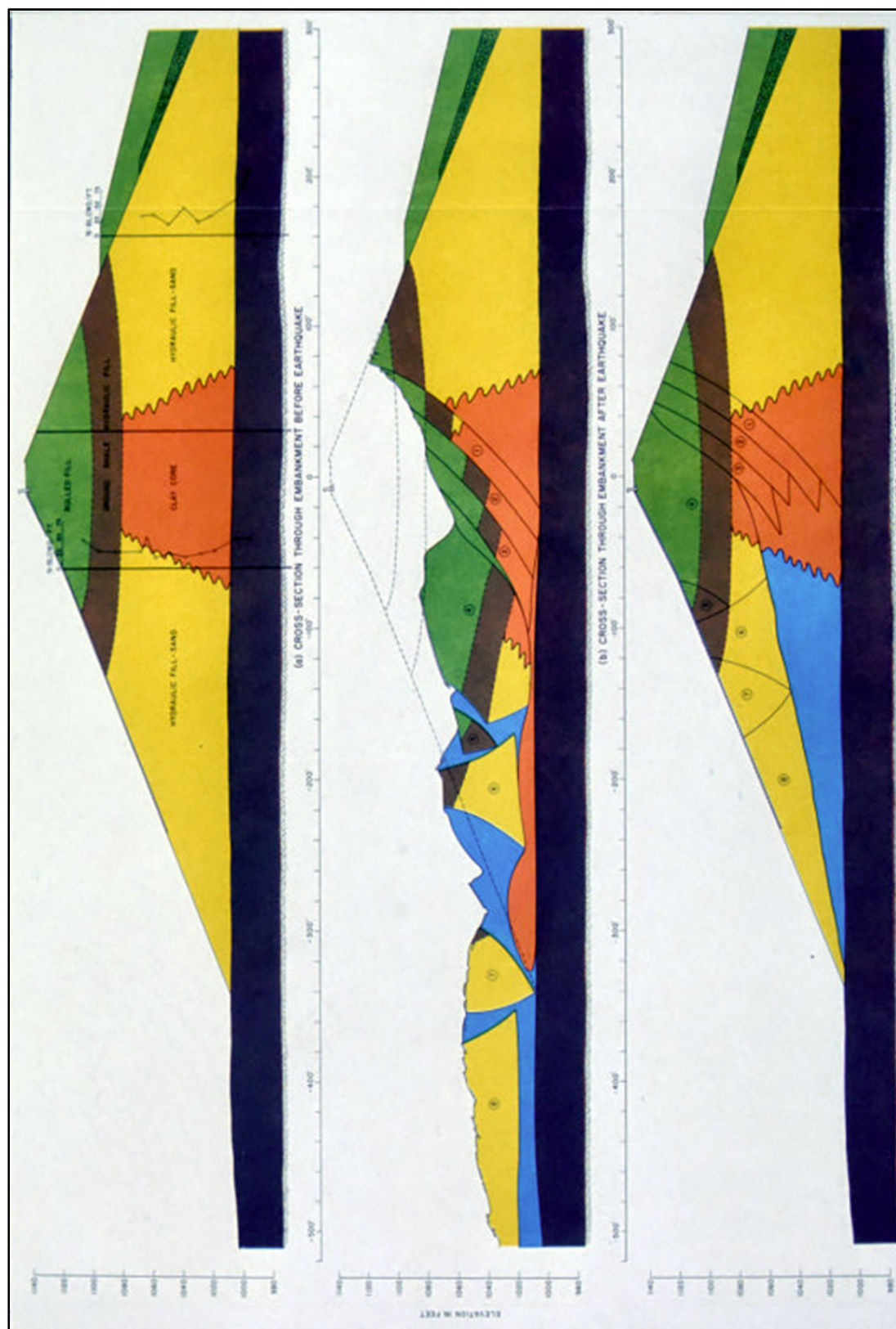


Figure 4-4: Plan view of the Lower San Fernando Dam showing original post-earthquake investigation cross-sections and exploration boring locations (Seed et al, 1973).

of a deep trench to investigate and map features of the central portion of the upstream flow slide at Cross-Section E-E', which is located near the center of the slide. It is this Cross-Section E-E' that will be back-analyzed in these current studies.

The exploratory trench at this cross-section was excavated as deeply towards and through the base of the upstream slide mass as stability and safety would allow, and as far into the central “puddled” clay core zone as stability and safety would allow. Features observed in the deep trench excavation were mapped in detail. Identifiable intact blocks of the original dam embankment were mapped and numbered, and the forensic investigation treated these displaced blocks as pieces of a “puzzle” that could then be re-assembled to recreate the original pre-failure geometry. This process produced a number of large, colored cross-section figures showing (1) “before” earthquake conditions/geometry, (2) “after” earthquake conditions/geometry (with numbered displaced blocks), and (3) “re-assembled” pre-earthquake geometry (Seed et al., 1973). Figure 4-5 shows reconstruction of the cross-section Section E-E' of the LSFD by Seed et al. (1973). The blocks are clearly identifiable in Figure 4-6.



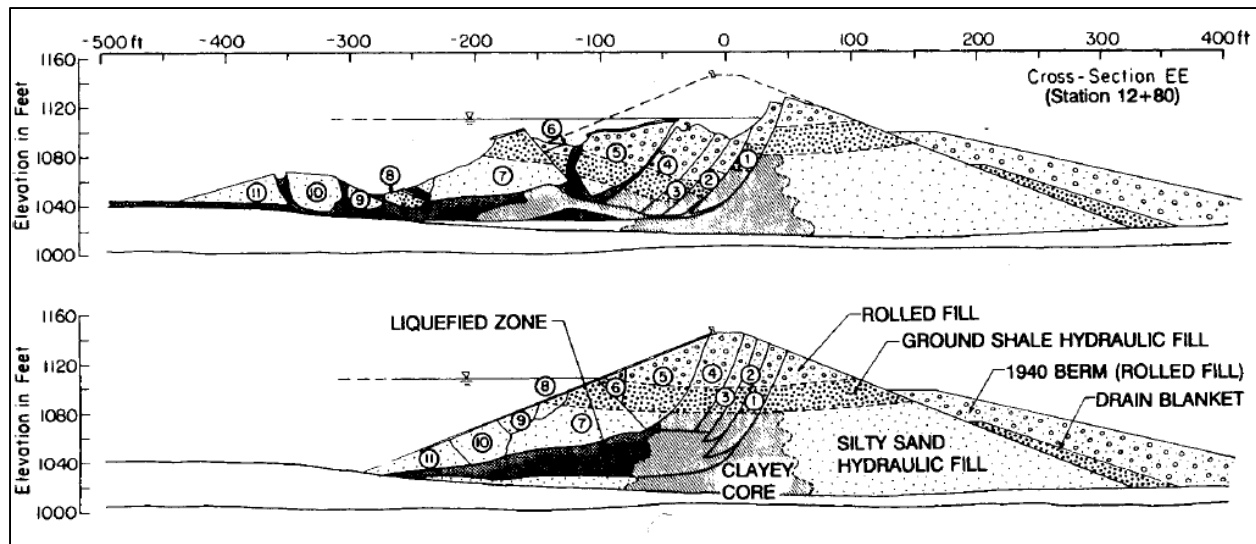


Figure 4-6: Pre-failure and post-failure cross-sections of the Lower San Fernando Dam at Cross-Section E-E' (from Seed et al., 1989; after Seed et al., 1973)

Figure 4-6 was developed by Seed et al., 1989 and Castro et al., 1992 to reproduce the original cross-sections of Seed et al. (1973) in a format more amenable to reproduction and use in the format of this current type of document. This figure serves well to illustrate the observed performance of the dam during the earthquake.

Once the numbered intact blocks of the post-earthquake cross-section had been delineated, numbered, and then “re-assembled”, it was clear that soil liquefaction had occurred in the very dark zone shown in Figure 4-6, at the base of the upstream hydraulic fill shell materials, and that the upstream flow slide had carried the overlying semi-intact blocks of the embankment back into the reservoir, borne along atop this liquefied material.

The post-earthquake investigations also found indications of some liquefaction within the downstream hydraulic fill shell zone (Seed et al, 1973) and these produced small, but non-zero displacements of downstream slope.

4.3 CONSTRUCTION OF THE LOWER SAN FERNANDO DAM

The Upper San Fernando Dam (USFD) and the Lower San Fernando Dam (LSFD) were both constructed to provide terminal storage reservoir capacity for the Los Angeles Aqueduct, at sufficient elevations for gravity distribution into the city.

The main sections of the LSFD were constructed by the hydraulic fill method, which involves the excavation and then aqueous suspension transport and deposition of materials. Relatively low wagon rolled “starter dikes” were first constructed along the upstream and downstream toes of the eventual embankment, to impound a shallow “lake” across the full width of the dam from upstream to downstream, and then soil materials excavated from the

streambed were mixed with water and the aqueous suspension was pumped through pipes to discharge points spaced along the upstream and downstream edges of the intended embankment. This is intended to produce an “ideally” graded embankment fill, as the coarser particles (in this case mainly sands and silty sands) would settle most quickly, and come to rest near the discharge points, and the finer (ideally clayey) materials would remain longer in suspension, and would settle towards the center of the dam embankment. The progressively evolving embankment fill in this process has its high points at both the upstream and downstream edges, and the fill elevation is somewhat lower at the center; giving rise to the term “puddled clay core”. After the fill has reached the tops of the first set of starter dikes, hydraulic fill placement is halted, and a new set of starter dikes are constructed at the progressively tapering upstream and downstream edges of the dam (partially atop the recently placed hydraulic fill), and the hydraulic deposition outlets are repositioned, and then the process is repeated.

In theory, this process would progressively/incrementally produce a dam embankment with a clayey core providing low permeability, with a gradual transition in gradation towards the coarser upstream and downstream toes; providing good filtration and drainage for the core. In actual practice, it is necessary to periodically halt material deposition from time to time in order to construct the next level of starter dikes, and equipment breakdowns and work shift changes also affect deposition. As a result, most hydraulic fills tend to have notoriously locally variable (layered) depositional structure, with inter-bedded coarser and finer layers occurring at multiple scales.

Figure 4-7 shows a photograph of the side wall of an excavation (trench) through the upstream hydraulic fill section of the dam that was performed as part of the post-failure investigations. The lighter layers are coarser, sandier layers (typically SP or SP-SM), with lower fines contents (mainly silty fines), and the darker layers are layers with higher silt contents, often SM, and in some cases ML. The silts in the shell zones tend to be of relatively low plasticity, but plasticity tends to increase towards the central “puddled” clay core.

The layers in the Photograph of Figure 4-7 can be clearly seen at this scale, but a closer examination of the “lighter” layers in this photo would reveal additional layering (lighter and darker, coarser and finer) at smaller scales (thinner layers). The hydraulic fill “shells” of the lower (main body) of the dam are layered at multiple scales, as was clear when opening and examining (and testing) tube samples obtained from the hydraulic fill shells (Seed et al., 1973, 1975; Seed et al., 1989, and Castro et al., 1992). Further illustration of this layering of the hydraulic fill shells is presented in Figure 4-8, which presents CPT data from a large number of CPT probes through the hydraulic fill “shell” zones as part of later (1985) studies (Castro, et al., 1992), as re-compiled and summarized by Olson (2001).

There are also “stringers” (thin and sometimes tapering layers) of finer, and even clayey, material extending laterally outwards to various distances from the puddled central clay core “zone” as a result of interruptions in hydraulic fill placement, and resulting settlement of fines over a broader area. Similarly, there are also “sandy” and silty layers and lenses or stringers extending to various lateral distances into the edges of the puddled central clay core zone, likely due to material variations during the excavation of the variable



Figure 4-7: Photograph of the side wall of a post-earthquake excavation through the upstream hydraulic fill showing distinct layering within the hydraulic fill zone. (H.B. Seed personal collection)

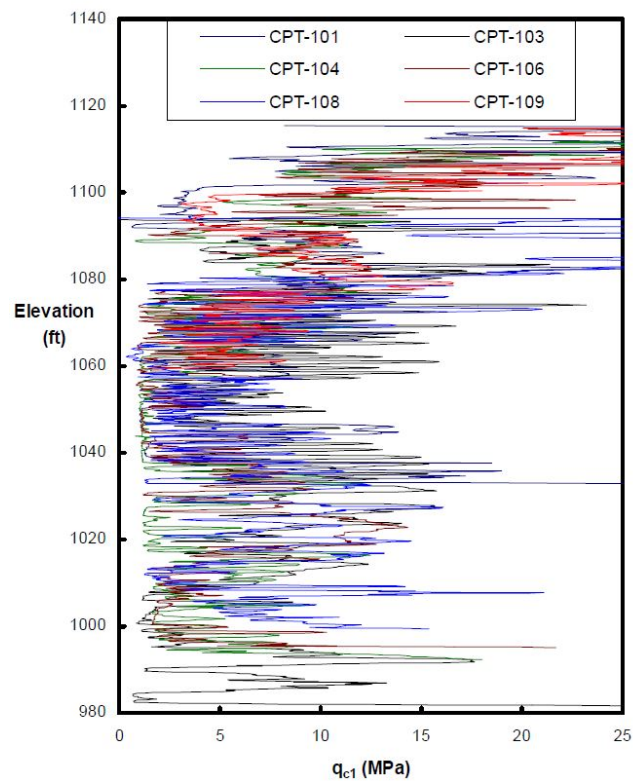


Figure 4-8: Summary of corrected CPT tip resistance q_{c1} (MPa) performed through the downstream hydraulic fill “shell” zones. (Olson, 2001).

streambed deposits used as the principal borrow source, and to periodic interruptions and variations in hydraulic fill emplacement operations.

As per Seed et al. (1973), the following is a brief summary of the LSFD foundation preparation and embankment construction.

- The construction of the LSFD began in 1912. The foundation alluvium was not stripped off prior to placing the embankment fill. This left potentially liquefiable sands and silty sands in place beneath the base of the embankment. There are reports of three cutoff trenches through the alluvium, which were backfilled with “hydraulicked” materials (or “puddled” clay).
- Based on available photographs and records, Seed et al. (1973) concluded that the lower, main body of the embankment was constructed by the hydraulic fill method described on the previous page. Between 1912 and 1915, the embankment was constructed by hydraulic fill to about Elevation 1080 ft. at the axis, and about 1090 ft. at the upstream and downstream edges, using materials hydraulicked from the stream bed.
- The borrow site then shifted and hydraulic fill construction continued using ground-up shale from a borrow area on the hillside at the left end of the dam, until the dam was built up to Elevation 1097 ft. at the axis.
- In 1916-17, the hydraulic fill section was capped by a rolled earthfill composed of shales from the east abutment. This fill was placed to about Elevation 1118 ft. for a narrow width at the upstream side and 1108 feet across the remainder of the dam. In 1920, additional fill was placed to bring the upstream edge to Elevation 1125 ft.
- In 1924, the embankment was again raised. This time, rolled fill was placed to about Elevation 1133 ft. along the upstream side and 1118 ft. on the downstream side. The material used was a combination of heavy clay and gravel from the hill at the right end of the dam.
- In 1929-30, the dam was raised for the last time, to Elevation 1144.6 ft. A trench was excavated through all of the previously placed upper fill zones and into the hydraulic fill. All shale materials encountered were removed and the new fill placed was reported to be a very plastic material.
- The shale materials excavated from the core trench were mixed with gravelly material from borrow pits at the right end and upstream side of the dam, and were placed in a downstream toe berm addition. This is called a “rock blanket” in summary notes recorded in the Field Report. This rock blanket was placed on a 3H:1V slope.
- In 1940, a final major modification was made with the construction of a rolled earth downstream toe berm addition terminating at Elevation 1096. This addition has a 4.5H:1V slope, except that it steepens a bit at the right abutment.
- The final dam had the dam had a maximum crest height of 43.3 meters (142 feet).

The original Lower San Fernando Dam has now been lowered, and significantly reconstructed/reconfigured, since the 1971 upstream slope failure to now serve as an emergency water retaining structure. The original reservoir base, now dry, serves primarily

as a Los Angeles Police Department (LAPD) training facility and LADWP stockpile area. In addition, an ultra-violet (UV) water treatment plant is currently being built, and a portion of the area is being prepared for temporary storm water storage (Tetone; personal communication).

4.4 GEOLOGICAL/GEOTECHNICAL ANALYSIS CROSS-SECTION AND ANALYSIS PLAN

4.4.1 Analysis Cross-Section

Seed et al. (1973) developed an idealized cross-section for back-analyses of the LSFD (Figure 4-9), which was subsequently utilized by multiple other researchers. This cross-section is analogous to a composite of Cross-Sections E-E' and F-F', the two center sections out of four cross sections through the upstream flow slide failure that were investigated during the post-earthquake studies. In this current study, the closely similar maximum height cross section was utilized (Figure 4-10).

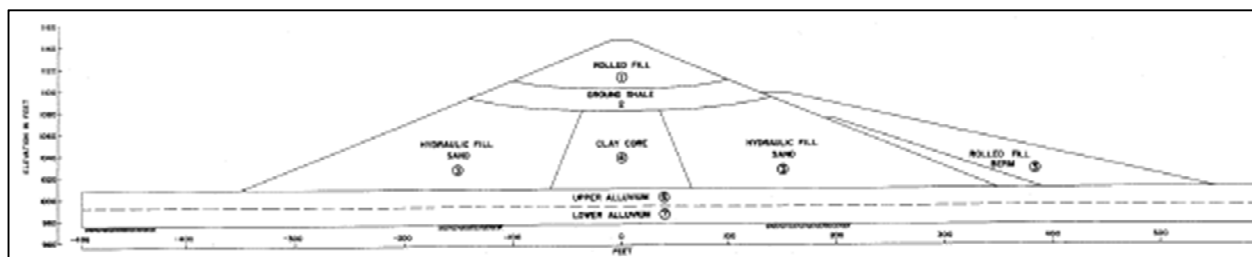


Figure 4-9: Representative cross-section of the LSFD (Seed et al., 1973)

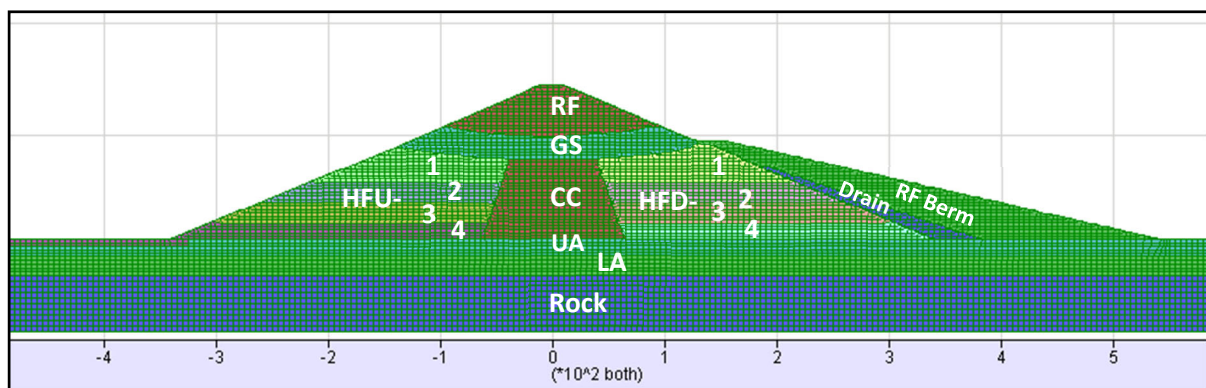


Figure 4-10: Analysis cross-section and principal material zones (current study)

As discussed in Section 4.2, the dam had a maximum height of 142 feet, and was constructed primarily by means of the hydraulic fill method, which produced relatively loose and primarily cohesionless upstream and downstream hydraulic fill “shells” [HF-U and HF-D, respectively], and a more cohesive “puddled” central clay core [CC]. A ground shale layer [GS], and then a rolled fill layer [RF], were later emplaced atop the hydraulic fill embankment

to achieve the final crest height. The chimney drain [Drain] adjacent to downstream slope face was then later installed, and finally a rolled fill berm [RF Berm] was placed on downstream side of the chimney drain. Foundation materials immediately below the dam consist of two alluvial units: Zones 6 and 7 in Figure 4-9; and Zones UA (Upper Alluvium) and LA (Lower Alluvium) in Figure 4-10.

The principal soils zones or soil strata modeled in these current studies (and in Figure 4-10) are identified using the following nomenclature:

Rolled Fill	-	RF
Hydraulic Fill Upstream	-	HFU (HFU-1 = upper, HFU-2 and HFU-3 = the two middle zones, and HFU-4 = lower most)
Clayey Core	-	CC
Hydraulic Fill Downstream	-	HFD (HFD-1 = upper, HFD-2 and HFD-3 = the two middle zones, and HFD-4 = lower most)
Rock Drain	-	Drain
Rolled Fill Berm	-	RFBerm
Upper Alluvium	-	UA
Lower Alluvium	-	LA

The principal potentially liquefiable materials/units are the upstream and downstream hydraulic fill “shells”, and the upper alluvium. The upstream side and downstream side hydraulic fill shells are each sub-divided into four sub-zones, by elevation, based on differences in penetration resistances. Similarly, the upper alluvium is separated from the underlying (and denser) lower alluvium based primarily on differences in penetration resistances. The lower alluvium is denser and is considered non-liquefiable. The upper alluvium was treated separately in these current studies, but a review of the available data showed that (1) SPT blow counts were higher in the upper alluvium than in the overlying hydraulic fill shell zones, and (2) SPT blow counts increased rapidly at small depths into the upper alluvium. As a result, the upper alluvium is also treated as non-liquefiable. Any areas of lower blow count upper alluvium would be localized, and relatively thin, and any corollary potential liquefaction behaviors would be suitably captured by the modeling of the overlying hydraulic fill shell materials.

4.4.2 Analysis Plan

These current studies employ a limited set of selected analytical models, and all of them are applied within a finite difference analysis framework using the code FLAC (Fast Lagrangian Analysis of Continua; Itasca, 2011). A suite of six sets of nonlinear seismic deformation analyses are performed for the LSFD, and the combinations of (1) analytical or

constitutive models, (2) soil liquefaction triggering models, and (3) post-liquefaction residual strength models employed in each of these analyses are listed in Table 4-1.

The nomenclature in this table revolves around the three principal choices made in developing each analysis: (1) the analytical model employed, (2) the liquefaction triggering relationship employed, and (3) the post-liquefaction residual strength (S_r) relationship employed.

The material behavior models employed in these analyses for potentially liquefiable soils are listed in Table 4-1. These were described previously in Section 2.2. Potentially liquefiable soil layers are modeled using four different models, and these are the (1) Roth, (2) UBCSAND, (3) PM4Sand, and (4) Wang2D constitutive models. Non-liquefiable soils are modeled using the FLAC Mohr-Coulomb model in all of the analyses performed. Each of these models require soil characterization as part of model parameterization.

The models for potentially liquefiable soils were each calibrated using one or more of three soil liquefaction triggering relationships, and these are (1) Youd et al. (2001) – [Y], (2) Boulanger and Idriss (2014)–[B&I], and (3) Cetin et al. (2018) – [C]. These relationships were described in Section 2.3. Each of these relationships were employed in conjunction with the K_σ relationships for the liquefaction triggering relationships employed. Each of these triggering relationships also require characterization of soil units for model parametrization.

Post-liquefaction residual strengths (S_r) were employed in the analyses performed, and three different relationships were employed for this purpose. These were the S_r relationships of (1) Seed and Harder (1990) – [S&H], (2) Idriss and Boulanger (2015) – [I&B], and (3) Weber et al. (2015) – [W]. These were described in Section 2.4. Each of these relationships also require characterization of soil units for model parametrization.

In addition, it is necessary to properly characterize, and model, the non-liquefiable materials in the analysis cross-section.

It is also necessary to develop, and apply, suitable “input” strong motion time histories to the analytical models developed.

Each of the above represent their own sets of challenges, and these will be addressed in the remaining sections of this chapter.

Table 4-1: Summary of the six analytical modeling schemes employed for the LSFD back-analyses performed in these current studies.

Analysis ID	Description
Analysis 1: Roth Model (C, W)	Constitutive model for liquefiable soils – Roth Liquefaction triggering – Cetin et al. (2018); K_σ – Youd et al. (2001) Post-liquefaction strength, S_r – Weber et al. (2015) [50 th percentile S_r applied during-shaking]
Analysis 2: UBCSAND (Y, S&H)	Constitutive model for liquefiable soils – UBCSAND Liquefaction triggering - Youd et al. (2001); K_σ – Youd et al. (2001) Post-liquefaction strength, S_r – Seed and Harder (1990) [Average S_r applied for post-shaking]
Analysis 3: UBCSAND (Y, W)	Constitutive model for liquefiable soils – UBCSAND Liquefaction triggering - Youd et al. (2001); K_σ – Youd et al. (2001) Post-liquefaction strength, S_r – Weber et al. (2015) [50 th percentile S_r applied for post-shaking]
Analysis 4: PM4Sand (B&I, I&B)	Constitutive model for liquefiable soils – PM4Sand Liquefaction triggering and K_σ – Boulanger and Idriss (2014) Post-liquefaction strength, S_r – Idriss and Boulanger (2015) [S_r relationship “with significant void redistribution” applied for post-shaking]
Analysis 5: PM4Sand (C, W)	Constitutive model for liquefiable soils – PM4Sand Liquefaction triggering – Cetin et al. (2018); K_σ – Youd et al. (2001) Post-liquefaction strength, S_r – Weber et al. (2015) [50 th percentile S_r applied for post-shaking]
Analysis 6: Wang2D (C, W)	Constitutive model for liquefiable soils – Wang2D Liquefaction triggering – Cetin et al. (2018); K_σ – Youd et al. (2001) Post-liquefaction strength, S_r – Weber et al. (2015) [50 th percentile S_r applied during shaking for durations with $R_{u,seis}$ greater than a specified value, and also during post-shaking analysis]

4.5 GEOTECHNICAL PARAMETERS FOR NONLINEAR SEISMIC DEFORMATION ANALYSES

4.5.1 Brief Summary of Available Data

After the 1971 San Fernando earthquake, the Division of Safety of Dams (DSOD) of the State of California Department of Water Resources (DWR) and the Los Angeles Department of Water and Power (LADWP) sponsored and performed a post-earthquake investigation program for both the Upper and Lower San Fernando Dams. The National Science Foundation (NSF) sponsored a grant to the University of California at Berkeley (UCB) and to the University of California, Los Angeles (UCLA) for the analytical studies as well as portions of the laboratory testing program. The investigation program and analytical studies were directed by the late Professors H.B. Seed of U.C. Berkeley and K.L. Lee of UCLA, and they are summarized in Seed et al. (1973; EERC 73-2).

A second significant field and laboratory investigation program was performed by Geotechnical Engineers, Inc. (GEI) in 1985 under a contract with the U.S. Army Corps of Engineers (USACE), with collaboration with a joint team from U.C. Berkeley and Stanford University. The main field work was performed by GEI Consultants, and laboratory testing programs and analyses were performed by both teams. This was part of a coordinated re-evaluation of the flow slide, and these studies involved two separate USACE contracts, one with GEI and the other with the University of California at Berkeley. The results of the GEI investigations are summarized in Castro et al. (1989) and the results of the U.C. Berkeley studies are summarized in Seed et al. (1989).

The parameters for the NDA analyses performed in this current study were developed based primarily on a re-evaluation of the data presented in Seed et al. (1973), Seed et al. (1989), Castro et al. (1989), and current State of Practice procedures for parameter evaluation and modeling employing the analytical tools and relationships used herein.

The 1971-1972 investigation program included trench excavation, 19 mud-rotary borings, and two bucket auger holes in the downstream section of the embankment, many field density tests, and a detailed laboratory testing program. Figure 4-4 shows a plan view of the principal explorations performed during the 1971-72 studies, including the locations of the mud-rotary borings. In the mud-rotary borings, a Standard Penetration Test (SPT) was performed, and a Shelby tube sample was taken, at approximately 5-foot intervals. The 1971-72 investigations also included laboratory strength tests of the puddled central core materials, and in situ density tests as well as corollary maximum and minimum density tests (for D_r evaluation purposes) of the hydraulic fill shell materials.

Figure 4-11 shows a plan view of borings, CPTs, and a deep (large diameter) exploration shaft performed for the 1985 field investigation program. Figure 4-12 shows the reconstructed/reconfigured embankment in which these 1985 investigations were performed. In the reconstructed configuration, the original upstream shell has been replaced by a compacted fill but the downstream shell below El. 1100 ft. remains essentially as it was at the time of the 1971 earthquake.

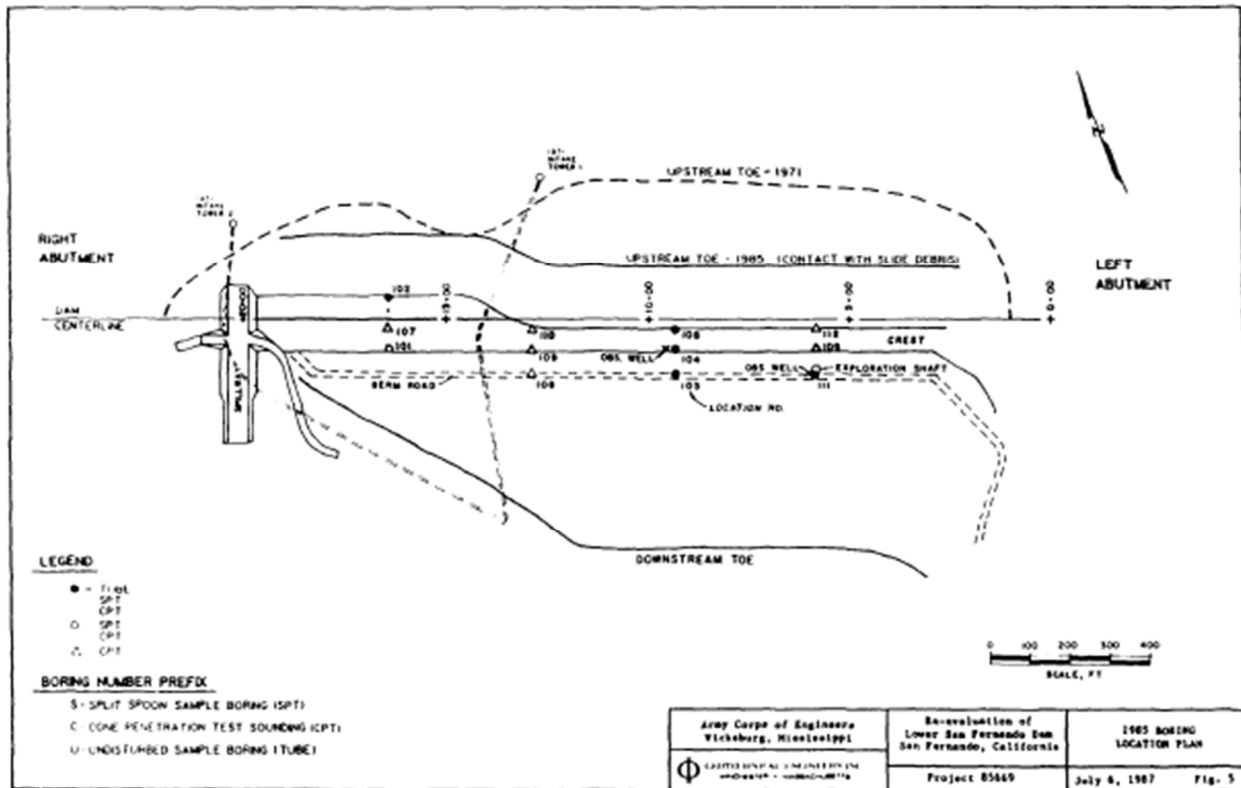


Figure 4-11: Plan view of field investigation program performed in 1985 by GEI Consultants for the USACE (Castro et al., 1989)

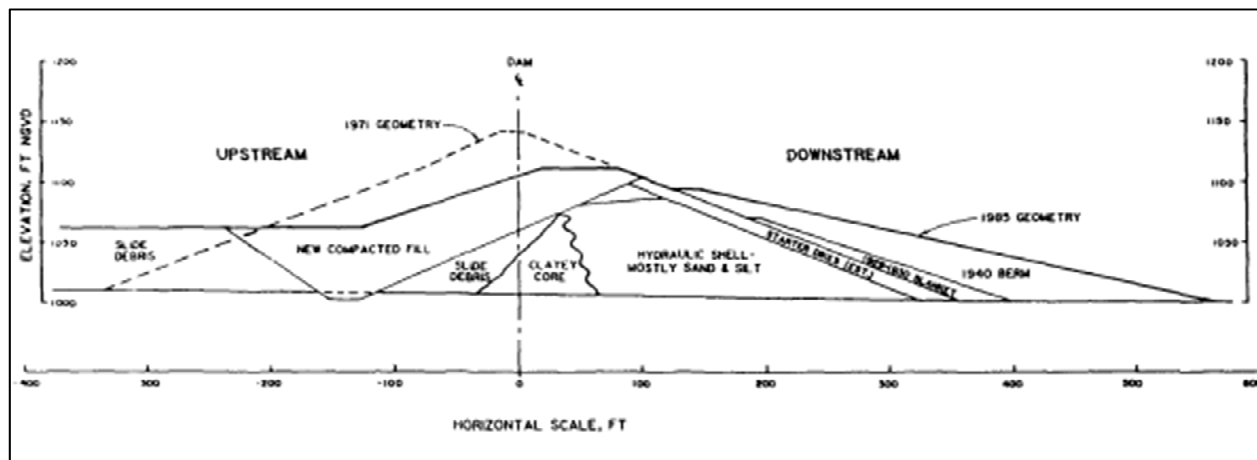


Figure 4-12: Cross-section through the reconstructed/reconfigured Lower San Fernando Dam as it existed in 1985 (Castro et al. 1989)

The 1985 field investigation program included:

1. Six borings (S101, S102, S103, S104, S105, and S106) with SPTs and sampling. Samples were taken at 5-foot intervals in Boring S104. In the remaining borings, split spoon samples were taken continuously through the hydraulic fill portion of the dam and intermittently above and below the hydraulic fill.
2. 12 Cone Penetration Testing (CPT), designated as C101 through C112. Six of these CPT soundings were performed adjacent to the SPT borings.
3. Six borings (U101, U12, U103, U104, U105, and U106), where undisturbed samples were obtained from selected zones of the dam.
4. An exploration shaft, from which hand-carved “undisturbed” samples of hydraulic fill shell materials were recovered using a special “tripod” procedure developed by GEI.

Considering that the original hydraulic fill embankment was probably reasonably symmetrical in configuration and properties about the center-line of the crest, based on excavation and emplacement of similar soils, by similar hydraulic fill methods, simultaneously on both sides of the hydraulic fill embankment, it was assumed that the properties of the soils forming the upstream shell can be evaluated with a reasonable degree of accuracy on the basis of the properties of the hydraulic fill comprising the remaining (largely intact) downstream portion of the embankment (Seed et al., 1973).

4.5.2 SPT Blow Counts for Potentially Liquefiable Materials

Parameterization for the geotechnical materials for this case history has been well developed, and a number of previous investigators and teams have back-analyzed this case history. The ground shale hydraulic fill was considered too cohesive to liquefy, though it might be potentially susceptible to both cyclic softening and strain softening. The upper rolled fill, and the rolled fill of the stability berm, were both non-saturated, and denser than the main hydraulic fill zones; they were thus considered not to be potentially susceptible to cyclic liquefaction. The upstream and downstream shell hydraulic fill materials are considered to be potentially susceptible to seismically induced soil liquefaction. These hydraulic fill “shells” were comprised of highly variable inter-layered sands, silty sands, and silts of low plasticity. There were also interbedded clay layers, mainly near the central “puddled” central clay core. The puddled central clay core was not considered potentially susceptible to classic liquefaction, but it was considered to be potentially susceptible to cyclic softening and also to strain softening. The underlying upper and lower alluvium layers were significantly denser and were not considered potentially susceptible to liquefaction. Thus, the principal materials considered to be potentially susceptible to seismically induced soil liquefaction was the saturated portions of the upstream and downstream hydraulic fill shells.

SPT blow counts from both the 1971 and 1985 studies, as well as the interpreted representative $N_{1,60}$ and $N_{1,60,cs}$ values utilized by previous studies, were evaluated as part of these current studies. Six new sets of independent evaluations of $N_{1,60,cs}$ values were also performed in these current studies, in accordance with procedures outlined by (1) Youd et

al. (2001), (2) Boulanger and Idriss (2014), (3) Cetin et al. (2018), (4) Seed and Harder (1990), (5) Idriss and Boulanger (2015) and (6) Weber et al. (2015).

Seven downstream borings from the 1971 investigations (D-1, E-1, E-2, F-1, F-2, and G-1, and G-2) were considered relevant for developing representative $N_{1,60}$ values for the hydraulic fill layers. Figure 4-13 presents $N_{1,60}$ values from these seven downstream shell borings, as presented in Seed et al. (1973), and it also shows the four elevational sub-zones selected by Seed et al. (1973) for analyses of the seismic performance of the LSFD based on SPT penetration resistances.

Similarly, four downstream borings from the 1985 investigations (S101, S103, S104, and S111) were also considered relevant for developing representative $N_{1,60}$ values for hydraulic fill layers. Figure 4-14 presents $N_{1,60}$ values from these four additional downstream shell borings, as presented in Seed et al. (1989), and showing the four elevational sub-zones as interpreted in the work of Seed et al. (1989).

Figure 4-15 presents a combined summary of $(N_1)_{60}$ values from both the 1971 and 1985 investigations. The overburden corrected $(N_1)_{60}$ values in Figures 4-13 through 4-15 were developed using the Seed, Tokimatsu, Harder, and Chung (1984) method. Table 4-2 presents both median and average values of pre-earthquake $(N_1)_{60}$ from the 1971 and 1985 studies, and “representative” $(N_1)_{60}$ values selected by Seed et al. (1989) based on these combined data.

Seed et al. (1973) noted that the density of the hydraulic fill layers has probably changed since the earthquake as evidenced by the settlement of observation points downstream side of the embankment. The resulting changes in penetration resistance at the time of the 1985 borings were likely a bit greater than those at the time of the 1971 post-

Table 4-2: Combined SPT $(N_1)_{60}$ values from 1971 and 1985 studies (Seed et al., 1989)

Elevation (feet)	Median Values of $(N_1)_{60}$		Average Values of $(N_1)_{60}$		Representative Average $(N_1)_{60}$
	1971 Data	1985 Data	1971 Data	1985 Data	
EL.1074-EL. 1057	17.0	20.0	16.5	21.0	~ 19.0
El. 1057-EL. 1039	14.5	13.0	15.5	14.0	~ 14.5
EL.1038-EL. 1024	21.5	25.5	21.5	28.5	~ 24.0
EL.1023-EL. 1000	16.0	13.0	16.0	14.5	~ 14.5

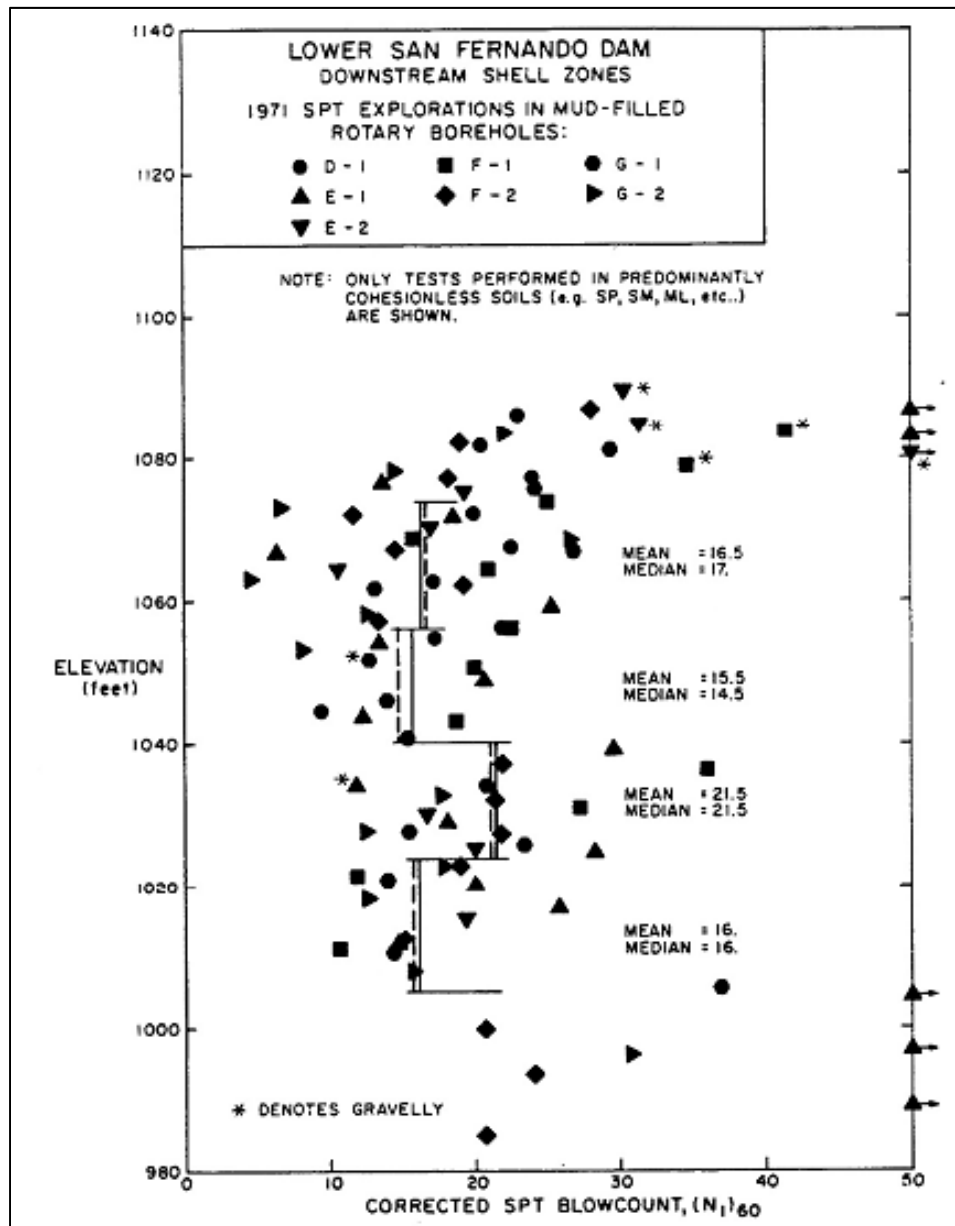


Figure 4-13: Summary of post-earthquake $(N_1)_{60}$ values (overburden, energy, and equipment corrected SPT values) from the 1971 investigation, as developed and compiled in Seed et al. (1973 and 1989)

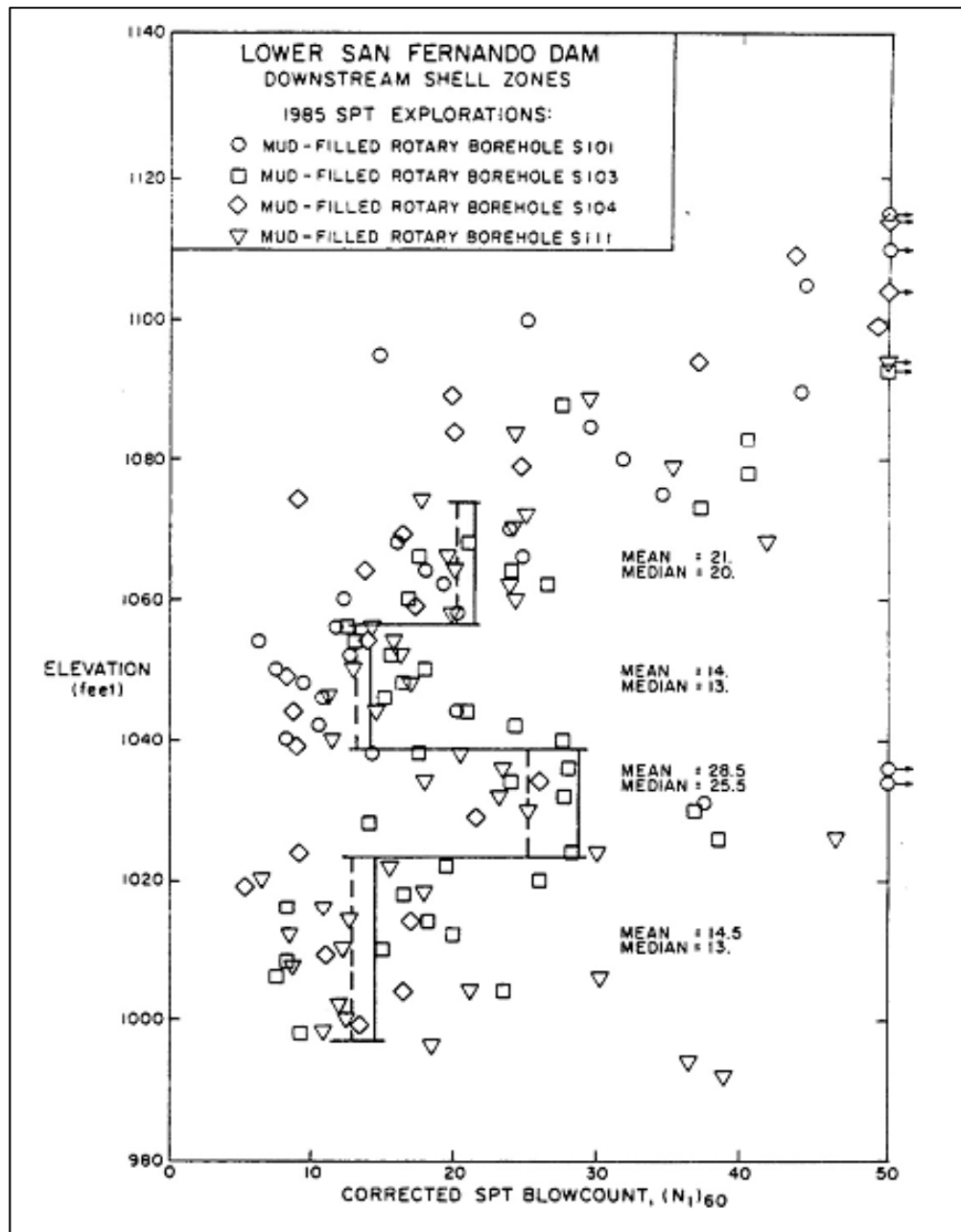


Figure 4-14: Summary of post-earthquake $(N_1)_{60}$ values (overburden, energy, and equipment corrected SPT values) from the 1985 investigation, as developed and compiled in Seed et al. (1989)

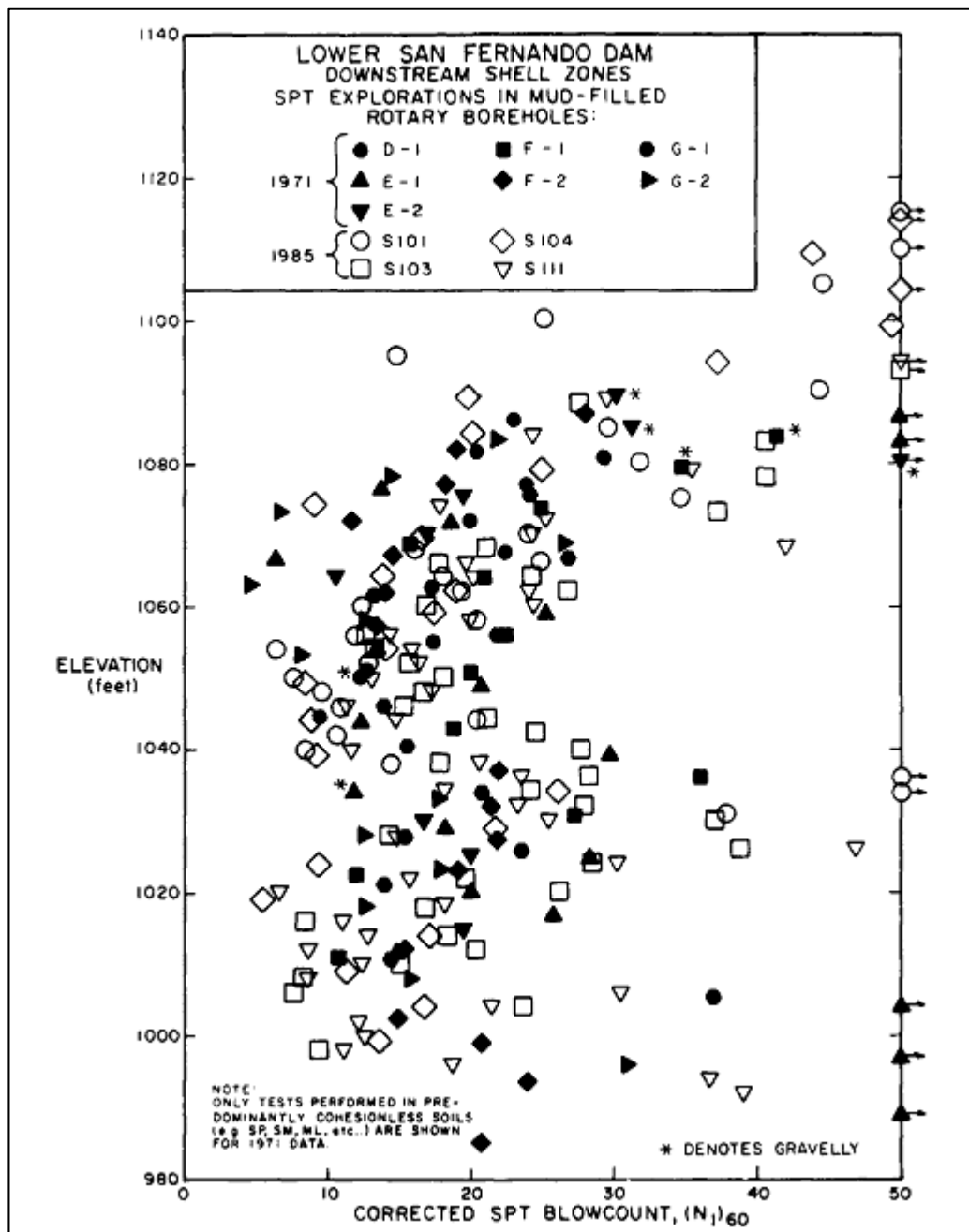


Figure 4-15: Summary of post-earthquake $(N_1)_{60}$ values (overburden, energy, and equipment corrected SPT values) from the 1971 and 1985 investigations, as compiled in Seed et al. (1989)

earthquake borings, which were performed in April and May of 1971, because “ageing effects” likely disrupted by high cyclic pore pressure generation during the earthquake would have begun to re-establish themselves. Based on an evaluation using Skempton (1986) for relative density, Seed et al. (1973) concluded that the $(N_1)_{60}$ values should be reduced by a value of approximately 2 blows/ft to best represent pre-earthquake conditions. This value has been relatively widely used by other investigators, and a similar approach will be taken in these current studies. As shown in Figures 4-13 through 4-15, there are no apparent systematic differences between the measured SPT penetration differences from the 1971 and 1985 field studies, and data from both studies will be treated equally herein.

Seed et al. (1973) and Castro et al. (1989) performed a number of grain size distribution analysis tests as part of the 1971 and 1985 site investigations of the LSFD. These grain size distribution analyses results were re-evaluated as part of this study. Table 4-3 presents a summary of fines contents from grain size distribution curves for relatively clean Sand (SW or SP) to Silty Sand (SM) samples with fines contents of less than 50 percent by weight. Average fines contents of both Sand and Silty Sand samples in hydraulic fill layers (46 samples) from the 1971 and 1985 studies is 24.3%, and Seed et al. (1989) suggested a value of 25 percent fines as a representative average value for hydraulic fill.

Table 4-3: Summary of grain size distributions for the hydraulic fill shells of the LSFD (samples comprised of sands and silty sands with less than 50% fines) from the 1971 and 1985 field studies

Study	Number of Grain Size Distribution Curves on Sand to Silty Sand (<50% fines)	33 rd Percentile	Mean	Median
1971 Investigation	14	Fines content range between 5 and 32 percent		
1985 Investigation	32	18.1	22.0	26.9

For this current study, a fines content of 25 percent has been adopted as a representative average value for fines correction for silty sand samples (SM), a fines content of 5 percent has been adopted for clean sand (SP) samples, and a fines content of 10 percent was adopted for SP-SM samples.

The available SPT data in hydraulic fill shell materials was re-processed anew in these current studies. The results were then cross-compared with the previous work and interpretations of Seed et al. (1989), Beaty (2001), and Weber et al. (2015). A number of different sets of corrections for (1) variations in SPT energy, equipment and procedures, (2) effective overburden effects (K_σ) and (3) fines were required for these current studies, as a number of the (1) liquefaction triggering relationships employed in these current studies,

and of the (2) post-liquefaction residual strength relationships (S_r) employed in these current studies each required their own sets of corrections in order to develop “energy, equipment, overburden and fines corrected” $N_{1,60,CS}$ values for use in the analyses performed herein.

Table 4-4 presents 33rd percentile, mean, and median values of $N_{1,60,CS}$ values developed in these current studies, based on the corrections procedures for SPT energy, equipment and procedures, as well as for fines content, and effective overburden stress, as recommended by each set of authors/developers of each of the three liquefaction triggering relationships used in these current analyses: the Youd et al. (2001), Boulanger and Idriss (2014), and Cetin et al. (2018) liquefaction triggering relationships. The four elevational sub-zones in the hydraulic fill do not precisely match either the elevational zones of Seed et al. (1973), nor of the other subsequent back-analysis teams against which cross-comparisons will be made, but these elevational zonings do not differ strongly. Each investigation or back-analysis team performed their own analyses, and sub-zoning choices (by elevation) varied a bit based on independent interpretations of the available data.

The approach taken in developing Table 4-4 warrants brief discussion. Values presented are (1) 33rd percentile values, (2) median (50th percentile) values, and (3) mean (average) values. Mean or median values tend to be the most used in current practice, and some of the liquefaction triggering relationships, and some of the post-liquefaction residual strength relationships, are clear as to which set of values were used in developing those specific relationships. There is still engineering judgment involved, however, as potentially anomalously high SPT N-values can occur, possibly as a result of coarse particles impeding the penetrometer. Similarly, a layer of softer soil (e.g. clay or silty material) can produce anomalously low N-values. It is recommended that all SPT samples retrieved be retained while SPT interpretations (and analytical parameterizations) are being performed, as opening and inspecting SPT samples can be useful here. When sample recovery is low, that can be indicative of coarser particle interference with the penetrometer. When softer, finer soils are included within the sample run, that can often be easily observed in the recovered sample. But when samples have been discarded, such checks cannot be made. Even when samples are retained, partial obstruction by coarse particles (gravel, cobbles, etc.) that do not massively impede SPT sample recovery can still increase measured N-values, and that can require judgment calls. Similarly, judgements must often be made as to the representative soil consistency of a given sample (e.g. is it potentially liquefiable, or not potentially liquefiable, based on gradation and fines plasticity, etc.), and/or laboratory evaluations can be made to help to assess material character.

Mean values of $N_{1,60,CS}$ can be biased upwards by inclusion of one or more spurious (non-representative) high measured N-values. Median values of $N_{1,60,CS}$ tend to be less biased by only one or a few such high values. But many of the relationships available (both triggering and S_r relationships) are based more on mean than median values. Having both values allows the engineer to exercise judgment. Similarly, 33rd percentile values are also useful for engineering judgment, as it reminds the engineer that it is not really the “average” properties that will likely actually control the strength and behavior of most soil units, but rather something closer to the weakest unit of the soil that can be consistently (continuous-

Table 4-4: Fines corrected pre-earthquake SPT $N_{1,60,CS}$ blow counts for hydraulic fill zones in the LSFD for the three liquefaction triggering relationships used in these current studies

Soil Layer and Elevation	Youd et al. (2001) $N_{1,60,CS}$			Boulanger and Idriss (2014) $N_{1,60,CS}$			Cetin et al. (2018) $N_{1,60,CS}$		
	33 rd Percen- tile	Mean	Median	33 rd Percen- Tile	Mean	Median	33 rd Percen- tile	Mean	Median
HFU-1 and HFD-1 (Elev. 1085 to 1058 ft.)	15.0	18.2	17.6	15.2	18.4	17.6	13.9	16.6	16.1
HFU-2 and HFD-2 (Elev. 1058 to 1039 ft.)	14.4	16.0	15.7	13.4	15.7	15.2	12.6	14.2	13.4
HFU-3 and HFD-3 (Elev. 1039 to 1021 ft.)	19.7	21.5	20.8	19.9	22.8	22.1	17.2	19.5	19.4
HFU-4 and HFD-4 (Elev. 1021 to 1007 ft.)	13.8	14.8	15.4	12.0	14.5	15.0	11.2	12.8	13.6

ly) accessed; or at least a combination of soil zones that can be accesses to form a contiguous failure “surface” or zone. 33rd percentile values cannot be used directly, however, as the liquefaction triggering and post-liquefaction S_r relationships are all based on back-analyses employing either mean or median $N_{1,60,CS}$ values, and employing 33rd percentile values would induce significant conservative bias.

For this current study, mean (or average) values of $N_{1,60,CS}$, as developed in accordance with the energy, equipment, overburden stress and fines corrections of each of the different liquefaction triggering relationships were utilized as representative values for the back-analyses performed. This approach is similar to Seed et al. (1973 and 1989), where average values of $N_{1,60,CS}$ values were considered as representative for the back-analyses of the LSFD and USFD.

A second set of energy, equipment, overburden stress and fines adjusted $N_{1,60,CS}$ values is also needed for the three post-liquefaction strength (S_r) relationships used in these current studies. The representative $N_{1,60,CS}$ - S_r values developed and employed for the three S_r relationships used in these current studies are presented in Table 4-5 (along with the values employed in the three triggering relationships). The S_r relationship of Seed and Harder (1990) employs energy, equipment, overburden stress and fines corrections as per the triggering relationship of Seed, Tokimatsu, Harder and Chung (1984). These are very

Table 4-5: Representative corrected pre-earthquake SPT $N_{1,60,CS}$ and SPT $N_{1,60,CS-S_r}$ blow counts for the LSFD for liquefaction triggering and post-liquefaction strength using different relationships used in these current studies

Soil Layer	Youd et al. (2001)		Boulanger and Boulanger (2014)		Cetin et al. (2018)
	Average Pre-EQ $N_{1,60,CS}$ for Liquefaction Triggering	Average Pre-EQ $N_{1,60,CS}$ for Seed and Harder, S_r (1990)	Average Pre-Earthquake $N_{1,60,CS}$ for Liquefaction Triggering	Average Pre-EQ $N_{1,60,CS}$ for Idriss and Boulanger, S_r (2015)	Average Pre-EQ $N_{1,60,CS}$ for both Liquefaction Triggering and Weber et al. (2015) S_r
HFU-1 and HFD-1	18.2	16.7	18.4	17.4	16.6
HFU-2 and HFD-2	16.0	13.9	15.7	14.1	14.2
HFU-3 and HFD-3	21.5	19.2	22.8	22.2	19.5
HFU-4 and HFD-4	14.8	12.5	14.5	12.6	12.8

similar to the recommended corrections of the Youd et al. (2001) triggering relationship, except that the overburden stress correction differs somewhat; producing slightly lower $N_{1,60,CS-S_r}$ values, as shown in Table 4-5. The fines correction for use in the S_r relationship of Idriss and Boulanger (2014) differs from that of their triggering relationship, and produces slightly lower $N_{1,60,CS-S_r}$ values, as shown in Table 4-5. The Weber et al. (2015) S_r relationship was developed using the energy, equipment, overburden stress and fines adjustments of the Cetin et al. (2004) triggering relationship. The fines correction (ΔN_{fc}) of the Cetin et al. (2018) triggering relationships differs a bit from that of the earlier 2004 triggering relationship, but the differences are not significant in the ranges of interest for the materials modeled here, producing values within a half blow count (or closer) to the $N_{1,60,CS}$ values employed for the Cetin et al. (2018) triggering relationship. Accordingly, the same $N_{1,60,CS}$ values were used for both the Cetin et al. (2018) triggering relationship, and the Weber et al. (2015) S_r relationship, as shown in Table 4-5.

4.5.3 Cross-Checks on $N_{1,60,CS}$ Values Developed

4.5.3.1 Cross-Comparisons of $N_{1,60,CS}$ Values with Previous Studies

A number of previous investigations and back-analyses have developed SPT-based characterizations of the potentially liquefiable materials of the LSFD. Cross-checks of the

values developed in previous studies, with the values developed in these current studies, is a useful exercise.

Table 4-6 shows a comparison between (1) the values selected for analysis by Seed et al. (1989) based on the combined field and lab data developed by the 1971-72 and 1985 field investigations reported in Seed et al. (1973), Castro et al. (1989), and Seed et al. (1989), and (2) those of this current study. The representative analysis values of Seed et al. (1989) were processed and corrected to $N_{1,60,CS}$ values based on the energy, equipment, procedure and overburden stress corrections of the Seed et al. (1984) liquefaction triggering relationship. The values developed in these current studies for the Youd et al. (2001) triggering relationship are based on similar corrections, with the only differences being corrections for effective overburden stress (K_σ). The comparison in Table 4-6 is therefore between these two sets of values. Elevational sub-divisions of the upstream and downstream hydraulic fills differed a bit between the two studies, so the comparison is not fully direct, but these differences in selected sub-layering divisions are not very pronounced. Agreement between the two sets of characterizations, allowing for differences in layering sub-divisions and K_σ , is considered very good.

Table 4-6: Comparison between representative $N_{1,60,CS}$ values developed by Seed et al. (1989) based on the corrections of Seed et al. (1984) vs. $N_{1,60,CS}$ values developed in these current studies based on the corrections of Youd et al. (2001)

Soil Layer	Seed et al. (1989): Processed for the Seed et al. (1984) Triggering Relationship	This Current Study: Processed for the Youd et al. (2001) Triggering Relationship
	Average Pre-Earthquake $N_{1,60,CS}$	Average Pre-Earthquake $N_{1,60,CS}$
HFU-1 and HFD-1	19.0 (Elev. 1074 to 1057)	18.2 (Elev. 1085 to 1058)
HFU-2 and HFD-2	14.5 (Elev. 1056 to 1039)	16.0 (Elev. 1058 to 1039)
HFU-3 and HFD-3	24.0 (Elev. 1038 to 1024)	21.5 (Elev. 1039 to 1021)
HFU-4 and HFD-4	14.5 (Elev. 1023 to 1000)	14.8 (Elev. 1021 to 1007)

Table 4-7 shows a comparison between (1) the values selected for analysis by Beaty (2001) based on the combined field and lab data developed by the 1971-72 and 1985 field investigations reported in Seed et al. (1975), Castro et al. (1989) and Seed et al. (1989), and (2) those of this current study. The representative analysis values of Beaty (2001) were processed and corrected to $(N_1)_{60}$ values based on the corrections of the Seed et al. (1984) liquefaction triggering relationship. Beaty (2001) used 33rd percentile $(N_1)_{60}$ values for the

LSFD analysis using a previous version of UBCSAND. The values developed in these current studies for the Youd et al. (2001) triggering relationship are based on similar corrections, with the only difference being in the corrections for effective overburden stress (K_σ). The comparison in Table 4-7 is therefore between these two sets of values. Elevational sub-divisions of the upstream and downstream hydraulic fills differed a bit between the two studies, so the comparison is again not fully direct. Agreement between the two sets of characterizations, allowing for differences in layering sub-divisions and in corrections for K_σ , is again considered very good.

Table 4-7: Comparison between 33rd percentile SPT (N_1)₆₀ values developed by Beaty (2001) based on the corrections of Seed et al. (1984) vs. 33rd percentile SPT (N_1)₆₀ values developed in these current studies based on the corrections of Youd et al. (2001)

Soil Layer	Beaty (2001): Processed for the Seed et al. (1984) Triggering Relationship	This Current Study: Processed for the Youd et al. (2001) Triggering Relationship
	33 rd Percentile Pre-Earthquake (N_1) ₆₀	33 rd Percentile Pre-Earthquake (N_1) ₆₀
HFU-1 and HFD-1	12 (Elev. 1074 to 1056)	12.8 (Elev. 1085 to 1058)
HFU-2 and HFD-2	9 (Elev. 1056 to 1039)	10.0 (Elev. 1058 to 1039)
HFU-3 and HFD-3	17 (Elev. 1039 to Elev. 1024)	14.5 (Elev. 1039 to 1021)
HFU-4 and HFD-4	9 (Elev. 1024 to 1000)	8.3 (Elev. 1021 to 1007)

Table 4-8 shows a comparison between the values selected for analyses by Weber et al. (2015) based on the combined field and lab data developed by the 1971-72 and 1985 field investigations reported in Seed et al. (1975), Castro et al. (1989) and Seed et al. (1989), and those of this current study. The representative analysis values of Weber et al. (2015) were processed and corrected to $N_{1,60,CS}$ values based on the corrections of the Cetin et al. (2004) liquefaction triggering relationship. The values developed in these current studies for the Cetin et al. (2018) triggering relationship are based on similar corrections, with the only difference being corrections for fines content (K_{fc}); and the differences in K_{fc} are relatively small in the range of interest for these current analyses. The comparison in Table 4-8 is therefore between these two sets of values. Elevational sub-divisions of the upstream and downstream hydraulic fills differed a bit between the two studies, so the comparison is again not fully direct. Agreement between the two sets of characterizations, allowing for differences in layering sub-divisions and K_{fc} , is again considered very good. The minor differences between two sets of values are mainly due to slightly different approaches for screening higher blow counts within the sub-layers.

Table 4-8: Comparison between representative $N_{1,60,CS}$ values developed by Weber et al. (2015) based on the corrections of Cetin et al. (2004) vs. $N_{1,60,CS}$ values developed in these current studies based on the corrections of Cetin et al. (2018)

Soil Layer	Weber et al. (2015): Processed for the Cetin et al. (2004) Triggering Relationship	This Current Study: Processed for the Cetin et al. (2018) Triggering Relationship
	Average Pre-Earthquake $N_{1,60,CS}$	Average Pre-Earthquake $N_{1,60,CS}$
HFU-1 and HFD-1	18.0	16.6
HFU-2 and HFD-2	14.7	14.2
HFU-3 and HFD-3	24.0	19.5
HFU-4 and HFD-4	13.7	12.8

4.5.3.2 Relative Density

Relative density is one of the most important parameters for seismic evaluations, and a second cross-check of the parameterizations for the potentially liquefiable soils in these current studies was made based on relative density; taking advantage of both the available SPT data, as well as data developed in the previous field studies including (1) in-situ density tests, (2) laboratory e_{max} and e_{min} tests for purposes of D_r evaluation, and (3) soils gradation data.

Relative density (D_R) can be estimated from $(N_1)_{60}$ values for coarse-grained soils, but there are intrinsic difficulties in accomplishing this. Studies by Skempton (1986) and Cubrinovski and Ishihara (1999) regarding cross-correlation between $(N_1)_{60}$ and D_r were evaluated as part of this current study.

Skempton (1986) evaluated Meyerhof's equation

$$(N_1)_{60} = (a + b) D_R^2 \quad \text{[Equation 4-1]}$$

where the parameters a and b are constants for a particular sand within a range of $0.35 < D_R < 0.85$ and $0.5 \text{ atm} < \sigma'_v < 2.5 \text{ atm}$. Skempton (1986) has shown that the parameters a and b (combined as $a + b = C_d$) tend to increase with increasing grain size, with increasing age of deposits, and with increasing overconsolidation ratio. Equation 4-2 shows a relationship between D_r and $(N_1)_{60}$. Skempton (1986) suggested that for normally consolidated natural

sands, an approximate value of $C_d \approx 60$ would produce similar results as the relative density relationship of Terzaghi and Peck (1967). He recommended use of $C_d \approx 55$ for fine sand and 65 for coarse sand. Skempton also considered ageing effects. Table 4-9 presents C_d values proposed by Skempton (1986) considering effects of aging.

$$D_R = \sqrt{\frac{(N_1)_{60}}{C_d}} \quad [\text{Equation 4-2}]$$

Table 4-9: Effect of aging on C_d Values (Skempton, 1986)

	Age of soil deposit (Years)	$C_d = (N_1)_{60}/D_R^2$
Laboratory Tests	10^{-2}	35
Recent Fills	10	40
Natural Deposits	$>10^2$	55

Cubrinovski and Ishihara (1999) compiled the results of 61 relative density measurements performed on samples of sands and gravels with SPT data of known $N_{1,78}$ blow counts (based on an assumed average Japanese SPT energy ratio of 78 percent). The results were summarized to develop relative density relationships based on D_{50} , $e_{\max} - e_{\min}$, and $N_{1,78}$ values. The following equations are based on the relationship of Cubrinovski and Ishihara (1999) for 78 percent SPT hammer energy ratio, but with the original $N_{1,78}$ -based Cubrinovski and Ishihara (1999) equation for C_d adjusted (modified) here for the 60 percent SPT hammer energy ratio (ER) common in U.S practice (and representing the $(N_1)_{60}$ standard employed in the three liquefaction triggering relationships, and in the three post-liquefaction S_r relationships, employed in these current studies) in Equation 4-5.

$$e_{\max} - e_{\min} = 0.23 + 0.06/D_{50} \quad [\text{Equation 4-3}]$$

$$C_d = 9/(e_{\max} - e_{\min})^{1.7} \quad \text{for ER}=78\% \quad [\text{Equation 4-4}]$$

$$C_d = 11.7/(e_{\max} - e_{\min})^{1.7} \quad \text{for ER}=60\% \quad [\text{Equation 4-5}]$$

Cubrinovski and Ishihara (1999) suggest that C_d values can vary between 10 and 100. Their data set included both sandy soils as well as coarser gravelly soils and cobbles. In this current study, the database of Cubrinovski and Ishihara (1999) was re-evaluated for a range of interest more suited for seismic evaluation of liquefaction-related behavior of primarily sandy and silty sand soils with: (1) $e_{\max} - e_{\min}$ of between 0.3 and 0.7, and (2) C_d values of between 20 and 70. $(N_1)_{78}$ values for soils conforming to this range in their larger data set were converted to $(N_1)_{60}$ values corresponding to 60 percent hammer energy ratio, and only D_R values of less than 100 percent were considered. A total of 28 values within this range remained, and these were used in developing a sub-relationship between C_d and $e_{\max} - e_{\min}$. Figure 4-16 shows resulting plots of (1) $e_{\max} - e_{\min}$ vs. D_{50} and (2) C_d vs. $e_{\max} - e_{\min}$ from the dataset of Cubrinovski and Ishihara (1999). Figure 4-17 shows a plot of C_d vs. $e_{\max} - e_{\min}$ based on re-evaluation of the Cubrinovski and Ishihara (1999) data set within the constrained ranges described above.

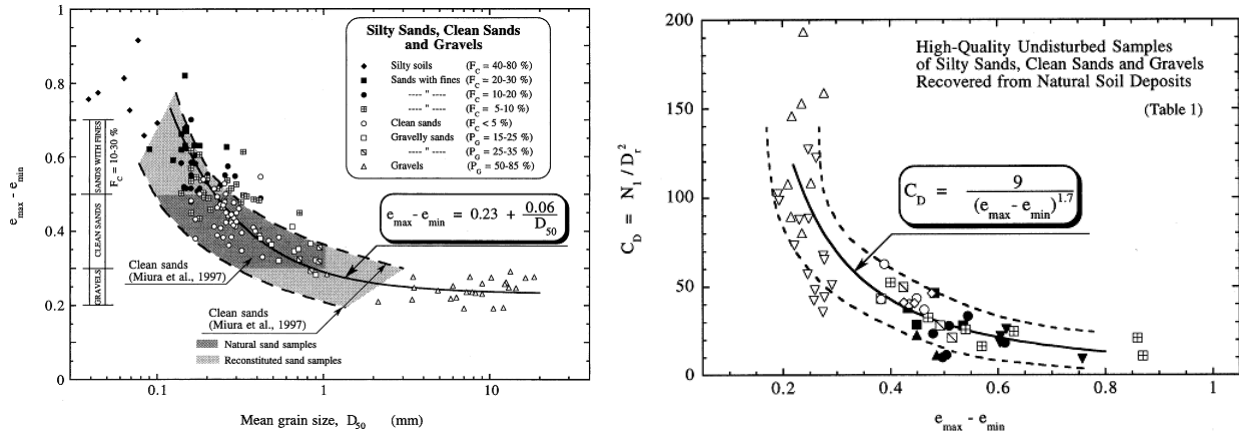


Figure 4-16: Plots of (a) $e_{\max} - e_{\min}$ vs. D_{50} and (b) C_d vs. $e_{\max} - e_{\min}$ Cubrinovski and Ishihara (1999)

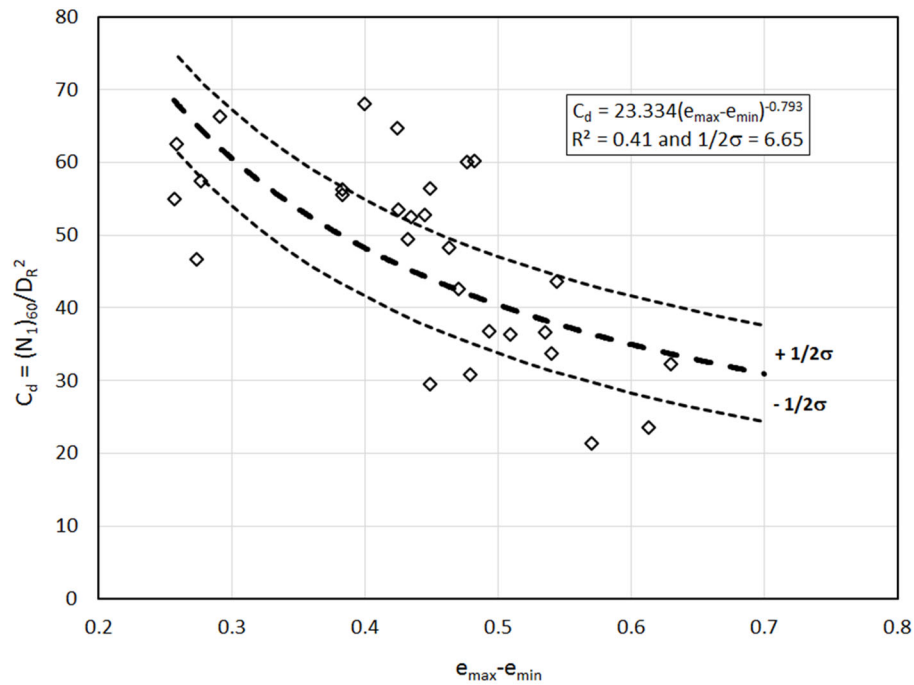


Figure 4-17: Modified plot of C_d vs. $e_{\max} - e_{\min}$ vs. C_d relationship (current study)

Based on this, the following equation (Equation 4-6) was developed in this study to relate void ratio range with C_d for sandy and silty sand soils.

$$C_d = 23.334(e_{\max} - e_{\min})^{-0.793} \quad [\text{Equation 4-6}]$$

It should be noted that the use of D_{50} -based $e_{\max} - e_{\min}$ may be a somewhat uncertain way to characterize or represent a soil layer, due to uncertainty in developing a

representative D_{50} and also considering that $e_{\max} - e_{\min}$ may be dependent on both D_{60} and D_{10} values. It may be more appropriate to estimate $e_{\max} - e_{\min}$ from commonly used values for soil types, such as presented in Cubrinovski and Ishihara (1999) and Mitchell and Soga (2012) or in-situ or laboratory tests.

As numerical modeling approaches are increasingly being simplified, and parameter selection is increasingly being correlated with $(N_1)_{60}$ -based relationships, a sensitivity study based on a range of possible D_R values for the same $(N_1)_{60}$ value and different C_d values may be appropriate for critical projects.

Table 4-10 shows a comparison of C_d values for different ranges of void ratio: (1) as recommended by Cubrinovski and Ishihara (1999) based on 78% SPT energy ratio (ER), (2) modified C_d values based on 60% ER, and (3) the further modified relationship developed in this study for a more appropriate range of soils for seismic studies of sandy and silty sand soils. The resulting further modified C_d values show a better correlation with Skempton's (1986) recommendations, which may be due in part to the more compatible range of soil material types to which it is likely to apply.

Relative density data were developed for soils at the USFD from post-earthquake laboratory and field studies (Seed et al. 1973). A comparison between those directly measured D_R values with estimated SPT-based values from the modified relationship

Table 4-10: Void ratio ranges ($e_{\max}-e_{\min}$) and C_d values from different relationships

Void Ratio Range from Cubrinovski and Ishihara (1999)				C_d from Cubrinovski and Ishihara (1999) with ER = 78%	C_d from Cubrinovski and Ishihara (1999) with ER = 60%	C_d from modified data sub-set from Cubrinovski and Ishihara (1999) (current study)	C_d values from Skempton (1986)
Soil Type	Fines Content (%)	Gravel (%)	$e_{\max} - e_{\min}$				
Silty Soils	40-80	< 5	> 0.7	< 17	< 21	< 31	55 for Silty Sand 65 for Coarse Sand
Silty Sand	20-30	< 5	0.60 to 0.70	21 to 17	28 to 21	35 to 31	
Silty Sand	10-20	< 5	0.50 to 0.60	29 to 21	38 to 28	40 to 35	
Silty Sand	5-10	< 5	0.45 to 0.55	35 to 25	45 to 32	44 to 37	
Clean Sand	< 5	< 5	0.30 to 0.50	70 to 29	91 to 38	61 to 40	40 for Recent Fill 55 for Natural Soil
Gravelly Sand	< 5	15-35	0.30 to 0.40	70 to 43	91 to 56	61 to 48	

Table 4-11 : Comparison between relative density for the LSFD from post-earthquake measurements and the modified equations (current study)

Layer	$e_{\max} - e_{\min}$ for coarse sand samples (Seed et al. 1976, Figure IV-7)	C_d using Equation 4-6 (this study) $C_d = 23.334^*$ $(e_{\max} - e_{\min})^{(1/0.793)}$	Post- Earthquake (N_1) ₆₀ from Cetin et al. (2018)	Relative Density, D_R (%) using C_d (Modified Cubrinovski and Ishihara, this study)	Measured and Estimated Relative Density, D_R (%) from Seed et al. (1973)
HFU-1	0.41 to 0.59	47.3 to 35.5	11.6	49.5 to 57.2 (average 53.4)	Direct Measure- ment $D_R \approx 50$ to 54 Percent and Estimated Values of $D_R \approx 45$ to 65 Percent
HFU-2			14.7	55.7 to 64.4 (average 60.1)	
UA			16.1	58.3 to 67.4 (average 62.9)	
HFD-1			11.9	50.1 to 57.9 (average 54.0)	
HFD-2			13.6	53.6 to 61.9 (average 57.8)	
HFD-3			14.6	55.5 to 64.2 (average 59.9)	

developed for this study (based on Cubrinovski and Ishihara (1999), but with a reduced dataset and a more limited range of applicability) is shown in Table 4-11. Based on post-earthquake in-situ testing and laboratory testing, and engineering evaluations, Seed et al. (1973) suggested that the relative density in the hydraulic fill typically ranges between 45 percent and 65 percent, which is comparable to the direct measurement values (50 to 54 percent). Average relative density values estimated based on the modified Equation 4-6 as described above vary between 53.4 percent and 62.9 percent, and these match well with the Seed et al. (1973) estimates and also with their actual measurements.

4.5.4 Shear Strengths and Strength Behaviors for Non-Liquefiable Soils

Non-liquefiable soil units were modeled in the nonlinear dynamic deformation analyses (NDA) of the Lower San Fernando Dam with the FLAC Mohr Coulomb model. There were suitable data available from the previous field and laboratory investigations for this purpose.

The central puddled clay core varied spatially, with thin layers and stringers of less plastic material, and even silty and sandy soils, near the upstream and downstream edges. Similarly, stringers of finer soils extended outward into the “shells”. The puddled clay core was considered to be essentially clay controlled, and it was found to be largely normally, with

a peak static undrained shear strength corresponding to $S_u/\sigma'_{vi} = 0.24$ (Seed et al., 1973). Atterberg Limits tests found representative values of $LL = 37$ to 60% , and $PI = 20$ to 40% . In-situ water content (w_i) varied a bit with depth, but the representative Liquidity Index was found to be $LI \approx 0.1$ to 0.35 , suggesting an associated strain sensitivity of $S_{u,peak} / S_{u,residual} \sim 2$ to 3 . This sensitivity value ranges between low to moderate sensitivity.

Castro et al. (1989) performed a laboratory vane shear test on an undisturbed clay core sample from the LSFD. This laboratory vane shear test indicated $S_u/\sigma'_{vi} = 0.3$ (peak), $S_u/\sigma'_{vi} = 0.16$ at 1 cm displacement, and $S_u/\sigma'_{vi} = 0.09$ at steady-state condition. These vane shear test results indicate a $S_{peak}/S_{steady-state} = 3.3$. Castro et al. (1989) utilized peak clay core strengths of between $S_u/\sigma'_{vi} = 0.2$ and 0.3 in their back-analyses for LSFD.

Weber et al. (2015) utilized a peak static undrained strength of $S_u/\sigma'_{vi} = 0.23$, and a steady-state (or fully residual) value $S_{steady-state}/\sigma'_{vi} = 0.07$ for the LSFD puddled central clay core in back-analyses of the LSFD to investigate post-liquefaction residual strength (S_r).

In the current studies, the puddled clay core was modeled as essentially clay controlled, and this clayey core was also modeled as essentially normally consolidated, with a peak static undrained shear strength corresponding to $S_u/\sigma'_{vi} \approx 0.24$. This central clay core was assumed to be vulnerable to both cyclic softening as well as strain softening, and the strength of the clay core was modeled as $S_u/\sigma'_{vi} = 0.192$ “during shaking”, representing a 20% reduction to account for both (1) cyclic softening and (2) partial strain softening. At the end of shaking, shear strains across the core zone were examined, and in those analyses where the development of large shear strains and shear offsets across narrowly banded shear zones across the core zone warranted, the shear strength of the central core zone was reduced to a value halfway between (1) the already softened strength of $S_u/\sigma'_{vi} = 0.192$ that was used during shaking to account for both cyclic softening and partial strain softening, and (2) the fully residual strength of $S_{u,residual}/\sigma'_{vi} = 0.08$. This intermediate strength is therefore modeled as $S_u/\sigma'_{vi} = (0.5)(0.192+0.08) = 0.136$. After implementation of this further reduced clay core strength, the analysis was then re-started and continued forward after the end of shaking.

If strains in the clay core continued to develop sufficiently, then clay strength was further reduced to a fully residual value of $S_{u,residual}/\sigma'_{vi} \approx 0.08$, and the analyses were again continued forward in time beyond the end of shaking unless and until either (1) deformations and displacements have ceased to occur, as the embankment is in a stable condition, or (2) mesh distortions are resulting in a need to perform significant (and time-consuming) re-meshing to continue the NDA deformation analysis, and the results at termination have become sufficient for purposes of engineering interpretation and decision-making, with recognition that deformations and displacements are still ongoing.

The hydraulically placed upper crushed shale fill was modeled with $c' = 500$ lbs/ft², and $\phi' = 27^\circ$. The top rolled fill was modeled with $c' = 300$ lbs/ft², and $\phi' = 31^\circ$. The downstream drain blanket was modeled with $c' = 0$, and $\phi' = 37^\circ$, and the downstream stability berm with $c' = 100$ lbs/ft², and $\phi' = 37^\circ$.

4.5.5 Hydraulic Conductivity and Pre-Earthquake Phreatic Surface for LSFD Analyses

Hydraulic conductivity values and seepage analyses are important to establish the initial (pre-earthquake) steady-state seepage conditions, which are in turn important to characterize the baseline (pre-earthquake) static effective stress conditions. In this study, a set of initial hydraulic conductivity values were assumed based on material descriptions and available data, as well as examination of values employed by previous analysts. Static (pre-earthquake) seepage analyses were then performed to develop an initial estimate of steady state conditions.

The results of these analyses were then compared with known details of the pre-earthquake hydraulic/phreatic conditions (based primarily on two piezometers in the embankment), and hydraulic conductivity values were then modified (within reasonable engineering bounds) and the seepage analyses were re-performed. The hydraulic conductivity values of the different soil units were then varied in a series of seepage analyses in FLAC to develop parameters that produce a good match with the pre-earthquake phreatic water surface elevations measured at two piezometers across a transverse cross-section. These piezometers were located approximately 250 feet and 445 feet downstream of the crest centerline, and the field piezometer levels prior to the earthquake were recorded as elevations of 1019 ft. and 1000 ft.

Table 4-12 presents a summary of the final hydraulic conductivity values developed and used for LSFD analyses in this study, and Figure 4-18 shows the results of steady state seepage analyses using these seepage parameters. This figure shows the LSFD cross-section FLAC model, and a comparison between the FLAC calculated phreatic surface and the pre-earthquake phreatic water levels in the two piezometers.

There may be different combinations of hydraulic conductivity values that would result in phreatic surfaces that also match reasonably well with recorded data, however for this study the values of Table 4-12 were considered appropriate, considering that (1) these are reasonable values based on understandings of the apparent soil material characteristics in the various soil zones and units, and (2) they provide a good match with the pre-earthquake piezometer readings.

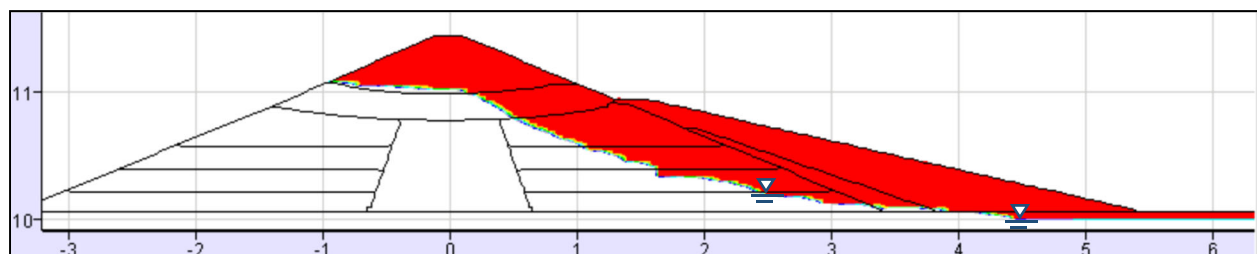


Figure 4-18: FLAC cross-section of LSFD showing the initial phreatic surface based on pre-earthquake steady state seepage analyses, and the degree of match with the available data from two embankment piezometers

Table 4-12: Hydraulic conductivity values for LSFD analyses

Soil Layer	Horizontal Hydraulic Conductivity, k_h (cm/sec)	Vertical Hydraulic Conductivity, k_v (cm/sec)	Anisotropy Ratio (k_h/k_v)
RF	5E-3	5E-4	10
GS	4E-5	1E-5	4
C	2E-5	5E-6	4
HFU-1	5E-4	5E-5	10
HFU-2	5E-4	5E-5	10
HFU-3	1E-4	1E-5	10
HFU-4	5E-4	5E-5	10
HFD-1	1E-4	1E-5	10
HFD-2	1E-4	1E-5	10
HFD-3	2E-5	2E-6	10
HFD-4	1E-4	1E-5	10
DRAIN	1E-2	1E-3	10
RFBERM	5E-4	5E-3	10
UA	4E-5	1E-5	4
LA	4E-5	1E-5	4
BEDROCK	1E-5	1E-5	1

4.5.6 Strength and Stiffness Parameters

Strength and stiffness parameters for LSFD were developed by Seed et al. (1973), based primarily on laboratory testing of samples collected after earthquake. These values have also been used by a number of different researchers in subsequent studies.

In these current studies, strength and stiffness parameters were re-evaluated. Strength and stiffness parameters were developed using commonly used relationships that are mainly either $(N_1)_{60}$ - based or D_R - based. The following relationships were used to develop stiffness parameters:

$$\text{Shear Modulus, } G_{\max} = 21.7 K_{2\max} P_a (\sigma'_m/P_a)^{1/2} \quad (\text{Seed et al., 1986}) \quad [\text{Eq. 4-7}]$$

$$\text{where } K_{2\max} = 20 N_{1,60,CS}^{0.33} \quad (\text{Seed et al. 1986}) \quad [\text{Eq. 4-8}]$$

$$\text{and/or } K_{2\max} = 0.6 D_R + 15 \quad (\text{Byrne et al. 1987}) \quad [\text{Eq. 4-9}]$$

$$\text{or } K_{2\max} = 625 \frac{OCR^k}{0.3+0.7e^2} \quad (\text{Hardin, 1978}) \quad [\text{Eq. 4-10}]$$

where k is a function of PI and stress history.

Equation 4-8 was originally developed for clean sand conditions. In this study, $N_{1,60,CS}$ values were used, as this better incorporates effects of fines on blow counts and resulting shear modulus. Table 4-13 presents elastic modulus numbers (K_{ge}) [$=21.7K_{2max}$] for LSFD to calculate shear modulus in FLAC models. The three columns of K_{ge} values in Table 4-13 correspond to the values used in nonlinear dynamic deformation analyses performed using each of the three referenced liquefaction triggering relationships. Table 4-14 presents strength parameters for use in Mohr-Coulomb elements and also for liquefiable elements before switching to dynamic properties.

Table 4-13: K_{ge} values for LSFD analyses

Soil Layer	Youd et al. (2016)	Boulanger and Idriss (2014)	Cetin et al. (2018)	Comment
RF	1,302			Byrne et al. (1987) with assumed $Dr=75\%$
GS	1,407			Hardin (1978) with assumed $PI=10$ and $OCR=3$
CC	893			Hardin (1978) with $PI=20$ and $OCR=1$
HFU-1 and HFD-1	1,136	1,136	1,098	Seed et al. (1986)
HFU-2 and HFD-2	1,087	1,077	1,042	Seed et al. (1986)
HFU-3 and HFD-3	1,198	1,236	1,157	Seed et al. (1986)
HFU-4 and HFD-4	1,061	1,050	1,009	Seed et al. (1986)
DRAIN	1,237			Byrne et al. (1987) with assumed $Dr=70\%$
RFBERM	1,302			Byrne et al. (1987) with assumed $Dr=75\%$
UA	1,367			Byrne et al. (1987) with assumed $Dr=80\%$
LA	1,432			Byrne et al. (1987) with assumed $Dr=85\%$

Table 4-14: Unit weights and drained or undrained shear strength parameters for LSFD analyses

Layer	Moist (γ_m) and Saturated (γ_{sat}) UnitWeight (pcf)	Cohesion, c' (psf)	Friction Angle, ϕ' (degrees)
RF	130/135	300	31
GS	120/126	500	27
CC	115/120	Peak static $S_u = 0.24 \sigma'_{v,i}$ During shaking: $S_u = 0.192 \sigma'_{v,i}$ Post-shaking: $S_u = 0.192 \sigma'_{v,i}$ to $0.136 \sigma'_{v,i}$ depending on strains developed Fully residual: $S_{u,residual} = 0.08 \sigma'_{v,i}$	0
HFU-1 and HFD-1	120/126	0	35
HFU-2 and HFD-2	120/126	0	34
HFU-3 and HFD-3	121/128	0	36
HFU-4 and HFD-4	120/126	0	33
DRAIN	120/125	0	37
RFBERM	124/130	100	37
UA	124/130	0	37
LA	124/130	0	37
BEDROCK	135/140	-	-

4.6 DEVELOPMENT OF INPUT GROUND MOTION TIME HISTORIES FOR LSFD AND USFD NONLINEAR SEISMIC DEFORMATION ANALYSES

4.6.1 Overview of Input Ground Motion Time Histories for These Two Case Histories

Most previous back-analyses of the Upper and Lower San Fernando Dams have been performed using an input time history developed by the late Prof. H. Bolton Seed (Seed, et al., 1973). That “classic” input motion was developed based upon the best available data and seismological understandings available, but it was developed at a time when near-field effects (e.g. pulse and fling step) on strong ground motions were not yet well understood.

The fault ruptures involved in the 1971 San Fernando Earthquake were relatively complex, and both the USFD and the LSFD were located in the near-field, and both were on the hanging wall of a ruptured fault surface. As a result: (1) both dams were strongly shaken, and (2) near field effects were significant.

A significant effort was undertaken as part of these current studies to re-evaluate the available strong motion data and other data (e.g. surface fault rupture mapping, etc.), and to bring to bear modern understandings of near-field effects and the best current understanding of the actual fault rupture details, as well as modern strong motion attenuation relationships developed as part of the NGA West-2 program (PEER, 2013) which are now better able to model and deal with near-field effects. Numerical simulations were also performed, employing the SCEC Broadband Platform (Maechling et al., 2015, Dreger et al, 2015) tools to model the 1971 rupture event and to develop resulting synthetic ground motions resulting from complex (and near-field) fault rupture events to shed further light on the development of suitable input strong motion time histories. The SCEC BBP was developed for these types of analyses, and the complex near-field 1971 event is an excellent subject for the BBP.

Section 4.6.2 will describe and summarize the development of the input motion time history as developed by the late Prof. H. Bolton Seed, and Section 4.6.3 will then present the investigations and development of the input strong motion time histories employed in these current studies.

4.6.2 Development of the Input Strong Motion Time Histories Used in Most Previous Back-Analyses of the USFD and the LSFD

Although the LSFD had seismic instrumentation, no strong motion recordings that were reliably directly useable as “input” motions for back-analyses were obtained at either the USFD or the LSFD during the 1971 San Fernando earthquake.

Two different types of strong motion recording instruments were in place in 1971 at a number of locations throughout the shaken region. One type of instruments were seismograph stations, usually consisting of pairs of seismographs oriented orthogonally to each other to record digitizable time histories in two orthogonal horizontal directions. These modern instruments recorded time histories that can be reliably processed and corrected for instrument effects, baseline drift, etc. to produce useful and reliable time histories. With two orthogonal horizontal records, the motions can also be rotated to produce horizontal records in any other (compass) direction desired. Vertical seismographs were co-located with the two horizontal instruments at a number of instrumented locations to record vertical motions.

The second type of recording instruments were of an older type of seismoscope. These instruments record the lateral motions by writing with a pen on top of a horizontally oriented round kerosene smoked “watch glass”, and thus recorded horizontal motions in all lateral directions simultaneously. Unfortunately, these seismoscopes are not considered

fully reliable for producing strong motion records that can be directly used for input motions. They are notoriously difficult to interpret, as there is no reliable time scale (it is not possible to reliably determine the precise time at which any given pen location on the watch glass occurred), and there are no well-accepted methods either for full interpretation nor for making the types of corrections for machine effects, etc. as are made for modern seismographs.

Two strong ground motion records were obtained at the Lower San Fernando Dam. Both of these were obtained on seismoscopes. One seismoscope (S-210) was located on the crest of the dam, near the center, and another seismoscope (S-213) was located on the sandstone sedimentary bedrock forming the east (right) abutment. Figures 4-19 and 4-20 show the locations both of these instruments. As the LSFD was subject to large deformations (a liquefaction induced upstream flow failure that carried away most of the crest), the crest seismograph subsided during the upstream side flow failure, and was found below the reservoir level during the post-earthquake survey (Figure 4-20). The abutment seismoscope was on stable ground. However, when the two watch glasses were retrieved from these two seismoscopes, it was found that they both retained clear traces of very strong motions recorded during the earthquake (Hudson, 1971).

Prof. Ronald F. Scott of Caltech performed a detailed study and interpretation of the trace of the seismoscope record from the east (left) abutment Seismoscope S-213 (Scott, 1973). A key source of difficulty in interpreting and processing data from seismoscopes is the lack of a time scale as the pen moves about atop the watch glass. Dr. Scott noticed a small “wobble” in the recoding of S-213, which appears to have been a characteristic of the instrument. As the period of this wobble appeared to be constant, it provided an approximate (though not fully reliable) time scale, and he was able to develop approximate time histories (1) transverse to the dam crest, and (2) parallel to the dam crest. Figure 4-21 shows the pen trace atop the watch glass for seismoscope S-213, and Figure 4-22 shows the two orthogonal times histories developed by Professor Scott from this trace.

The acceleration time histories (Figure 4-22) developed by Ronald F. Scott included a number of peaks in the range of 0.6 to 0.8g. However, there were some uncertainties; especially where the instrument reached its maximum travel and bounced against its support, and/or the pen went off scale. Considering the uncertainties, Scott (1973) suggested that peak earthquake accelerations of perhaps 0.65g to 0.8g on the filtered (10Hz) records might reasonably have been obtained at two peak points of the records, if the pendulum had been unrestrained, but he also privately noted that the peak acceleration might have been a bit lower (Prof. H. Bolton Seed, personal communication). Those peaks of 0.65 to 0.8 g will be important as this discussion continues.

As shown in Figure 4-22, the two time histories developed/interpreted by Prof. Scott are oriented (a) perpendicular to the crest of the LSFD, and (b) parallel to the crest of the LSFD. The interpreted peak acceleration in the record perpendicular to the crest of the LSFD is ~0.65g (acceleration spike C in the crest perpendicular record of Figure 4-22(a)), and the interpreted peak acceleration in the record parallel to the crest of the LSFD is ~0.78g (the

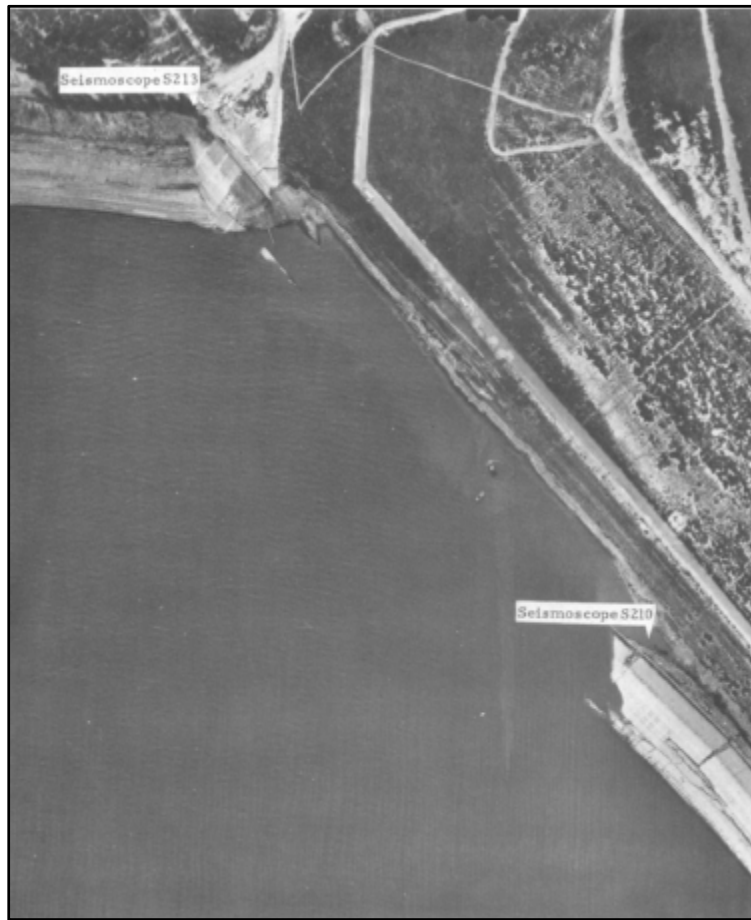


Figure 4-19: Locations of the two seismoscopes in a post-earthquake aerial plan view photograph of the LSFD (Scott, 1973)

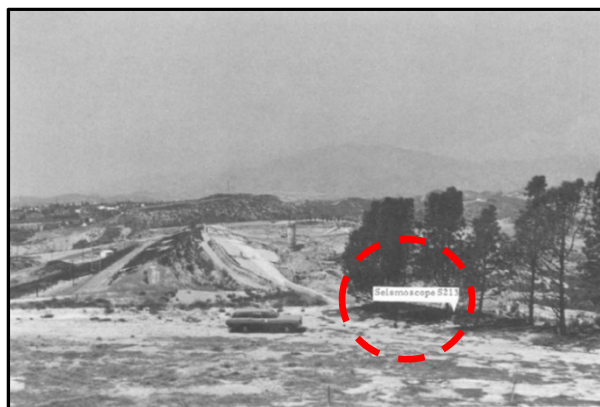


Figure 4-20: (a) Location of the crest seismoscope (S-210) and (b) location of the right abutment seismoscope (S-213) of the LSFD (Scott, 1973)

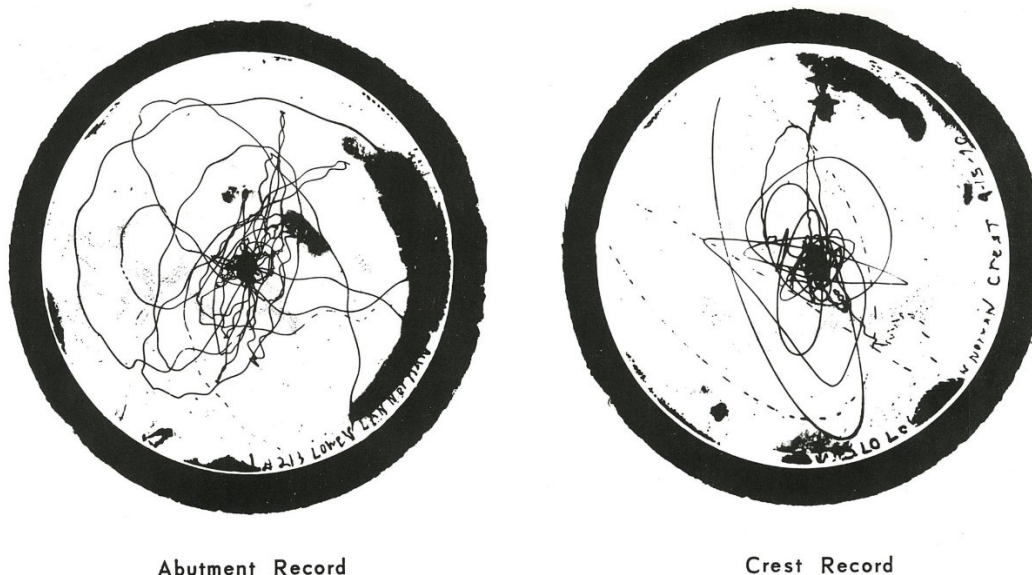


Figure 4-21: Recorded pen traces on the watch glasses of seismoscopes S-210 (crest) and S-213 (left abutment) of the Lower San Fernando Dam (Scott, 1973)

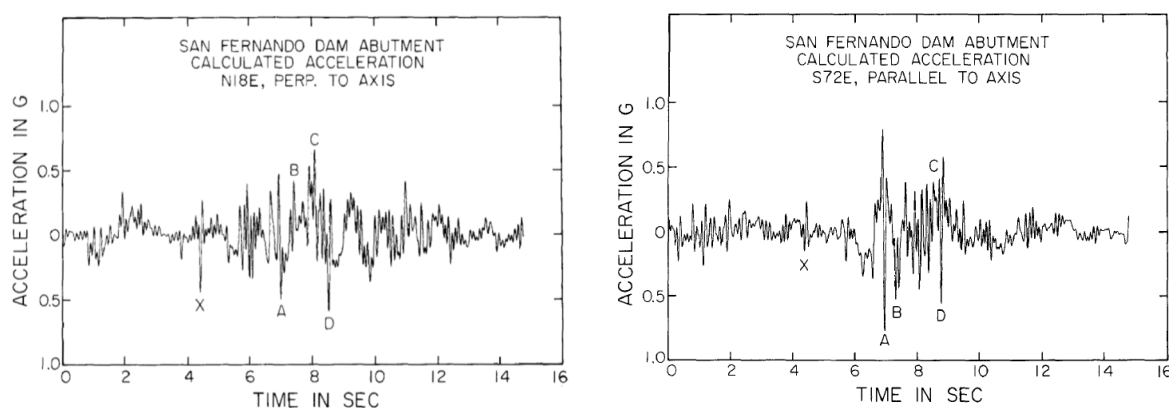


Figure 4-22: Acceleration time histories developed by Scott (1973) at (a) perpendicular to the LSFD crest (axis) of the dam, and (b) parallel to the LSFD axis based on Seismoscope S-213

unlabeled acceleration spike immediately before spike A in the crest parallel record of Figure 4-22(b)).

The seismoscope records developed by Prof. Scott showed several very strong velocity pulses that were considered somewhat “unusual” in 1971. With modern understanding of near-field effects, these are now understood to represent classical near-field effects due to elastic rebound or “fling” and rupture directivity that are dependent on the fault rupture geometry, rupture mechanisms, and the relative locations of the instruments involved.

The nearby Pacoima Dam (approximately 5.5 to 6 miles to the south-east from the USFD and LSFD, respectively) had a modern seismograph station on its abutment, and the abutment recordings obtained there were also considered somewhat unusual. The peak recorded horizontal acceleration of the Pacoima dam abutment record was 1.25 g, which was the highest peak lateral acceleration recorded up to that time, and the record also contained several very strong velocity pulses. A number of investigations and studies were undertaken to determine whether this was an anomalous recording, perhaps reflecting topographic effects or other issues, but none of those efforts showed a clear cause of error, bias, or inconsistency. Today, with modern understanding of near-field effects, the Pacoima Dam abutment records appear both reasonable, and understandable; but there may also be some topographic amplification effects due to the geometry of the abutment recording station location and the surrounding canyon geometry.

That was not the case in the immediate aftermath of the 1971 earthquake, however, as the recorded near-field motions appeared to be somewhat unusual, and the extensive post-earthquake forensic and field investigations of the performances of both the USFD and the LSFD in the aftermath of the 1971 San Fernando earthquake led to the need to develop suitable “input” motions for back-analyses of the two dams.

The late Prof. H. Bolton Seed (Seed, et al., 1973) developed a plot of the maximum accelerations recorded at “rock” sites at different distances from the epicenter of the 1971 San Fernando earthquake (Figure 4-23). Based on this plot, Seed et al. (1973) postulated that a maximum acceleration of on the order of 0.5g to 0.6g in the vicinity of the LSFD seemed reasonable.

Considering the approximations required to obtain the record developed by Scott (1973) from the record of Seismoscope S-213, and as (1) it had the highest horizontal peak acceleration ever recorded up to that date, and (2) it contained some unusually strong low-frequency components (velocity pulses) that would likely have strong effect on the embankment response, and (3) interpretation and processing of the seismoscope record was fraught with uncertainties and there were no well-established methods for making corrections to the resulting records, Prof. H.B. Seed utilized a different approach to develop a ground motion record for use as an input motion for back-analyses of the LSFD and USFD case histories. He modified the (modern) seismograph abutment ground motion record at the Pacoima Dam [the recording in a direction parallel to the crest (axis) of Pacoima Dam] using the following modification approach:

- (1) He truncated the amplitudes of any acceleration pulses exceeding 0.9g, to allow for the effects of topographic features of the Pacoima recording station site, and then
- (2) He further reduced all ordinates of the resulting (trimmed) acceleration record by a factor of 2/3 to produce a time history of rock motions having a maximum acceleration of 0.6g; which he considered to be in good accord with (a) the peak acceleration of 0.50 to 0.60g suggested by his attenuation plot of Figure 4-23,

and (b) the peak acceleration of approximately 0.65g from the seismoscope record (perpendicular to the crest) at the left abutment of the LSFD, as interpreted by Scott (1973).

Figure 4-24 shows a comparison between the resulting modified Pacoima Dam abutment seismograph record (Figure 4-24(b)), as modified by Prof. Seed (Seed, et al., 1973), and the acceleration time history developed by Scott (1973) from the LSFD left abutment seismoscope (S-213) record (Figure 4-24(a), and also Figure 4-22) after Scott “trimmed” the acceleration spike “C” from the preceding Figure 4-22(a) to $a_{max} \approx 0.6g$. [Note: The two

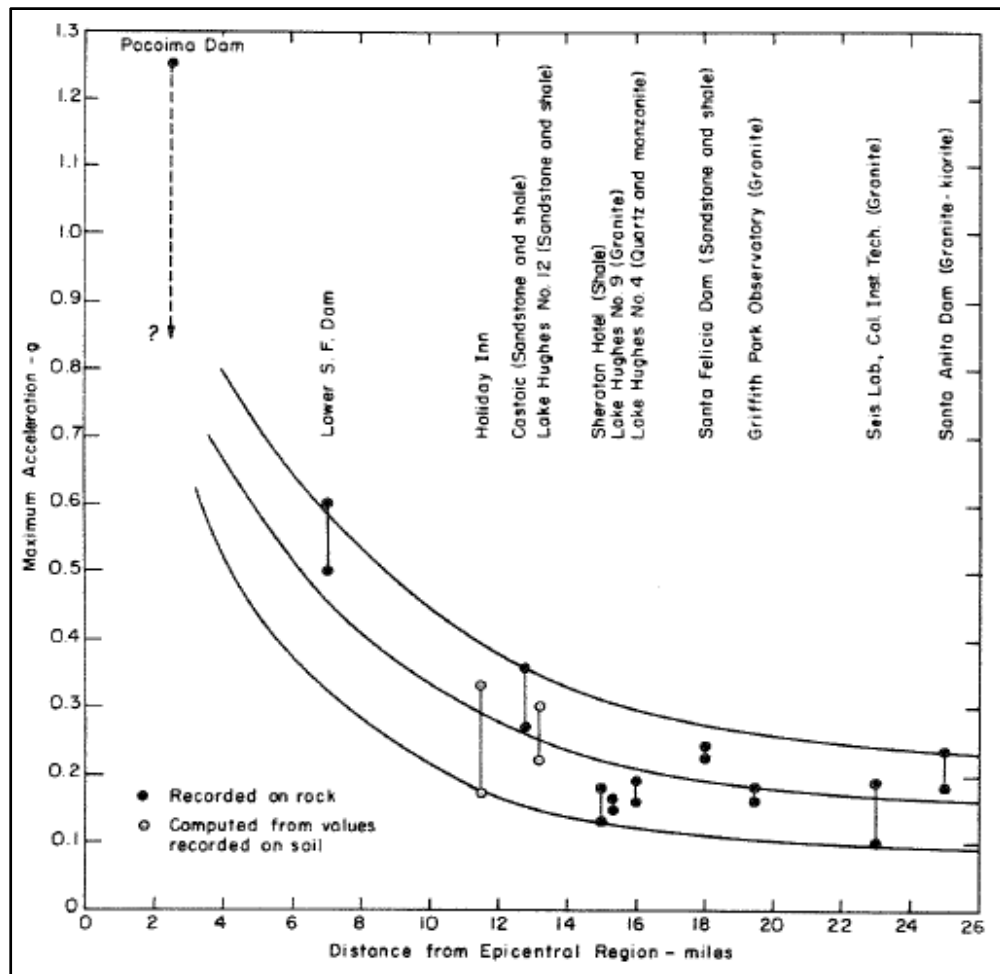


Figure 4-23: Maximum accelerations recorded at sites on rock in the 1971 San Fernando earthquake (Seed et al., 1973)

interpretations of Figures 4-24(a) and 4-22(a) differ slightly, and both are considered here to be roughly equally viable.]

The two motions in Figure 4-24(a) and (b) have a number of similar characteristics, but they are not the same. Because the seismograph recordings are more reliable, and more reliably processable, the modified and scaled Pacoima abutment record of Seed, et al. (1973)

has since been widely utilized as an “input” ground motion by different researchers and investigators in performing seismic back-analyses of both the USFD and LSFD [e.g. Seed et al. (1973), Serff (1976), Seed and Harder (1990), Inel et al. (1993), Moriwaki et al. (1998), and Beaty (2001)].

There are now known to be a number of short-comings to some of the approaches used to develop this “classic” input acceleration time history. As a result, in these current studies a significant effort was undertaken to re-consider and re-analyze the available data (including strong motion data, geological data, etc.) in the light of more modern understandings of near-field site effects, and to develop more defensible “input” strong motions for back-analyses of both the USFD and the LSFD.

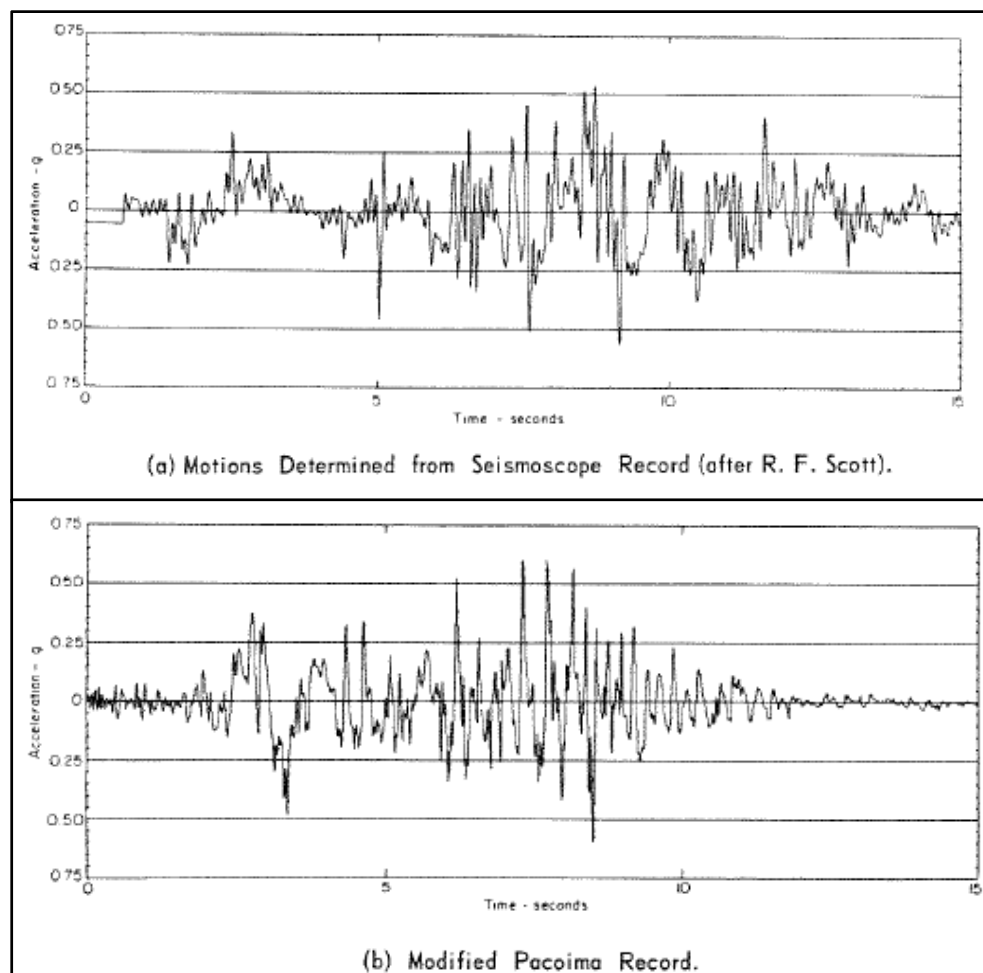


Figure 4-24: Acceleration time history from (a) interpretation of the seismoscope (S-213) at the LSFD left abutment by Scott (1973), and (b) the modified Pacoima Dam abutment [Parallel to axis of Pacoima Dam] record as per Seed, et al. (1973)

One of the shortcomings was made apparent as a result of further (and subsequent) field mapping of surface fault rupture evidence from the 1971 San Fernando earthquake, and by further seismological studies of the apparent deeper-seated fault rupture mechanisms and mechanics (based on inversions of strong motion recordings, aftershock studies, etc.), which established a better overall understanding of the rupture mechanics of the February 9, 1971 event.

Figures 4-25 and 4-26 show cross-sectional views of two fault rupture models postulated based primarily on inversions of strong motion records from multiple recording sites, as well as aftershock location data. Figure 4-25 shows the initial

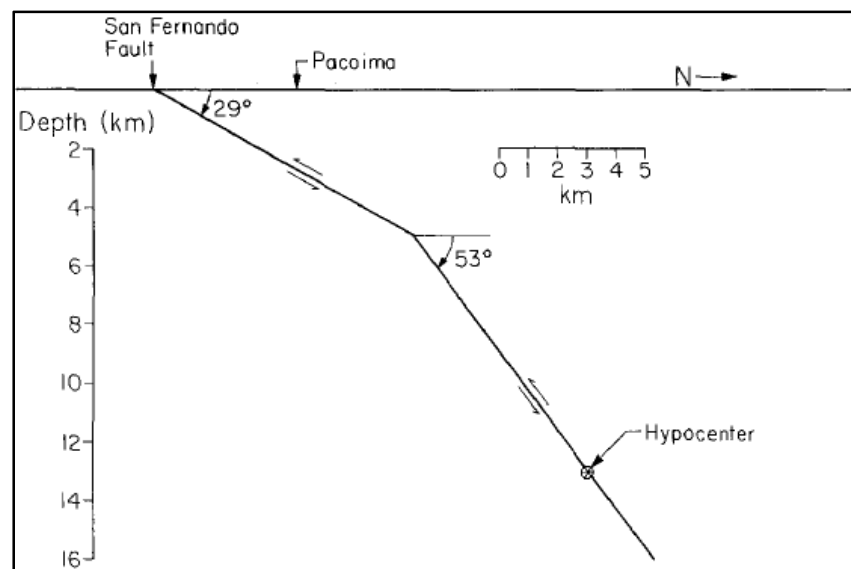


Figure 4-25: Cross-section of fault geometry of a single fault with a shallower near-surface dip with decreasing depth, as postulated by Langston (1978). (Figure source: Heaton, 1982)

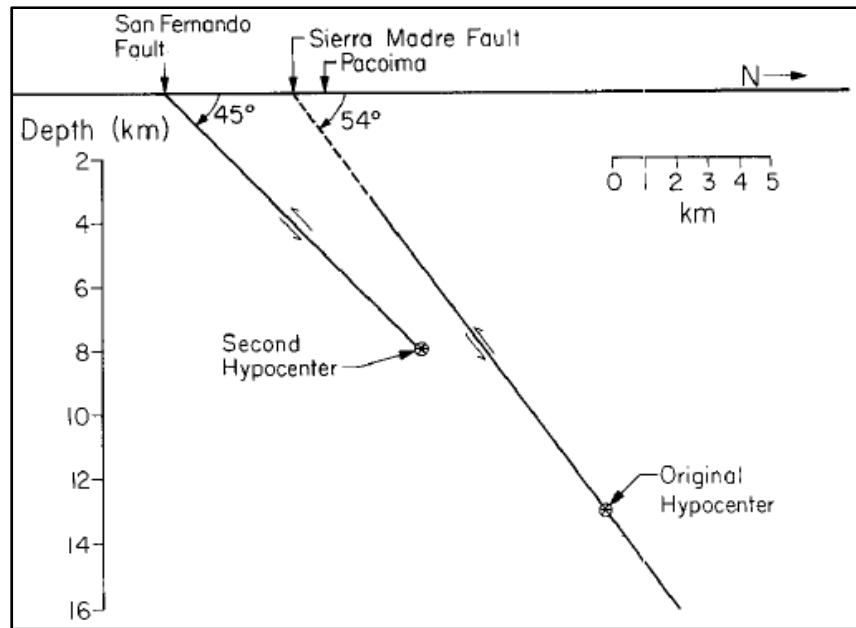


Figure 4-26: Cross-section of fault geometry of two parallel thrust faults, as postulated by Heaton (1982)

fault rupture mechanism postulated by Langston (1978). In this model, the fault rupture initiates at depth on the steeply dipping reverse fault, and then propagates upwards toward the surface, making a “bend” to a shallower dip angle as it nears the surface. This single fault is inferred to be the San Fernando fault.

Figure 4-26 shows an alternate model postulated by Heaton (1982), and it involves two co-parallel, and steeply dipping, thrust faults. Rupture initiates at depth on the Sierra Madre fault, but the rupture of the Sierra Madre fault does not propagate fully to the ground surface. The second fault (the San Fernando fault, slightly to the south) nucleates a second rupture at medium depth, and this rupture does propagate fully up to the ground surface, producing the principal observed and mapped surface rupture features.

Both cross-sections show an arrow marked “Pacoima” which and represents the location of the Pacoima Dam. The locations of the Upper and Lower San Fernando Dams are not shown, but they would be located to the south of the Pacoima Dam (south is to the left in these two figures), on the hanging wall side of the fault that produces rupture to the ground surface, and in very close proximity to the ground surface faulting. Pacoima Dam is located approximately at the lateral center of the rupture, the LSFD and USFD are located on the western edge of the ruptured fault, approximately 5 miles west of Pacoima Dam. As a result; in either model all three dams (Pacoima dam, USFD and LSFD) are (1) on the hanging wall of a steeply dipping thrust fault, and (2) in close proximity to the rupture. All three dams would therefore be expected to experience significant near-field effects including (1) “pulse-like” motions due to the rupture propagating towards the dams, (2) “fling steps” as the dams all

experience permanent underlying ground displacement offsets, and (3) hanging wall effects also potentially affecting energy concentrations in the near field on the up-thrown block.

Figure 4-27 shows a plan view of the region, with yellow “pins” indicating the locations of USFD, LSFD and Pacoima Dam. The red lines represent mapped surface fault rupture traces. The southern-most of these (and the most extensive) delineate the surface expressions of the San Fernando fault rupture. The blue star shows the initial estimated location of the epicenter (directly overlying the initial estimated hypocenter) as it was interpreted in the early 1970’s. It was this epicenter location upon which the late Prof. H. B. Seed based his attenuation plot (Figure 4-23). As further data and studies evolved, the hypo-

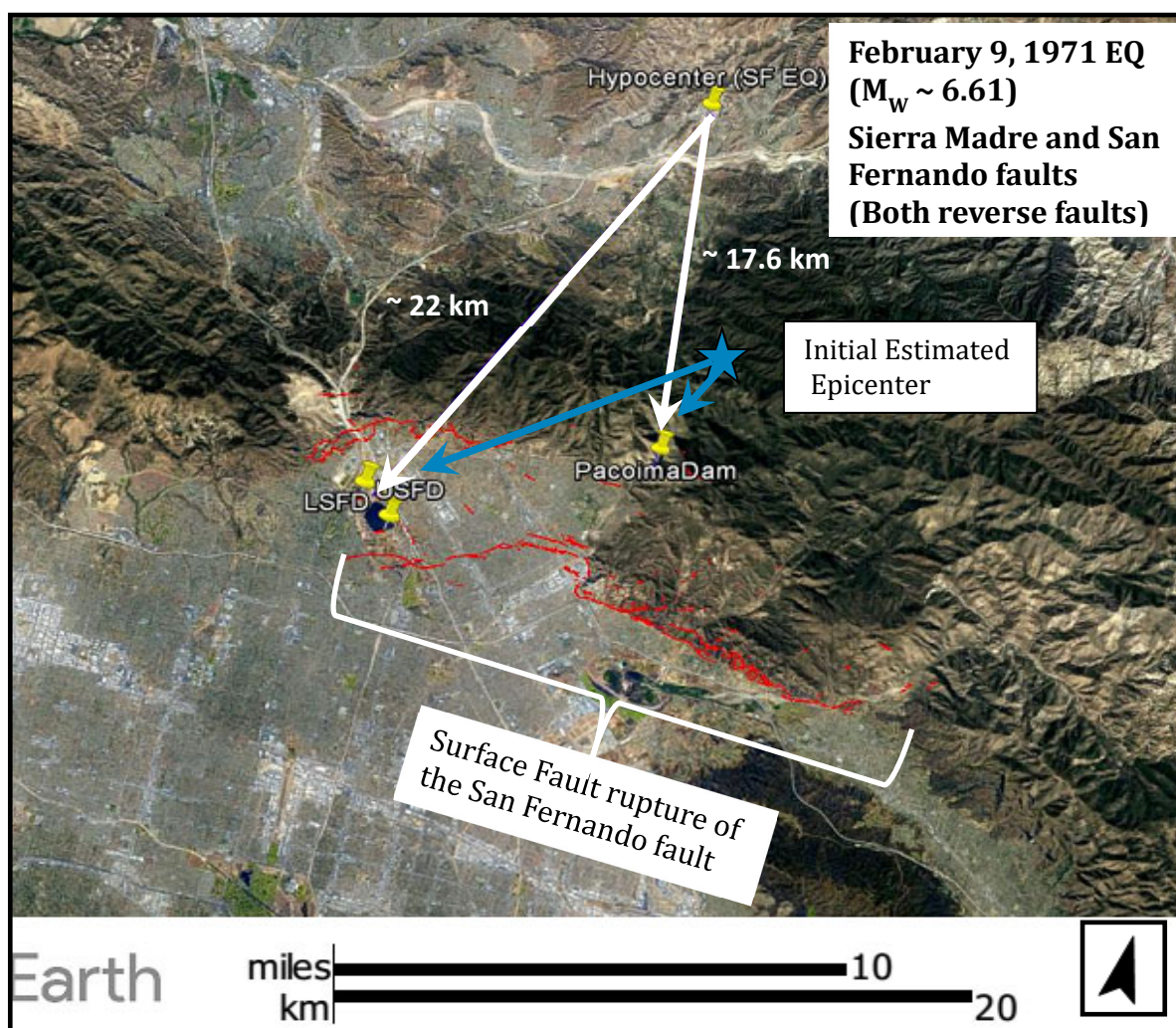


Figure 4-27: Map of the 1971 San Fernando earthquake epicentral and near-field region showing two postulated epicenters, and mapped surface fault rupture expressions

center (and thus also the epicenter in plan view) was eventually re-located further to the north, as also shown in Figure 4-27. This updated geometry would not match as well with the plot of Figure 4-23. As a result, the inference of a peak acceleration of approximately 0.5 to 0.6 g at the USFD and LSFD, based on Figure 4-23, is not well supported by the more recent data and understandings of the causative fault rupture mechanisms.

4.6.3 Approaches for Development of Input Acceleration Time Histories for These Current Studies

The ground motions recorded in 1971 San Fernando earthquake at the Pacoima Dam had the highest recorded peak ground acceleration ($a_{\max} = 1.25g$ in the north-south direction) that had ever been recorded up to that date (Trifunac and Hudson, 1971). The modified input ground motion (as discussed in Section 4.6.1) that has been widely used over the past several decades for back-analyses of the USFD and LSFD seismic performance case histories was developed by Seed et al. (1973) at a time when near-field directivity effects (e.g. pulse and fling step) were not yet well understood. It was a reasonable judgment call at that time, but four decades later it does not stand up as well (1)-to modern understandings of near-field effects, and (2) to a significant amount of new data developed since 1973.

Recent studies (e.g. Bray and Rodriguez-Marek, 2004; etc.) of near field source effects on ground motions now utilize the Pacoima Dam abutment record as one of the “classic” data points for evaluation of near-field directivity effects (e.g. pulse and fling step). In addition, ground motions were again recorded at the Pacoima Dam in the 1994 Northridge earthquake, which had similar thrust-fault type rupture mechanisms. After evaluation of the ground motions from Northridge earthquake, the validity of the Pacoima Dam abutment ground motion record as recorded during the 1971 San Fernando earthquake is no longer as much in question (Nuss et al. 2017).

Also, the 1971 San Fernando earthquake is now understood to have been a complex rupture event involving two steeply dipping oblique thrust faults (Heaton, 1982). The rupture initiated at depth on the Sierra Madre fault, as shown in Figure 4-26, and then a second rupture initiated at a shallower depth on the San Fernando fault. Both ruptures propagated up-plane. The Pacoima Dam (where the potentially useful abutment strong motion recording from a seismograph was recorded) is located close to the Sierra Madre fault, and on the hanging wall side, and the Upper and Lower San Fernando Dams were all located on the hanging wall side of the shallower San Fernando fault rupture. Pacoima Dam is located relatively near to central portion of the San Fernando fault rupture, and both the USFD and LSFD are located very near to the surface expression of the western-most end of the San Fernando fault rupture. As a result, the motions at all three dams were significantly affected by near-field directivity effects.

In this current study, the input ground motions for the back-analyses of the USFD and LSFD were developed utilizing the following two approaches:

Approach 1: Scaled Ground Motions

A set of ground motions for the USFD and LSFD were developed by rotating and scaling the Pacoima Dam abutment records from 1971 San Fernando earthquake in order to develop input ground motions suitable for application in directions transverse (perpendicular) to the crests of (1) the USFD and (2) the LSFD. A rotation was performed to develop the crest perpendicular input ground motions for the LSFD. As the Pacoima Dam parallel direction is very close (difference of ~ 2 degrees) to the crest perpendicular direction for the USFD axis perpendicular direction, no additional rotation was performed for the USFD. Scaling factors were developed based on (1) an evaluation of the anticipated ground motions using the NGA-West2 ground motion attenuation relationships (PEER, 2013) (also known as NGA-West2 ground motion prediction equations, or GMPEs), which specifically address near-field effects, (2) consideration of details of the initial ground motion development approaches by Seed et al. (1973) and Scott (1973), (3) locally available seismogram and seismograph records at and near the USFD, LSFD and Pacoima Dam, and (4) lessons and insights from the SCEC broadband platform (BBP) simulations performed in Approach 2.

Approach 2: Validation of Approach 1 by Simulated Earthquake Scenarios Modeled with the SCEC BBP

Considering the uncertainty in ground motion records for USFD and LSFD, a series of simulations of potential slip mechanisms and scenarios during the 1971 earthquake were performed by using the SCEC broadband platform (BBP) software, developed by the Southern California Earthquake Center (Maechling et al., 2015, Dreger et al., 2015). This software allows detailed and fully three-dimensional modeling of complex fault rupture events, and resulting propagation of waves and energy to sites and hypothetical recording stations. The principal objectives of the simulated ground motions approach were (1) to inform and evaluate the validity of the rotations and scaling factors used in Approach 1 above, with an additional benefit of (2) also examining the ability of the SCEC BBP to simulate a very complex rupture event.

4.6.3.1 Fault Mechanisms for the 1971 San Fernando Earthquake

The fault mechanism or rupture scenario for San Fernando Earthquake has been a subject of keen interest among seismologists for decades since the earthquake. In these current studies, the fault maps including surface rupture traces and aftershocks, and initial and recent hypotheses regarding the San Fernando earthquake, as well as inferred rupture zones and zones of energy release based on inversions of strong motion and aftershock data, as well as mapping of surface rupture expressions, were evaluated to develop a fault rupture scenario for use (1) in the SCEC BPP simulations, and (2) in the application of a suite of NGA-West2 ground motion prediction equations (GMPEs) to the problem of developing a suitable set of input motions.

The main shock of the San Fernando earthquake occurred at 6 AM, on February 9, 1971. Many aftershocks were recorded following the earthquake. Thirty-five aftershocks with Richter magnitude of 4.0 or larger were recorded within seven minutes following the main shock. The aftershock activities continued until the end of the year. Allen et al. (1975) noted that fifty-five aftershocks with Richter magnitude of 4.0 or larger were recorded until December 31, 1971. Figure 4-28 shows the location of the mainshock, and of aftershocks of Richter magnitude 4.0 or larger (Allen et al. 1975). These aftershocks were recorded at permanent stations across the area, as well as by portable stations deployed by Caltech.

Allen et al. (1975) performed an evaluation of the focal mechanisms and tectonic interpretations based on an evaluation of (1) previous studies and (2) aftershocks. Allen et al. (1975) postulated that the hypocentral locations of the main shock and aftershocks

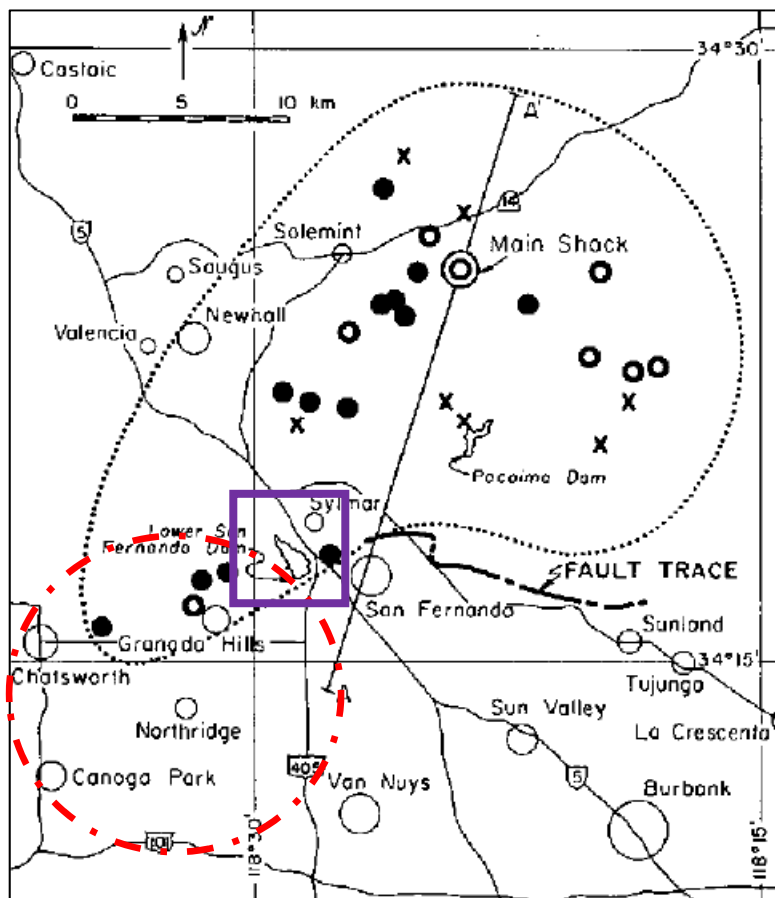


Figure 4-28: Main Shock and Aftershocks of Richter Magnitude 4.0 or greater through December 31, 1971. Solid circles represent locations with estimated an accuracy of ± 2 km horizontal and ± 4 km vertical, open circles represent locations with an estimated accuracy of ± 4 km horizontal and ± 8 km vertical, and heavy 'X' locations are less accurate. Dotted line shows limits of most aftershock activity, including many smaller shocks than those shown. Red circle in the southwest corner includes the aftershocks observed near Granada Hills area (Allen et al. 1975).

support the idea of displacement on a north-dipping fault, and that it seems particularly likely that the lunate distribution of aftershock epicenters reflects the edge of the disc-shaped segment of the fault plane that slipped during the earthquake, where stresses remained high following the main shock. They observed that very few aftershocks occurred in the vicinity of the surface break, presumably because stresses had been relieved in those areas. Allen et al. (1975) also pointed out two observations that indicate that the fault mechanism may be more complex than just simple thrust faulting: (1) aftershocks near Granada Hills and Chatsworth, at the southwest end of the aftershock zone, are south of the projected surface of the thrust fault (shown in the red circle in Figure 4-28) and therefore do not ideally fit a simple thrust fault scenario, and (2) focal-mechanism studies of aftershocks (Whitcomb, 1971a and 1971b) found the aftershocks to include many shocks of strike-slip character.

As an explanation for the aftershocks in the Granada Hills area, and the strike slip nature of many of the aftershocks, Allen et al. (1975) suggest that a flexure exists along the zone of strike slip aftershocks, as schematically illustrated in Figure 4-29. Allen et al. (1975) suggest that one geometric effect of the flexure would be to displace the trace of the thrust fault to the south on the west side of the flexure and that may explain the strong aftershocks in the Granada Hills area, where one of the aftershocks (Mw 4.6 on March 31, 1971) locally caused more damage than the main shock. Also, they suggested that the rock characteristics of the area such as exposed basement rock in the eastern area and sedimentary rock in the western area support the concept of a flexural down-step to the west in this area.

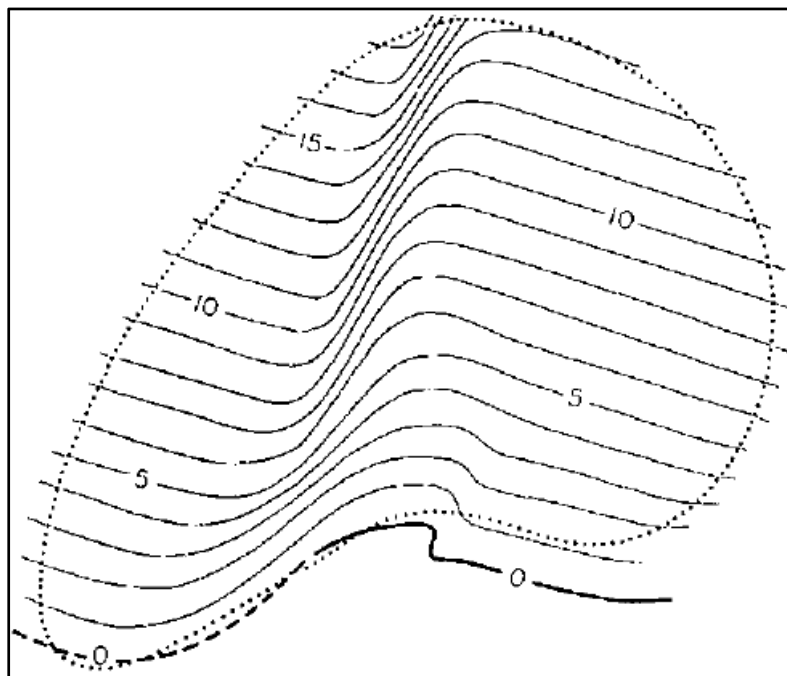


Figure 4-29: Schematic structural contour map showing simplified contours of fault plane (in km) with monoclinal flexure that might explain strike slip aftershock mechanisms on steep west-dipping flanks of flexure in the fault surface (Allen et al., 1975).

Studies of surface rupture, focal mechanism, and hypocentral locations continued after the earthquake due to the complex nature of faulting, and it was recognized that a constantly dipping fault plane which is compatible with P-wave first-motion observations would not intersect both the hypocenter and the surface rupture (Allen et al. 1975, Heaton, 1982). Langston (1978) proposed a finite-fault model of the San Fernando earthquake, which explained many of the features of both the long-period and short-period tele-seismic body waves recorded for this event. Figure 4-25 shows Langston's (1978) finite-fault model, which consists of a uniform rupture that propagates up-dip at an angle of 53° and at a rupture velocity of 1.8 km/sec, and then decreases dip angle to 29° at a depth of about 5 km. Even though Langston's (1978) model was found to fit the tele-seismic long periods, it did not adequately explain both the local and tele-seismic data simultaneously (Heaton, 1982).

Heaton (1982) postulated that the 1971 San Fernando earthquake may have been a double event that occurred on two separate, subparallel thrust faults, as illustrated previously in Figure 4-26. Heaton postulated that the initial rupture occurred at depth on the Sierra Madre fault zone, which runs along the base of the San Gabriel Mountains. Rupture is postulated to have occurred from a depth of about 13 km to a depth of about 3 km. A second event is thought to have initiated about 4 seconds later on another steeply dipping thrust fault, which is located about 4 km south of the Sierra Madre fault zone. The surface trace of this fault matches with the surface rupture associated with the San Fernando fault system from the 1971 San Fernando earthquake.

Figure 4-26 shows a cross-section with a two-faults system, as postulated by Heaton (1982). Table 4-15 presents source parameters of the two faults, as per Heaton (1982).

Table 4-15: Source parameters for Heaton's (1982) two-fault mechanism for the 1971 San Fernando Earthquake

Parameter	Sierra Madre Fault (Deep Fault)	San Fernando Fault (Shallow Fault)
Strike	290°	285°
Dip	54°	45°
Rake	76°	90°
Moment ($\times 10^{26}$ dyne-cm)	0.7	1.0
Rupture Velocity (km/sec)	2.8	2.8
Hypocentral Depth (km)	13.0	8.0
Time Lag (sec)	-	4.0

Figure 4-30 shows a plan view of the detailed fault mechanism geometry modeling scenario for one of the simulations performed using the SCEC BBP simulator in the current studies using SCEC BPP version 16.5.0. In this figure, the deeper fault rupture surface of the inclined (north dipping) Sierra Madre fault is at the north end of the figure (and is fainter, representing greater depth), and the rupture surface of the also north-dipping San Fernando fault is shown as two separate rectangles to the south; largely bounded by the mapped

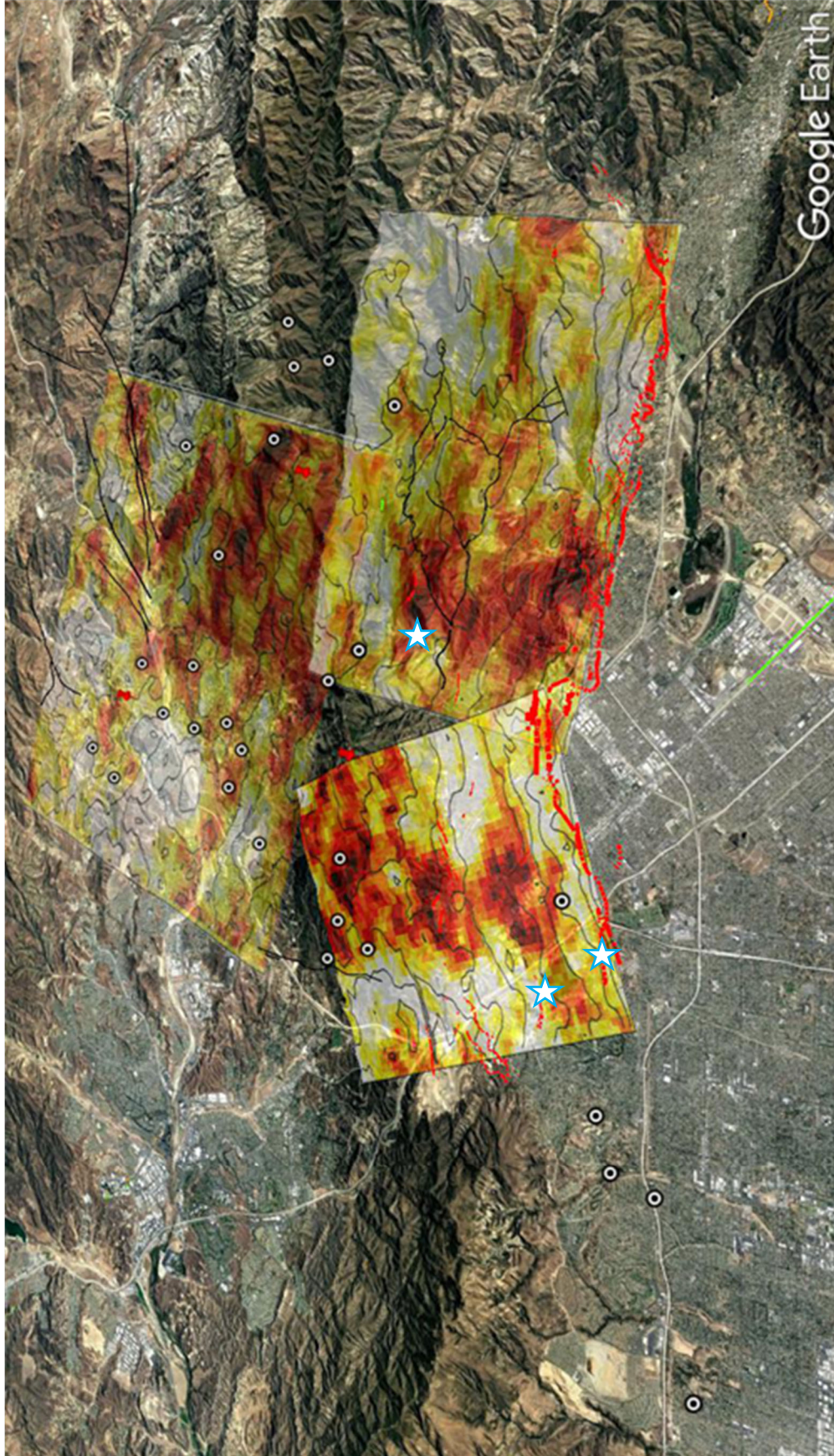


Figure 4-30: Three segment fault model for the 1971 San Fernando earthquake showing the random slip distributions (scenario210). White circles show aftershocks. The two southern planes are placed to be consistent with the observation of surface faulting in the earthquake (thin red fault lines). The blue stars show Pacoima Dam (STA1), Lower San Fernando Dam (STA45) and Upper San Fernando Dam (STA46) sites. The red push pins show the hypocenters of the respective faults. The earthquake nucleated on the deep-north plane and rupture up-dip on the south-dipping fault system.

surface fault rupture expressions. These two rectangles are essentially part of the San Fernando fault,; however they were modeled separately to account for the monoclinical flexure of the overall rupture surface (as posited in Figure 4-29); When rupture of the first plane reaches the nearest edge of the two shallower planes, rupture is initiated, and then spreads across the respective planes. Figure 4-30 also shows the locations of (1) the USFD, (2) the LSFD, and (3) Pacoima Dam. Overall, Figure 4-30 is the best graphical representation of the fault rupture mechanism modeled in these current studies (1) with NGA attenuation relationships, and (2) with the SCEC BBP simulator.

4.6.3.2 Development of Scaling Factors for Development of Input Motions for Back Analyses of the LSFD and USFD

An evaluation of the ground motions at the Pacoima Dam, LSFD, and USFD was performed using the NGA-West 2 attenuation relationships and tools; available at the PEER website (<http://peer.berkeley.edu/>). Fault mechanisms of the San Fernando Earthquake, as postulated by Heaton (1982), NGA-West2 database information regarding the 1971 San Fernando earthquake, surface rupture maps by USGS (2018), and the discussions of the previous section, as reflected in Figure 4-29, were utilized in estimating spectral accelerations at different periods from 0.01 sec to 10 sec. An equal 0.25 weight factor was used for each of the four (out of five available) NGA-West2 ground motion prediction equations (GMPE's) employed here. These four NGA-West2 GMPE's are (1) Abrahamson, Silva, and Kamai (2014), (2) Boore, Stewart, Seyhan, and Atkinson (2014), (3) Campbell and Bozorgnia (2014), and (4) Chiou and Youngs (2014).

The NGA-West2 database considers $M_w=6.61$ as the representative Moment-Magnitude (M_w) for the 1971 San Fernando earthquake based on fifteen source documents on the event with an estimated seismic moment (M_o) of $9.36E+25$ dyne-cm (Darragh, 2018). In these current studies, the double-fault mechanism of Heaton (1982) was utilized, and the resultant M_w was assumed to be equal to $M_w=6.61$. The total energy was distributed nearly evenly between the two sub-parallel thrust fault rupture surfaces on the Sierra Madre and San Fernando faults.

Considering that the 1971 San Fernando earthquake was the result of slips along two sub-parallel thrust faults, ground motions were developed for each individual fault (the Sierra Madre fault and the San Fernando fault). The ground motions estimated from each individual fault rupture were then combined utilizing an approach based on findings of a recent study on ground motion characterization for the southwestern United States (GeoPentech, 2015). That study used four alternative methods for using GMPE's to compute the ground motion for complex rupture scenarios involving multiple fault segments, including fault segments with major changes in the rake, dip, and rupture width as well as ruptures of a splay fault off a main rupture. The four alternative methods were:

Method 1: Square root of the sum of squares (SRSS) of the PSA from multiple fault segments using Equation 4-11.

$$PSA_{SRSS} = \sqrt{PSA_{fault1}^2 + PSA_{fault2}^2} \quad [\text{Eq. 4-11}]$$

Method 2: Approximate as a single fault using fault parameters weighted by the area of the fault. This method calculates the average fault parameters (rake, dip, and down-dip width) along strike, weighted by the area of each of the individual participating segments. The distance metrics (R_{RUP} , R_{JB} , and R_X) are based on the distances for the closest point on the rupture plane from the site of interest. The magnitude is the magnitude of the combined overall rupture.

Method 3: Calculates the average fault parameters (rake, dip, and down-dip width) weighted by $1/R^2$, where R is the distance from the site to a point on the rupture plane. Average dip (and similar equations for rake and rupture width) is computed using Equation 4-12,

$$Dip_{ave} = \frac{\sum \frac{Dip_i}{R_i^2}}{\sum \frac{1}{R_i^2}} \quad [\text{Eq. 4-12}]$$

The distance metrics (e.g. R_{RUP} , R_{JB} , and R_X) are based on the distances for the closest point on the rupture plane from the site of interest. The magnitude is the magnitude for the combined overall ruptures.

Method 4: Approximate as a single fault using closest segment parameters. This is the simplest among the four approaches, where the fault parameters and the distance metrics are taken from the closest point along the rupture to the site of interest. The magnitude used is the magnitude for the combined overall ruptures.

As part of the GeoPentec (2015) study, two cases of complex fault systems and two cases of splay ruptures, were simulated by using the SCEC broadband platform (BBP), and the results were then compared with NGA-West 2 GMPEs using each of methods 1 through 4. Based on the comparisons, the Technical Integrator (TI) team for the study selected Method 1 to estimate ground motions for both complex and splay ruptures. Considering this exercise, and the conclusions of the GeoPentec (2015) study, Method 1 was adopted for these current studies to estimate ground motions from NGA-West2 GMPE's for the complex 1971 San Fernando earthquake event.

Figure 4-31 shows pseudo-spectral acceleration (PSa) plots (5% damping) for the Pacoima Dam, LSFD, and USFD based on the NGA-West 2 GMPE's and the Method 1 approach to combine contributions from the two faults. The NGA-West 2 GMPE's provide the predicted values for earthquakes considering all events considered in developing the database suitable to NGA-West. This prediction of motions for the 1971 San Fernando earthquake event was developed by also considering the "event terms", as per Abrahamson, Silva, and Kamai (2014). Table 4-16 presents the event terms used in developing pseudo-spectral acceleration values for the Pacoima Dam, LSFD, and USFD sites.

Table 4-16: Event terms for the four NGA-West2 GMPEs used to “predict” PSa values
For (1) USFD, (2) LSFD, and (3) Pacoima Dam

Period	Event term (Ln units) From Abrahamson et al. (2014) Attenuation model
0	0.16
0.02	0.17
0.03	0.22
0.05	0.17
0.075	0.18
0.10	0.09
0.15	0.2
0.20	0.21
0.25	0.17
0.30	0.12
0.40	0.06
0.50	-0.02
0.75	-0.05
1.00	0.05
1.50	0.1
2.00	-0.03
3.00	-0.02
4.00	0.28
5.00	0.37
7.50	0.4

The pseudo-spectral acceleration values at the Pacoima Dam, LSFD, and USFD were developed using the following steps:

- (1) The pseudo-spectral acceleration values were developed using the event parameters of the San Fernando earthquake and fault parameters for Sierra Madre and San Fernando faults.
- (2) The resulting PSa values from Sierra Madre and San Fernando faults were combined using square root of the sum of squares (SRSS) - (Method 1).
- (3) Event terms (as per Abrahamson et al., 2014) for the San Fernando earthquake were applied on the combined PSa values to obtain PSa plots, as shown in Figure 4-31. The PSa values obtained from Method 1 were multiplied by the exponential of event terms.

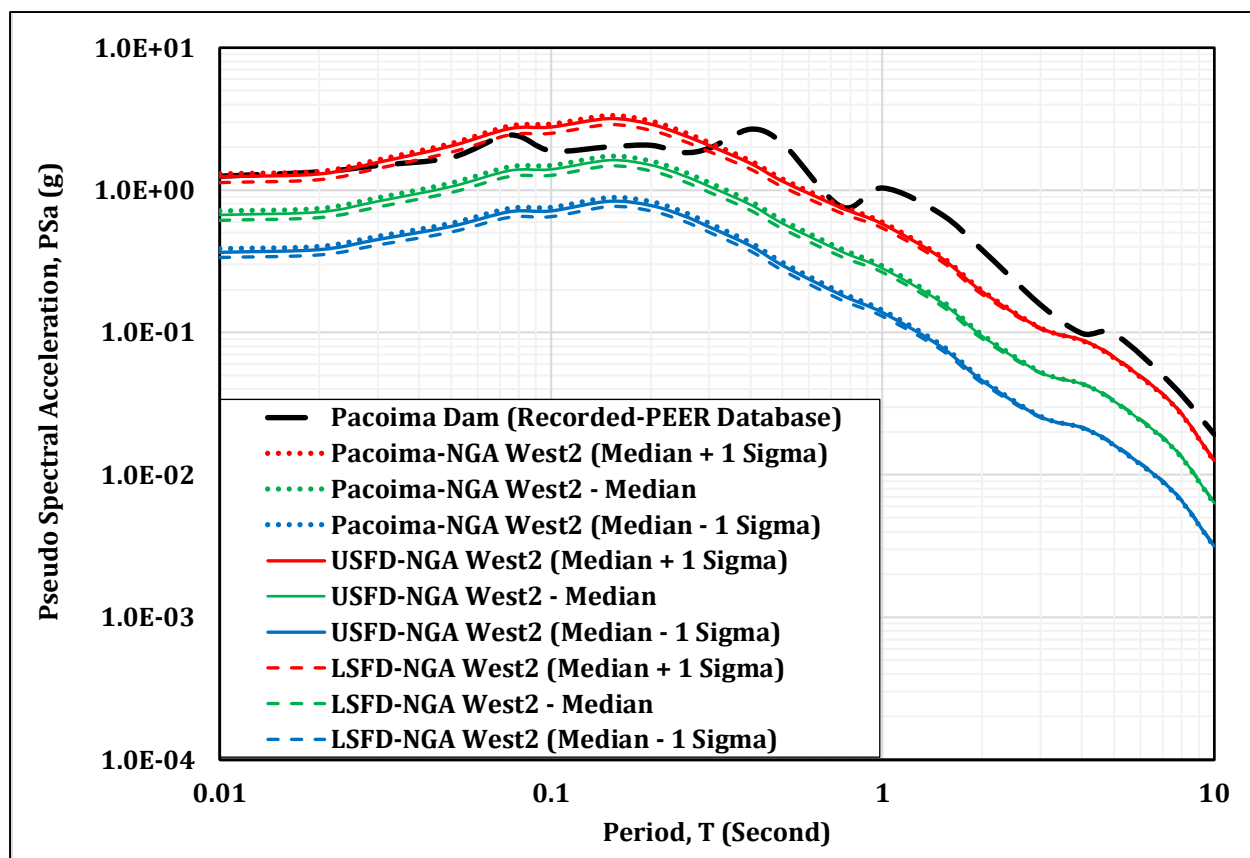


Figure 4-31: Comparison between pseudo spectral acceleration values obtained from NGA-West2 GMPE's vs. recorded ground motions from the seismograph at the left abutment of Pacoima Dam.

As shown in Figure 4-31, the actual recorded PSa values from the seismograph at the left abutment of the Pacoima Dam (S16°E; dam-axis direction) match reasonably well with approximately the Median + 1 standard deviation PSa values from the NGA-West2 GMPEs, including the peak horizontal ground surface accelerations. The Pacoima Dam abutment record PSa is presented for the single direction of maximum peak lateral acceleration (a_{max}), while the NGA-West2 GMPEs “predict” a non-directional [root mean squared] value of a_{max} , and also similarly non-directional [root mean squared] PSa values, and these would on average be expected to be somewhat lower than the values in the single direction of maximum a_{max} . They would also be higher than motions in some of the other directions. The NGA-West2 results also suggests the possibility that the local motions at Pacoima Dam in that direction were a bit more “energetic”, possibly (1) because the event released more energy than “average” at the very near-field instrument location, or (2) local directivity effects (discussed previously) and local source effects (e.g. concentrations of energy on portions of the fault near to the instrument station) were “adverse” near the Pacoima Dam, or (3) there may have been topographic effects at the Pacoima dam abutment instrument site. There is an argument to be made here for topographic effects, and it is possible that

some combination of two or more of these possible factors contributed to the observed motions.

Figure 4-31 also shows that the predicted ground motions at all three dam locations (Pacoima Dam, LSFD, and USFD), developed based on the NGA-West2 GMPEs, are very close to each other due to the three dams sharing (1) relatively similar and close proximities to surface rupture and (2) generally similar relative locations with regard to being on the hanging wall sides of the closest thrust fault (the San Fernando fault), and at nearly equal distance from the rupture surface (energy release zone) of the slightly more distant and deeper Sierra Madre fault.

The NGA-West2 GMPEs indicate that the recorded motions at the Pacoima Dam abutment seismograph, and at the Lower San Fernando Dam abutment seismoscope, represent motions that should not be considered surprising. They do not, however, fully define the best possible choices for development of “input” ground motion time histories for the USFD and the LSFD.

Morrill (1972) and Duke et al. (1972) studied recordings from both (1) seismoscopes and (2) seismographs that recorded ground motions during the 1971 San Fernando earthquake, in order to assess the reliability and potential usefulness of the older seismoscopes. The detailed interpretations of the pen-drawn traces on the watch glasses of the seismoscopes were considered less reliable as a basis for development of full acceleration time histories, and there were also issues with regard to reliability of detailed corrections for machine effects, etc. But they found that upon plotting a_{\max} values for both types of instruments as a function of distance from the epicenter, and also by examining sites where both seismoscopes and accelerometers were co-located (including strong aftershock measurements when additional temporary accelerometers had been installed), that with some scatter the maximum peak accelerations obtained from the seismoscope records were approximately the same as the peak accelerations recorded on more modern seismographs (strong motion accelerometers).

The interpreted acceleration time histories developed by Scott (1973) from the LSFD abutment seismoscope had peak horizontal accelerations of $a_{\max} = 0.65g$ in the direction (N18E) perpendicular to the LSFD crest, and $a_{\max} = 0.80g$ in the crest parallel direction (S72E).

In the current study, the NGA-West2 GMPE-based PSa indicate that a peak ground acceleration value of $a_{\max} \approx 0.70 g$ at both the USFD and the LSFD would be approximately the median value estimated from these modern predictive relationships. But these are non-directional, root mean square NGA-West2 GMPE predictions, so a_{\max} could be higher or lower in any specific compass direction. The root mean square of the peak horizontal accelerations recorded at the LSFD abutment seismoscope is $0.72g$, which is very close to NGA-West 2 prediction of $0.70 g$.

The peak lateral accelerations interpreted from the LSFD abutment seismoscope by Scott (1973) are supported by the studies of Morrill (1972) and Duke et al. (1972), and they are now also supported by the NGA-West2 GMPEs.

The two maximum accelerations interpreted by Scott at the LSFD are an unusually valuable set of “directional” values, and they are likely among the best indications of a_{\max} in the directions parallel and perpendicular to the crest of the LSFD.

The USFD and LSFD dams are unusually close together (approximately 0.5 miles apart), and the motions at the two dams would be expected to be similar. The two dam crests are oriented in different directions, however, and the motions to be applied in the fully nonlinear seismic deformation back-analyses will be applied in a direction perpendicular to the axis of the crest (crest perpendicular) for each dam.

Arguably an important pair of data points are provided by Prof. Scott’s interpretations of the seismoscope record on the abutment of the LSFD, which showed an apparent PGA of 0.65 g in the crest perpendicular direction, and 0.8 g in the crest parallel direction. Those numbers now appear to be reasonably well supported by the NGA-West2 GMPE’s, with a better understanding of the complex fault rupture mechanism and geometry, and also by the SCEC BBP simulations.

Based on the available data, models, GMPE’s, simulations, etc. it appears that a reasonable range of PGA’s for the LSFD crest perpendicular input motion would be in the range of 0.65 to 0.8 g. Input motions for the Lower San Fernando Dam analyses for this study were developed by (1) rotating the horizontal ground motion seismograph recordings at Pacoima Dam to a direction transverse to the crest of the LSFD (N18E), and then (2) scaling the motions achieve two “input” ground motions as follow:

LSFD Input Motion No. 1: Rotating the Pacoima Dam seismograph recordings to a direction perpendicular to the crest of the LSFD (N18E), and then scaling the rotated acceleration time by a factor of 0.433 to a PGA of 0.65g, in agreement with the “measured” crest perpendicular PGA of the LSFD abutment seismoscope record as interpreted by Scott (1973).

LSFD Input Motion No. 2: Rotating the Pacoima Dam seismograph recordings to a direction perpendicular to the crest of the LSFD (N18E), and then scaling the rotated acceleration time by a factor of 0.534 to a PGA of 0.80g; allowing for uncertainties in the data and judgments involved, and in recognition of the NGA-West2 GMPE’s that predicted/suggested the possibility of a somewhat higher PGA than that of USFD Input Motion 1.

It is suggested that these two motions likely suitably envelope “best estimated” input motions for back-analyses of the LSFD. Figures 4-32 and 4-33 show these two input motions for back-analyses of the LSFD. All six of the “primary” back-analyses of the LSFD will be performed using both of these motions. The analysis results with the higher motion (PGA=0.80g) are presented in this chapter. The analysis results with the lower motion (PGA=0.65g) will be presented as part of future studies as part of this current effort, and the results will be presented in an overall U.C. Berkeley geotechnical research report.

Motions at the nearby USFD would be expected to be similar to those at the nearby LSFD, but the direction of interest (perpendicular to the crest of the USFD) would be different. The crest perpendicular direction at the USFD is S18E, which is only 2° different

than the crest parallel direction (and abutment recording) at Pacoima Dam. Accordingly, the seismograph recording for the horizontal motion parallel to the Pacoima Dam axis (S16E) was utilized in the current studies without rotation. These motions were, however, scaled to develop an input motion for the USFD back-analyses. This approach is similar to a number of previous studies on USFD, where the un-rotated Pacoima Dam abutment motion in the direction parallel to the dam axis was utilized for USFD analyses, with scaling.

The nearby peak accelerations (PGA's) interpreted by Scott (1973) from the nearby LSFD abutment seismoscope are (1) $a_{\max} = 0.65g$ in the LSFD crest perpendicular direction which is (N18E), and (2) $a_{\max} = 0.65g$ in the crest parallel direction of LSFD which is (S72W). Because the motions from the LSFD abutment seismoscope are not fully reliably digitizable and correctable, it is not possible to reliably "rotate" these to the crest perpendicular direction of the USFD (which is S18E). It cannot be reliably determined whether the PGA from the LSFD abutment seismoscope would be higher, lower, or in between the two PGA's interpreted by Prof. Scott.

Similarly, the NGA-West2 GMPEs suggest that a best estimate of the root mean squared PGA might be in the range of approximately $a_{\max} = 0.70g$, but with some uncertainty as to how this would translate into a PGA in the direction of interest (S18E).

An additional data point can be obtained at the relatively nearby Pacoima dam, where the crest parallel motion (S16E) recorded at the abutment seismoscope is almost perfectly aligned with the USFD crest perpendicular direction of S18E. The PGA of the crest parallel abutment motion recorded at the Pacoima Dam seismograph was 1.25g. It is possible that some topographic amplification affected this PGA.

Considering all of the available data and analyses, this project team postulate that the likely "best estimate" "input" motion for back-analyses of the USFD would be obtained by (1) using the Pacoima Dam abutment seismograph in direction parallel to dam axis (S16E) without any rotation for use in USFD dam-perpendicular direction (S18E), and then (2) scaling the rotated motion to a PGA of between approximately 0.7 to 0.85g. The USFD case history involves an embankment that remained "stable" and experienced moderate deformations. The USFD back-analyses will therefore represent an examination of ability of the nine combinations of analytical models and engineering relationships to reasonably accurately "predict" the observed magnitudes of deformations and displacements, and the apparent mechanisms responsible for these movements.

Instead of developing two "input" motions to bound this range, for the USFD back-analyses a single input motion was developed near the middle of the range estimated above. The input motion for the back-analyses of the USFD case history was developed as follows: USFD Input Motion No.1: The Pacoima Dam abutment seismograph record PUL164 (S16E) was scaled by a factor of 0.656 to a PGA of 0.80g to develop the "best estimate" input ground motion for back-analyses of the USFD. Figure 4-34 shows this input motion for back-analyses of the USFD. This motion will be used for all USFD back-analyses, but it is suggested that there is similar uncertainty for the USFD input motion(s) as for the LSFD input motions, and that scaling this rotated input motion for the USFD to a PGA of between 0.7g to 0.85g

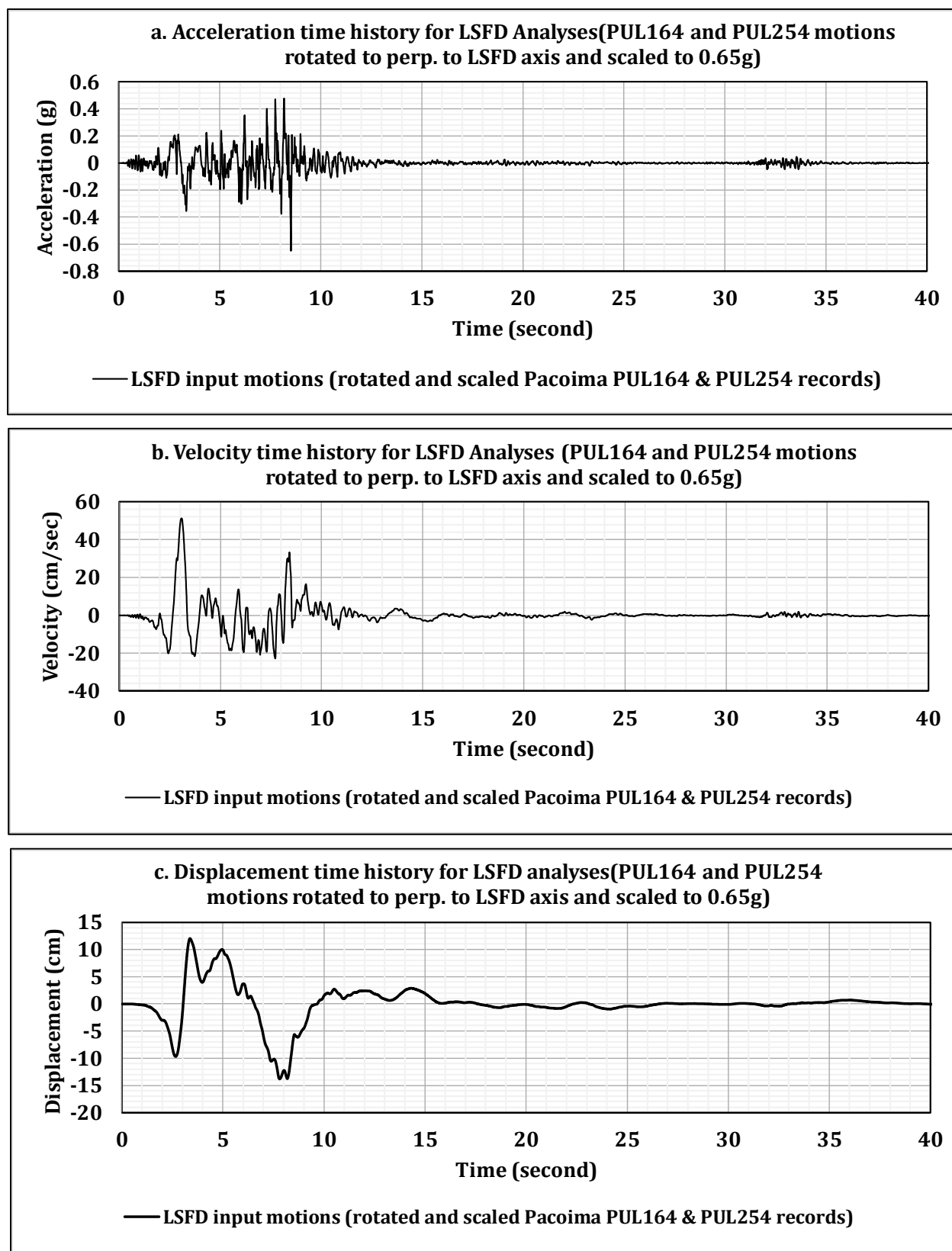


Figure 4-32: Lower San Fernando Dam Input Motion No. 1 ($a_{\max} = 0.65g$)

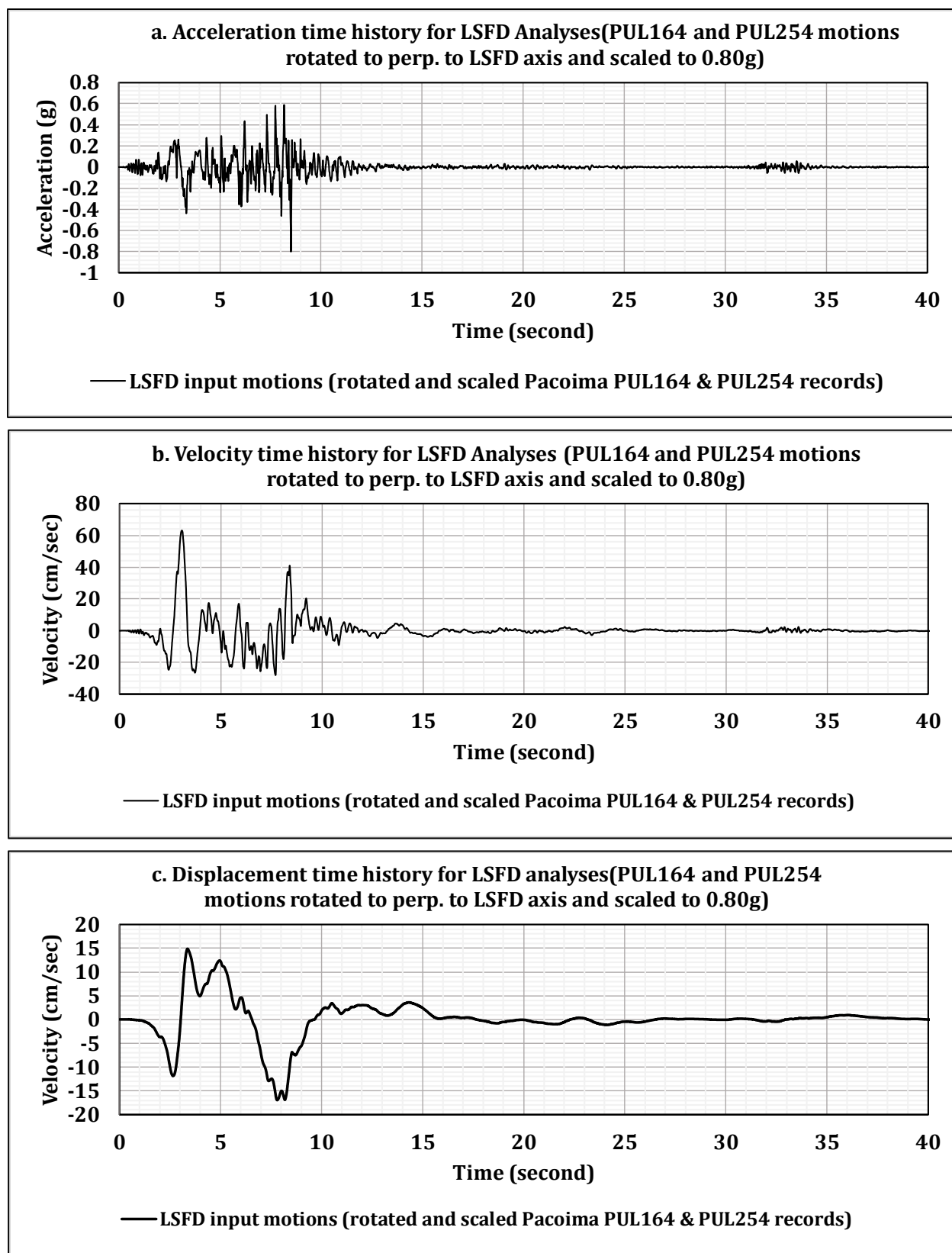


Figure 4-33: Lower San Fernando Dam Input Motion No. 2 ($a_{max} = 0.80g$)

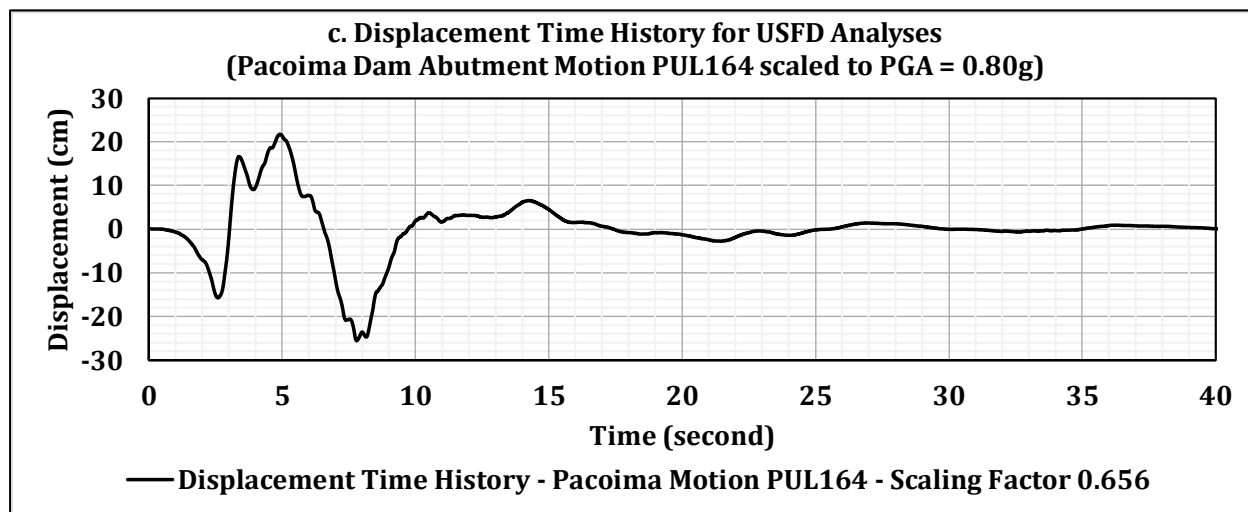
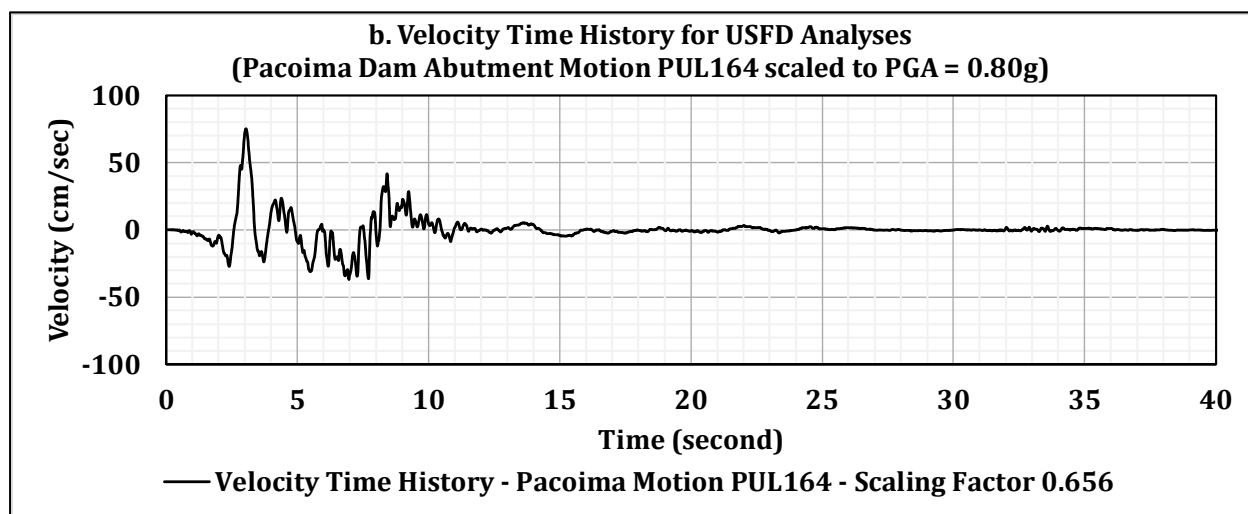
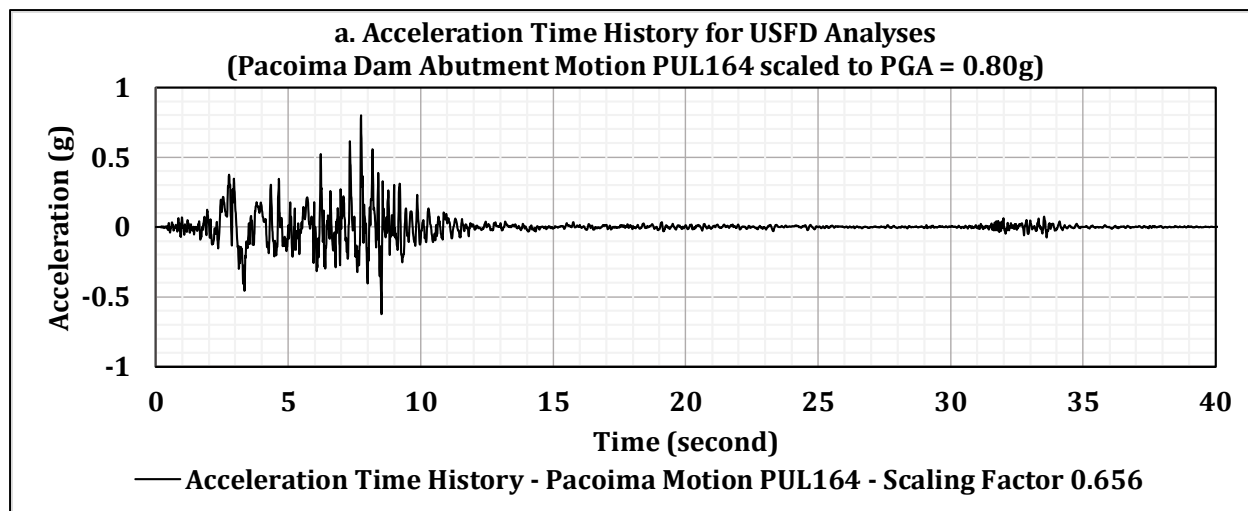


Figure 4-34: Upper San Fernando Dam input motion ($a_{\max} = 0.80g$)

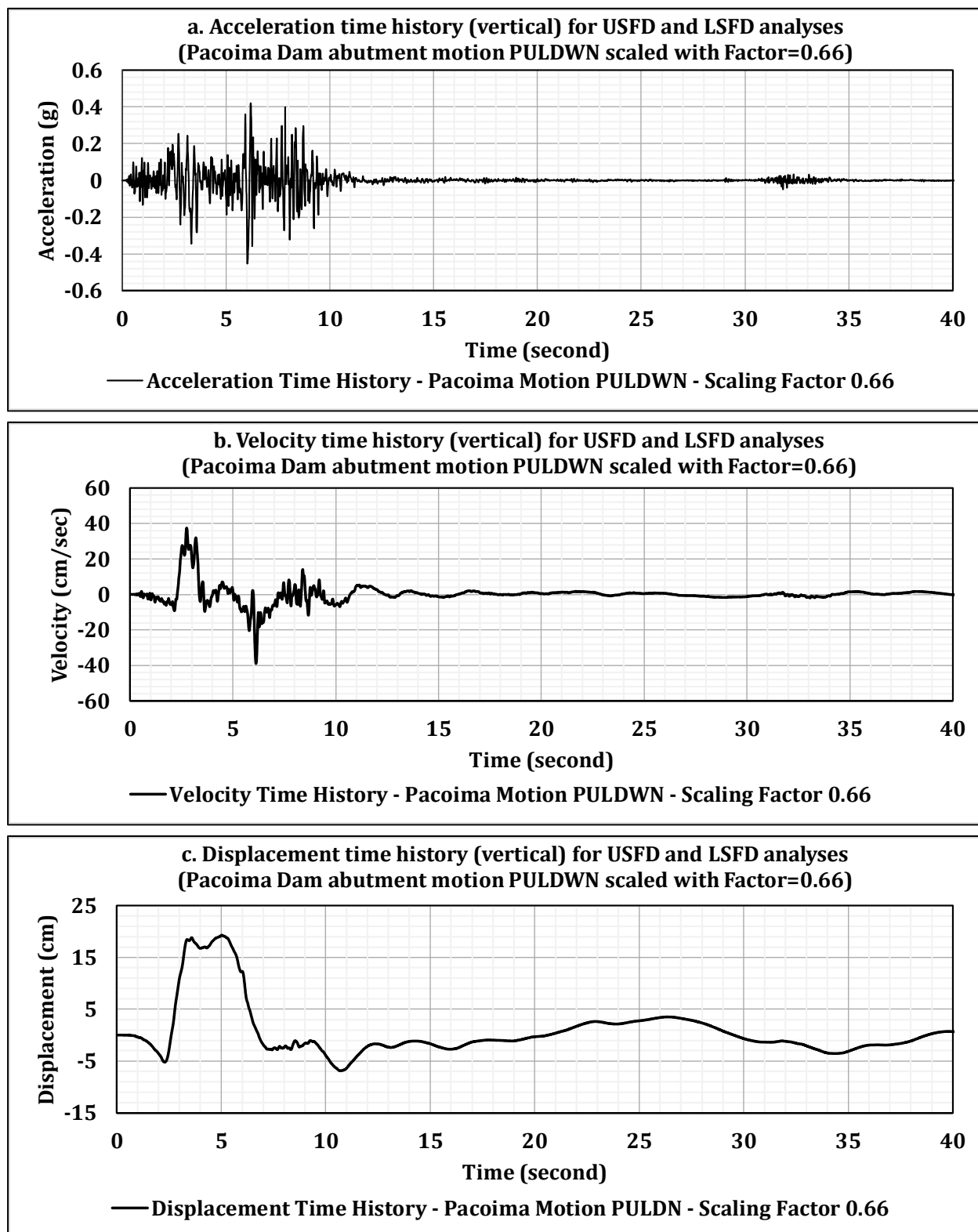


Figure 4-35: Vertical input motion for back-analyses of both USFD and LSFD ($a_{\max} = 0.45g$)

Table 4-17: Intensity parameter values for USFD and LSFD input ground motions

Intensity Parameters from SeismoSignal Version 2016	LSFD Motion No. 2: Horizontal Component (PGA=0.8g)	USFD Motion: Horizontal Component	USFD and LSFD: Vertical Component
Max. Acceleration (g)	0.80	0.80	0.4537
Time of Max. Acceleration (sec)	7.75	8.52	6.03
Max. Velocity (cm/sec)	75.093	63.15337	39.09346
Time of Max. Velocity (sec)	3.05	3.09	6.13
Max. Displacement (cm)	25.59659	16.94024	19.33849
Time of Max. Displacement (cm)	7.8	7.8	5.02
Vmax/Amx: (sec)	0.09572	0.08051	0.08783
Acceleration RMS: (g)	0.0774	0.07191	0.05387
Velocity RMS: (cm/sec)	9.97136	8.28187	5.24408
Displacement RMS: (cm)	6.38985	3.99502	5.21418
Arias Intensity: (m/sec)	3.85048	3.32074	1.86518
Characteristic Intensity (Ic)	0.13907	0.12448	0.08075
Specific Energy Density (cm ² /sec)	4147.1403	2858.80786	1147.03931
Cumulative Absolute Velocity (cm/sec)	1380.5572	1276.60975	888.22266
Acceleration Spectrum Intensity	0.56144	0.51406	0.39952
Velocity Spectrum Intensity	248.17807	234.12725	109.96417
Housner Intensity (cm)	231.5358	217.04435	101.84199
Sustained Maximum Acceleration (cm ² /sec)	0.61414	0.58085	0.34577
Sustained Maximum Velocity (cm/sec)	37.01604	28.01264	31.92199
Effective Design Acceleration (cm ² /sec)	0.78229	0.7252	0.47303
A95 parameter (g)	0.79367	0.7936	0.448
Predominant Period (sec)	0.38	0.4	0.3
Mean Period (sec)	0.48828	0.51317	0.3032

could also be justified, based on the data and understandings currently available. Figure 4-34 shows the crest perpendicular input motion used for the nine primary back-analyses of the USFD.

A similar approach (and scaling) was utilized for vertical components, and a scaling factor of 0.66 was applied to the Pacoima Dam abutment motion to obtain the vertical component of ground motions for both the USFD and LSFD analyses. The resulting peak

vertical acceleration is $a_{\max} = 0.45g$. Figure 4-35 shows the resulting vertical motion. This vertical input motion was used for all back-analyses of both the USFD and the LSFD.

Table 4-17 presents suites of ground motion parameters generated by SeismoSignal 2016 for the 3 horizontal input motions for USFD and LSFD, and for the vertical input motion.

4.6.4 Ground Motion Processing with Different Filtering Bands

Seismic ground motions at a far-field or near-field location depend on several parameters such as source parameters (Moment magnitude, stress drop), path parameters (geometrical spreading coefficient, anelastic attenuation along ray path, and effective distance), and site parameters (kappa, amplification factor for the impedance contrast from source to site) (Abrahamson, 2018). Corner frequency of an amplitude spectrum is one of the important parameters in evaluating the effects of different parameters on the resulting ground motion at a site. The far-field spectrum is reasonably well-characterized by three parameters, (1) the low-frequency level, which is proportional to seismic moment, (2) the corner frequency, and (3) the power of the high-frequency asymptote. According to Brune (1970), a corner frequency is defined as the frequency at the intersection of the low and high-frequency asymptotes in the spectrum.

Aki (1967) developed two kinematic models, the ω -square and ω -cube models to describe the far-field displacement spectrum. Aki and Richards (2009) suggested that the ω -cube model contradicts the observations on peak accelerations for $6 < M < 8$, where the peak accelerations observed at short distances are at frequencies higher than 1 Hz, and they are greater for larger earthquakes at a given distance; however, Aki's (1967) ω -square model gives more satisfactory results. Based on Aki's (1967) ω -square model, the far-field spectrum is given by

$$S(\omega) = \frac{S(0)}{1 + (\omega/\omega_0)^2} \quad [\text{Equation 4-13}]$$

where $S(0)$ is proportional to seismic moment and ω_0 is the corner frequency. Figure 4-36 shows a family of spectral curves fitted by Aki (1967), based on Berckhemer (1962) data that included six earthquake pairs recorded at Stuttgart station for between 1931 and 1951. In the Berckhemer (1962) dataset, the seismogram records from two different earthquakes with the same epicenter were utilized to eliminate the path and receiver effects, and to compare the effects of the source parameters.

Figure 4-37 shows a seismic amplitude spectrum to illustrate the ω -square model (Lay and Wallace, 1995). In Figure 4-37, the amplitude spectrum content of a seismic pulse should be flat at periods longer than the rupture time of the fault. At periods between the rise time and rupture time, the spectra will decay approximately as $1/\omega$, and at high frequencies the spectra will decay approximately in proportion to $1/\omega^2$. In practice, only

one corner (corner frequency) is used, which is defined as the intersection of the asymptote of the plateau and the asymptote of the $1/\omega^2$ decay.

As shown on Figure 4-36, a low-pass filter of ~ 0.01 to 0.05 Hz would be ideal for processing of recorded ground motion for the San Fernando earthquake, considering that the Moment magnitude of the earthquake was $M_w \approx 6.6$, as it would be outside of the vicinity of relevant corner frequency for $M_w \approx 6.6$. Thus, an appropriate low-pass filter, and an adequate high-pass filter, should not alter the corner frequencies of the ground motions at the recorded location (Pacoima Dam abutment station), and would effectively preserve the ground motion characteristics specific to the 1971 San Fernando earthquake.

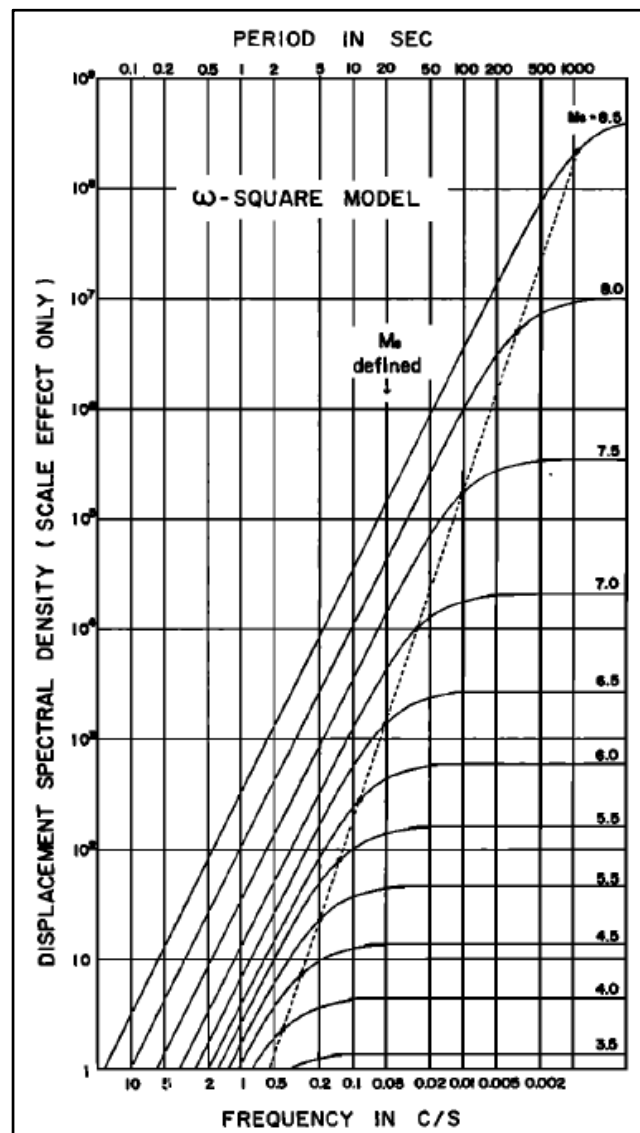


Figure 4-36: Spectra of far-field body-wave displacement observed at a fixed distance from earthquakes with different Magnitudes, using the ω -square model. The broken line is the locus of ω_0 , or corner frequency [Aki, 1967].

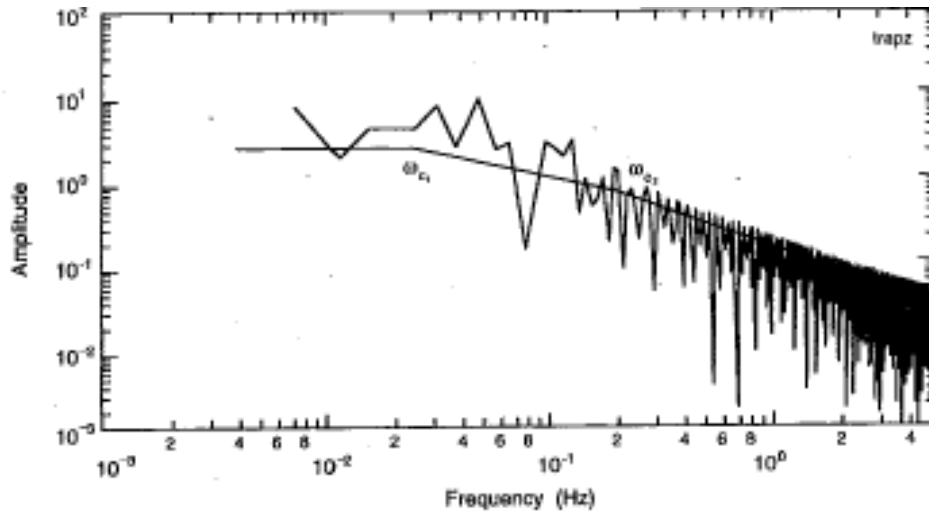


Figure 4-37: Amplitude spectrum of a trapezoid (two boxcars convoluted together) with two corner frequencies, ω_{c1} and ω_{c2} [Lay and Wallace, 1995]

During the initial phases of these current studies, the ground motions from the Pacoima Dam abutment recording station were processed using a filtering band of 0.1 Hz and 25 Hz, in addition to baseline correction, using the ground motion processing software SeismoSignal (SeismoSoft, 2016). The results of the deformation analyses using these ground motions were presented in two GEESD 2018 conference papers (Chowdhury et al., 2018a and 2018b). However, in subsequent evaluations of the ground motions, including consultations with Professors Norman Abrahamson and Douglas Dreger of the University of California at Berkeley, it was found that the narrower filtering band used might not be appropriate for the study considering a relatively higher $M_w \sim 6.6$, as it had inadvertently changed the corner frequency of the ground motions, which is a function of the magnitude of the earthquake and other factors.

The ground motion records available in PEER website include processed records, where the processing was performed with two main objectives: (1) correction for the response of the strong motion instrument itself, and (2) reduction of random noise in the recorded signals (Darragh, Silva, and Gregor, 2011). The standard procedure used by PEER to process strong motion time histories includes bandpass filtering motions based on the frequency range with substantial signal to noise ratios. Based on Gregor (2018), a frequency range from 0.07Hz to 35 Hz was utilized to process Pacoima Dam abutment records, as available in PEER website.

In these current studies, the “PEER-processed” strong motion time histories from the PEER website have now been adopted without any additional filtering and baseline correction (i.e. PEER motions processed with a filtering band of between 0.07 and 35 Hz are used). The strong motion time histories from the PEER database were compared with the strong motions previously processed using a narrower (0.1 Hz to 25Hz) filtering band. Tables 4-18 and 4-19 present intensity parameter values for these differently processed

Table 4-18: Intensity parameter values for the Pacoima Dam _PUL164 motion with different filtering ranges

Intensity Parameters from SeismoSignal Version 2016	PEER Database (Processed with filtering band of 0.07Hz to 35Hz)	Narrower Filtering Band (Processed with filtering band of 0.1Hz to 25Hz)
Max. Acceleration (g)	1.21904	1.23307
Time of Max. Acceleration (sec)	7.75	7.77
Max. Velocity (cm/sec)	114.47103	93.25472
Time of Max. Velocity (sec)	3.05	3.03
Max. Displacement (cm)	39.01919	32.55935
Time of Max. Displacement (cm)	7.8	9.1
Vmax/Amax: (sec)	0.09572	0.07709
Acceleration RMS: (g)	0.11799	0.11709
Velocity RMS: (cm/sec)	15.20024	14.98564
Displacement RMS: (cm)	9.74063	8.75213
Arias Intensity: (m/sec)	8.94762	8.81124
Characteristic Intensity (I _c)	0.26175	0.25875
Specific Energy Density (cm ² /sec)	9636.98202	9366.7948
Cumulative Absolute Velocity (cm/sec)	2104.50792	2082.74565
Acceleration Spectrum Intensity	0.85586	0.84458
Velocity Spectrum Intensity	378.32022	377.02229
Housner Intensity (cm)	352.95092	356.86127
Sustained Maximum Acceleration (cm ² /sec)	0.93619	0.93062
Sustained Maximum Velocity (cm/sec)	56.4269	63.88454
Effective Design Acceleration (cm ² /sec)	1.19252	1.1708
A95 parameter (g)	1.20986	1.22379
Predominant Period (sec)	0.38	0.38
Mean Period (sec)	0.48828	0.48858

Table 4-19: Intensity parameter values for the Pacoima Dam _PUL254 motion with different filtering bands

Intensity Parameters from SeismoSignal Version 2016	PEER Database (Processed with filtering band of 0.07Hz to 35Hz)	Narrower Filtering Band (0.1Hz and 25Hz)
Max. Acceleration (g)	1.23832	1.0974
Time of Max. Acceleration (sec)	8.52	8.53
Max. Velocity (cm/sec)	57.27904	53.44636
Time of Max. Velocity (sec)	8.34	8.35
Max. Displacement (cm)	12.80136	10.25822
Time of Max. Displacement (cm)	3.33	3.29
Vmax/Amax: (sec)	0.04715	0.04965
Acceleration RMS: (g)	0.11261	0.11192
Velocity RMS: (cm/sec)	8.74847	8.71963
Displacement RMS: (cm)	2.63969	2.27206
Arias Intensity: (m/sec)	8.1507	8.05062
Characteristic Intensity (Ic)	0.24406	0.24181
Specific Energy Density (cm2/sec)	3192.30394	3171.29368
Cumulative Absolute Velocity (cm/sec)	1997.00041	1998.29111
Acceleration Spectrum Intensity	0.83321	0.83714
Velocity Spectrum Intensity	260.05069	257.66799
Housner Intensity (cm)	227.90445	227.60716
Sustained Maximum Acceleration (cm2/sec)	0.71306	0.73899
Sustained Maximum Velocity (cm/sec)	48.71101	47.08237
Effective Design Acceleration (cm2/sec)	1.08512	1.08399
A95 parameter (g)	1.229	1.08359
Predominant Period (sec)	0.42	0.42
Mean Period (sec)	0.38493	0.38508

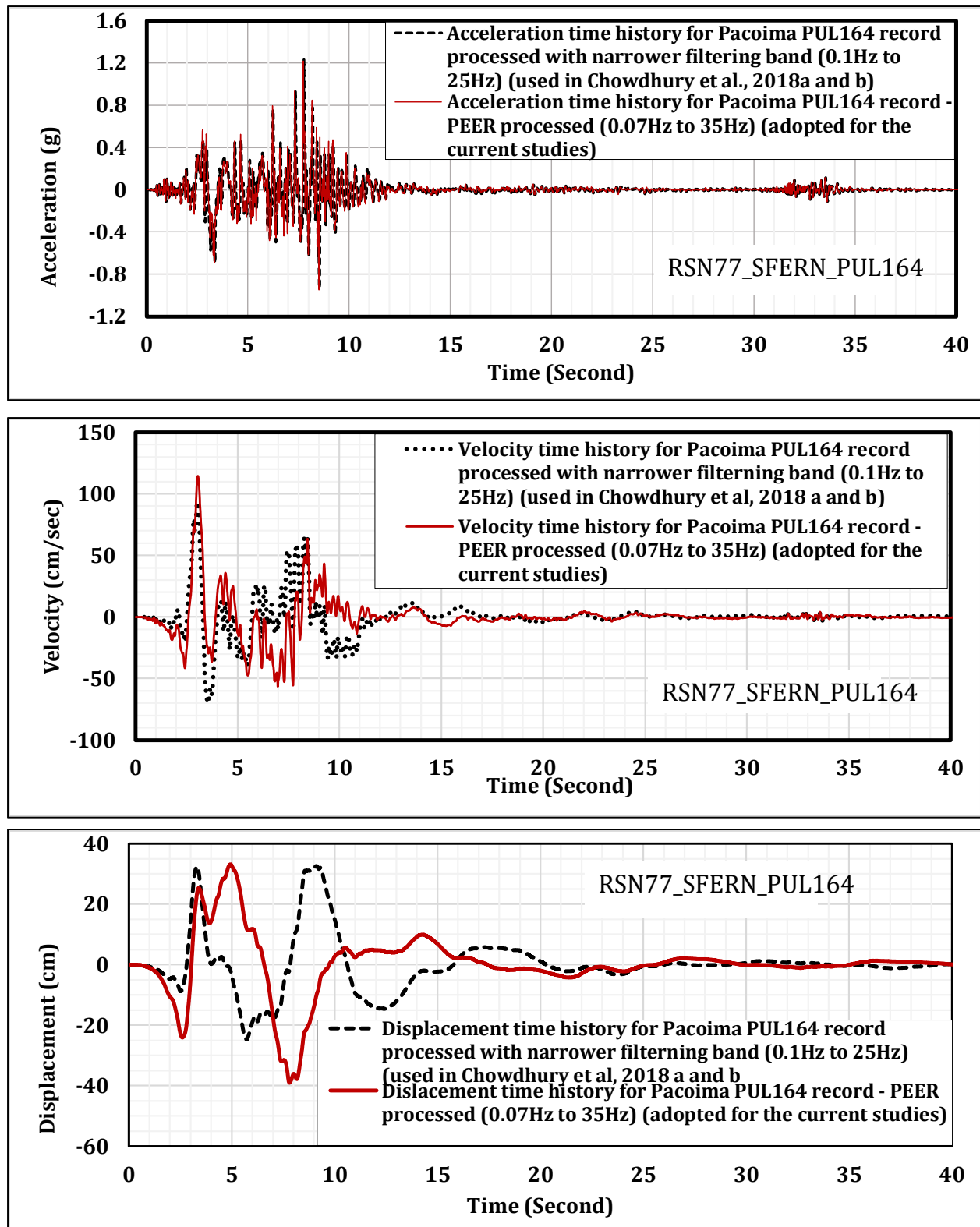


Figure 4-38: Comparison of acceleration, velocity, and displacement time histories with different ground motion processing schemes and without scaling (Pacoima PUL164)

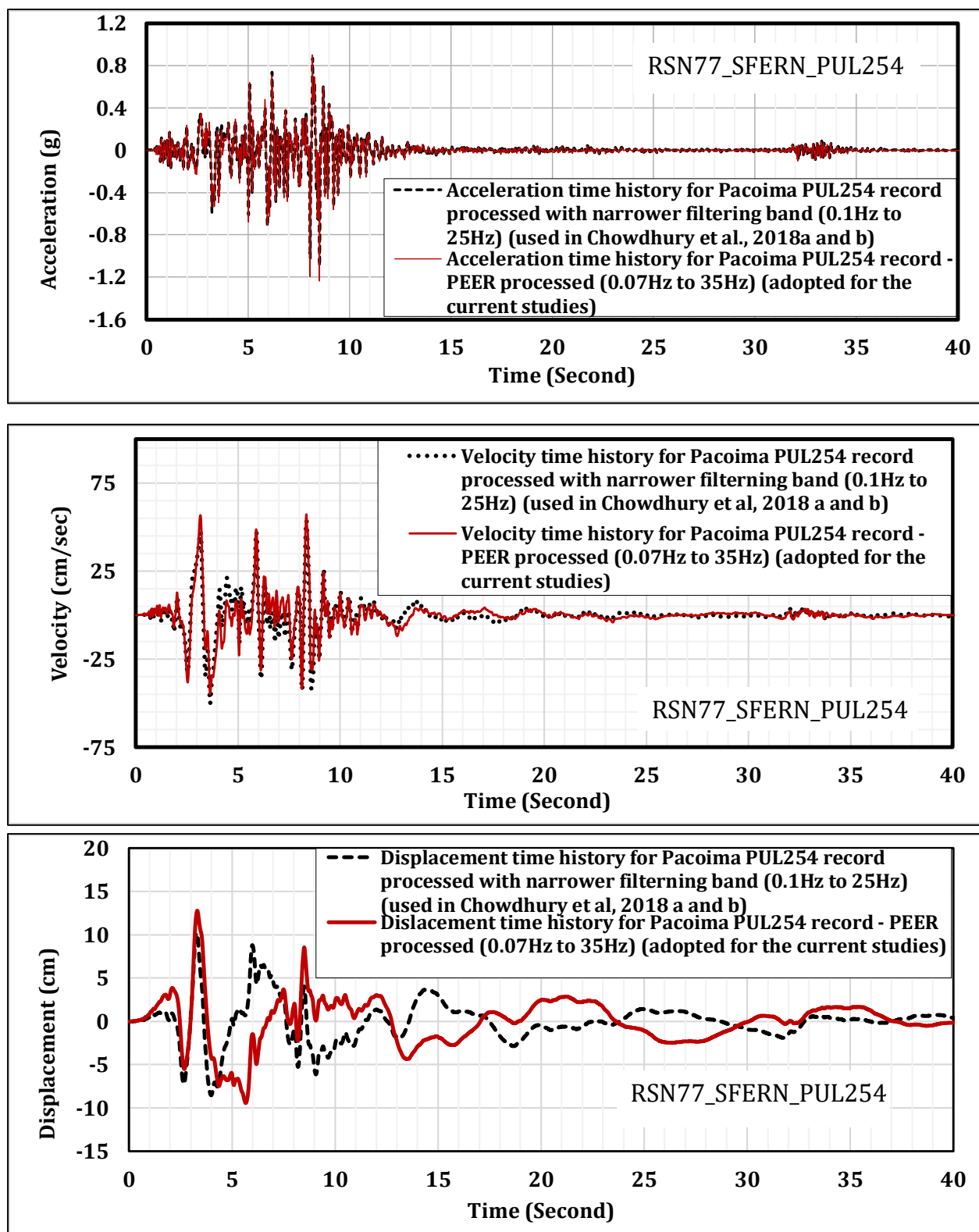


Figure 4-39: Comparison of acceleration, velocity, and displacement time histories with different ground motion processing schemes and without scaling (Pacoima PUL254)

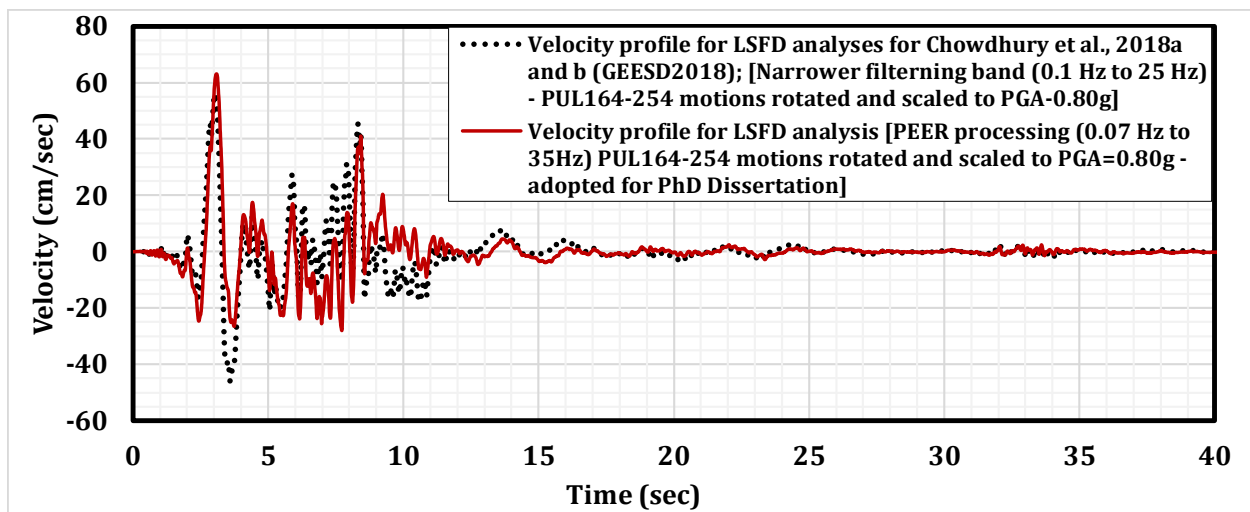
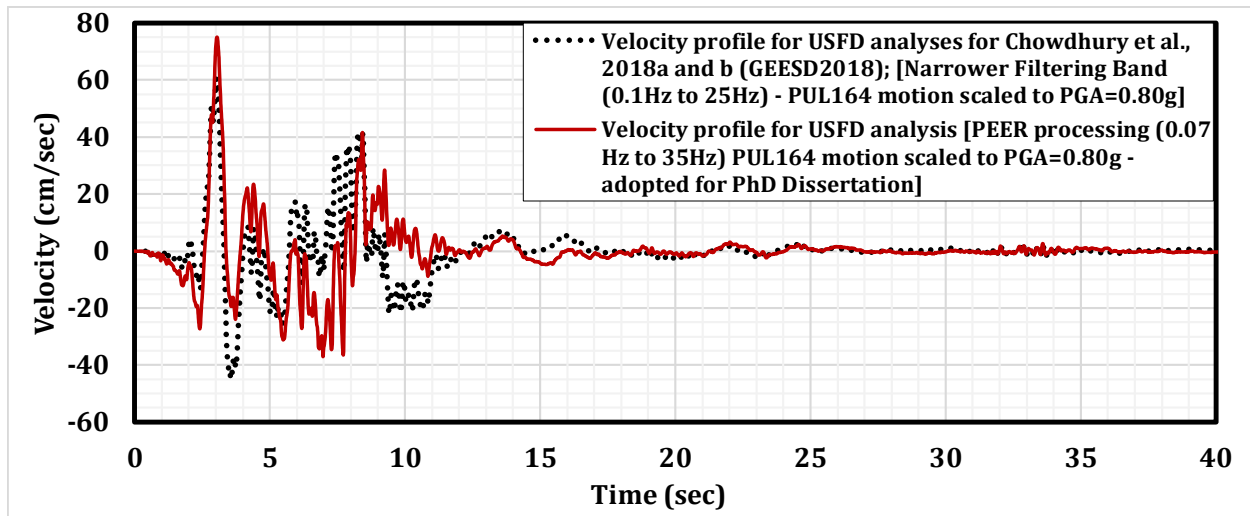


Figure 4-40: Comparison of Velocity Time Histories for USFD and LSFD with the narrower filtering band (0.1 Hz to 25Hz) (used in Chowdhury et al., 2018(a) and (b)) vs. the Time Histories from the PEER ground motion database (with filtering band from 0.07 Hz to 35 Hz) as adopted for these current studies

a narrower filtering band (0.1Hz to 25 Hz) (Chowdhury et al., 2018a and b) and the seismic deformation analyses for this dissertation were performed using the strong motions processed by PEER. The approaches for scaling and rotations are presented in Section 4.6.3. The overall results of 14 out of 15 deformation analyses performed in this study have changed negligibly from the deformation values presented in Chowdhury et al. (2018a and 2018b). The results of one of the LSFD analyses has changed significantly, however, and this is discussed in Section 4.8.4.

4.6.5 Ground Motion Processing with Estimated Permanent Displacement

Ground motions in the near-source regions of earthquakes can be significantly affected by rupture directivity and tectonic fling. These two conditions, i.e. rupture directivity (or pulse) and tectonic fling (or fling step) can result in large, long-period pulses of ground motions.

Rupture directivity is related to the direction of propagation of the rupture front. It is identified as forward directivity if rupture propagates towards the site, and backward directivity if rupture propagation is away from the site. Figure 4-41 shows both forward and

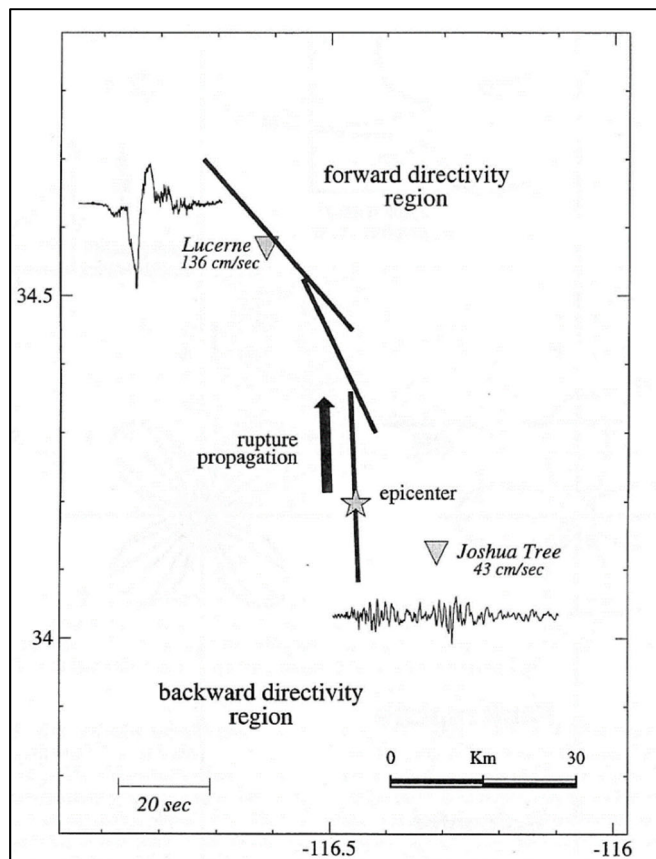


Figure 4-41: Map of the Landers region showing (1) the location and propagation of the rupture of the 1992 Landers EQ , which progressed across 3 fault segments, (2) the epicenter, and (3) the locations of the recording stations at Lucerne and Joshua Tree. The strike-normal velocity time histories recorded at Lucerne and Joshua tree are also shown. These exhibit forward and backward rupture directivity effects, respectively.

backward directivity effects from the 1992 Landers earthquake (Somerville, 1995). Forward rupture directivity occurs at locations towards which the rupture propagates (in this case the Lucerne recording station in the northeast corner of the figure, as the rupture initiated at the south end of the three fault rupture sequence), and it typically results in a two-sided velocity pulse due to constructive interference of shear waves generated from parts of the rupture located between the site and the originating epicenter (Abrahamson, 2018). The two-sided velocity pulse can produce large velocities, but it produces little or no permanent (residual) displacement. The constructive interference occurs if slip direction is aligned with the rupture direction. The velocity time history recorded at the Lucerne station is shown in Figure 4-41, and the large and two-sided velocity pulse can be clearly seen.

Reverse directivity occurs at locations that the evolving fault ruptures away from (in this case the Joshua Tree recording station, located south of the northwards propagating rupture. As shown in Figure 4-41, the velocity time history shows velocity pulses to be “stretched out”, and there are no pulses nearly as large as those in the forward directivity velocity time history of the Lucerne station.

Fling results from the overall (net) tectonic displacement of the fault, and it occurs on the fault-parallel component for strike-slip rupture, or on the fault normal component for reverse (thrust) rupture (Dreger et al., 2011, Graves, 2011). Fling effects are independent of epicenter location, but they only occur in relatively close proximity to fault rupture surfaces where the ground undergoes non-negligible overall permanent displacements. Fling motions are manifested by a one-sided pulse in ground velocity. This one-sided velocity pulse rises to a peak value, and then decreases back to zero; but it does not reverse. The result is the occurrence of displacements initially at an increasing rate, then at a decreasing rate, producing potentially significant overall (permanent) displacement offset.

Conventional processing techniques can typically recover directivity pulses from seismograph records, but accurate recovery of fling requires complete resolution of the residual displacement, which can be non-unique and quite sensitive to the processing approaches (Graves, 2011). Conventional ground motion processing typically involves bandpass filtering and baseline correction. The standard ground motion processing procedures used by PEER include bandpass filtering of the recorded motions based on the frequency range with substantial signal to noise ratios (Abrahamson and Silva, 1997 and Darragh, Silva, and Gregor, 2011). Due to application of the filtering band, and baseline correction, the ground motion records in the PEER database cannot preserve overall (net) static displacements.

Gregor, Silva, and Darragh (2002) used the methodology proposed by Grazier (1979) and Boore (1999, 2000) to perform baseline correction of several recorded motions that experienced near-source effects to obtain estimates of static displacements. Figures 4-42 (a) to (c) show a comparison between the peak values (PGA, PGV, and PGD) for the ground motions processed (1) using PEER standard procedures (including standard baseline correction to zero velocity and to zero net displacement) vs. (2) the static baseline correction procedures (to zero net velocity) that preserve the estimated static offset (Darragh, Silva, and Gregor, 2011). In Figures 4-42(a) through (c) the values shown on the vertical axes are the results of “conventional” baseline correction to zero final velocity and zero net displacement, and the values shown on the horizontal axes are the results of “static” baseline correction to zero final velocity, but preserving net displacement. As shown on Figure 4-42(a), the PGA values are very similar between the two processing procedures, i.e. the data points generally fall along the 1:1 line. As shown in Figure 4-42(b), the PGV values also fall along the 1:1 line, but show slightly larger scatter than the PGA values. As shown in Figure 4-42(c), the “static” correction procedure (which) produces net displacements also tends to produce larger maximum (or peak) ground displacements (PGD), while the conventional correction procedure that zeros out permanent (or net) ground displacements as part of the correction process also tends to produce lower PGD’s.

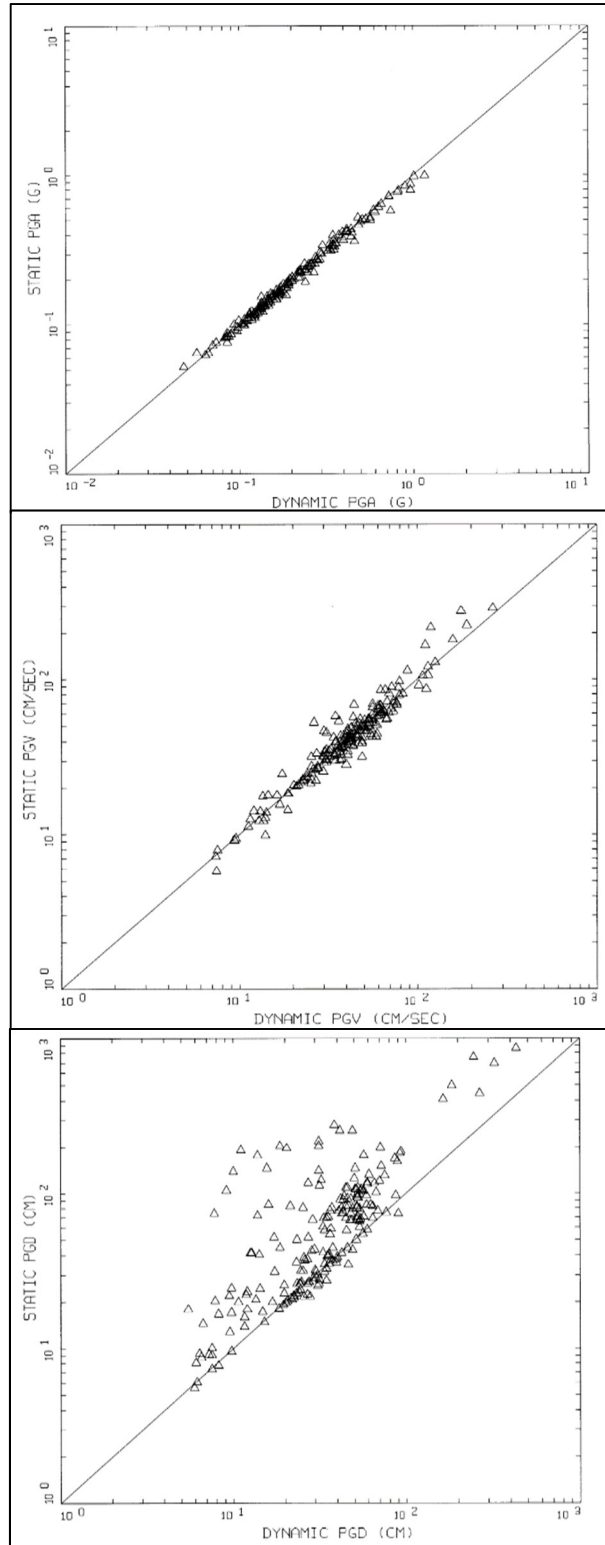


Figure 4-42: Comparison between the (a) PGA, (b) PGV, and (c) PGD values for the “static” baseline corrected time histories vs. the PEER NGA-West1 database time histories with “conventional” (or “static and dynamic”) baseline correction (Darragh, Silva, and Gregor, 2011)

Because Pacoima Dam, USFD and LSFD are all within 16 km of the hypocenter of the 1971 San Fernando earthquake, and in close proximity to fault rupture surfaces, and on the hanging block of the San Fernando fault, all of these sites experienced near-source effects. These would include permanent ground displacement (or ground offset). To investigate the potential effects of this, the input motions for both the USFD and LSFD seismic deformation back-analyses were re-processed to preserve the static offset.

The Pacoima Dam horizontal records in both directions (PUL164 and PUL254) were baseline corrected by Prof. Norm Abrahamson using a two-step baseline correction process such that it preserves the static offset. In this processing scheme, the baseline drift in the first 1.5 seconds (before the first S-wave arrival) was removed using a conventional baseline correction. In these records, a baseline drift was observed after the large velocity pulse arrival at about 4.5 seconds. This drift was removed using a baseline correction from 4.5 seconds to the end of the recording which preserved static offset or displacement.

Figures 4-43 and 4-44 show a comparison of acceleration, velocity, and displacement time histories for the ground motion records at Pacoima Dam abutment (PUL164 and PUL254) with two different processing approaches. The figures present the motions developed using (1) the PEER ground motions (with conventional baseline correction) and (2) the ground motions processed with static offset preserved.

Figure 4-43 shows a comparison of acceleration, velocity, and displacement time histories for the USFD crest-perpendicular input ground motion (scaled to $PGA = 0.80g$), and Figure 4-44 shows for the LSFD crest-perpendicular input ground motion (scaled to $PGA = 0.80g$), processed (1) with and (2) without preservation of permanent ground displacements. The seismic deformation analyses for the current studies as presented in this dissertation have been performed using the ground motions processed by PEER.

However, a sensitivity analysis using a ground motion with permanent static offset was performed for the USFD. This research effort will continue beyond the filing of this dissertation, and one element of the additional work will involve performing a number of additional analyses of both the USFD and the LSFD with input motions that preserve static offset.

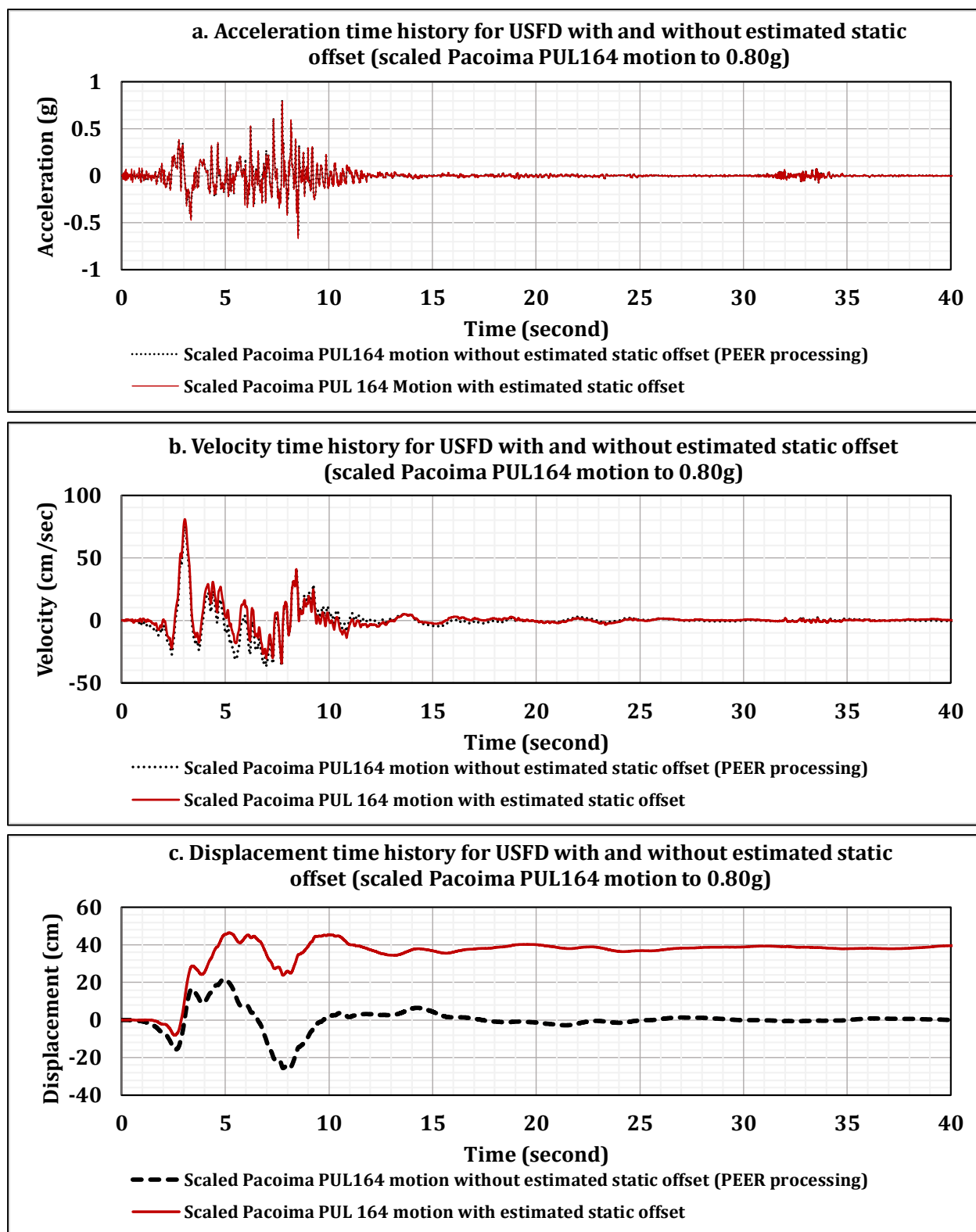


Figure 4-43: Comparison between horizontal motions for USFD analysis [scaled Pacoima PUL164 motion to $PGA=0.80g$] with and without preservation of estimated permanent displacement

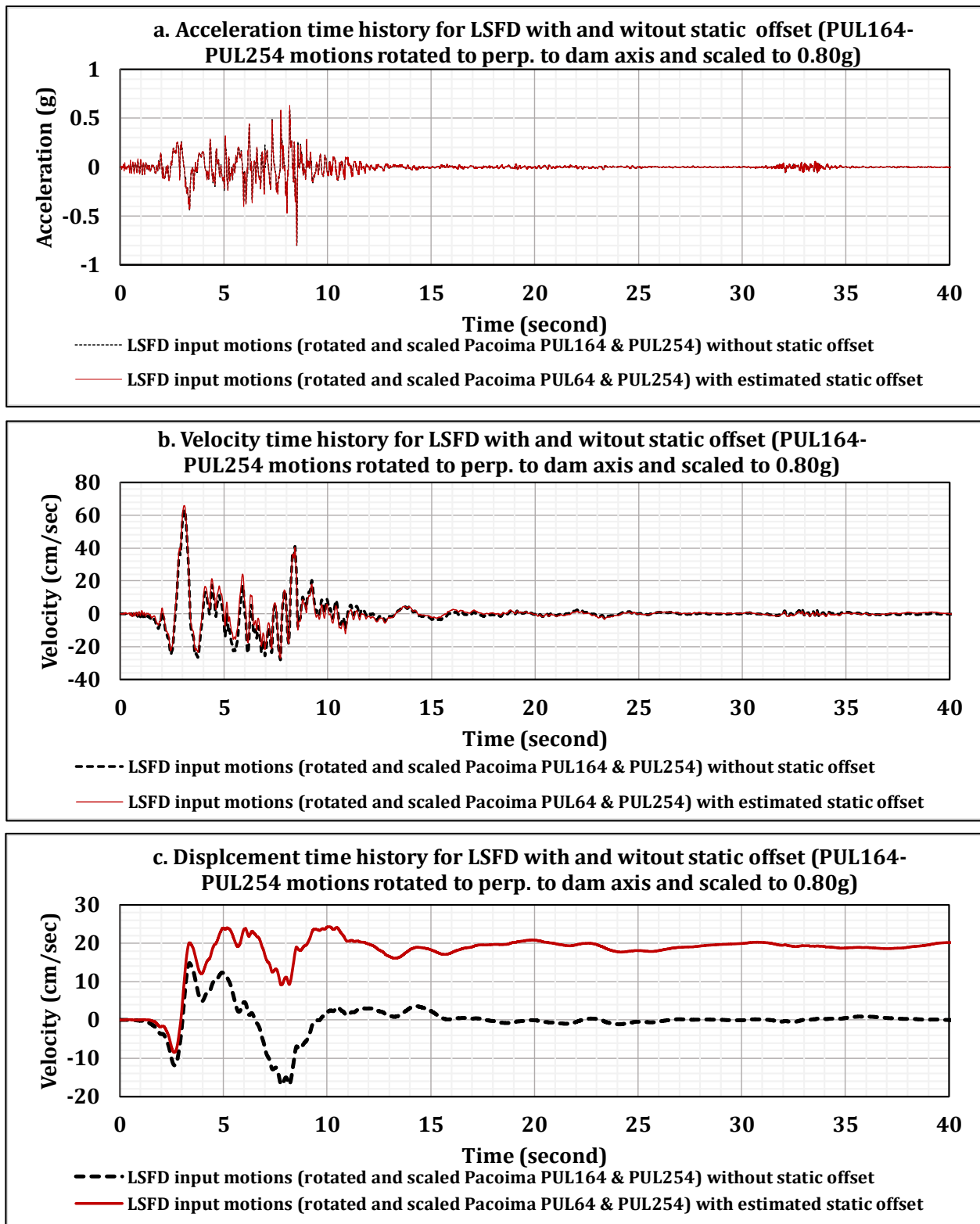


Figure 4-44: Comparison between horizontal motions for LSFD analysis [rotated and scaled Pacoima PUL164-PUL254 motions to $PGA=0.80g$] with and without preservation of estimated permanent displacement

4.6.6 Simulated Ground Motions for Use as Input Motions for Back-Analyses of the USFD and LSFD Case Histories (Approach 2)

4.6.6.1 SCEC Broadband Platform Simulation Approach for the Current Study

The Southern California Earthquake Center (SCEC) Broadband Platform (BPP) is an open source software system that contains physics-based seismological ground motion models capable of generating 0-100 Hz seismograms for historical and scenario earthquakes. The resource database of the BPP is currently well-populated for sites in California, Eastern North America, and Japan (Maechling et al. 2015, SCEC, 2018).

Figure 4-45 shows an overview of the simulation workflow of the SCEC-BPP. The BPP simulation is generally implemented through three processing stages and two post-processing stages.

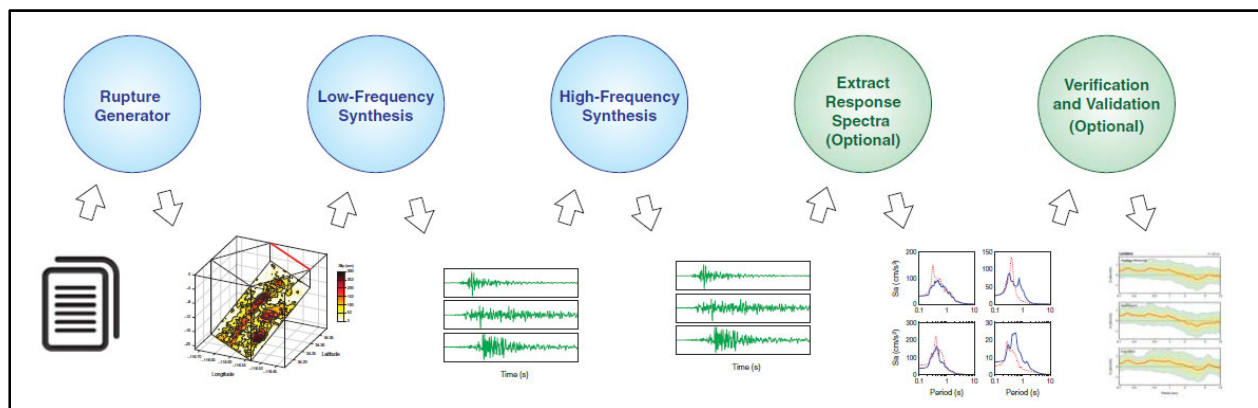


Figure 4-45: SCEC-BPP simulation workflow showing how a ground motion simulation is implemented in three processing stages (blue circles) and two postprocessing stages (green circles) (<https://scec.usc.edu/scecpedia/Broadband Platform>).

The three processing stages include (1) rupture generation, (2) low-frequency synthesis, and (3) high-frequency synthesis.

Rupture generators are user-defined rupture earthquake event scenarios that contain details of rupture geometry (for one or more faults), magnitude (M_w) or overall energy release on each contributing fault: details include fault length, fault width, strike, rake, dip, latitude and longitude at the center of the fault rupture zone, hypocenter along strike, hypocenter down dip, dimensions for discretization, corner frequency, and seed values (produced by a random scenario generator). Rupture generation (propagation of rupture across the fault rupture surface modeled) can be implemented as a largely randomized process, within the constraints of user-specified event parameters.

For the 1971 San Fernando Earthquake, there are relatively good understandings of energy release patterns on the principal rupture surfaces of the two causative faults; the San Fernando fault and the Sierra Madre fault, due to inversions of ground motion recordings in the region. The SCEC-BBP is developed to be able to address localized details of rupture features and geometries, and thus a good level of detail can either be input, or can be provided by algorithmic “randomizers”.

Energy “packets” incrementally released from small zones of fault surfaces as they progressively rupture (as ruptures stochastically propagate) travel as “wavelets” or Green’s functions, and they interact with geometry and geology (including the ground surface, and modeled regional ground and “basement” conditions and properties). Resulting “outputs” (or ground motions) can be calculated at any number of user-specified locations. Low-frequency generation (typically from DC to 20 Hz) is performed for any given (randomized) scenario event by means of propagating Green’s functions, and based on stochastically roughened and randomized fault rupture propagation (based on different selected models in different methods) to develop calculated simulations of low-frequency motions at any specified location. Higher frequency generation (> 20 Hz) is based on either (1) one of three different finite-source simulation models, or (2) one of two semi-deterministic approaches, in the currently available set of tools in the SCEC-BBP.

The five broadband, finite-source simulation methods currently implemented in the SCEC-BBP include two deterministic approaches; (1) CSM (Anderson, 2015), and (2) UCSB (Crempien and Archula, 2015); a band-limited stochastic white noise method (3) called EXSIM (Atkinson and Assatourians, 2015); and two hybrid approaches, referred to as (4) G&P (Graves and Pitarka, 2015) and (5) SDSU (Olsen and Takedatsu, 2015). In the post-processing stages, the BPP also includes software tools to assist in evaluating ground-motion models and comparing simulation results to observed ground-motion recordings and against ground motion prediction equations. In the first post-processing stage, ground motion time series are converted to peak pseudospectral acceleration (PSA) at different periods, and in the second post-processing stage, BPP validation processing compares observed ground motions against ground-motion prediction equations (GMPEs) (Maechling et al., 2015).

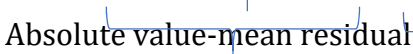
One of the supported methods of the SCEC BBP is the Graves and Pitarka (2015) hybrid broadband simulation approach. In this model, as the fault model ruptures “energy packets” are incrementally released from small zones of fault surfaces as they progressively rupture. This radiated field is convolved with Green’s functions that account for the wave propagation from the fault surface to the recording stations, and accounts for how the wavefield interacts with geologic structure (assumed in this case to be one-dimensional). The calculated wavefield thusly accounts for 1) rupture directivity effects, 2) hanging wall effects (for dip-slip fault geometry), 3) the static offsets due to the elastic rebound of the material adjacent to the fault (“fling”), as well as 4) the reflection, refraction, and generation of surface wave motions due to interactions of the wavefield with the layered geologic velocity structure. Resulting “outputs” (or ground motions) can be calculated at any number of user-specified locations. In the hybrid approach low-frequency generation (typically from DC to 20 Hz) is performed for any given (randomized) scenario event by means of

propagating deterministically the theoretical Green's functions for the specified one-dimensional layered velocity model. Higher frequency generation (> 20 Hz) is based on the integration of stochastic motions that are shaped for the source spectrum, over the same randomized slip-time rupture model. The low-frequency (deterministic) and the high-frequency (stochastic) fields are then matched at approximately 1 Hz to produce the full broadband spectral response of the simulated motions.


A validation exercise was performed using the SCEC-BPP Version 14.3 to evaluate the performance of five broadband, finite-source models relative to recordings from past earthquakes (Part A) and ground motion prediction equations (GMPEs – Part B) (Dreger et al., 2015 and Goulet et al. 2015). This validation exercise was based on evaluation of the performance of the five different methodologies in matching the pseudospectral acceleration spectra (PSA) of (1) recorded ground motions and (2) empirical relations GMPEs) for a set of selected earthquake scenarios and recording stations. The target validation metric was the RotD50 5%-damped PSA for the spectral periods in the 0.01 to 10 seconds range. RotD50 is the median value PSA of the resultant of two horizontal components of ground motions as computed over each degree of compass rotation from 1° to 180° (Boore, 2010). As RotD50 is independent of the sensor orientation, it was considered an appropriate index for validation purposes here. The Part A validation involved the comparison of simulated and observed PSA's for twelve earthquake events, with each having 40 (analytical) "stations" to provide good azimuthal and site to source distance coverage. The basis for the Part B validation (the empirical data, or GMPE-based, data-to-simulation; Dreger et al., 2015) was evaluated primarily in terms of residuals of RotD50 PSAs. For a given period, the residual is defined as the difference between the natural logarithm of the observed PSA (data) and the simulations (models), which can be written as $\ln(\text{data}/\text{model})$. The residuals were aggregated to four different period bins (0.01-0.1 sec, 0.1-1 sec, 1-3 sec, and 3-10 sec) and into four distance bins (0-5 km, 5-20 km, 20-70 km, and >70 km). A combined goodness of fit (CGOF) was computed as the equally weighted sum of the absolute value of the mean residuals and the mean of the absolute value of the residuals using the following equation.

$$\text{CGOF} = \frac{1}{2} \langle |\ln(\text{data}/\text{model})| \rangle + \frac{1}{2} \langle |\ln(\text{data}/\text{model})| \rangle$$

[Equation 4-14]



Absolute value-mean residual



Mean-absolute value of residuals

The threshold adopted for the BPP evaluation considered a CGOF exceeding a factor of 2.0 (0.69 ln units) as a 'fail' condition, whereas a CGOF less than a factor of 1.4 (0.35 ln units) was given a 'pass'. In the validation process, all four of the methods employed (UCSB, EXSIM, G&P, and SDSU) performed well in the distance ranges 5-20 and 20-70 km distance ranges, and in the 0.01-0.1 s, 0.1-1.0 s, and 1-3 s period ranges. Also, the UCSB, EXSIM, G&P, and SDSU methods were judged to have performed better than the GMPEs (NGA-West1) in 36%, 56%, 53%, and 49% of the cases, and worse than GMPEs in 41%, 16%, 17%, and 21% of the cases.

In Part B of the validation, Dreger et al. (2015) compared mean $\ln(\text{PSa})$ from simulations and GMPEs (NGA-West1) for M 5.5. (reverse), 6.2 (strike-slip), and 6.6 (reverse

and strike-slip) events at distances of 20 km and 50 km for the 0.01-3 s period range. As an example, Figure 4-38 shows a comparison of four models for a M 6.2, strike-slip scenario at a distance of 50 km. The solid squares in Figure 4-46 show the mean motion, the boxes show the standard deviation, and the error bars show the maximum range of simulated motions for 50 (randomized) source realizations. The effective range of the acceptance criteria corresponds to a range of about ± 1.46 (± 0.38 ln units).

Considering that the primary purpose of the SCEC-BPP simulations for this current study was to evaluate and inform the selection of scaling factors developed in Approach 1, and given the significant amount of data that was available from this well-studied event, a single model was selected for the simulations of the 1971 San Fernando earthquake in these current studies. Based on an evaluation of the validations performed (Dreger et al., 2015), the GP2010 model (Graves and Pitarka, 2010) was considered to be a reasonable relationship for the current study and was selected for SCEC broadband simulations of the 1971 San Fernando earthquakes scenarios.

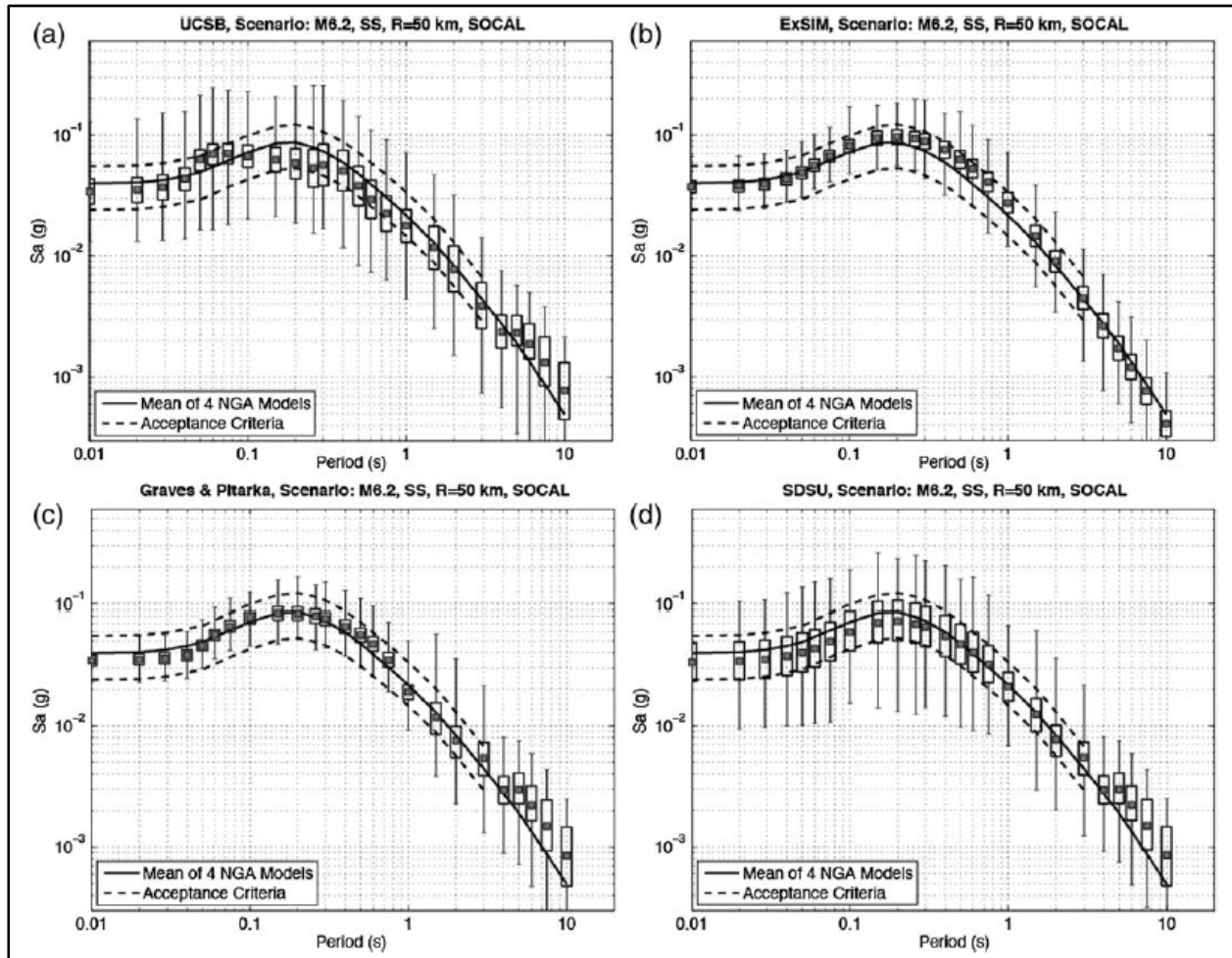


Figure 4-46: Comparison of four (a) UCSB, (b) EXCIM, (c) G&P, and (d) SDSU PSa for an $M_w = 6.2$, strike-slip scenario at a distance of 50 km (Dreger et al. 2015)

The GP2010 method can be described as a hybrid simulation approach in which: (1) for frequencies less than 1 Hz, deterministic ground motions are simulated using Green's functions for an appropriate 1D seismic velocity model, and (2) for frequencies greater than 1 Hz, a finite-source stochastic simulation (e.g. Boore; 1983, 2009) is utilized. As implemented, the method simulates motions from DC to 20 Hz (40 Hz sampling frequency). Since the Green's functions used in the simulation are complete with respect to near-, intermediate- and far-field terms of the elasto-dynamic equations of motion, the method is capable of simulating static offsets, which could be important at sites located up-dip and on the hanging wall of the fault: as with the locations of both the USFD and the LSFD, as well as Pacoima Dam. The method thusly accounts for 1) directivity effects, 2) static offset or "fling" effects, 3) hanging wall effects for dipping faults, and 4) complete seismic wave propagation including direct wave, reflected and refracted, multiply reflected and refracted body waves, and Love and Rayleigh surface waves for the specified one-dimensional velocity model to compute the utilized Green's functions.

4.6.6.2 Slip Models for SCEC-BPP Simulations of the 1971 San Fernando Earthquake in These Current Studies

The simulation procedure begins by generating kinematic slip models that have stochastic heterogeneity in slip, rise time, and rupture velocity. To simulate motions for the 1971 San Fernando earthquake, which exhibited complex surface faulting and compound ruptures (Heaton, 1982), a multi-segmented model was developed (Figure 4-47). In the current studies, SCEC BPP version 16.5.0 was utilized.

The more northern plane segment shown in Figure 4-47 represents the Sierra Madre fault. This fault initiated the overall event, and it initiated rupture at greater depth than the rupture on the nearly co-parallel San Fernando fault to its south. The Sierra Madre fault dips relatively steeply to the north, and it did not rupture fully to the ground surface (see Figure 4-26). As a result, the ruptured portion of the Sierra Madre fault is at greater depth than the ruptured portions of the San Fernando fault, and it is shown "fainter" in Figure 4-47 than the shallower rupture surfaces of also steeply dipping San Fernando fault to its south. The rupture on the Sierra Madre fault is modeled here as rupturing upwards from the overall hypocenter, and terminating at a depth of 3 km.

The southern-most two rectangular planes in Figure 4-47 represent the San Fernando fault rupture surfaces. The San Fernando fault ruptured fully to the ground surface, and as a result its surface intersection is defined in part by post-earthquake surface fault mapping studies. The red lines in Figure 4-47 represent mapped surface fault rupture for this event. The orientations of the two San Fernando plane segments generally follow the Heaton (1982) imbricate faulting model, and they dip relatively steeply to the north (see Figure 4-26). These two rupture planes will be referred to as (1) San Fernando fault rupture west (SF-R-West) and (2) San Fernando fault rupture east (SF-R-East). These two rectangles are essentially part of the San Fernando fault, however they are modeled separately to account for the monoclinial flexure of the overall rupture surface (as posited in Figure 4-47); when

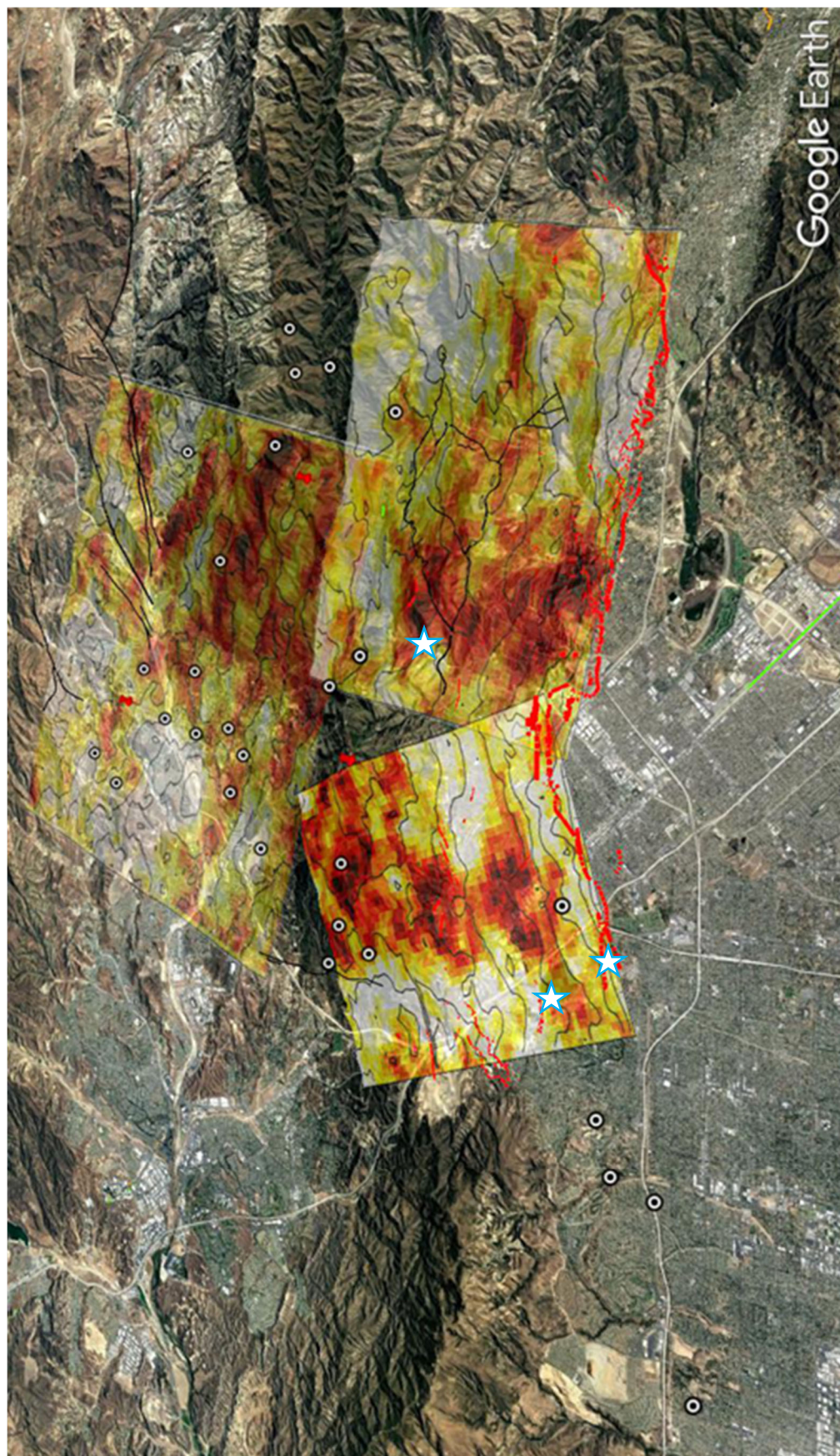


Figure 4-47: Three segment fault model for the 1971 San Fernando earthquake showing the random slip distributions (scenario210). White circles show aftershocks. The two southern planes are placed to be consistent with the observation of surface faulting in the earthquake (thin red fault lines). The blue stars show Pacoima Dam (STA1), Lower San Fernando Dam (STA45) and Upper San Fernando Dam (STA46) sites. The red push pins show the hypocenters of the respective faults. The earthquake nucleated on the deep-north plane and rupture up-dip on the south-dipping fault system.

rupture of the first plane reaches the nearest edge of the two shallower planes, rupture is initiated, and then spreads across the respective planes.

The shallower San Fernando fault plane rupture reaches the surface and was adjusted to be consistent with the reported/mapped surface faulting (thin red lines), and the monoclinial dipping flexure inferred by Allen et al. (1975), as shown in Figure 4-29. The surface rupture of the 1971 San Fernando earthquake extends approximately to the LSFD, and includes a bend that starts with an apparent offset located at about 12 km west of the eastern most limit of the surface rupture.

Modeling of the complex fault rupture of the February 9, 1971 San Fernando earthquake with the SCEC-BBP simulation/models was based on available data including mapped surface traces, the evidence for the dipping monoclinial model for the San Fernando fault, inferred energy radiation distributions on the various rupture surfaces based on inversions of strong motion recordings, locations of aftershocks, estimates of overall magnitude(s) or energy release, and NGA-West 2 documentation for the 1971 San Fernando earthquake.

Rupture is modeled as initiating at the hypocenter (the red “push pin near the base of the Sierra Madre fault rupture plane in Figure 4-47), and it propagates upwards and initiates a second rupture sequence (approximately 3.5 seconds later) on the eastern-most of the two shallower San Fernando fault planes, which then cross-connects and then initiates rupture on the second (western) San Fernando fault plane

Characterization and parameterization of the input and modeling characteristics for the SCEC-BBP simulations is as follows.

Table 4-15 (from Section 4.6.2.1) is repeated below as Table 4-20, showing Heaton’s (1982) source parameters for his two-fault mechanism for the 1971 San Fernando earthquake. Modeling with the SCEC-BBP in these current studies is similar, but a two-segment model (two rupture planes) will be used for the San Fernando fault rupture surface. Heaton’s model was more general, and aimed to match/explain observations and recordings at multiple ordinates and distances. The current SCEC-BBP simulations are primarily focused on predictions of very near-field motions at the sites of the USFD, LSFD and Pacoima Dam, though a check will be made against regional recordings.

Based on interpretation of currently available data and understandings, the source parameter modeling for the SCEC-BBP simulations is shown in Table 4-21.

The modeled magnitudes of the deeper San Madre fault rupture, and of the shallower San Fernando fault ruptures (west and east planes) are $M_w = 6.4, 6.3$, and 6.1 , respectively, giving a total M_w of 6.61 (total scalar seismic moment of $1.03e+26$ dyne-cm). The combined M_w of 6.61 is the representative M_w in NGA-West2 database for the 1971 San Fernando Earthquake; and is based on 15 publications and expert synthesis. The total rupture area of the model is consistent with the scaling laws of Leonard (2010), as shown in Figure 4-48.

A total of 8,000 random slip distributions for each of the faults were generated with the SCEC-BBP to permit cross-correlating of the generated slip with a slip stencil representing the inversion-based slip model presented in the Heaton (1982) paper. Randomized rupture realizations (slip distributions) judged to conform generally with Heaton's inferred slip models of (1) the San Madre fault rupture surface, and (2) the east rupture area of the San Fernando fault, were retained for further processing. For the west plane of the San Fernando fault there is no published slip model, so random models were generated and visually selected such that they had coherent rupture patches as well as surface slip that is consistent with observation and mapping.

Table 4-20: Source parameters for Heaton's (1982) two-fault mechanism for the 1971 San Fernando Earthquake

Parameter	Sierra Madre Fault (Deeper Fault)	San Fernando Fault (Shallower Fault)
Strike	290 ⁰	285 ⁰
Dip	54 ⁰	45 ⁰
Rake	76 ⁰	90 ⁰
Moment (x 10 ²⁶ dyne-cm)	0.7	1.0
Magnitude (M _w)	6.5	6.4
Rupture Velocity (km/sec)	2.8	2.8
Hypocentral Depth (km)	13.0	8.0
Time Lag (sec)	-	4.0

Table 4-21: Source parameters for SCEC-BBP simulations of the 1971 San Fernando earthquake for these current studies, with a two-fault mechanism and two modeled fault rupture zones (east and west) for the San Fernando fault.

Parameter	Sierra Madre Fault (Deeper Fault)	San Fernando Fault (Shallower Fault) (East Section)	San Fernando Fault (Shallower Fault) (West Section)
Strike	290 ⁰	285 ⁰	253 ⁰
Dip	54 ⁰	45 ⁰	45 ⁰
Rake	76 ⁰	90 ⁰	90 ⁰
Moment (x 10 ²⁵ dyne-cm)	5.01	3.55	1.78
Magnitude (M _w)	6.4	6.3	6.1
Rupture Velocity (km/sec)	2.8	2.8	2.8
Hypocentral Depth (along plane) (km)	14.0	12.0	12.0
Time Lag (sec)	-	3.5	3.5

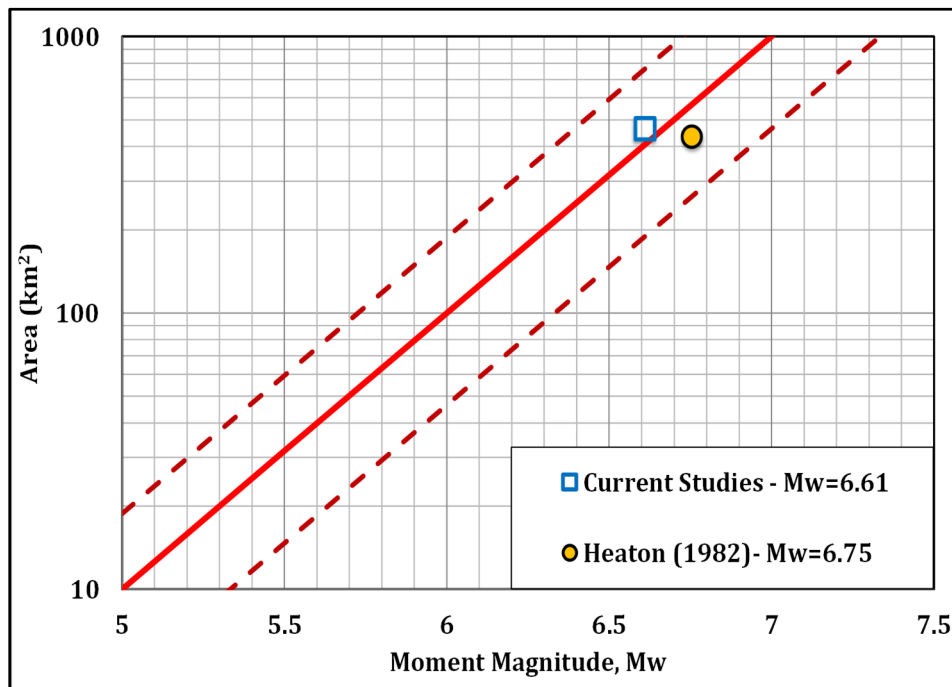


Figure 4-48: Comparison of the total area of the three-segment fault model and the Leonard (2010) scaling law (red line). The dashed lines show the range of uncertainty of the Leonard relationship intercept parameter. The top, middle and bottom lines are for stress drops of ~ 10 , ~ 30 , and ~ 100 bars, respectively.

Kinematically, each BBP earthquake scenario begins at the hypocenter at a depth of ~ 14 km and ruptures up-dip, spreading to the two shallow rupture planes. The segments are run separately and the resulting time series are summed to produce composite source ground motion time histories after applying delay times consistent with the arrival of the rupture front or radiated S-waves to the motions from the two shallow planes. The GP2015 simulation method also accounts for frequency-dependent, nonlinear site effects through the use of the V_{S30} parameter. The Green's functions for the low-frequency deterministic part of the simulation were computed with the Los Angeles Basin model from the BBP software distribution.

Figure 4-49 shows comparisons of simulated and observed PGA and PGV for five selected scenarios that were considered reasonable for this study. Four of these are randomized realizations of the two-fault model with two sub-planes (west and east) for the San Fernando fault rupture surface, and the fifth (SCEC212) is an alternate model with the western section of the San Fernando fault rupture surface deleted, however, the eastern fault was widened to capture the total length. In addition to regional strong motion stations that recorded the actual 1971 San Fernando earthquake on modern seismographs, an additional "station" (and comparison point) was added at the LSFD, where the seismoscope record at

the abutment was interpreted by Scott (1973). Prof. Scott's interpreted motions (and PGA's) are in the crest parallel and crest perpendicular directions, and it is not possible to reliably rotate these, so the "Recorded" PGA of 0.72g at this "station" is taken as the geometric mean of the two directions (crest parallel and crest perpendicular) As shown in Figure 4-49, this is in reasonably good agreement with the SCEC-simulation scenario results.

For the five scenarios, the agreement with PGA is very good over the entire distance range, though the closest station, Pacoima Dam, is under predicted. This is likely due to the local topographic amplification effects that were not included in the ground motion simulations. The comparison with PGV is also good over the full distance range (Figure 4-50).

The results of the SCEC simulations correlate well with the NGA_West2 GMPE results, and support the scaling factors used to develop USFD and USFD input motions for the seismic deformation analyses for the current studies.

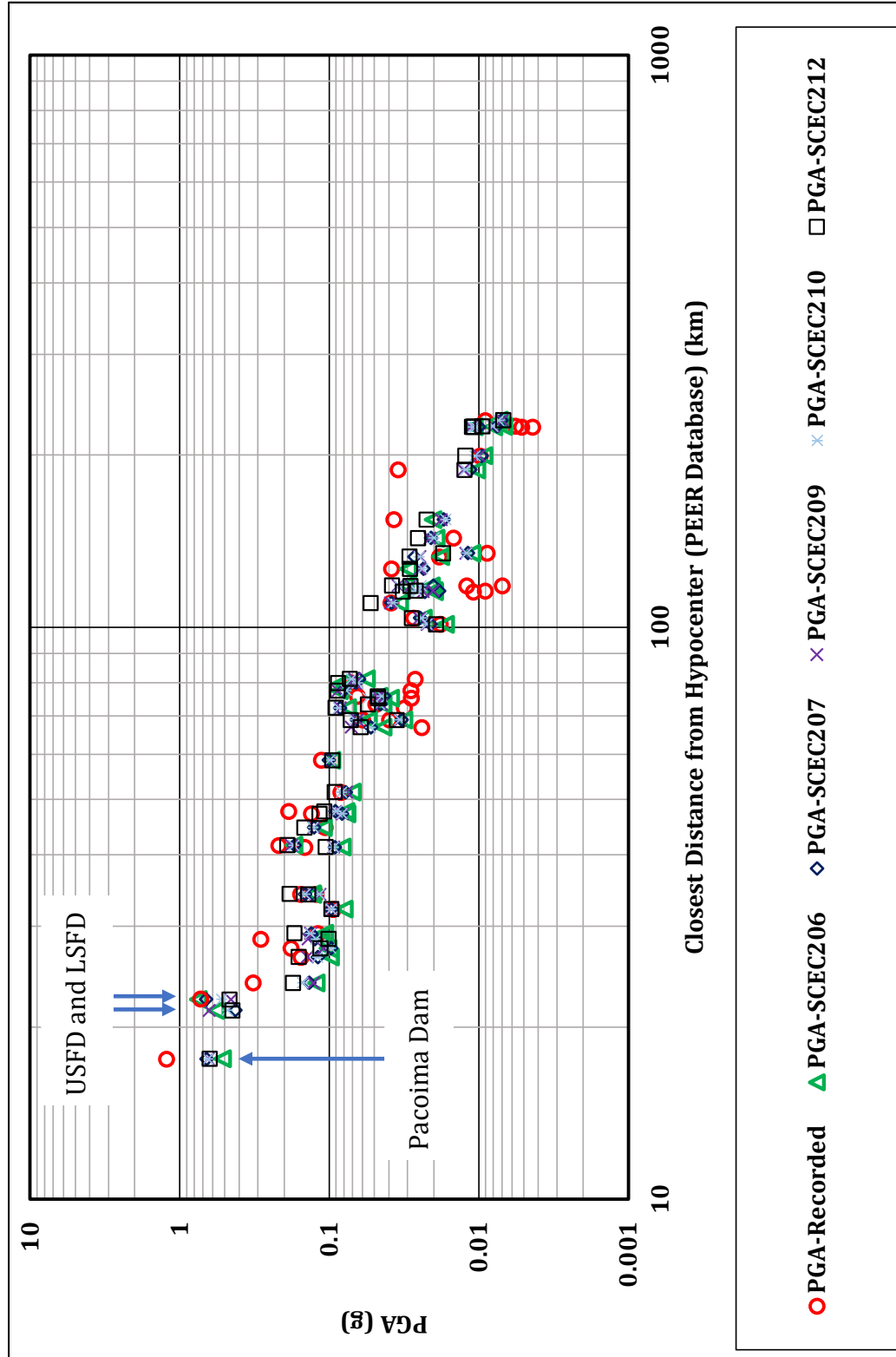


Figure 4-49: Comparison of observed (red circles) vs. simulated peak ground acceleration with distance. The ground motion values are the geometric mean of the two horizontal components. The distance is with respect to the hypocenter location on the deeper Sierra Madre fault.

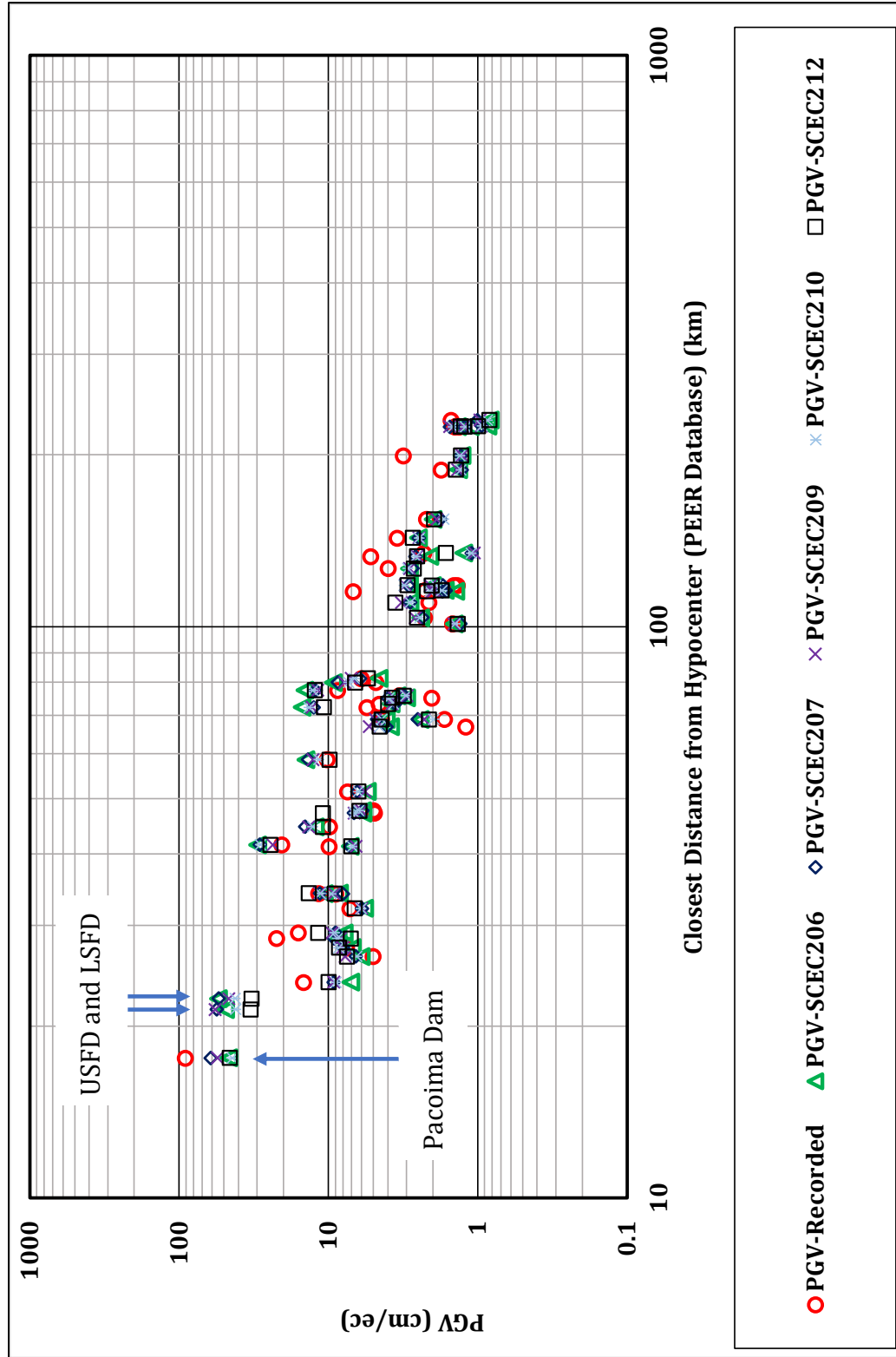


Figure 4-50: Comparison of observed (red circles) vs. simulated peak ground velocity with distance. The ground motion values are the geometric mean of the two horizontal components. The distance is with respect to the hypocenter location on the deeper Sierra Madre fault.

4.7 NONLINEAR SEISMIC DEFORMATION ANALYSES OF THE LOWER SAN FERNANDO DAM

The seismic deformation analyses in these current studies were performed in accordance with the perceived current state of practice with regard to tools, programs, models, and engineering approaches and protocols used in recent projects by different agencies and top-level engineering firms. Perlea and Beaty (2010) was utilized as a base resource to develop many of the seismic deformation protocols for these studies; with adjustments as needed based on lessons learned during the research. Some of the analyses also employed variations in some of the protocols and analysis details. These are explained as they arise. The intricacies of the parameterization and use of various models and analysis protocols were also discussed with some of the different constitutive model developers, and also with well-experienced practitioners.

The three main phases of nonlinear seismic deformation analyses in FLAC are:

- (1) Model construction and static analysis,
- (2) Seismic deformation analyses with input seismic ground motions, and
- (3) Post-shaking analyses; with post-liquefaction strength, S_r in liquefied elements, and often (if appropriate) also reduced shear strengths to model strain softening in non-liquefiable (cohesive) soils.

4.7.1 Model Construction and Static Analyses

Element Size: The element sizes in FLAC models should be developed such that they ensure accurate wave transmission through different layers with different material properties. Kuhlemeyer and Lysmer (1973) presented results of a study concerning the accuracy of displacements caused by a single, harmonic, one-dimensional elastic wave propagating through a finite element mesh. They used a finite rod represented by a system of finite elements that permitted a rigorous analysis of the finite element method for approximating the elastic continuum in steady-state wave propagation problems. Their study found that the calculated displacement field for the homogeneous rod varied between 1% and 4% for element lengths varying between one-sixth and one-twelfth, respectively, of the wavelength of the elastic wave propagating downward to infinity. Kuhlemeyer and Lysmer (1973) recommended a maximum element length equal to one-eighth of the wavelength of the slowest body wave propagating in the elastic materials for analysis of two- or three-dimensional layered media. Based on the Kuhlemeyer and Lysmer (1973) study, the spatial element size, Δl , should ideally be smaller than approximately one-eighth of the wave-length associated with the highest significant frequency component of input wave:

$$\Delta l < \lambda/8 \quad \text{[Equation 4-15]}$$

where l is the wavelength associated with the highest frequency component that contains appreciable energy.

With modern, higher-order elements, these wavelength size targets can be slightly relaxed, but given the nature of this research effort these more rigorous targets were employed for the vertical sizes of elements in the LSFD analyses, and lateral element dimensions were permitted to be slightly larger.

In deformation analyses of dams, the element size is usually developed considering both the initial shear wave velocity and the softened condition with increased strain and pore pressure. Table 4-23 presents a summary of conditions that were used to develop element sizes for nonlinear seismic deformation analyses of the LSFD using FLAC.

Table 4-23: Calculation of element size to transmit shear waves in LSFD Analyses

Soil Layer	Condition (Initial or Deformed)	Shear Wave Velocity (ft/sec)	Frequency (Hz)	Maximum Element Size (feet) ($\Delta l < \lambda/8$)
Hydraulic Fill - LSFD	Initial	750	25	3.8
	Deformed Condition (assuming ~ 15% of G_{max})	290	10	3.6
Lower Alluvium - LSFD	Initial	1500-1800 (avg. 1650)	25	8.3
	Deformed Condition (assuming ~ 15% of G_{max}) (Note: This is a conservative estimate, as Lower Alluvium was considered non- liquefiable and was unlikely to experience large deformation)	639	10	8.0

Considering the criteria, as presented in Table 4-23, a vertical element size of 3 feet for embankment layers and a vertical element size of 3.3 feet for lower Alluvium were selected for the LSFD model. Lateral element sizes of up to 5 feet were allowed.

In the USFD model (see Chapter 5), the elements sizes are slightly larger than ideal. The maximum vertical element size for the USFD model is 5 feet, and the maximum lateral element size is 5 feet. A sensitivity analysis of the USFD, performed with smaller elements, indicated that the use of smaller elements in the USFD model increased the FLAC run times several-fold, but that the change in deformation values was found to be negligible. Considering that the number of deformation analyses to be performed for the USFD is more than ten cases, including the sensitivity analyses and an alternate case with a modified input

motion; a maximum vertical element size of 5 feet was adopted for the USFD analyses. In general, however, for forward analyses the element size selection protocol for the LSFD should be considered more appropriate. If larger element sizes are to be employed, they should be justified based on sensitivity analyses (as were performed for the USFD analyses).

Boundary Conditions: During the static analysis, both the horizontal and vertical directions are fixed against movement at the base of the model. The upstream and downstream vertical boundaries allow vertical movement, but are laterally “fixed” to prevent horizontal movements. A free pore pressure condition is assigned to the bottom of the model, which allows change in pore pressure, but restricts flow across the boundary. A hydrostatic stress state is applied to the left and right vertical boundaries. The pore pressures on the upstream boundary are defined by the reservoir head. The pore pressures on the downstream edge of the mesh are defined by the phreatic surface below the ground surface at the downstream edge of the model, which must be located at a significant distance from the downstream toe of the dam. Steady state seepage analyses are then performed (as described and presented previously in Section 4.5.5) to develop the initial (pre-earthquake) phreatic surface through the dam, and through the foundation if necessary. These analyses should, ideally, be calibrated based on available data (e.g. piezometers, etc.) within the embankment.

Model Construction Sequence: The principal purpose of the pre-earthquake static analyses is to obtain the initial distribution of effective stresses and pore pressures within the dam and foundation soils at the beginning of the dynamic analysis (establishing the pre-earthquake initial conditions). The steps in these static analyses include (1) mesh and soil zonation generation, (2) materials properties assignment with initial (simplified) Mohr-Coulomb and seepage (permeability) parameters, (3) sequential “construction” of the dam (as closely as possible modeling the actual dam construction sequence) to develop initial effective stresses within soil elements without developing an instability, and (4) addition of increasing reservoir pool elevations in sequence and performance of iterative steady-state seepage analyses, varying seepage parameters as necessary and reasonable to achieve a good match with observed data, in order to obtain the final pre-earthquake phreatic surface and the initial effective stress conditions within each soil element.

The stiffness parameters for the current studies were developed based on empirical relationships that are based on initial effective stress and relative density (expressed in terms of $N_{1,60,CS}$). Either SPT blow counts, and/or shear wave velocity measurements, can be used as a basis for evaluation of initial stiffness parameters of soils. For these dams, most initial stiffness parameters were based primarily on the large amounts of SPT data available. Equations 4-7 through 4-10, along with Table 4-13, presented the relationships and values used to evaluate and model initial dynamic stiffnesses. The bulk and shear moduli modeled were determined using the following relationships

$$\text{Shear Modulus,} \quad G_{max} = K_{ge} * P_a \left(\frac{\sigma'_m}{P_a} \right)^{0.5} \quad [\text{Equation 4-16}]$$

$$\text{Modulus of Elasticity,} \quad E = 2G (1 + \nu) \quad [\text{Equation 4-17}]$$

$$\text{Bulk Modulus,} \quad K = E/3(1 - 2\nu) \quad [\text{Equation 4-18}]$$

For Mohr-Coulomb elements (employed to model non-liquefiable geotechnical materials, such as clayey central core soils, denser lower alluvium, upper rolled fills, and non-saturated zones such as portions of the downstream hydraulic fills, and the two downstream berms), a factor of 0.7 was applied to convert G_{\max} to a secant shear modulus value, appropriate for seismic deformation analyses.

A Poisson's ratio of $\nu = 0.35$ was used for soil layers, and $\nu = 0.25$ was used for rock.

FLAC computes the total density of an element from the dry density of the soil, the density of water, porosity, and current degree of saturation. As FLAC computes/defaults to a saturation of zero above the phreatic surface, a subroutine was used to achieve moist unit weights, as necessary, above the phreatic surface in order to achieve the appropriate initial effective stresses.

4.7.2 Dynamic or Earthquake Shaking Analyses

The dynamic (or earthquake shaking) analyses are performed in the time domain. The primary information and data that are carried forward from the static analyses are (1) geometric descriptions of stratigraphy and mesh design, (2,3) the phreatic surface and initial pore pressures in each element, (4,5) initial effective stresses and shear stresses, and (6) material properties that are still applicable to the dynamic analyses.

A number of important features of dynamic analyses are described below:

Constitutive Models and Material Properties: The constitutive models for all liquefiable and non-liquefiable layers “during shaking” are defined in this stage. The material properties for liquefiable layers are constitutive model dependent, and sometimes also specific to each different analytical scheme. For example, if the Wang2D constitutive model is utilized in an analysis with the Cetin et al. (2018) liquefaction triggering relationship and the Weber et al. (2015) post-liquefaction strength relationship, then the applicable Wang2D input parameters are developed based on model calibration to match the triggering relationship, and by direct application (when appropriate) of the post-liquefaction residual strengths to liquefied elements, based on user-specified criteria. Section 4.8 of this Chapter presents the input parameters for different numerical modeling schemes with different combinations of liquefaction triggering and post-liquefaction strength relationships. The FLAC Mohr-Coulomb model was used for the non-liquefiable layers (e.g. central puddled clay core, denser lower alluvium, upper rolled fills, non-saturated soils, etc.) in the LSFD and USFD analyses. Each of the constitutive models provides a framework for modeling stress state-dependent and strain-dependent, and in some cases stress history-dependent, changes in both (1) shear modulus and (2) hysteretic damping, as described in Chapter 2, Section 2.2.

Viscous Damping: Damping is an important characteristic in seismic analyses performed using FLAC. Some amount of viscous damping is needed to remove/reduce energy carried as high frequency “noise” (or “ringing”) generated in the numerical analyses. The use of too much viscous damping, however, can overdamp the mesh and can reduce overall seismic response; producing potentially unconservative calculations of (1) cyclic pore pressure generation and (2) seismically-induced deformations. Viscous damping is applied in FLAC as Rayleigh damping.

Figure 4-50 shows the mass-proportional, stiffness-proportional, and combined damping behaviors with increasing angular frequencies. A damping matrix, C is the sum of mass (M)-proportional and stiffness (K)-proportional matrices ($C=\alpha M + \beta K$), where α =the mass-proportional damping constant and β =the stiffness-proportional damping constant. In FLAC, the mass-proportional term is analogous to a dashpot connecting each FLAC gridpoint to “ground”. The stiffness-proportional term is analogous to a dashpot across each FLAC zone (responding to the strain rate) (Itasca, 2011). Mass-proportional damping does not impact timestep, may reduce large displacements, and does not significantly damp high frequencies. Stiffness-proportional damping is good at damping high frequencies, does not impact low frequencies as much, and can significantly reduce timestep (Beaty, 2017).

Even though damping is frequency dependent, as shown on Figure 4-50, an approximately frequency-independent response can be obtained over a limited frequency range. In Figure 4-50, it appears that the damping ratio is almost constant over at least a 3:1 frequency range, from $\omega=5$ to 15 radians per second, considering, $\omega_{min}=10$ radians per second (Itasca, 2011). As shown on Figure 4-51, a spectral analysis of typical velocity records might produce a response such as the one shown on Figure 4-51. The flat region in Figure 4-51 covers approximately one-third of the spectrum centered at the predominant frequency. Based on Figures 4-50 and 4-51, the FLAC manual (Itasca, 2011) suggests that Rayleigh damping is considered to be frequency independent over a span of roughly 3:1 (or one-third) of the frequency range of the velocity record.

In FLAC models for dams, the predominant period of the dam is used as the center frequency for Rayleigh damping. In the LSFD and USFD seismic deformation models, the predominant period for each analysis was developed considering both embankment and foundation V_s , potential dynamic modulus degradation during earthquake analysis, and geometry. The amount of damping was selected considering material type, recommendations in the applicable constitutive model documentations, and precedent in previous projects. Table 4-24 presents constitutive models, materials, damping ratio (percent of critical) at the center frequency, and the center frequency for the LSFD and USFD models.

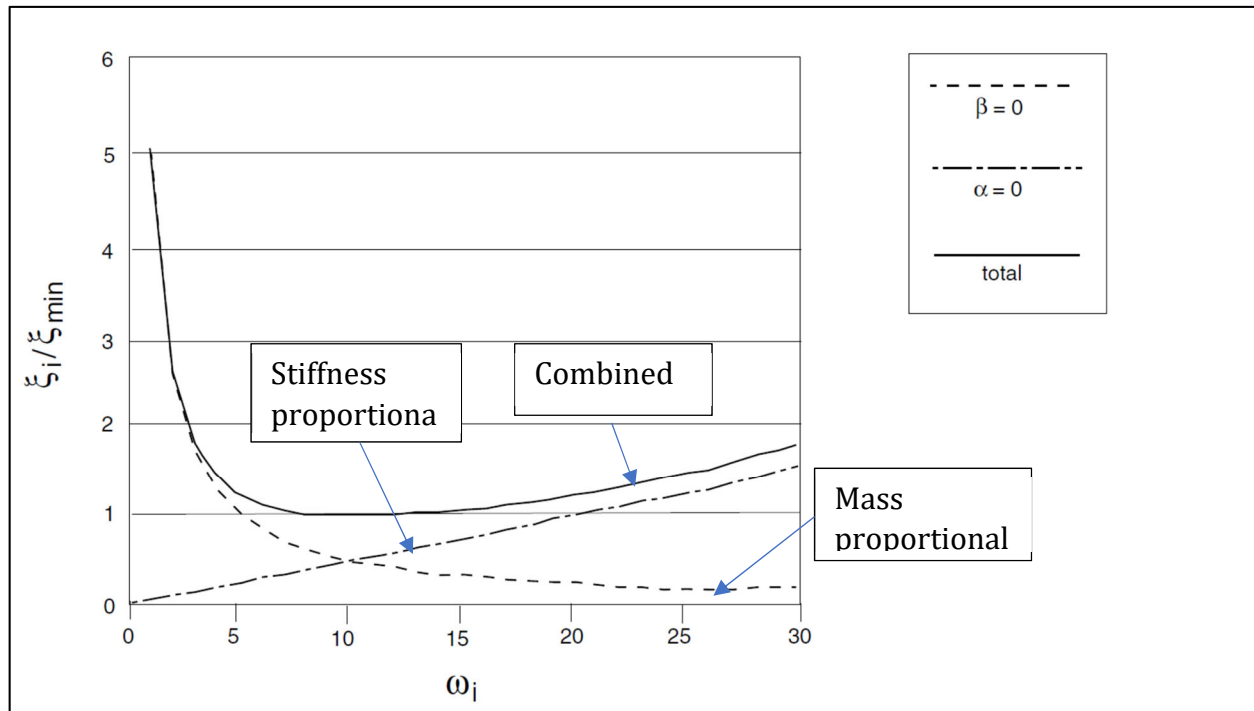


Figure 4-50: Variation of normalized critical damping ratio with angular frequency (Itasca, 2011)

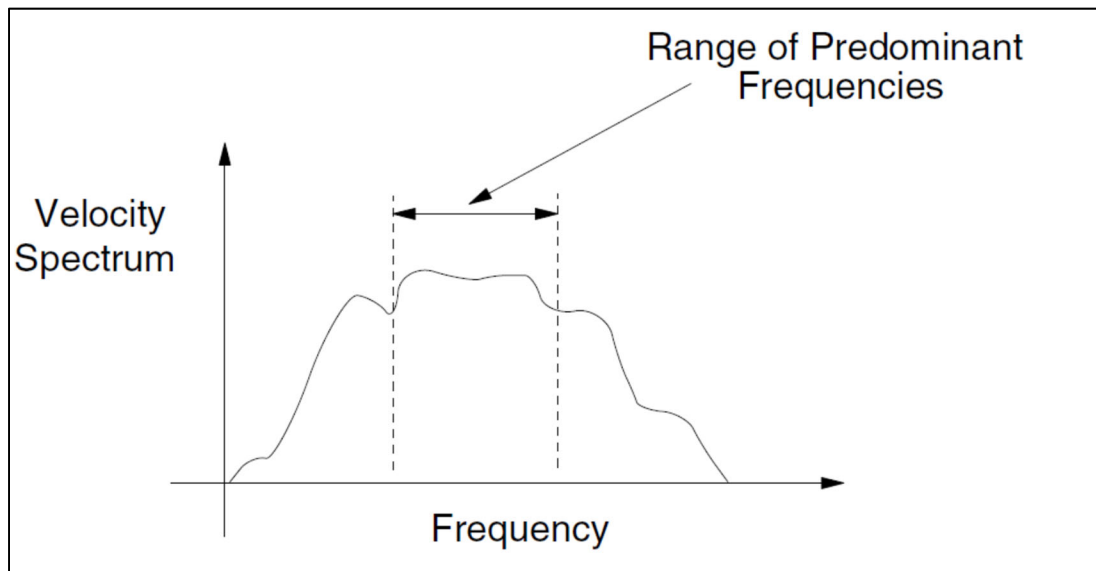


Figure 4-51: Plot of velocity spectrum versus frequency (Itasca, 2011)

Table 4-24: Rayleigh viscous damping parameters for the LSFD and USFD

Constitutive Model	Material Zones	Damping Ratio (b) as percent of critical damping)	Center Frequency (Hz)
Rock	Rock	0.5 percent	2.35 for LSFD and 3.1 for USFD
Mohr-Coulomb Model	Non-Liquefiable layers in the embankment and foundation	3 percent	
Constitutive Models (Roth, UBCSAND, PM4Sand, Wang2D)	Potentially liquefiable layers	0.5 to 1 percent	

Boundary Conditions: Boundary conditions at the bottom of the model, and at the upstream and downstream foundation edges, are assigned in the dynamic stage.

Boundary Conditions at the Vertical Edges: Free-field mechanical boundary conditions were used for the vertical upstream and downstream edges. However, considering that the free-field boundary can be distorted during dynamic analyses, elastic elements were used in the boundary zones with appropriate stiffness (3 columns of elements on each side). This adjustment may increase the spurious reflections off the boundary; however, the resulting behavior is still considered a better option. In addition, the free-field boundaries in the LSFD and USFD models are located at significant distances from the dam, to minimize the potential influence of spurious reflections on seismic response of the dam embankment and its underlying foundation materials.

Boundary Conditions at the Base of the Model: A compliant base boundary condition was assigned to the bottom of the model. This was achieved by applying a quiet boundary condition in both the x- and y-directions and then applying the ground motions as equivalent shear waves (horizontal motion) or compression waves (vertical motion). These boundaries approximate a half-space existing below the model with the same elastic stiffness and mass properties as the lowest element row of the 2-D model. In the LSFD model, a 50-foot thick rock layer and in the USFD model, a 50-foot thick rock layer was modeled as the deepest foundation layer, and the quiet boundary conditions were applied below this rock layer.

The use of compliant boundary conditions is discussed in Mejia and Dawson (2006). FLAC uses a viscous boundary scheme consisting of two sets of dashpots attached independently to the mesh in the normal and shear directions. In the shear direction, the dashpots provide a viscous shear traction given by:

$$\sigma_s = \rho V_s v_s \quad \text{[Equation 4-19]}$$

where ρ and V_s are the density and shear wave velocity of the base material, and v_s is the shear-component of particle velocity at the boundary. The viscous dashpots of the quiet boundary absorb downward propagating waves so that they are not reflected back into the model.

For the vertical component of the seismic motion, the vertical upward propagating compressive stress can be computed by:

$$\sigma_p = \rho V_p v_p \quad [\text{Equation 4-20}]$$

where ρ and V_p are the density and compressional wave velocity of the base material, and v_p is the compressive-component of particle velocity at the boundary.

In the LSFD and USFD analyses for the current studies, the input motions were applied as rock outcrop motions using Equations 4-19 and 4-20.

4.7.3 Transitioning to S_r and Post-Shaking Analyses

The constitutive models based on critical state soil mechanics such as UBCSAND, PM4SAND, and Wang2D do not transition to post-liquefaction strengths during the earthquake shaking phase of the analysis. Therefore, the deformations estimated from earthquake analysis during shaking by these constitutive models, if erroneously considered to be the final deformations, can significantly underestimate the actual final deformations. In some cases, progressive failure can develop after the “end of shaking”, and it is therefore important to continue the analysis after the end of applied earthquake shaking. The simpler, incremental Roth model progressively transitions to post-liquefaction strengths (S_r), during shaking; but is also potentially unconservative to end the Roth model analyses at the end of shaking in certain conditions. This will also be discussed below.

In these current studies, the nonlinear seismic deformation analyses performed using any of the three “cyclic/constitutive” models (UBCSAND, PM4Sand, and Wang2D) are temporarily halted “at the end of shaking”, and both (1) strains and (2) seismically generated pore pressures are evaluated. Based on these evaluations (for each individual element of potentially liquefiable soil), properties within the element (and sometimes also the material model employed) may be changed prior to re-commencing the “post-shaking” part of the nonlinear deformation analysis. For potentially liquefiable soils, each analytical model and analysis scheme employed in these current studies has a protocol (and criteria) for transitioning the behavior in a given potentially liquefiable element to post-liquefaction residual strength (S_r) behavior.

In the analyses performed with the Roth model, potentially liquefiable soil elements that satisfy criteria specific to the Roth model are transitioned (individually) to S_r during the actual analysis time-step (if and when) they meet the Roth model criteria for that.

For some non-liquefiable elements (e.g. cohesive, clayey soils) shear strains are also evaluated at the end of shaking, and so are shear offsets across relatively narrow shear zones; and shear strengths in these cohesive soils may also be modified at the end of shaking to model reduced shear strengths to account for strength reduction (strain-softening) due to the development of large shear strains. This topic will be further discussed in this dissertation. It is important to note that strain-softening of cohesive, clayey soils, and also potential cyclic softening of cohesive, clayey soils, is often overlooked in seismic analyses involving potential liquefaction; where the primary focus is often instead on the potentially liquefiable soils. This can be a potentially dangerously unconservative oversight, as evidenced in the nonlinear seismic deformation analyses of the LSFD that follow.

Most commonly used constitutive models for cyclic behavior of potentially liquefiable soils have been calibrated to match behaviors of laboratory-based monotonic and cyclic tests; but these do not directly address the material and behavioral changes associated with potential void redistribution effects associated with development of “soil liquefaction”. In addition, conventional definitions of “onset of soil liquefaction”, initially developed based on either laboratory cyclic triaxial, or cyclic simple shear, or cyclic torsional shear tests without initial “driving shear stresses” ($K_\alpha = 0$ conditions) are not appropriate, nor directly applicable, to the $K_\alpha > 0$ conditions that dominate seismic deformation analyses for dams.

For $K_\alpha = 0$ conditions, common criteria for “onset of liquefaction” include double amplitude cyclic triaxial strains of $\pm 5\%$, or double amplitude cyclic simple shear strains of $\pm 3\%$ or $\pm 5\%$, or achievement of a cyclic pore pressure ratio of $R_{u,seis} \approx 1.0$. These types of criteria are, however, neither applicable nor useful for field conditions with $K_\alpha > 0$.

For $K_\alpha > 0$ conditions (1) soil elements can “fail” in shear at $R_{u,seis}$ of less than 1.0 because the “downslope” static driving shear stress of greater than zero does not require strength to be reduced fully to zero in order to develop uncontrolled downslope shear strains, and (2) soil elements deform preferentially towards the downslope direction during cyclic loading so that achievement of a roughly symmetric criteria of $\pm X\%$ shear strain is inappropriate; instead criteria based on development of some level of maximum downslope-biased shear strain is necessary.

Transitions to S_r , and criteria for transitioning to S_r , in each of the four analytical models employed in these current analyses is handled as follow:

(1) Roth Model:

As discussed in Section 2.2.1, the Roth model is the only one of the four models used in these current studies that can currently readily be programmed to transition to post-liquefaction residual strength (S_r) “during shaking”. In the Roth Model analyses performed herein, the transition to post-liquefaction strength (S_r) in each individual element occurs when the shear strength (S) of the element is reduced to a value of $S \leq S_r$. As a result, individual elements incrementally transition to S_r as the “during shaking” analysis proceeds. This differs from approach taken to the transition to S_r in analyses performed with the other

three analytical models. There are no strain criteria for transition to S_r in the Roth model analyses “during shaking”; only the achievement of a shear strength (reduced by cyclic pore pressure generation, or $R_{u,seis}$) to a value of $\text{Strength} \leq S_r$. At the end of shaking, the analysis is temporarily halted, and shear strains in non-liquefiable soils (e.g. clayey soils) are evaluated, and decisions are made as to whether or not to reduce shear strengths in these cohesive soils to model strain softening effects. The Roth model protocol is then to continue the nonlinear deformation analysis after the end of shaking until either (1) deformations and displacements have ceased to occur, as the embankment is in a stable condition, or (2) mesh distortions are resulting in a need to perform significant (and time-consuming) re-meshing to continue the NDA deformation analysis, and the analysis results at termination have become sufficient for purposes of engineering interpretation and decision-making, with recognition that deformations and displacements are still ongoing.

(2) UBCSAND Model:

The protocol for the UBCSAND analyses performed as part of these current studies is to handle the potential transition to post-liquefaction residual strength (S_r) in elements comprised of potentially liquefiable soils within the UBCSAND framework by considering the analysis to progress in two steps or stages (1) during shaking, and (2) after the end of shaking. During shaking, there is no implementation of S_r . After the end of shaking, the analysis is temporarily halted, and S_r is applied within potentially liquefiable soil elements that satisfy either of two criteria: (1) occurrence of $R_{u,seis} \geq 0.7$ at any stage during shaking ($R_{u,seis,max} \geq 0.7$) or (2) development of a peak shear strain of $\gamma \geq 10\%$ at the end of shaking in saturated materials. Shear strains developed in cohesive soils are also evaluated, and this can lead to strength reductions in cohesive soils to account for strain softening effects, as discussed above. The UBCSAND protocol in these current studies is then to continue the nonlinear deformation analysis after the end of shaking until either (1) deformations and displacements have ceased to occur, as the embankment is in a stable condition, or (2) mesh distortions are resulting in a need to perform significant (and time-consuming) re-meshing to continue the NDA deformation analysis, and the analysis results at termination have become sufficient for purposes of engineering interpretation and decision-making, with recognition that deformations and displacements are still ongoing.

(3) PM4Sand Model:

The protocol for the PM4Sand analyses performed as part of these current studies is the same as for the UBCSAND analyses.

(4) Wang2D Model:

The protocol for the Wang2D analyses performed as part of these current studies is slightly different than for the UBCSAND and PM4SAND analyses. The potential transition to post-liquefaction residual strength (S_r) in elements comprised of potentially liquefiable soils is handled within the Wang2D analysis framework by considering the analysis to progress in two steps or stages (1) during shaking, and (2) after the end of shaking. During shaking, there is an option to utilize S_r above a user-specified $R_{u,seis}$ level. Wang and Ma (2016) in

introduced a $R_{u,seis}$ parameter in the updated Wang2D version (also available in Itasca UDM site). This allows an user to define a $R_{u,seis}$ parameter for S_r application during shaking analysis. This unique feature softens the effects of dilation in elements that liquefy during shaking by transitioning to a post-liquefaction residual strength (S_r) for elements that experience a pore pressure ratio above a user specific $R_{u,seis}$ value. This softening occurs in elements that would otherwise utilize a higher strength than S_r , even when $R_{u,seis}$ is high enough to induce liquefaction. For example, in these current studies, an $R_{u,seis}$ value of 0.85 was used for S_r application during shaking. As a result, the elements utilized S_r after they achieved $R_{u,seis}$ greater than 0.85, but only until dilation reduced $R_{u,seis}$ back below 0.85.

After the end of shaking, the analysis is temporarily halted, and S_r is applied within potentially liquefiable soil elements that satisfy either of two criteria: (1) occurrence of $R_{u,seis} \geq 0.7$ at any stage during shaking ($R_{u,seis,max} \geq 0.7$) or (2) development of a peak shear strain of $\gamma \geq 10\%$ at the end of shaking in saturated materials. Shear strains developed in cohesive soils are also evaluated, and this can lead to strength reductions in cohesive soils to account for strain softening effects, as discussed above. The protocol is then to continue the nonlinear deformation analysis after the end of shaking until either (1) deformations and displacements have ceased to occur, as the embankment is in a stable condition, or (2) mesh distortions are resulting in a need to perform significant (and time-consuming) re-meshing to continue the NDA deformation analysis, and the results at termination have become sufficient for purposes of engineering interpretation and decision-making, with recognition that deformations and displacements are still ongoing.

Previous analysts have dealt with the issue of transitioning to post-liquefaction strengths. Due to recognition of the intrinsic limitations in the ability of current constitutive models to transition to post-liquefaction strengths, largely because these models were developed for targeting cyclic pore pressure generation and associated cyclic stress-strain behaviors, and the resulting inability of these “cyclic” models to capture the material and behavioral changes that occur with localized void redistribution (see Section 2.4), there has been some recent evolution in this regard.

Beaty and Byrne (2011) recognized this important limitation of the UBCSAND model (and other constitutive models) that have been calibrated to match with laboratory test behaviors of soils or with empirical liquefaction triggering relationships during cyclic loading up to the point of “liquefaction”, but which are not suited to modeling post-liquefaction S_r behaviors as exhibited in field case histories, nor as predicted by S_r relationships developed based on back-analyses of full-scale field performance failure case histories. They proposed a procedure that could be used to compute deformations that would be more consistent with liquefaction-induced deformation case histories, and thus correct some of the limitations of FLAC modeling for earthquake analysis of liquefiable soils. Beaty and Byrne (2011) state that “*while UBCSAND will predict a significantly softened stress-strain behavior after liquefaction, the resulting mobilized strength may not be consistent with common interpretations of residual strength.*”

The procedure for post-earthquake analysis that was adopted in Beaty and Byrne (2011) was developed and applied in USACE seismic dam projects such as the Tuttle Creek

Dam seismic retrofit, and the Success Dam seismic evaluations projects. Vlad Perlea, Francke Walberg, and David Serafini of USACE, and Ethan Dawson of URS, were participants in those discussions regarding development of post-shaking analyses procedures; including transition of elements to post-liquefactions (S_r) strengths.

Beaty and Byrne (2011) suggested that a criterion based on the maximum pore pressure ratio, $R_{u,seis}$ in any element can be utilized as a criterion for S_r application in the post-shaking analysis stage. The USACE adopted a value of $R_{u,seismic} \geq 0.7$ as a criterion in all major seismic dam evaluation projects such as Tuttle Creek Dam, Lake Isabella Dam, and Success Dam.

$R_{u,seis}$ (referring to cyclic, or seismically generated pore pressure ratio) differs from the more commonly calculated value of r_u (pore pressure ratio). Pore pressure ratio (r_u) is simply the ratio of current pore pressure in an element of soil divided by the total vertical stress in that element, as

$$r_u = u / \sigma_v \quad \text{[Equation 4-21]}$$

where u = pore pressure,

and σ_v = total vertical stress

$R_{u,seis}$, on the other hand, is the seismically generated (or cyclically generated) increase in pore pressure in an element of soil, divided by the cyclic increase in pore pressure that would be required to reduce the effective stress in that element fully to zero. This is expressed as

$$R_{u,seis} = 1 - (\sigma'_v / \sigma'_{v,i}) = \Delta u_{cyclic} / \sigma'_{v,i} \quad \text{[Equation 4-22]}$$

where u = pore pressure,

σ'_v = effective vertical stress, and

$\sigma'_{v,i}$ = initial (pre-earthquake) effective vertical stress, and

Δu_{cyclic} = cyclically induced change in pore pressure

As discussed in Section 2.2, soils with initial static driving shear stresses (e.g. downslope driving shear stresses in dams) representing conditions of $K_\alpha > \text{zero}$ do not generally develop $r_u = 1.0$ and they also may not fully develop $R_{u,seis} = 1.0$ for two sets of reasons: (1) with initial static driving shear stresses, the soil elements can fail in shear before either of these measures of pore pressure ratio rises fully up to 1.0, and (2) cyclic dilation of granular, particulate soils cyclically loaded under $K_\alpha > \text{zero}$ conditions produces K_α -biased (downslope) shear deformations that can result in downslope shear-induced dilation that can limit the maximum pore pressure ratios that can be developed.

The use of a value of $R_{u,seis} = 0.7$ as a criteria for transition to post-liquefaction residual strength represents some degree of “averaging”, as the actual appropriate value would vary somewhat as a function of (1) the level of K_α , and (2) the relative density (or penetration resistance, as a proxy for relative density) of the soil, and (3) the initial effective vertical stress ($\sigma'_{v,i}$).

It is the consensus of the analysis team for these current studies that the criteria of $R_{u,seis} \geq 0.7$ as a basis for transition to S_r is potentially incomplete; for conditions (and soil elements) with very high values of K_α , dilation will suppress $R_{u,seis}$ and a strain-based criteria would be appropriate. Accordingly, the transition to post-liquefaction residual strength imposed at the end of shaking in the three cyclic constitutive models employed in these current studies (1) UBCSAND, (2) PM4Sand, and (3) Wang2D is considered to be appropriate if any given (saturated) element of potentially liquefiable soil achieves either of two criteria: (1) a maximum value of $R_{u,seis} \geq 0.7$ at any time during shaking, or (2) development of a peak shear strain of $\gamma \geq 10\%$ at the end of shaking in saturated materials. There are also good precedents for the use of dual criteria, and for the use of $\gamma \geq 10\%$ as part of these dual criteria.

Both of these values ($R_{u,seis} \geq 0.7$, and/or $\gamma \geq 10\%$) represent some degree of engineering judgment, and these are the consensus values selected and employed in these current studies.

In all nonlinear seismic deformation analyses performed as part of these current studies, analyses performed using any of these three models employ a protocol that involves temporarily halting the analysis at the end of shaking, examining each potentially liquefiable element and transition that element to S_r if that element reached either of the above two criteria at any point during shaking, and then continuing the analysis after the end of shaking. That entails constantly tracking both $R_{u,seis}$ and shear strain (γ) in each element, and updating $R_{u,seis,max}$ and γ_{max} as the analyses during shaking proceed; these are easily accomplished with FISH functions.

For the Roth analytical model, the situation is a bit different as it is relatively easy to program FLAC to “transition” potentially liquefiable soil elements to S_r “during shaking” with this model. Accordingly, the criteria discussed previously above are not employed to transition elements to S_r . In the Roth Model analyses performed herein, the transition to post-liquefaction residual strength (S_r) in each individual element occurs in the analysis when the shear strength (S) of the element is reduced to a value of $S \leq S_r$. As a result, individual elements incrementally transition to S_r as the “during shaking” analysis proceeds. This differs from approach taken to the transition to S_r in analyses performed with the other three analytical models. There are no strain criteria for transition to S_r in the Roth model analyses “during shaking”; only the achievement of a shear strength (reduced by cyclic pore pressure generation, or $R_{u,seis}$) to a value of Strength $\leq S_r$.

The Roth model thus potentially transitions some of the potentially liquefiable elements to S_r during shaking, as appropriate, but at the end of shaking the analysis is temporarily halted and shear strains developed in cohesive soils are evaluated, and if appropriate shear strengths in cohesive soil elements may be reduced to account for strain

softening. The analysis is then resumed, and continues until either of the two criteria for terminating the analysis is met.

4.8 RESULTS OF LOWER SAN FERNANDO DAM NONLINEAR SEISMIC DEFORMATION ANALYSES

Table 4-25 repeats Table 4-1, and lists the six analyses performed as the primary back-analyses of the LSFD to evaluate the performance of different analytical schemes including (1) four different analytical or constitutive models, (2) three different liquefaction triggering relationships, (3) several different K_σ and K_α relationships, and (4) two different post-liquefaction strength (S_r) relationships. This table lists the six different combinations of each of these models and relationships employed in LSFD Analyses 1 through 6.

Analysis details, and protocols, often specific to particular models and/or combinations of models or relationships, will be discussed as they arise in each of the nine back-analyses performed.

LSFD Analysis 1 employs the Roth analytical model, with the Cetin et al. (2018) liquefaction triggering relationship, and the Youd et al. (2001) K_σ relationship (which is recommended for use with the Cetin et al. triggering relationship), and it uses the Weber et al. (2015) post-liquefaction residual strength (S_r) relationship.

LSFD Analyses 2 and 3 both employ the UBCSAND model, and both use the Youd et al. (2001) liquefaction triggering and K_σ relationships. Analysis 2 uses the Seed and Harder (1990) post-liquefaction residual strength (S_r) relationship, and Analysis 3 uses the Weber et al. (2015) S_r relationship.

LSFD Analyses 4 and 5 both employ the PM4Sand model. Analysis 4 uses the Boulanger and Idriss (2014) liquefaction triggering and K_σ relationships, and the Idriss and Boulanger (2015) post-liquefaction residual strength (S_r) relationship.

Analysis 5 uses the Cetin et al. (2018) liquefaction triggering relationship, with the Youd et al. (2001) K_σ relationship, and uses the Weber et al. (2015) S_r relationship.

Analysis 6 employs the Wang2D model, with the Cetin et al. (2018) liquefaction triggering relationship, and the Youd et al. (2001) K_σ relationship (which is recommended for use with the Cetin et al. triggering relationship), and it uses the Weber et al. (2015) post-liquefaction residual strength (S_r) relationship.

Table 4-25: Summary of the six analytical modeling schemes employed for the LSFD back-analyses performed in these current studies.

Analysis ID	Description
Analysis 1: Roth Model (C, W)	Constitutive model for liquefiable soils – Roth Liquefaction triggering – Cetin et al. (2018); K_σ – Youd et al. (2001) Post-liquefaction strength, S_r – Weber et al. (2015) [50 th percentile S_r applied during-shaking]
Analysis 2: UBCSAND (Y, S&H)	Constitutive model for liquefiable soils – UBCSAND Liquefaction triggering - Youd et al. (2001); K_σ – Youd et al. (2001) Post-liquefaction strength, S_r – Seed and Harder (1990) [Average S_r]
Analysis 3: UBCSAND (Y, W)	Constitutive model for liquefiable soils – UBCSAND Liquefaction triggering - Youd et al. (2001); K_σ – Youd et al. (2001) Post-liquefaction strength, S_r – Weber et al. (2015) [50 th percentile S_r]
Analysis 4: PM4Sand (B&I, I&B)	Constitutive model for liquefiable soils – PM4Sand Liquefaction triggering and K_σ – Boulanger and Idriss (2014) Post-liquefaction strength, S_r – Idriss and Boulanger (2015) [S_r relationship “with significant void redistribution”]
Analysis 5: PM4Sand (C, W)	Constitutive model for liquefiable soils – PM4Sand Liquefaction triggering – Cetin et al. (2018); K_σ – Youd et al. (2001) Post-liquefaction strength, S_r – Weber et al. (2015) [50 th percentile S_r applied during-shaking]
Analysis 6: Wang2D (C, W)	Constitutive model for liquefiable soils – Wang2D Liquefaction triggering – Cetin et al. (2018); K_σ – Youd et al. (2001) Post-liquefaction strength, S_r – Weber et al. (2015) [50 th percentile S_r applied during shaking for durations with $R_{u,seis}$ greater than a specified value, and also during post-shaking]

4.8.1 LSFD Analysis 1: Roth Model, with the Cetin et al. (2018) Liquefaction Triggering Relationship, Youd et al. (2001) K_σ , and the Weber et al. (2015) S_r Relationship

Analysis 1 utilizes the Roth model, with the Cetin et al. (2018) liquefaction triggering relationship, the Youd et al. (2001) K_σ relationship, the Idriss and Boulanger (2003) K_α relationship, and the Weber et al. (2015) post liquefaction (median) S_r relationship in the Roth modeling scheme for the potentially liquefiable hydraulic fill layers. The analysis-specific input parameters are summarized in Table 4-26.

As discussed in Chapter 2, the engineering protocol for use of the Roth model analysis, and the liquefaction triggering and K_σ relationships combination of Analysis 1, is that a cyclic strength curve is first defined to develop relationships between cyclic stress ratio (τ_{cy}/σ'_v) and number of equivalent cycles. The CSR curve in LSFD Analysis 1 was developed based on CSR_{15} and $B (=1/b)$ values based on Cetin et al. (2018) for each of the hydraulic fill layers. The model then monitors the shear stress time history of each element (monitored as the shear stress on a horizontal plane, τ_{xy}) and “counts” the shear stress cycles (half cycles as determined by shear stress reversals). As soon as a stress cycle is detected the excess pore pressure is positively incremented (increased) by an amount dependent on the cyclic stress ratio of that cycle. The strength envelope follows a Mohr-Coulomb relationship from the beginning of analysis, until (and if) strength drops to a user-defined post-liquefaction strength (S_r), which in this LSFD Analysis 1 is taken as the Weber et al. (2015) S_r .

Table 4-26: Input Parameters for analysis 1 of LSFD using Roth model with Cetin et al. (2018) liquefaction triggering, Youd et al. (2001) K_σ , Idriss and Boulanger (2003) K_α , and Weber et al. (2015) S_r

Soil Layer	$N_{1,60,CS}$ (Cetin et al., 2018)	$B (=1/b)$ (Cetin et al. 2018)	CSR_{15} (Cetin et al, 2018)	Friction Angle, ϕ' (Table 4-8)	f for K_σ (Youd et al. 2001)
HFU-1 and HFD-1	16.6	2.324	0.156	35	0.679
HFU-2 and HFD-2	14.2	2.324	0.127	34	0.704
HFU-3 and HFD-3	19.5	2.324	0.200	36	0.653
HFU-4 and HFD-4	12.8	2.324	0.113	33	0.719

The non-liquefiable layers were modeled with Mohr-Coulomb parameters, as presented in Table 4-8. The “puddled” central clay core strength was modeled as $S_u/\sigma'_{v,i} = 0.192$ at the beginning of the dynamic analysis, representing a 20% reduction from the peak

static strength of $S_u/\sigma'_{v,i} = 0.24$ to account for both (1) cyclic softening, and (2) strain softening. Later in the analysis, the strength of the clay core would potentially be reduced further to account for further strain softening, if very large shear strains develop.

Figures 4-52 and 4-53 present the results of nonlinear seismic deformation analyses performed with the combination of models and relationships of Analysis 1, and with the crest-perpendicular input motion of Figure 4-33 (with $a_{max} = 0.80$ g). Figure 4-52 shows conditions at the end of 7.8 seconds of seismic shaking, and Figure 4-53 shows conditions at the end of analysis.

Ordinarily, and in most of the rest of the analyses presented in Chapters 4 and 5, the first set of figures (Figures 4-52(a) through (c)) would show conditions at the end of shaking. In LSFD Analysis 1, however, the deformations at the end of 7.8 seconds of shaking are sufficient that re-meshing is necessary to overcome numerical difficulties (or “mesh-lock”) due to large deformations at the base of the upstream side hydraulic fill “shell” zone”. Because it is necessary to temporarily “pause” the analysis to re-mesh, this opportunity was also used to evaluate shear strains and shear displacement offset across the central “puddled” clay core zone. It was judged that these shear strains (see Figure 4-52 (b)) are sufficiently large, and still progressing, as to warrant a reduction of clay core strength to a fully residual value of $S_{u,residual}/\sigma'_{v,i} = 0.08$. The analysis was then re-started, with re-meshing as needed to continue the analysis until a decision was made to terminate the analysis because (1) re-meshing was becoming less effective, and (2) the deformations had advanced sufficiently that a suitable engineering interpretation of the results (recognizing that deformations were still ongoing) could be achieved.

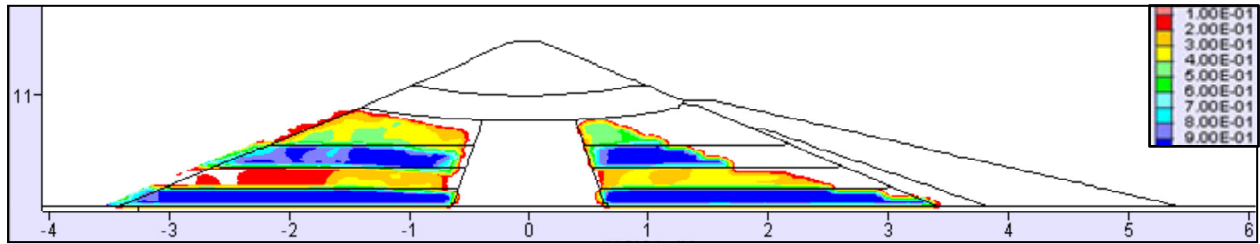
The temporary pause at 7.8 seconds occurred near the tail end of significant shaking; as a result it was not necessary to again make a pause at the formal end of shaking, especially as it had already been concluded that reduction of clay core strengths to fully residual values was warranted, and that strength reduction had already been implemented.

Figure 4-53 shows the analysis results at the “end of analysis”. The analysis was terminated at 25 seconds based on the criteria above. The blue arrows indicate that deformations and displacements towards the upstream side are still ongoing at the end of analysis.

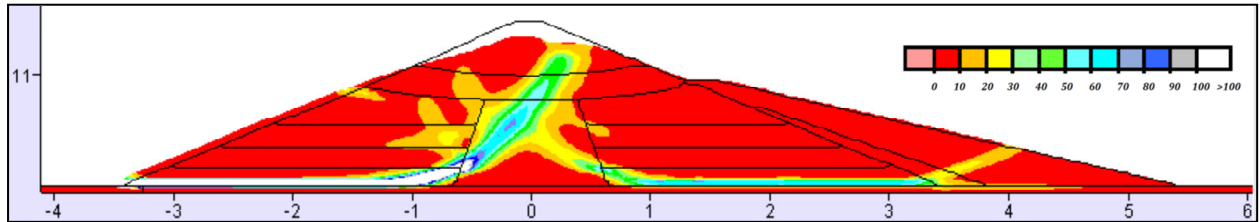
As shown in Figures 4-52(a) and 4-53(a), significant pore pressures were generated in the upstream side hydraulic fill shell zones (especially HFU-2 and HFU-4), and also in the saturated portions of the hydraulic fill shell zones on the downstream side (especially HFD-2 and HFD-4).

As shown in Figure 4-52(b), these cyclically-induced pore pressures, in conjunction with seismic inertial forces, led to the development of two sets of concentrated shear strain zones representing potential shear failure surfaces. One of these began at the upstream toe, passed laterally along the base of the upstream hydraulic fill shell zone, and then arced upwards across the central “puddled” clay core to exit high on the upper portion of the down-

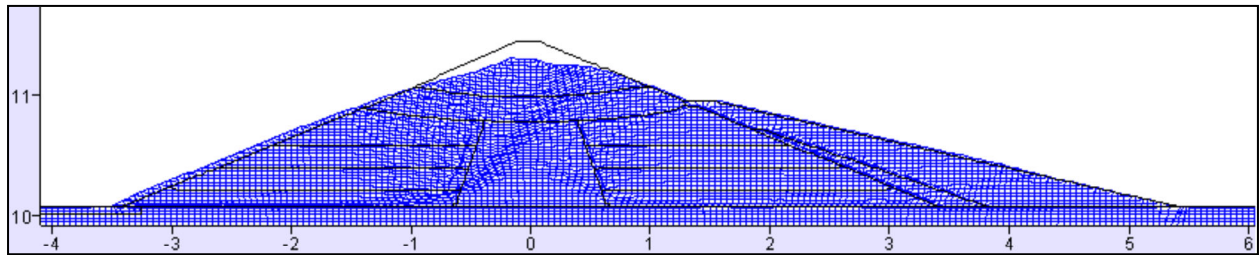
LSFD Analysis 1: Roth model, with the Cetin et al. (2018) Triggering Relationship, the Youd et al. (2001) K_σ , and the Weber et al. (2015) S_r Relationship



(a) Maximum value of $R_{u, \text{seismic}}$ recorded in each element at the end of 7.8 seconds



(b) Shear strain (percent), with the inset shear strain scale set to maximum of 100 percent



(c) Deformed mesh at the end of 7.8 seconds

Figure 4-52: Results of LSFD Analysis 1 at the end of 7.8 seconds of shaking

stream face of the dam. This represented a potential slope failure surface towards the upstream side of the dam. As also shown in Figure 4-52(b), a second potential failure surface occurred across the base of the downstream hydraulic fill shell zone. This second potential failure surface also arced upwards as it traversed the “puddled” central clay core, towards an exit high on the upper portion of the upstream face of the dam. This second potential failure surface would suggest the possibility of eventual development of a second slope failure towards the downstream side.

At the time represented by Figure 4-52 ($t = 7.8$ seconds, near the “end of shaking”), it is already clear that the upstream side failure has begun to occur, and that significant lateral displacements towards the upstream side have also begun to occur, and so have significant vertical displacements of the dam’s crest section. The partially developed potential failure surface towards the upstream toe has moved far enough at this juncture to begin to cut the top heel mass off of the top of the second (and similar) potential failure surface towards the downstream side, as seen most clearly in Figure 4-52(b).

LSFD Analysis 1: Roth model, with the Cetin et al. (2018) Triggering Relationship, the Youd et al. (2001) K_σ , and the Weber et al. (2015) S_r Relationship

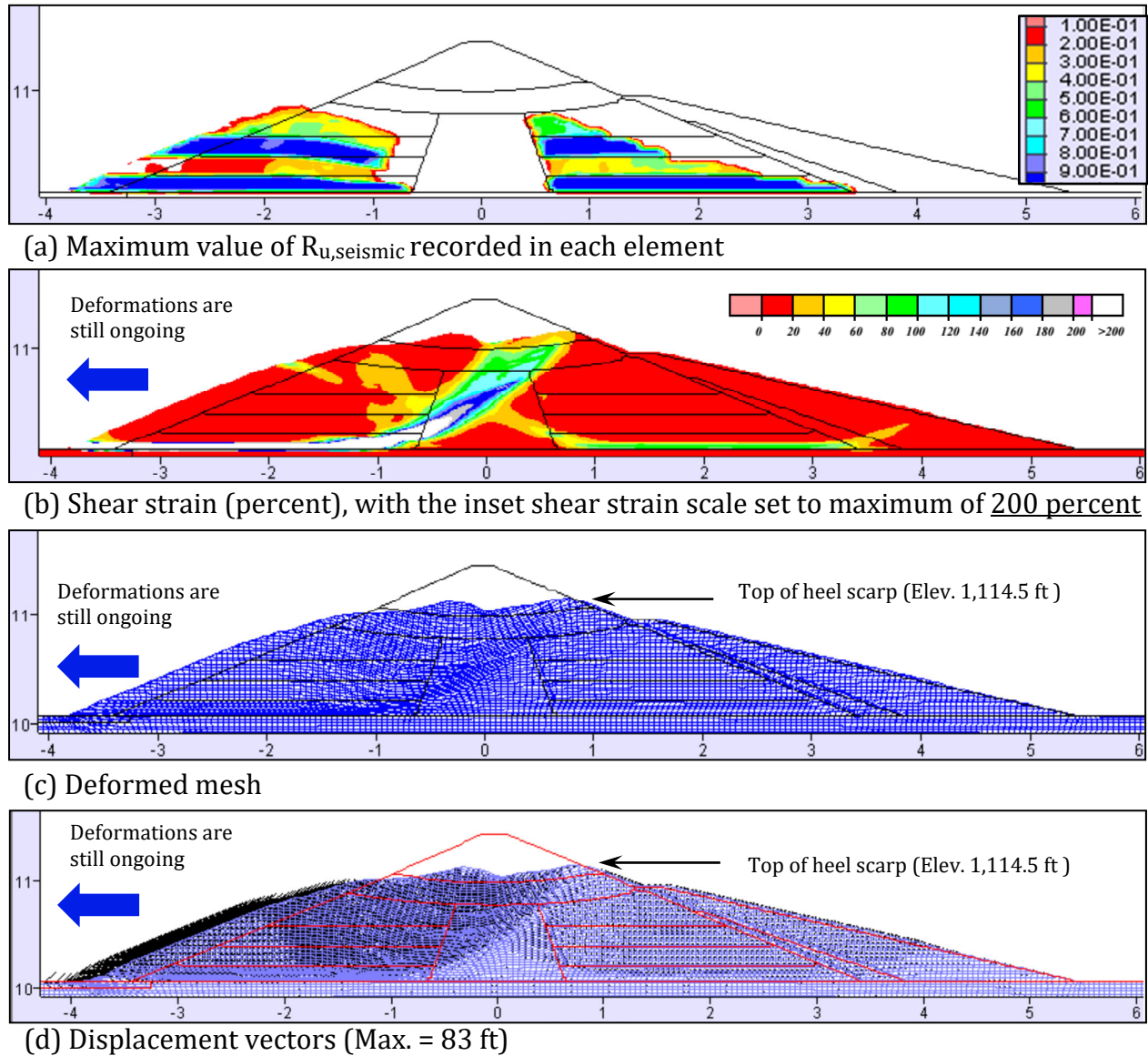
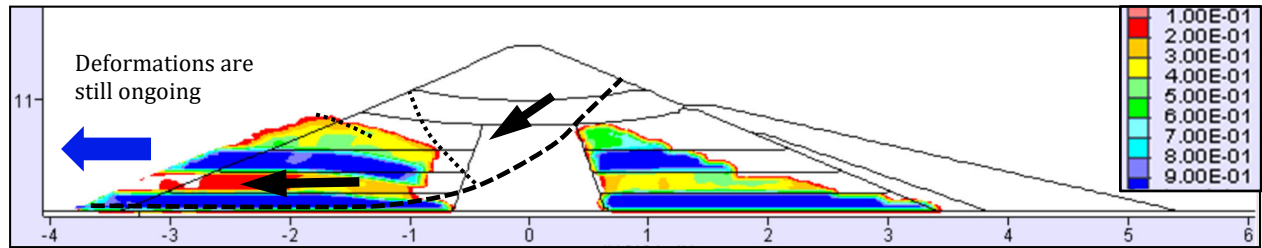


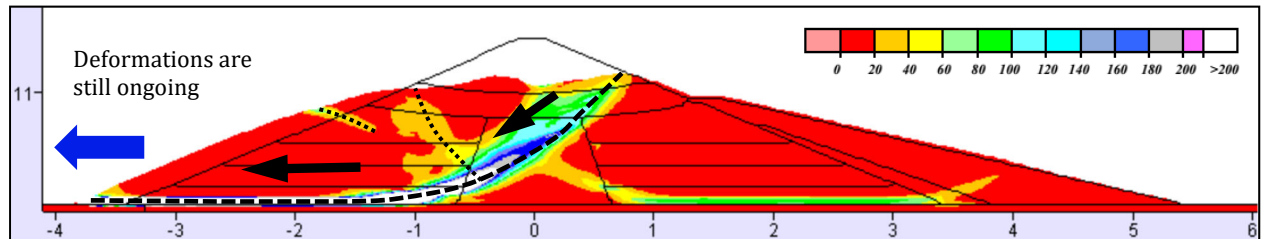
Figure 4-53: Results of LSFD Analysis 1 at the end of analysis

Figure 4-53 shows conditions at the end of analysis. The analysis was terminated at this point because the re-meshing necessary in order to continue to advance the analysis in the face of large deformations had become tedious and time-consuming, and the engineering outcome (suitable for engineering interpretation) was already clearly established.

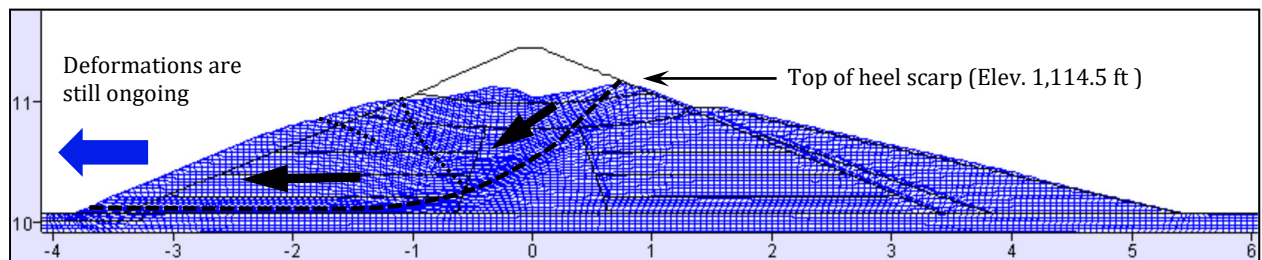
As shown in Figure 4-53, the upstream side failure continued to develop, but there was no further development of the potential (or incipient) downstream side slope failure; the downstream side had remained statically stable at the end of analysis.



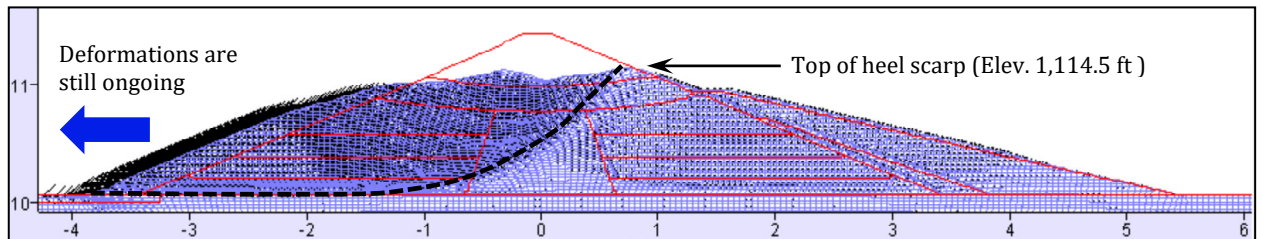
(a) Maximum value of $R_{u,seismic}$ recorded in each element



(b) Shear strain (percent), with the inset shear strain scale set to maximum of 200 percent



(c) Deformed mesh



(d) Displacement vectors (Max. = 83 ft.)

Figure 4-54: Results of LSFD Analysis 1 at the end of analysis (after 25 seconds of earthquake shaking) - Annotated

Figure 4-54 repeats Figure 4-53, but this time with annotation indicating and/or highlighting selected elements of the observed analysis results.

As indicated by the blue arrows in Figures 4-54 (b), (c) and (d), the upstream side slope stability failure continued to develop, and both deformations and displacements towards the upstream side were still ongoing when the analysis was halted. The correct engineering interpretation is that the upstream flow slide would continue to proceed considerably further.

At termination of analysis, the top of the original dam crest has been lowered nearly below the “lip” of the slide heel scarp at the top of the remaining downstream face of the dam, and deformations were still ongoing; so this heel scarp feature will now control/define the available crest height (minus further reductions due to potential transverse cracking, etc. of the top portion of this scarp feature or “lip”). As indicated in Figures 4-54(b), (c) and (d) the top of this analytically predicted heel scarp feature is located at elevation 1,114.5 ft., which matches well with the actual heel scarp (remaining top of crest, or lip) elevation of 1,114 ft. that was actually observed in the immediate aftermath of the 1971 earthquake.

It should be noted that the actual “useful” or effective (or functional) remaining crest height would, of course, likely be somewhat less due to localized transverse cracking of this heel scarp “lip” section; the depth of cracking of this lip section was not conclusively established in the aftermath of the earthquake. As a result, comparisons between analytical “predictions” and observed performance will be based on the top of lip, rather than on the useful/functional post-earthquake crest height as reduced by cracking. Engineers should note that analytically calculated remaining crest heights for these situations (in forward analyses) should be further reduced to account for potential cracking. Examples of procedures for estimating cracking for this type of situation are presented in USBR (2015).

The prediction of the upstream side failure, and the prediction of no occurrence of a downstream side failure, matches well with the observed field performance. The nature of the upstream failure; a deep-seated translational failure across the base of the upstream hydraulic fill shell zone, and then a rotational slippage feature arcing upwards across the central core zone to exit at a heel scarp high on the upper portion of the upstream face, also matches well with the observed field performance (see Section 4.2).

A final detail shown in this LSFD Analysis 1 also warrants mention. There was a crest seismoscope on the failure section of the Lower San Fernando Dam, and although the crest was carried away atop the upstream side flow failure, it was subsequently recovered (from a submerged location in the reservoir), and one interpretation of the recovered seismoscope record suggested that the upstream side flow failure had occurred after the end of the strongest shaking (as the seismoscope pen record appeared to potentially indicate systematic “tilting” of the seismoscope after shaking had been either completed, or largely completed; though that was never fully confirmed (Seed, 1987). This current Analysis 1 would suggest the possibility that significant movements occurred during the later stages of shaking, and continued after the end of shaking. Examining Figure 4-52 shows that the analysis predicts very little “tilting” of the dam crest after 7.8 seconds (near the end of significant shaking), but Figure 4-53 shows that tilting increases as subsequent deformations continue.

The analysis was halted at 25 seconds, in part because the engineering conclusions were clear at that point, and also because it was not possible to continue the analysis onwards through the full development of the very large final displacements observed due to numerical difficulties and limitations involved in these types of continuum analyses which cannot “bifurcate” (produce sharp shear displacement offsets), and cannot produce tensile failures between soil masses. As shown previously in Figures 4-5 and 4-6, the upper portion

of the dam dis-aggregated as the very large field deformations and displacements continued to develop, and the resulting disaggregated semi-intact “blocks” of the dam were carried back into the reservoir atop the underlying liquefied materials. FLAC is a continuum analysis, and cannot model (1) fully localized shear bifurcation (shear slippage, instead of shear strains distributed across a shear zone of finite but non-zero width), and (2) tensile separations between adjacent soils. Both shear bifurcation, and tensile failures (and resulting tensile separations) are indicated in the post-earthquake cross-sections of Figures 4-5 and 4-6.

It is important to note that these limitations do not in any way limit the usefulness of the analytical predictions. It is clear that an upstream side flow failure is underway, and that it will continue to progress further. And the geometry of the upper “lip” of the upstream failure heel scarp is very well predicted.

An interesting effect of the difficulty of modeling bifurcation and dis-aggregation for this particular case history, and analysis, (and for these types of large-deformation analyses in general) is that the actual pre-earthquake dam crest currently remains at about the same height as the heel scarp feature at the top of the remaining downstream face at the time the analysis was halted, and thus might appear to define the apparent “remaining crest”. In reality, this original crest is still displacing, as indicated by the blue arrows in Figure 4-53, and the correct engineering interpretation is to recognize that movements are ongoing and will likely proceed significantly further, and thus then take the heel scarp crest (or lip) as the remaining effective crest (minus further allowance for expected cracking of this heel scarp crest feature). If a conventional static limit equilibrium stability analysis is performed at this “end of analysis” stage using the deformed shape of the dam from FLAC, it would be missing ongoing inertial effects, and it would also be misleading to perform such static analysis with the assumption that the upper portion of the upstream slide mass as shown in Figure 4-53 will continue to behave as an intact soil mass. Instead, it will next experience both tensile cracking and shear cracking that will result in blocky disaggregation (see Figure 4-6). Upstream slope failure deformations and displacements will continue significantly further. Such an engineering interpretation (that movements will continue to develop further; and that the heel scarp feature will define the available freeboard, minus considerations for cracking) is not always made in engineering practice, and the result here would then be misleadingly unconservative, and potentially dangerously so.

In addition, there are two more potential phenomena associated with the upstream flow slide that cannot currently be analytically treated with good precision (Weber et al. (2015)). The first of these is the possibility of “hydro-planing” as the upstream toe of the dam entered at significant (and increasing) velocity into the reservoir, and potentially trapped some reservoir waters beneath portions of the advancing toe, and the second is “plowing” of the advancing upstream toe of the slide feature both over and through “soft or loose” (and weak) reservoir sediments at the toe; the shear strengths of these sediments cannot be reliably ascertained. It should be noted that these two issues are sometimes addressed in offshore applications, but that they are not yet routinely addressed in onshore seismic dam applications. It is not necessary to deal rigorously with these two issues in this current case; only to recognize that they will likely further exacerbate the still ongoing displacements.

This does not in any way diminish the usefulness, nor the apparent accuracy, of this LSFD Analysis1 analytical “prediction” of seismic dam performance for this earthquake. The engineering “match” with observed behavior is excellent, and it would provide a suitable and useful prediction of expected seismic performance for this input motion, and a suitable basis for engineering evaluation of associated downstream risk or hazard exposure.

In addition, another feature observed in this analysis is the revelation of two “competing” potential shear surfaces; one towards the upstream side of the dam, and one towards the downstream side of the dam (as shown in Figure 4-52(a)), and a nuance associated with their geometries. The location at which the incipient potential downstream failure heel scarp feature passes diagonally across the upstream side of the dam (as indicated by shear zone contours in Figure 5-53(b), and by the uppermost finely dashed black line in Figure 4-54(b) represents the approximate location above which (above and to the right) the main observed dis-aggregation of multiple independent “semi-intact blocks” of the dam developed. This suggests that the second “incipient” failure surface towards the downstream side did not develop fully, but that it did help to constrain the location and nature of blocky dis-aggregation of the upper dam embankment zones that were transported back into the reservoir atop the underlying liquefied materials.

Table 4-27 shows a summary and comparison of five selected key indices of (1) analytically “predicted” field performance vs. (2) actual observed field performance for LSFD Analysis 1. These five indices will be examined for all of the LSFD back-analyses performed as part of these studies. As indicated in Table 4-27, this analysis produced good agreement with observed field performance.

Overall, LSFD Analysis 1 provided very good engineering predictions of the principal mechanisms of dam distress and deformation, and with good matching of the magnitudes of actual displacements, as well as the location (elevation) of the top lip of the upstream slide scarp feature that controlled (with suitable allowance for additional transverse cracking of this lip feature) the available useful freeboard in the immediate aftermath of the earthquake. These are excellent results, and they would represent a good engineering basis for “predicting” expected performance under this level of seismic loading, and also a good basis for evaluation of downstream risk or hazard exposure.

Table 4-27: LSFD Analysis 1; Comparison between analysis results and actual observed field performance

	Analysis	Observed
1. Occurrence of U/S flow failure	Yes	Yes
2. Correct U/S failure plane/mechanism	Yes	(Yes)
3. Elevation of top of heel scarp feature	1,114.5 ft	1,114 ft
4. Occurrence of D/S flow failure	No	No
5. Maximum D/S face lateral displacement	6.1 ft	~ 0.8 ft

4.8.2 LSFD Analysis 2: UBCSAND Model, with the Youd et al. (2001) Liquefaction Triggering Relationship, and the Seed and Harder (1990) S_r Relationship

LSFD Analysis 2 utilizes the UBCSAND model, parameterized to implement the Youd et al. (2001) liquefaction triggering relationship, with the Youd et al. (2001) K_σ relationship, and an approximation of the Boulanger and Idriss (2003) K_α relationship, and it utilizes the Seed and Harder (1990) post liquefaction S_r (average) relationship, within the UBCSAND modeling scheme for the potentially liquefiable hydraulic fill layers. This is the first of two LSFD back-analyses performed using the UBCSAND model. The UBCSAND constitutive model Version 904aR requires only $N_{1,60,CS}$ values as input parameters, as all other model parameters have been parametrized or calibrated to relate (to be self-setting) as a function of $N_{1,60,CS}$.

The current UBCSAND model is parametrized in such a way that it is expected to show soil behaviors consistent with the Youd et al. (2001) liquefaction triggering relationship, and the Youd et al. (2001) K_σ relationship, and behaviors consistent with the Boulanger and Idriss (2003) K_α relationship, when $N_{1,60,CS}$ values based on the energy, equipment, procedural and effective overburden stress corrections, and fines corrections, of Youd et al. (2001) are assigned in the potentially liquefiable soil elements (in the upstream and downstream hydraulic fill shells). As part of this parameterization of the UBCSAND model, K_σ behavior has been parametrized by means of a conversion relating D_r with $N_{1,60,CS}$ using a value of $C_d = 46$ in Equation 4-2.

Table 4-28 presents the input parameters used in LSFD Analysis 2 for modeling of the potentially liquefiable soils. The non-liquefiable layers were modeled with Mohr-Coulomb parameters, as presented in Table 4-8. Shear strength of the puddled central clay core was modeled as $S_u/\sigma'_{vi} = 0.192$ during shaking in Analysis 2, which assumes approximately a 20% reduction of undrained shear strength (from peak static, or monotonic, shear strength of $S_u/\sigma'_{vi} = 0.24$) for the normally consolidated clayey core to account for both (a) cyclic softening and (b) strain softening.

The protocol for the UBCSAND analyses in these current studies is to handle the potential transition to post-liquefaction residual strength (S_r) in elements comprised of potentially liquefiable soils within the UBCSAND framework by considering the analysis to progress in two steps or stages (1) during shaking, and (2) after the end of shaking. During shaking, there is no implementation of S_r . After the end of shaking, S_r is applied within potentially liquefiable soil elements that satisfy either of two criteria: (1) occurrence of $R_{u,seis} \geq 0.7$ at any stage during shaking ($R_{u,seis,max} \geq 0.7$) or (2) development of a peak shear strain of $\gamma \geq 10\%$ at the end of shaking in saturated materials. The UBCSAND protocol is then to continue the nonlinear deformation analysis after the end of shaking until either (1) deformations and displacements have ceased to occur, as the embankment is in a stable condition, or (2) mesh distortions are resulting in a need to perform significant (and time-consuming) re-meshing to continue the NDA deformation analysis, and the results at termination have become sufficient for purposes of engineering interpretation and decision-making, with recognition that deformations and displacements are still ongoing.

Table 4-28: Input Parameters for LSFD Analysis 2 using the UBCSAND model, with the Youd et al. (2001) Liquefaction Triggering Relationship and K_σ Relationship, and the Seed and Harder (1990) S_r Relationship

Soil Layer	$N_{1,60,CS}$ (Youd et al., 2001)	$N_{1,60,CS-Sr}$ (Seed and Harder, 1990)
HFU-1	18.2	16.7
HFU-2	16.0	13.9
HFU-3	21.5	19.2
HFU-4	14.8	12.5
HFD-1	18.2	16.7
HFD-2	16.0	13.9
HFD-3	21.5	19.2
HFD-4	14.8	12.5

Similarly, it is also part of the UBCSAND protocol to also examine non-liquefiable soils (e.g. the normally consolidated central clayey core zone) at the end of shaking, and to consider whether strength reduction (or further strength reduction) is warranted as a result of large shear strain development in sensitive cohesive soils. This will be discussed further below. If appropriate, cohesive strengths are reduced (or further reduced) at this juncture, and the analysis then proceeds after the end of shaking.

Figures 4-55 and 4-56 present the results of nonlinear seismic deformation analyses performed with the combination of models and relationships of LSFD Analysis 2. Figure 4-55 shows conditions calculated “at the end of shaking”, but the analyses are continued after the end of input seismic excitation, as deformations can continue after the end of shaking due to ongoing deformations under static (gravity loading). In some cases, the post-shaking deformations can lead to development, or discovery, of progressive development of large deformations or even instability failures. Accordingly, it is important to continue the analyses after the end of shaking.

The analysis was temporarily halted at the end of shaking, and elements of potentially liquefiable soils that had achieved either (1) maximum cyclic pore pressure ratios of $R_{u,seis} \geq 0.7$, or (2) development of a peak shear strain of $\gamma \geq 10\%$ at the end of shaking in saturated materials were transitioned to post-liquefaction strength (S_r).

Similarly, as the analysis was temporarily halted at the end of shaking, the shear strains and deformations within the “puddled” central clay core zone were also evaluated. It was judged that these shear strains (see Figure 4-55 (b)) are sufficiently large (mostly greater than 25 to 30 percent, and still progressing) as to warrant a reduction of clay core strength to a fully residual value of $S_{u,residual}/\sigma'_{vi} = 0.08$.

LSFD Analysis 2: UBCSAND model, with the Youd et al. (2001) Liquefaction Triggering and $K\sigma$ Relationships, and the Seed and Harder (1990) S_r Relationship

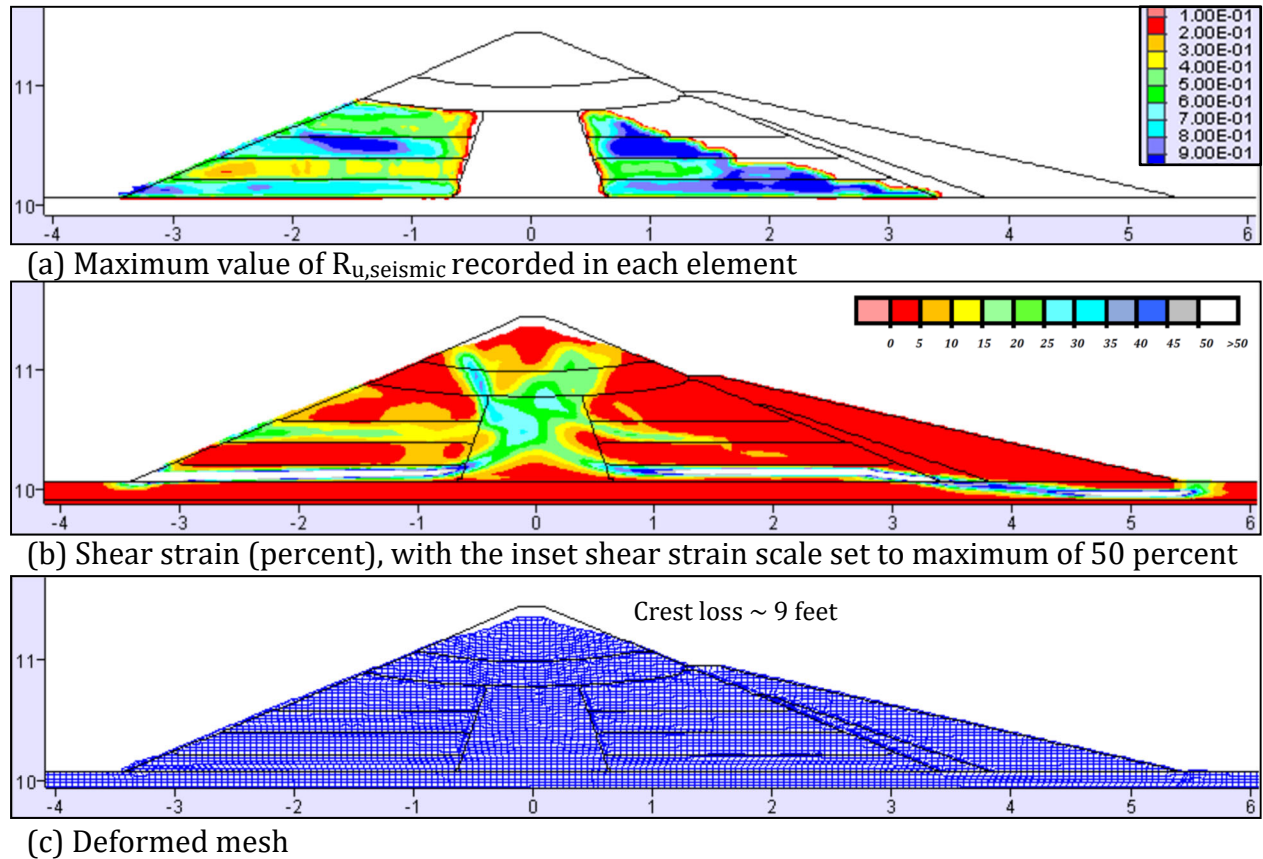


Figure 4-55: Results of LSFD Analysis 2 at the end of shaking

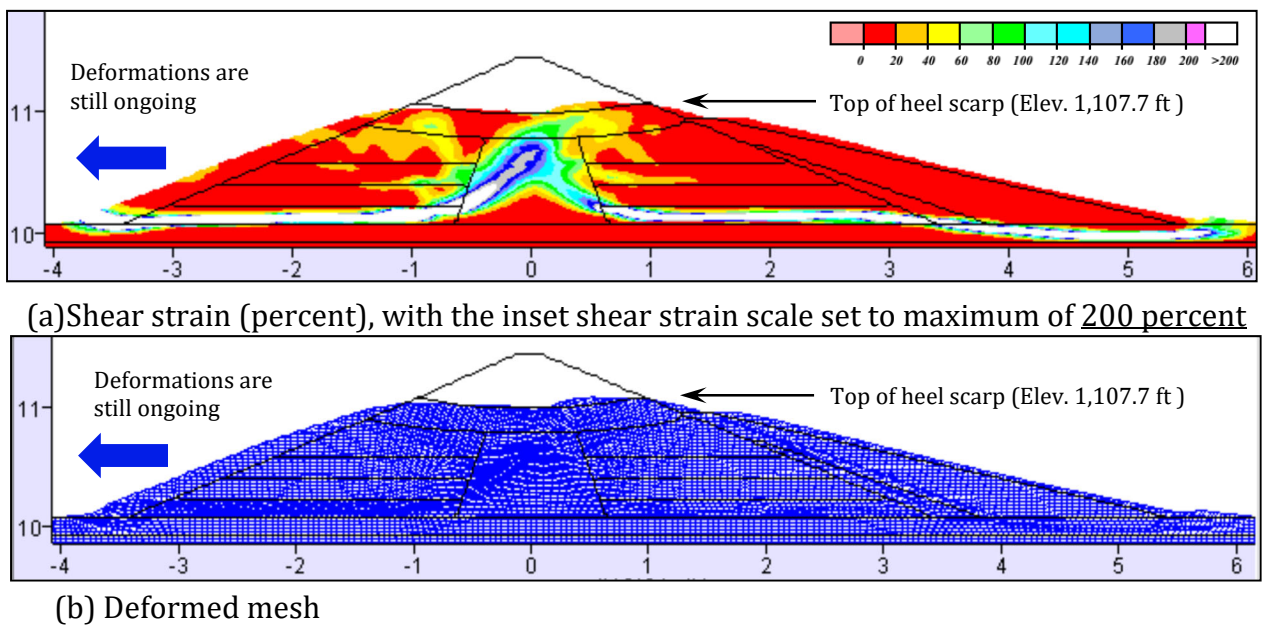


Figure 4-56: Results of LSFD Analysis 2 at the end of analysis

The analysis was then re-started, with re-meshing as needed to continue the analysis until a decision was made to terminate the analysis because (1) re-meshing was becoming less effective, and (2) the deformations had advanced sufficiently that a suitable engineering interpretation of the results (recognizing that deformations were still ongoing) could be achieved. The conditions at termination (or “end of analysis”) are shown in Figure 4-56. There is no need to show an additional maximum cyclic pore pressure figure as part of Figure 4-56, as there has been no further development of higher cyclic pore pressures after the end of shaking, so Figure 4-55(a) represents the highest cyclic pore pressures achieved.

As shown in Figure 4-55(a), significant cyclic pore pressure generation occurs in the saturated upstream hydraulic fill shell zones (especially HFU-2 and HFU-4. Significant cyclic pore pressure generation also occurs in the saturated portions of the downstream hydraulic fill shell zones (especially HFD-2 and HFD-4).

As shown in Figures 4-55(b) and (c), these cyclic pore pressures, in conjunction with cyclic inertial forces, produce only moderate deformations and displacements during shaking [vertical crest loss in Figures 4-55(b) and (c) is approximately 9 feet], and they have also produced two sets of shear strain concentrations (see Figure 4-55(b)) indicating the development of two incipient or potential shear failure surfaces: (1) one of these is an potential upstream failure surface, originating at the upstream toe, passing along the base of the upstream hydraulic fill shell zones, and then arcing upwards across the central puddled clay core zone to exit high on the upper portion of the downstream face of the dam, and (2) the second, and similar, potential or incipient failure surface is a downstream failure surface, originating at the downstream toe, passing along the base of the downstream hydraulic fill shell zones, and then arcing upwards across the central puddled clay core zone to exit high on the upper portion of the upstream face of the dam. These two nearly symmetrical potential failure surfaces are very similar to the two (also upstream and downstream) incipient or potential failure surfaces observed previously approximately at the end of strong shaking in LSFD Analysis 1. It is not possible “at the end of shaking” to determine, based on engineering judgment, whether either (or even both) of these two potential failure surfaces will continue to develop further.

As shown in Figures 4-56(a) and (b), the upstream side potential failure surface does continue to develop after the end of shaking. The blue arrows in Figures 4-56(a) and (b) indicate that deformations and displacements towards the upstream side are also still continuing to develop at the “end of analysis”.

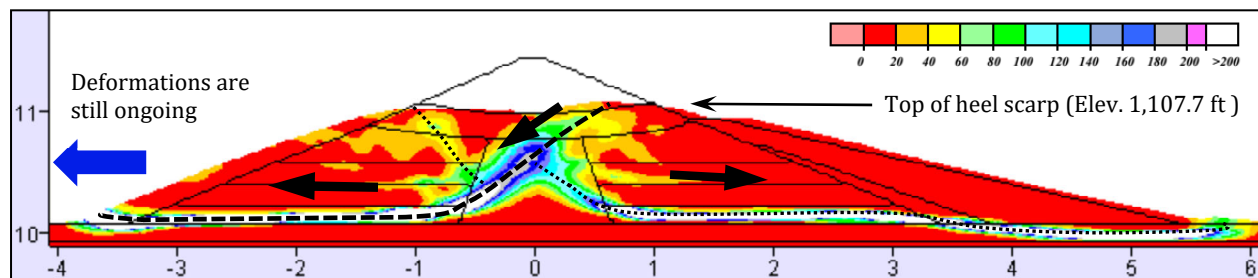
The downstream side potential failure surface, on the other hand, develops lesser (but non-negligible) deformations and then remains stable. These moderate deformations (maximum lateral downstream slope displacement = 21.6 ft.) appear to be larger than those observed (~1 ft.), and they have a non-negligible effect on the overall analysis results.

The post-liquefaction residual strength (S_r) relationship employed in LSFD Analysis 2 was the Seed and Harder (1990) relationship. As discussed in Section 2.4, this S_r relationship predicts S_r as a function of only $N_{1,60,CS}$, rather than as a function of both $N_{1,60,CS}$

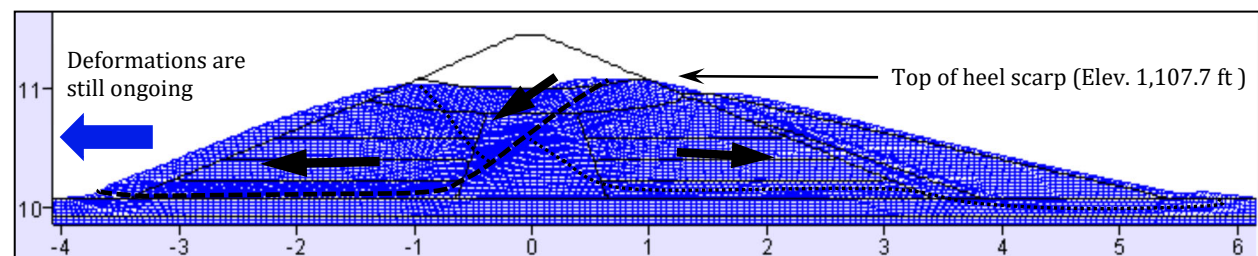
and initial effective vertical stress ($\alpha'_{v,i}$), and as a result it is overconservative (under-predicts S_r) at high initial effective overburden stresses.

The hydraulic fill shell zones at the base of both the upstream and downstream hydraulic fill shell zones are regions of high initial effective stress, and the under-prediction of S_r in these zones produced a condition of marginal instability on the downstream side. The downstream side potential or incipient failure surface has a greater level of stability than the upstream side instability feature, however, due in large part to the shear strengths of the non-saturated hydraulic fill and berm materials at and near the downstream toe. As a result, the upstream slide feature was displacing more rapidly than the similar downstream slide feature as the analysis was re-stated after the end of shaking.

This produced an interesting effect. Figures 4-57(a) and (b) repeat Figures 4-56(a) and (b), but this time with annotations to highlight several features. The heavier dashed lines in Figures 4-56(a) and (b) indicate the upstream side slope instability feature's principal failure surface, and the lighter (and finer) dashed lines indicate the shear displacement zone of the downstream instability feature. As clearly shown in this feature, the faster moving upstream side failure "cuts off" the crest section of the dam and carries it away from the heel area downstream side failure feature. This removes significant driving mass from the top heel area of the downstream side feature, and this limits the downstream side movements. As shown in Figures 4-56(a) and (b), the more dominant upstream slide feature also "cuts off" the upper portion of the downstream slide shear surface, and carries it away from the remaining downstream slide feature.



(a) Shear strain (percent), with the inset shear strain scale set to maximum of 200 percent



(b) Deformed mesh

Figure 4-57: Results of LSFD Analysis 2 at the end of analysis; annotated

Because the upper “lip” of the heel scarp of the upstream slide feature was initially lowered by movements of both the upstream and the downstream slide features, this important “lip” (which, with allowances for likely transverse cracking) controlled effective remaining crest height in the immediate aftermath of the earthquake, was lowered more in LSFD Analysis 2 than was actually observed in the earthquake. The analytically predicted elevation of +1,108 feet of this upstream scarp “lip” is lower than the actual observed post-earthquake elevation of +1,114 ft.

The analysis was halted at the stage shown in Figure 4-56, in part because the engineering conclusions were clear at that point, and also because it was not possible to continue the analysis onwards through the full development of the very large final displacements observed. As shown in Figures 4-5 and 4-6, the upper portion of the dam disaggregated as the very large field deformations and displacements continued to develop, and the resulting disaggregated semi-intact “blocks” of the dam were carried back into the reservoir atop the underlying liquefied materials. FLAC is a continuum analysis, and cannot model (1) fully localized shear bifurcation (shear slippage, instead of shear strains distributed across a shear zone of finite but non-zero width), and (2) tensile separations between adjacent soils. Both shear bifurcation, and tensile failures (and resulting tensile separations) are indicated in the post-earthquake cross-sections of Figures 4-5 and 4-6.

The decision to halt the analysis at stage of Figure 5-56 was based on (1) the observation that the engineering information was sufficient, as the original dam crest had subsided vertically to a point that it was below the “lip” of the upstream slide scarp feature, and so the lip of the scarp feature would control the useful crest height, or freeboard, with allowances for expected cracking of this lip section, and (2) re-meshing was becoming tedious and progressively less effective, and it would not be possible to reliably model full runout of the upstream “flow failure” because of the intrinsic limitations of current continuum analyses (see discussion in Section 4.8.1).

Table 4-29 shows a summary and comparison of five selected key indices of (1) analytically “predicted” field performance vs. (2) actual observed field performance for LSFD Analysis 2. These five indices will be examined for all of the LSFD back-analyses performed as part of these studies. The matches with actual observed field behavior are only moderate, including the location and elevation of the top of the “lip” of the heel scarp feature that largely defines available useful crest height (and freeboard) in the immediate aftermath of the 1971 earthquake, with appropriate consideration of likely effects of some transverse cracking of this heel scarp lip section, and the fact that downstream displacements were over-predicted.

The mechanism of failure “predicted” by LSFD Analysis 2 matches well for the upstream flow failure. However, LSFD Analysis 2 “over-predicted” downstream deformations; lateral displacement at the downstream slope of 21.6 feet was calculated, but this was not observed in the field. Also, the elevation of the top “lip” of the upstream slide heel scarp from LSFD Analysis 2 is about 5 feet lower than the observed heel scarp lip. These larger than observed deformations in the downstream slope and toe, and larger displacements in the heel scarp area, are the result of continued deformations and displacements of the downstream side slope instability feature that is indicated with the

“dotted” line in Figures 4-57(a) and (b). These movements, which were not observed in the field, can be attributed the use of the Seed and Harder (1990) post-liquefaction S_r relationship. This relationship predicts S_r as a function only of $N_{1,60,CS}$, rather than as a function of both $N_{1,60,CS}$ and initial effective vertical stress($\sigma'_{v,i}$), and as a result it tends to under-predict S_r at relatively high effective overburden stresses, such as occur near the base of the downstream hydraulic fill shell zone near to the core.

LSFD Analysis 3 tests this hypothesis, by repeating Analysis 2, but replaces the Seed and Harder (1990) S_r relationship with the S_r relationship of Weber et al. (2015) which predicts S_r as a function of both $N_{1,60,CS}$ and initial effective vertical stress($\sigma'_{v,i}$).

Overall, LSFD Analysis 2 was judged to be partially unsuccessful. It provided moderately useful engineering predictions of the upstream side instability (flow failure) feature, but it also predicted partial development of a downstream side instability feature which produced (1) significantly larger (but not unlimited) downstream side lateral displacements than were observed, and (2) lowering of the critical “lip” of the upstream flow slide scarp to an elevation well below what was actually observed. These relatively poor results were not the fault of the analytical model (UBCSAND), nor of the triggering relationship (Youd et al., 2001). Instead, they were due to the post-liquefaction residual strength (S_r) relationship employed (S_r as per Seed and Harder, 1990), which conservatively under-predicted S_r in the hydraulic fill materials at the base of the downstream side “shell zone” adjacent to and near to the central clayey core. This produced a downstream instability (slide) feature that was later halted when the faster (more dominant) upstream side instability (flow slide) feature carried away the top crest section of the dam, reducing the “driving” forces at the upper heel of the downstream slide feature. This partially unsuccessful analysis thus serves to indicate the importance of selection and use of a suitable post-liquefaction (S_r) relationship as part of the overall analysis package.

Table 4-29 shows a summary and comparison of five selected key indices of (1) analytically “predicted” field performance vs. (2) actual observed field performance for LSFD Analysis 2. Agreement between the analytical results, and the actual field performance observed, was poor.

Table 4-29: LSFD Analysis 2; Comparison between analysis results and actual observed field performance

	Analysis	Observed
1. Occurrence of U/S flow failure	Yes	Yes
2. Correct U/S failure plane/mechanism	Yes	(Yes)
3. Elev. of top of heel scarp feature	1,107.7 ft	1,114 ft
4. Occurrence of D/S flow failure	Yes/No*	No
5. Maximum D/S face lateral displacement	21.6 ft	~ 0.8 ft

*A downstream side slippage initiates, but is slowed when the upstream side flow failure cuts off the upper driving mass of the central crest region and carries it to the upstream side.

4.8.3 LSFD Analysis 3: UBCSAND Model, with the Youd et al. (2001) Soil Liquefaction Triggering Relationship, and the Weber et al. (2015) Post-Liquefaction S_r Relationship

LSFD Analysis 3 repeats Analysis 2, but this time substitutes the post-liquefaction S_r relationship of Weber et al. (2015) in place of the S_r relationship of Seed and Harder (1990). Unlike the Seed and Harder (1990) S_r relationship, and the Idriss and Boulanger (2015) S_r/σ'_{vi} relationship, the relationship of Weber et al. varies S_r (and varies S_r/σ'_{vi}) as a function of both initial effective vertical stress and $N_{1,60,CS}$. In LSFD Analysis 2, the Seed and Harder (1990) post-liquefaction strength, S_r relationship appears to have under-predicted S_r at relatively high initial effective overburden stresses ($\sigma'_{v,i}$) at the bases of the hydraulic fill shells near the central clay core; likely causing the observed calculation of (1) significantly larger than actually observed displacements at the downstream toe, and (2) a final elevation of the “lip” of the upstream flow slide that is too low. In this LSFD Analysis 3, the switch to the S_r relationship of Weber et al. (2015) is implemented to see (1) if the analysis continues to over-predict displacements at the downstream toe and too low an elevation of the critical heel scarp feature, and (2) if the analysis will continue to correctly predict the upstream side flow failure.

The only new model-specific parameters needed in Analysis 3 are those for the Weber et al. (2015) S_r relationship, and those were presented previously in Table 4-26.

The engineering protocols of Analysis 3 are exactly the same as those described in Analysis 2.

Figures 4-55(a) through (c) showing conditions at the end of shaking are unchanged (from Analysis 2) for Analysis 3, and do not need to be repeated. Figures 4-58 (a) through (c) then present the results of Analysis 3 for post-earthquake conditions. Once again, when the analysis was temporarily halted at the end of shaking (1) the shear strains in the clay core were evaluated, and based on this the shear strength of the puddled central clay core was reduced to $S_{u,residual}/\sigma'_{vi} = 0.08$, and (2) both $R_{u,seis}$ and shear strains within the hydraulic fill layers were evaluated, and post-liquefaction residual strength (S_r) was implemented in potentially liquefiable soil elements that had achieved either (1) maximum cyclic pore pressure ratios of $R_{u,seis} \geq 0.7$, and/or (2) development of a peak shear strain of $\gamma \geq 10\%$ at the end of shaking in saturated materials. The analysis was then re-started, and continued forward after the end of shaking.

Figures 4-58(a) through (c) show conditions at the end of analysis. Two potential or incipient failure surfaces were shown to have developed at the end of shaking (see Figures 4-55(b) and (c)). As shown in Figure 4-58, the upstream potential shear failure surface again is the one that continues to propagate to full failure, but this time the potential downstream failure surface remains stable and experiences only very limited deformations and displacements. The blue arrows in Figures 4-58(a) through (c) again indicate that deformations and displacements towards the upstream side are continuing to develop at the termination of analysis.

LSFD Analysis 3: UBCSAND model, with the Youd et al. (2001) Liquefaction Triggering and K_σ Relationships, and the Weber et al. (2015) S_r Relationship

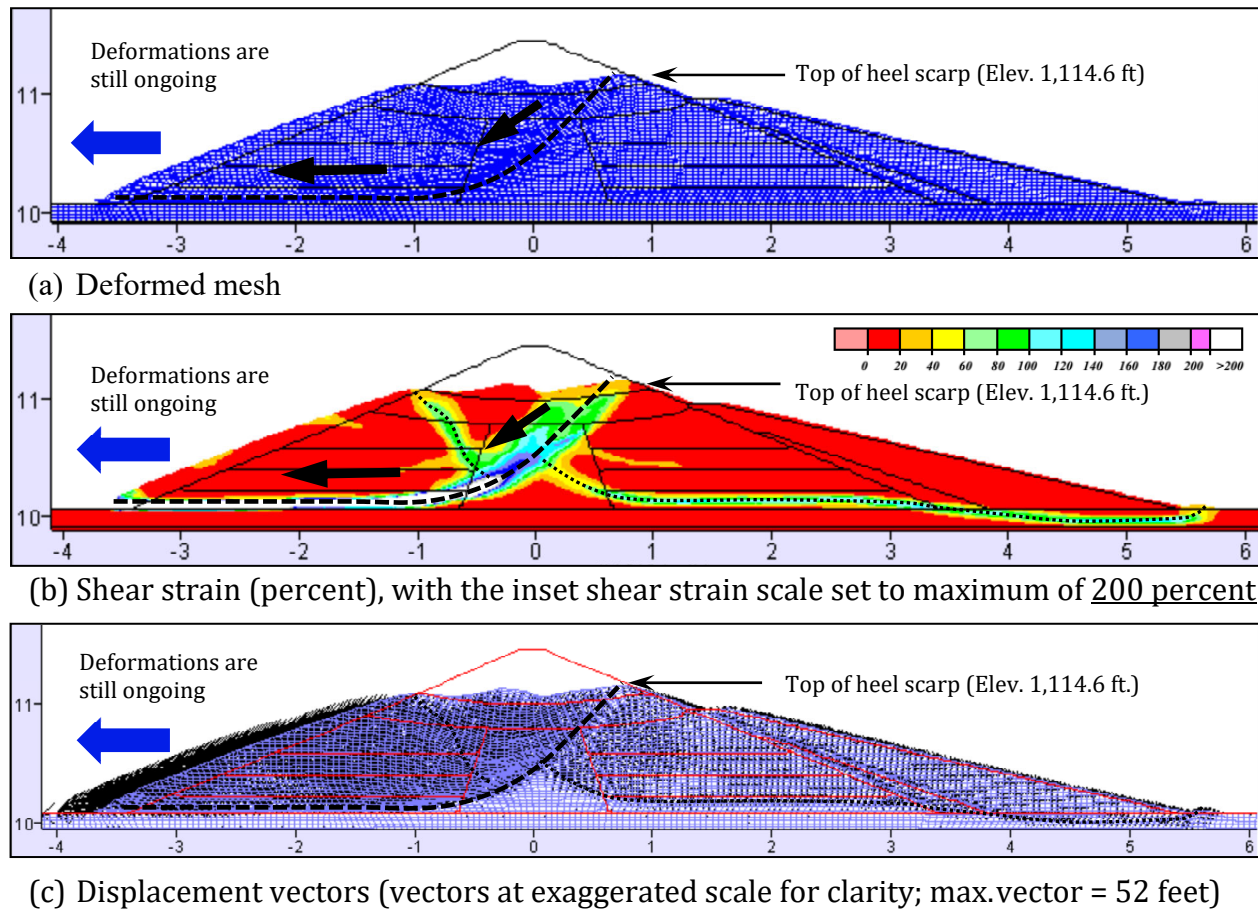


Figure 4-58: Results of LSFD Analysis 3 at the end of analysis

With the improved S_r values, the incipient slope stability feature towards the downstream side does not develop, and as a result the “lip” of the upstream side flow slide does not settle due in part to partial slope instability movements towards the downstream side. As shown in Figure 4-58, the calculated elevation of this critical “lip” which (with allowance for expected transverse cracking) controls the useful or effective crest elevation in the immediate aftermath of the earthquake now occurs at elevation +1,114.6 feet, very closely matching the actual observed elevation of 1,114 feet.

The substitution of the S_r relationship of Weber et al. (2015), which predicts S_r as a function of both $N_{1,60,CS}$ and $\sigma'_{v,i}$, in place of the S_r relationship of Seed and Harder (1990), which predicts S_r as a function of only $N_{1,60,CS}$ (as was used in LSFD Analysis 2) “fixes” the problems of the largely unsuccessful LSFD Analysis 2, and as a result LSFD Analysis 3 now produces excellent results.

Table 4-30 shows a summary and comparison of five selected key indices of (1) analytically “predicted” field performance vs. (2) actual observed field performance for LSFD

Analysis 3. These five indices will be examined for all of the LSFD back-analyses performed as part of these studies. The matches with actual observed field behavior are excellent, including the location and elevation of the top of the “lip” of the heel scarp feature that largely defines available useful crest height (and freeboard) in the immediate aftermath of the 1971 earthquake, with appropriate consideration of likely effects of some transverse cracking of this heel scarp lip crest.

Overall, LSFD Analysis 3 provided very good engineering predictions of the principal mechanisms of dam distress and deformation, and with very good matching of the magnitudes of actual displacements, as well as the location (elevation) of the top lip of the upstream flow slide scarp feature that controlled available useful freeboard (with considerations of likely transverse cracking) in the immediate aftermath of the earthquake. These are excellent results, and they would represent a very good engineering basis for “predicting” expected performance of the dam under this level of seismic loading, and also a good basis for evaluation of downstream risk or hazard exposure.

Table 4-30: LSFD Analysis 3; Comparison between analysis results and actual observed field performance

	Analysis	Observed
1. Occurrence of U/S flow failure	Yes	Yes
2. Correct U/S failure plane/mechanism	Yes	(Yes)
3. Elev. of top of heel scarp feature	1,114.6 ft	1,114 ft
4. Occurrence of D/S flow failure	No	No
5. Maximum D/S face lateral displacement	9.0 ft	~ 0.8 ft

4.8.4 LSFD Analysis 4: PM4Sand Model, with Boulanger and Idriss (2014) Liquefaction Triggering Relationship, and the Idriss and Boulanger (2015) S_r Relationship

LSFD Analysis 4 utilizes the PM4Sand model, the Boulanger and Idriss (2014) liquefaction triggering and K_σ relationships, the Idriss and Boulanger (2003) K_α relationship, and the Idriss and Boulanger (2015) post liquefaction S_r/σ'_{vi} relationship (for soils potentially susceptible to void redistribution). The PM4Sand model is employed in the potentially liquefiable soils (the upstream and downstream hydraulic fill shell zones).

The current PM4Sand model is parametrized in such a way that it is expected to show soil behaviors consistent with the Boulanger and Idriss (2014) liquefaction triggering and K_σ relationships, and behaviors at least generally consistent with the Boulanger and Idriss (2003) K_α relationship.

The analysis specific input parameters for PM4Sand in this LSFD Analysis 4 are summarized in Table 4-31. The contraction parameter, h_{po} was calibrated using the single element direct simple shear tests, as per PM4Sand version 3 manual (Ziotopoulou and Boulanger, 2015). For comparison, the calibration was first performed using the examples in the PM4Sand manual. The primary input parameters, as shown in Table 4-22, were assigned in Analysis 4 and all of the secondary parameters were kept unchanged, i.e. default values of PM4Sand were used.

The non-liquefiable layers were modeled with Mohr-Coulomb parameters, as presented in Table 4-8. The “puddled” central core strength was modeled as $S_u/\sigma'_{vi} = 0.192$ during shaking, representing a 20% reduction from the peak static strength of $S_u/\sigma'_{vi} = 0.24$ to account for both (1) cyclic softening, and (2) strain softening.

Table 4-31: Input Parameters for LSFD Analysis 4 using the PM4Sand model parameterized to match with the with Boulanger and Idriss (2014) liquefaction triggering

PM4Sand Manual /LSFD	Soil Layer	Input Parameter for PM4Sand Calibration					Output from PM4Sand Calibration (Number of Cycles)		
		$N_{1,60,CS}$	$CRR_{Mw=7.5}$ (Boulanger and Idriss, 2014)	Relative Density, D_R	Shear Modulus Coefficient, G_0	Contraction Rate Parameter, h_{po}	98% _ru	1% _strain	3% _strain
PM4Sand Manual Table 4.1		6	0.092	0.36	486.9	0.53	14.5	14.0	15
		14	0.147	0.55	677.0	0.40	13.0	13.0	15
		26	0.312	0.75	890.0	0.63	17.5	11.5	14.5
LSFD (Boulanger and Idriss 2014 Triggering)	HFU-1 and HFD-1	18.4	0.188	0.632	763.4	0.38	14	13	15
	HFU-2 and HFD-2	15.7	0.162	0.584	712.4	0.39	14	13.5	15
	HFU-3 and HFD-3	22.8	0.246	0.704	840.0	0.45	14	14	15
	HFU-4 and HFD-4	14.5	0.152	0.561	688.6	0.40	14.5	14	15

The protocol for the PM4Sand analyses performed as part of these current studies is to handle the potential transition to post-liquefaction residual strength (S_r) in elements comprised of potentially liquefiable soils within the PM4Sand framework by considering the

analysis to progress in two steps or stages (1) during shaking, and (2) after the end of shaking. During shaking, there is no implementation of S_r . After the end of shaking, S_r is applied within potentially liquefiable soil elements that satisfy either of two criteria: (1) occurrence of $R_{u,seis} \geq 0.7$ at any stage during shaking ($R_{u,seis,max} \geq 0.7$) or (2) development of a peak shear strain of $\gamma \geq 10\%$ at the end of shaking in saturated materials. The PM4Sand protocol in these current studies is then to continue the nonlinear deformation analysis after the end of shaking until either (1) deformations and displacements have ceased to occur, as the embankment is in a stable condition, or (2) mesh distortions are resulting in a need to perform significant (and time-consuming) re-meshing to continue the NDA deformation analysis, and the results at termination have become sufficient for purposes of engineering interpretation and decision-making, with recognition that deformations and displacements are still ongoing.

Similarly, it is also part of the PM4Sand protocol in these current studies to also examine non-liquefiable soils (e.g. the normally consolidated central clayey core zone) at the end of shaking, and to consider whether strength reduction (or further strength reduction) is warranted as a result of large shear strain development in sensitive cohesive soils.

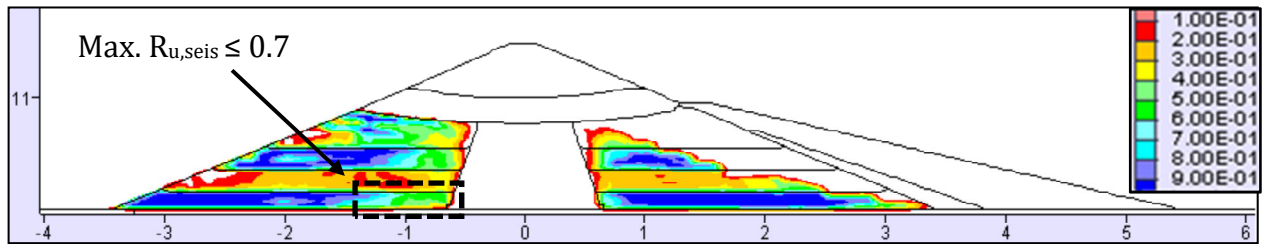
Figure 4-59 shows the results of Analysis 4 at the end of shaking, and Figure 4-60 shows the results of Analysis 4 at the end of analysis.

Figure 4-59(a) shows the maximum values of $R_{u,seis}$ achieved in each potentially liquefiable element at any time during shaking. As shown in this figure, significant seismically induced pore pressures occur in portions of the saturated upstream hydraulic fill shell zones (especially in HFU-2 and HFU-4), and in the saturated portions of the downstream side hydraulic fill shell zones (especially in HFD-2 and HFD-4). Despite these significant seismically induced pore pressures, and the seismic inertial forces of the earthquake, the resulting deformations and displacements at the end of shaking are small, as shown in Figures 4-59(b) and (c).

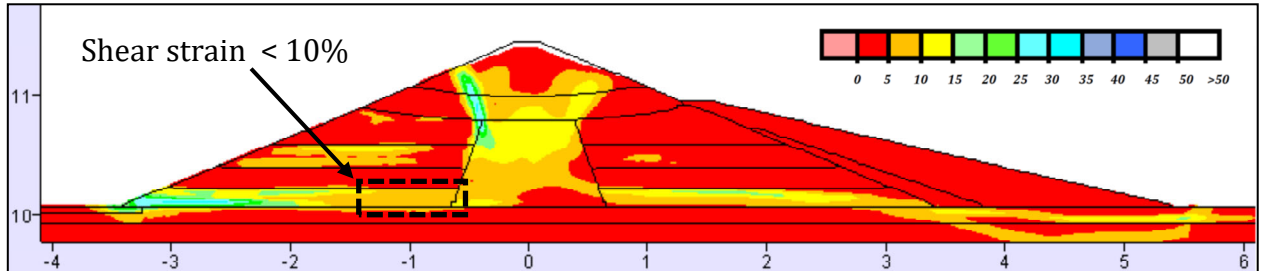
As per the analysis protocol for the constitutive models employed in these current studies, the analysis was temporarily halted at the end of shaking, and elements of potentially liquefiable soils that had achieved either (1) maximum cyclic pore pressure ratios of $R_{u,seis} \geq 0.7$, or (2) peak shear strain of $\gamma \geq 10\%$ at the end of shaking were transitioned to post-liquefaction strength (S_r).

Similarly, when the analysis was temporarily halted at the end of shaking, the shear strains and displacement offsets across narrowly banded shear zones within the “puddled” central clay core zone were also evaluated. As shown in Figure 4-59(b) shear the strains across the clay core were on the order of $\gamma \approx 7$ to 15%. At those levels of shear strain, it is unlikely but also somewhat uncertain whether or not significant further reduction in the shear strength of the clay core is necessary to account for additional strain softening.

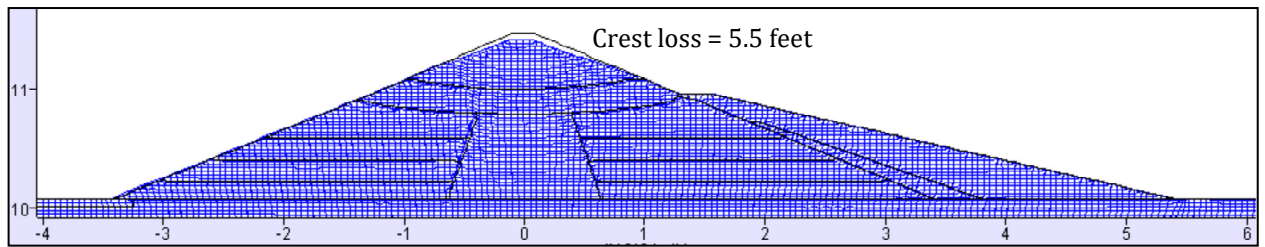
LSFD Analysis 4: PM4Sand model, with the Boulanger and Idriss (2014) Liquefaction Triggering Relationship, and Idriss and Boulanger (2015) S_r Relationship



(a) Maximum value of $R_{u,seismic}$ recorded in each element

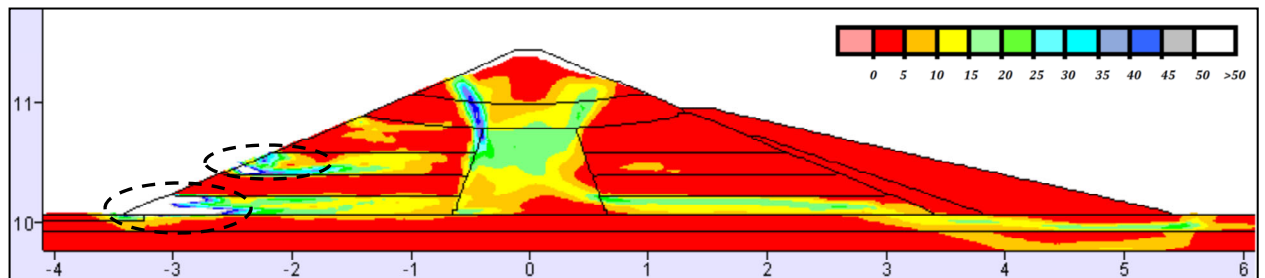


(b) Shear strain (percent), with the inset shear strain scale set to maximum of 50 percent

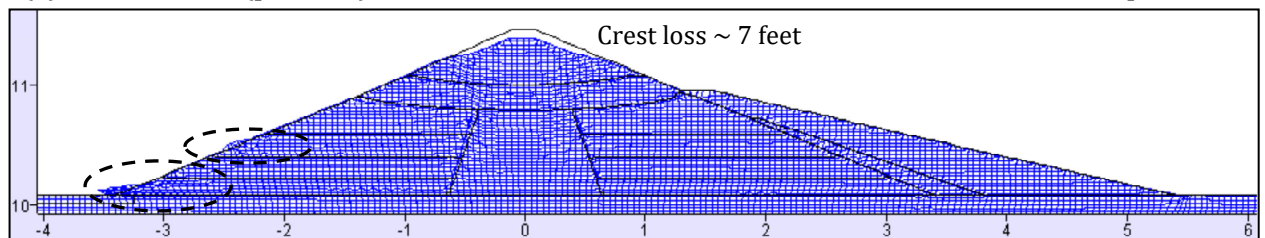


(c) Deformed mesh

Figure 4-59: Results of LSFD Analysis 4 at the end of shaking



(a) Shear strain (percent), with the inset shear strain scale set to maximum of 50 percent



(b) Deformed mesh

Figure 4-60: Results of LSFD Analysis 4 at the end of analysis

In these current analyses, if shear strains at the end of shaking across a clayey soil zone, or along a section of potential (or incipient) shear surface in clayey materials, are mainly greater than about 25%, especially if they are still progressing at the end of shaking, then further strength reduction to account for strain softening is implemented. If shear strains are mainly less than about 10 to 15% at the end of shaking, especially if deformations are slowing as shaking subsides, then additional strength reductions to account for strain softening are generally not implemented (a possible exception would be more “highly” sensitive clays).

In the range of shear strain between these two, engineering judgment (and possibly further analysis) is needed. There are several engineering options available here, and it was judged necessary for these current studies to develop a protocol for dealing with this issue. For these current studies, the following approaches are considered:

1. One approach can be to “try” a worst case scenario, to see if this issue may potentially have a significant effect on the engineering analysis results. This “hypothetical” approach involves continuing forward with analyses “after the end of shaking” by reducing the clay strength to a fully residual value of $S_{u,residual}/P = 0.08$, and then continuing the analysis forward to examine whether or not a reduction to fully residual clay strength significantly affects the overall analysis results. If the reduction to fully residual clay strength does not significantly change the analysis results, then the question is moot.
2. A second approach (more realistic) can be to reduce the clay strengths to a level intermediate between (1) the shear strengths used “during shaking” and (2) the fully residual shear strengths. In this case, the shear strength during shaking was modeled as $S_u/\sigma'_{v,i} = 0.192$ (representing a 20% reduction from the peak static strength of $S_u/\sigma'_{v,i} = 0.24$ in order to account for both cyclic softening and some strain softening). The fully residual (or steady state) strength is $S_{u,residual} = 0.08$. A strength mid-way between the already slightly softened “during analysis” shear strength and the fully residual (very large strain/displacement) strength would then be $S_u/\sigma'_{v,i} = (0.5)(0.192 + 0.08) = 0.136$. This shear strength can be implemented at the stoppage at the end of shaking, and the analysis can then be re-started and continue forward. If uncontrolled additional deformations and displacements continue to develop, then the analysis should at some point again be halted, and fully residual shear strength should be implemented and the analysis should again be continued forward. If only moderate additional deformations and displacements occur, and the deformation analysis stabilizes (not due to mesh-locking), then the final shear strains and shear offsets across any potential shear surfaces should be evaluated, and an engineering decision would need to be made as to whether or not to further reduce shear strengths to fully residual values based on shear strains (and shear displacement offsets across a narrow shear zone), and then again continue forward with the post-shaking analysis.

The largely normally consolidated puddled central clay core materials are “moderately sensitive”, with a sensitivity of $S_{u,residual} / S_{u,peak} = 3$. This is a fairly “typical” level

of strain sensitivity for clays, so this back-analysis may have useful lessons for other dams. For more highly sensitive clays, additional judgment may likely be required.

It was judged that these shear strains at the end of shaking (see Figure 4-59 (b)) which have maximum values of less than about 15% shear strain, are not sufficiently large as to warrant a reduction of clay core strength towards a fully residual value of $S_{u,residual}/\sigma'_{vi} = 0.08$. But it was also not clear that a reduction towards a somewhat lower shear strength was not warranted.

The approach taken was therefore to begin with Approach 2 above. The shear strengths of the central clay core were reduced to a value of $S_u/\sigma'_{vi} = 0.136$, which is halfway between (1) the already 20% softened value of $S_u/\sigma'_{vi} = 0.196$ and (2) the fully residual value of $S_{u,residual}/\sigma'_{vi} = 0.08$, and the analysis was then re-started. As shown in Figures 4-60(a) and (b) only minor additional displacements and deformations occurred (e.g. vertical crest loss increased from 5.0 ft. to 7.2 ft.), and the analysis was then terminated as the embankment became stable. It was judged that the additional shear strains developed across the central clay core did not warrant further reduction of clay core strengths to a fully residual value of $S_{u,residual}/\sigma'_{vi} = 0.08$.

Reduction of the puddled central clay core zone to a fully residual strength of $S_{u,residual}/\sigma'_{vi} = 0.08$ was not warranted. However, as a hypothetical worst case scenario for LSFD Analysis 4, the puddle clay core strength was then reduced to fully residual strength of clay, and the analysis was again re-started and carried forward. It added additional 1.8 feet of crest loss (e.g. crest loss increased from 7.2 feet to 9.0 feet) and the dam was again stable.

This LSFD Analysis 4 failed to correctly predict the occurrence of an upstream side flow failure, as actually occurred in the field during the 1971 earthquake.

Figure 4-59(a) shows a dashed rectangle near the base of the upstream side hydraulic fill (Layer HFU-4) near to the central puddled clay core. Cyclic pore pressures within this rectangle did not generate sufficiently high cyclic pore pressures to transition to post-liquefaction residual strength (S_r). The required criteria for transition to S_r would have been $R_{u,seis,max} \geq 0.7$. The soil elements within this rectangle also failed to mobilize shear strains of $\gamma \geq 10\%$, which is the other (second) criteria for transition to S_r . As a result, these elements did not transition to post-liquefaction strengths.

This resulted in a zone of non-liquefied soils adjacent to the core, at the base of the upstream hydraulic fill shell. The strength and stiffness of this zone served to inhibit the development of larger shear strains across the base of the upstream hydraulic fill by and acting as a “buttress” for the adjacent central clayey core zone, preventing the development of an upstream side instability failure.

The failure to generate sufficient cyclic pore pressures in the inboard portions of the lower layer of the upstream hydraulic fill shell materials (HFU-4) closest to the clayey core zone was not surprising, as the liquefaction triggering relationship of Boulanger and Idriss

(2014) is the least conservative of the three triggering relationships employed in these current studies. A discussion of this, and some of the reasons for potential lack of conservatism, can be found in Chapter 2, Section 2.3.

It should be noted that shallow sloughing occurred in toe areas of two of the upstream hydraulic fill shell zones (HFU-2 and HFU-4) in LSFD Analysis 2, as shown in the dashed ovals in Figures 4-60(a) and (b). These were localized features, and they did not retrogress inwards or upwards, and they produced no larger-scale instabilities.

Table 4-32 shows a summary and comparison of five selected key indices of (1) analytically “predicted” field performance vs. (2) actual observed field performance for LSFD Analysis 4. These five indices will be examined for all of the LSFD back-analyses performed as part of these studies. The matches with actual observed field behavior are very poor.

Overall, LSFD Analysis 4 provided very poor engineering predictions of the field behavior actually observed in the 1971 earthquake. These results would represent an unconservative engineering basis for “predicting” expected performance of the dam under this level of seismic loading, and also an unconservative basis for evaluation of downstream risk or hazard exposure.

Table 4-32: LSFD Analysis 4; Comparison between analysis results and actual observed field performance

	Analysis	Observed
1. Occurrence of U/S flow failure	No	Yes
2. Correct U/S failure plane/mechanism	No	(Yes)
3. Elev. of top of heel scarp feature	N/A	1,114 ft
4. Occurrence of D/S flow failure	No	No
5. Maximum D/S face lateral displacement	2.9 ft	~ 0.8 ft

4.8.5 LSFD Analysis 5: PM4Sand Model, with the Cetin et al. (2018) Liquefaction Triggering Relationship, the Youd et al. (2001) K_σ relationship, and the Weber et al. (2015) S_r Relationship

LSFD Analysis 5 largely repeats LSFD Analysis 4, but this time utilizes the Cetin et al. (2018) liquefaction triggering relationship, with the Youd et al. (2001) K_σ relationship (which is recommended for use with the Cetin et al. (2018) triggering relationship), to parameterize the PM4Sand model with regard to cyclic pore pressure generation, and employs the post-liquefaction residual strength (S_r) relationship of Weber et al. (2015). All

other modeling and analysis protocols are the same as those described previously in LSFD Analysis 4.

In this Analysis 5, the PM4Sand model is re-parametrized in such a way that it is expected to show soil behaviors consistent with the Cetin et al. (2018) liquefaction triggering relationship and the Youd et al. (2001) K_σ relationship, and behaviors at least generally consistent with the Idriss and Boulanger (2003) K_α relationship, when $N_{1,60,CS}$ values based on the energy, equipment, procedural and effective overburden stress corrections of Boulanger and Cetin et al. (2018) are used as a basis for parameterization.

The analysis specific input parameters for Analysis 5 are summarized in Table 4-33. The contraction parameter, h_{po} was calibrated in these current studies using single element direct simple shear tests, as per the PM4Sand version 3 manual (Ziotopoulou and Boulanger, 2015). For comparison, the calibration was first performed using the examples in the PM4Sand manual. The primary input parameters, as shown in Table 4-33, were assigned in Analysis 5 and all secondary parameters were kept unchanged, i.e. the default values of PM4Sand were used.

The PM4Sand model is used in the potentially liquefiable soils (which are the upstream and downstream hydraulic fill shell zones). Non-liquefiable soils (the central clayey core, the upper rolled fill, and the downstream berms, and the lower alluvium) are modeled using the FLAC Mohr-Coulomb model. The non-liquefiable layers were modeled

Table 4-33: Input parameters for LSFD Analysis 5, using the PM4Sand model calibrated with the Cetin et al. (2018) liquefaction triggering relationship, and the Youd et al. (2001) K_σ relationship

		Input Parameters for PM4Sand Calibration					Output from PM4Sand Calibration (Number of Cycles)		
		$N_{1,60,CS}$	$CRR_{Mw=7.5}$ (Cetin et al., 2018)	Relative Density, D_R	Shear Modulus Coefficient, G_0	Contraction Rate Parameter, h_{po}	98% _ru	1% _strain	3% _strain
PM4Sand Manual /LSFD	Soil Layer								
PM4Sand Manual Table 4.1		6	0.092	0.36	486.9	0.53	14.5	14.0	15
		14	0.147	0.55	677.0	0.40	13.0	13.0	15
		26	0.312	0.75	890.0	0.63	17.5	11.5	14.5
LSFD (Cetin et al. 2018)	HFU-1 HFD-1	16.6	0.119	0.617	729.8	0.15	14	13	15
	HFU-2 HFD-2	14.2	0.095	0.571	682.5	0.12	14	13.5	15
	HFU-3 HFD-3	19.5	0.141	0.669	783.3	0.23	14	14	15
	HFU-4 HFD-4	12.8	0.082	0.542	653.2	0.11	14.5	14	15

with Mohr-Coulomb parameters, as presented in Table 4-8. Shear strength of the semi-puddled central clay core was modeled as $S_u/\sigma'_{v,i} = 0.192$ during shaking in Analysis 5, which assumes approximately a 20% reduction of undrained shear strength (from peak static, or monotonic, shear strength of $S_u/\sigma'_{v,i} = 0.24$) for the normally consolidated clayey core to account for both (a) cyclic softening and (b) strain softening.

Figures 4-61 and 4-62 show the results of nonlinear seismic deformation analyses performed with the combination of models and relationships of LSFD Analysis 5. Figure 4-61 shows conditions at the end of shaking, and Figure 4-62 shows condition at the end of analysis.

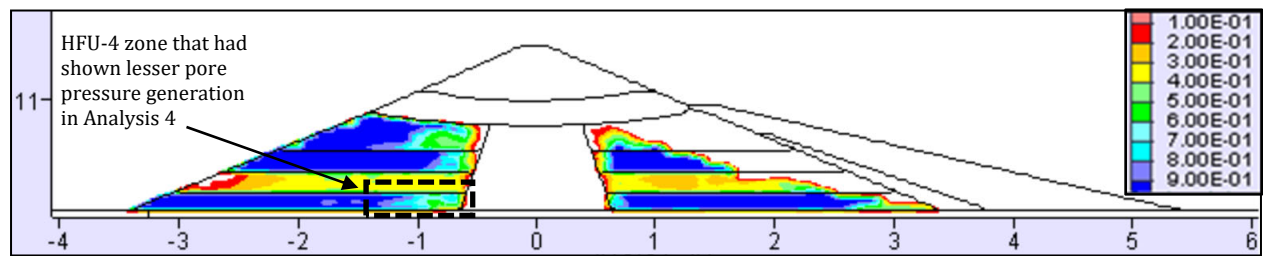
As shown on Figure 4-61(a), higher maximum pore pressure ratios developed in both the upstream and downstream hydraulic fill layers than had developed in Analysis 4 using the same PM4Sand constitutive model, due to the use of the Cetin et al. (2018) liquefaction triggering relationship in Analysis 5. The dashed box in Figure 4-61(a) indicates the zone of the lower layer of upstream hydraulic fill (HFU-4) adjacent and near to the clayey core that had failed to generate pore pressures with $R_{u,seis} \geq 0.7$, and shear strains of greater than 10% in the previous Analysis 4. In Analysis 4, slightly more than 90 percent of the elements in this box had failed to generate values of $R_{u,seis} \geq 0.7$. As shown in Figure 4-61(a), a nearly continuous zone of $R_{u,seis} \geq 0.7$ extends nearly all the way across to the core in this current Analysis 5. This eliminates the “buttressing” effect of a (stronger) non-liquefied hydraulic fill zone against the base of the upstream side of the central clay core that had helped to prevent development of an upstream side stability failure in Analysis 4.

As shown in Figures 4-61(b) and (c), this increase in cyclic pore pressure generation produced only slightly increased deformations and displacements at the end of shaking (vs. those of Analysis 4). The vertical crest loss at the end of shaking was 6.8 feet in Analysis 5 (vs. 5.5 feet in Analysis 4), and maximum shear strains across the puddled central clay core zone were approximately <10 percent to 18 percent in Analysis 5 (vs. <10 percent to 15 percent in Analysis 4). As discussed previously in Section 4.8.4 (LSFD Analysis 4), at these levels of shear strain there is no full certainty as to whether it is necessary or appropriate to further reduce shear strengths in the clay core zone to account for strain softening. But a majority of the potentially liquefiable soil elements of HFU-4 in this zone met or exceeded the criteria of $R_{u,seis} \geq 0.7$ or shear strain >10 percent in Analysis 5, and thus they met the criteria for transition to post-liquefaction strength (S_r) at the end of shaking.

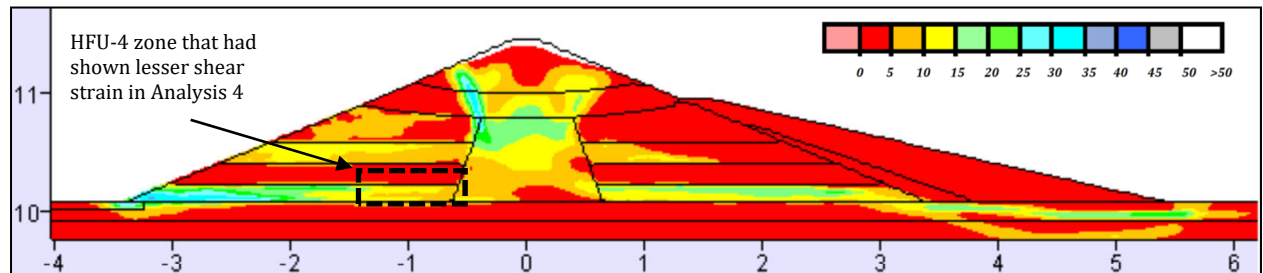
The post-shaking analyses for Analysis 5 were performed by transitioning to post-liquefaction residual strengths (S_r) in the potentially liquefiable soil elements which had (1) achieved $R_{u,seis} \geq 0.7$, or (2) development of a peak shear strain of $\gamma \geq 10\%$ at the end of shaking in saturated materials.

The protocol of Section 4.8.4 was used to examine whether the shear strengths in the clay core zone should be further reduced towards a more fully residual strength of $S_{u,residual}/\sigma'_{v,i} = 0.08$ for the post-shaking continuation of analysis. The shear strains across

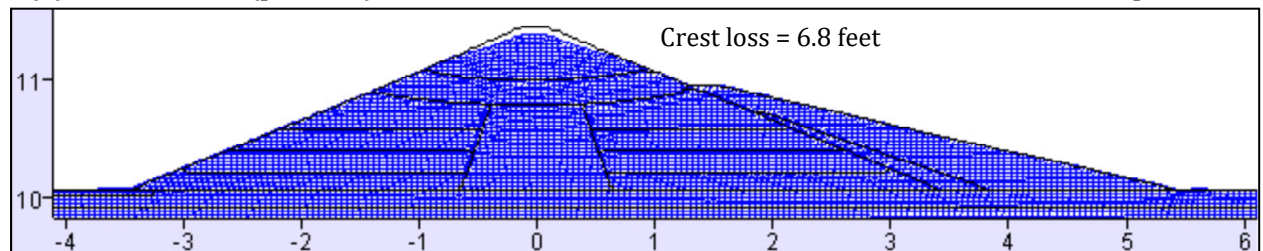
LSFD Analysis 5: PM4SAND model, with the Cetin et al. (2018) Liquefaction Triggering Relationship, and the Weber et al. (2015) S_r Relationship



(a) Maximum value of $R_{u, \text{seismic}}$ recorded in each element

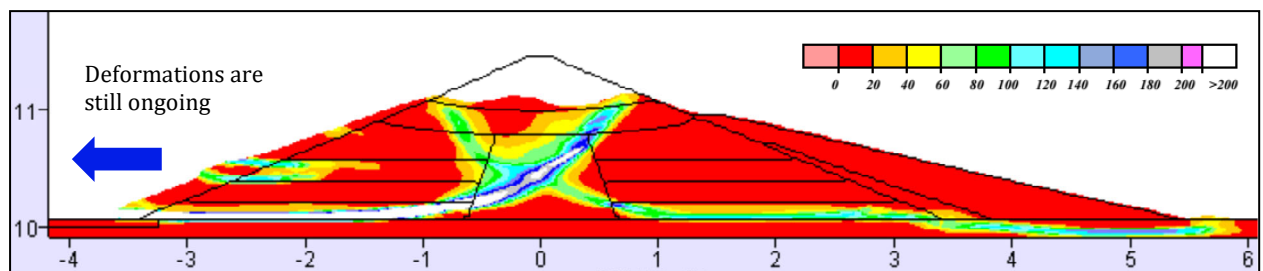


(b) Shear strain (percent), with the inset shear strain scale set to maximum of 50 percent

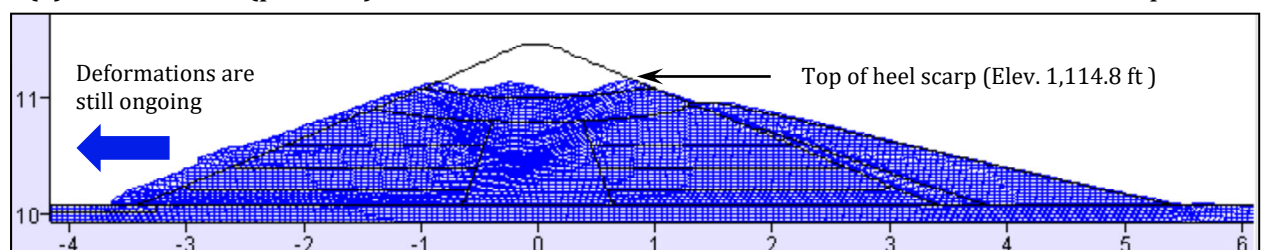


(c) Deformed mesh

Figure 4-61: Results of LSFD Analysis 5 at the end of shaking



(a) Shear strain (percent), with the inset shear strain scale set to maximum of 200 percent



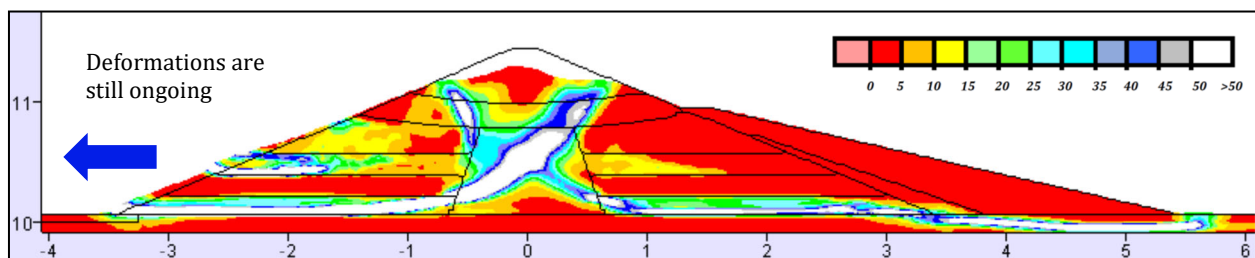
(b) Deformed mesh

Figure 4-62: Results of LSFD Analysis 5 at the end of analysis

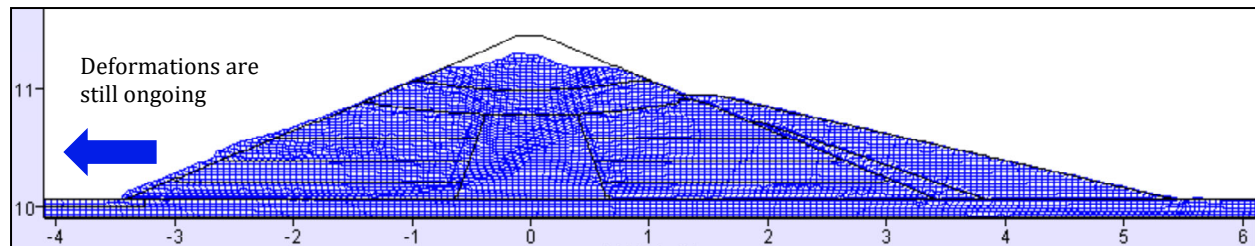
the central clay core were between $\sim 9\%$ to 18% along potential through-passing shear surfaces; again in a range where it was not certain whether or not further reduction in clay strengths to $S_{u,residual}/P = 0.08$ was warranted. An intermediate strength of $S_u/\sigma'_{vi} = 0.136$ was therefore implemented in the post-shaking analysis, along with post-liquefaction S_r in liquefied elements, and the analysis was re-started. This intermediate clay strength is taken as halfway between (1) the already softened strength of $S_u/\sigma'_{vi} = 0.192$ that was used during shaking to account for both cyclic softening and partial strain softening, and (2) the fully residual strength of $S_{u,residual}/\sigma'_{v,i} = 0.08$. The intermediate strength was therefore modeled as $S_u/\sigma'_{v,i} = (0.5) (0.192 + 0.08) = 0.136$.

With this transition to $S_u/\sigma'_{vi} = 0.136$, and the transition of liquefied elements to post-liquefaction S_r , the shear strains in the clay core increased significantly as the post-shaking analyses were continued, until a path across the clayey core zone with elements that exceeded 50 percent shear strains was created. At this point, the analysis was halted, and the fully residual clay core strength of $S_{u,residual}/\sigma'_{v,i} = 0.08$ was applied. With application of the $S_{u,residual}$ in the puddled central clay core, and the transition of liquefied soil elements to post-liquefaction residual strength (S_r), the upstream side potential (or incipient) failure surface continued to develop, and an upstream flow failure occurred.

Figure 4-63 shows the results of this “interim step” post-shaking continuation of analysis. As shown in Figures 4-63(a) and (b), additional post-shaking deformation and displacements continued to develop, and shear strains across the puddled central clay core continued to increase. The analysis was halted at the stage shown in Figure 4-63, and



(a) Shear strain (percent), with the inset shear strain scale set to maximum of 50 percent



(b) Deformed mesh

Figure 4-63: Results of LSFDA Analysis 5; analysis re-started at the end of shaking, employing shear strengths in the puddled central clay core that are intermediate between those employed during shaking, and fully residual clay strengths

shear strains and shear offsets across the central clay core zone were again evaluated. As shown in Figure 4-63, a path fully across the central clay core with shear strains greater than 50% was created and an additional assessment of shear strains and shear offset displacements led the analysis team to conclude that additional shear strength reduction was warranted because (1) the larger shear strains now warranted further reduction, and (2) shear strains were continuing to develop.

Figure 4-62 shows conditions at the end of analysis with both post-liquefaction residual strengths (S_r) applied and fully residual clay core shear strengths applied. The analysis was halted at the stage shown in Figure 4-62, in part because the engineering conclusions were clear at that point, and also because it was not possible to continue the analysis onwards through the full development of the very large final displacements actually observed.

Figure 4-64 repeats this end of analysis Figure 4-62, with annotation, and adds an additional Figure 4-64(c) showing displacement vectors.

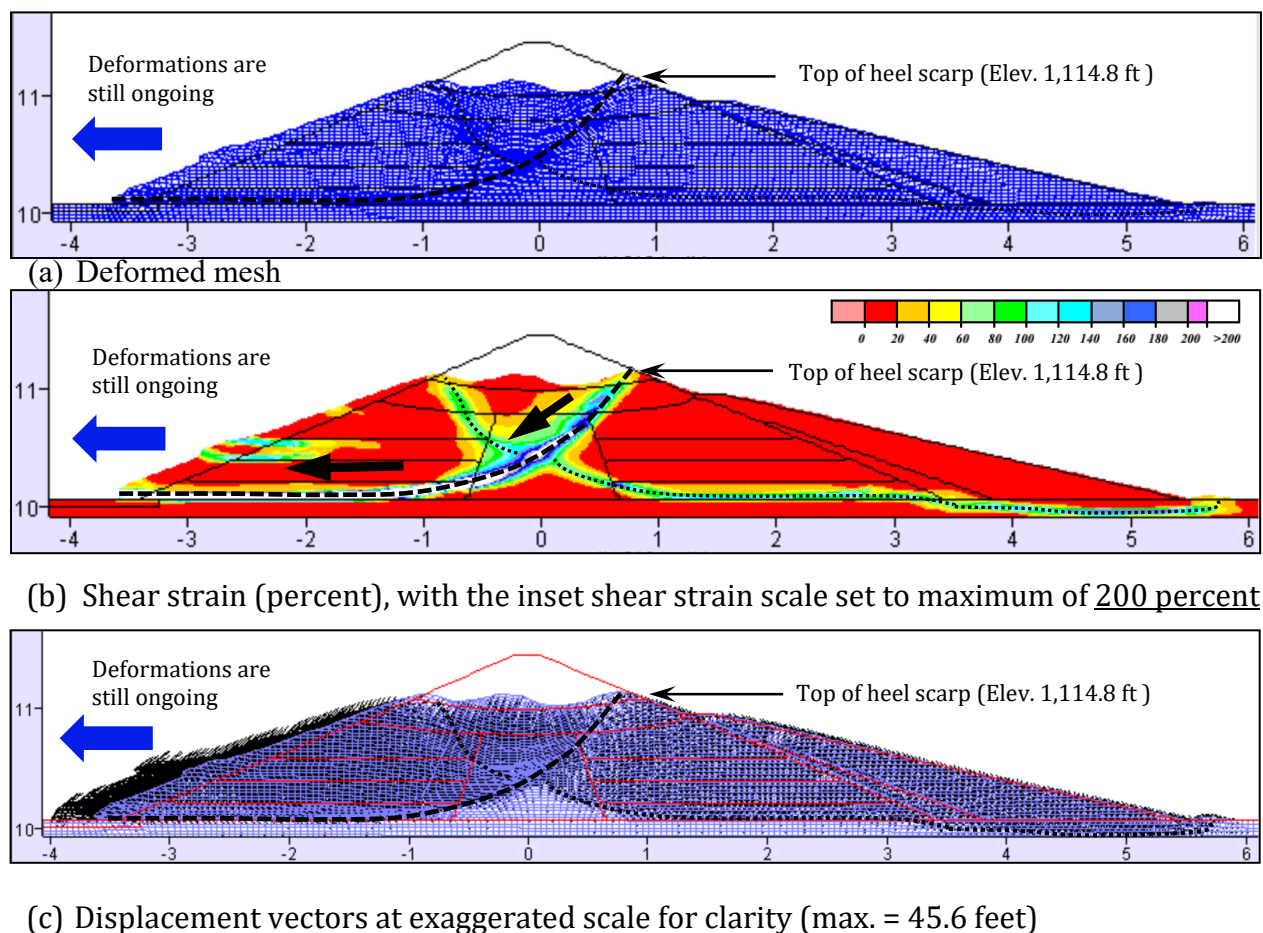


Figure 4-64: Results of LSFD Analysis 5 at the end of analysis; annotated

LSFD Analysis 5 correctly predicts the apparent mechanisms of distress and upstream failure, in good agreement with Analyses 1, 2, and 3. As shown in Figure 4-61(b), initially two incipient (potential) failure surfaces begin to form; one towards the upstream side, and one towards the downstream side.

As shown in Figures 4-63 and 4-64, the upstream side stability failure continues to develop, and becomes an uncontrolled upstream flow failure. This upstream side failure begins at the base of the upstream toe, traverses laterally across the base of the upstream hydraulic fill shell zone, then arcs upwards across the puddled central clay core to exit high on the upper portion of the downstream face.

The location and elevation of the “lip” of the upstream slide heel scarp feature is again very well predicted; it occurs at an elevation of 1,114.8 feet (vs. 1,114 feet actually observed in the field in the immediate aftermath of the 1971 earthquake). This “lip”, with appropriate considerations for likely transverse cracking, controlled the effective (useful) crest elevation and freeboard immediately after the earthquake.

Table 4-34 shows a summary and comparison of five selected key indices of (1) analytically “predicted” field performance vs. (2) actual observed field performance for LSFD Analysis 5. These five indices will be examined for all of the LSFD back-analyses performed as part of these studies. The matches with actual observed field performance, including the mechanisms of distress, and the magnitudes of movements, and the post-earthquake interim crest geometry (heel scarp) are very good, except that lateral displacements at the downstream toe are over-estimated. These analytical results would provide a good basis for evaluation of expected engineering performance in an earthquake of this severity, and they would also provide a good basis for evaluation of downstream risk and hazard exposure.

Table 4-34: LSFD Analysis 5; Comparison between analysis results and actual observed field performance

	Analysis	Observed
1. Occurrence of U/S flow failure	Yes	Yes
2. Correct U/S failure plane/mechanism	Yes	(Yes)
3. Elev. of top of heel scarp feature	1,114.8 ft	1,114 ft
4. Occurrence of D/S flow failure	No	No
5. Maximum D/S face lateral displacement	10.5 ft	~ 0.8 ft

4.8.6 LSFD Analysis 6: Wang2D Model, with the Cetin et al. (2018) Liquefaction Triggering Relationship, and the Weber et al. (2015) S_r Relationship

LSFD Analysis 6 utilizes the Wang2D plasticity model, parameterized to match the Cetin et al. (2018) liquefaction triggering relationship, the Youd et al. (2001) K_σ relationship, which is recommended in conjunction with the Cetin et al. triggering relationship, and the Idriss and Boulanger (2003) K_α relationship. Post-liquefaction residual strengths (S_r) are determined in Analysis 6 using the S_r relationship of Weber et al. (2015). The Wang2D model is used in all potentially liquefiable soils.

The Wang2D model is parametrized in such a way that it is expected to show soil behaviors consistent with Cetin et al. (2018) liquefaction triggering, Youd et al. (2001) K_σ , and Idriss and Boulanger (2003) K_α , when model parameters are developed in accordance with the calibration protocol of the Wang2D model for the potentially liquefiable layers. Wang and Ma (2018) developed and refined both the model, and the parameterization procedures, to be in good agreement with the above-referenced relationships, and also in good agreement with the cyclic DSS database of Wu and Kammerer (Wu, 2003). Wang and Ma calculated both K_α and K_σ behaviors for different initial effective stress ($\sigma'_{v,i}$) and K_α conditions and found that K_α behaviors in Wang2D generally match well with the (1) Cetin et al. (2018) liquefaction triggering and cyclic pore pressure generation, (2) Youd et al. (2001) K_σ , (3) the K_α relationship of Idriss and Boulanger (2003), and (4) the behaviors exhibited in the undrained cyclic DSS tests of Wu and Kammerer.

Wang2D model parameters for these current studies were developed using the calibration file provided by Dr. Fenggang Ma (personal communication, 2016) (also available in Itasca-UDM site), and in general accordance with the procedures described in Wang and Ma (2018). The analysis specific input parameters are summarized in Tables 4-35(a) and (b).

The Wang2D model is used in potentially liquefiable soils (which are the saturated semi-hydraulic fill shell zones). Non-liquefiable soils (the central clayey core, the upper rolled fill, and the upper and lower alluvium) are modeled using the FLAC Mohr-Coulomb model. The non-liquefiable layers were modeled with Mohr-Coulomb parameters, as presented in Table 4-8. Shear strength of the semi-puddled central clay core was modeled as $S_u/\sigma'_{vi} = 0.192$ throughout during shaking analysis of LSFD Analysis 6, which assumes approximately a 20% reduction of undrained shear strength (from peak static, or monotonic, shear strength of $S_u/\sigma'_{vi} = 0.24$) for the normally consolidated clayey core to account for both (a) cyclic softening and (b) strain softening.

The protocol for the Wang2D analyses performed as part of these current studies is to handle the potential transition to post-liquefaction residual strength (S_r) in elements comprised of potentially liquefiable soils within the framework of considering the analysis to progress in two steps or stages: (1) during shaking, and (2) after the end of shaking. During shaking, there is an option to utilize S_r above a user-specified $R_{u,seis}$ level. In these current studies, an $R_{u,seis}$ value of 0.85 was used for S_r application during shaking. As a result, the elements utilized S_r after they achieved $R_{u,seis}$ greater than 0.85. After the end of shaking,

Table 4-35(a): Input Parameters for the WANG2D-Sr Model

Soil Layer	Relative Density, D_R (%)	Void Ratio, e	Friction Angle, ϕ'	Poisson Ratio, ν	Elastic Shear Modulus Coefficient, G_0
HFU-1	64.1	0.53	35	0.35	281.4
HFU-2	59.3	0.55	34	0.35	276.7
HFU-3	69.5	0.50	36	0.35	285.0
HFU-4	56.3	0.57	33	0.35	273..6
HFD-1	64.1	0.53	35	0.35	281.4
HFD-2	59.3	0.55	34	0.35	276.7
HFD-3	69.5	0.50	36	0.35	285.0
HFD-4	56.3	0.57	33	0.35	273..6
<ul style="list-style-type: none"> • D_R: Relative density measured using $N_{1,60,CS}$ (Cetin et al. 2018) and $C_d=40.4$ • $e = e_{max} - (e_{max}-e_{min})*D_R$ with $e_{max}-e_{min}=0.5$ for Silty Sand • $\phi' =$ Table 4-8 using Hatanaka and Uchida (1997) and Cetin et al. (2018) corrected SPT $N_{1,60,CS}$ • G_0: Calculated using $G_{max} = p_a G_0 \frac{(2.973-e)^2}{1+e} \sqrt{\frac{p}{p_a}}$ and • $G_{max} = 1000K_{2max}p^{0.5}$, where p is mean effective stress, G_{max} is in psf and K_{2max} are in Table 4-9 					

S_r is applied within potentially liquefiable soil elements that satisfy either of two criteria: (1) occurrence of $R_{u,seis} \geq 0.7$ at any stage during shaking ($R_{u,seis,max} \geq 0.7$) or (2) development of a peak shear strain of $\gamma \geq 10\%$ at the end of shaking in saturated materials. The protocol is then to continue the nonlinear deformation analysis after the end of shaking until either (1) deformations and displacements have ceased to occur, as the embankment is in a stable condition, or (2) mesh distortions are resulting in a need to perform significant (and time-consuming) re-meshing to continue the NDA deformation analysis, and the results at termination have become sufficient for purposes of engineering interpretation and decision-making, with recognition that deformations and displacements are still ongoing.

Similarly, it is also part of the Wang2D protocol in these current studies to also examine non-liquefiable soils (e.g. the normally consolidated central clayey core zone) at the end of shaking, and to consider whether strength reduction (or further strength reduction) is warranted as a result of large shear strain development in sensitive cohesive soils.

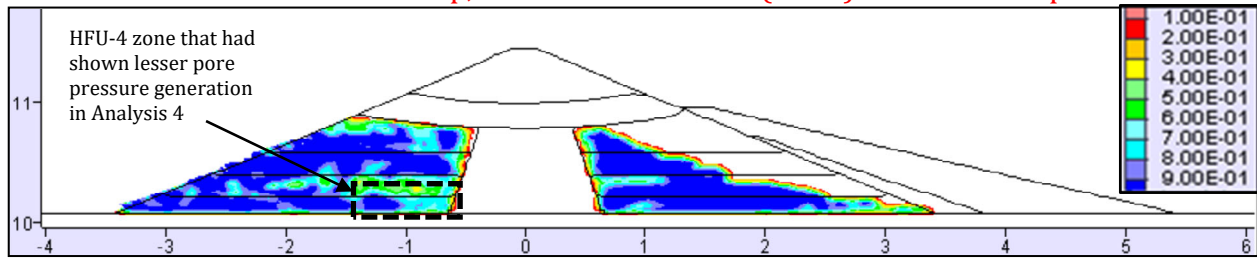
Figures 4-65 and 4-66 present the results of nonlinear seismic deformation analyses performed with the combination of models and relationships of LSFD Analysis 6. Figure 4-65 shows conditions calculated “at the end of shaking”, but the analyses are continued after the end of input seismic excitation, as deformations can continue after the end of shaking due to ongoing deformations under static (gravity loading).

Table 4-35(b): Input Parameters for the Wang2D Model

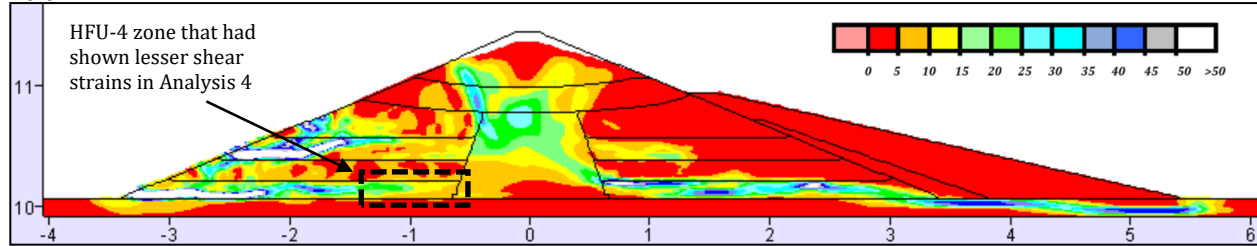
Soil Layer	kr	b	γ	η	Plastic Shear Modulus Coefficient, hr	d	Phase Transformation Ratio, $f_p (=R_p/R_f)$	Ru for Sr Application During Shaking
HFU-1	0.3	2	27.9	10.9	0.28	4.0	0.75	0.85
HFU-2	0.3	2	24.5	9.9	0.26	3.2	0.80	0.85
HFU-3	0.3	2	31.3	11.9	0.22	5.8	0.75	0.85
HFU-4	0.3	2	22.7	9.3	0.20	2.7	0.80	0.85
HFD-1	0.3	2	27.9	10.9	0.26	4.1	0.75	0.85
HFD-2	0.3	2	24.5	9.9	0.22	3.2	0.80	0.85
HFD-3	0.3	2	31.3	11.9	0.18	5.8	0.75	0.85
HFD-4	0.3	2	22.7	9.3	0.16	2.9	0.80	0.85

- **d**: Coefficient that controls the development of excess pore pressure due to cyclic loading under undrained conditions (or shear-induced volumetric change under drained condition). It was developed for each layer by calibrating the DSS single element tests to match CSR vs. N_{cyc} using Cetin et al. (2018) liquefaction triggering relationships and N_{cyc} based on Idriss (1999).
- **hr**: Plastic shear modulus coefficient. It was developed using Wang2D-Sr modulus reduction relationship by Wang and Ma (2018) for each layer using mean initial effective stress at the middle of the layer, G_{max} and strength parameters. The hr parameter is calibrated to match with established modulus reduction relationships. In the current studies, both Seed and Idriss (1970) and Darendeli (2001) with Yee et al. (2013) strength adjustments relationships were utilized.
- **$f_p (=R_p/R_f)$** : Phase transformation line is the ratio of the phase transformation line and failure line from laboratory tests. In the current studies, $R_p/R_f=0.8$ was used for $Dr \leq 60$ percent and $R_p/R_f=0.75$ was used for $Dr > 60$ based on an evaluation of Wu et al. (2003).
- **gamma**: Defines the plastic shear modulus reduction due to accumulation of strains. It impacts the post-liquefaction behavior during earthquake analysis. Used $\gamma = (2/3) * Dr(\%) - 15$.
- **ita**: Defines the plastic bulk modulus reduction due to accumulation of strains. It impacts the post-liquefaction behavior during earthquake analysis. Used $ita = (1/5) * Dr(\%) - 2$.
- **Ru**: Defines excess pore pressure ratio ($R_{u,seis}$), at which post-liquefaction strength values are used as an instantaneous strength. The strength is not capped at S_r , rather acts as an instantaneous strength for Ru values greater than or equal to a user-defined value. In the current studies, considering that post-earthquake stage applies S_r at elements with $Ru \geq 0.7$ to check for deformations that were not realized from earthquake analysis, a slightly higher Ru (≥ 0.85) was utilized in earthquake analysis for Sr application.

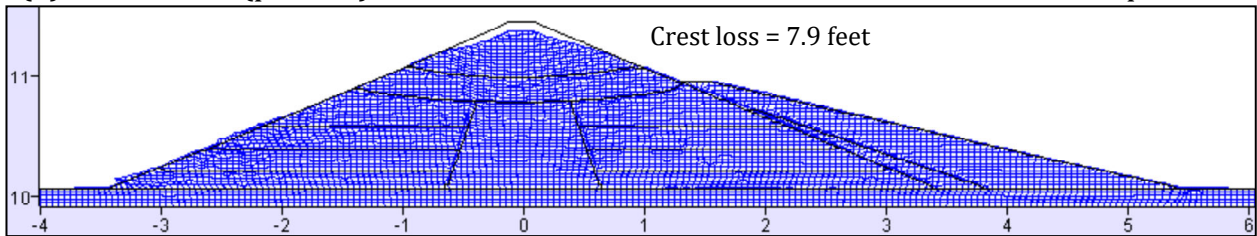
LSFD Analysis 6: Wang2D model, with the Cetin et al. (2018) Liquefaction Triggering Relationship, and the Weber et al. (2015) S_r Relationship



(a) Maximum value of $R_{u, \text{seismic}}$ recorded in each element

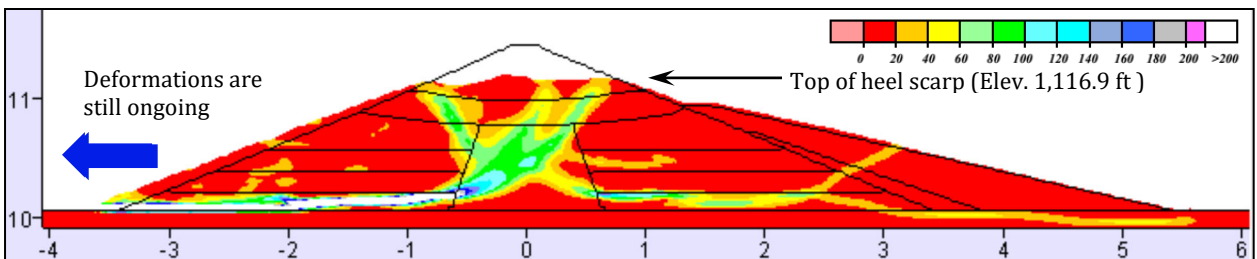


(b) Shear strain (percent), with the inset shear strain scale set to maximum of 50 percent

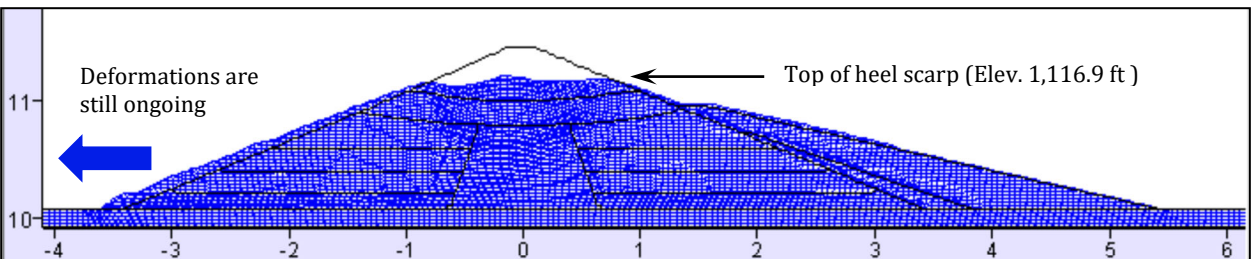


(c) Deformed mesh

Figure 4-65: Results of LSFD Analysis 6 at the end of shaking



(a) Shear strain (percent), with the inset shear strain scale set to maximum of 200 percent



(b) Deformed mesh

Figure 4-66: Results of LSFD Analysis 6 at the end of analysis

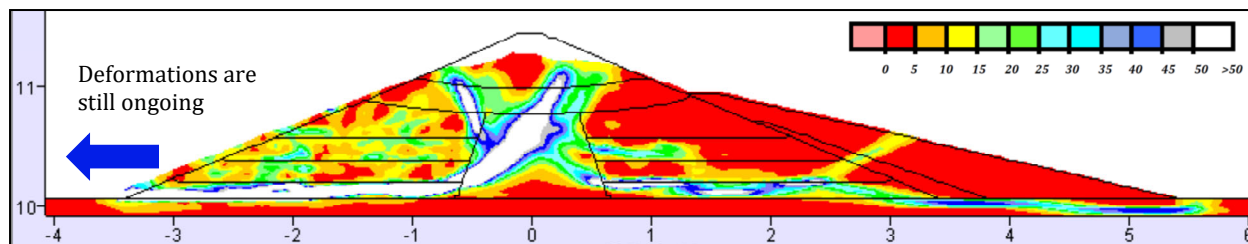
As shown in Figure 4-65(a) significant seismically induced pore pressures occur in saturated zones of both the upstream and downstream hydraulic fill shells.

As shown in Figures 4-65(b) and (c), this increase in cyclic pore pressure generation produced only slightly increased deformations and displacements at the end of shaking (vs. those of Analyses 4 and 5). The vertical crest loss at the end of shaking was 7.9 feet in Analysis 6 (vs. 5.5 feet, and 6.8 feet, in Analyses 4 and 5 respectively), and maximum shear strains across the puddled central clay core zone were approximately 14 to 32 percent (vs. approximately 9 to 18 percent in Analysis 5, and approximately 7 to 15 percent in Analysis 4). As discussed previously in Section 4.8.4 (LSFD Analysis 4), at these levels of shear strain there is no full certainty as to whether it is necessary or appropriate to further reduce shear strengths in the clay core zone to account for strain softening.

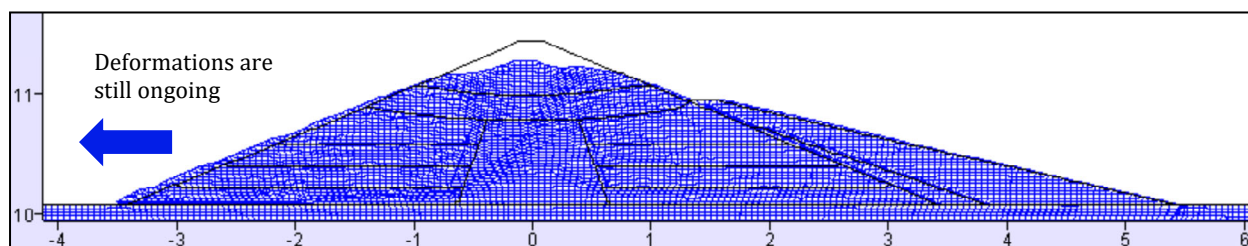
The post-shaking analyses for Analysis 6 were performed by transitioning to post-liquefaction residual strengths (S_r) in the potentially liquefiable soil elements which had achieved either (1) $R_{u,seis} \geq 0.7$, or (2) shear strain of $\gamma \geq 10\%$ at any time during shaking.

The protocol of Section 4.8.4 was then used to examine whether the shear strengths in the clay core zone should be further reduced towards a more fully residual strength of $S_{u,residual}/\sigma'_{vi} = 0.08$ for the post-shaking continuation of analysis. Because the observed end of analysis shear strains across the central clay core were in the indeterminate range, an intermediate strength of $S_u/\sigma'_{vi} = 0.136$ was implemented for the post-shaking strength along with S_r in liquefied elements, and the analysis was then re-started. This intermediate strength is taken as the half of initial softened strength ($S_u/\sigma'_{vi} = 0.192$) and fully residual strength of clay ($S_u/\sigma'_{vi} = 0.136$) [$S_u/\sigma'_{vi} = (0.5) (0.192 + 0.08) = 0.136$]. With this transition to $S_u/\sigma'_{vi} = 0.136$, and the transition to S_r in liquefied elements, the shear strains in clay core continued to increase and exceeded 50 percent shear strains. At this point, the analysis was again halted, and fully residual strength of $S_{u,residual}/\sigma'_{vi} = 0.08$ was applied in the central clay core, and then the analysis was again re-started. The upstream side potential (or incipient) failure surface continued to develop, and an upstream flow failure occurred.

Figure 4-67 shows the results of this “interim step” post-shaking continuation of analysis. As shown in Figures 4-67(a) and (b), additional post-shaking deformation and displacements continued to develop, and shear strains across the puddled central clay core zone continued to increase. The analysis was halted at the stage shown in Figure 4-67, and an additional assessment of shear strains and shear offset displacements across the central clayey core zone led the analysis team to conclude that additional shear strength reduction was warranted because (1) the larger shear strains now warranted further reduction, and (2) shear strains were continuing to develop. These shear strains, and the shear displacements across the narrowly banded shear zone across the clay core, clearly warranted a further reduction to a fully residual shear strength of $S_{u,residual}/\sigma'_{v,i} = 0.08$, as shown in Figure 4-67. This further reduction in clay strengths was implemented, and the analysis was again re-started.



(a) Shear strain (percent), with the inset shear strain scale set to maximum of 50 percent



(b) Deformed mesh

Figure 4-67: Results of LSFD Analysis 6; hypothetical analysis re-started at the end of shaking, and employing shear strengths in the puddled central clay core that are intermediate between those employed during shaking, and fully residual clay strengths

Figure 4-66 shows conditions at the end of analysis. The analysis was terminated at this juncture because re-meshing was becoming less effective, and the engineering interpretation was already clear. The blue arrows in Figure 4-66 again indicate that deformations and displacements were still ongoing when the analysis was terminated.

Figure 4-68 repeats this “end of analysis” Figure 4-66, with annotation, and adds an additional Figure 4-66(c) showing displacement vectors.

LSFD Analysis 6 correctly predicts the apparent mechanisms of distress and upstream failure, in good agreement with Analyses 1, 3, and 5, and in good agreement with observed field performance during the 1971 San Fernando earthquake. As shown in Figure 4-61(b), once again two incipient (potential) failure surfaces begin to form; one towards the upstream side, and one towards the downstream side.

As shown in Figures 4-65 and 4-66, the upstream side stability failure continues to develop, and becomes an uncontrolled upstream flow failure. This upstream side failure begins at the base of the upstream toe, traverses laterally across the base of the upstream hydraulic fill shell zone, then arcs upwards across the puddled central clay core to exit high on the upper portion of the downstream face

The location and elevation of the “lip” of the upstream slide heel scarp feature is again very well predicted; it occurs at an elevation of 1,116.9 feet (vs. 1,114 feet actually observed in the field in the immediate aftermath of the 1971 earthquake). This “lip”, with appropriate

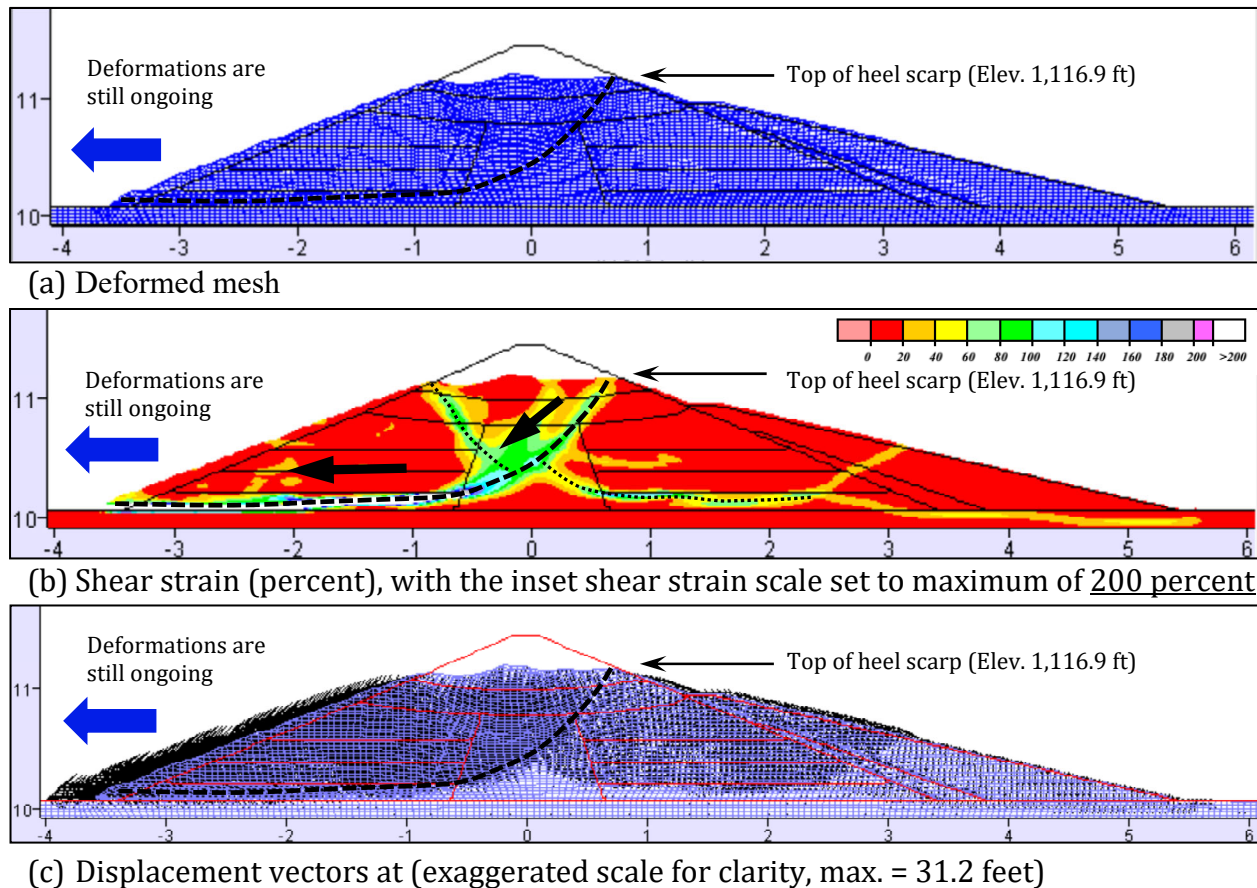


Figure 4-68: Results of LSFD Analysis 6 at the end of analysis; annotated

considerations for likely transverse cracking, controlled the effective (useful) crest elevation and freeboard immediately after the earthquake.

Table 4-36 shows a summary and comparison of five selected key indices of (1) analytically “predicted” field performance vs. (2) actual observed field performance for LSFD Analysis 6. These five indices will be examined for all of the LSFD back-analyses performed as part of these studies. The matches with actual observed field performance, including the mechanisms of distress, and the magnitudes of movements, and the post-earthquake interim crest geometry (heel scarp) are very good.

Overall, LSFD Analysis 6 provided very good engineering predictions of the principal mechanisms of dam distress and deformation, and with very good matching of the magnitudes of actual displacements, as well as the location (elevation) of the top lip of the upstream slide scarp feature that controlled available useful freeboard (with considerations of likely transverse cracking) in the immediate aftermath of the earthquake. These are excellent results, and they would represent a very good engineering basis for “predicting” expected performance of the dam under this level of seismic loading, and also a good basis for evaluation of downstream risk or hazard exposure.

Table 4-36: LSFD Analysis 6; Comparison between analysis results and actual observed field performance

	Analysis	Observed
1. Occurrence of U/S flow failure	Yes	Yes
2. Correct U/S failure plane/mechanism	Yes	(Yes)
3. Elev. of top of heel scarp feature	1,116.9 ft	1,114 ft
4. Occurrence of D/S flow failure	No	No
5. Maximum D/S face lateral displacement	6.6 ft	~ 0.8 ft

4.9 SUMMARY AND CONCLUSIONS

Six nonlinear seismic deformation analyses were performed as back-analyses of the performance of the LSFD in the 1971 San Fernando Dam earthquake. Table 4-37 presents a summary of five selected indices of the relative matches between each of the analytical results vs. the actual observed field behavior. The combinations of analytical models and engineering relationships employed in each of the six analyses are listed in Table 4-1, and are repeated in Table 4-25. Individual results for each analysis, including figures showing cyclic pore pressure generation, shear strains, deformed meshes at various stages of analysis, displacement vectors, inferred concentrated shear strain zones (and inferred incipient and also well-developed shear failure surfaces), etc. are presented and discussed in detail in Sections 4.8.1 through 4.8.6.

Four of these nonlinear seismic deformation analyses were successful (LSFD Analyses 1, 3, 5, and 6); producing good matches with the observed field behavior, including principal mechanisms of deformation, and details such as the elevation of the “lip” of the heel scarp of the upstream flow failure, which (with allowance for likely transverse cracking) represented the remaining crest, and freeboard, in the immediate aftermath of the earthquake.

One analysis (LSFD Analysis 4) was unsuccessful, and failed to predict the upstream side liquefaction-induced flow failure that actually occurred.

And one analysis (LSFD Analysis 2) was moderately unsuccessful; predicting the upstream side flow failure, but (1) over-estimating lateral deformations and displacements towards the downstream side, and (2) predicting a final elevation of the “lip” of the upstream flow slide heel scarp that (with appropriate allowance for expected transverse cracking) defined the useful (or effective) dam crest and freeboard in the immediate aftermath of the earthquake at too low an elevation (1,108 feet as calculated vs. 1,114 feet actually observed).

Table 4-37: Summary comparisons between analytical results and observed field behavior during the 1971 San Fernando earthquake.

Analysis ID and Key Comparison Items	Analysis	Observed
LSFD Analysis 1: Roth Model – Cetin et al. (2018) liquef. trig. and Weber et al. (2015) S_r		
1. Occurrence of U/S flow failure	Yes	Yes
2. Correct U/S failure plane/mechanism	Yes	(Yes)
3. Elev. of top of heel scarp feature	1,114.5 ft	1,114 ft
4. Occurrence of D/S flow failure	No	No
5. Maximum D/S face lateral displacement	6.1 ft	~ 0.8 ft
LSFD Analysis 2: UBCSAND model – Youd et al. (2001) liquef. trig. and Seed and Harder (1990) S_r		
1. Occurrence of U/S flow failure	Yes	Yes
2. Correct U/S failure plane/mechanism	Yes	(Yes)
3. Elev. of top of heel scarp feature	1,107.7 ft	1,114 ft
4. Occurrence of D/S flow failure	Yes/No*	No
5. Maximum D/S face lateral displacement	21.6 ft	~ 0.8 ft
*A downstream side slippage initiates, but is slowed when the upstream side flow failure cuts off the upper driving mass of the central crest region and carries it to the upstream side		
LSFD Analysis 3: UBCSAND model – Youd et al. (2001) liquef. trig. and Weber et al. (2015) S_r		
1. Occurrence of U/S flow failure	Yes	Yes
2. Correct U/S failure plane/mechanism	Yes	(Yes)
3. Elev. of top of heel scarp feature	1,114.6 ft	1,114 ft
4. Occurrence of D/S flow failure	No	No
5. Maximum D/S face lateral displacement	9.0 ft	~ 0.8 ft
LSFD Analysis 4: PM4Sand model – Boulanger and Idriss (2014) liq. trig. and Idriss and Boulanger (2015) S_r		
1. Occurrence of U/S flow failure	No	Yes
2. Correct U/S failure plane/mechanism	No	(Yes)
3. Elev. of top of heel scarp feature	N/A	1,114 ft
4. Occurrence of D/S flow failure	No	No
5. Maximum D/S face lateral displacement	2.9 ft	~ 0.8 ft

Analysis ID and Key Comparison Items	Analysis	Observed
LSFD Analysis 5: PM4Sand model - Cetin et al. (2018) liquef. trig. and Weber et al. (2015) S _r		
1. Occurrence of U/S flow failure	Yes	Yes
2. Correct U/S failure plane/mechanism	Yes	(Yes)
3. Elev. of top of heel scarp feature	1,114.8 ft	1,114 ft
4. Occurrence of D/S flow failure	No	No
5. Maximum D/S face lateral displacement	10.5 ft	~ 0.8 ft
LSFD Analysis 6: Cetin et al. (2018) liquef. triggering. and Weber et al. (2015) S _r		
1. Occurrence of U/S flow failure	Yes	Yes
2. Correct U/S failure plane/mechanism	Yes	(Yes)
3. Elev. of top of heel scarp feature	1,116.9 ft	1,114 ft
4. Occurrence of D/S flow failure	No	No
5. Maximum D/S face lateral displacement	6.6 ft	~ 0.8 ft

All six analyses predicted the early development of incipient, or potential, shear failure surfaces towards both the upstream and downstream sides of the dam. These were relatively symmetrical with each other (with allowances for different details in embankment and foundation geometry and stratigraphy). The upstream side feature began at the upstream toe, passed along near the base of the upstream hydraulic fill shell zone, and then arced upwards across the core to exit high on the upper portion of the downstream face of the dam. The downstream side feature was similar, beginning at the downstream toe, passing laterally nearly along the base of the downstream side hydraulic fill shell zone, and then arcing upwards across the core to exit high on the upper portion of the upstream face of the dam.

In the four successful analyses (LSFD Analyses 1, 3, 5, and 6), the upstream side feature continued to develop, and became an uncontrolled upstream slope stability failure (flow failure), and the downstream side incipient or potential shear stability feature did not develop; the downstream side deformations and displacements remained small. This matched well with the actual observed behavior. The analytical match with observed field performance was also very good with in these four analyses with regard to their predictions of the elevation of the “lip” of the upstream slide heel scarp feature that would control effective crest elevation (and freeboard) in the immediate aftermath of the earthquake; all four of these analyses predicted the elevation of the top of this “lip” feature with an accuracy of +/- 1.5 feet or better. As shown in Table 4-37, the accuracy of these four analytical “predictions” was very good. Analyses 1, 3, 5 and 6 predicted the top of this scarp lip at elevations of 1,114.5 ft, 1,114.6 ft, 1,114.8 ft. and 1,116.9 ft., respectively (vs. 1,114 ft. actually observed).

Analysis 3 was unsuccessful. This analysis employed the PM4Sand model, calibrated with the Boulanger and Idriss (2014) liquefaction triggering relationship with regard to cyclic pore pressure generation behavior, and it used the Idriss and Boulanger (2015) post-liquefaction residual strength (S_r) relationship. The inability to successfully predict the occurrence of the upstream flow failure (which actually occurred in the field) was mainly due to the lack of pore pressure generation in the lowest level of the upstream hydraulic fill “shell” zone at locations adjacent and near to the central clay core; as shown in Figure 4-59. This left a zone of higher strength materials adjacent at the upstream base of the core that “buttressed” the core and prevented the full development of the upstream flow failure that actually occurred. As discussed in Chapter 2, Section 2.3, this liquefaction triggering relationship is the least conservative of the three triggering relationships used in these current studies: it has three known errors in its derivation, and it also employs the least conservative K_σ relationship; further adding to the likely unconservative bias.

Analysis 4 exactly repeated Analysis 3, but this time employing the liquefaction triggering relationship of Cetin et al. (2018), along with the K_σ relationship of Youd et al. (2001) which is the relationship recommended by Cetin et al. This produced higher cyclically-induced pore pressures in the zone adjacent to the upstream side of the clay core, at the base of the hydraulic fill, which eliminated the buttressing effect of Analysis 4, and the upstream side flow failure was successfully predicted.

The analysis that was only largely successful was Analysis 2. This analysis successfully predicted the upstream flow failure, but it also predicted the inception and partial development of a second, downstream side slope instability feature (which was not observed in the 1971 earthquake). This was due to the use of the Seed and Harder (1990) S_r relationship, which predicts S_r as a function of only $N_{1,60,CS}$ (rather than as a function of both $N_{1,60,CS}$ and also initial vertical effective stress, $\sigma'_{v,i}$). Due to the failure to also account for $\sigma'_{v,i}$, this relationship tends to under-predict S_r at high initial effective overburden stresses (e.g. at the base of the downstream hydraulic fill shell zone, especially near the core), and the result was the inception of a downstream side instability feature in addition to the upstream side stability that was also initiated. As shown in Figures 4-58(a) through (c), the upstream slide progressed more rapidly, and it eventually “cut the top” off of the downstream slide feature by transporting the dam’s upper crest section laterally upstream towards the reservoir. The removal of the driving mass of the top crest section of the dam from the upper heel of the downstream slide feature reduced the driving shear stresses and eventually limited the downstream side movements. The partial development of the downstream slippage feature did, however, produce additional vertical settlements of the “lip” of the upstream slide feature, which is located in the heel area of the downstream slide feature, and as a result this is the analysis that shows the lowest predicted final elevation of this important lip feature (Elev. 1,107.7 ft. vs. 1,114 ft. actually observed). The partial development of a downstream slide feature also resulted in prediction of larger lateral displacements at the downstream toe (~21.6 feet) than were actually observed (~1 foot) in the field after the earthquake.

As a test of this hypothesis that these of the S_r relationship of Seed and Harder was principally responsible for the poor results of LSFD Analysis 2, Analysis 3 exactly reproduced Analysis 2, but this time employed the S_r relationship of Weber et al. (2015) which predicts S_r as a function of both $N_{1,60,CS}$ and also initial vertical effective stress, $\sigma'_{v,i}$. This analysis was fully successful, and provided a good match with observed field performance with regard to both mechanisms and magnitudes of deformations and displacements.

One of the important additional lessons learned was the importance of suitably treating the issues associated with potential strain softening of the cohesive soils of the puddled central clay core. This was a critical issue in all six of the analyses. It is noted here that geotechnical earthquake engineers involved in “liquefaction analyses” can sometimes tend to be focused on the potentially liquefiable soils. It is important to also deal with the properties and behaviors of the non-liquefiable materials; including strain sensitive clays.

Overall, these back-analyses demonstrated an ability to produce very good engineering “predictions” of both observed mechanisms of displacements and distress, as well as magnitudes of deformations and displacements.

Accomplishing this appears to require the following:

1. Suitable analytical or constitutive models.
2. Calibration of these models with respect to cyclic (seismic) pore pressure generation with suitable liquefaction triggering relationships, including both K_α and K_σ relationships.
3. Use of suitable post-liquefaction residual strength (S_r) relationships.
4. Suitable procedures and protocols for transition to S_r behaviors in potentially liquefiable soils.
5. Suitable treatment of potential cyclic softening, and strain softening, behaviors in sensitive clayey soils.
6. Suitable characterization of geometry and stratigraphy, and suitable evaluation of material properties and behaviors.
7. Suitable development and application of appropriate seismic “input” motions.
8. Appropriate evaluation and interpretation of the analysis results, with an understanding of the models and relationships employed, and also the intrinsic limitations of the continuum analysis methods employed with regard to accurate analyses of very large deformations and displacements.
9. And engineering judgment.

Chapter 5

The Upper San Fernando Dam Seismic Performance Case History During the 1971 San Fernando Earthquake

5.1 INTRODUCTION

The Upper San Fernando Dam (USFD) experienced well-documented small to moderate deformations during the 1971 San Fernando earthquake ($M_w \approx 6.61$) on February 9, 1971. This makes this case history an excellent paring with the case history of the nearby Lower San Fernando Dam (LSFD), as discussed and presented in Chapter 4. The nearby LSFD experienced a liquefaction-induced flow slide failure, carrying much of the dam embankment back into the reservoir. The toe of the upstream flow failure traveled approximately 140 feet back into the reservoir.

The USFD, in contrast, experienced significant liquefaction, but only moderate deformations, including crest loss (vertical settlements) of approximately 2.5 to 3 feet, lateral displacements of the crest of up to 5 to 6 feet, and lateral displacements of the downstream slope of up to 7 to 9 feet.

Although less dramatic than the LSFD case history, the USFD may be the more challenging, and the more important, of the two paired case histories. The engineering challenge of attempting to accurately and reliably “predict” the limited deformations and displacements observed, as well as the causative mechanism(s), is very significant. It is arguably easier to predict the “on/off” nature (and associated risk exposure) of the upstream flow slide of the LSFD, than to make accurate predictions of more “limited” (small to moderate) deformations and displacements.

The engineering importance of this second back-analysis case history is primarily because:

- (1) moderate deformation cases often represent the most challenging situations for forward assessment of existing seismic dam risk exposure, as it can be difficult to accurately assess risk exposure and thus relative prioritization for risk mitigation (vs. dams likely to suffer either “negligible” or more “catastrophic” larger deformations),
- (2) accurate analyses of limited to moderate deformations are often needed to evaluate and develop interim reservoir restrictions, until final overall mitigation can be implemented, and thus they can have consequences regarding interim reservoir operations and water supply and/or power generation as well as public safety, and
- (3) mitigation design and implementation usually involves the targeting of adequately small deformations and displacements as to suitably protect public safety, again requiring suitably accurate engineering “predictions” of small to moderate deformations.

Multiple post-earthquake studies of the USFD have produced significant amounts of both field and laboratory data (e.g.: Seed et al., 1973; Serff, 1976, Castro et al., 1989, Seed et al., 1989; etc.). As a result, this field performance case history is a good candidate for assessing the impacts of numerical modeling approaches and details on the results of nonlinear dynamic analyses of dams. A re-evaluation of the USFD seismic case history was performed (1) to develop an understanding of the principle mechanisms that had influenced the observed field performance, (2) the abilities of a suite of current analytical frameworks, models, and engineering relationships to suitably capture those behaviors, and (3) the accuracy and reliability of the various analytical methods and combinations of engineering relationships and modeling and analysis protocols employed.

5.2 CONSTRUCTION OF THE UPPER SAN FERNANDO DAM

The USFD and LSFD were both constructed to provide terminal storage reservoir capacity for the Los Angeles Aqueduct, at sufficient elevation for gravity distribution into the city. The LSFD was constructed first, beginning in 1912, followed by the USFD beginning in 1921 (Seed et al., 1973).

Figure 5-1 shows a cross-section of the USFD as constructed, with earthquake-induced displacements shown.

The USFD was constructed directly on alluvial soils, without any excavation of the upper alluvium; leaving potentially liquefiable sandy and silty sand alluvium in place beneath the base of the dam embankment. A cutoff trench extending to a depth of 4 feet was constructed with an upstream-downstream width of approximately 30 feet, beneath approximately the center of the embankment.

The main body of the dam was constructed by the “semi-hydraulic fill” method. The semi-hydraulic portion of the dam was constructed to about Elevation 1,200 ft. in 1921 by using approximately 50,000 cubic yards of materials excavated from the valley floor. As with the hydraulic fill method of the LSFD, starter dikes were constructed at the upstream and

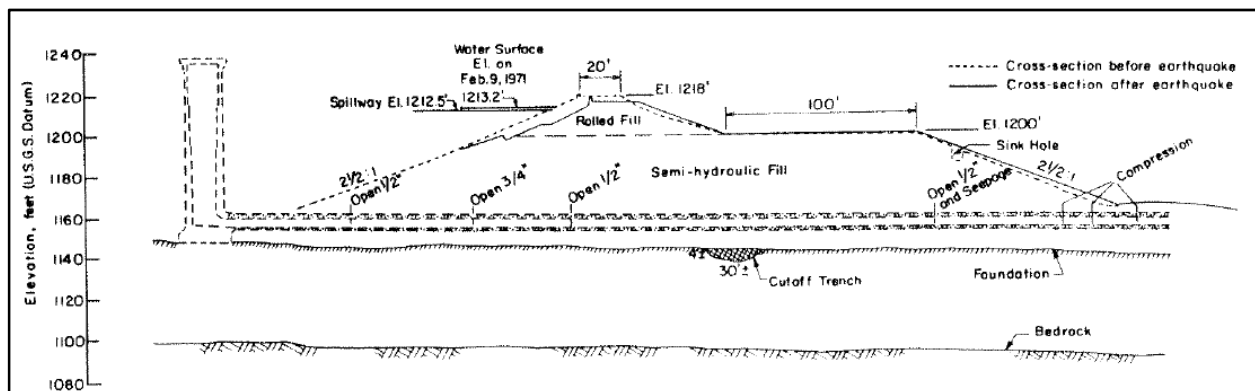


Figure 5-1: Cross section through the Upper San Fernando Dam (L.A. Department of Water and Power) (Seed et al., 1973)

downstream edges of the eventual embankment, and water was then ponded between these dikes. The excavated valley floor materials were hauled from the borrow areas to the edges of the starter dikes at both the upstream and downstream edges by wagons, dumped into the pond, and dispersed by spraying by monitors (high volume pump nozzles) working from floating barges. This process was repeated iteratively, constructing new starter dikes atop the upstream and downstream edges of the evolving embankment, filling the pond, and depositing and then dispersing the fill materials with monitors. This produced a semi-hydraulic fill embankment with properties and attributes relatively similar to the hydraulic fill embankment section of the nearby LSFD; with generally coarser sandy materials settling near the upstream and downstream edges, and progressively finer materials (silty sands, sandy silts, and eventually clayey materials) settling towards the center of the pond.

This semi-hydraulic fill method was intended to produce an “ideally” graded dam embankment fill, as the coarser particles (in this case mainly sands and silty sands) would settle most quickly, and come to rest near the upstream and downstream edges and the finer (ideally clayey) materials would remain longer in suspension, and would settle towards the center of the dam embankment. In theory, this process would produce a dam embankment with a clayey core providing low permeability, with a gradual transition in gradation towards the coarser upstream and downstream toes; providing good filtration and drainage, and good lateral support, for the core. In actual practice, as with the hydraulic fill of the LSFD, the result was a locally variable (layered) depositional structure, with coarser and finer layers occurring at multiple scales. The resulting central “clayey” core appears to have been cohesive/clay dominated, and the resulting shells were generally comprised of sands and silty sands, with some sandy silts.

After completion of the semi-hydraulic portion of the embankment up to approximately Elev. 1,200 ft., the dam embankment was next raised to Elevation 1,218 ft. by placing compacted “dry fill” atop the upstream side of the much wider semi-hydraulic fill embankment section. The dry fill materials represented a “rolled fill”, consisting of crushed shale, which was obtained from side hill borrow, spread in thin layers, sprinkled, and wagon-rolled. This rolled fill section served as the upper crest section of the embankment.

As shown on Figure 5-1, the completed cross-section of the dam had a 2.5H:1V concrete paved upstream slope, a crest width of 20 feet, and a downstream slope of 2.5H:1V to Elevation 1,200 ft. The completed dam was 70 feet tall at the maximum height section.

5.3 OBSERVED PERFORMANCE OF THE UPPER SAN FERNANDO DAM DURING THE 1971 SAN FERNANDO EARTHQUAKE

5.3.1 Observed Performance

The USFD suffered liquefaction-induced damage, and displacements, during the 1971 San Fernando earthquake. Figures 5-2 and 5-3 show damage to the crest of the dam, and to



Figure 5-2: Repair of damage to the crest and upstream concrete facing of the Upper San Fernando Dam after the 1971 San Fernando earthquake (Steinbrugge Collection, NICEE library, U.C. Berkeley)



Figure 5-3: Slide scarp on upstream face of the USFD after the 1971 San Fernando earthquake (Seed et al. 1973)

the concrete facing near the top of the upstream face of the embankment. Figure 5-2 is a photograph taken after the earthquake showing repair of the damage to the upstream side concrete facing. Figure 5-3 shows an earlier photograph of the seismically offset concrete facing sections, prior to repair. The original photo has been augmented in this current report with a dashed red line, and an arrow, indicating the direction and magnitude of offset between the original concrete facing sections. The damage to the upper portion of the concrete facing extended along nearly the full length of the upstream face, and this feature is now recognized to represent the heel scarp of a slide feature that extended to the base of the embankment, passed along the base, and exited at the downstream toe. The importance of this heel scarp feature had not been well recognized in the early investigations, but these current studies and back-analyses clearly demonstrate the nature of this feature.

Figure 5-4 shows a plan view of the USFD, and shows the locations of three cross-sections studied in the post-earthquake investigations. Observable displacements were mapped along these three cross-sections, and the resulting displaced cross-sections (as well as the original pre-earthquake cross-sections) are shown in Figures 5-5(a) through (c). The reservoir was not drawn down fully after the earthquake, so displacements were observed, measured and mapped only to the downstream side of the intersection between the lowest interim top of the reservoir and the upstream face of the dam. Detailed displacements of the lower portions of the upstream side of the embankment, and at the upstream toe, are not known with specificity.

As shown in Figures 5-5(a) through (c), the slide scarp feature near the top of the upstream face shown in Figures 5-2 and 5-3 occurs in all three cross-sections. Similarly, all three cross-sections also show lateral displacements of the downstream toe of the embankment. Based on measurements off these cross-sections, the dam crest suffered approximately 2.5 to 3 feet of vertical crest loss, and the crest translated laterally approximately 5 to 6 feet toward the downstream side. The downstream toe of the dam translated approximately 4 to 9 feet toward the downstream side at various locations, with the largest displacements occurring at or near the most central Cross-Section B-B'. The movements at and near the upstream toe are not known with certainty, as the reservoir water level was not fully lowered in the immediate aftermath of the earthquake.

Serff (1976) summarized horizontal and vertical displacements measured at six locations (including five survey monuments) on or near to the maximum height cross-section of the dam (Cross-Section B-B' in Figures 5-4 and 5-5(b)). Figure 5-6 shows locations of these displacement measuring points, and the measured displacements (both vertical and horizontal) at these locations. These locations were: (1) on the crest upstream parapet wall, (2) at the mid-point of the downstream slope of the upper rolled embankment fill, (3,4) at the upstream and downstream ends of the top deck of the downstream berm, (5) at the mid-point of the downstream berm slope, and (6) at the downstream toe. At this cross-section, the dam crest displaced 4.9 feet toward the downstream side, and the maximum measured lateral displacement was a downstream translation of 7.2 feet at the hinge point at the top of the downstream berm. The maximum settlement measured was 2.5 feet at the crest parapet wall. The California Department of Water Resources (DWR, 1989) also presented additional settlement measurements along the crest at four more locations, and on the downstream

berm and slope at four additional locations. Figure 5-7 shows the locations and values of these additional settlement measurements.

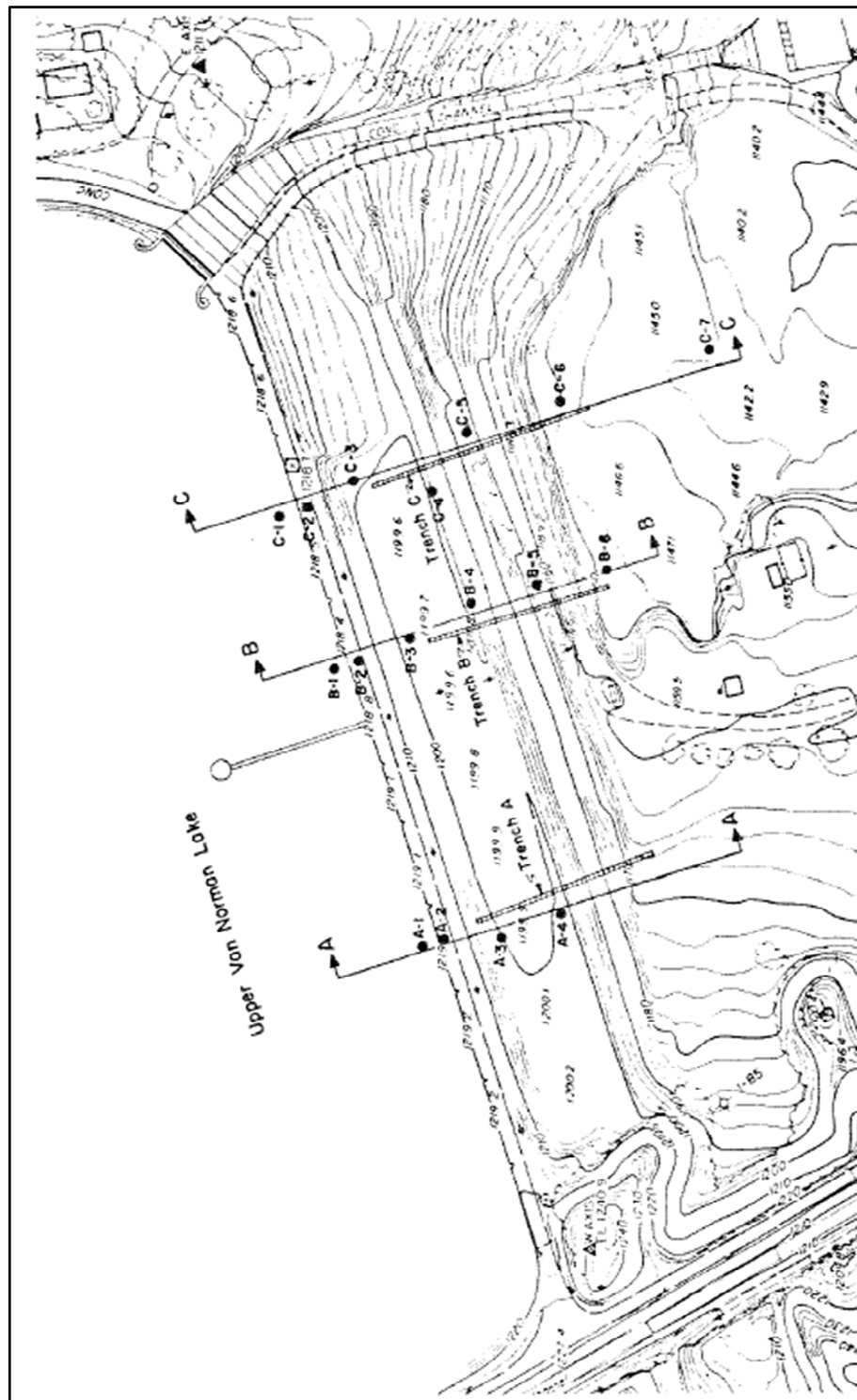


Figure 5-4: Plan view of the USFD showing cross-sections, borings, and trench locations from the post-earthquake study (Seed et al., 1973)

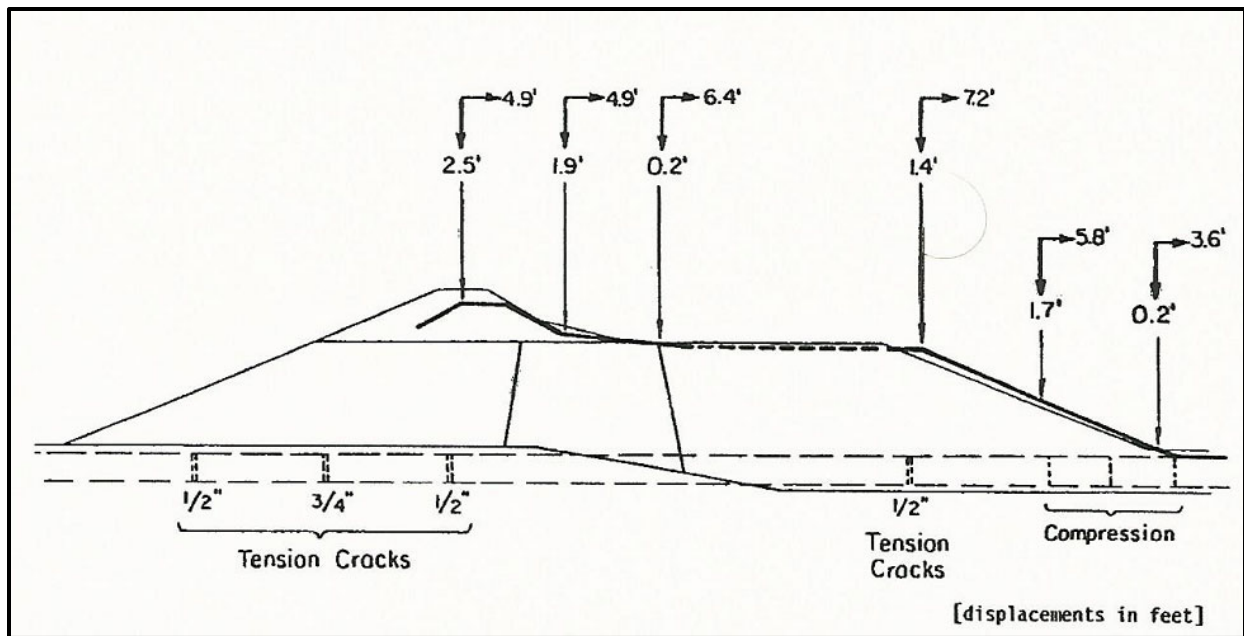


Figure 5-6: Displacements measured at the USFD after the 1971 San Fernando earthquake (Serff, 1976)

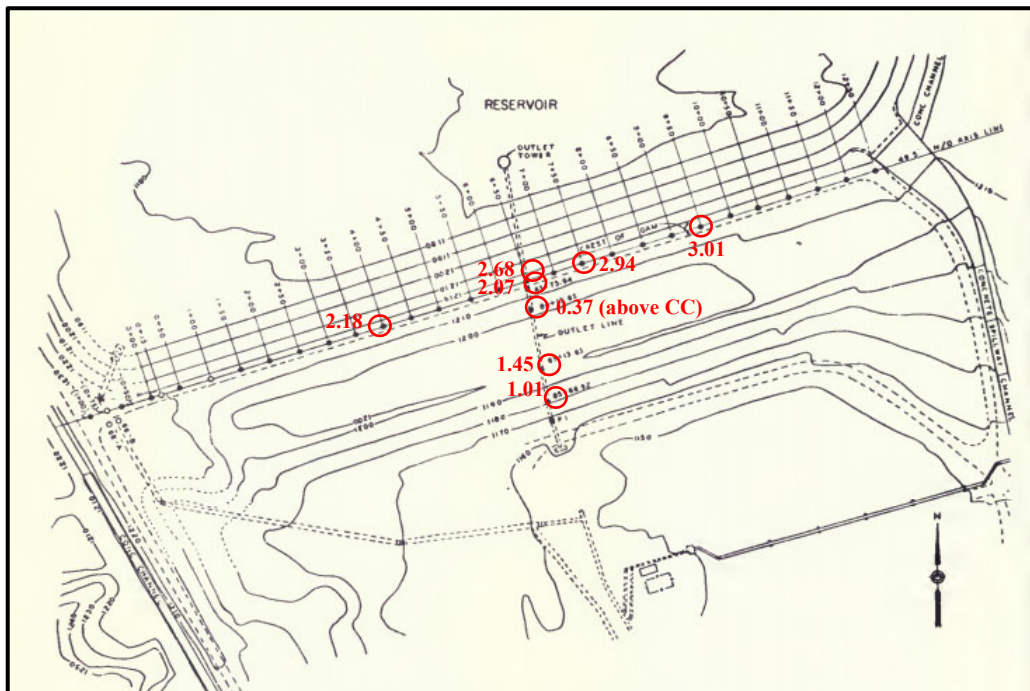


Figure 5-7: Plan view of the USFD with settlement measurement locations and settlement magnitudes (measured in feet) [Red circles and numbers were added for clarity in this current, annotated figure] (DWR, 1989)

5.3.2 Principal Distress Mechanisms of the USFD; Deep Seated Basal Shear Surface Due to Liquefaction and Strain Softening of Soils, and Strong Influence of Near-Source Seismic Ground Motions

The USFD seismic performance case history from the 1971 San Fernando earthquake has been studied and back-analyzed by multiple teams of researchers as a moderate deformation case history with emphasis on liquefaction of hydraulic fill layers and resulting displacements and settlements. In this current study, one of the objectives of the back-analyses performed was to re-evaluate the principal distress mechanisms and mechanics that produced the observed deformations and displacements.

As shown in Figure 5-8, a potential deep-seated basal shear surface can be inferred from the upstream face damage and offset near the crest (see also Figures 5-2 and 5-3), passing diagonally across the main dam embankment, and then forming a basal shear surface that extends laterally to exit at the downstream toe. The upstream face damage would then represent the top of a heel scarp, and the scarp would be the back heel of a massive lateral translational movement of a majority of the overall dam embankment as a largely monolithic block or mass. This lateral movement of the embankment was primarily the result of liquefaction within the semi-hydraulic fill materials, and resulting lateral “lurching” due to the seismic inertial motions imparted by the earthquake. Due to the proximity of the USFD from the hypocenter of the earthquake, and the nearest fault rupture surfaces, near-source directivity effects might have been a factor in development of the downslope lurching. Even with liquefaction of hydraulic fill layers, and strain softening of the clay core, the downstream movement of the USFD is of only a moderate amount (about 7 to 9 feet).

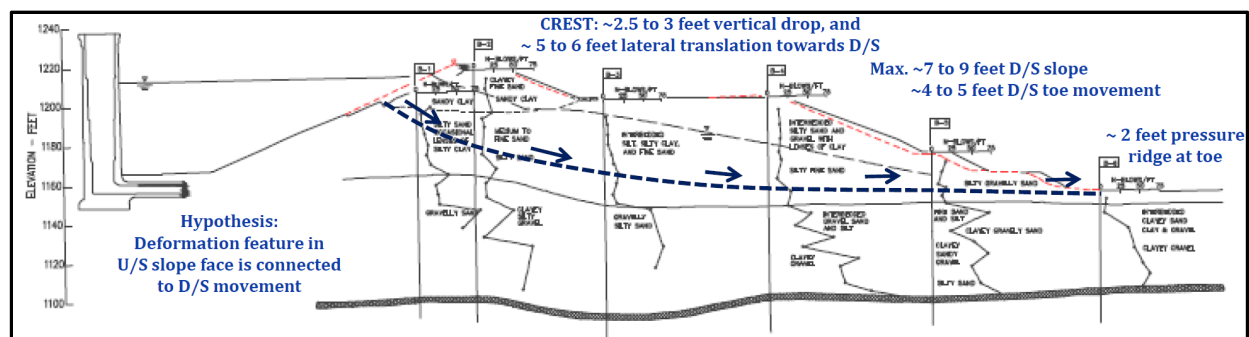


Figure 5-8: Idealized potential deep-seated basal shear surface in the USFD (Section B-B') connecting the upstream heel scarp with observed downstream toe movements

This potential explanatory mechanism for the observed behavior was first proposed in back-analyses of the USFD performed by Weber et al. (2015). Because those back-analyses were targeted at evaluating the post-liquefaction strength (S_r) of liquefied materials in the semi-hydraulic fill shells, they were not performed with nonlinear continuum analysis methods; they were narrowly focused on S_r and could not conclusively verify the hypothesized mechanism. Weber et al. (2015) also hypothesized that the post-liquefaction residual shear strengths (S_r) in the semi-hydraulic fill layers were adequate to prevent the occurrence of flow failure conditions in the USFD.

In the back-analyses performed for these current studies, it was not necessary to make any “a priori” assumptions as to causative mechanisms for the observed behaviors. Instead, all back-analyses began with (1) evaluation of pre-earthquake stresses and phreatic conditions and pore pressures, and then (2) proceeded to impose seismic input motions to evaluate (a) seismic/cyclic pore pressure generation and liquefaction behaviors, and resulting deformations and displacements during shaking, and then (b) post-seismic (post-shaking) deformations, as analyses were continued after the end of strong shaking. Mechanisms responsible for the observed field performance were clearly elucidated in these back-analyses (Section 5-8), and the principal causative mechanisms for the observed field behaviors were clearly determined in a majority of the back-analyses performed.

5.4 GEOLOGICAL/GEOTECHNICAL CROSS-SECTION AND BACK-ANALYSIS PLAN

Seed et al. (1973) prepared an idealized “representative” analysis cross-section of the USFD (Figure 5-9) that has been used, sometimes with variations as to details, by a number of researchers and analysts for subsequent numerical modeling and back-analyses of the USFD field performance case history. This cross-section is a compromise, or melding, of Cross-Sections A-A', B-B' and C-C' presented in Figures 5-4 and 5-5, and was developed to be “representative” of conditions at the maximum height cross-section.

Instead of using this fictitious “representative” analysis cross-section, these current studies used one of the actual dam cross-sections, Section B-B' (Figure 5-5b), which was selected (1) because it is located near center of the dam, nearly at the maximum height cross-section, and (2) because it aligns closely with the available surveyed lateral and vertical displacements in the central portion of the dam. Figure 5-10 shows the geological and geotechnical conditions modeled at this back-analysis Cross-Section B-B'. These are closely similar to the representative cross-section of Figure 5-9, but have the advantage of being an actual cross-section of the dam.

The dam had a maximum height of 70 feet and was constructed primarily by means of the semi-hydraulic fill method, which produced relatively loose and primarily cohesionless upstream and downstream “shells”, and a more cohesive “puddled” central clay core. A rolled fill, consisting of crushed shale, was placed atop the hydraulic fill embankment to achieve the final crest height. Foundation materials immediately below the dam consist of two alluvial units: Zones 4 and 5 in Figure 5-9; and Zones UA (Upper Alluvium) and LA (Lower Alluvium) in Figure 5-10. These alluvial soils are primarily sands and silty sands. Unlike the LSFD, at the USFD the uppermost alluvial materials (UA) underlying the upstream side of the dam were not very dense, and so were potentially liquefiable materials. The lower alluvium was significantly denser, and was not potentially vulnerable to soil liquefaction.

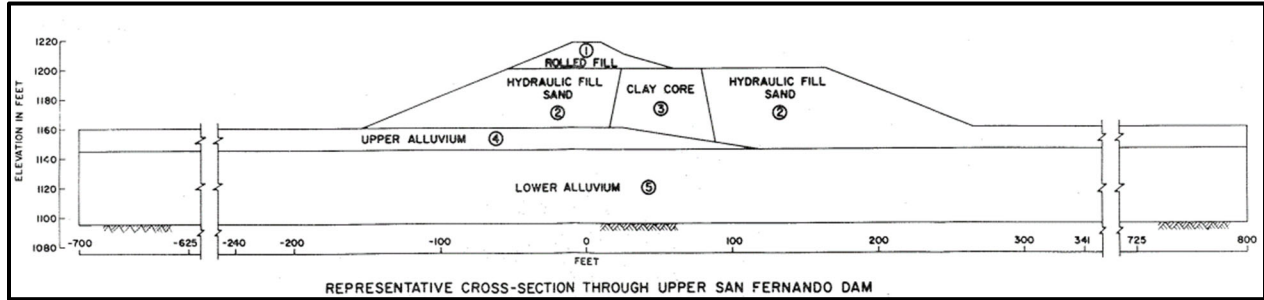


Figure 5-9: Representative Cross-Section of USFD (Seed et al., 1973)

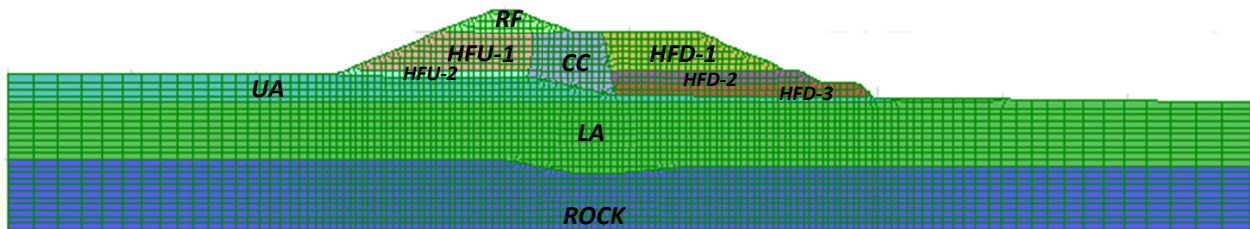


Figure 5-10: Analysis Cross-Section B-B' and principal material zones (current study)

Figure 5-10 shows an analysis cross-section of the USFD, and the principal soil zones modeled in these current studies. This figure also shows the mesh used in these current studies for back-analyses of USFD performance by means of nonlinear dynamic deformation analyses (NDA) performed using FLAC (Fast Lagrangian Analysis of Continua; Itasca, 2011). The soil strata in these current studies (Figure 5-10) are identified using the following nomenclature:

Hydraulic Fill Upstream	-	HFU (HFU-1 = upper, and HFU-2 = lower)
Hydraulic Fill Downstream	-	HFD (HFD-1 = upper, HFD-2 = middle, and HFD-3 lower)
Upper Alluvium	-	UA
Lower Alluvium	-	LA
Rolled Fill	-	RF
Clayey Core	-	CC

These current studies employ a limited set of selected analytical models, and all of them are applied within a finite difference analysis framework using the code FLAC. A suite of nine principal nonlinear seismic deformation analyses were performed for the USFD, and the combinations of (1) analytical or constitutive models, (2) soil liquefaction triggering models, and (3) post-liquefaction residual strength models employed in each of these nine analyses are listed in Table 5-1.

Table 5-1: Summary of analytical modeling schemes for the USFD back-analyses performed.

Analysis ID	Description
USFD Analysis 1: Roth (Y,SH)	Constitutive model for liquefiable soils – Roth Liquefaction Triggering and K_σ – Youd et. al. (2001) Post Liquefaction Residual Strength, S_r – Seed and Harder (1990) [Average S_r applied during-shaking/earthquake analysis]
USFD Analysis 2: Roth (B&I,I&B)	Constitutive model for liquefiable soils – Roth Liquefaction Triggering and K_σ – Boulanger and Idriss (2014) Post Liquefaction Residual Strength, S_r – Idriss and Boulanger (2015) [S_r “with significant void redistribution” curve applied during-shaking/earthquake analysis]
USFD Analysis 3: Roth (C,W)	Constitutive model for liquefiable soils – Roth Liquefaction Triggering – Cetin et al. (2018); K_σ – Youd et al. (2001) Post Liquefaction Residual Strength, S_r – Weber et al. (2015) [50 th percentile S_r applied during-shaking/earthquake analysis]
USFD Analysis 4: UBCSAND (Y,SH)	Constitutive model for liquefiable soils – UBCSAND Liquefaction triggering and K_σ – Youd et al. (2001) Post-liquefaction Residual Strength, S_r – Seed and Harder (1990) [Average S_r applied during post-shaking analysis]
USFD Analysis 5: UBCSAND (B&I,I&B)	Constitutive model for liquefiable soils – UBCSAND Liquefaction Triggering and K_σ – Youd et al. (2001); Post Post Liquefaction Residual Strength, S_r – Idriss and Boulanger (2015) [S_r “with significant void redistribution” curve applied during post- shaking]
USFD Analysis 6: UBCSAND (Y,W)	Constitutive model for liquefiable soils – UBCSAND Liquefaction Triggering and K_σ – Youd et al. (2001); Post Liquefaction Residual Strength, S_r – Weber et al. (2015) [50 th percentile S_r applied during post- shaking analysis]
USFD Analysis 7: PM4Sand (B&I,I&B)	Constitutive model for liquefiable soils – PM4Sand Liquefaction Triggering and K_σ – Boulanger and Idriss (2014); Post Liquefaction Residual Strength, S_r – Idriss and Boulanger (2015) [S_r “with significant void redistribution” curve applied during post-shaking analysis]
USFD Analysis 8: PM4Sand (C,W)	Constitutive model for liquefiable soils – PM4Sand Liquefaction Triggering – Cetin et al. (2018); K_σ – Youd et al. (2001); Post Liquefaction Residual Strength, S_r – Weber et al. (2015) [50 th percentile S_r applied during post-shaking analysis by a FISH function]
USFD Analysis 9: Wang2D (C,W)	Constitutive model for liquefiable soils – Wang2D Liquefaction Triggering – Cetin et al. (2018); K_σ – Youd et al. (2001); Post Liquefaction Residual Strength, S_r – Weber et al. (2015) [50 th percentile S_r applied during shaking for durations with $R_{u,seis}$ greater than a specified value, and also during post-shaking analysis by a FISH function]

The nomenclature in this table revolves around the three principal choices made in developing each analysis: (1) the analytical model employed, (2) the liquefaction triggering relationship employed, and (3) the post-liquefaction residual strength (S_r) relationship employed. As examples: USFD Analysis 4: UBCSAND (Y,SH) indicates that Analysis 4 employed the UBCSAND analytical model, with liquefaction triggering calibrated within the UBCSAND Model using the Youd et al. (2001) [Y] triggering relationship, and also employing the Seed and Harder (1990) [SH] residual strength (S_r) relationship, and USFD Analysis 9: Wang2D [C,WEA] indicates that Analysis 9 employed the Wang2D analytical model, with liquefaction triggering calibrated within the Wang2D model using the Cetin et al. (2018) [C] triggering relationship, and also employing the Weber et al. (2015) [WEA] post-liquefaction residual strength (S_r) relationship.

The constitutive or analytical material behavior models employed in these analyses for potentially liquefiable soils are listed in Table 5-1. These were described previously in Section 2.2. Potentially liquefiable soil layers are modeled using four different models, and these are the (1) Roth, (2) UBCSAND, (3) PM4Sand, and (4) Wang2D constitutive/analytical models. Non-liquefiable soils are modeled using the FLAC Mohr-Coulomb model in all of the analyses performed. Each of these analytical models require soil characterization as part of model parameterization.

The models for potentially liquefiable soils were each calibrated using one or more of three soil liquefaction triggering relationships, and these are the (1) Youd et al. (2001) – [Y], (2) Boulanger and Idriss (2014)-[B&I], and (3) Cetin et al. (2018) – [C] triggering relationships. These relationships were described in Section 2.3. Each of these relationships were employed in conjunction with the K_σ relationships for the specific liquefaction triggering relationships employed. Each of these triggering relationships also require characterization of soil units for model parametrization.

Post-liquefaction residual strengths (S_r) were also employed in the analyses performed, and three different relationships were employed for this purpose. These were the S_r relationships of (1) Seed and Harder (1990) – [S&H], (2) Idriss and Boulanger (2015) – [I&B], and (3) Weber et al. (2015) – [W]. These were described in Section 2.4. Each of these relationships also require characterization of soil units for model parametrization.

In addition, it is also necessary to properly characterize, and model, the non-liquefiable materials in the analysis cross-section.

It is also necessary to develop, and apply, suitable “input” strong motion time histories to the analytical models developed.

Each of the above represent their own sets of challenges, and these will be addressed in the sections that follow.

5.5 GEOTECHNICAL PARAMETERS FOR DEFORMATION ANALYSES

After the 1971 San Fernando earthquake, the Division of Safety of Dams (DSOD) of the State of California Department of Water Resources (DWR) and the Los Angeles Department of Water and Power (LADWP) sponsored and performed a post-earthquake investigation program for both the Upper and Lower San Fernando Dams. For the Upper San Fernando Dam, this consisted of 17 SPT borings with 231 SPT measurements, several trenches, cross-hole geophysical studies, and laboratory testing. The National Science Foundation (NSF) sponsored a grant to the University of California at Berkeley (UCB) and to the University of California at Los Angeles (UCLA) for the analytical studies as well as portions of the laboratory testing program. The investigation program and analytical studies were directed by the late Professors H.B. Seed of U.C. Berkeley and K.L. Lee of UCLA, and they are summarized in Seed et al. (1973, EERC 73-2). The parameters for this study were developed based on a re-evaluation of the data presented in EERC 73-2, subsequent research studies performed, and current State of Practice procedures for parameter evaluation and modeling employing the various analytical tools and engineering models and relationships employed in the analyses presented herein.

5.5.1 SPT Blow Counts

A total of 17 SPT borings were performed across three transverse (upstream to downstream) cross-sections, at the locations shown in Figure 5-4, and these provided a total of 231 SPT blow counts at different locations and in different strata. Figure 5-4 shows a plan view of the field boring locations, and Figures 5-5 (a) to (c) show individual SPT locations and the N-values measured. In most previous studies, data from 11 borings from (a) upstream, (b) crest, and (c) downstream locations were utilized to develop average or representative $(N_1)_{60}$ and $N_{1,60,CS}$ values for USFD seismic back-analyses, and properties were considered to be similar in the potentially liquefiable material zones on both the upstream and downstream zones at each elevation range. In these current studies, the upstream and downstream sections were considered separately and characterized on a more localized basis.

California DWR performed an additional evaluation of the USFD data as part of the post-1975 Oroville earthquake investigation for the Oroville Dam (DWR, 1989). In this evaluation, DWR used settlement values measured at the crest and the top deck of the downstream shell to estimate post-earthquake re-consolidation (densification), and reduced the average SPT blow counts by 4.5 blows/foot to obtain better estimates of pre-earthquake conditions. Beaty (2001) correctly noted that the settlements measured would include both (1) vertical settlement from kinematic movement of the slide mass, and (2) volumetric post-earthquake consolidation (densification), and suggested that a reduction of between 2 and 4 blows/foot would be more appropriate. Beaty (2001) reduced average blow counts by 3 to obtain best estimates of average “pre-earthquake” blow counts for his back-analyses. Beaty and Byrne (2011) re-processed the data set, producing nearly the same median $(N_1)_{60}$ values, except for the lower hydraulic fill layer (HFD-3). This time Beaty and Byrne (2011) estimated the same $(N_1)_{60}$ value reduction as the previous DWR (1989) study. Table

5-2 presents a summary of the average blow counts developed by DWR (1989), Beaty (2001) and Beaty and Byrne (2011).

Table 5-2: SPT $(N_1)_{60}$ and $N_{1,60,CS}$ values from the DWR (1989), Beaty (2001), and Beaty and Byrne (2011) studies

Soil Layer	DWR Study (1989)		Beaty (2001)	Beaty and Byrne (2011)	
	Average Post-Earthquake $(N_1)_{60}$	Average Pre-Earthquake $(N_1)_{60}$	Median Pre-Earthquake $(N_1)_{60}$	Median Pre-Earthquake $(N_1)_{60}$	Median Pre-Earthquake $N_{1,60,CS}$
HFU-1 (EL.1200-EL. 1170)	13.5	9	9	10	15
HFU-2 (EL. 1170-1160)	17.5	13	15	14.5	19.5
HFD-1 (EL.1200-EL. 1170)	13.5	9	9	10	15
HFD-2 (EL.1170-EL. 1160)	17.5	13	15	14.5	19.5
HFD-3 (EL.1160-EL. 1145)	17.5	13	15	13	18

In these current studies, crest and upstream borings were treated separately from downstream borings, and SPT data were separately processed to develop characterizations for the upstream and downstream zones. Blow count data within each of the zones were fully re-processed, and then a blow count reduction of 2 blows/foot was applied to the post-earthquake $(N_1)_{60}$ values to obtain best estimates of pre-earthquake $(N_1)_{60}$ values for both upstream and downstream layers. This reduction factor is similar to that employed in a recent study by Weber et al. (2015), and differs by only 1 blow/foot from that employed by Beaty (2001). This is smaller than the adjustment made by Beaty and Byrne (2011). The adjustment by a reduction of 2 blows/ft in these current studies is based on (1) the observation that deviatoric deformations may have contributed slightly more strongly to observed settlements, so that volumetric densification would have been slightly smaller, and (2) the observation that increases in SPT N-values due to seismically-induced densification would be partially offset by reductions in N-values due to loss of “ageing” effects (which also affect penetration resistances). SPT blow counts were screened to include SPT from only non-plastic soil strata.

In these current studies, the Upper Alluvium layer on the upstream side was separated from the downstream side lower hydraulic fill layer. These two layers are located at approximately the same elevations, but overburden-corrected blow counts from the upstream side alluvial unit are slightly higher than those of the downstream side hydraulic fill unit in Section B-B'.

Average fines contents of both sand and silty sand samples in the semi- hydraulic fill layers (46 samples) from the 1971 and 1985 studies for the LSFD were evaluated in this study to obtain a representative fines content for the hydraulic fill layers. The mean fines content of these 46 samples is 24.3%, which is very close to the value of 25% estimated by Seed et al. (1989). For this current study, a fines content of 25% has been adopted as a representative average value for fines correction of the SPT $N_{1,60,CS}$ values for the semi-hydraulic fill “shells” using each of the different liquefaction triggering relationships, and post-liquefaction residual strength (S_r) relationships. Beaty and Byrne (2011) also used a representative fines content of 25% to develop $N_{1,60,CS}$ values.

Table 5-3 presents 33rd percentile, mean, and median values of $N_{1,60,CS}$ using different (a) fines corrections, (b) equipment, energy and procedure corrections, and (c) effective overburden stress corrections (K_σ), for each of the three different liquefaction triggering relationships. These corrected and normalized $N_{1,60,CS}$ blow counts for these current studies were developed by applying the equipment, energy, procedural and effective overburden corrections, and the fines corrections, of each of the three liquefaction triggering relationships of (1) Youd et al. (2001), (2) Boulanger and Idriss (2014), and (3) Cetin et al. (2018). Several samples were specifically classified as clean sand, where a fines content of 5 percent was used for fines adjustments. Otherwise, a representative fines content of 25% was assumed for silty sand.

For these current studies, mean or average $N_{1,60,CS}$ values, as calculated in accordance with each of the liquefaction triggering relationships, were utilized as representative values for the analyses performed.

A second set of energy, equipment, overburden stress and fines adjusted $N_{1,60,CS}$ values is also needed for the three post-liquefaction strength (S_r) relationships used in these current studies. The representative $N_{1,60,CS-S_r}$ values developed and employed for the three S_r relationships used in these current studies are presented in Table 5-4 (along with the values employed in the three triggering relationships). The S_r relationship of Seed and Harder (1990) employs energy, equipment, and overburden stress corrections as per the liquefaction triggering relationship of Seed, Tokimatsu, Harder and Chung (1984) and fines correction as per Seed (1987). These are very similar to the corrections of the Youd et al. (2001) recommended triggering relationship, except that the fines correction and the overburden stress corrections differ somewhat; producing lower $N_{1,60,CS-S_r}$ values, as shown in Table 5-4.

The values presented in Tables 5-3 and 5-4 are the characterizations employed in the nonlinear seismic deformations analyses of the USFD performed in these current studies.

Table 5-3: Compilation of 33rd percentile, mean, and median values of fines corrected pre-earthquake SPT $N_{1,60,CS}$ blow counts for the three different triggering relationships employed in these current studies

Soil Layer	Youd et al. (2001) $N_{1,60,CS}$			Boulanger and Idriss (2014) $N_{1,60,CS}$			Cetin et al. (2018) $N_{1,60,CS}$		
	33 rd Per-centile	Mean	Median	33 rd Per-centile	Mean	Median	33 rd Per-centile	Mean	Median
HFU-1	10.6	13.6	12.5	10.6	13.4	12.3	8.7	11.7	10.4
HFU-2	14.7	18.4	20.7	14.3	17.9	20.1	12.0	15.4	17.6
UA	18.3	19.5	21.6	17.9	19.3	21.2	15.4	16.7	18.5
HFD-1	13.6	15.8	15.7	13.4	15.2	15.2	10.5	12.6	13.1
HFD-2	15.2	17.3	15.6	14.8	16.6	15.1	12.2	14.3	12.8
HFD-3	17.9	18.3	18.4	17.4	17.8	17.7	14.9	15.3	15.9

The fines correction for use in the S_r relationship of Idriss and Boulanger (2015) differs from that of their triggering relationship, which was developed using the fines correction of the Seed and Harder (1990) and Seed (1987) relationships, and this produces slightly lower $N_{1,60,CS-S_r}$ values, as shown in Table 5-4. The Weber et al. (2015) S_r relationship was developed using the energy, equipment, overburden stress and fines adjustments of the Cetin et al. (2004) triggering relationship. The fines correction (ΔN_{fc}) of the Cetin et al. (2018) triggering relationships differs a bit from that of the earlier 2004 triggering relationship, but the differences are not significant in the ranges of interest ($\sim 25\%$ fines) for the materials modeled here, producing mean and median values within a half blow count (or closer) to the $N_{1,60,CS}$ values employed for the Cetin et al. (2018) triggering relationship. Accordingly, the same $N_{1,60,CS}$ values were used for both the Cetin et al. (2018) triggering relationship, and the Weber et al. (2015) S_r relationship, as shown in Table 5-4.

Finally, as an illustrative example, Figures 5-11 and 5-12, show the processed $N_{1,60,CS}$ values developed based on the equipment, energy, procedural, and effective overburden stress corrections, and fines content adjustments of Cetin et al. (2018) for each of the six principal soil units analyzed in these studies, and this figure serves to illustrate the variabil-

Table 5-4: Fines Corrected $N_{1,60,CS}$ SPT Blow Counts for This Study

Soil Layer And Elevation (ft)	Youd et al. (2001)		Boulanger and Idriss (2014)		Cetin et al. (2018)
	Average Pre- Earthquake $N_{1,60,CS}$ for Triggering	Average Pre- Earthquake $N_{1,60,CS-Sr}$ for Seed and Harder (1990) S_r	Average Pre- Earthquake $N_{1,60,CS}$ for Triggering	Average Pre- Earthquake $N_{1,60,CS-Sr}$ for Idriss and Boulanger (2015) S_r	Average Pre- Earthquake $N_{1,60,CS}$ for Triggering and Weber et al. (2015) S_r
HFU-1 (EL.1200-1170)	13.6	11.6	13.4	11.6	11.7
HFU-2 (EL. 1170- 1160)	18.4	14.7	17.9	14.8	15.4
UA (EL.1160-1145)	19.5	16.1	19.3	16.6	16.7
HFD-1 (EL.1200-1170)	15.8	12.3	15.2	12.1	12.6
HFD-2 (EL.1170-1160)	17.3	13.7	16.6	13.5	14.3
HFD-3 (EL.1160-1145)	18.3	14.6	17.8	14.7	15.3

ity of the individual values in each unit. Similar figures can be presented for each of the other two approaches (Youd et al., 2001, and Boulanger and Idriss, 2014), and variability within each unit, and following each approach, would be similar.

5.5.2 Shear Strengths and Strength Behaviors for Non-Liquefiable Soils

Non-liquefiable soil units were modeled in the nonlinear dynamic deformation analyses (NDA) with the FLAC Mohr Coulomb model. There were suitable data and information available from the previous field and laboratory investigations for this purpose.

The puddled clay core was modeled as essentially clay controlled, and this clayey core was also modeled as essentially normally consolidated, with a peak static undrained shear strength corresponding to $S_u/\sigma'_{v,i} \approx 0.24$. As with the LSFD (discussed in Chapter 4), this central clay core was assumed to be vulnerable to both cyclic softening as well as strain softening, and the strength of the clay core was modeled as $S_u/\sigma'_{v,i} = 0.192$ “during shaking”, representing a 20% reduction to account for both (1) cyclic softening and (2) partial strain softening. At the end of shaking, shear strains across the core zone were examined, and in those analyses where the development of large shear strains and shear offsets across nar-

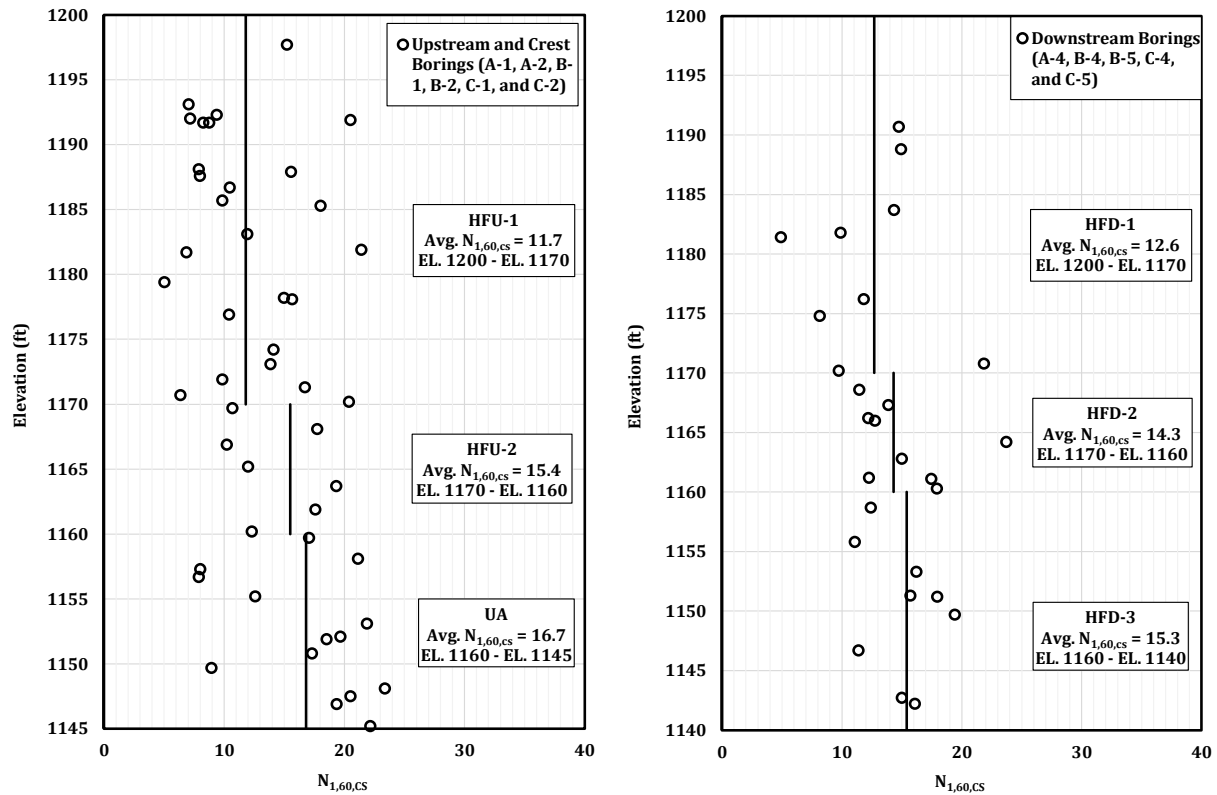


Figure 5-11: SPT blow counts (pre-earthquake) for (a) the upstream hydraulic fill shell materials and upper alluvium, and (b) the downstream hydraulic fill shell materials and upper alluvium; using Cetin et al. (2018) for energy, equipment, procedural and effective over-burden stress corrections, fines corrections, and an adjustment of -2 blows/ft to account for earthquake-induced reconsolidation/densification.

rowly banded shear zones across the core zone warranted, the shear strength of the central core zone was reduced to a value halfway between (1) the already softened strength of $S_u/\sigma'_{v,i} = 0.192$ that was used during shaking to account for both cyclic softening and partial strain softening, and (2) the fully residual strength of $S_{u,residual}/\sigma'_{v,i} = 0.08$. This intermediate strength is therefore modeled as $S_u/\sigma'_{v,i} = (0.5)(0.192+0.08) = 0.136$. After implementation of this further reduced clay core strength, the analysis was then re-started and continued forward after the end of shaking.

If strains in the clay core continued to develop sufficiently, then clay strength was further reduced to a fully residual value of $S_{u,residual}/\sigma'_{v,i} \approx 0.08$, and the analyses were again continued forward in time beyond the end of shaking unless and until either (1) deformations and displacements have ceased to occur, as the embankment is in a stable condition, or (2) mesh distortions are resulting in a need to perform significant (and time-consuming) re-meshing to continue the NDA deformation analysis, and the results at termination have become sufficient for purposes of engineering interpretation and decision-making, with recognition that deformations and displacements are still ongoing.

In six of the nine USFD analyses, the dam was stable with $S_u/\sigma'_{v,i} = 0.136$, and further strength reduction in the clay core was not warranted.

The rolled fill of the upper crest section of the embankment was modeled with the parameters, $c' = 300 \text{ lbs/ft}^2$ and $\phi' = 31^\circ$.

5.5.3 Hydraulic Conductivity and Pre-Earthquake Phreatic Surface

Hydraulic conductivity values and seepage analyses are important to establish the pre-earthquake steady-state seepage conditions, which are in turn important to characterize the baseline (pre-earthquake) static effective stress conditions and pore pressures. In these current studies, a range of hydraulic conductivity values were initially developed using the equation of Chapuis (2004), which is based on d_{10} and density values. These hydraulic conductivity values were then iteratively varied in a series of seepage analyses in FLAC to develop “analytically calibrated” parameters that produce a good match with the pre-earthquake phreatic water surface elevations measured at three piezometers across a transverse cross-section of the downstream side dam embankment. These piezometers were located approximately 20 feet, 45 feet, and 175 feet downstream of the crest centerline, and the piezometer levels were recorded as El. 1196, El. 1194, and El. 1174. Table 5-5 presents a summary of the resulting hydraulic conductivity values for USFD analyses in this study, and Figure 5-12 shows the degree of agreement between the “calculated” phreatic surface, and the phreatic surface data at the three downstream piezometers. The phreatic surface from Seed et al. (1973) was also evaluated for the current studies in developing the overall phreatic surface. There may be different combinations of hydraulic conductivity values that would result in phreatic surfaces that also match reasonably well with recorded data, however for this study the values of Table 5-6 were considered appropriate, as (1) they are judged to be reasonable, based on material descriptions and data, and (2) they provide a good match with the available pre-earthquake piezometer readings.

Table 5-5: Hydraulic Conductivity Values for USFD Analyses

Soil Layer	Horizontal Hydraulic Conductivity, k_h (cm/sec)	Vertical Hydraulic Conductivity, k_v (cm/sec)	Anisotropy Ratio (k_h/k_v)
RF	4E-5	1E-5	4
CC	4E-5	1E-5	4
HFU-1	5E-4	5E-5	10
HFU-2	5E-4	5E-5	10
UA	4E-5	1E-5	4
HFD-1	2.5E-4	2.5E-5	10
HFD-2	5E-4	5E-5	10
HFD-3	5E-4	5E-5	10
LA	4E-5	1E-5	4
BEDROCK	1E-7	1E-7	1

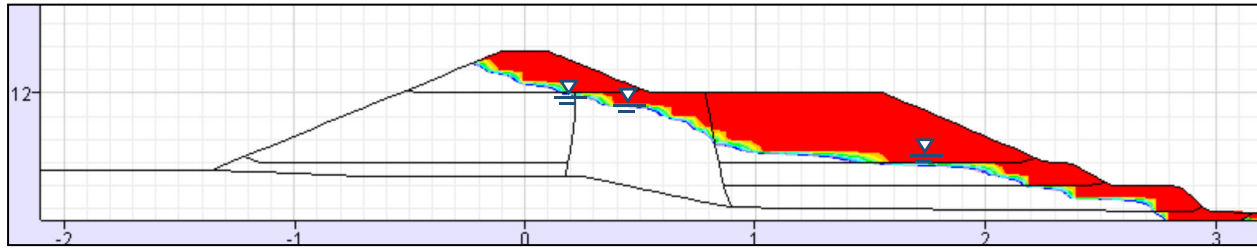


Figure 5-12: FLAC cross-section of USFD showing the initial phreatic surface based on pre-earthquake steady state seepage analyses, and the degree of match with the available data from three embankment piezometers

5.5.4 Strength and Stiffness Parameters

Strength and stiffness parameters for USFD were developed by Seed et al. (1973) based primarily on laboratory testing of samples collected after the earthquake. These values have also been used by a number of different researchers in subsequent studies. In these current studies, strength and stiffness parameters were re-evaluated. As laboratory testing in coarse-grained liquefiable soils is not routinely performed, and as undisturbed samples are difficult to obtain for these soils, strength and stiffness parameters for cohesionless soils were developed primarily using commonly used relationships that are mainly either $(N_1)_{60}$ - based or D_R - based. Strength and stiffness parameters were developed using the same protocols as were used for the LSFD analyses, as described in Section 4-5, and the stiffness parameters developed are shown in Table 5-6. Finally, Table 5-7 presents a summary of moist and saturated unit weights, drained shear strengths, and undrained strength S_u for the clay core, employed in these current studies.

Table 5-6: Stiffness parameter, K_{ge} values for USFD back-analyses

Soil Layer	Youd et al. (2016)	Boulanger and Idriss (2014)	Cetin et al. (2018)	Comment
RF	1302			Byrne et al. (1987) with assumed $D_r=75\%$
CC	893			Hardin (1978) with $PI=20$ and $OCR=1$
HFU-1	1027	1022	977	Seed et al. (1986)
HFU-2	1135	1124	1070	Seed et al. (1986)
UA	1157	1153	1099	Seed et al. (1986)
HFD-1	1079	1065	1001	Seed et al. (1986)
HFD-2	1112	1097	1044	Seed et al. (1986)
HFD-3	1133	1122	1068	Seed et al. (1986)
LA	1432			Byrne et al. (1987) with assumed $D_r=85\%$

Table 5-7: Moist and saturated unit weights, drained and undrained shear strength parameters for USFD analyses

Layer	Moist (γ_m) and Saturated (γ_{sat}) UnitWeight (pcf)	Cohesion, c' (psf)	Friction Angle, ϕ' (degrees)
RF	128/134	300	31
CC	114/120	Peak static $S_u = 0.24 \sigma'_{v,i}$ During shaking: $S_u = 0.192 \sigma'_{v,i}$ Post-shaking: $S_u = 0.192 \sigma'_{v,i}$ to $0.136 \sigma'_{v,i}$ depending on strains developed Fully residual: $S_{u,residual} = 0.08 \sigma'_{v,i}$	-
HFU-1	120/126	0	32
HFU-2	120/126	0	34
UA	121/128	0	35
HFD-1	120/126	0	33
HFD-2	120/126	0	34
HFD-3	120/126	0	34
LA	124/130	0	37
BEDROCK	134/140	-	-

5.6 INPUT GROUND MOTION TIME HISTORY FOR THE UPPER SAN FERNANDO DAM (USFD) SEISMIC DEFORMATION ANALYSES

Chapter 4, Section 4.6, provides details of evaluations of the fault mechanisms of the 1971 San Fernando earthquake, and resulting ground motions, for the purpose of re-evaluating and developing suitable “input” ground motion time histories for these current back-analyses of both the USFD and the LSFD. That discussion will not be repeated here.

As discussed in Section 4.6.3, the input motion employed in these current back-analyses of the USFD as the crest-perpendicular input motion is the 1971 strong motion recording (acceleration time history) obtained at the Pacoima Dam abutment station (recording direction: 164 degrees, measured from north); scaled with a ratio of 0.656 to produce an “input” acceleration time history for application in the transverse direction (USFD transverse direction at ~162 degrees) with $a_{max} = 0.80g$. A similar approach was utilized for development of a suitable vertical component input time history, and a scaling factor of 0.66 was applied to the recorded Pacoima Dam abutment vertical time history to develop a vertical component input motion with a peak acceleration of 0.80g. Figures 5-13 and 5-14 repeat Figures 4-34 and 4-35, and show the horizontal (perpendicular to the dam crest axis) and vertical motions employed as “input” motions for back-analyses of the USFD.

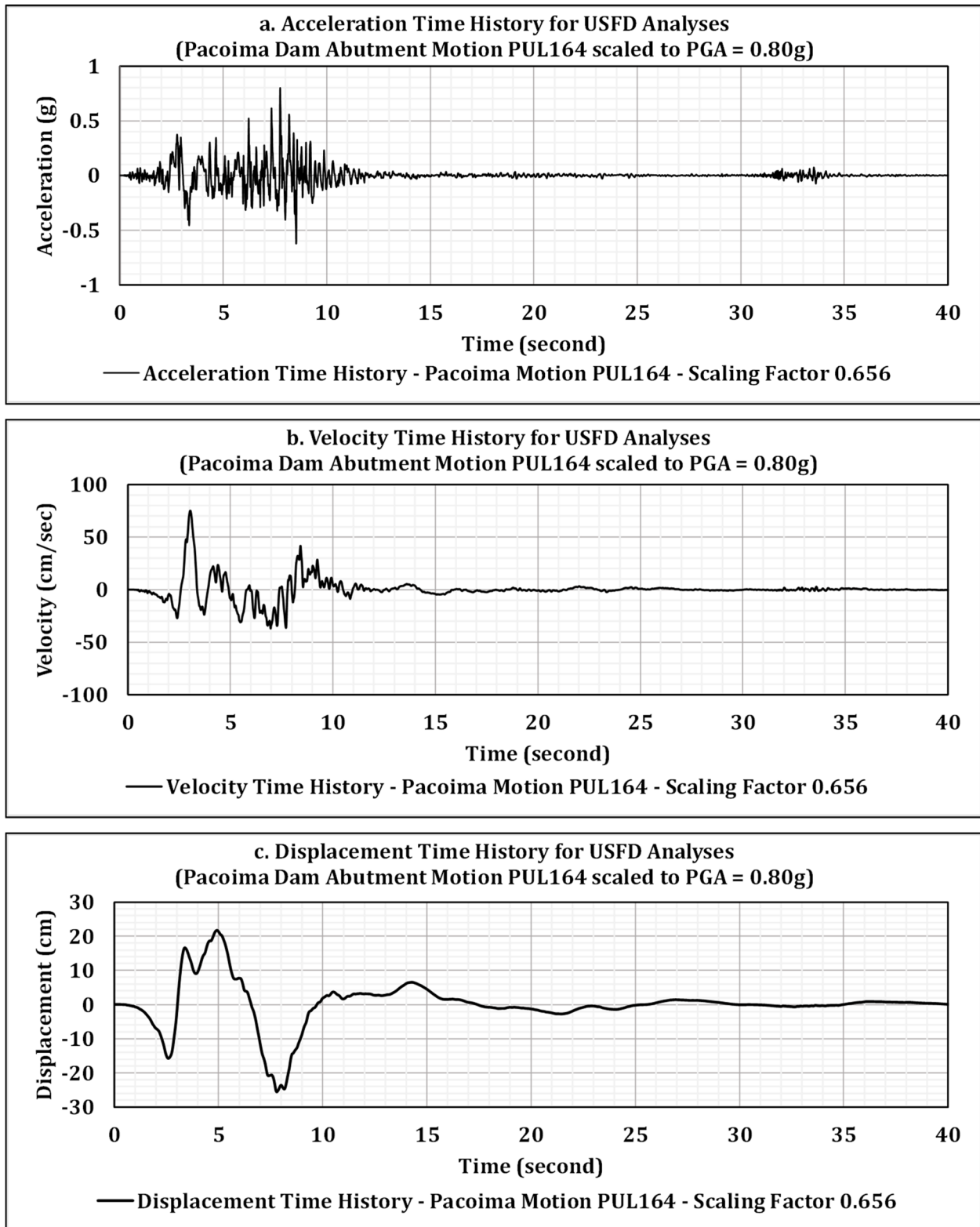


Figure 5-13: Horizontal input time history, perpendicular to the crest, for back-analyses of USFD (PGA = 0.80g)

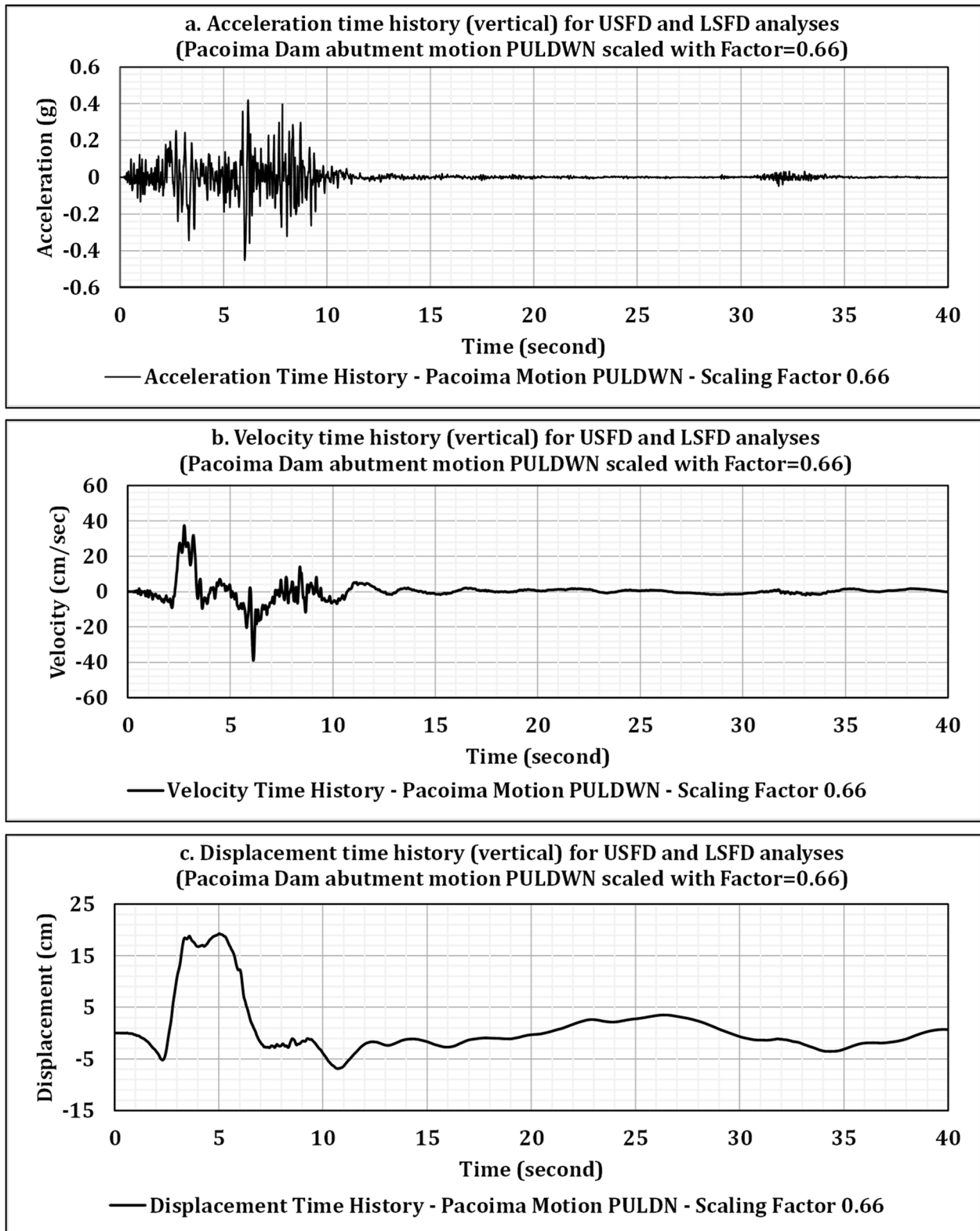


Figure 5-14: Vertical input time history for back-analyses of USFD

5.7 FLAC MODEL DEVELOPMENT FOR USFD SEISMIC DEFORMATION ANALYSES

Chapter 4 provides details of a number of important features of nonlinear seismic deformation analyses (NDA) using FLAC, which employs the finite difference method for computations of deformations. The details described previously for the LSFD analyses (Chapter 4) with regard to model development and implementation are similar to those for the USFD analyses. One of the basic principles of the suites of seismic deformation analyses performed in this study was to perform all steps of seismic deformation analyses as if the observed performances of the two dams were not “known”, in order to assess the accuracy and reliability of the various analytical approaches, details, and protocols. The protocols for seismic deformations analyses for forward analyses should ideally be the same for a wide range of expected deformations encompassing potential outcomes ranging from (1) limited deformations to (2) large or “flow failure” conditions in an embankment dam due to an earthquake. The protocols and practices employed in the different analyses of LSFD in Chapter 4 were thus largely repeated for the USFD in Chapter 5. That includes mesh development, boundary conditions, application of input acceleration time histories, transitions to S_r in different analytical models, continuation of analyses after the end of shaking, etc.

5.8 RESULTS OF UPPER SAN FERNANDO DAM NONLINEAR SEISMIC DEFORMATION ANALYSES

Table 5-8 repeats Table 5-1, and lists the nine analyses performed as the primary analyses to evaluate the performance of different analytical schemes including (1) four different analytical or constitutive models, (2) three different liquefaction triggering relationships, (3) several different K_σ and K_α relationships, and (4) three different post-liquefaction strength (S_r) relationships. This table lists the nine different combinations of each of these models and relationships employed in USFD Analyses 1 through 9.

Analysis details, and protocols, often specific to particular models and/or combinations of models or relationships, will be discussed as they arise in each of the nine back-analyses performed.

USFD Analyses 1 through 3 all employ the Roth analytical model, and they use three different combinations of (1) liquefaction triggering and (2) post-liquefaction S_r relationships in the potentially liquefiable layers. These combinations are (1) the Youd et al. (2001) liquefaction triggering relationship, with the Seed and Harder (1990) S_r (average) relationship [USFD Analysis 1], (2) the Boulanger and Idriss (2014) liquefaction triggering relationship, with the Idriss and Boulanger (2015) S_r relationship [USFD Analysis 2], and (3) the Cetin et al. (2018) liquefaction triggering relationship, with the Weber et al. (2015) S_r (50 percentile) relationship [USFD Analysis 3]. Analyses 1 through 3 also utilize the Idriss and Boulanger (2003) K_α relationship. USFD Analyses 1 and 3 also utilize the Youd et al. (2001) K_σ relationship, and Analysis 2 utilizes the Boulanger and Idriss (2014) K_σ relationship.

Table 5-8: Summary of analytical modeling schemes for the USFD back-analyses performed.

Analysis ID	Description
USFD Analysis 1: Roth (Y,SH)	Constitutive model for liquefiable soils – Roth Liquefaction Triggering and K_σ – Youd et. al. (2001) Post Liquefaction Residual Strength, S_r – Seed and Harder (1990) [Average S_r applied during shaking and post-earthquake analyses]
USFD Analysis 2: Roth (B&I,I&B)	Constitutive model for liquefiable soils – Roth Liquefaction Triggering and K_σ – Boulanger and Idriss (2014) Post Liquefaction Residual Strength, S_r – Idriss and Boulanger (2015) [S_r “with significant void redistribution” curve applied during shaking and post-earthquake analyses]
USFD Analysis 3: Roth (C,WEA)	Constitutive model for liquefiable soils – Roth Liquefaction Triggering – Cetin et al. (2018); K_σ – Youd et al. (2001) Post Liquefaction Residual Strength, S_r – Weber et al. (2015) [50 th percentile S_r applied during shaking and post-earthquake analyses]
USFD Analysis 4: UBCSAND (Y,SH)	Constitutive model for liquefiable soils – UBCSAND Liquefaction triggering and K_σ – Youd et al. (2001) Post-liquefaction Residual Strength, S_r – Seed and Harder (1990) [Average S_r applied during post-shaking analyses]
USFD Analysis 5: UBCSAND (B&I,I&B)	Constitutive model for liquefiable soils – UBCSAND Liquefaction Triggering and K_σ – Youd et al. (2001); Post Post Liquefaction Residual Strength, S_r – Idriss and Boulanger (2015) [S_r “with void redistribution” curve applied during post-shaking analyses]
USFD Analysis 6: UBCSAND (Y,WEA)	Constitutive model for liquefiable soils – UBCSAND Liquefaction Triggering and K_σ – Youd et al. (2001); Post Liquefaction Residual Strength, S_r – Weber et al. (2015) [50 th percentile S_r applied during post- shaking analysis]
USFD Analysis 7: PM4Sand (B&I,I&B)	Constitutive model for liquefiable soils – PM4Sand Liquefaction Triggering and K_σ – Boulanger and Idriss (2014); Post Liquefaction Residual Strength, S_r – Idriss and Boulanger (2015) [S_r “with void redistribution” curve applied during post- shaking analyses]
USFD Analysis 8: PM4Sand (C,WEA)	Constitutive model for liquefiable soils – PM4Sand Liquefaction Triggering – Cetin et al. (2018); K_σ – Youd et al. (2001); Post Liquefaction Residual Strength, S_r – Weber et al. (2015) [50 th percentile S_r applied during post- shaking analyses]
USFD Analysis 9: Wang2D (C,WEA)	Constitutive model for liquefiable soils – Wang2D Liquefaction Triggering – Cetin et al. (2018); K_σ – Youd et al. (2001); Post Liquefaction Residual Strength, S_r – Weber et al. (2015) [50 th percentile S_r applied during shaking for durations with $R_{u,seis}$ greater than a specified value, and also during post-shaking analyses]

USFD Analyses 4 through 6 all employ the UBCSAND model, and they all use the Youd et al. (2001) liquefaction triggering relationship. They use three different S_r relationships: (1) Seed and Harder (1990) (average) S_r [USFD Analysis 4], (2) Idriss and Boulanger (2015) S_r [USFD Analysis 5], and Weber et al. (2015) (50 percentile) S_r [USFD Analysis 6].

USFD Analyses 7 and 8 employ the PM4Sand model and use two different combinations of (1) liquefaction triggering and (2) post-liquefaction S_r relationships. These combinations are (1) the Boulanger and Idriss (2014) liquefaction triggering relationship, with the Idriss and Boulanger (2015) S_r relationship [USFD Analysis 7], and (2) the Cetin et al. (2018) liquefaction triggering relationship, with the Weber et al. (2015) (50 percentile) S_r relationship [USFD Analysis 8]. Analysis 8 also employs the Youd et al. (2001) K_σ relationship.

USFD Analysis 9 employs the Wang2D model, with (1) the Cetin et al. (2018) liquefaction triggering relationship, and (2) the Weber et al. (2015) post-liquefaction S_r relationship.

5.8.1 USFD Analysis 1: Roth Model, with the Youd et al. (2001) Liquefaction Triggering Relationship, and the Seed and Harder (1990) S_r Relationship

USFD Analysis 1 utilizes the Roth analytical model. This model is calibrated with the Youd et al. (2001) liquefaction triggering relationship, the Youd et al. (2001) K_σ relationship, and the Idriss and Boulanger (2003) K_α relationship for USFD Analysis 1. The Seed and Harder (1990) (average, or mean curve) post-liquefaction S_r relationship is applied to elements that experience soil liquefaction.

As is standard with the Roth analytical model, the transition to post-liquefaction strength (S_r) in each individual element occurs in this analysis when the shear strength (S) of the element is reduced to a value of $S \leq S_r$. As a result, elements incrementally transition to S_r as the analysis proceeds (“during shaking”). This differs from approach taken to the transition to S_r in analyses performed with the other three analytical models. There are no strain criteria for transition to S_r in the Roth model analyses; only the achievement of a shear strength (reduced by cyclic pore pressure generation, or $R_{u,seis}$) to a value of $\text{Strength} \leq S_r$.

Modeling and characterization parameters were described in Sections 5-5 and 5-7, and the analysis-specific input parameters are summarized in Table 5-9. As discussed in Chapters 2 and 4, the engineering protocol for use of the Roth analytical model (and the relationship(s) combination) of USFD Analysis 1 is that a cyclic strength curve is first defined to develop the relationship between cyclic stress ratio (τ_{cy}/σ'_v) and the number of equivalent cycles. The cyclic strength curve used in USFD Analysis 1 was developed based on CSR_{15} values from the Youd et al (2001) liquefaction triggering relationship, with modifications for the K_α relationship, and the $B (=1/b)$ value from Youd et al. (2001) for each of the hydraulic fill layers and the UA layer. The model then monitors the shear stress time history of each

Table 5-9: Input Parameters for USFD Analysis 1 using the Roth model, with Youd et al. (2001) liquefaction triggering, Youd et al. (2001) K_σ , and the Seed and Harder (1990) S_r relationship

Soil Layer	$N_{1,60,CS}$ (Youd et al., 2001)	$N_{1,60,CS-Sr}$ (Seed and Harder, S_r , 1990)	$B (=1/b)$ (Idriss, 1999)	CSR_{15} (Youd et al. 2001)	Friction Angle, ϕ' (Table 4-8)	f for K_σ (Youd et al., 2001)
HFU-1	13.6	11.6	2.97	0.147	32	0.710
HFU-2	18.4	14.7	2.97	0.196	34	0.663
UA	19.5	16.1	2.97	0.209	35	0.653
HFD-1	15.8	12.3	2.97	0.168	33	0.687
HFD-2	17.3	13.7	2.97	0.184	34	0.673
HFD-3	18.3	14.6	2.97	0.195	34	0.663

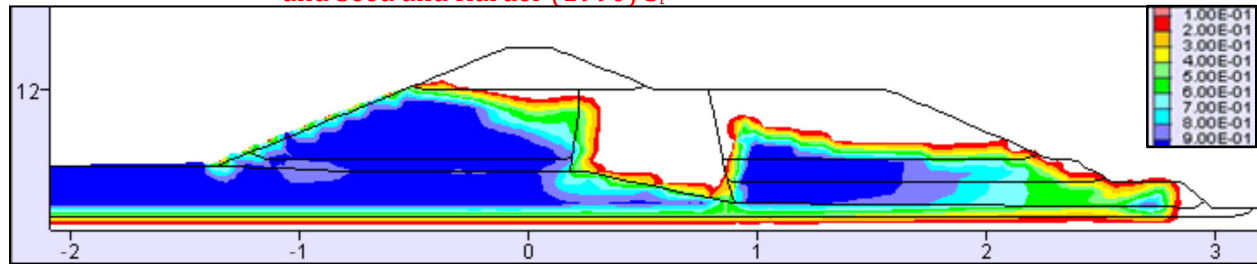
element of potentially liquefiable soil (monitored as the shear stress on the horizontal plane, τ_{xy} , for each half-cycle seismic shear loading), with reversal of shear direction on the horizontal plane representing the end of each half-cycle of loading, with “counting” of the accumulating shear stress cycles (half cycles determined by shear stress reversals) and incrementing cyclic pore pressure generation (increase) based on a scaled “damage accumulation” approach. As soon as a one-half stress cycle is detected, the excess pore pressure is incremented by an amount dependent on the cyclic stress ratio of that cycle. The strength envelope follows a Mohr-Coulomb relationship from the beginning of analysis, until (and if) the element’s shear strength transitions to a user-defined post-liquefaction strength; in this USFD Analysis 1 to S_r as determined by Seed and Harder (1990).

The Roth model is used in potentially liquefiable soils (which are the semi-hydraulic fill shell and upper alluvium zones). Non-liquefiable soils (the central clayey core, the upper rolled fill, and the lower alluvium) are modeled using the FLAC Mohr-Coulomb model. The non-liquefiable layers were modeled with Mohr-Coulomb parameters, as presented in Table 5-8. Shear strength of the semi-puddled central clay core was modeled as $S_u/\sigma'_{vi} = 0.192$ during shaking in USFD Analysis 1, which represents approximately a 20% reduction of undrained shear strength (from a peak static, or monotonic, shear strength of $S_u/\sigma'_{vi} = 0.24$) for the normally consolidated clayey core to account for both (1) cyclic softening and (2) strain softening.

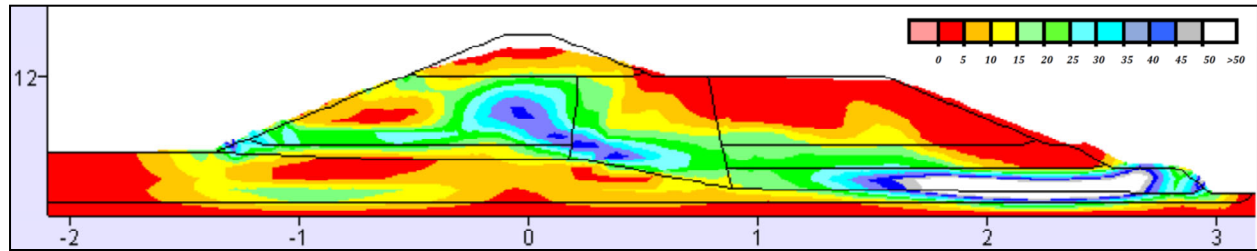
Figures 5-15 and 5-16 present the results of nonlinear seismic deformation analyses performed with the combination of models and relationships of USFD Analysis 1. Figure 5-15 shows conditions at the end of shaking, and 5-16 show conditions at the end of analysis.

The Roth model is the only one of the four analytical models used in these current studies that transitions “incrementally” to post-liquefaction residual strength as the analysis proceeds during shaking (transition to S_r occurs when the strength of an individual element

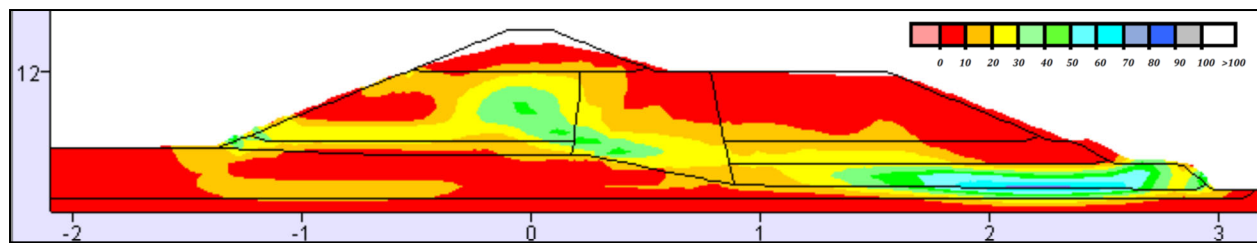
USFD Analysis 1: Roth model, Youd et al. (2001) liquefaction triggering, Youd et al. (2001) K_{σ} , and Seed and Harder (1990) S_r



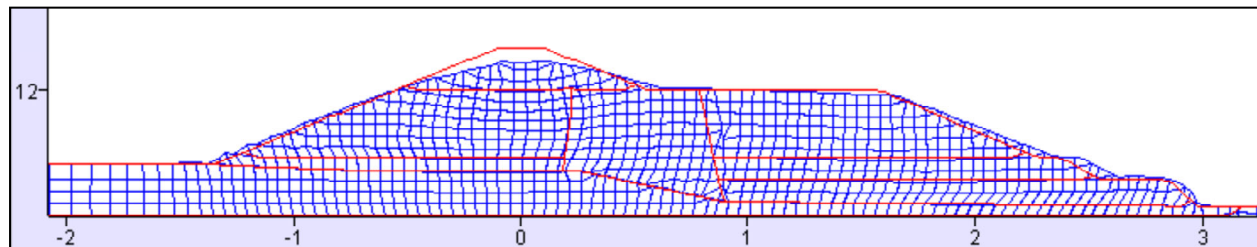
(a) Maximum value of $R_{u, \text{seismic}}$ recorded in each element



(b) Shear strain (percent), with the inset shear strain scale set to max. of 50 percent



(c) Shear strain (percent), with the inset shear strain scale set to max. of 100 percent



(d) Deformed mesh

Figure 5-15: Results of USFD Analysis 1 at the end of strong shaking (12.5 seconds)

decreases to $S \leq S_r$ as a result of incremental seismic pore pressure generation). As a result, all elements that will transition to S_r will have done so by the end of shaking.

An assessment is then made at the end of shaking of shear strains, and of shear displacement offsets across narrowly banded shear zones, in potentially strain sensitive cohesive soils, and if warranted the strengths of these soils may be further reduced, and then the NDA analysis is re-started and continued after the end of shaking. In this case (see Figure 5-15(b)), shear strains across the central clay core zone were between 23% to 41%. These

were sufficient as to potentially warrant additional reductions in clay strengths to account for strain softening, but they were not sufficient as to warrant a reduction to a fully residual value of $S_{u,residual} = 0.08$.

As per the protocol described in Section 5.5.2, the strength of the central clayey core was reduced to a value intermediate between (1) the already 20% softened clay core strength value of $S_u/\sigma'_{v,i} = 0.192$ and (2) a fully residual value of $S_{u,residual}/\sigma'_{vi} = 0.08$, to a strength of $S_u/\sigma'_{v,i} = (0.5)(0.192 + 0.08) = 0.136$, and then the analysis was re-started and continued past the end of shaking. In USFD Analysis 1, this intermediate clay strength was applied at 12.5 seconds, approximately at the end of strong shaking.

This reduction in the strength of the central clayey core materials resulted in small to moderate additional displacements and deformations, but the embankment continued to be stable and the deformations came to a halt. Figure 5-16 shows conditions at the end of this post-shaking analysis with partially reduced shear strengths of $S_u/\sigma'_{v,i} = 0.136$ in the clayey core zone. Maximum vertical crest loss had increased from 6.2 feet at the end of strong shaking condition of Figure 5-15, to 7.7 feet (Figure 5-16), and maximum lateral translation at the downstream slope had increased from 8.1 feet at the end of strong shaking condition of Figure 5-15, to a value of 11.7 feet (Figure 5-16).

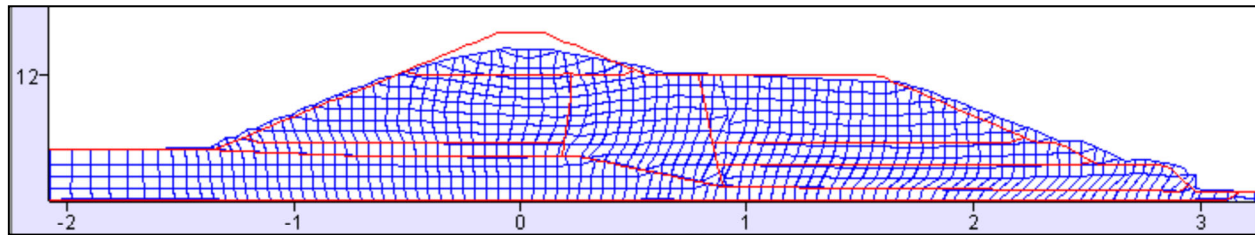
Re-evaluation of shear strains, and of shear displacement offsets across narrowly banded shear deformation zones across the central clayey core, shown in Figure 5-16 indicated that no further reduction of clay strengths was warranted below the now reduced value of $S_u/\sigma'_{v,i} = 0.136$. Maximum shear strains across the central core zone were now approximately 51% with an average of 16% across the central clay core. At these levels, reductions from the 20% softened value of $S_u/\sigma'_{vi} = 0.192$ were warranted, but not a transition below the now more significantly reduced value of $S_u/\sigma'_{v,i} = 0.136$.

As a hypothetical worst case scenario for LSFD Analysis 1, the puddled clay core strength was next reduced to the fully residual strength of $S_{u,residual}/\sigma'_{vi} = 0.08$, of clay, and the analysis was again re-started and continued forward. This added an additional 1.2 feet of crest loss (e.g. crest loss increased from 7.7 feet to 8.9 feet), and an additional 4.5 feet of lateral slope movement (maximum lateral slope displacement increased from 11.7 feet to 16.2 feet), and the dam remained stable. This indicated that the hypothetical further reduction did not lead to instability.

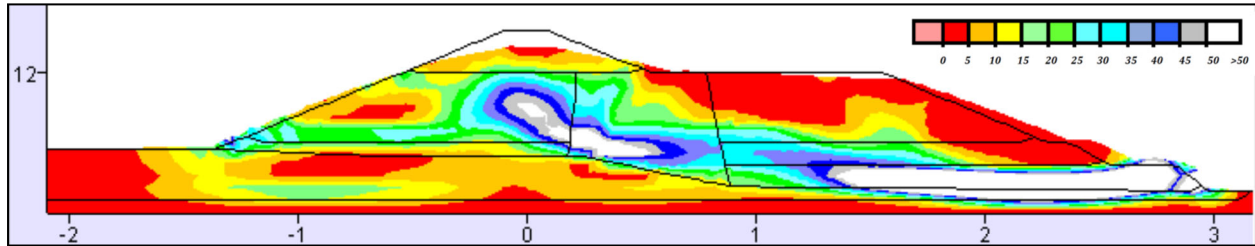
As a result, Figures 5-16(a) through (d) represent the “end of analysis” conditions for USFD Analysis 1. It is not necessary to repeat Figure 5-15(a) in Figure 5-16, because there are no additional increases in cyclic pore pressures in the post-shaking analysis. Figure 5-16 therefore shows updates of Figures 5-15(b) through (d), and adds an additional figure showing displacement vectors (at exaggerated scale for clarity).

As shown in Figure 5-15(a), USFD Analysis 1 generates significant seismically-induced pore pressures in the saturated semi-hydraulic fill shell materials on the upstream side of the dam (layers HFU-1 and HFU-2) and also in the underlying upper alluvium (UA) beneath the upstream side of the dam. High seismically-induced pore pressures are also

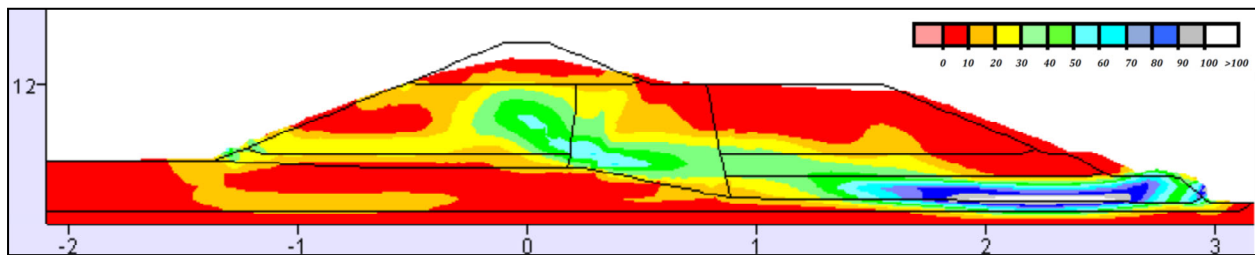
USFD Analysis 1: Roth model, Youd et al. (2001) liquefaction triggering, Youd et al. (2001) K_σ , and Seed and Harder (1990) S_r



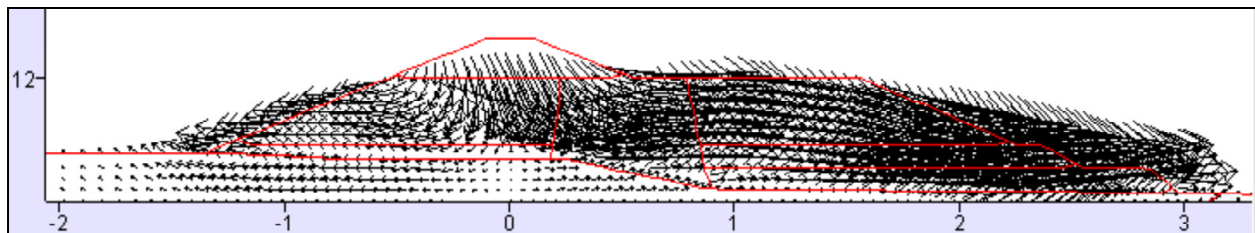
(a) Deformed mesh



(b) Shear strain (percent), with the inset shear strain scale set to max. of 50 percent



(c) Shear strain (percent), with the inset shear strain scale set to max. of 100 percent



(d) Displacement vectors (exaggerated scale for clarity w/ maximum vector set at 7 feet)

Figure 5-16: Results of USFD Analysis 1 at the end of analysis

generated on the downstream side of the dam, in the saturated portions of the semi-hydraulic fill downstream shell materials (layers HFD-2 and HFD-3).

Figures 5-15(b) and (c) show contours of maximum shear strains developed (at two different scales; set to maximum shear strains of 50 percent and 100 percent), and Figure 5-15(d) shows the deformed mesh at the end of shaking. As shown in Figure 5-15, the combination of seismic pore pressure generation, and resulting strength and stiffness

reductions, combined with the seismic inertial shaking forces, produced moderate displacements and deformations at the end of shaking.

Figure 5-17 repeats Figure 5-16, but with annotation to indicate some of the observed engineering behaviors. Figures 5-17(b) through (d) are annotated to show the concentrated shear zone exhibited in these analysis results. The shear zone represents a deep basal shear mechanism originating at the base of the downstream toe, traversing laterally along the base of the downstream side hydraulic fill shell zone, and then arcing upwards as it crosses the central clay core zone, to exit high on the upstream face of the dam at a location relatively

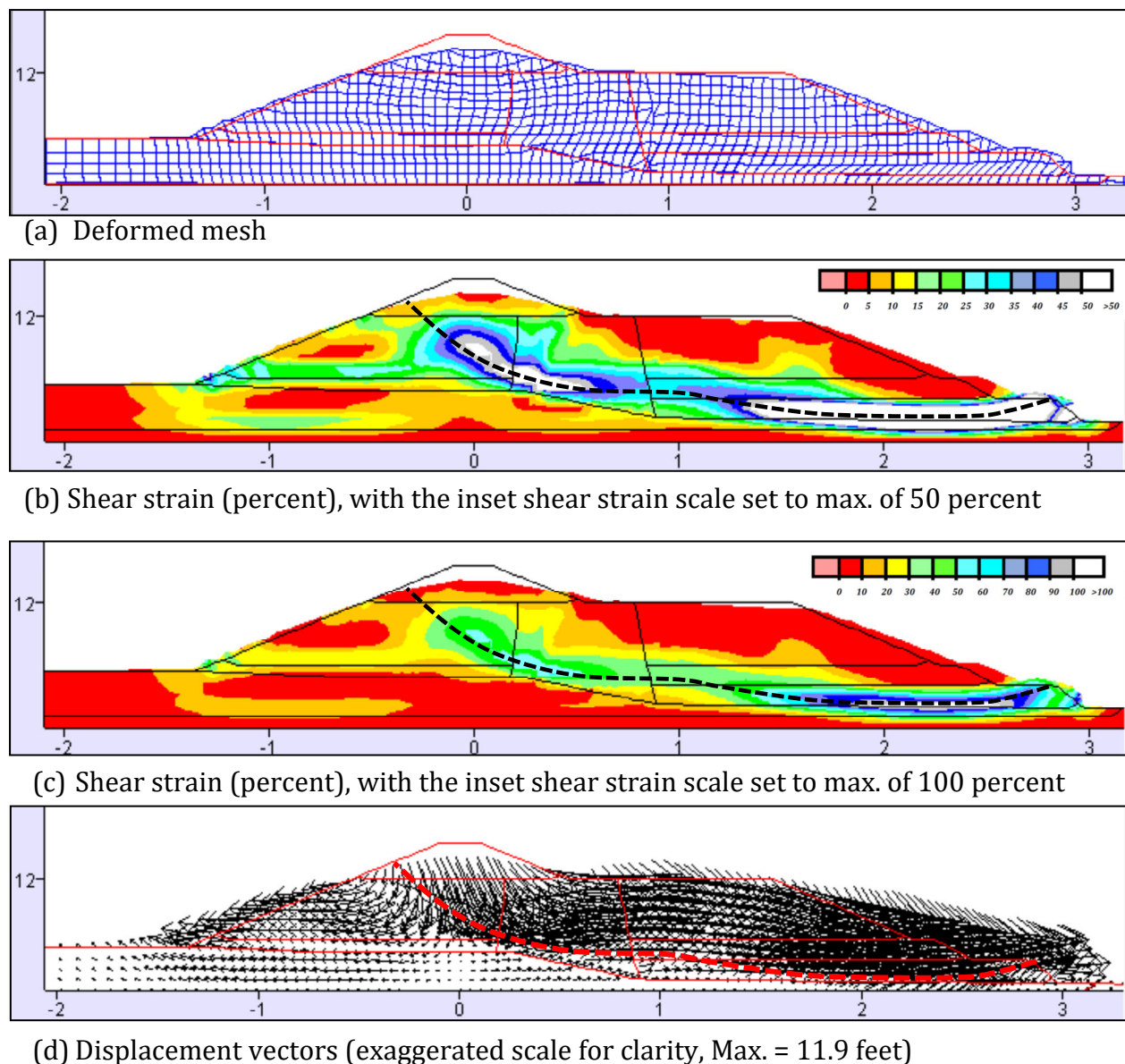


Figure 5-17: Results of USFD Analysis 1 at the end of analysis, annotated

closely matching the zone of damage to the upstream side concrete facing (See Figures 5-1, 5-2, 5-3, 5-5 and 5-8); which can now be recognized as the likely heel scarp of an only partially displaced overall deep-seated slippage mechanism.

The shear offset in the upstream slope face concrete lining is not well-developed at the upstream face (1) because the deformations at the upstream face are small, and (2) because these FLAC nonlinear seismic deformation analyses are continuum analyses, and they do not allow for modeling of full shear strain localization and bifurcation (direct shear offset). Despite this intrinsic shortcoming of continuum analyses, USFD Analysis 1 captures the apparent deformation mechanisms well, and explains both the upstream face distress as well as the observed downstream toe displacements. As the rear heel (upstream end) of this slope displacement feature is curved (semi-rotational) in shape, this analysis also explains the observed vertical crest settlements, and as the shear zone (or inferred potential slippage surface) transitions to become principally laterally translational towards the downstream side of the embankment and it also explains the observed lateral translation of the downstream toe.

Table 5-10 presents a summary comparison of displacements calculated by USFD Analysis 1 vs. measured displacements at several key locations where surveyed or measured displacements available. These locations (and displacements) are (1) settlement of the crest, (2) lateral translation of the crest, (3) lateral translation of the downstream slope face of the dam embankment, and (4) lateral translation of the downstream toe of the embankment. Movements in the lower portion of the upstream slope and at the upstream toe are not known, as the reservoir was only partially lowered after the earthquake to facilitate repairs to the heel scarp feature and damage near the top of the upstream face. Agreement between calculated displacements and actual observed displacements is generally good, but vertical crest settlements are conservatively overestimated, which is a common observation with the

Table 5-10: Comparison between results of USFD Analysis 1 [Roth Model – Y, SH] and observed displacements of the USFD at four key locations

Displacement Location and Direction	Measured Displacements	Analysis Results
Maximum crest loss	2.5 to 3.0 feet	7.0 feet to 7.7 feet
Maximum crest lateral translation towards the D/S	4.9 to 6.0 feet	3.4 feet
Maximum lateral translation of the D/S slope face	7.2 to 8.7 feet	11.7 feet
Maximum lateral translation of the D/S toe	3.6 to 5.3 feet	7.3 feet

Roth model, and which is targeted to compensate for the current lack of a well-vetted approach for evaluation of post-earthquake reconsolidation settlements (Beatty, personal communication).

Overall, USFD Analysis 1 provides very good, and useful, engineering results. It usefully reveals the principal mechanism of displacements and deformations: a deep shear surface originating at the downstream toe, passing laterally across the base of the embankment, and then curving upwards across the central clay core to intersect near the top of the upstream face. The magnitudes of displacements calculated agree well with observed displacements, except that vertical crest settlements are conservatively over-estimated. If this analysis had been performed as a “forward” assessment of likely performance for these input ground motions, the engineering interpretation would likely have been that this earthquake would produce significant liquefaction, and that this liquefaction in conjunction with the seismic dynamic inertial forces would produce moderate crest loss (settlement) and moderate lateral displacements towards the downstream direction at both the crest and near the downstream toe. It is noteworthy that this analysis also closely predicts the location of the rear heel scarp of the downstream slippage feature; and thus also closely predicts the observed damage to the concrete lining near the top of the upstream face.

5.8.2 USFD Analysis 2: Roth Model, with the Boulanger and Idriss (2014) Liquefaction Triggering Relationship, and the Idriss and Boulanger (2015) S_r Relationship

USFD Analysis 2 is the second back-analysis of the USFD performed using the Roth analytical model. In this analysis, the Roth model is calibrated with the Boulanger and Idriss (2014) liquefaction triggering relationship, the Boulanger and Idriss (2014) K_σ relationship, and the Idriss and Boulanger (2003) K_α relationship. The Idriss and Boulanger (2015) post-liquefaction S_r relationship (the S_r/σ'_{vi} curve for soils potentially susceptible to void redistribution) is applied to elements that experience soil liquefaction.

As is standard with the Roth analytical model, the transition to post-liquefaction strength (S_r) in each individual element occurs in this analysis when the shear strength (S) of the element is reduced to a value $S \leq S_r$. As a result, elements incrementally transition to S_r as the analysis proceeds (“during shaking”). This differs from analyses performed with the other three analytical models. There are no strain criteria for transition to S_r ; only the achievement of a shear strength (reduced by cyclic pore pressure generation, or $R_{u,seis}$) to a value of $\text{Strength} \leq S_r$.

Modeling and characterization parameters were described in Sections 5-5 and 5-7, and the analysis-specific input parameters are summarized in Table 5-11. As discussed in Chapters 2 and 4, the engineering protocol for use of the Roth analytical model (and the relationship(s) combination) of USFD Analysis 2 is that a cyclic strength curve is first defined to develop the relationship between cyclic stress ratio (τ_{cy}/σ'_v) and number of equivalent

Table 5-11: Input Parameters for USFD Analysis 2 using the Roth model, with the Boulanger and Idriss (2014) Liquefaction Triggering Relationship, and the Idriss and Boulanger (2015) S_r Relationship

Soil Layer	$N_{1,60,CS}$ (Youd et al., 2001)	$N_{1,60,CS-Sr}$ (Idriss and Boulanger, 2015)	$B (=1/b)$ (Idriss, 1999)	CSR_{15} (Boulanger and Idriss, 2014)	Friction Angle, ϕ' (Table 4-8)
HFU-1	13.4	11.6	2.97	0.143	32
HFU-2	17.9	14.8	2.97	0.182	34
UA	19.3	16.6	2.97	0.198	35
HFD-1	15.2	12.1	2.97	0.182	33
HFD-2	16.6	13.5	2.97	0.170	34
HFD-3	17.8	14.7	2.97	0.158	34

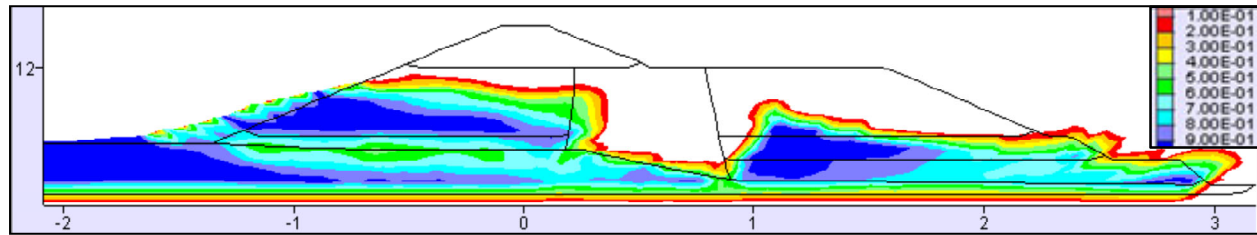
uniform cycles. The cyclic strength curve used in USFD Analysis 2 was developed based on CSR_{15} values from the Boulanger and Idriss (2014) liquefaction triggering relationship, with modifications for the K_α relationship of Idriss and Boulanger (2003), and the $B (=1/b)$ value from Idriss (1999) for each of the hydraulic fill layers and the UA layer. The model then monitors the shear stress time history of each element (monitored as the shear stress on the horizontal plane, τ_{xy} , for each half-cycle of seismic shear loading), with reversal of shear direction on the horizontal plane representing the end of each half-cycle of loading, and “counting” of the accumulating shear stress cycles (half cycles determined by shear stress reversals) and then increments cyclic pore pressure generation (increase) based on a scaled “damage accumulation” approach. As soon as a one-half stress cycle is detected, the excess pore pressure is incremented by an amount dependent on the cyclic stress ratio of that cycle.

The strength envelope follows a Mohr-Coulomb relationship from the beginning of analysis, until (and if) the element’s shear strength transitions to a user-defined post-liquefaction strength; in this USFD Analysis 2 to S_r as determined by Idriss and Boulanger (2015).

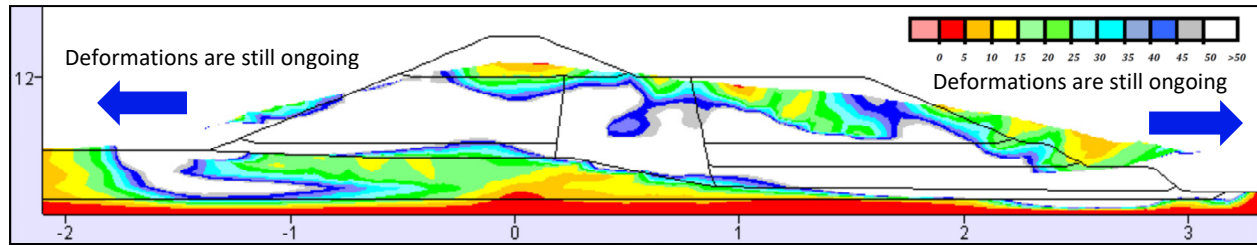
The Roth model is used in potentially liquefiable soils (which are the semi-hydraulic fill shell zones, and the upper alluvium). Non-liquefiable soils (the central clayey core, the upper rolled fill, and the lower alluvium) are modeled using the FLAC Mohr-Coulomb model. The non-liquefiable layers were modeled with Mohr-Coulomb parameters, as presented in Table 5-8. Shear strength of the semi-puddled central clay core was modeled as $S_u/\sigma'_{vi} = 0.192$ during shaking in USFD Analysis 2, which represents approximately a 20% reduction of undrained shear strength (from peak static, or monotonic, shear strength of $S_u/\sigma'_{vi} = 0.24$) for the normally consolidated clayey core to account for both (1) cyclic softening and (2) strain softening.

Figure 5-18 presents the results of nonlinear seismic deformation analyses performed with the combination of models and relationships of USFD Analysis 2. Figure 5-

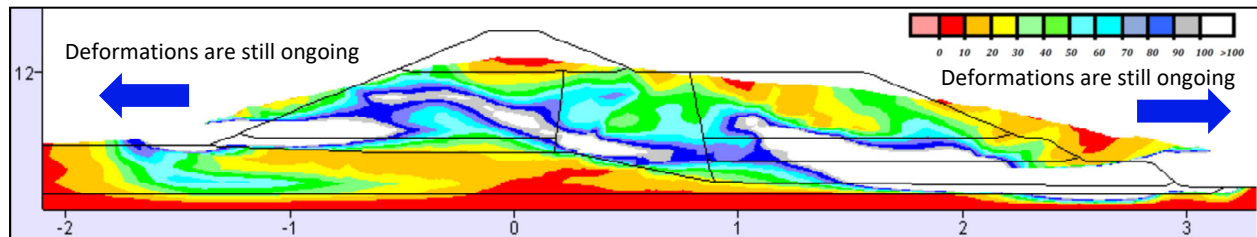
USFD Analysis 2: Roth model, with the Boulanger and Idriss (2014) Liquefaction Triggering Relationship, and the Idriss and Boulanger (2015) S_r Relationship



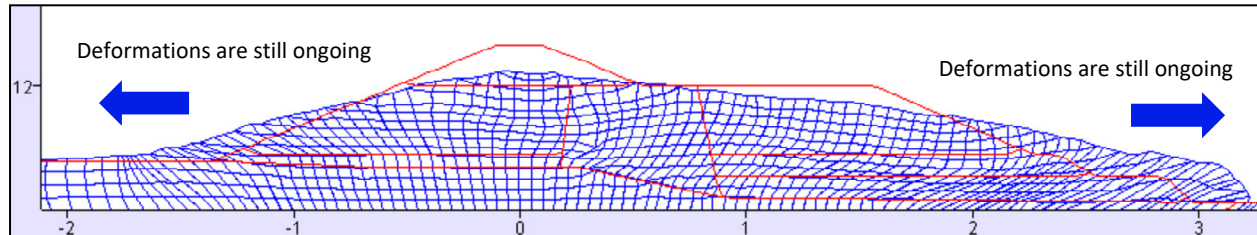
(a) Maximum value of $R_{u, seismic}$ recorded in each element



(b) Shear strain (percent), with the inset shear strain scale set to max. of 50 percent



(c) Shear strain (percent), with the inset shear strain scale set to max. of 100 percent



(d) Deformed mesh

Figure 5-18: Results of USFD Analysis 2 at the “end of shaking” and “end of analysis”

18 also shows conditions calculated “at the end of shaking”, which are the same as “end of analysis” for this USFD Analysis 2 (unstable conditions; with deformations still ongoing). It should be noted that “post-shaking” analyses are necessary in Roth model analyses only if (1) the “end of shaking” analysis indicates ongoing deformations in Roth model analyses, and the amount of deformations are not yet adequate to make an engineering interpretation and decision, or (2) shear strains developed across potentially strain sensitive cohesive (clayey) soils suggest that further reduction in strengths of these cohesive soils are warranted to account for strain softening.

In this case, the embankment was unstable at the end of shaking, and displacements and deformations were still ongoing. Re-meshing was necessary to continue the analysis. As this remeshing becomes increasingly tedious, and as the solution accuracy eventually declines, the protocol in these current studies is to make an engineering decision to stop the analysis when the engineering results are sufficient for decision-making.

Figure 5-18 also represents conditions at “the end of analysis”. In this case (USFD Analysis 2), when the analysis was halted, there were two uncontrolled slope stability failures still underway on both the upstream and downstream sides of the embankment, with deformations and displacements still ongoing as indicated by the blue arrows in Figure 5-18. Vertical crest loss was already very large, and was still progressing as the embankment displaced laterally towards both the upstream and downstream directions. The slides toward both the upstream and downstream sides of the dam represent liquefaction-induced flow slides.

As shown in these figures, and in Figure 5-19 below, which shows a further-annotated copy of Figure 5-18(c) a downstream side uncontrolled stability failure (or flow slide) is underway, with a shear displacement surface originating at the base of the downstream toe, and then arcing upwards to exit at a heel scarp feature that occurs at a point near to where the downstream “deck” intersects the base of the upper “crest section”. A second “lobe” has formed upslope, behind this downstream flow failure lobe, and it is carrying the top crest section of the dam obliquely downwards and laterally towards the downstream direction. A third uncontrolled stability failure originates at the upstream toe. The top of this second feature has been cut off by the heel of the second (upper) lobe of the upper lobe of the downstream stability failure feature.

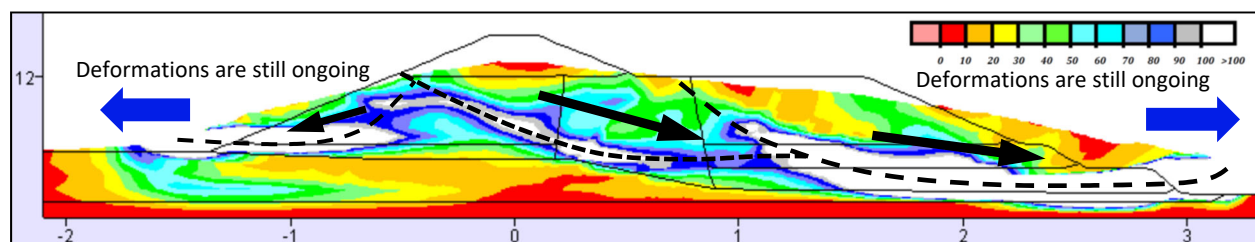


Figure 5-19: Shear strains and deformed embankment shape at the end of analysis for USFD Analysis 2, with dashed lines and black arrows indicating the inferred shear displacement surfaces and mechanisms

The analysis was terminated because the useful engineering result had been reached. With embankment deformations still ongoing (stability has not yet been re-established), the dam crest has been lowered by approximately 13 feet, and was continuing to drop. Uncontrolled flow slides were occurring on both the upstream and downstream sides of the embankment.

These two analytically predicted flow failures, which did not occur in the actual earthquake, represent very poor analytical results.

These poor results are not primarily the fault of the Roth model, which performed well in USFD Analyses 1 and 3, nor of the Boulanger and Idriss (2014) liquefaction triggering relationship, which is the least conservative of the three liquefaction triggering relationships employed in these current studies (see Section 2.3) and would not have over-estimated cyclic pore pressure generation. Instead, these poor analytical results appear to be mainly the result of underestimation of post-liquefaction residual strengths (S_r) by the Idriss and Boulanger (2015) S_r relationship, and the resulting erroneous prediction of stability failures on both the upstream and downstream sides of the dam. As discussed in Section 2.4, in this S_r relationship the ratio of predicted $S_r/\sigma'_{v,i}$ is a function only of $N_{1,60,CS}$; this ratio does not also vary as a function of initial effective overburden stress ($\sigma'_{v,i}$). As a result, this relationship is overly conservative (under-predicts S_r) at low initial effective overburden stresses. Both of the stability failures initiated at and near the upstream and downstream toes, where elements with low initial effective overburden stresses occur.

Table 5-12 shows a comparison between predicted, and observed, displacements at three key locations. Agreement between the analytical results, and observed performance, was very poor.

Table 5-12: Comparison between results of USFD Analysis 2 [Roth Model – B&I, I&B] and observed displacements of the USFD at four key locations

Displacement Location and Direction	Measured Displacements	Analysis Results
Maximum crest loss	2.5 to 3.0 feet	> 13 feet*
Maximum crest lateral translation to D/S (+ towards D/S)	4.9 to 6.0 feet	> 4.7 feet*
Maximum lateral translation of the D/S slope face	7.2 to 8.7 feet	> 45 feet*
Maximum lateral translation of the D/S toe	3.6 to 5.3 feet	> 36 feet*

*Upstream and downstream liquefaction-induced flow failures are still ongoing.

5.8.3 USFD Analysis 3: Roth Model, with the Cetin et al. (2018) Liquefaction Triggering Relationship, Youd et al. (2001) K_σ Relationship, and the Weber et al. (2015) Post-Liquefaction S_r Relationship

USFD Analysis 3 is the third and final back-analysis of the three USFD back-analyses performed using the Roth analytical model. This time the Roth model is calibrated with the Cetin et al. (2018) liquefaction triggering relationship, the Youd et al. (2001) K_σ relationship, and the Idriss and Boulanger (2003) K_α relationship. The Weber et al. (2015) post-liquefaction S_r relationship is applied to elements that experience soil liquefaction.

As is standard with the Roth analytical model, the transition to post-liquefaction strength (S_r) in each individual element occurs in this analysis when the shear strength (S) of the element is reduced to a value of $S \leq S_r$. As a result, elements incrementally transition to S_r as the analysis proceeds (“during shaking”). This differs from approach taken to the transition to S_r in analyses performed with the other three analytical models. There are no strain criteria for transition to S_r in the Roth model analyses; only the achievement of a shear strength (reduced by cyclic pore pressure generation, or $R_{u,seis}$) to a value of Strength $\leq S_r$.

Modeling and characterization parameters were described in Sections 5-5 and 5-7, and the analysis-specific input parameters are summarized in Table 5-13. As discussed in Chapters 2 and 4, the engineering protocol for use of the Roth analytical model (and the relationship(s) combination) of USFD Analysis 3 is that a cyclic strength curve is first defined to develop the relationship between cyclic stress ratio (τ_{cy}/σ'_v) and number of equivalent cycles. The cyclic strength curve used in USFD Analysis 3 was developed based on CSR_{15} values from the Cetin et al. (2018) liquefaction triggering relationship, with modifications for the K_α relationship of Idriss and Boulanger (2003), and the $B (=1/b)$ value from Cetin et al. (2018) for each of the hydraulic fill layers and for the UA layer. The model then monitors the shear stress time history of each element (monitored as the shear stress on the horizontal plane, τ_{xy} , for each half-cycle of seismic shear loading), with a reversal of shear direction on the horizontal plane representing the end of each half-cycle of loading, and then by “counting” the accumulating shear stress cycles (half cycles determined by shear stress reversals) and incrementing cyclic pore pressure generation (increase) based on a scaled “damage accumulation” approach. As soon as a one-half stress cycle is detected, the excess pore pressure is incremented by an amount dependent on the cyclic stress ratio of that cycle. The strength envelope follows a Mohr-Coulomb relationship from the beginning of analysis, until (and if) the element’s shear strength transitions to a user-defined post-liquefaction strength; in this USFD Analysis 3 to S_r as determined by Weber et al. (2015).

The Roth model is used in potentially liquefiable soils (which are the semi-hydraulic fill shell zones, and the upper alluvium). Non-liquefiable soils (the central clayey core, the upper rolled fill, and the lower alluvium) are modeled using the FLAC Mohr-Coulomb model. The non-liquefiable layers were modeled with Mohr-Coulomb parameters, as presented in Table 5-8. Shear strength of the semi-puddled central clay core was modeled as $S_u/\sigma'_{vi} = 0.192$ throughout USFD Analysis 3, which assumes approximately a 20% reduction of undrained shear strength (from a peak static, or monotonic, shear strength of $S_u/\sigma'_{vi} = 0.24$)

for the normally consolidated clayey core to account for both (1) cyclic softening and (2) strain softening.

Table 5-13: Input Parameters for USFD Analysis 3 using the Roth model, with the Cetin et al. (2018) Liquefaction Triggering Relationship, and the Weber et al. (2015) Post-Liquefaction S_r Relationship

Soil Layer	$N_{1,60,CS}$ (Cetin et al., 2018)	$N_{1,60,CS-S_r}$ (Weber et al., 2015)	$B (=1/b)$ (Cetin et al. 2018)	CSR_{15} (Cetin et al, 2018)	Friction Angle, ϕ' (Table 4-8)	f for K_σ (Youd et al., 2001)
HFU-1	11.7	11.7	2.325	0.098	32	0.731
HFU-2	15.4	15.4	2.325	0.135	34	0.691
UA	16.7	16.7	2.325	0.150	35	0.679
HFD-1	12.6	12.6	2.325	0.106	33	0.721
HFD-2	14.3	14.3	2.325	0.123	34	0.703
HFD-3	15.3	15.3	2.325	0.134	34	0.692

Figure 5-20 present the results of nonlinear seismic deformation analyses performed with the combination of models and relationships of USFD Analysis 3. Figure 5-20 shows conditions calculated “at the end of shaking”, which are the same as “end of analysis” for the Roth model when stable conditions occur at the end of shaking, and shear strain development at the end of shaking does not warrant additional reductions of strengths of cohesive soils to account for strain softening. The “end of shaking” conditions for analyses performed with the Roth model are also the same as “end of analysis” conditions when additional strength reductions in cohesive soils (to account for strain softening) do not produce any significant further deformations or displacements.

The Roth model is the only one of the four analytical models used in these current studies that transitions “incrementally” to post-liquefaction residual strength as the analysis proceeds during shaking (transition to S_r occurs when the strength of an individual element decreases to $S \leq S_r$ as a result of incremental seismic pore pressure generation). As a result, all elements that will transition to S_r will have done so before the end of shaking.

An assessment is then made at the end of shaking of shear strains, and of shear displacement offsets across narrowly banded shear zones, in potentially strain sensitive cohesive soils, and if warranted the strengths of these soils may be further reduced, and then the NDA analysis is re-started and continued after the end of strong shaking. In this case (USFD Analysis 3), shear strains across the central clay core zone were sufficient as to potentially warrant additional reductions in clay strengths to account for strain softening. Maximum shear strains across the central core zone were 56%, with an average of 17%. As per the protocol described in Section 5.5.2, the strength of the central clayey core was reduced to a value intermediate between (1) the already 20% softened clay core strength value of $S_u/\sigma'_{vi} = 0.192$ and (2) a fully residual value of $S_{u,residual}/\sigma'_{vi} = 0.08$, to a strength of $S_u/\sigma'_{vi} = (0.5)(0.192 + 0.08) = 0.136$, and then the analysis was re-started and continued past the end of shaking.

USFD Analysis 3: Roth model, with the Cetin et al. (2018) Liquefaction Triggering Relationship, Youd et al. (2001) K_σ , and the Weber et al. (2015) S_r Relationship

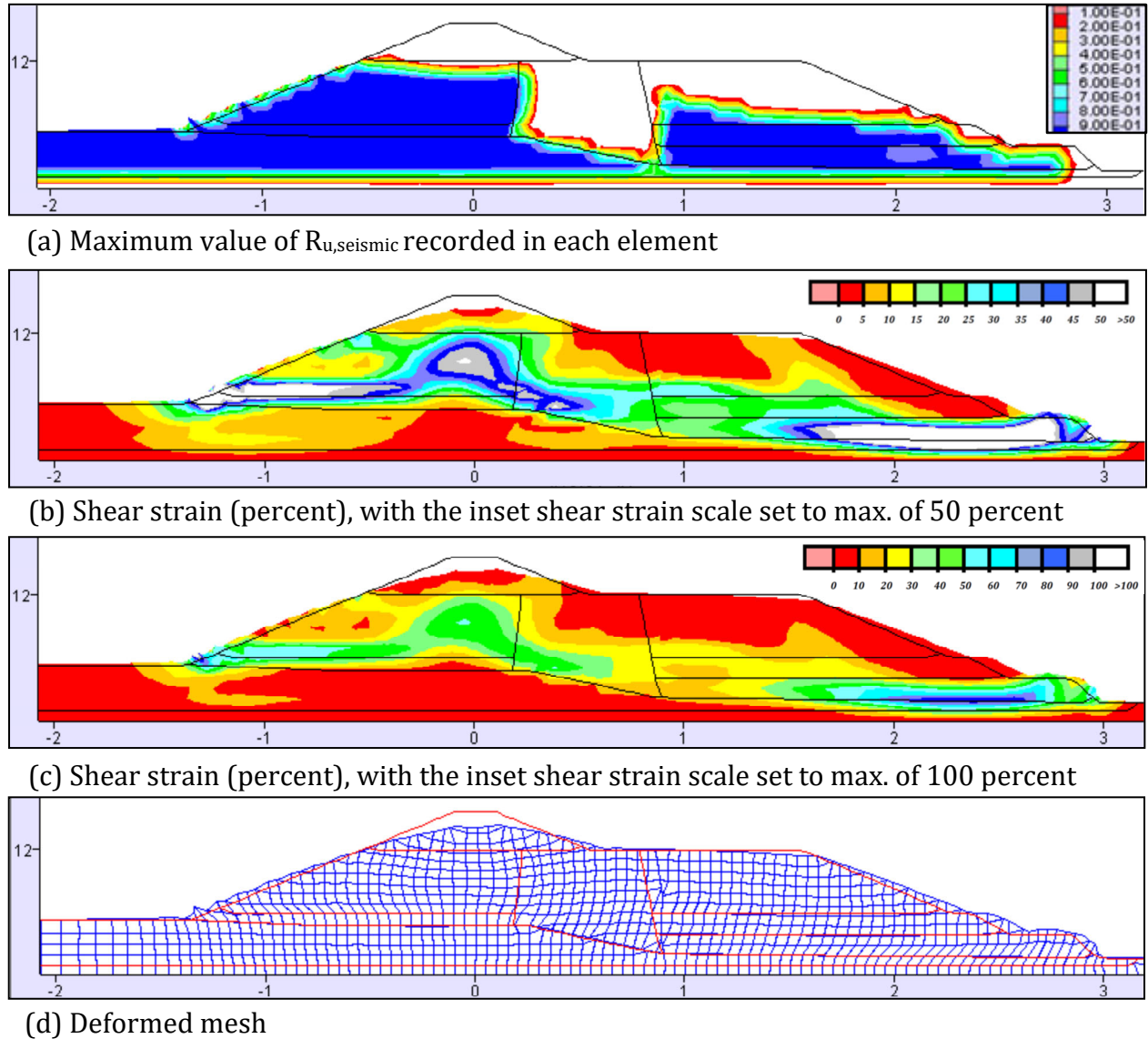


Figure 5-20: Results of USFD Analysis 3 at the end of shaking and end of analysis

The embankment was stable with these reduced clay core strengths, and no further significant deformations or displacements developed. The shear strengths of the upstream and downstream shells, and upper alluvium, including large numbers of elements that had transitioned to post-liquefaction residual strengths (S_r), were sufficient to maintain stability and to help support the weakened central core. Upon application of this reduction of clayey core strengths to $S_u/\sigma'_{vi} = 0.136$, crest loss from 6.2 to 7.3 feet. Similarly, maximum lateral translation at the downstream slope increased from 9.5 feet to 9.7 feet. The embankment was stable and stationary, and there were no significant increases in shear strains that would result in consideration of further clay strength decreases to account for strain softening.

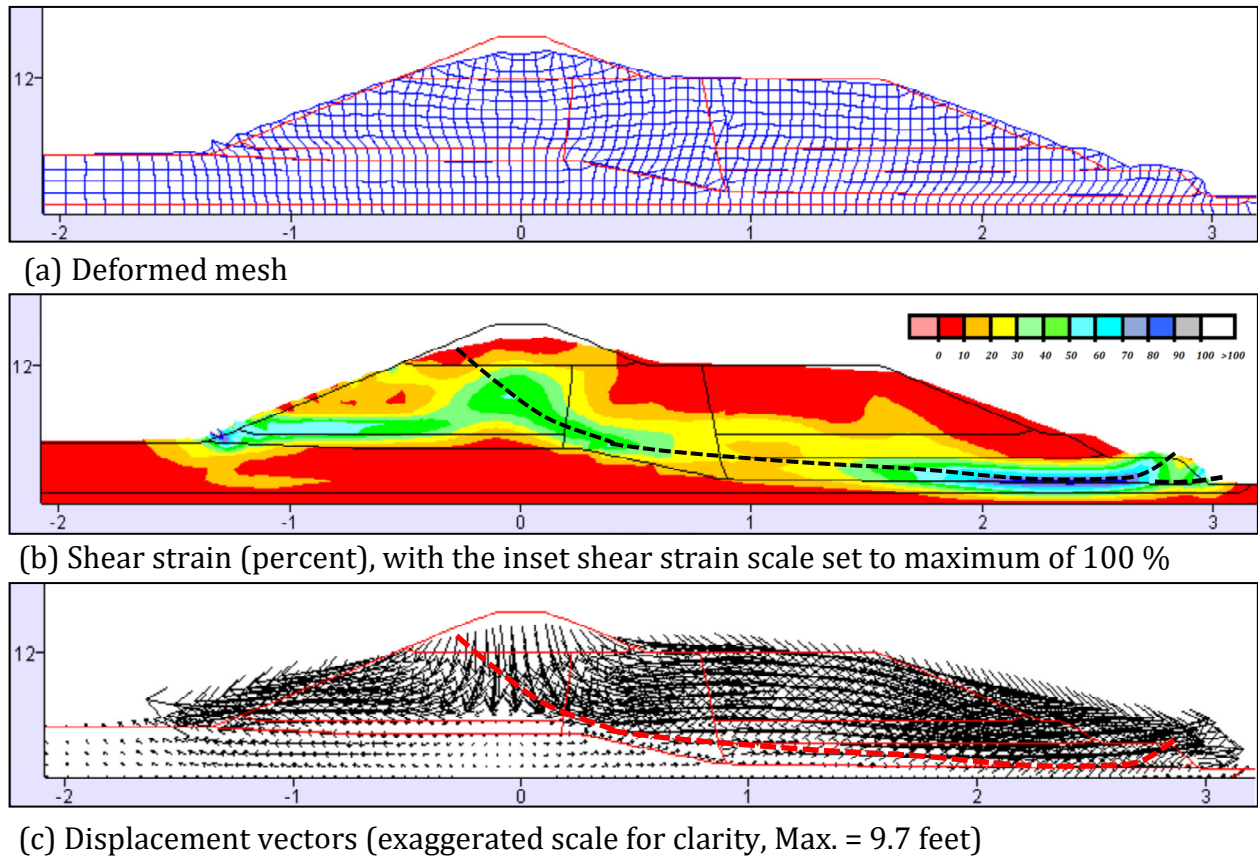


Figure 5-21: Results of USFD Analysis 3 at end of analysis; annotated

As a result, the “end of analysis” conditions are the same as the “end of shaking” conditions, as shown in Figure 5-20.

As a hypothetical worst case scenario for LSFD Analysis 3, the puddled clay core strength was next reduced to the fully residual strength of $S_{u,residual}/\sigma'_{vi} = 0.08$ of clay, and the analysis was again re-started and continued forward. This added an additional 0.2 feet of crest loss (e.g. crest loss increased from 7.3 feet to 7.5 feet), and maximum lateral slope displacement increased from 9.7 feet to 9.9 feet, and the dam remained stable.

As shown in Figure 5-20(a), USFD Analysis 3 generates significant seismically-induced pore pressures in the saturated semi-hydraulic fill shell materials on the upstream side of the dam (layers HFU-1 and HFU-2) and also in the underlying upper alluvium (UA) beneath the upstream side of the dam. Significant seismically-induced pore pressures are also generated on the downstream side of the dam, in the saturated portions of the semi-hydraulic fill downstream shell materials (layers HFD-2 and HFD-3).

Figures 5-20(b) and (c) show contours of maximum shear strains developed (at two different scales; set to maximum shear strains of 50 percent and 100 percent), and Figure 5-20(d) shows the deformed mesh at the end of shaking and end of analysis. As shown in,

these four figures, the combination of seismic pore pressure generation, and resulting strength and stiffness reductions, combined with the seismic inertial shaking forces, produces moderate displacements and deformations.

Figure 5-21 repeats Figures 5-20(d) and (c), and adds an additional figure showing displacement vectors (at exaggerated scale for clarity). Figures 5-21(b) and (c) are annotated to show the concentrated shear zone exhibited in these analysis results. The zone represents a deep basal shear mechanism originating at the base of the downstream toe, traversing laterally along the base of the downstream side hydraulic fill shell zone, and then arcing upwards as it crosses the central clay core zone to exit high on the upstream face of the dam at a location again relatively closely matching the zone of damage to the upstream side concrete facing (See Figures 5-1, 5-2, 5-3, 5-5 and 5-8); which can now be recognized as the likely heel scarp of an only partially displaced overall deep-seated slippage mechanism.

The shear offset in upstream slope face is not well-developed at the upstream face (1) because the deformations at the upstream face are small, and (2) because these FLAC NDA analyses are continuum analyses, and they do not allow for modeling of full shear strain localization and bifurcation (direct shear offset). Despite this intrinsic shortcoming of continuum analyses, USFD Analysis 1 captures the apparent deformation mechanisms well, and explains both the upstream face distress (the rear heel of the slippage feature exits the upstream face very near to the location of observed damage to the upstream side concrete facing) as well as the observed downstream toe displacements. As the rear heel (upstream end) of this slope displacement feature is curved (semi-rotational) in shape, this analysis also explains the observed crest settlements, and as the shear zone (or inferred potential slippage surface) transitions to become principally laterally translational towards the downstream side of the embankment and it also explains the observed lateral translation of the downstream toe.

Table 5-14 presents a summary comparison of displacements calculated by USFD Analysis 3 vs. measured displacements at several key locations where surveyed or measured displacements available. These locations (and displacements) are (1) settlement of the crest, (2) lateral translation of the crest, (3) lateral translation of the downstream slope face of the dam embankment, and (4) lateral translation of the downstream toe of the embankment. Movements in the lower portion of the upstream slope and at the upstream toe are not known, as the reservoir was only partially lowered after the earthquake to facilitate repairs to the heel scarp feature and damage near the top of the upstream face. Agreement between calculated displacements and actual observed displacements is generally very good. Vertical crest settlements are conservatively overestimated, which is a common observation with the Roth model which compensates for the lack of a well-vetted approach for evaluation of post-earthquake reconsolidation settlements.

Overall, USFD Analysis 3 provides very good, and useful, engineering results. It usefully reveals the principal mechanism of displacements and deformations: a deep shear surface originating at the downstream toe, passing laterally across the base of the embankment, and then curving upwards across the central clay core to intersect near the top of the upstream face. The magnitudes of displacements calculated agree well with observed displacements, except that vertical crest loss is again conservatively over-estimated. If this

analysis had been performed as a “forward” assessment of likely performance for these input ground motions, the engineering interpretation would likely have been that this earthquake would produce significant liquefaction, and that this liquefaction in conjunction with the seismic dynamic inertial forces would produce moderate crest loss (settlement) and moderate lateral displacements towards the downstream direction at both the crest and near the downstream toe.

Table 5-14: Comparison between results of USFD Analysis 3 [Roth Model – C, W] and observed displacements of the USFD at four key locations

Displacement Location and Direction	Measured Displacements	Analysis Results
Maximum crest loss	2.5 to 3.0 feet	6.3 to 7.3 feet
Maximum crest lateral translation to D/S (+ towards D/S)	4.9 to 6.0 feet	1.1 feet
Maximum lateral translation of the D/S slope face	7.2 to 8.7 feet	9.7 feet
Maximum lateral translation of the D/S toe	3.6 to 5.3 feet	6.0 feet

5.8.4 USFD Analysis 4: UBCSAND Model, with the Youd et al. (2001) Liquefaction Triggering Relationship and the Seed and Harder (1990) S_r Relationship

USFD Analysis 4 utilizes the UBCSAND model, parameterized to implement the Youd et al. (2001) liquefaction triggering relationship, with the Youd et al. (2001) K_σ relationship, and the Idriss and Boulanger (2003) K_α relationship, within the UBCSAND modeling scheme for the potentially liquefiable hydraulic fill and upper alluvium layers. This is the first of three USFD back-analyses performed using the UBCSAND model. The UBCSAND constitutive model Version 904aR requires only $N_{1,60,CS}$ values as input parameters, as all other model parameters have been parametrized or calibrated to relate (to be self-setting) as a function of $N_{1,60,CS}$. The post-shaking analysis requires post-liquefaction strength, S_r , and in Analysis 4 this will be based on the Seed and Harder (1990) S_r relationship (average values).

The current UBCSAND model is parametrized in such a way that it is expected to show soil behaviors consistent with the Youd et al. (2001) liquefaction triggering relationship, and the Youd et al., 2001 K_σ relationship, and behaviors at least generally consistent with the Boulanger and Idriss (2003) K_α relationship, when $N_{1,60,CS}$ values based on the energy,

equipment, procedural and effective overburden stress corrections of Youd et al. (2001) are assigned in the potentially liquefiable soil elements (the saturated elements in the upstream and downstream semi-hydraulic fill shells, and the upper alluvium underlying the upstream side of the dam embankment). As part of this parameterization of the UBCSAND model, K_σ behavior has been parametrized by means of a conversion relating D_r with $N_{1,60,CS}$ using a value of $C_d = 46$ in Equation 4-2.

Table 5-15 presents the input parameters used in Analysis 4 for modeling of the potentially liquefiable soils. The non-liquefiable layers were modeled with Mohr-Coulomb parameters, as presented in Table 5-8. Shear strength of the semi-puddled central clay core was modeled as $S_u/\sigma'_{vi} = 0.192$ throughout during shaking analyses of USFD Analysis 4, which assumes approximately a 20% reduction of undrained shear strength (from peak static, or monotonic, shear strength of $S_u/\sigma'_{vi} = 0.24$) for the normally consolidated clayey core to account for both (a) cyclic softening and (b) strain softening.

The protocol for the seismic deformation analyses performed as part of these current studies is to handle the potential transition to post-liquefaction residual strength (S_r) in elements comprised of potentially liquefiable soils within the constitutive model framework by considering the analysis to progress in two steps or stages (1) during shaking, and (2) after the end of shaking. During shaking, there is no implementation of S_r in UBCSAND model. After the end of shaking, S_r is applied within potentially liquefiable soil elements that satisfy either of two criteria: (1) occurrence of $R_{u,seis} \geq 0.7$ at any stage during shaking ($R_{u,seis,max} \geq 0.7$) or (2) development of a peak shear strain of $\gamma \geq 10\%$ at the end of shaking in saturated materials. The UBCSand protocol used in the current studies is then to continue the nonlinear deformation analysis after the end of shaking until either (1) deformations and displacements have ceased to occur, as the embankment is in a stable condition, or (2) mesh distortions are resulting in a need to perform significant (and time-consuming) re-meshing to continue the NDA deformation analysis, and the results at termination have become sufficient for purposes of engineering interpretation and decision-making, with recognition that deformations and displacements are still ongoing.

Similarly, it is also part of the UBCSAND protocol in these current studies to examine non-liquefiable soils (e.g. the normally consolidated central clayey core zone) at the end of shaking, and to consider whether strength reduction (or further strength reduction) is

Table 5-15: Input Parameters for USFD Analysis 4 using the UBCSAND model, with the Youd et al. (2001) Liquefaction Triggering Relationship, and the Seed and Harder (2015) S_r Relationship

Soil Layer	$N_{1,60,CS}$ (Youd et al., 2001)	$N_{1,60,CS-Sr}$ (Seed and Harder, S_r , 1990)
HFU-1	13.6	11.6
HFU-2	18.4	14.7
UA	19.5	16.1
HFD-1	15.8	12.3
HFD-2	17.3	13.7
HFD-3	18.3	14.6

warranted as a result of large shear strain development in strain sensitive cohesive soils. This will be discussed further below. If appropriate, strengths are reduced (or further reduced) at this juncture, and the analysis then proceeds after the end of shaking.

Figures 5-22 and 5-23 present the results of nonlinear seismic deformation analyses performed with the combination of models and relationships of USFD Analysis 4. Figure 5-22 shows conditions calculated “at the end of shaking”, but the analyses are continued after residual strengths (S_r) are applied in elements that satisfy either of two criteria: (1) occurrence of $R_{u,seis} \geq 0.7$ at any stage during shaking ($R_{u,seis,max} \geq 0.7$) or (2) development of a peak shear strain of $\gamma \geq 10\%$ at the end of shaking in saturated materials. In some cases the post-shaking deformations can lead to development, or discovery, of progressive development of large deformations or even instability failures (see Chapter 4). Accordingly, it is important to continue the analyses after the end of shaking.

Figure 5-23 therefore presents conditions at “the end of analysis”. The end of analysis is the point in time when the analysis team elects to end (discontinue) the NDA analysis. Reasons for ending the analysis can include (1) deformations and displacements have ceased to occur, as the embankment is in a stable condition, or (2) mesh distortions are resulting in a need to perform significant (and time-consuming) re-meshing to continue the NDA deformation analysis, and the results at termination have become sufficient for purposes of reduction of strength by 20% in the central clayey core zone to account for both cyclic softening and moderate strain softening.

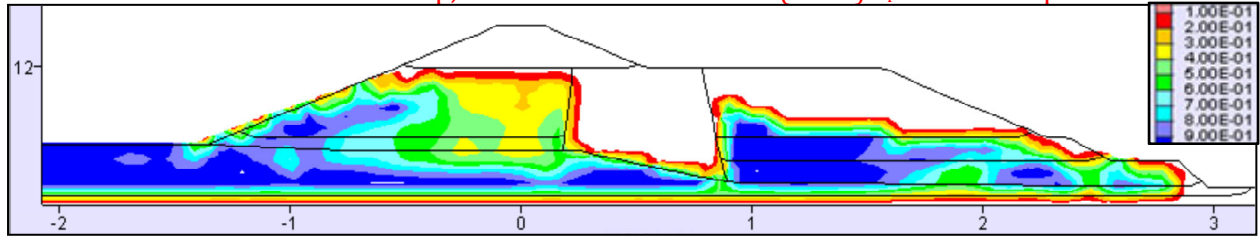
Examination of shear strains at the end of shaking (Figure 5-22) across zones of strain sensitive puddled clay core materials indicated shear strains of approximately maximum of 27%, with an average of 12% across the central clay core along potential shear zones. As discussed in Section 4.8.4, at this range of shear strains it was not fully clear whether or not additional reduction of clay shear strengths to account for strain softening was warranted, as there was already a reduction of strength by 20% in the central clay core zone to account for both cyclic softening and moderate strain softening during shaking.

The engineering judgment of the analysis team was that the strength of the central clayey core should be reduced to a value intermediate between (1) the already 20% softened clay core strength value of $S_u/\sigma'_{vi} = 0.192$ and (2) a fully residual value of $S_{u,residual}/\sigma'_{vi} = 0.08$, to a strength of $S_u/\sigma'_{vi} = (0.5)(0.192 + 0.08) = 0.136$ in the post-shaking stage. This reduction to intermediate clay strength should not add significant deformations, if the dam is stable.

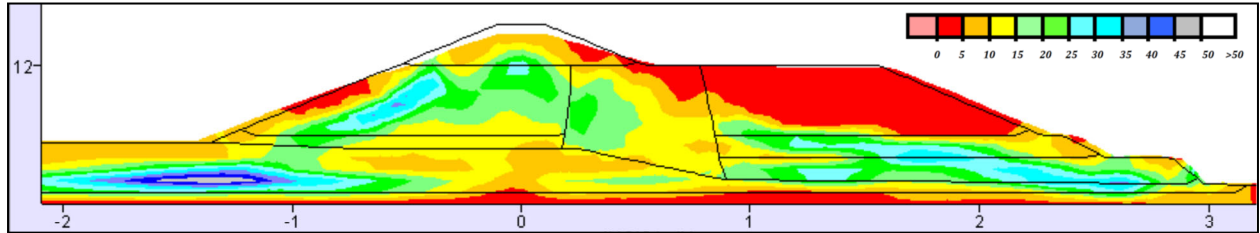
In addition, at this end of shaking stoppage a transition to post-liquefaction residual strength (S_r) was implemented in potentially liquefiable elements that had experienced either (1) $R_{u,seismic} \geq 0.7$, or (2) shear strain of greater than 10% at any time during shaking.

After the implementation of the reduced clay core strengths, and the implementation of post-liquefaction S_r in liquefied elements, the analysis was re-started and continued past the end of shaking.

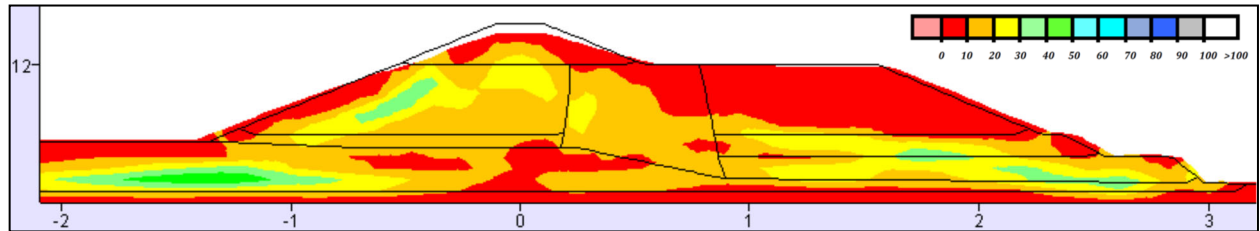
USFD Analysis 4: UBCSAND model, with the Youd et al. (2001) Liquefaction Triggering Relationship, and the Seed and Harder (1990) S_r Relationship



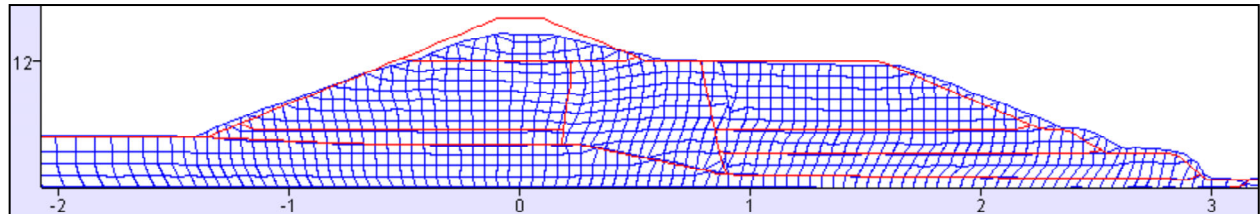
(a) Maximum value of $R_{u, seismic}$ recorded in each element



(b) Shear strain (percent), with the inset shear strain scale set to max. of 50 percent



(c) Shear strain (percent), with the inset shear strain scale set to max. of 100 percent

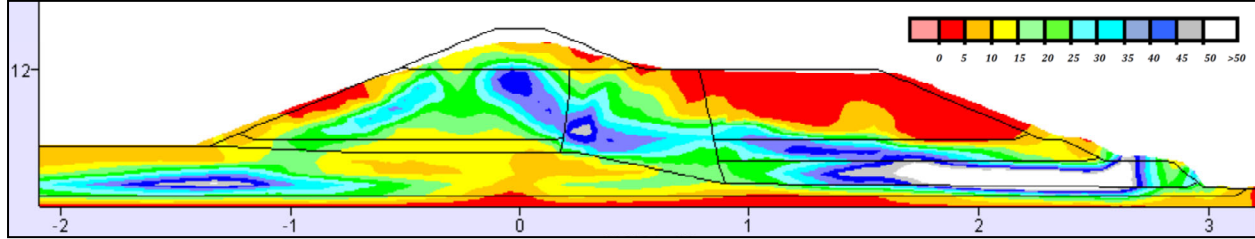


(d) Deformed mesh

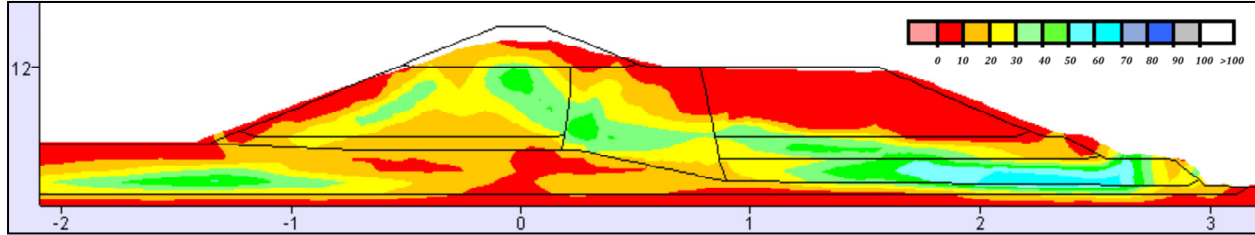
Figure 5-22: Results of USFD Analysis 4 at the end of shaking

Crest settlement was 4.8 feet at the end of shaking, and increased to 7.2 feet at the end of analysis after (1) post-liquefaction residual strengths (S_r) were implemented, and (2) further softened clay core strengths of $S_u/\sigma'_{vi} = 0.136$ were applied, and the analysis was re-started. Similarly, maximum lateral translation of the downstream slope was 6.3 feet at the end of shaking, and increased to 10.1 feet at the end of analysis. At the end of analysis, the embankment was stable. This is the “end of analysis” condition shown in Figures 5-23 and 5-24.

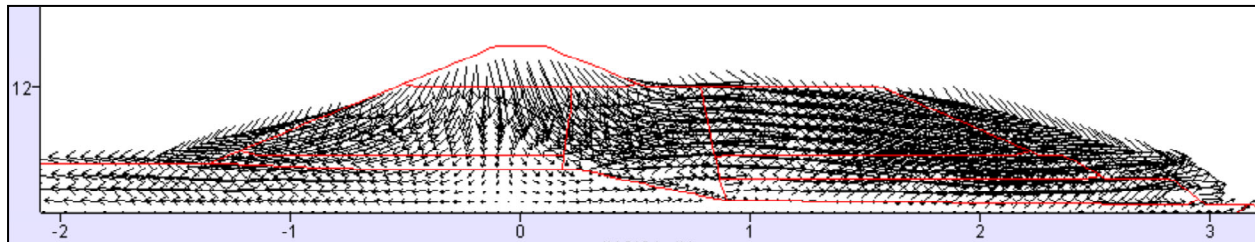
USFD Analysis 4: UBCSAND model, with the Youd et al. (2001) Liquefaction Triggering Relationship, and the Seed and Harder (1990) S_r Relationship



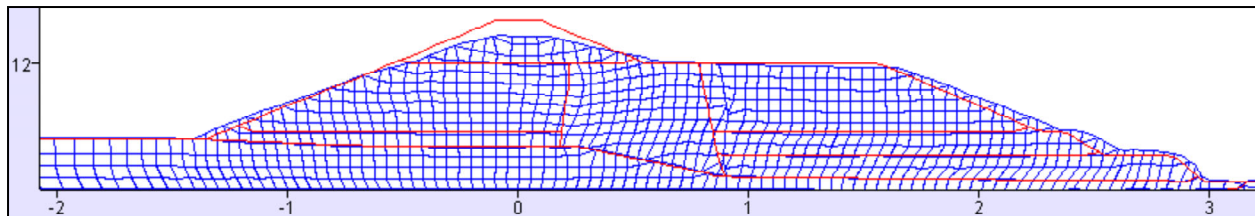
(a) Shear strain (percent), with the inset shear strain scale set to max. of 50 percent



(b) Shear strain (percent), with the inset shear strain scale set to max. of 100 percent



(c) Displacement vectors (exaggerated scale for clarity, Max. = 10.2 feet)



(d) Deformed mesh

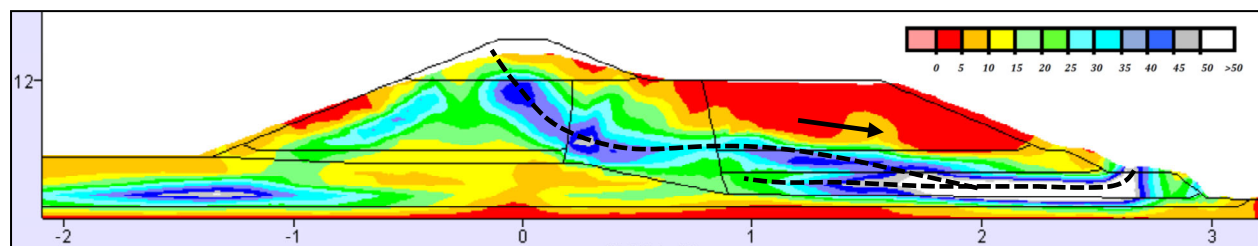
Figure 5-23: Results of USFD Analysis 4 at the end of analysis

As a hypothetical worst case scenario for LSFD Analysis 4, the puddled clay core strength was next reduced to the fully residual strength of $S_{u,residual}/P = 0.08$ of clay, and the analysis was again re-started and continued forward. This added an additional 2.6 to 3.2 feet of crest loss (e.g. crest loss increased from 7.2 feet to 10.4 feet), and maximum lateral slope displacement increased from 10.1 feet to 15.4 feet, and the dam remained stable, but marginally so.

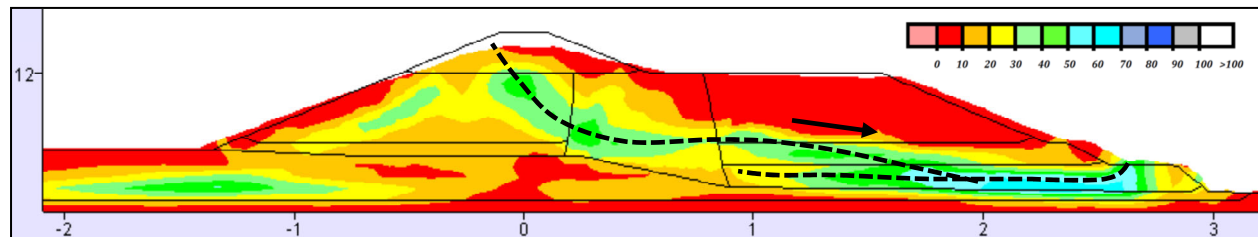
Shear strains and shear offsets across the central clay core zone had not increased sufficiently as a result of this hypothetical further reduction to fully residual clay strength as

to warrant further reduction of clay strength below $S_u/P = 0.136$, verifying the hypothetical nature of this additional analysis check. As a result, the end of analysis had occurred at the end of the post-shaking analysis with clay strengths of $S_u/P = 0.136$. This is the condition shown in Figures 5-23 and 5-24.

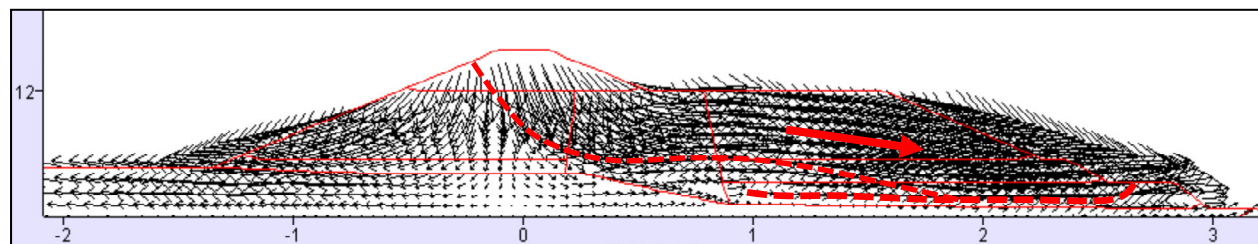
As shown in Figure 5-22 (a), significant cyclic pore pressures are generated in USFD Analysis 4 in the upstream semi-hydraulic fill shell zones, as well as in the upper alluvium underlying the upstream side of the embankment, and significant pore pressures are also generated in Analysis 4 in the saturated portions of the downstream side semi-hydraulic fill shell zones.



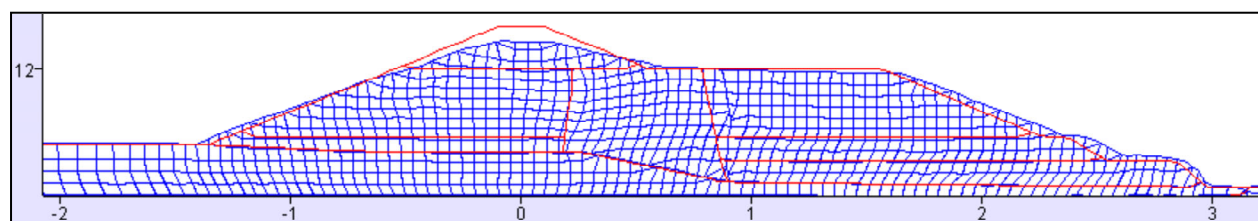
(a) Shear strain (percent), with the inset shear strain scale set to max. of 50 percent



(b) Shear strain (percent), with the inset shear strain scale set to max. of 100 percent



(c) Displacement vectors (exaggerated scale for clarity, Max. = 10.2 feet)



(d) Deformed mesh

Figure 5-24: Results of USFD Analysis 4 at the end of analysis, annotated

As indicated in Figures 5-22(b) through (d) and 5-23(a) through (d), these seismically induced pore pressures, in conjunction with the seismic inertial forces of the earthquake, again produced moderate deformations, with the principal movements occurring along a narrowly confined shear zone originating at and near the downstream toe, and then passing laterally across the lower portion of the embankment to the core, then arcing upwards across the core to exit high in the upstream face of the dam.

Figure 5-24 repeats Figure 5-23, but this time the figures are annotated to highlight selected features. There are two potential shear zone paths from the downstream toe towards the upstream side heel scarp; one passing more deeply along near the base of the embankment, and one heading upwards more quickly as it moves towards the upstream side. In USFD Analyses 1 and 3, the deeper failure surface, exiting relatively high on the upstream face (approximately at the observed location of damage to the upstream concrete facing) appears to “win”, and captures a majority of these movements; producing an upstream slide scarp exit at a location near the intersection of the horizontal crest deck and the very top of the upstream face. These two potential shear displacement surfaces will continue to compete with each other in a number of the remaining USFD analyses.

USFD Analysis 4 again predicts a deep, basal shear mechanism from the downstream toe, arcing upwards across the core and then exiting high on the upstream face; in good agreement with both the observed field performance, but exiting on the upstream face at the crest deck hinge point, which is higher than the observed exit point after the 1971 San Fernando earthquake (see Figures 5-1, 5-2, 5-3, 5-5 and 5-8) and the hypothesized mechanism, as discussed in Section 5.4.

Table 5-16 shows a comparison between predicted, and observed, displacements at four key locations. Agreement between the analytical results, and observed performance, was generally good, except that vertical crest loss was conservatively over-estimated. Minor (conservative) over-estimation of crest settlements is noted in a number of UBCSAND analyses, and it compensates for the lack of a well-established method or procedure for evaluation of post-earthquake volumetric reconsolidation, and associated vertical settlements. In this case, the over-prediction is a bit larger, and it is suspected that the use of the Seed and Harder (1990) S_r relationship, which does not account for both $N_{1,60,CS}$ and $\sigma'_{v,i}$, may also have been a contributing factor. This hypothesis will be tested in USFD Analysis 6, which exactly repeats this current Analysis 4, except that it substitutes the S_r relationship of Weber et al. (2015) for the S_r relationship of Seed and Harder (1990).

Overall, USFD Analysis 4 provided good engineering “predictions” of the actual observed field performance. It correctly predicted the occurrence of a deep, basal slippage originating at the downstream toe and then arcing upwards across the core zone to exit high on the upstream face, and it provided usefully accurate predictions of the magnitudes of deformations and displacements. The engineering interpretation of USFD Analysis 4 would be that this earthquake would produce moderate displacements and deformations, resulting in moderate crest loss and moderate downstream displacements.

Table 5-16: Comparison between results of USFD Analysis 4 [UBCSAND Model – Y, SH] and observed displacements of the USFD at four key locations

Displacement Location and Direction	Measured Displacements	Analysis Results
Maximum crest loss	2.5 to 3.0 feet	6.4 feet to 7.2 feet
Maximum crest lateral translation to D/S (+ towards D/S)	4.9 to 6.0 feet	3.3 feet
Maximum lateral translation of the D/S slope face	7.2 to 8.7 feet	10.1 feet
Maximum lateral translation of the D/S toe	3.6 to 5.3 feet	4.1 feet

5.8.5 USFD Analysis 5: UBCSAND Model with Youd et al. (2001) Liquefaction Triggering and Idriss and Boulanger (2015) S_r Relationship

USFD Analysis 5 repeats USFD Analysis 4, but substitutes the post-liquefaction residual strength, S_r relationship of Idriss and Boulanger (2015), in place of the S_r relationship of Seed and Harder (1990). That is the only difference between USFD Analyses 4 and 5. All other modeling and analysis procedures and protocols remain the same. (See the previous discussions and parameterizations in Section 5.8.4.).

The only new parameters needed for USFD Analysis 5 are $N_{1,60,CS}$ values based on corrections for energy, equipment, procedural and effective overburden stress effects as per the S_r relationship of Idriss and Boulanger (2015). These are listed in Table 5-17.

The protocol for the seismic deformation analyses performed as part of these current studies is to handle the potential transition to post-liquefaction residual strength (S_r) in elements comprised of potentially liquefiable soils within the constitutive model framework by considering the analysis to progress in two steps or stages (1) during shaking, and (2) after the end of shaking. During shaking, there is no implementation of S_r in the UBCSAND model. After the end of shaking, S_r is applied within potentially liquefiable soil elements that satisfy either of two criteria: (1) occurrence of $R_{u,seis} \geq 0.7$ at any stage during shaking ($R_{u,seis,max} \geq 0.7$) or (2) development of a peak shear strain of $\gamma \geq 10\%$ at the end of shaking in saturated materials. The protocol used in the current studies is then to continue the nonlinear deformation analysis after the end of shaking until either (1) deformations and displacements have ceased to occur, as the embankment is in a stable condition, or (2) mesh

Table 5-17: Input Parameters for use of the Idriss and Boulanger (2015) S_r Relationship in USFD Analysis 5

Soil Layer	$N_{1,60,CS-Sr}$ (Idriss and Boulanger, 2015)
HFU-1	11.6
HFU-2	14.8
UA	16.6
HFD-1	12.1
HFD-2	13.5
HFD-3	14.7

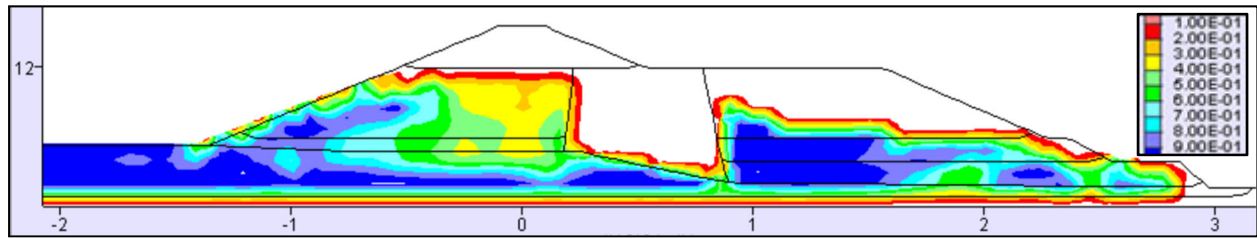
distortions are resulting in a need to perform significant (and time-consuming) re-meshing to continue the NDA deformation analysis, and the results at termination have become sufficient for purposes of engineering interpretation and decision-making, with recognition that deformations and displacements are still ongoing.

Similarly, it is also part of the UBCSAND protocol in the current studies to also examine non-liquefiable soils (e.g. the normally consolidated central clayey core zone) at the end of shaking, and to consider whether strength reduction (or further strength reduction) is warranted as a result of large shear strain development in sensitive cohesive soils.

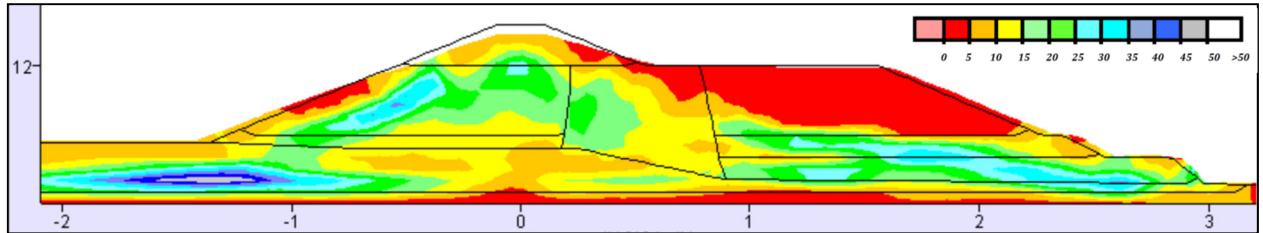
Figures 5-25 and 5-26 present the results of nonlinear seismic deformation analyses performed with the combination of models and relationships of USFD Analysis 5. Figure 5-25 shows conditions calculated “at the end of shaking”, but the analyses are continued after the end of input seismic excitation, as deformations can continue after the end of shaking due to ongoing deformations under static (gravity loading) when post-liquefaction residual strength, S_r are applied in elements that satisfy either of two criteria: (1) occurrence of $R_{u,seis} \geq 0.7$ at any stage during shaking ($R_{u,seis,max} \geq 0.7$) or (2) development of a peak shear strain of $\gamma \geq 10\%$ at the end of shaking in saturated materials. In some cases the post-shaking deformations can lead to development, or discovery, of progressive development of large deformations or even instability failures. Accordingly, it is important to continue the analyses after the end of shaking.

Figure 5-26 therefore presents conditions at “the end of analysis”. The end of analysis is the point in time when the analysis team elects to end (discontinue) the NDA analysis. Reasons for ending the analysis can include (1) deformations and displacements have ceased to occur, as the embankment is in a stable condition, or (2) mesh distortions are resulting in a need to perform significant (and time-consuming) re-meshing to continue the NDA deformation analysis, and the results at termination have become sufficient for purposes of engineering interpretation and decision-making, with recognition that deformations and displacements are still ongoing.

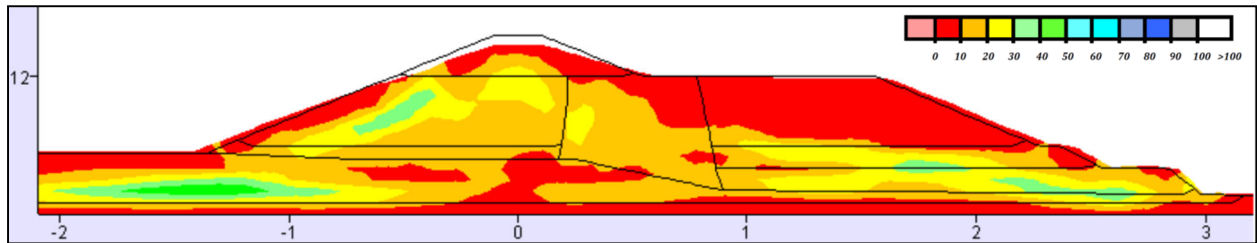
USFD Analysis 5: UBCSAND model, with the Youd et al. (2001) Liquefaction Triggering Relationship, and the Idriss and Boulanger (2015) S_r Relationship



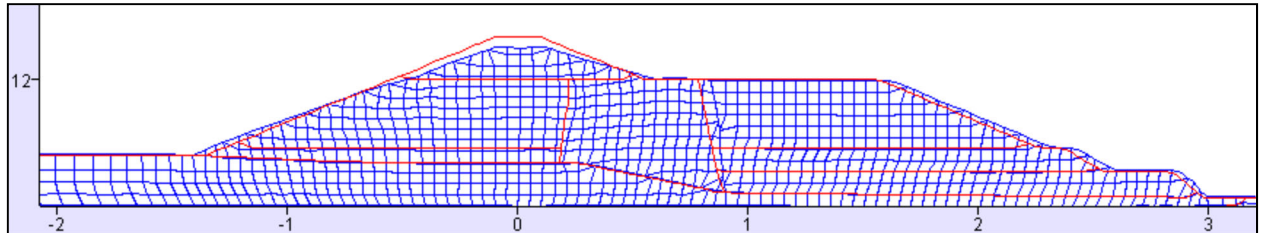
(a) Maximum value of $R_{u, seismic}$ recorded in each element



(b) Shear strain (percent), with the inset shear strain scale set to max. of 50 percent



(c) Shear strain (percent), with the inset shear strain scale set to max. of 100 percent



(d) Deformed mesh

Figure 5-25: Results of USFD Analysis 5 at the end of shaking

In this case, USFD Analysis 5, the deformations and displacements that occurred after the end of shaking were very large, and they were still ongoing as the analysis was halted, as indicated by the blue arrows in Figures 5-26(a) through (d).

Figures 5-25(a) to (d) show conditions calculated at the end of shaking. Because the same models and parameterizations were used as in the preceding Analysis 4, Figures 5-25(a) through (d) are identical to Figures 5-22(a) through (d) from USFD Analysis 4.

USFD Analysis 5: UBCSAND model, with the Youd et al. (2001) Liquefaction Triggering Relationship, and the Idriss and Boulanger (2015) S_r Relationship

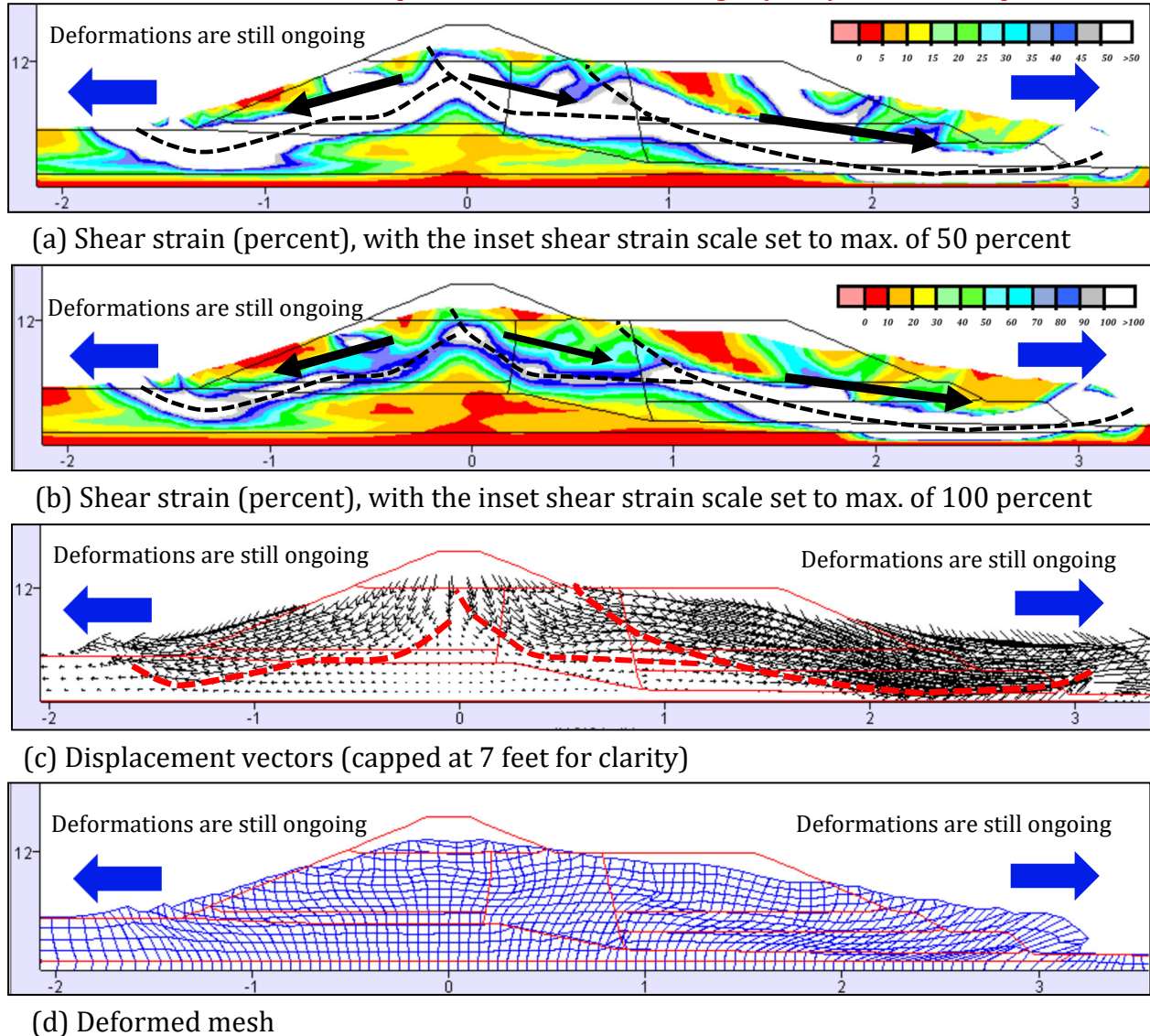


Figure 5-26: Results of USFD Analysis 5 at the end of analysis, annotated

As discussed in Section 5.8.4, examination of shear strains at the end of shaking across zones of strain sensitive puddled clay core materials indicated shear strains of approximately maximum of 27%, with an average of 12%. As discussed in Section 4.8.4, at this range of shear strains it was not fully clear whether or not additional reduction of clay shear strengths to account for strain softening was warranted, as there was already a reduction of strength by 20% in the central clay core zone to account for both cyclic softening and moderate strain softening.

The engineering judgment of the analysis team was that the strength of the central clayey core should be reduced to a value intermediate between (1) the already 20% softened

clay core strength value of $S_u/\sigma'_{v,i} = 0.192$ and (2) a fully residual value of $S_{u,residual}/\sigma'_{v,i} = 0.08$, to a strength of $S_u/\sigma'_{v,i} = (0.5)(0.192 + 0.08) = 0.136$ in the post-shaking stage. This reduction to intermediate clay strength should not add significant deformations, if the dam is stable.

As per the protocol for analyses performed with the UBCSAND model in the current studies, when the analysis was halted at the end of shaking post-liquefaction residual strengths (S_r) were implemented in potentially liquefiable soil elements which had achieved either (1) $R_{u,seis, max} \geq 0.7$ or (2) maximum shear strains of $\gamma \geq 10\%$, and the analysis was then re-started.

The result of implementation of post-liquefaction strengths, and a reduction of clay core strengths, and then re-starting the post-shaking analysis was uncontrolled deformations and displacements towards both the upstream and downstream sides of the dam embankment, as shown in Figure 5-26.

As shown in Figures 5-26(a) through (d), transitioning to S_r in elements that have liquefied, and continuing the analysis here (Analysis 5) resulted in ongoing uncontrolled displacements and deformations representing flow slide conditions towards both the upstream and downstream sides of the dam. These were very similar to the upstream and downstream flow slide features exhibited previously in USFD Analysis 2 (see Figure 5-19). A large downstream failure occurred, with a shear surface originating at the downstream toe and arcing back and upwards to approximately the point where the top deck of the downstream berm intersects the downstream end of the top crest section. A secondary slippage feature, representing the potential beginning of a second “lobe” of the downstream slide, develops as the upper portion of the downstream slope becomes un-buttressed as the toe slide feature displaces; as also highlighted with a dashed line. The downstream slide feature was still moving when the analysis was halted due to difficulties with regard to re-meshing to overcome mesh-lock, and it is interpreted to be a flow-type feature that would continue to displace. A smaller, and shallower, second flow slide feature also occurred on the upstream face. This second feature was not moving very rapidly when the analysis was halted, and it is thus not clear how far it would have traveled. As these FLAC NDA analyses are continuum analyses, and they do not allow for modeling of full shear strain localization and bifurcation (direct shear offset), there is a potential that they may underestimate formation of secondary slope failures.

As with USFD Analysis 2, which also used the Idriss and Boulanger (2015) S_r relationship, the use of this S_r relationship again underestimated S_r at relatively low to moderate initial effective overburden stresses, creating a situation of both upstream and downstream instability upon transition to S_r .

As discussed in Section 2.2.3, the Idriss and Boulanger (2015) S_r/σ'_{vi} relationship varies as a function of $N_{1,60,CS-sr}$, but the ratio of S_r/σ'_{vi} does not vary as a function of initial effective stress (σ'_{vi}). As a result, the relationship is unconservative (over-predicts S_r) at high initial effective overburden stresses, and it is over-conservative (under-predicts S_r) at low

initial effective stresses. The two analytically predicted slope failures initiated (1) at the downstream toe, and (2) at shallow depth on the upstream face. Initial effective vertical stresses (σ'_{vi}) were low in both of these locations, and so these are zones in which S_r would have been underestimated by the S_r relationship employed here.

Analysis 5 was an unsuccessful back-analysis, failing to correctly predict either (1) the principal mechanisms of the actual observed field performance, or (2) the approximate magnitudes of the actual observed field deformations and displacements. That was due to the incorrect prediction of the occurrence of two uncontrolled embankment failures (which did not occur in the actual field performance) on both the upstream and downstream sides of the embankment. These incorrect predictions of the occurrences of upstream and downstream failures appear to have been caused by under-prediction of S_r at and near the toes of the slopes, and at shallow depths near the slope faces.

This analysis failed to predict the deeper, basal slippage feature observed in the actual field performance, and it failed to provide good predictions of the observed field deformations and displacements.

Table 5-18 shows a comparison between predicted, and observed, displacements at four key locations. Agreement between the analytical results, and observed performance, was very poor, and the deformations (especially on the downstream side) were still ongoing when the analysis was halted.

Table 5-18: Comparison between results of USFD Analysis 5 [UBCSAND Model – Y, I&B] and observed displacements of the USFD at four key locations

Displacement Location and Direction	Measured Displacements	Analysis Results
Maximum crest loss	2.5 to 3.0 feet	> 14 feet*
Maximum crest lateral translation to D/S (+ towards D/S)	4.9 to 6.0 feet	> 8.2 feet*
Maximum lateral translation of the D/S slope face	7.2 to 8.7 feet	> 70 feet*
Maximum lateral translation of the D/S toe	3.6 to 5.3 feet	> 50 feet*

*Upstream and downstream liquefaction-induced flow failures are still ongoing.

5.8.6 USFD Analysis 6: UBCSAND Model with the Youd et al. (2001) Liquefaction Triggering Relationship, and the Weber et al. (2015) S_r Relationship

USFD Analysis 6 again repeats Analysis 4, but this time swaps in the post-liquefaction S_r relationship of Weber et al. (2015) (50th percentile). The Weber et al. (2015) S_r relationship predicts S_r as a function of both $N_{1,60,CS-Sr}$ and initial effective stress, σ'_{vi} .

USFD Analyses 4, 5 and 6 all employ the UBCSAND model, and all three calibrate the UBCSAND model with the Youd et al. (2001) liquefaction triggering relationship. The only differences between these three analyses are the S_r relationships employed. Analysis 4 uses the S_r relationship of Seed and Harder (1990), Analysis 5 uses the S_r relationship of Idriss and Boulanger (2015), and Analysis 6 uses the S_r relationship of Weber et al. (2015). All other modeling and analysis procedures and protocols remain the same. (See the previous discussions and parameterizations in Section 5.8.4.).

The only new parameters needed for USFD Analysis 6 are $N_{1,60,CS}$ values based on corrections for energy, equipment, procedural and effective overburden stress effects as per the S_r relationship of Weber et al. (2015). These are listed in Table 5-19.

Table 5-19: Input Parameters for use of the Weber et al. (2015) S_r Relationship in USFD Analysis 6

Soil Layer	$N_{1,60,CS-Sr}$ (Weber et al., 2015)
HFU-1	11.7
HFU-2	15.4
UA	16.7
HFD-1	12.6
HFD-2	14.3
HFD-3	15.3

The protocol for the seismic deformation analyses performed as part of these current studies is to handle the potential transition to post-liquefaction residual strength (S_r) in elements comprised of potentially liquefiable soils within the constitutive model framework by considering the analysis to progress in two steps or stages (1) during shaking, and (2) after the end of shaking. During shaking, there is no implementation of S_r in UBCSAND model. After the end of shaking, S_r is applied within potentially liquefiable soil elements that satisfy either of two criteria: (1) occurrence of $R_{u,seis} \geq 0.7$ at any stage during shaking ($R_{u,seis,max} \geq 0.7$) or (2) development of a peak shear strain of $\gamma \geq 10\%$ at the end of shaking in saturated materials. The PM4Sand protocol used in the current studies is then to continue the nonlinear deformation analysis after the end of shaking until either (1) deformations and displacements have ceased to occur, as the embankment is in a stable condition, or (2) mesh

distortions are resulting in a need to perform significant (and time-consuming) re-meshing to continue the NDA deformation analysis, and the results at termination have become sufficient for purposes of engineering interpretation and decision-making, with recognition that deformations and displacements are still ongoing.

Similarly, it is also part of the UBCSAND protocol in the current studies to also examine non-liquefiable soils (e.g. the normally consolidated central clayey core zone) at the end of shaking, and to consider whether strength reduction (or further strength reduction) is warranted as a result of large shear strain development in sensitive cohesive soils.

Figures 5-27 and 5-28 present the results of nonlinear seismic deformation analyses performed with the combination of models and relationships of USFD Analysis 6. Figure 5-27 shows conditions calculated “at the end of shaking”, but the analyses are continued after the end of input seismic excitation, as deformations can continue after the end of shaking due to ongoing deformations under static (gravity loading) when post-liquefaction residual strength, S_r are applied in elements that satisfy either of two criteria: (1) occurrence of $R_{u,seis} \geq 0.7$ at any stage during shaking ($R_{u,seis,max} \geq 0.7$) or (2) development of a peak shear strain of $\gamma \geq 10\%$ at the end of shaking in saturated materials. In some cases the post-shaking deformations can lead to development, or discovery, of progressive development of large deformations or even instability failures. Accordingly, it is important to continue the analyses after the end of shaking.

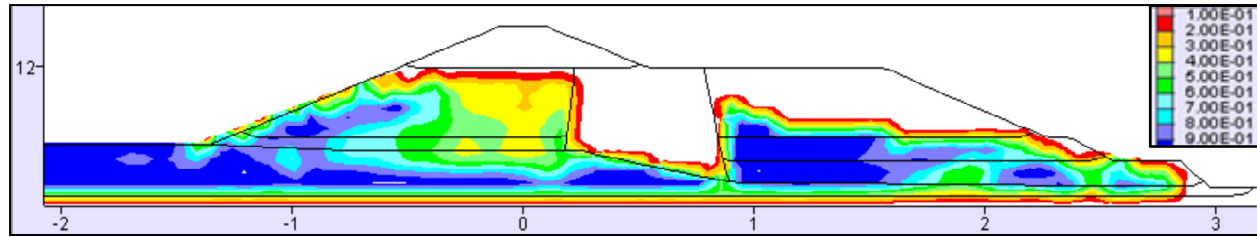
Figure 5-28 therefore presents conditions at “the end of analysis”. The end of analysis is the point in time when the analysis team elects to end (discontinue) the NDA analysis. Reasons for ending the analysis can include (1) deformations and displacements have ceased to occur, as the embankment is in a stable condition, or (2) mesh distortions are resulting in a need to perform significant (and time-consuming) re-meshing to continue the NDA deformation analysis, and the results at termination have become sufficient for purposes of engineering interpretation and decision-making, with recognition that deformations and displacements are still ongoing.

In this case, USFD Analysis 6, the deformations and displacements that occurred after the end of shaking were not very large, and the mesh was both stable and stationary at the end of analysis.

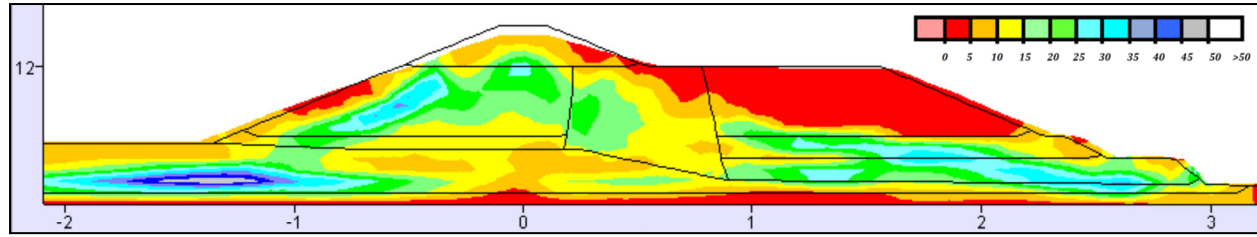
Figures 5-27(a) to (d) show conditions calculated at the end of shaking. Because the same models and parameterizations were used as in the preceding USFD Analyses 4 and 5, Figures 5-27(a) through (d) are identical to Figures 5-22(a) through (d) from USFD Analysis 4, and they are also identical to the end of shaking Figures 5-25(a) through (d) from USFD Analysis 5.

As discussed in Section 5.8.4, examination of shear strains at the end of shaking across zones of strain sensitive puddled clay core materials indicated maximum shear strains of approximately 27%, with an average of 12% across the puddled central clay core along potential shear zones. As discussed in Section 4.8.4, at this range of shear strains it was not fully clear whether or not additional reduction of clay shear strengths to account for strain

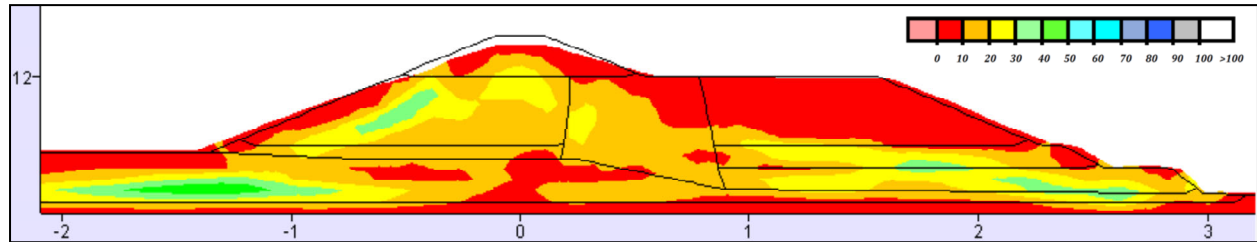
USFD Analysis 6: UBCSAND model, with the Youd et al. (2001) Liquefaction Triggering Relationship, and the Weber et al. (2015) S_r Relationship



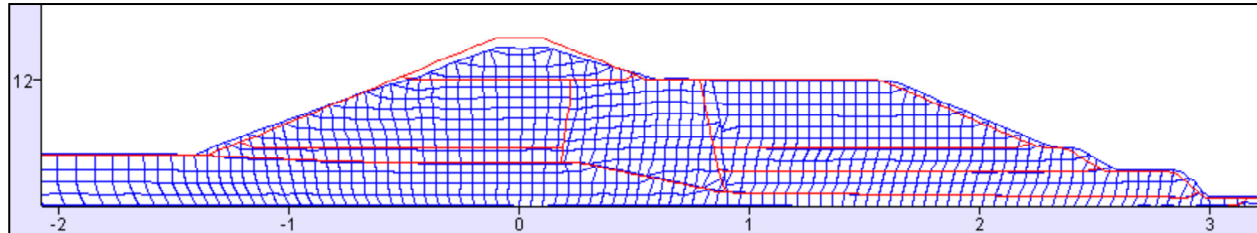
(a) Maximum value of $R_{u, seismic}$ recorded in each element



(b) Shear strain (percent), with the inset shear strain scale set to max. of 50 percent



(c) Shear strain (percent), with the inset shear strain scale set to max. of 100 percent



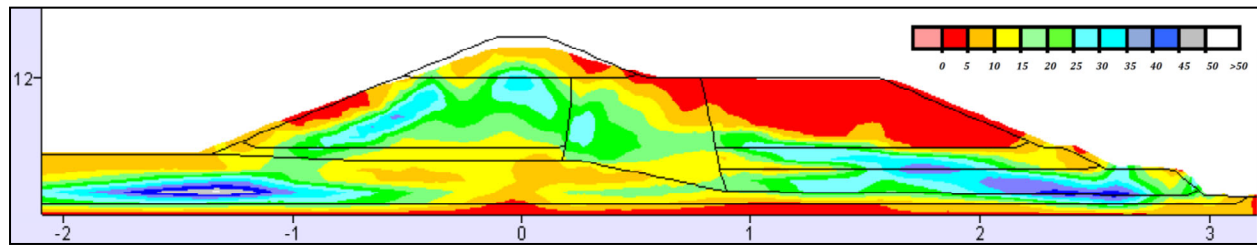
(d) Deformed mesh

Figure 5-27: Results of USFD Analysis 6 at the end of shaking

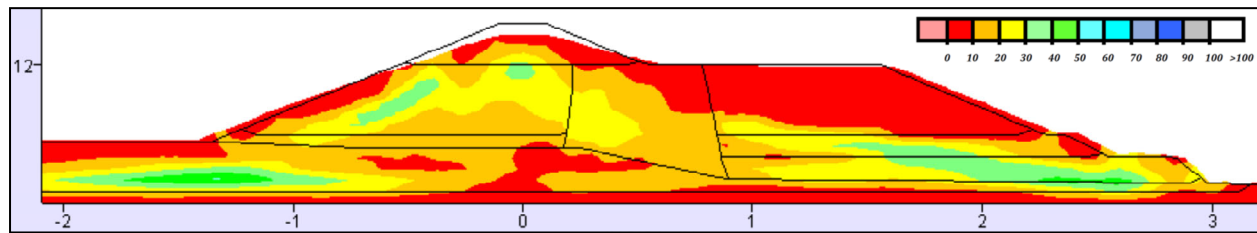
softening was warranted, as there was already a reduction of strength by 20% in the central clay core zone to account for both cyclic softening and moderate strain softening.

The engineering judgment of the analysis team was that the strength of the central clayey core should be reduced to a value intermediate between (1) the already 20% softened clay core strength value of $S_u/\sigma'_{vi} = 0.192$ and (2) a fully residual value of $S_{u, residual}/\sigma'_{vi} = 0.08$, to a strength of $S_u/\sigma'_{vi} = (0.5)(0.192 + 0.08) = 0.136$ in the post-shaking stage. This reduction to intermediate clay strength should not add significant deformations, if the dam is stable. The analysis was re-started and continued past the end of shaking.

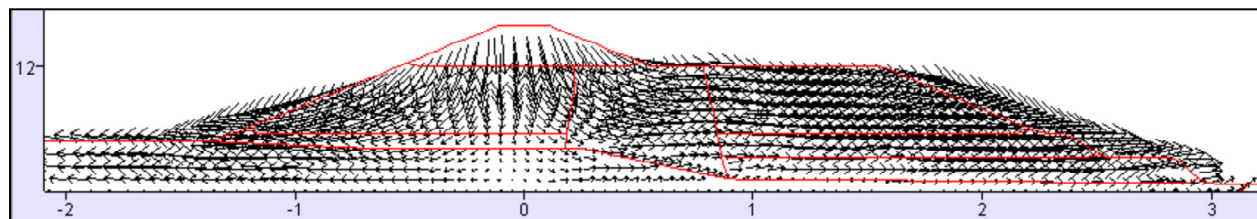
USFD Analysis 6: UBCSAND model, with the Youd et al. (2001) Liquefaction Triggering Relationship, and the Weber et al. (2015) S_r Relationship



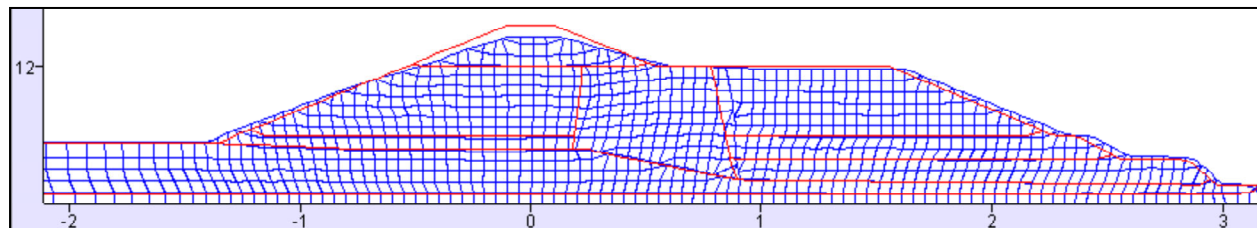
(a) Shear strain (percent), with the inset shear strain scale set to max. of 50 percent



(b) Shear strain (percent), with the inset shear strain scale set to max. of 100 percent



(c) Displacement vectors (exaggerated scale for clarity). Max. = 7.3 feet.



(d) Deformed mesh

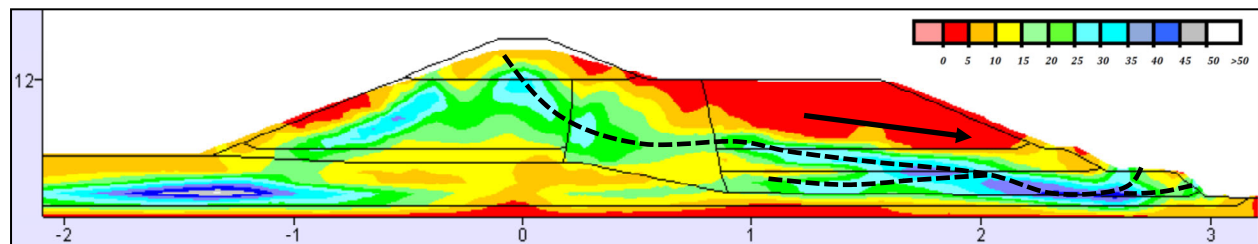
Figure 5-28: Results of USFD Analysis 6 at the end of analysis

Crest settlement was 4.8 feet at the end of shaking, and increased to 5.6 feet at the end of analysis when (1) post-liquefaction residual strengths (S_r) and (2) softened clay core strengths of $S_u/\sigma'_{vi} = 0.136$ were applied, and the analysis was again re-started. Similarly, maximum lateral translation of the downstream slope was 6.3 feet at the end of shaking, and increased to 7.3 feet at the end of analysis. At the end of analysis, the embankment was stable. This is the “end of analysis” condition shown in Figure 5-28.

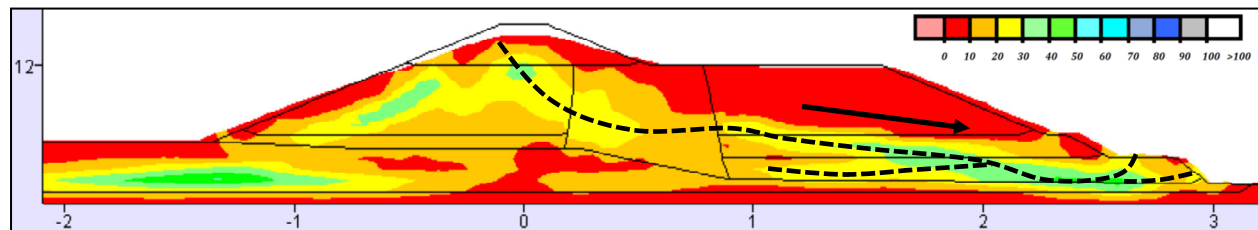
As a hypothetical worst case scenario for LSFD Analysis 6, the puddled clay core strength was then reduced to fully residual strength of clay, and the post-shaking analysis

was again re-started. Crest loss increased from 5.6 feet to 6.9 feet, and lateral downstream slope displacement increased from 7.3 feet to 9.0 feet, and the dam was stable.

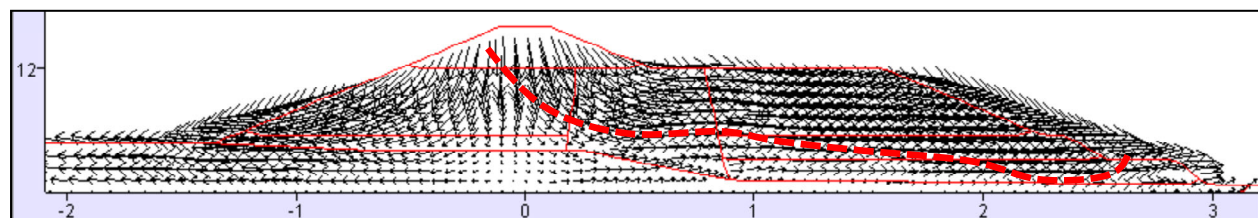
Figure 5-29 repeats Figure 5-28, showing end of analysis conditions, but this time with annotation to highlight selected details. As shown in Figure 5-29, the principal displacements towards the downstream side again occur on a deep-seated shear zone or slip surface that originates near the downstream toe, traverses largely laterally across the lower portion of the downstream hydraulic fill shell zone, and then arcs upwards at it passes across the central clayey core to exit near to the intersection of the horizontal top deck of the crest and the top of the inclined upstream face. This exit point is again a bit higher than the apparent heel scarp feature observed in the field, and this analysis again shows a slightly deeper, and not so fully developed, competing shear surface that would likely have even



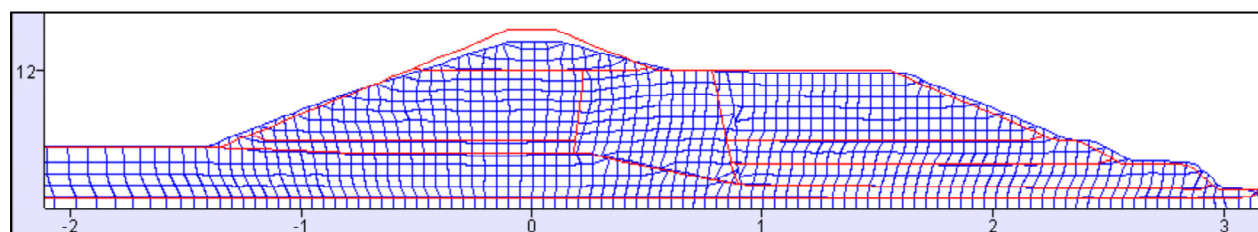
(a) Shear strain (percent), with the inset shear strain scale set to max. of 50 percent



(b) Shear strain (percent), with the inset shear strain scale set to max. of 100 percent



(c) Displacement vectors (exaggerated scale for clarity, Max. = 7.3 feet)



(d) Deformed mesh

Figure 5-29: Results of USFD Analysis 6 at the end of analysis, annotated

better matched the actual observed upstream heel scarp location, but that is beaten out by the slightly shallower feature.

Table 5-20 shows a comparison between predicted, and observed, displacements at four key locations. Agreement between the analytical results, and observed performance, was very good, and represented an accurate and useful “prediction” of the actual observed behavior.

Table 5-20: Comparison between results of USFD Analysis 6 [UBCSAND Model – Y, W] and observed displacements of the USFD at four key locations

Displacement Location and Direction	Measured Displacements	Analysis Results
Maximum crest loss	2.5 to 3.0 feet	5.1 feet to 5.6 feet
Maximum crest lateral translation to D/S (+ towards D/S)	4.9 to 6.0 feet	1.7 feet
Maximum lateral translation of the D/S slope face	7.2 to 8.7 feet	7.3 feet
Maximum lateral translation of the D/S toe	3.6 to 5.3 feet	3.6 feet

It is noted that the only differences between USFD Analyses 4, 5 and 6 were the post-liquefaction residual strength (S_r) relationships employed. Analysis 5 (with the S_r relationship of Idriss and Boulanger (2015)) incorrectly predicted liquefaction-induced flow failures towards both the upstream and downstream sides of the embankment. Analysis 4 correctly predicted end of earthquake stability, and provided a reasonable prediction of the observed deep-seated shear displacement mechanism towards the downstream side, and generally good predictions of the magnitudes of the movements actually observed; except that it over-predicted vertical crest loss. It is hypothesized that a contributing factor in this conservative over-estimation of crest loss in Analysis 4 may have been the use of the Seed and Harder (1990) S_r relationship, which predicts S_r as a function of only $N_{1,60,CS}$, rather than as a function of both $N_{1,60,CS}$ and initial effective vertical stress ($\sigma'_{v,i}$). The very good predictions provided by Analysis 6, which substituted the S_r relationship of Weber et al. (2015), and which provided a very good match for observed behaviors and displacements, including eliminating the over-prediction of crest loss of Analysis 4, appears to support this hypothesis.

Overall, USFD Analysis 6 provided good engineering “predictions” of the actual observed field performance. It correctly predicted the occurrence of a deep, basal slippage originating at the downstream toe and then arcing upwards across the core zone to exit high on the upstream face, and it provided usefully accurate predictions of the magnitudes of deformations and displacements. The engineering interpretation of USFD Analysis 4 would be that this earthquake would produce moderate displacements and deformations, resulting in moderate crest loss and moderate downstream displacements.

5.8.7 USFD Analysis 7: PM4Sand Model, with the Boulanger and Idriss (2014) Liquefaction Triggering Relationship, and the Idriss and Boulanger (2015) S_r Relationship

USFD Analysis 7 utilizes the PM4Sand model, the Boulanger and Idriss (2014) liquefaction triggering and K_σ relationships, the Idriss and Boulanger (2003) K_α relationship, and it uses the Idriss and Boulanger (2015) post liquefaction S_r/σ'_{vi} relationship (for soils potentially susceptible to void redistribution) to model post liquefaction strengths. The PM4Sand model is employed in the potentially liquefiable soils (the saturated elements in the upstream and downstream semi-hydraulic fill shells).

The current PM4Sand model is parametrized in such a way that it is expected to show soil behaviors consistent with the Boulanger and Idriss (2014) liquefaction triggering and K_σ relationships, and behaviors generally consistent with the Boulanger and Idriss (2003) K_α relationship, when single element simple shear test calibration-based contraction parameters, h_{po} , are developed using USFD Analysis 7 parameters. $N_{1,60,CS}$ values based on the energy, equipment, procedural and effective overburden stress corrections of Boulanger and Idriss (2014) are used as a basis for parameterization.

Table 5-21 presents the $N_{1,60,CS}$ values used as a basis for parameterization of the PM4Sand model for USFD Analysis 7, and also summarizes the analysis specific input parameters are summarized in this analysis. The contraction parameter, h_{po} was calibrated in these current studies using single element direct simple shear tests, as per the PM4Sand version 3 manual (Ziotopoulou and Boulanger, 2015). For comparison, the calibration was first performed using the examples in the PM4Sand manual. The primary input parameters, as shown in Table 5-21, were assigned in USFD Analysis 7 and all secondary parameters were kept unchanged, i.e. the default values of PM4Sand were used.

Table 5-21 presents the input parameters used in USFD Analysis 7 for modeling of the potentially liquefiable soils. The non-liquefiable layers were modeled with Mohr-Coulomb parameters, as presented in Table 5-8. Shear strength of the semi-puddled central clay core was modeled as $S_u/\sigma'_{vi} = 0.192$ during shaking in USFD Analysis 7, which assumes approximately a 20% reduction of undrained shear strength (from peak static, or monotonic, shear strength of $S_u/\sigma'_{vi} = 0.24$) for the normally consolidated clayey core to account for both (a) cyclic softening and (b) strain softening.

Table 5-21: Input Parameters for USFD Analysis 7 using the PM4Sand model with the Boulanger and Idriss (2014) liquefaction triggering relationship

		Input Parameter for PM4Sand Calibration					Output from PM4Sand Calibration (Number of Cycles)		
PM4Sand Manual And USFD	Soil Layer	$N_{1,60,CS}$	$CRR_{Mw=7.5}$ (Boulanger and Idriss, 2014)	Relative Density, D_R	Shear Modulus Coefficient, G_0	Contraction Rate Parameter, h_{po}	98% _ru	1% _strain	3% _strain
PM4Sand Manual Table 4.1		6	0.092	0.36	486.9	0.53	14.5	14.0	15
		14	0.147	0.55	677.0	0.40	13.0	13.0	15
		26	0.312	0.75	890.0	0.63	17.5	11.5	14.5
USFD (Boulanger and Idriss, 2014 liq. trig. and K_σ)	HFU-1	13.4	0.143	0.540	665.9	0.40	13.0	13.0	15.0
	HFU-2	17.9	0.183	0.624	754.3	0.37	13.0	13.0	15.0
	UA	19.3	0.198	0.648	779.7	0.37	12.5	12.5	15.0
	HFD-1	15.2	0.158	0.575	702.6	0.40	13.5	13.0	15.0
	HFD-2	16.6	0.170	0.601	729.8	0.39	13.5	13.0	15.0
	HFD-3	17.8	0.182	0.622	752.4	0.37	12.5	12.0	15.0

Additional parameters are needed for the Idriss and Boulanger (2015) post-liquefaction residual strength (S_r) relationship, and these are $N_{1,60,CS-S_r}$ values developed based on the energy, equipment, procedural and effective overburden stress corrections of Idriss and Boulanger (2014) and fines adjustment, as per Idriss and Boulanger (2015). These are presented in Table 5-22.

Table 5-22: $N_{1,60,CS-S_r}$ values used in USFD Analysis 7 for the post-liquefaction residual strength relationship of Idriss and Boulanger (2015)

Soil layer	$N_{1,60,CS-S_r}$
HFU-1	11.6
HFU-2	14.8
UA	16.6
HFD-1	12.1
HFD-2	13.5
HFD-3	14.7

The protocol for the seismic deformation analyses performed as part of these current studies is to handle the potential transition to post-liquefaction residual strength (S_r) in

elements comprised of potentially liquefiable soils within the constitutive model framework by considering the analysis to progress in two steps or stages (1) during shaking, and (2) after the end of shaking. During shaking, there is no implementation of S_r in the PM4Sand model. After the end of shaking, S_r is applied within potentially liquefiable soil elements that satisfy either of two criteria: (1) occurrence of $R_{u,seis} \geq 0.7$ at any stage during shaking ($R_{u,seis,max} \geq 0.7$) or (2) development of a peak shear strain of $\gamma \geq 10\%$ at the end of shaking in saturated materials. The PM4Sand protocol used in the current studies is then to continue the nonlinear deformation analysis after the end of shaking until either (1) deformations and displacements have ceased to occur, as the embankment is in a stable condition, or (2) mesh distortions are resulting in a need to perform significant (and time-consuming) re-meshing to continue the NDA deformation analysis, and the results at termination have become sufficient for purposes of engineering interpretation and decision-making, with recognition that deformations and displacements are still ongoing.

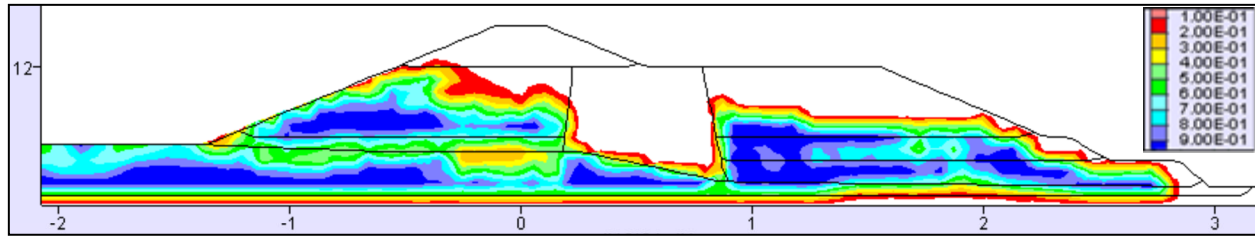
Similarly, part of the PM4Sand protocol for the current studies is to also examine non-liquefiable soils (e.g. the normally consolidated central clayey core zone) at the end of shaking, and to consider whether strength reduction (or further strength reduction) is warranted as a result of large shear strain development in sensitive cohesive soils.

Figures 5-30 and 5-31 present the results of nonlinear seismic deformation analyses performed with the combination of models and relationships of USFD Analysis 7. Figure 5-30 shows conditions calculated “at the end of shaking”, but the analyses are continued after the end of input seismic excitation, as deformations can continue after the end of shaking due to ongoing deformations under static (gravity loading) when post-liquefaction residual strength, S_r are applied in elements that satisfy either of two criteria: (1) occurrence of $R_{u,seis} \geq 0.7$ at any stage during shaking ($R_{u,seis,max} \geq 0.7$) or (2) development of a peak shear strain of $\gamma \geq 10\%$ at the end of shaking in saturated materials. In some cases the post-shaking deformations can lead to development, or discovery, of progressive development of large deformations or even instability failures. Accordingly, it is important to continue the analyses after the end of shaking.

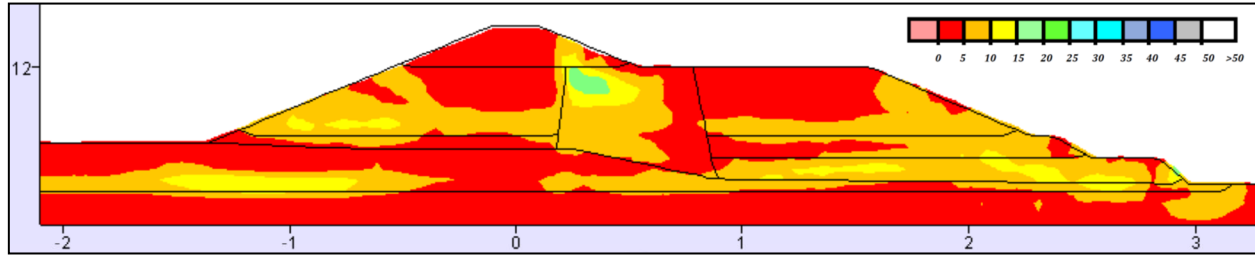
Figure 5-31, therefore presents conditions at “the end of analysis”. The end of analysis is the point in time when the analysis team elects to end (discontinue) the NDA analysis. Reasons for ending the analysis can include (1) deformations and displacements have ceased to occur, as the embankment is in a stable condition, or (2) mesh distortions are resulting in a need to perform significant (and time-consuming) re-meshing to continue the NDA deformation analysis, and the results at termination have become sufficient for purposes of engineering interpretation and decision-making, with recognition that deformations and displacements are still ongoing.

As shown in Figure 5-30(a), significant seismically induced pore pressures are generated in the saturated portions of both the upstream and downstream hydraulic fill shell zones, as well as in the upper alluvium.

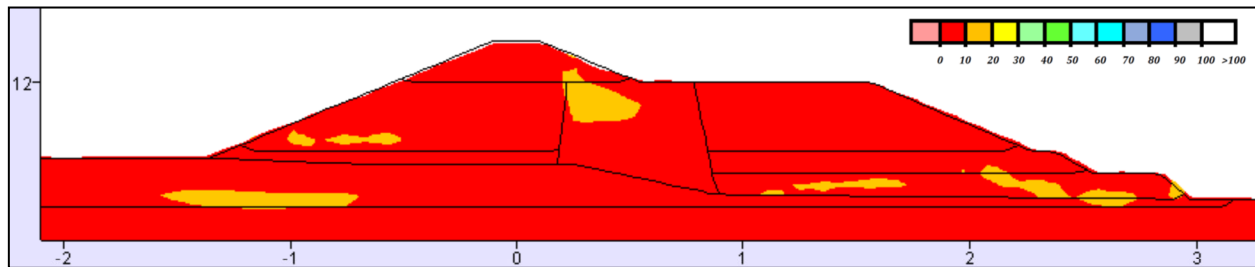
Analysis 7: PM4Sand model, with the Boulanger and Idriss (2014) Liquefaction Triggering Relationship, and the Idriss and Boulanger (2015) S_r Relationship



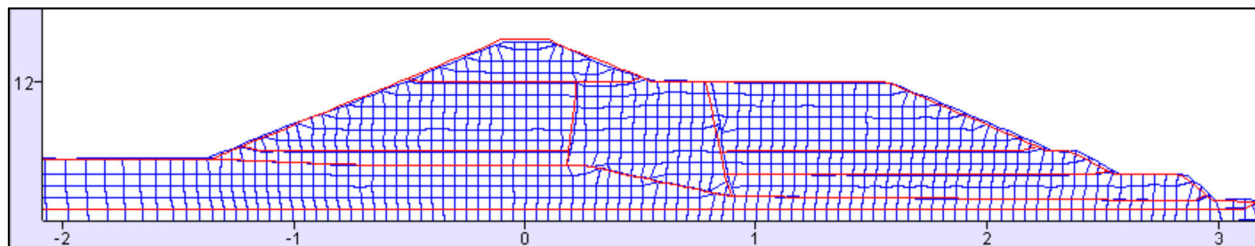
(a) Maximum value of $R_{u, seismic}$ recorded in each element



(b) Shear strain (percent), with the inset shear strain scale set to max. of 50 percent



(c) Shear strain (percent), with the inset shear strain scale set to max. of 100 percent



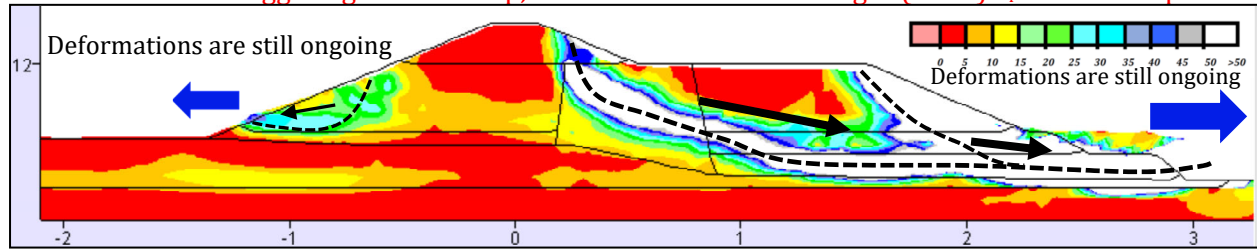
(d) Deformed mesh

Figure 5-30: Results of USFD Analysis 7 at the end of shaking

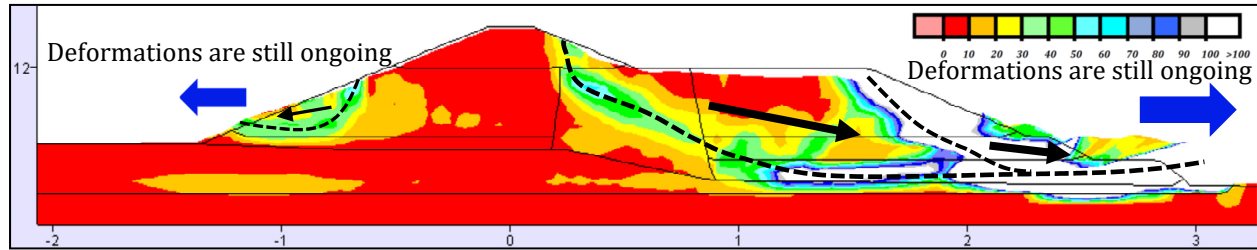
As shown in Figures 5-30(b) through (d) these pore pressures, in conjunction with seismic inertial forces, produce only minor to moderate displacements and deformations. The PM4Sand model is one of the stiffest models used in these current studies.

As per protocol, post-liquefaction residual strengths (S_r) were implemented at the end of shaking, and the analysis was then re-started and continued forward to the end of analysis. Post-liquefaction strengths were implemented in elements that satisfy either of

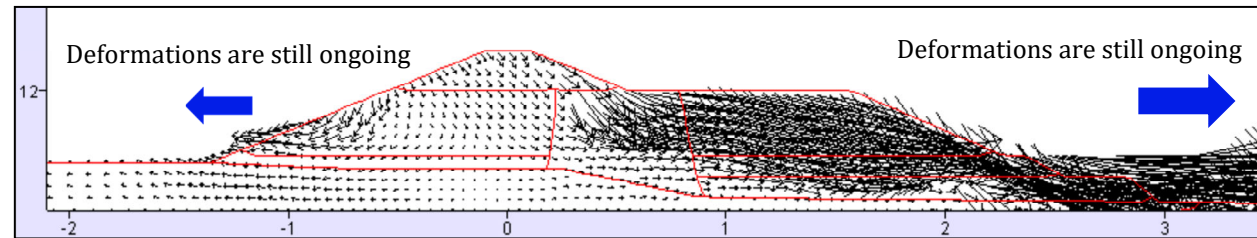
Analysis 7: PM4Sand model, with the Boulanger and Idriss (2014) Liquefaction Triggering Relationship, and the Idriss and Boulanger (2015) S_r Relationship



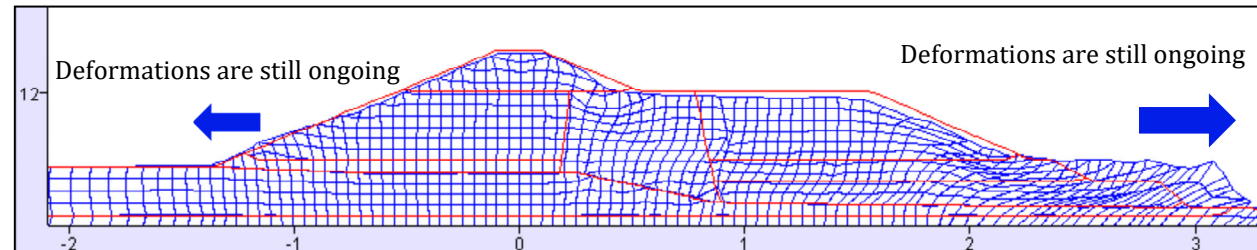
(a) Shear strain (percent), with the inset shear strain scale set to max. of 50 percent



(b) Shear strain (percent), with the inset shear strain set to max. of 100 percent



(c) Displacement vectors (exaggerated for clarity, Max = 46.9 feet)



(d) Deformed mesh

Figure 5-31: Results of USFD Analysis 7 at the end of analysis

two criteria: (1) occurrence of $R_{u,seis} \geq 0.7$ at any stage during shaking ($R_{u,seis,max} \geq 0.7$) or (2) development of a peak shear strain of $\gamma \geq 10\%$ at the end of shaking in saturated materials. Shear strains across the central clayey core zone at the end of shaking were also examined.

As discussed in Section 5.8.4, examination of shear strains at the end of shaking across zones of strain sensitive puddled clay core materials indicated maximum shear strains of approximately 24% with an average of 6.5% across the puddled central clay core along potential shear zones. These strains within clay core are low and do not warrant any further

reduction of clay core strength, as there as there was already a reduction of strength by 20% in the central clay core zone to account for both cyclic softening and moderate strain softening.

As per the protocol for analyses performed with the UBCSAND model in the current studies, the analysis was halted at the end of shaking and post-liquefaction residual strengths (S_r) were implemented in potentially liquefiable soil elements which had achieved either (1) $R_{u,seis,max} \geq 0.7$ or (2) maximum shear strains of $\gamma \geq 10\%$, and the analysis was then re-started. The result was uncontrolled deformations and displacements towards both the upstream and downstream sides of the dam embankment. The clay strength was also reduced to an intermediate strength of $S_u/\sigma'_{vi} = 0.136$ at this stage, as it was apparent that very large shear strains and displacements were occurring.

As shown in Figure 5-31(a) to (d), transitioning to S_r in elements that have liquefied, and then continuing the analysis in USFD Analysis 7 resulted in ongoing displacements and deformations. A large downstream flow failure occurred, with a shear surface originating at the downstream toe and arcing back and upwards to approximately the point where the top deck of the downstream berm intersects the downstream end of the top crest section. The initial failure occurred right at the toe, and then as deformations continued a second “lobe” developed and extended further up the slope, with a heel scarp intersecting the downstream face of the rolled fill dam crest section. This downstream slide feature was still moving when the analysis was halted due to difficulties with regard to re-meshing to overcome mesh-lock, and it is interpreted to be a flow-slide feature that would continue to displace. It cannot (yet) be determined whether or not a third regressive “lobe” would develop directly affecting available dam crest height. As these FLAC NDA analyses are continuum analyses, and they do not allow for modeling of full shear strain localization and bifurcation (direct shear offset), there is a potential that they underestimate formation of secondary slope failures.

A smaller, and shallower, second instability feature also occurred on the upstream face. This second feature was not moving very rapidly when the analysis was halted, and it is thus not clear how far it would have traveled; it may have represented a relatively modest and localized upstream surficial slippage feature.

As discussed in Section 2.4, the Idriss and Boulanger (2015) S_r/σ'_{vi} relationship varies as a function of $N_{1,60,CS-Sr}$, but the ratio of S_r/σ'_{vi} does not vary as a function of initial effective stress (σ'_{vi}). As a result, the relationship is unconservative (over-predicts S_r) at high initial effective overburden stresses, and it is over-conservative (under-predicts S_r) at low initial effective stresses. The two analytically predicted slope failures initiated (1) at the downstream toe, and (2) at shallow depth on the upstream face. Initial effective vertical stresses (σ'_{vi}) were low in both of these locations, and so these are zones in which S_r would have been significantly underestimated by the S_r relationship employed here.

Analysis 7 was an unsuccessful back-analysis, failing to correctly predict either (1) the principal mechanisms of the actual observed field performance, or (2) the approximate magnitudes of the actual observed field deformations and displacements. This was due to

the incorrect prediction of (1) a large downstream liquefaction-induced flow failure (which was not observed in the field), and (2) a smaller instability feature on the upstream slope.

Table 5-23 shows a comparison between predicted, and observed, displacements at four key locations. Agreement between the analytical results, and observed performance, was very poor, and the deformations (especially on the downstream side) were still ongoing when the analysis was halted.

Table 5-23: Comparison between results of USFD Analysis 7 [PM4Sand Model – B&I, I&B] and observed displacements of the USFD at four key locations

Displacement Location and Direction	Measured Displacements	Analysis Results
Maximum crest loss	2.5 to 3.0 feet	1.3 feet to 1.4 feet*
Maximum crest lateral translation to D/S (+ towards D/S)	4.9 to 6.0 feet	1.2 feet*
Maximum lateral translation of the D/S slope face	7.2 to 8.7 feet	> 46 feet*
Maximum lateral translation of the D/S toe	3.6 to 5.3 feet	> 28 feet*

*A downstream liquefaction-induced flow failure is still ongoing.

5.8.8 USFD Analysis 8: PM4Sand Model, with the Cetin et al. (2018) Liquefaction Triggering Relationship, the Youd et al. (2001) K_σ Relationship, and the Weber et al. (2015) S_r Relationship

USFD Analysis 8 utilizes the PM4Sand model, the Cetin et al. (2018) liquefaction triggering relationship, the Youd et al. (2001) K_σ relationship (which is recommended for use with Cetin et al. (2018)), and the Weber et al. (2015) post liquefaction S_r relationship. The PM4SAND model is employed in the potentially liquefiable soils (in the upstream and downstream semi-hydraulic fill shells, and the upper alluvium).

In this USFD Analysis 8, the PM4Sand model is re-parametrized in such a way that it is expected to show soil behaviors consistent with the Cetin et al. (2018) liquefaction triggering relationship and the Youd et al. (2001) and K_σ relationship, when single element

simple shear test calibration-based contraction parameter, h_{po} are developed using USFD Analysis 8 parameters.

The analysis specific input parameters are summarized in Table 5-24. The contraction parameter, h_{po} was calibrated in these current studies using single element direct simple shear tests, as per the PM4Sand version 3 manual (Ziotopoulou and Boulanger, 2015). For comparison, the calibration was first performed using the examples in the PM4Sand manual. The primary input parameters, as shown in Table 5-24, were assigned in USFD Analysis 8 and all secondary parameters were kept unchanged, i.e. the default values of PM4Sand were used.

Table 5-24 presents the input parameters used in USFD Analysis 8 for modeling of the potentially liquefiable soils. The non-liquefiable layers were modeled with Mohr-Coulomb parameters, as presented in Table 5-8. Shear strength of the semi-puddled central clay core was modeled as $S_u/\sigma'_{vi} = 0.192$ during shaking in USFD Analysis 8, which assumes approximately a 20% reduction of undrained shear strength (from peak static, or monotonic, shear strength of $S_u/\sigma'_{vi} = 0.24$) for the normally consolidated clayey core to account for both (a) cyclic softening and (b) strain softening.

No additional parameters are needed for the Weber et al. (2015) post-liquefaction residual strength (S_r) relationship, as the $N_{1,60,CS}$ values developed for the Cetin et al. (2018) triggering relationships are based on the same energy, equipment, procedural and effective overburden stress corrections as those employed in the Weber et al. (2015) S_r relationship. The fines correction for the Weber et al. (2015) S_r relationship differs slightly, but this difference is negligible (maximum differences of less than half a blow count) in the ranges of interest here.

The protocol for the seismic deformation analyses performed as part of these current studies is to handle the potential transition to post-liquefaction residual strength (S_r) in elements comprised of potentially liquefiable soils within the constitutive model framework by considering the analysis to progress in two steps or stages (1) during shaking, and (2) after the end of shaking. During shaking, there is no implementation of S_r in PM4Sand model. After the end of shaking, S_r is applied within potentially liquefiable soil elements that satisfy either of two criteria: (1) occurrence of $R_{u,seis} \geq 0.7$ at any stage during shaking ($R_{u,seis,max} \geq 0.7$) or (2) development of a peak shear strain of $\gamma \geq 10\%$ at the end of shaking in saturated materials. The PM4Sand protocol used in the current studies is then to continue the nonlinear deformation analysis after the end of shaking until either (1) deformations and displacements have ceased to occur, as the embankment is in a stable condition, or (2) mesh distortions are resulting in a need to perform significant (and time-consuming) re-meshing to continue the NDA deformation analysis, and the results at termination have become sufficient for purposes of engineering interpretation and decision-making, with recognition that deformations and displacements are still ongoing.

Table 5-24: Input Parameters for USFD Analysis 8 using the PM4Sand model with the Cetin et al. (2018) liquefaction triggering relationship, and the Youd et al. (2001) K_σ Relationship

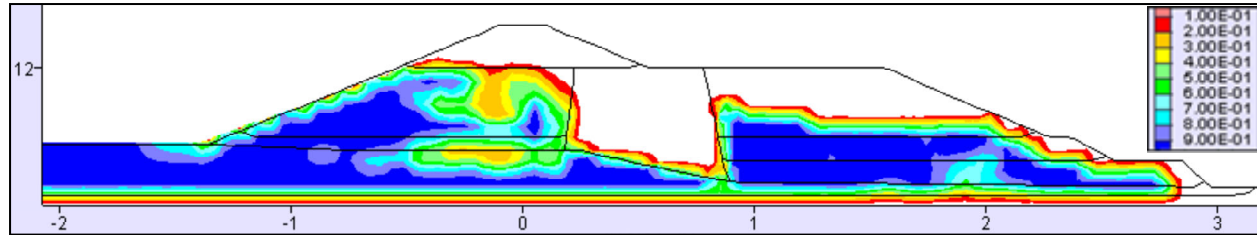
PM4Sand Manual USFD	Soil Layer	Input Parameter for PM4Sand Calibration					Output from PM4Sand Calibration (Number of Cycles)		
		$N_{1,60,CS}$	$CRR_{Mw=7.5}$ (Boulanger and Idriss, 2014)	Relative Density, D_R	Shear Modulus Coefficient, G_0	Contraction Rate Parameter, h_{po}	98% _ru	1% _strain	3% _strain
PM4Sand Manual Table 4.1		6	0.092	0.36	486.9	0.53	14.5	14.0	15
		14	0.147	0.55	677.0	0.40	13.0	13.0	15
		26	0.312	0.75	890.0	0.63	17.5	11.5	14.5
USFD (Cetin et al., 2018 liq. trig. and Youd et al., 2001 K_σ)	HFU-1	11.7	0.094	0.504	629.3	0.12	13.0	13.5	15.0
	HFU-2	15.4	0.120	0.579	706.6	0.17	13.5	13.5	15.0
	UA	16.7	0.129	0.603	731.8	0.19	13.5	13.5	15.0
	HFD-1	12.6	0.106	0.523	648.9	0.13	12.5	13.0	15.0
	HFD-2	14.3	0.112	0.558	684.5	0.15	13.5	13.5	15.0
	HFD-3	15.3	0.117	0.577	704.6	0.165	14.0	13.5	15.0

Similarly, it is part of the protocol for the current studies is to also examine non-liquefiable soils (e.g. the normally consolidated central clayey core zone) at the end of shaking, and to consider whether strength reduction (or further strength reduction) is warranted as a result of large shear strain development in sensitive cohesive soils.

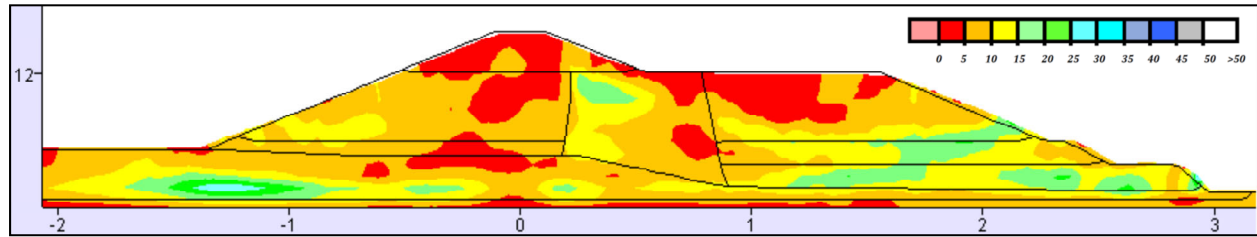
Figures 5-32 and 5-33 present the results of nonlinear seismic deformation analyses performed with the combination of models and relationships of USFD Analysis 8. Figure 5-32 shows conditions calculated “at the end of shaking”, but the analyses are continued after the end of input seismic excitation, as deformations can continue after the end of shaking due to ongoing deformations under static (gravity loading) when post-liquefaction residual strength, S_r are applied in elements that satisfy either of two criteria: (1) occurrence of $R_{u,seis} \geq 0.7$ at any stage during shaking ($R_{u,seis,max} \geq 0.7$) or (2) development of a peak shear strain of $\gamma \geq 10\%$ at the end of shaking in saturated materials. In some cases the post-shaking deformations can lead to development, or discovery, of progressive development of large deformations or even instability failures. Accordingly, it is important to continue the analyses after the end of shaking.

Figure 5-33, therefore presents conditions at “the end of analysis”. The end of analysis is the point in time when the analysis team elects to end (discontinue) the NDA analysis. Reasons for ending the analysis can include (1) deformations and displacements have ceased to occur, as the embankment is in a stable condition, or (2) mesh distortions are resulting in a need to perform significant (and time-consuming) re-meshing to continue the

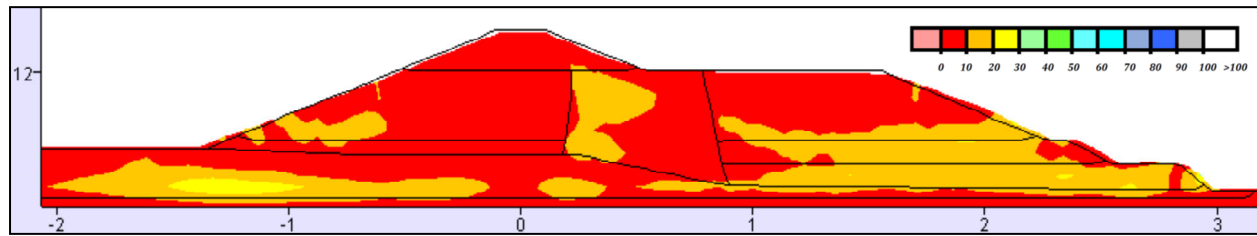
USFD Analysis 8: PM4Sand model, with the Cetin et al. (2016) Liquefaction Triggering Relationship, and the Weber et al. (2015) S_r Relationship



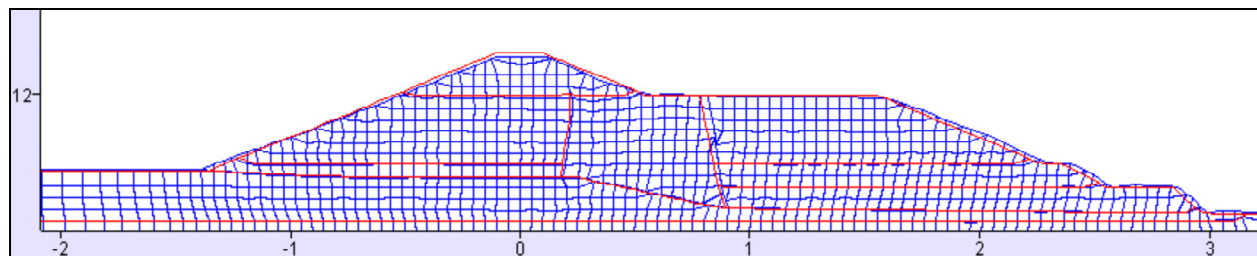
(a) Maximum value of $R_{u, \text{seismic}}$ recorded in each element



(b) Shear strain (percent), with the inset shear strain scale set to max. of 50 percent



(c) Shear strain (percent), with the inset shear strain scale set to max. of 100 percent



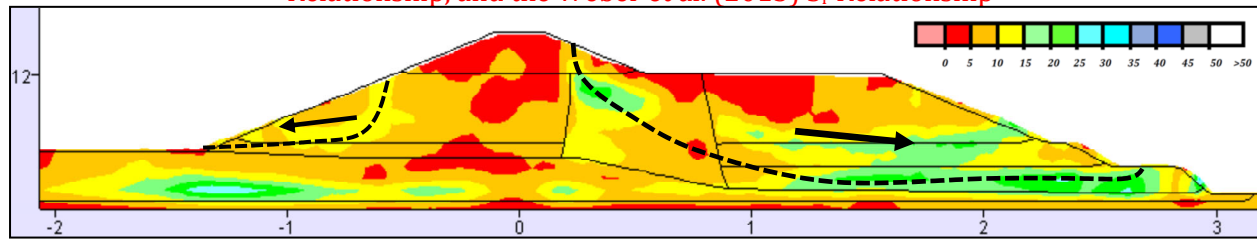
(d) Deformed mesh

Figure 5-32: Results of USFD Analysis 8 at the end of shaking

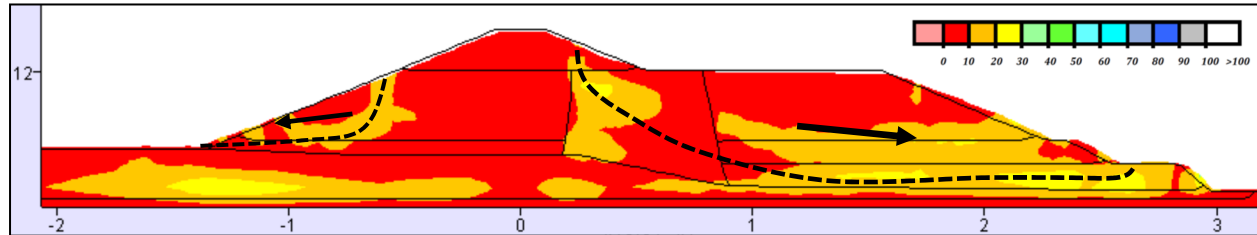
nonlinear seismic deformation analysis, and the results at termination have become sufficient for purposes of engineering interpretation and decision making, with recognition that deformations and displacements are still ongoing.

As anticipated, the use of the Cetin et al. (2018) liquefaction triggering relationship in USFD Analysis 8 produced somewhat higher levels of cyclically generated pore pressures during shaking (see Figure 5-32(a)) than those produced in the previous Analysis 7 (see Figure 5-30(a)). Deformations and displacements at the end of shaking are again small, however, as shown in Figures 5-32(b) through (d).

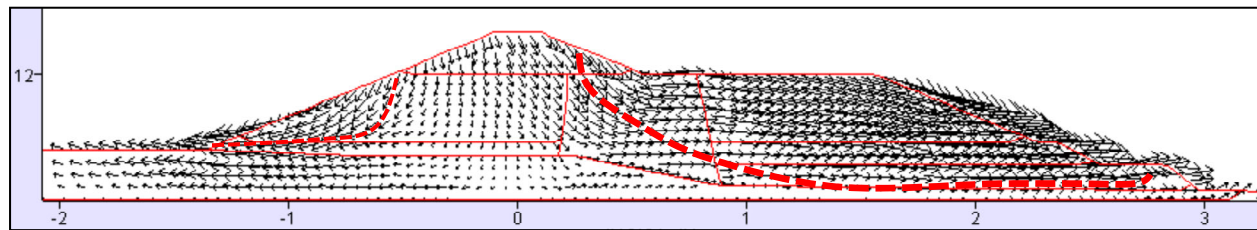
USFD Analysis 8: PM4Sand model, with the Cetin et al. (2016) Liquefaction Triggering Relationship, and the Weber et al. (2015) S_r Relationship



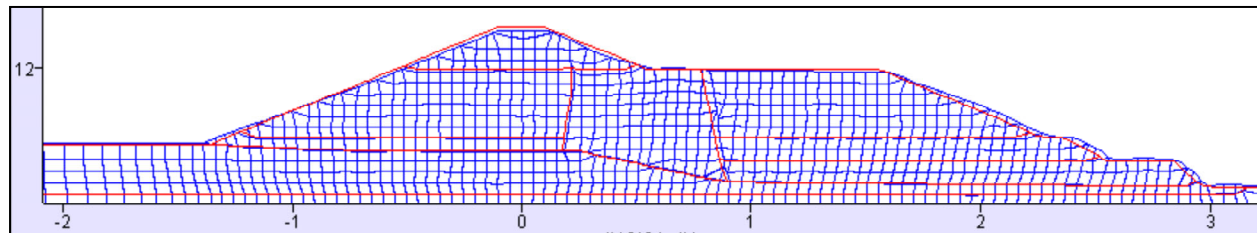
(a) Shear strain (percent), with the inset shear strain scale set to max. of 50 percent



(b) Shear strain (percent), with the inset shear strain scale set to max. of 100 percent



(c) Displacement vectors (exaggerated for clarity, Max. = 7.1 feet)



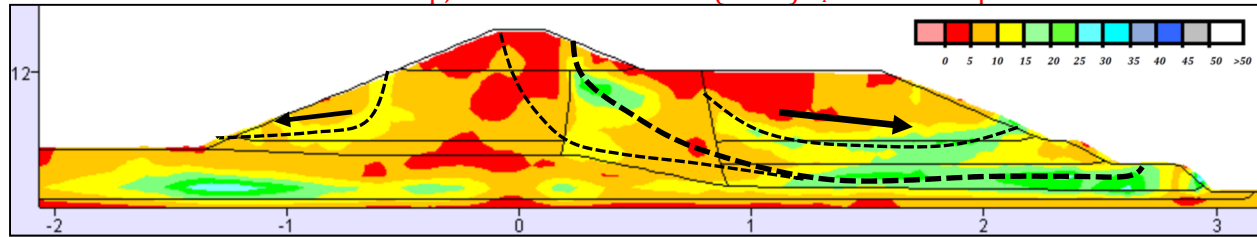
(d) Deformed mesh

Figure 5-33: Results of USFD Analysis 8 at the end of analysis, annotated

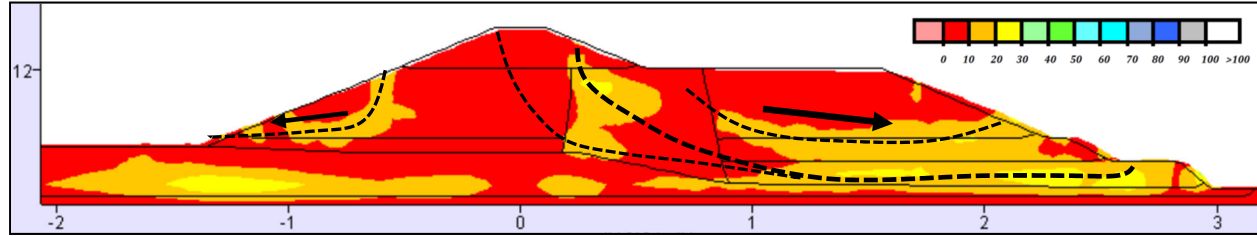
As per protocol, post-liquefaction residual strengths (S_r) were implemented at the end of shaking, and the analysis was then re-started and continued forward to the end of analysis. Post-liquefaction strengths were implemented in elements that satisfy either of two criteria: (1) occurrence of $R_{u,seis} \geq 0.7$ at any stage during shaking ($R_{u,seis,max} \geq 0.7$) or (2) development of a peak shear strain of $\gamma \geq 10\%$ at the end of shaking in saturated materials. Shear strains across the central clayey core zone at the end of shaking were also examined.

Examination of shear strains at the end of shaking across zones of strain sensitive puddled clay core materials indicated maximum shear strains of approximately 22% with

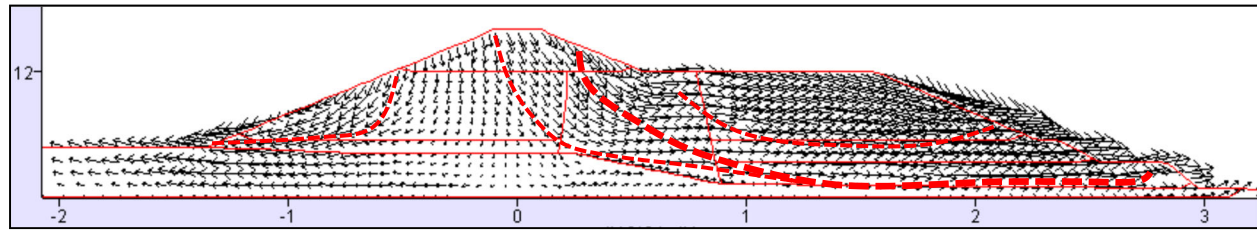
USFD Analysis 8: PM4Sand model, with the Cetin et al. (2016) Liquefaction Triggering Relationship, and the Weber et al. (2015) S_r Relationship



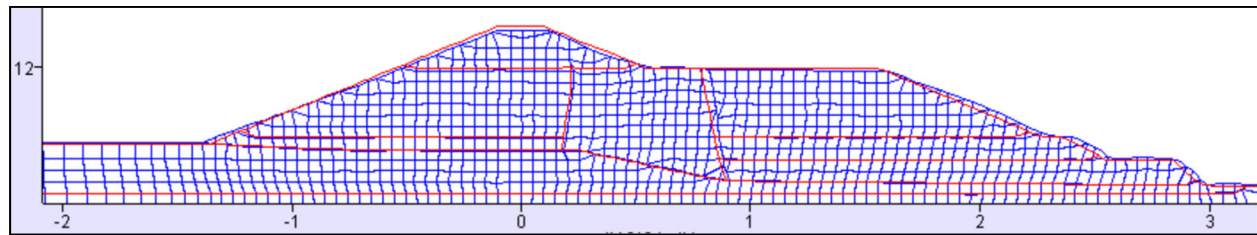
(a) Shear strain (percent), with the inset shear strain scale set to max. of 50 percent



(b) Shear strain (percent), with the inset shear strain scale set to max. of 100 percent



(c) Displacement vectors (exaggerated for clarity, Max. = 7.1 feet)



(d) Deformed mesh

Figure 5-33(a): Results of USFD Analysis 8 at the end of analysis, further annotated

an average of 8.4%, across the puddled central clay core along potential shear zones. As discussed in Section 4.8.4, at this range of shear strains it was not fully clear whether or not additional reduction of clay shear strengths to account for strain softening was warranted, as there was already a reduction of strength by 20% in the central clay core zone to account for both cyclic softening and moderate strain softening.

However, the engineering judgment of the analysis team was that the strength of the central clayey core should be reduced to a value intermediate between (1) the already 20% softened clay core strength value of $S_u/\sigma'_{v,i} = 0.192$ and (2) a fully residual value of $S_{u,residual}/\sigma'_{v,i} = 0.08$, to a strength of $S_u/\sigma'_{v,i} = (0.5)(0.192 + 0.08) = 0.136$ in the post-

shaking stage, to check if the embankment would remain stable and not experience significant additional deformations. If so, then the reduction to $S_u/\sigma'_{v,i} = 0.136$ would have been shown to be unnecessary. This was mainly performed to be consistent with other USFD analyses performed in these current studies. The hypothesis for performing this analyses was that the reduction to intermediate clay strength should not add significant deformations, if the dam is stable. The analysis was re-started and continued past the end of shaking.

Crest settlement was 1.75 feet at the end of shaking, and increased to 1.8 feet at the end of analysis when (1) post-liquefaction residual strengths (S_r) and (2) softened clay core strengths of $S_u/\sigma'_{v,i} = 0.136$ were applied, and the analysis was again re-started. Similarly, maximum lateral translation of the downstream slope was 6.5 feet at the end of shaking, and increased to 7.2 feet at the end of analysis. These minor deformations and displacements did not appreciably increase the shear strains or deformations across the central clayey core zone, and the embankment remained stable. It was therefore judged that the hypothetical partial reduction in clay strength to $S_u/\sigma'_{v,i} = 0.136$ had been shown to be unnecessary, and had not significantly affected the end of analysis conditions.

These “end of analysis” conditions are shown in Figure 5-33. The dashed lines in this figure represent the incipient or slightly developed shear zones that would ordinarily be identified at this level of displacement. As shown in this figure, USFD Analysis 8 again predicts a deep, basal shear mechanism originating at the downstream toe, passing laterally across the lower portion of the downstream side hydraulic fill shell zone, and then arcing upwards across the core; in reasonable agreement with the nature of the observed field performance, except that the heel scarp emerges at the top of the downstream face of the rolled crest section rather than high on the upstream face of the dam as was observed in the actual field performance (see Figures 5-1, 5-2, 5-3, 5-5 and 5-8) and the hypothesized mechanism, as discussed in Section 5.4.

Figure 5-33(a) repeats Figure 5-33, but with additional annotation for this current discussion. Nonlinear seismic deformation analyses “evolve” as the analysis progresses. It can be interesting and useful for the engineers and analysts to “play back” colored graphical renderings of an analysis, watching as incoming inertial forces or waves move the dam back and forth, and as pore pressures cyclically increase and decrease on opposite sides of the embankment with reversing upslope and downslope inertial dynamic forces. Also to watch as both shear strains and displacements evolve.

The shear strains and embankment displacements developed in this analysis are “small to moderate”, and no fully well-developed principal shear surfaces have yet evolved at the end of analysis. The dashed lines in Figure 5-33 represent the best-developed (partially developed) shear surfaces or shear mechanisms at the end of shaking (and end of analysis), but it is not yet clear whether these two shear surfaces would continue to be the principal upstream and downstream shear mechanisms if the earthquake shaking had been either longer or stronger, and deformations had progressed further. That is because (1) there are “competing” alternative mechanisms also partially developing, and (2) overall (final) displacements are only small to moderate.

In the analyses of the Lower San Fernando dam presented in Chapter 4, two sets of potential shear surfaces develop in the early stages of earthquake shaking; one representing a potential slide towards the downstream side of the dam, and one towards the upstream side. In those LSFD analyses, it was not until significantly greater shear strains and displacements had developed that the analysts could see that (1) the upstream slide “wins” the race and becomes an upstream flow slide, and (2) the downstream slide feature remains stable with only nominal (essentially negligible) displacements.

Close examination of USFD Analysis 8, as shown in Figure 5-33(a) is a useful exercise, as it can help to give engineers and analysts insight with regard to interpretation of apparent or likely shear displacement mechanisms based on nonlinear seismic deformation analyses; especially when deformations and displacements are not large.

The finer dashed lines in Figure 5-33(a) show alternate incipient or potential shear surfaces that might develop if further deformations occur. One of these is an alternate incipient potential shear surface that would produce a heel scarp that intersects the top of the upstream face; a location above but near to the upstream face heel scarp feature actually observed in the field. The USFD case history is a complex and challenging one, and the ability of nonlinear seismic deformation analyses to provide insight has been shown to be impressive.

Table 5-25 shows a comparison between predicted, and observed, displacements at four key locations. Agreement between the analytical results, and observed performance, was moderately good, and was slightly unconservatively biased.

Overall, Analysis 8 provided a fairly good engineering “prediction” of the actual observed field performance. It correctly predicted the deep, basal slippage originating at the downstream toe and then arcing upwards across the core zone, but did not very accurately determine the location at which the exiting heel scarp feature of this slippage would emerge to exit either high on the upstream face of the dam, or at the crest road. Analysis 8 also underestimated deformations and displacements to some extent, as shown in Figures and 5-33(b), and in Table 5-25. The engineering interpretation of Analysis 8 would be that this earthquake would produce moderate displacements and deformations, but it would somewhat under-estimate effective crest loss and associated risk of overtopping.

Given that the liquefaction triggering relationship of Cetin et al. (2018) is the least conservative of the three triggering relationships employed in these current studies, and produces the highest levels of seismically induced cyclic pore pressure generation, the moderate levels of under-estimation of observed displacements (see Table 5-25) appear to be due to somewhat overly “stiff” performance of the PM4Sand model during strong shaking. Calculated displacements are generally within a factor of two or better of these actually observed, but they tend to be a bit unconservatively biased.

Table 5-25: Comparison between results of USFD Analysis 8 [PM4Sand Model – C, W] and observed displacements of the USFD at four key locations

Displacement Location and Direction	Measured Displacements	Analysis Results
Maximum crest loss	2.5 to 3.0 feet	1.7 feet to 1.8 feet
Maximum crest lateral translation to D/S (+ towards D/S)	4.9 to 6.0 feet	1.0 feet
Maximum lateral translation of the D/S slope face	7.2 to 8.7 feet	7.2 feet
Maximum lateral translation of the D/S toe	3.6 to 5.3 feet	3.3 feet

5.8.9 USFD Analysis 9: Wang2D Model, with the Cetin et al. (2018) Liquefaction Triggering Relationship, and the Weber et al. (2015) S_r Relationship

USFD Analysis 9 utilizes the Wang2D plasticity model, parameterized to match the Cetin et al. (2018) liquefaction triggering relationship, and the Youd et al. (2001) K_σ relationship, which is recommended in conjunction with the Cetin et al. (2018) triggering relationship. Post-liquefaction residual strengths (S_r) are determined in Analysis 9 using the S_r relationship of Weber et al. (2015). The Wang2D model is used in all potentially liquefiable soils (in the upstream and downstream hydraulic fill shells, and the upper alluvium).

Wang and Ma (2018) developed and refined both the Wang2D model, and the associated parameterization procedures, to be in good agreement with the cyclic direct simple shear testing (DSS) database of Wu et al. (2003). Wang and Ma calculated both K_α and K_σ behaviors for different initial effective stress ($\sigma'_{v,i}$) and K_α conditions and demonstrated that K_α behaviors in Wang2D generally match well with the K_α and K_σ behaviors exhibited in the undrained cyclic DSS tests of Wu et al. (2003) and also the K_σ behaviors of Youd et al. (2001), and the K_α relationship of Idriss and Boulanger (2003).

Wang and Ma (2018) also introduced an $R_{u,seismic}$ parameter in the updated Wang2D version (also available in Itasca UDM site). This allows a user defined $R_{u,seismic}$ parameter for S_r application during shaking analysis. In these current studies, an $R_{u,seismic}$ value of 0.85 was used, and as a result potentially liquefiable soil elements utilized prescribed S_r values (as per Weber et al. (2015) in this analysis) for durations during shaking when they achieved $R_{u,seis}$ greater than 0.85. The current implementation does not, however, restrict dilation and

when $R_{u,seismic}$ drops below 0.85 the model performs without any effect of the prescribed limiting value. As a result, at present this feature has relatively little effect on the analyses performed in these current studies.

Wang2D model parameters for these current studies were developed using the calibration file (single element DSS testing) provided by Dr. Fenggang Ma (2018) (also available in Itasca-UDM site), and in general accordance with the procedures described in Wang and Ma (2018). Tables 5-26 (a) and (b) present the input parameters used in USFD Analysis 9 for modeling of the potentially liquefiable soils. The non-liquefiable layers were modeled with Mohr-Coulomb parameters, as presented in Table 5-8. Shear strength of the semi-puddled central clay core was modeled as $S_u/\sigma'_{vi} = 0.192$ during shaking analysis of USFD Analysis 9, which assumes approximately a 20% reduction of undrained shear strength (from peak static, or monotonic, shear strength of $S_u/\sigma'_{vi} = 0.24$) for the normally consolidated clayey core to account for both (a) cyclic softening and (b) strain softening.

One set of additional parameters are needed for Analysis 9, and these are the $N_{1,60,CS}$ values processed and developed according to the energy, equipment, procedural and effective stress corrections of the post-liquefaction S_r relationship of Weber et al. (2015). These are presented in Table 5-27.

Table 5-26(a): Input parameters for USFD Analysis 9 using the Wang2D model; calibrated with the Cetin et al. (2018) liquefaction triggering relationship, the Youd et al. (2001) K_σ relationship, and the Boulanger and Idriss (2003) K_α relationship

Soil Layer	$N_{1,60,CS}$	Relative Density, D_R	Void Ratio, e	Friction Angle, ϕ'	Poisson Ratio, ν	Elastic Shear Modulus Coefficient, G_0
HFU-1	11.7	0.54	0.58	32	0.35	270.2
HFU-2	15.4	0.62	0.54	34	0.35	279.1
UA	16.7	0.64	0.53	35	0.35	281.4
HFD-1	12.6	0.56	0.57	33	0.35	272.8
HFD-2	14.3	0.59	0.55	34	0.35	276.9
HFD-3	15.3	0.62	0.54	34	0.35	278.9
<ul style="list-style-type: none"> D_R: Relative density measured using $N_{1,60,CS}$ (Cetin et al. 2018) and $C_d=40.4$ $e = e_{max} - (e_{max}-e_{min})*D_R$ with $e_{max}-e_{min}=0.5$ for Silty Sand $\phi' =$ Table 4-8 using Hatanaka and Uchida (1997) and Cetin et al. (2018) corrected SPT $N_{1,60,CS}$ G_0: Calculated using $G_{max} = p_a G_0 \frac{(2.973-e)^2}{1+e} \sqrt{\frac{p}{p_a}}$ and $G_{max} = 1000 K_{2max} p^{0.5}$, where p is mean effective stress, G_{max} is in psf and K_{2max} are in Table 4-9 						

Table 5-26(b): Input parameters for USFD Analysis 9 using the Wang2D model; calibrated with the Cetin et al. (2018) liquefaction triggering relationship, the Youd et al. (2001) K_σ relationship, and the Boulanger and Idriss (2003) K_α relationship

Soil Layer	kr	b	gamma	η	Plastic Shear Modulus Coefficient, hr	d	Phase Transformation Ratio, $f_p (=R_p/R_f)$	Ru for S_r Application During Shaking
HFU-1	0.3	2	20.9	8.8	0.24	2.2	0.80	0.85
HFU-2	0.3	2	26.2	10.3	0.22	3.8	0.75	0.85
HFU-3	0.3	2	27.9	10.9	0.18	4.3	0.75	0.85
HFD-1	0.3	2	22.2	9.2	0.28	2.5	0.80	0.85
HFD-2	0.3	2	24.7	9.9	0.19	3.3	0.80	0.85
HFD-3	0.3	2	26.0	10.3	0.18	3.8	0.75	0.85

- **d:** Coefficient that controls the development of excess pore pressure due to cyclic loading under undrained conditions (or shear-induced volumetric change under drained condition). It was developed for each layer by calibrating the DSS single element tests to match CSR vs. N_{cyc} using the Cetin et al. (2016) liquefaction triggering relationship and N_{cyc} based on Idriss (1999).
- **hr:** Plastic shear modulus coefficient. It was developed using Wang2D-Sr modulus reduction relationship by Wang and Ma (2018) for each layer using mean initial effective stress at the middle of the layer, G_{max} and strength parameters. The hr parameter is calibrated to match with established modulus reduction relationships. In the current studies, both Seed and Idriss (1970) and Darendeli (2001) with Yee et al. (2013) strength adjustments relationships were utilized.
- **$f_p (=R_p/R_f)$:** Phase transformation line is the ratio of the phase transformation line and failure line from laboratory tests. In the current studies, $R_p/R_f=0.8$ was used for $D_r \leq 60$ percent and $R_p/R_f=0.75$ was used for $D_r > 60$ percent, based on an evaluation of Wu et al. (2003).
- **gamma:** Defines the plastic shear modulus reduction due to accumulation of strains. It impacts the post-liquefaction behavior during earthquake analysis. Used $\gamma = (2/3)*D_r(\%)-15$.
- **ita:** Defines the plastic bulk modulus reduction due to accumulation of strains. It impacts the post-liquefaction behavior during earthquake analysis. Used $ita = (1/5)*D_r(\%)-2$
- **Ru:** Defines excess pore pressure ratio, at which post-liquefaction strength values are used as an instantaneous strength. The strength is not capped at S_r , rather acts as an instantaneous strength for Ru values greater than or equal to a user-defined value. In the current studies, considering that post-earthquake stage applies S_r at elements with $R_u \geq 0.7$ to check for deformations that were not realized from earthquake analysis, a slightly higher Ru (≥ 0.85) was utilized in earthquake analysis for S_r application.

The protocol for the seismic deformation analyses performed as part of these current studies is to handle the potential transition to post-liquefaction residual strength (S_r) in elements comprised of potentially liquefiable soils within the constitutive model framework by considering the analysis to progress in two steps or stages (1) during shaking, and (2) after the end of shaking. After the end of shaking, S_r is applied within potentially liquefiable soil elements that satisfy either of two criteria: (1) occurrence of $R_{u,seis} \geq 0.7$ at any stage during shaking ($R_{u,seis,max} \geq 0.7$) or (2) development of a peak shear strain of $\gamma \geq 10\%$ at the end of shaking in saturated materials. The PM4Sand protocol used in the current studies is then to continue the nonlinear deformation analysis after the end of shaking until either (1) deformations and displacements have ceased to occur, as the embankment is in a stable condition, or (2) mesh distortions are resulting in a need to perform significant (and time-consuming) re-meshing to continue the NDA deformation analysis, and the results at termination have become sufficient for purposes of engineering interpretation and decision-making, with recognition that deformations and displacements are still ongoing.

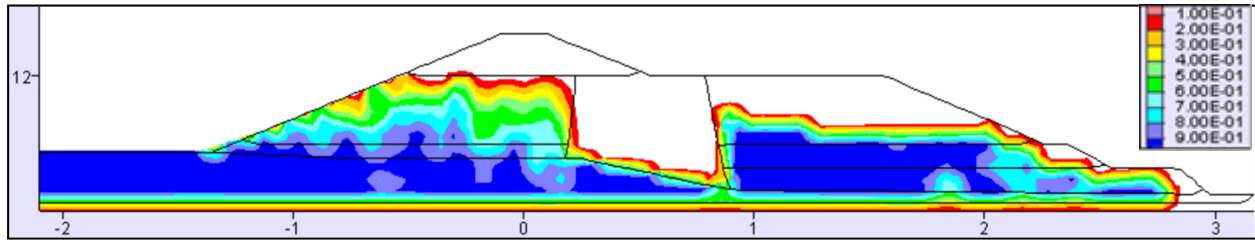
Similarly, it is part of the Wang2D protocol for the current studies to also examine non-liquefiable soils (e.g. the normally consolidated central clayey core zone) at the end of shaking, and to consider whether strength reduction (or further strength reduction) is warranted as a result of large shear strain development and resulting strain softening in sensitive cohesive soils.

Table 5-27: Input Parameters for use of the Weber et al. (2015) S_r Relationship in USFD Analysis 9

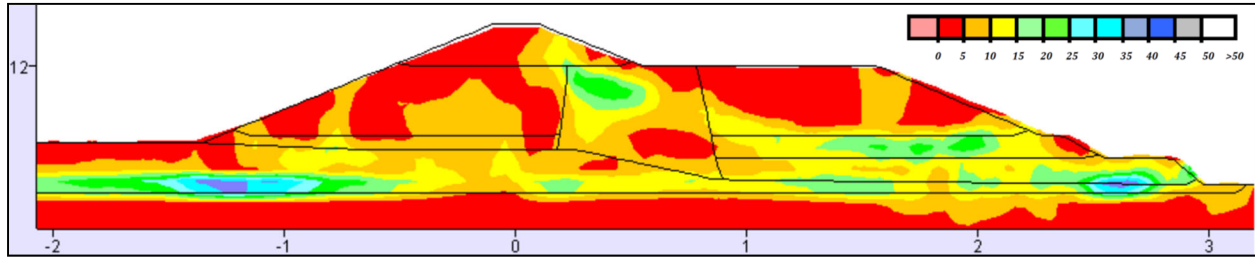
Soil Layer	$N_{1,60,CS-Sr}$ (Weber et al., 2015)
HFU-1	11.7
HFU-2	15.4
UA	16.7
HFD-1	12.6
HFD-2	14.3
HFD-3	15.3

Figures 5-34 and 5-35 present the results of nonlinear seismic deformation analyses performed with the combination of models and relationships of USFD Analysis 9. Figure 5-34 shows conditions calculated “at the end of shaking”, but the analyses are continued after the end of input seismic excitation, as deformations can continue after the end of shaking due to ongoing deformations under static (gravity loading) when post-liquefaction residual strength, S_r are applied in elements that satisfy either of two criteria: (1) occurrence of $R_{u,seis} \geq 0.7$ at any stage during shaking ($R_{u,seis,max} \geq 0.7$) or (2) development of a peak shear strain

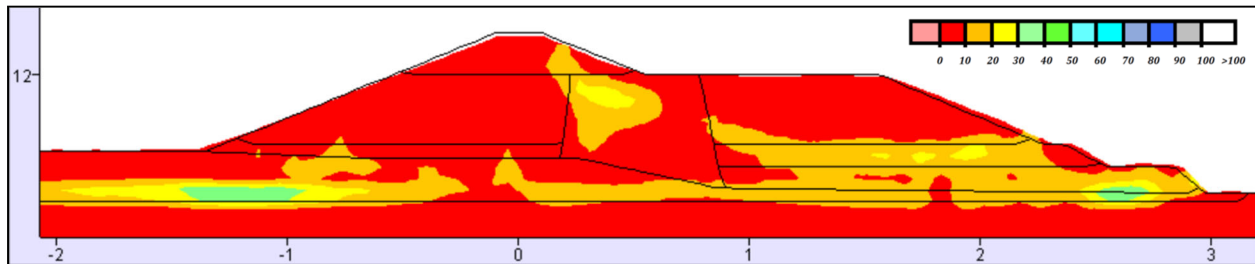
USFD Analysis 9: Wang2D model, with the Cetin et al. (2016) Liquefaction Triggering Relationship, and the Weber et al. (2015) S_r Relationship



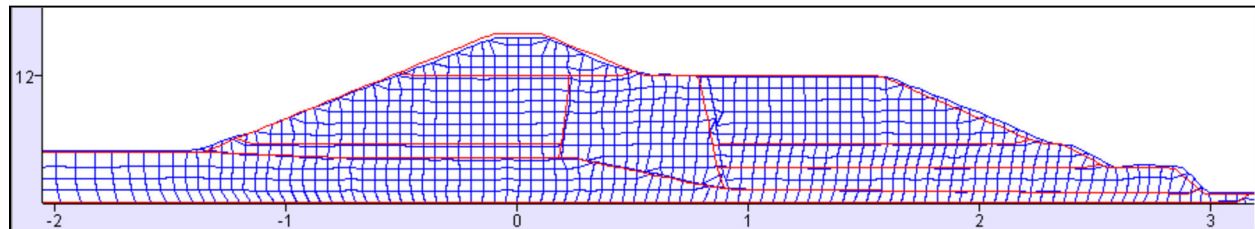
(a) Maximum value of $R_{u, seismic}$ recorded in each element



(b) Shear strain (percent), with the inset shear strain scale set to max. of 50 percent



(c) Shear strain (percent), with the inset shear strain scale set to max. of 100 percent



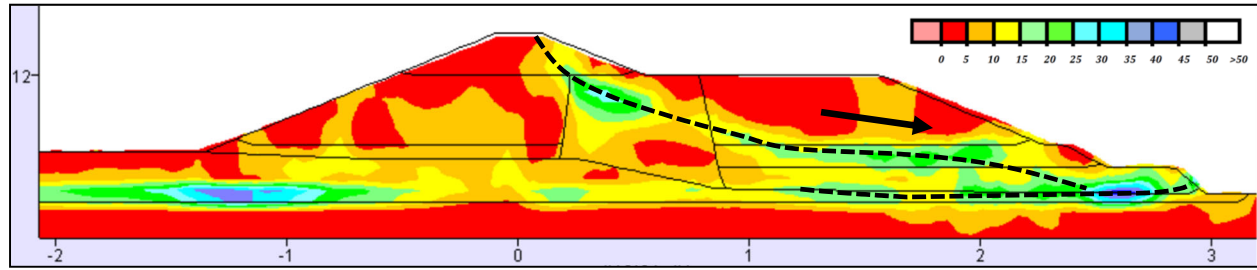
(d) Deformed mesh

Figure 5-34: Results of USFD Analysis 9 at the end of shaking

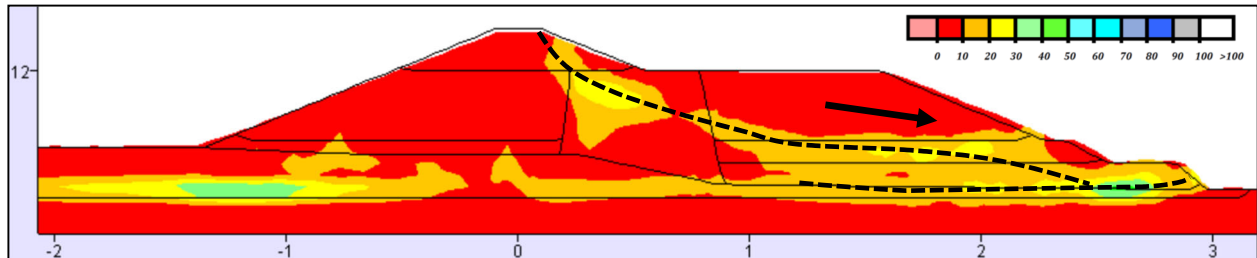
of $\gamma \geq 10\%$ at the end of shaking in saturated materials. In some cases, the post-shaking deformations can lead to development, or discovery, of progressive development of large deformations or even instability failures. Accordingly, it is important to continue the analyses after the end of shaking.

Figure 5-35 therefore presents conditions at “the end of analysis”. The end of analysis is the point in time when the analysis team elects to end (discontinue) the NDA analysis. Reasons for ending the analysis can include (1) deformations and displacements have ceased

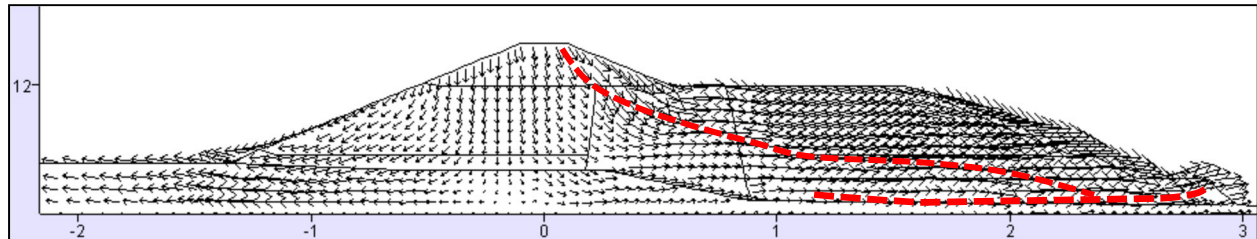
USFD Analysis 9: Wang2D model, with the Cetin et al. (2016) Liquefaction Triggering Relationship, and the Weber et al. (2015) S_r Relationship



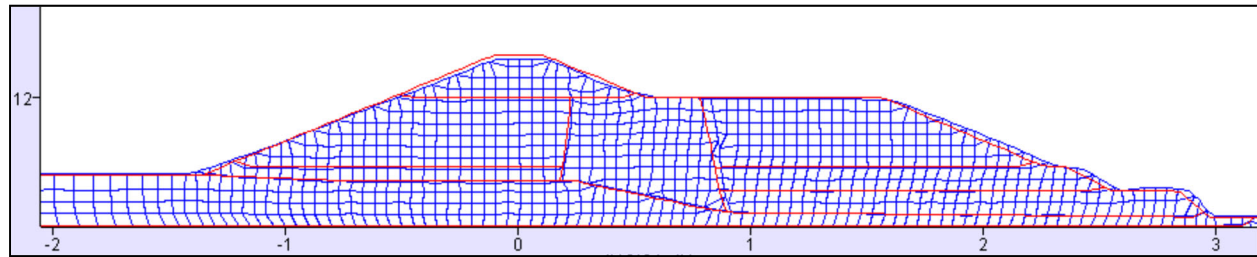
(a) Shear strain (percent), with the inset shear strain scale set to max. of 50 percent



(b) Shear strain (percent), with the inset shear strain scale set to max. of 100 percent



(c) Displacement vectors (capped at 7 feet for clarity), Maximum 6.3 feet



(d) Deformed mesh

5-35: Results of USFD Analysis 9 at the end of analysis

to occur, as the embankment is in a stable condition, or (2) mesh distortions are resulting in a need to perform significant (and time-consuming) re-meshing to continue the NDA deformation analysis, and the results at termination have become sufficient for purposes of engineering interpretation and decision-making, with recognition that deformations and displacements are still ongoing.

Examination of shear strains at the end of shaking across zones of strain sensitive puddled clay core materials indicated maximum shear strains of approximately of 27%, with

an average of 9% across the puddled central clay core along potential shear zones. As discussed in Section 4.8.4, at this range of shear strains it was not fully clear whether or not additional reduction of clay shear strengths to account for strain softening was warranted, as there was already a reduction of strength by 20% in the central clay core zone to account for both cyclic softening and moderate strain softening.

However, the engineering judgment of the analysis team was that the strength of the central clayey core should be reduced to a value intermediate between (1) the already 20% softened clay core strength value of $S_u/\sigma'_{v,i} = 0.192$ and (2) a fully residual value of $S_{u,residual}/\sigma'_{v,i} = 0.08$, to a strength of $S_u/\sigma'_{v,i} = (0.5)(0.192 + 0.08) = 0.136$ in the post-shaking stage, to check if the embankment would remain stable and not experience significant additional deformations. If so, then the reduction to $S_u/\sigma'_{v,i} = 0.136$ would have been shown to be unnecessary. This was mainly done to be consistent with other USFD analyses performed in these current studies. The hypothesis for performing this analyses was that the reduction to intermediate clay strength should not add significant deformations, if the dam is stable. The analysis was re-started and continued past the end of shaking.

Crest settlement was 1.9 feet at the end of shaking, and increased to 2.0 feet at the end of analysis when (1) post-liquefaction residual strengths (S_r) and (2) softened clay core strengths of $S_u/\sigma'_{vi} = 0.136$ were applied, and the analysis was again re-started. Similarly, the maximum lateral translation of the downstream slope was 5.7 feet at the end of shaking, and increased to 6.3 feet at the end of analysis. These minor deformations and displacements did not appreciably increase the shear strains or deformations across the central clayey core zone, and the embankment remained stable. It was therefore judged that the hypothetical partial reduction in clay strength to $S_u/\sigma'_{vi} = 0.136$ had been shown to be unnecessary, and had not significantly affected the end of analysis conditions. At the end of analysis, the embankment was stable. This is the “end of analysis” condition shown in Figure 5-35.

As a hypothetical worst-case scenario for LSFD Analysis 9, the puddled clay core strength was then reduced to fully residual strength of clay, and the analysis was again re-started. The additional deformations were negligible (less than 0.1 feet of additional crest loss, and less than 0.1 feet of additional downstream toe displacement), and the dam remained stable.

In this case, USFD Analysis 9, only limited to moderate additional deformations and displacements that occurred after the end of shaking, as the embankment stabilized after cyclic (seismic) inertial forces abated.

As shown in Figure 5-34(a), significant cyclic pore pressures are generated in USFD Analysis 9 in the upstream semi-hydraulic fill shell zones, as well as in the upper alluvium underlying the upstream side of the embankment, and significant pore pressures are also generated in the saturated portions of the downstream side semi-hydraulic fill shell zones. Despite these high pore pressures, the embankment continues to be stable both during and after shaking; due to the availability of sufficient post-liquefaction strength (S_r) in conjunction with the strengths available in other, non-liquefied zones.

This is a recurring pattern in many of the back-analyses of the USFD performed in these current studies, with various analytical model and engineering relationship combinations; significant to high cyclic pore pressures are generated, and embankment lurching-type deformations are developed during strong shaking, but post-liquefaction residual strengths are sufficient to maintain overall static stability, so only moderate deformations develop during shaking, and deformations do not continue to increase very significantly after the end of shaking.

As indicated in Figures 5-34(b) through (d), and Figure 5-35(a) through(d), these seismically induced pore pressures, in conjunction with the seismic inertial forces of the earthquake, again produce moderate deformations, with the principal movements occurring along a narrowly confined shear zone originating at and near the downstream, and then passing laterally across the base of the embankment to the core, then arcing upwards across the core to exit at the crest of the dam. USFD Analysis 9 again predicts a deep, basal shear mechanism from the downstream toe, and then arcing upwards across the core; in good general agreement with the observed field performance, except that the heel scarp emerges at a point near the downstream edge of the level top deck of the crest, rather than high on the upstream face of the dam as was observed in the actual field performance (see Figures 5-1, 5-2, 5-3, 5-5 and 5-8) and the hypothesized mechanism, as discussed in Section 5.4.

Table 5-28 shows a comparison between predicted, and observed, displacements at three key locations. Agreement between the analytical results, and observed performance, was very good.

Table 5-28: Comparison between results of USFD Analysis 9 [Wang2D – C, W] and observed displacements of the USFD at four key locations

Displacement Location and Direction	Measured Displacements	Analysis Results
Maximum crest loss	2.5 to 3.0 feet	1.9 to 2.0 feet
Maximum crest lateral translation to D/S (+ towards D/S)	4.9 to 6.0 feet	1.0 feet
Maximum lateral translation of the D/S slope face	7.2 to 8.7 feet	6.3 feet
Maximum lateral translation of the D/S toe	3.6 to 5.3 feet	3.4 feet

Overall, Analysis 9 provided good engineering “predictions” of the actual observed field performance. It correctly predicted the deep, basal slippage originating at the downstream toe and then arcing upwards across the core zone to exit high on crest of the dam (but it missed the actual heel scarp exit point which was high on the upstream face), and it provided usefully accurate predictions of the magnitudes of deformations and displacements. The overall matches between the magnitudes of calculated vs. observed displacements (e.g. Table 5-25) from USFD Analysis 9 were the best among the nine USFD analyses performed; despite not fully accurately predicting the heel scarp exit point of the downstream side slippage. As discussed in Section 5.8.8 (USFD Analysis 8) there appear to be multiple partially developed or incipient slippage surfaces at this stage of deformation development, and the crest section was suitably lowered (suffered 1.9 to 2.0 feet of crest loss) across the full width of the crest deck. The engineering interpretation of USFD Analysis 9 would be that this earthquake would produce moderate displacements and deformations, resulting in moderate crest loss and likely repairable damage to the upper portions of the upper crest section of the dam.

5.9 SENSITIVITY ANALYSIS WITH GROUND MOTIONS WITH STATIC PERMANENT OFFSET

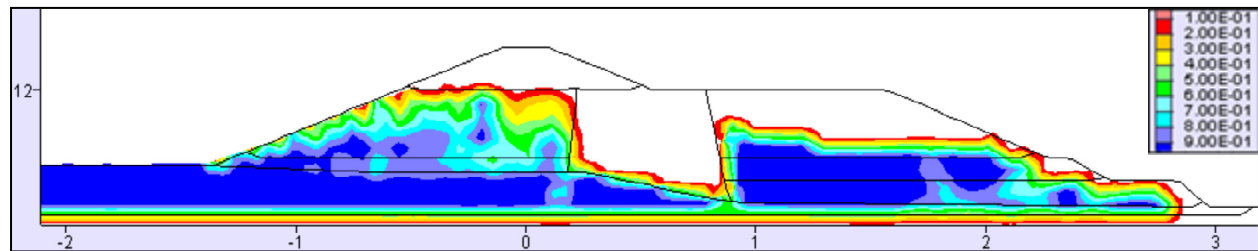
Ground motions in the near-source regions of earthquakes can be significantly affected by rupture directivity and tectonic fling. These two conditions can result in large, long-period pulses of ground motions, and permanent ground displacements. Conventional ground motion processing involves bandpass filtering and baseline correction. Conventional record processing techniques can typically recover directivity pulses, however, accurate recovery of fling requires complete resolution of the residual displacement, which can be non-unique and quite sensitive to the processing approaches [Dreger et al. (2011), Graves (2011)].

In these current studies, the recorded ground motions at Pacoima Dam were processed to capture the permanent offset or residual displacement to perform a sensitivity analysis for USFD, using the USFD Analysis 9 model; with Cetin et al. (2018) liquefaction triggering, and Weber et al. (2015) Sr.

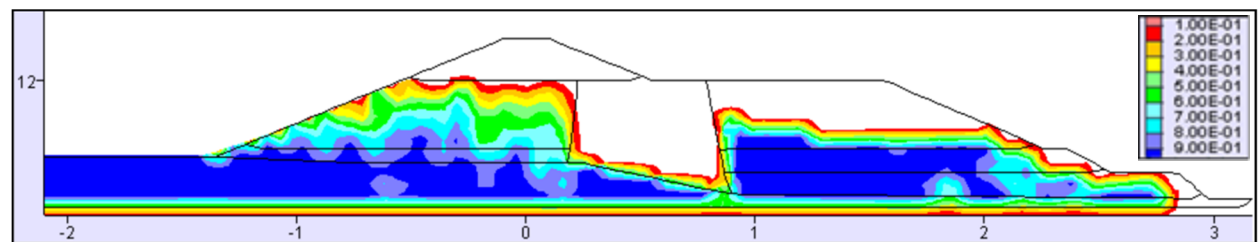
Figure 5-36(a) and (b) show a comparison of maximum $R_{u, seismic}$ values for the input motions with, and without, permanent offset preserved. Figure 5-36(c) and (d) show a similar comparison of shear strains at the end of shaking. Figure 5-37 shows a comparison of displacement vectors at the end of shaking, and Figure 5-38 show the final deformed shapes from these two analyses.

A comparison of USFD Analysis 9 using PEER-processed scaled motions, and scaled motions processed to preserve permanent offset, shows that the ground motions with permanent offset resulted in more displacement vectors directing toward downslope. The deformation magnitudes did not differ significantly (maximum crest loss: 2.1 feet with permanent static offset compared with 2.0 feet without permanent static offset; landside max. slope displacement: 5.9 feet with static offset compared with 6.3 feet without permanent static offset) in this study mainly due to presence of a wider downstream berm

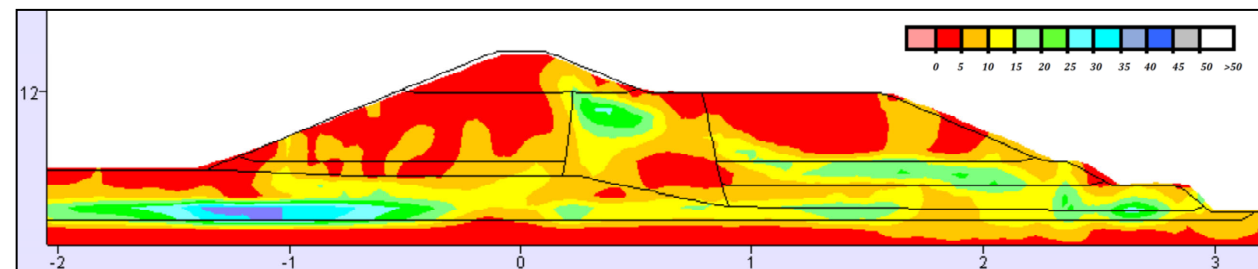
in USFD.; however, the use of ground motions with permanent offset may be important for forward analyses, where a weaker embankment zone aligned with ground motion directivity and fling may be a more accurate modeling of expected deformations.



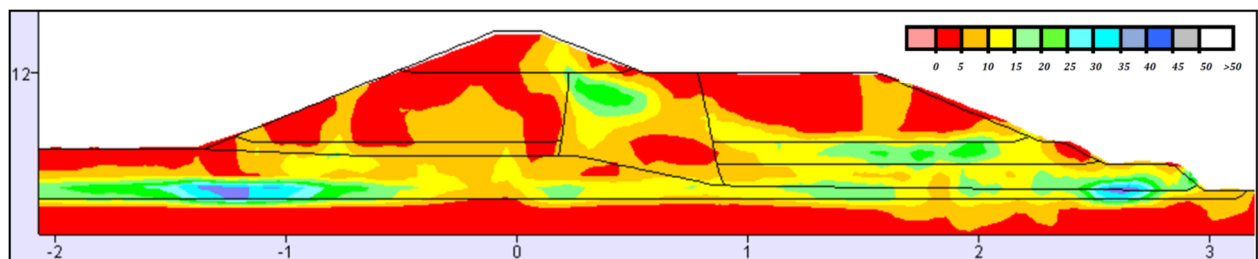
(a) With permanent static offset ground motions: Maximum value of $R_{u,seismic}$ recorded in each element



(b) Without permanent static offset ground motions (PEER processing): Maximum value of $R_{u,seismic}$ recorded in each element

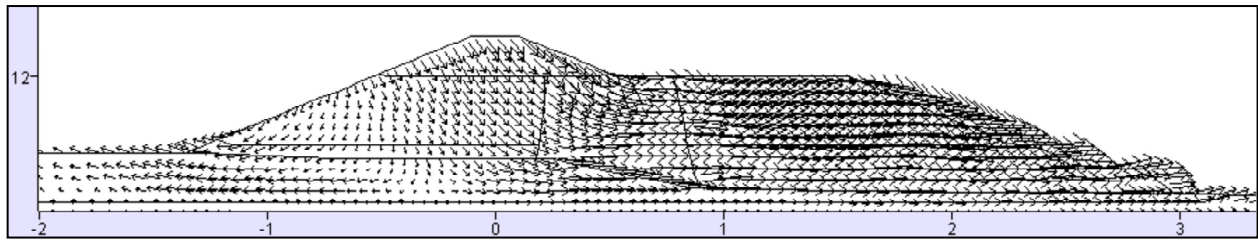


(c) With permanent static offset ground motions: Shear strain (percent), with the inset shear strain scale set to max. of 50 percent

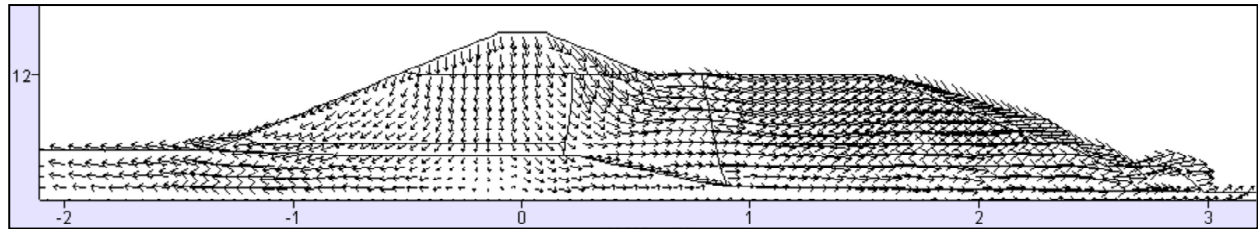


(d) Without permanent static offset ground motions (PEER processing): Shear strain (percent), with the inset shear strain scale set to max. of 50 percent

Figure 5-36: Results of USFD Analysis 9 (maximum $R_{u,seismic}$ and shear strains) with input ground motions with and without permanent static offset; end of shaking conditions are shown



(a) With permanent static offset ground motions: Displacement vectors (capped at 7 feet for clarity), Maximum = 6.6 feet



(b) Without permanent static offset ground motions (PEER processing): Displacement vectors (capped at 7 feet for clarity), Maximum = 5.6 feet

Figure 5-37: Results of USFD Analysis 9 (displacement vectors) with ground motions with permanent static offset and without permanent static at the end of shaking

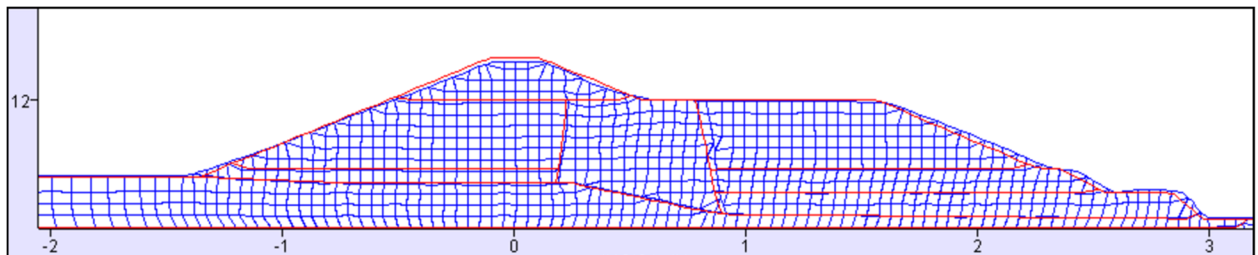
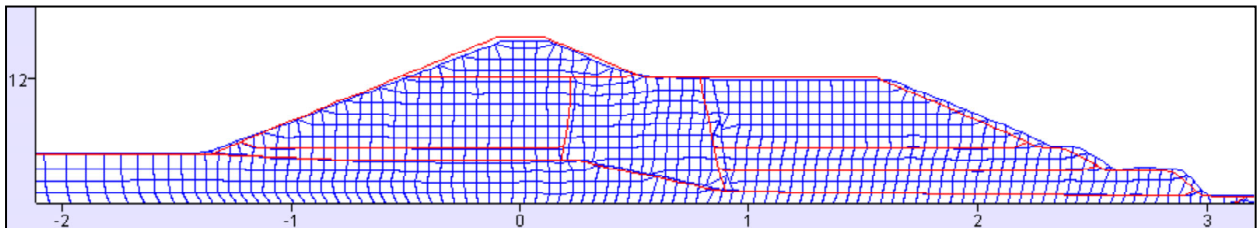


Figure 5-38: Deformed shape of USFD Analysis 9 with ground motions with permanent static offset and without permanent static at the end of analyses (after post-shaking analyses)

5.10 SUMMARY AND CONCLUSIONS

The Upper San Fernando Dam (USFD) seismic performance case history from the 1971 San Fernando earthquake represents an excellent pairing or couplet with the Lower San Fernando dam (LSFD) case history presented in the previous Chapter 4 with regard to examination of the accuracy, reliability, and likely engineering usefulness of nonlinear seismic deformation analysis (NDA) methods. The Lower San Fernando dam experienced liquefaction-induced flow failure on its upstream side during the earthquake, which transported a majority of the embankment back into the reservoir leaving a slide heel scarp on the downstream side as the only functioning/remaining crest. The Upper San Fernando dam, on the other hand, suffered only moderate deformations and displacements, despite having been constructed as part of the same overall project, and with similar materials and largely similar methods. These two very different ranges of observed performance in the same earthquake pose two very different sets of challenges for nonlinear seismic deformation analyses. As a result, they are a good and instructive pair of test cases.

Nine nonlinear seismic deformation analyses were performed as back-analyses of the performance of the USFD in the 1971 San Fernando Dam earthquake. Table 5-1 presented a summary of the combinations of (1) four analytical models or constitutive relationships, (2) three liquefaction triggering relationships, and (3) three post-liquefaction residual strength relationships employed in each of these nine analyses, and it is repeated here as Table 5-29 for easy reference.

Table 5-30 presents a summary overview of five selected indices of the relative matches between each of the analytical results vs. the actual observed field behavior. The combinations of analytical models and engineering relationships employed in each of the nine analyses are listed in Table 5-30. Individual results for each analysis, including figures showing cyclic pore pressure generation, shear strains, deformed meshes at various stages of analysis, displacement vectors, inferred concentrated shear strain zones (and inferred incipient and also well-developed shear failure surfaces), etc. are presented and discussed in detail in Sections 5.8.1 through 5.8.9.

Six of these nonlinear seismic deformation analyses (Analyses 1, 3, 4, 6, 8 and 9) were either successful or very successful, producing good matches with the observed field behavior, including discerning principal mechanisms of deformation, as well as details such as (1) the magnitudes of crest loss and (2) magnitudes of lateral translation of the downstream slope and toe.

All six of these analyses correctly predicted the apparent principal mechanism of displacement that produced the moderate deformations and displacements observed after the 1971 earthquake. This was a largely monolithic slippage towards the downstream side of approximately two-thirds of main body of the dam, along a deep-seated basal shear zone or shear surface that originated near the downstream toe, traversed laterally across the lower portion of the downstream side hydraulic fill “shell” zones, and then arced upwards as it crossed the central clayey core zone, to exit with a heel scarp either high on the upstream

Table 5-29: Summary of analytical modeling schemes for the USFD back-analyses performed

Analysis ID	Description
USFD Analysis 1: Roth (Y,SH)	Constitutive model for liquefiable soils – Roth Liquefaction Triggering and K_σ – Youd et. al. (2001) Post Liquefaction Residual Strength, S_r – Seed and Harder (1990) [Average S_r applied during-shaking/earthquake analysis]
USFD Analysis 2: Roth (B&I,I&B)	Constitutive model for liquefiable soils – Roth Liquefaction Triggering and K_σ – Boulanger and Idriss (2014) Post Liquefaction Residual Strength, S_r – Idriss and Boulanger (2015) [S_r “with significant void redistribution” curve applied during-shaking/earthquake analysis]
USFD Analysis 3: Roth (C,W)	Constitutive model for liquefiable soils – Roth Liquefaction Triggering – Cetin et al. (2018); K_σ – Youd et al. (2001) Post Liquefaction Residual Strength, S_r – Weber et al. (2015) [50 th percentile S_r applied during-shaking/earthquake analysis]
USFD Analysis 4: UBCSAND (Y,SH)	Constitutive model for liquefiable soils – UBCSAND Liquefaction triggering and K_σ – Youd et al. (2001) Post-liquefaction Residual Strength, S_r – Seed and Harder (1990) [Average S_r applied during post-shaking analysis]
USFD Analysis 5: UBCSAND (B&I,I&B)	Constitutive model for liquefiable soils – UBCSAND Liquefaction Triggering and K_σ – Youd et al. (2001); Post Post Liquefaction Residual Strength, S_r – Idriss and Boulanger (2015) [S_r “with significant void redistribution” curve applied during post- shaking]
USFD Analysis 6: UBCSAND (Y,W)	Constitutive model for liquefiable soils – UBCSAND Liquefaction Triggering and K_σ – Youd et al. (2001); Post Liquefaction Residual Strength, S_r – Weber et al. (2015) [50 th percentile S_r applied during post- shaking analysis]
USFD Analysis 7: PM4Sand (B&I,I&B)	Constitutive model for liquefiable soils – PM4Sand Liquefaction Triggering and K_σ – Boulanger and Idriss (2014); Post Liquefaction Residual Strength, S_r – Idriss and Boulanger (2015) [S_r “with significant void redistribution” curve applied during post-shaking analysis]
USFD Analysis 8: PM4Sand (C,W)	Constitutive model for liquefiable soils – PM4Sand Liquefaction Triggering – Cetin et al. (2018); K_σ – Youd et al. (2001); Post Liquefaction Residual Strength, S_r – Weber et al. (2015) [50 th percentile S_r applied during post-shaking analysis by a FISH function]
USFD Analysis 9: Wang2D (C,W)	Constitutive model for liquefiable soils – Wang2D Liquefaction Triggering – Cetin et al. (2018); K_σ – Youd et al. (2001); Post Liquefaction Residual Strength, S_r – Weber et al. (2015) [50 th percentile S_r applied during shaking for durations with $R_{u,seis}$ greater than a specified value, and also during post-shaking analysis by a FISH function]

Table 5-30: Summary comparison between selected analytical results and observed field performance of the USFD

Analysis ID No. and Model	Liquefaction Triggering Relationship	Post-Liquefaction Residual Strength (S_r) Relationship	Maximum crest loss	Maximum crest lateral translation to D/S	Maximum lateral translation of the D/S slope face	Maximum lateral translation of the D/S toe
Observed Performance	-	-	2.5 to 3.0 feet	4.9 to 6.0 feet	7.2 to 8.7 feet	3.6 to 5.3 feet
1 Roth	Youd et al. (2001)	Seed and Harder (1990)	7.0 to 7.7 feet	3.4 feet	11.7 feet	7.3 feet
2 Roth	Boulanger and Idriss (2014)	Idriss & Boulanger (2015)	> 13.0 feet (and ongoing)	> 4.7 feet (and ongoing)	> 45.0 feet (and ongoing)	> 36.0 feet (and ongoing)
3 Roth	Cetin et al. (2018)	Weber et al. (2015)	6.3 to 7.3 feet	1.1 feet	9.7 feet	6.0 feet
4 UBCSAND	Youd et al. (2001)	Seed and Harder (1990)	6.4 to 7.2 feet	3.3 feet	10.1 feet	4.1 feet
5 UBCSAND	Youd et al. (2001)	Idriss & Boulanger (2015)	> 14.0 feet (and ongoing)	> 8.2 feet (and ongoing)	> 70.0 feet (and ongoing)	> 50.0 feet (and ongoing)
6 UBCSAND	Youd et al. (2001)	Weber et al. (2015)	5.1 to 5.6 feet	1.7 feet	7.3 feet	3.6 feet
7 PM4SAND	Boulanger and Idriss (2014)	Idriss & Boulanger (2015)	1.3 to 1.4 feet (and ongoing)	1.2 feet (and ongoing)	> 46.0 feet (and ongoing)	> 28.0 feet (and ongoing)
8 PM4SAND	Cetin et al. (2018)	Weber et al. (2015)	1.7 to 1.8 feet	1.0 feet	7.2 feet	3.3 feet
9 WANG2D	Cetin et al. (2018)	Weber et al. (2015)	1.9 to 2.0 feet	1.0 feet	6.3 feet	3.4 feet

face of the dam, or at the crest of the dam. That mechanism had been postulated by Weber et al. (2015) based on the post-earthquake investigations and cross-sections, but it took these types of more advanced nonlinear seismic deformation analyses (NDA) to analytically demonstrate the feasibility and likelihood of this mechanism.

Three of the nine USFD back-analyses were unsuccessful (USFD Analyses 2, 5, and 7); incorrectly predicting the occurrence of liquefaction-induced full flow failures towards the downstream side of the dam that were not observed in the field. Two of these analyses also incorrectly predicted upstream side flow failures, and the third incorrectly predicted a smaller slump or localized failure on the central upstream face. The two analyses that incorrectly predicted flow failures towards both the upstream and downstream sides of the embankment were USFD Analyses 2, and 5, and it was Analysis 7 that incorrectly predicted upstream side localized slumping. As shown in Table 5-30, each of these employed a different analytical or constitutive model (Roth, PM4Sand, and UBCSAND, respectively), and they employed two different triggering relationships (the Boulanger and Idriss, 2015 triggering relationship for Analyses 2 and 7, and the Youd et al., 2001 triggering relationship for Analysis 5). All three of these analyses employed the same post-liquefaction residual strength relationship; the Idriss and Boulanger (2015) S_r relationship. As discussed in Section 2.4, that relationship predicts the ratio of $S_r/\sigma'_{v,i}$ as a function of only $N_{1,60,CS}$, rather than as a function of both $N_{1,60,CS}$ and $\sigma'_{v,i}$, and as a result it is over-conservative and under-predicts S_r for low to moderate initial effective overburden stresses ($\sigma'_{v,i}$). All of the incorrectly predicted flow failures originated near the toes of the dam, in areas of low initial effective stress ($\sigma'_{v,i}$).

USFD Analysis 3 repeats Analysis 2, except that the Cetin et al. (2018) liquefaction triggering relationship, and the Weber et al. (2015) S_r relationship, are substituted in place of the Boulanger and Idriss (2014) liquefaction triggering relationship and the Idriss and Boulanger S_r relationship that were used in Analysis 2. Similarly, USFD Analysis 6 exactly repeats Analysis 5, except that the Weber et al. (2015) S_r relationship is used in place of the Idriss and Boulanger S_r relationship that was employed in Analysis 5. USFD Analyses 3 and 6 both produce very good results.

Similarly, USFD Analysis 8 largely repeats Analysis 7, except that it employs an even more conservative triggering relationship (Cetin et al., 2018) which results in prediction of even higher seismic (cyclic) pore pressure generation, but it also employs the Weber et al. (2015) S_r relationship in place of the Idriss and Boulanger (2015) S_r relationship, and the post-liquefaction strengths are again sufficient to maintain post-shaking stability and as a result, Analysis 8 also produces very good predictive results.

There is an important lesson here, and that is the largely co-equal importance of employing a suitable post-liquefaction S_r relationship as well as a suitable liquefaction triggering relationship. Engineers to date have often tended to be more focused on the liquefaction triggering relationship; but it is apparent that the post-liquefaction S_r relationship can be of co-equal importance. Failure to employ a suitable S_r relationship can produce very poor analytical results in these types of nonlinear seismic deformation analyses.

In the six successful USFD back-analyses, a recurring theme is that the analyses show significant seismic (cyclic) pore pressure generation in the saturated portions of the upstream and downstream hydraulic fill shell zones, as well as in the upper alluvium underlying the upstream shell, but the post-liquefaction residual strengths are sufficient to maintain overall stability of the embankment.

Each of the four different analytical models produced at least one successful analysis. The Roth model produced good results in Analyses 1 and 3; though it showed a minor tendency to conservatively over-predict vertical crest loss. This is a recognized issue, and it is part of the Roth model intent; it provides for behavior that tends to compensate for the lack of a well-vetted approach to evaluation and modeling of post-liquefaction volumetric reconsolidation settlements (Dawson, personal communication, 2019). These analyses produced useful engineering results.

The UBCSAND model produced good analytical results in Analyses 4 and 6, though it also had an apparent tendency to conservatively slightly over-predict vertical crest loss. Again, this compensates for the lack of a well-vetted approach to evaluation and modeling of post-liquefaction volumetric reconsolidation settlements. These analyses also produced useful engineering results.

The PM4Sand model produced good analytical results in Analysis 8, though it showed a tendency in Analysis 8 (and also in Analysis 7, despite the prediction of a downstream flow failure) to under-predict vertical crest loss. An argument can be made that this will be corrected, at least in part, when well-vetted approaches become available for evaluation and modeling of post-liquefaction volumetric reconsolidation settlements. This analysis also produced useful engineering results.

The Wang2D model (Analysis 9) also produced good analytical results. It produced the best overall matches with observed field performance for the four different displacement indices listed in Table 5-31, but it should be noted that both Analyses 8 (with PM4Sand) and 9 (with Wang2D) predicted the upstream side heel scarp feature to exit somewhat higher on the crest of the dam rather than high on the upstream face as was actually observed in the aftermath of the 1971 earthquake. These two analyses correctly identified the deep basal slippage mechanism, originating at the downstream toe and then passing laterally across the dam before arcing upwards across the central clayey core zone; but both predicted higher exit points for the upstream side heel scarp than was observed in the field. These two analyses, both employing higher order plasticity models, also both “discovered” two sets of potential failure surfaces (or slippage surface paths) from the downstream toe laterally across the dam and then up to a heel scarp high on the upper crest section of the dam. Both models/analyses found the upper-most path (exiting on the crest deck, rather than high on the upstream face of the dam as was actually observed) to be the most likely.

All six successful analyses (USFD Analyses 1, 3, 4, 6, 8, and 9) have caused to claim success; and there was no clear overall “winner”. Each of the four analytical models showed itself well able to produce useful and accurate engineering “predictions”, so long as it was

calibrated and used in conjunction with (1) a suitable liquefaction triggering relationship, and (2) a suitable post-liquefaction S_r relationship.

Neglecting the three analyses that were unsuccessful due to the incorrect prediction of flow failures due to the use of an un-suitable post-liquefaction S_r relationship, and then considering the remaining six analysis results:

1. The Roth model is the oldest, and the simplest of the four analytical models employed. It did the best job (in both Analyses 1 and 3) of predicting the observed exit location of the heel scarp (high on the upstream face) of the massive downstream side slippage feature; very closely matching the heel scarp location. But it conservatively over-predicted the observed crest loss, by factors of approximately $7.7 \text{ ft} / 3.0 \text{ ft} = 2.57$ and $7.3 \text{ ft} / 3.0 \text{ ft} = 2.43$ in these two analyses. It provided predictions of lateral displacements of the downstream slope face, and of the downstream toe, that were all within a factor of 1.43 or less relative to the displacements observed.
2. The UBCSand model represents a mid-level range of complexity between that of the Roth model, and the two higher-order plasticity models (PM4Sand and Wang2D). In USFD Analyses 4 and 6, the UBCSand model predicted the exit point of the heel scarp of the deep-seated downstream side deep-seated displacement feature to occur at the very top of the upstream face of the dam; essentially at the heel point where the upstream face meets the horizontal crest deck. The actually observed exit location of the heel scarp was a bit lower (still near the top of the upstream face); this represented a good (and useful) prediction. The UBCSand model conservatively slightly over-predicted the observed crest loss, by factors of approximately $7.2 \text{ ft} / 3.0 \text{ ft} = 2.40$, and $5.6 \text{ ft} / 3.0 \text{ ft} = 1.87$, in these two analyses. It provided predictions of lateral displacements of the downstream slope face, and of the downstream toe, that were also all within a factor of 1.16 or less relative to the displacements observed.
3. The PM4Sand model is one of the two higher-order plasticity models employed. In USFD Analysis 8, this model predicted an exit location of the heel scarp of the downstream side deep-seated displacement feature high in the downstream side of the upper crest section of the dam. This was the least successful prediction of this heel scarp location. But it should also be noted that in a forward engineering this would likely still have been of some concern. The PM4Sand model under-predicted crest loss by a factor of $1.8 \text{ ft.} / 3.0 \text{ ft.} = 0.60$, and it under-predicted lateral translation of the downstream face of the dam, and of the downstream toe, by factors of $7.2 \text{ ft.} / 8.7 \text{ ft.} = 0.82$ and $3.3 \text{ ft.} / 5.3 \text{ ft.} = 0.62$, respectively. These were all unconservative results.
4. The Wang2D model is the other higher-order plasticity model employed. In USFD Analysis 9, this model predicted an exit location of the heel scarp of the downstream side deep-seated displacement feature on the top deck of the crest, near the downstream end of the deck. This was a somewhat better prediction than the PM4Sand Analysis 8, but it was not as good as any of the four successful Roth and UBCSand analyses. The Wang2D Analysis 9 provided the closest predictions of (1) crest loss (2.0 feet vs. 3.0 feet observed), and close predictions of maximum lateral translation of the downstream face (6.3 ft. calculated

vs. 8.7 ft. observed) and (2) lateral translation of the downstream toe (3.4 ft. vs. 5.3 ft. observed).

With suitable diligence on the part of the engineering team, it appears that these types of analyses can suitably identify potentially critical deformation and/or failure mechanisms, and that they can also provide engineering predictions of expected magnitudes of deformations and displacements within a factor of approximately 2 or so. That was a somewhat surprising and positive outcome of these back-analyses of a challenging case history involving “moderate” seismically induced deformations, with challenging geometry, and significant occurrence of soil liquefaction.

As a result, it may be expected that different model developers will each claim some levels of vindication based on these results.

More important from an engineering perspective is to understand the accuracies, tendencies and apparent reliabilities of each of these analytical models; and also the nature of their interactions with (1) the different liquefaction triggering relationships employed, (2) the different post-liquefaction residual strength (S_r) relationships employed, (3) the different K_σ relationships employed, as well as (4) the different analysis protocols used by different engineering/analysis teams.

These nonlinear seismic deformation analyses can produce very good and useful engineering results, and they can also fail to produce good results. There are a large number of contributing pieces and operations and models and relationships that must all be well selected, and well executed, and which must function both well and compatibly with each other, in order to produce suitably accurate, reliable, useful engineering results.

The over-arching lessons from these back-analyses appear to be two-fold. The first is that these types of nonlinear seismic deformation analyses can provide accurate and useful engineering results. Overall, these back-analyses demonstrated an ability to produce very good engineering “predictions” of both observed mechanisms of displacements and distress, as well as the magnitudes of deformations and displacements.

Accomplishing this appears to require the following:

1. Suitable analytical or constitutive models.
2. Calibration of these models with respect to cyclic (seismic) pore pressure generation with suitable liquefaction triggering relationships, including both K_α and K_σ relationships.
3. Use of suitable post-liquefaction residual strength (S_r) relationships.
4. Suitable procedures and protocols for transition to S_r behaviors in potentially liquefiable soils.

5. Suitable treatment of potential cyclic softening, and strain softening, behaviors in strain sensitive clayey soils.
6. Suitable characterization of geometry and stratigraphy, and suitable evaluation of material properties and behaviors.
7. Suitable development and application of appropriate seismic “input” motions.
8. Appropriate evaluation and interpretation of the analysis results, with an understanding of the models and relationships employed, and also the intrinsic limitations of the continuum analysis methods employed with regard to accurate analyses of very large deformations and displacements.
9. And engineering judgment.

These are largely the same findings produced from the back-analyses of the LSFD, as presented in Chapter 4. It is perhaps not surprising that both sets of back-analyses would produce this list of key issues to address and suitably handle.

Chapter 6 presents overall lessons learned from the studies, and those include a number of lessons that can only be gleaned by considering both the USFD and LSFD back-analyses jointly. The summary of lessons learned that is presented in Chapter 6 will therefore be the more detailed and comprehensive set.

Chapter 6

Summary Findings and Conclusions

6.1 INTRODUCTION

The principal objective of these studies was to evaluate the accuracy, performance and reliability of current state-of-practice fully nonlinear seismic deformation analyses as applied to the evaluation of expected seismic performance of dams potentially susceptible to seismically-induced soil liquefaction. Applications would include (1) evaluation of existing risk for dams, (2) dam inventory prioritization for eventual seismic hazard mitigation, (3) establishment of interim reservoir restrictions and other measures until seismic hazard can be mitigated, and (4) design and implementation of seismic mitigation.

The approach taken was to apply suites of combinations of (1) four different analytical models, (2) three liquefaction triggering relationships, (3) three post-liquefaction residual (S_r) relationships, and (4) various additional analysis protocols to a series of three well-documented seismic performance field case histories.

The three field performance case histories were (1) seismic site response and performance of the Port Island vertical strong motion array in the 1995 Kobe, Japan earthquake, (2) performance of the Lower San Fernando Dam during the 1971 San Fernando earthquake, and (3) performance of the Upper San Fernando dam during the 1971 San Fernando earthquake.

This chapter presents a summary of the lessons and findings that resulted from these studies.

6.2 LESSONS LEARNED FROM BACK-ANALYSES OF THE PORT ISLAND VERTICAL ARRAY DURING THE 1995 KOBE $M_w = 6.9$ EARTHQUAKE

The strong motion recordings obtained at the Port Island Vertical Array site during the 1995 Kobe earthquake represent a unique data set, and they were used as a basis for assessing the ability of the four analytical models employed in these current studies to suitably and adequately perform one-dimensional seismic site response analyses in a situation with (a) strong shaking, (b) widespread occurrence of liquefaction in the upper fill soils, and (3) available strong motion recordings at depths of 83m, 32m, 16m, and at the ground surface. It was considered important to assess this before electing to carry forward each of these models for use in the two-dimensional nonlinear seismic deformation analyses (NDA) of the Upper and Lower San Fernando Dam case histories.

Literature review showed that two of these four models had been used previously for back-analyses of the Port Island case history, and with good results. Accordingly, the Wang2D model, and the UBCSAND model, were carried forward to the two-dimensional NDA analyses of the two dams.

Ziotoupolou et al. (2012) had applied the PM4Sand model to the Port Island case history, and they had concluded that the calculated site response provided a good engineering match with the recorded site performance. It was the judgment of this investigation team that the match between the analysis results and the recorded performance was not very good, but that it might be adequate in a two-dimensional application. As PM4Sand is currently being relatively widely used for two-dimensional nonlinear seismic deformation analyses of dams, it was decided to also carry the PM4Sand model forward to the analyses of the two dams.

Ziotoupolou et al. (2012) had also applied the Roth model to the Port Island case history, and they had found that the model performed very poorly, producing a poor match with the actual ground surface recordings. Investigation of this revealed that they had made two apparent errors in their back-analysis of the Port Island case history with the Roth model. They had failed to rotate the recordings obtained at a depth of 83 meters to correctly align them with the motions of the three sets of overlying recording stations; this was a relatively minor error. The more significant error was the mis-application of the Roth model. The Roth model cycle-counting algorithm for computing cyclic pore pressure increase will generate pore pressure increases up to full elimination of effective stress ($r_u = 100\%$). The correct implementation of this model, and the one employed in these current studies, is to transition “liquefied” elements to post-liquefaction residual strength (S_r) when the pore pressure generation reduces the effective stresses enough that the strength of the soil to $\text{Strength} \leq S_r$.

Ziotoupolou et al. (2012) had not implemented a transition to S_r . Instead, the upper fill soils reached $r_u = 100\%$, reducing effective stress fully to zero, and thus creating materials with zero strength and stiffness. The analytically calculated surface motions “died” at approximately 14.5 seconds into the earthquake as the upper fill soils ceased to behave as soils, and instead behaved as a heavy fluid.

This analysis was repeated as part of these current studies, with implementation of S_r in potentially liquefiable elements when pore pressures increase and reach a condition where $\text{Strength} \leq S_r$. Chapter 3 presents details of these analyses. The results of that new one dimensional site response analysis provided a much better set of results, and justified the carrying forward of the Roth model to the two-dimensional nonlinear seismic deformation analyses of the two dams.

6.3 LESSONS LEARNED FROM BACK-ANALYSES OF THE LOWER SAN FERNANDO DAM DURING THE 1971 SAN FERNANDO Mw=6.61 EARTHQUAKE

6.3.1 Overview

Seismic deformation analyses for LSFD were performed with combinations of four constitutive models for potentially liquefiable soils, three liquefaction triggering relationships, and three post-liquefaction strength relationships.

Chapter 4 presents details of these analyses, and Table 4-1 presents an overview of the combinations of analytical models, triggering relationships, and post-liquefaction S_r relationships employed in each of the six nonlinear seismic deformation analyses performed. The following is a brief summary of key lessons learned.

6.3.2 Lessons Learned

Six nonlinear seismic deformation analyses were performed as back-analyses of the performance of the LSFD in the 1971 San Fernando Dam earthquake. Table 6-1 presents a summary of five selected indices of the relative matches between each of the analytical results vs. the actual observed field behavior. The combinations of analytical models and engineering relationships employed in each of the six analyses are also listed in Table 6-1.

Figures 6-1 through 6-3 present the side by side comparisons of (1) maximum cyclic excess pore pressure ratio, $R_{u, seismic}$ experienced at any time during shaking analyses of six LSFD analyses, (2) shear strains at the end of shaking, and (3) deformed mesh at the end of shaking for all six analyses. Figures 6-4 and 6-5 then present (1) shear strains and (2) deformed meshes at the end of analysis for all six analyses. It is important to continue the analyses past the end of shaking until either (1) deformations cease to develop, and the embankment becomes stable, or (2) deformations have progressed to a point where re-meshing to continue the analysis forward is becoming less effective and the deformations have advanced sufficiently that the engineering interpretations and conclusions are clear.

Four of these NDA analyses were very successful (LSFD Analyses 1, 3, 5, and 6); producing good matches with the observed field behavior, including principal mechanisms of deformation, and details such as the elevation of the “lip” of the heel scarp of the upstream flow failure, which (with allowance for likely transverse cracking) represented the remaining crest, and freeboard, in the immediate aftermath of the earthquake.

One analysis (LSFD Analysis 4) was unsuccessful, and failed to predict the upstream side liquefaction-induced flow failure that actually occurred.

And one analysis (LSFD Analysis 2) was only moderately successful; predicting the upstream side flow failure, but (1) over-estimating lateral deformations and displacements towards the downstream side, and (2) predicting a final elevation of the “lip” of the upstream

Table 6-1: Summary comparisons between analytical results and the observed field behavior for five selected indices during the 1971 San Fernando earthquake

Analysis ID and Key Comparison Items	Analysis	Observed
LSFD Analysis 1: Roth Model – Cetin et al. (2018) liquef. triggering, and Weber et al. (2015) S_r		
1. Occurrence of U/S flow failure	Yes	Yes
2. Correct U/S failure plane/mechanism	Yes	(Yes)
3. Elev. of top of heel scarp feature	1,114.5 ft	1,114 ft
4. Occurrence of D/S flow failure	No	No
5. Maximum D/S face lateral displacement	6.1 ft	~ 0.8 ft
LSFD Analysis 2: UBCSAND model – Youd et al. (2001) liquef. trig., and Seed and Harder (1990) S_r		
1. Occurrence of U/S flow failure	Yes	Yes
2. Correct U/S failure plane/mechanism	Yes	(Yes)
3. Elev. of top of heel scarp feature	1,107.7 ft	1,114 ft
4. Occurrence of D/S flow failure	Yes/No*	No
5. Maximum D/S face lateral displacement	21.6 ft	~ 0.8 ft
*A downstream side slippage initiates, but is slowed when the upstream side flow failure cuts off the upper driving mass of the central crest region and carries it to the upstream side		
LSFD Analysis 3: UBCSAND model – Youd et al. (2001) liquef. trig., and Weber et al. (2015) S_r		
1. Occurrence of U/S flow failure	Yes	Yes
2. Correct U/S failure plane/mechanism	Yes	(Yes)
3. Elev. of top of heel scarp feature	1,114.6 ft	1,114 ft
4. Occurrence of D/S flow failure	No	No
5. Maximum D/S face lateral displacement	9.0 ft	~ 0.8 ft
LSFD Analysis 4: PM4Sand model – Boulanger and Idriss (2014) liq. trig., and Idriss and Boulanger (2015) S_r		
1. Occurrence of U/S flow failure	No	Yes
2. Correct U/S failure plane/mechanism	No	(Yes)
3. Elev. of top of heel scarp feature	N/A	1,114 ft
4. Occurrence of D/S flow failure	No	No
5. Maximum D/S face lateral displacement	2.9 ft	~ 0.8 ft

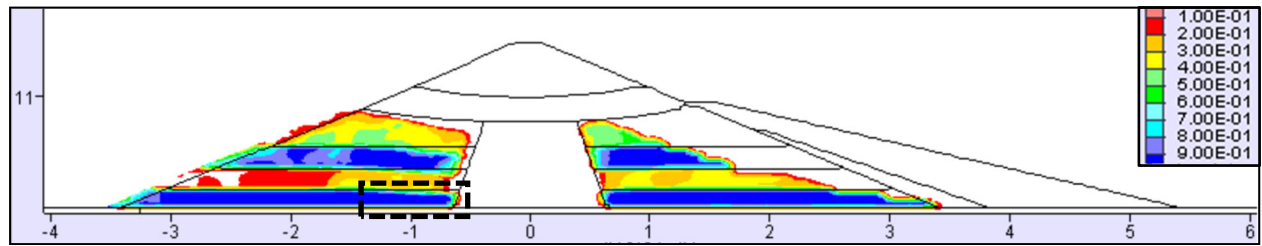
Table 6-1 (Cont'd)

Analysis ID and Key Comparison Items	Analysis	Observed
LSFD Analysis 5: PM4Sand model - Cetin et al. (2018) liquef. trig. and Weber et al. (2015) S _r		
1. Occurrence of U/S flow failure	Yes	Yes
2. Correct U/S failure plane/mechanism	Yes	(Yes)
3. Elev. of top of heel scarp feature	1,114.8 ft	1,114 ft
4. Occurrence of D/S flow failure	No	No
5. Maximum D/S face lateral displacement	10.5 ft	~ 0.8 ft
LSFD Analysis 6: Cetin et al. (2018) liquefaction triggering, and Weber et al. (2015) S _r		
1. Occurrence of U/S flow failure	Yes	Yes
2. Correct U/S failure plane/mechanism	Yes	(Yes)
3. Elev. of top of heel scarp feature	1,116.9 ft	1,114 ft
4. Occurrence of D/S flow failure	No	No
5. Maximum D/S face lateral displacement	6.6 ft	~ 0.8 ft

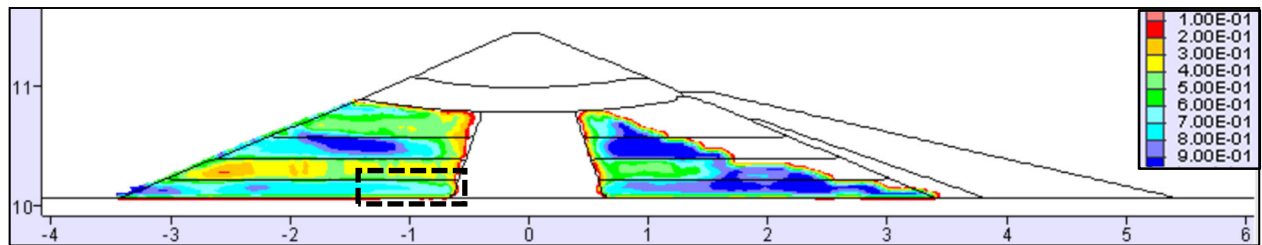
flow slide heel scarp that (with appropriate allowance for expected transverse cracking) defined the useful (or effective) dam crest and freeboard in the immediate aftermath of the earthquake at too low an elevation (1,108 feet as calculated vs. 1,114 feet actually observed).

Lesson 6.1: These are all well-used analytical models and engineering relationships, but some of the analysis combinations produced unsuccessful results, or partially unsuccessful results. This occurred in analyses performed for both the Upper San Fernando dam, as well as for the Lower San Fernando Dam. Engineers must make suitable choices with regard to selection of models and engineering relationships, and they must understand the interactions between these models and relationships.

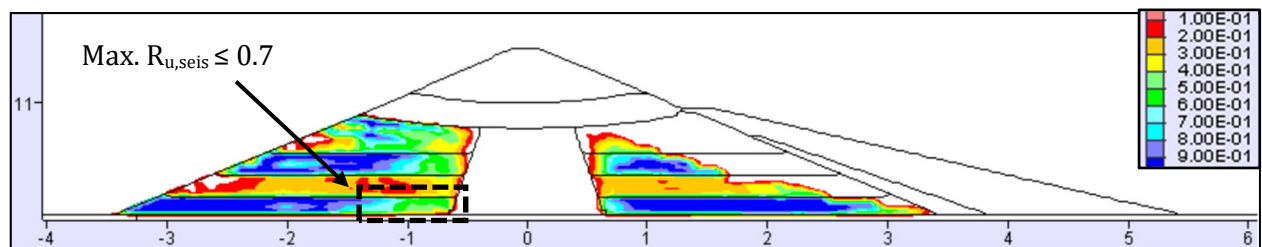
As shown in Figures 6-2(a) through (e), all six analyses predicted the early development of incipient, or potential, shear failure surfaces towards both the upstream and downstream sides of the dam. [Figure 6-2(b) shows the end of shaking results for both Analyses 2 and 3, because they are the same.] These upstream and downstream incipient failure surfaces were relatively symmetrical with each other (with allowances for different details in geometry and stratigraphy). The upstream side feature began at the upstream toe, passed along near the base of the upstream hydraulic fill shell zone, and then arced upwards across the core to exit high on the upper portion of the downstream face of the dam. The downstream side feature was similar, beginning at the downstream toe, passing laterally nearly along the base of the downstream side hydraulic fill shell zone, and then arcing upwards across the core to exit high on the upper portion of the upstream face of the dam.



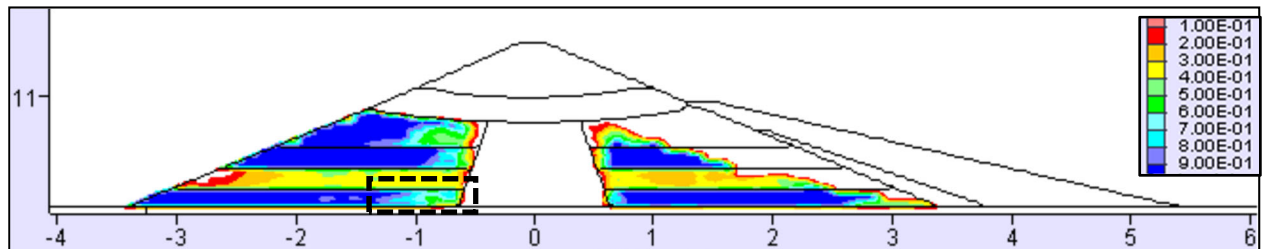
(a) LSD Analysis 1: Roth model, with the Cetin et al. (2018) Triggering Relationship, the Youd et al. (2001) K_σ , and the Weber et al. (2015) S_r Relationship



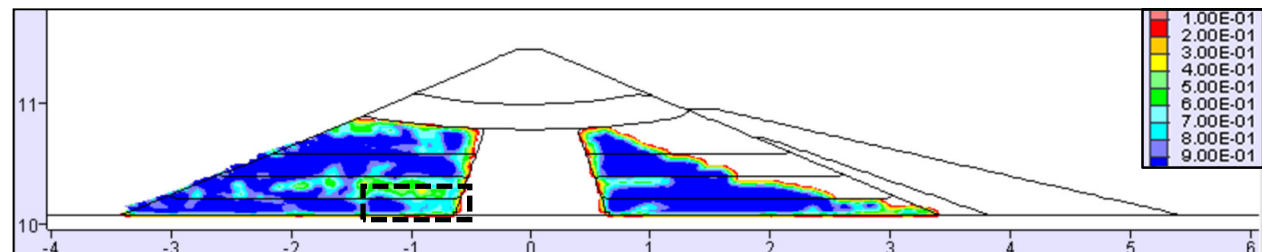
(b) LSD Analyses 2 and 3: UBCSAND model, with the Youd et al. (2001) Liquefaction Triggering and K_σ Relationships, and the Seed and Harder (1990) S_r (Analysis 2) or the Weber et al. (2015) S_r (Analysis 3)



(c) LSD Analysis 4: PM4Sand model, with the Boulanger and Idriss (2014) Liquefaction Triggering Relationship, and the Idriss and Boulanger (2015) S_r Relationship



(d) LSD Analysis 5: PM4SAND model, with the Cetin et al. (2018) Liquef. Triggering Relationship, Youd et al. (2001) K_σ Relationships, and the Weber et al. (2015) S_r Relationship



(e) LSD Analysis 6: Wang2D model, with the Cetin et al. (2018) Liquefaction Triggering Relationship, and the Weber et al. (2015) S_r Relationship

Figure 6-1: Excess Pore Pressure Ratio (Max. $R_{u,seismic}$) recorded at any time during shaking in LSD Analyses 1 through 6

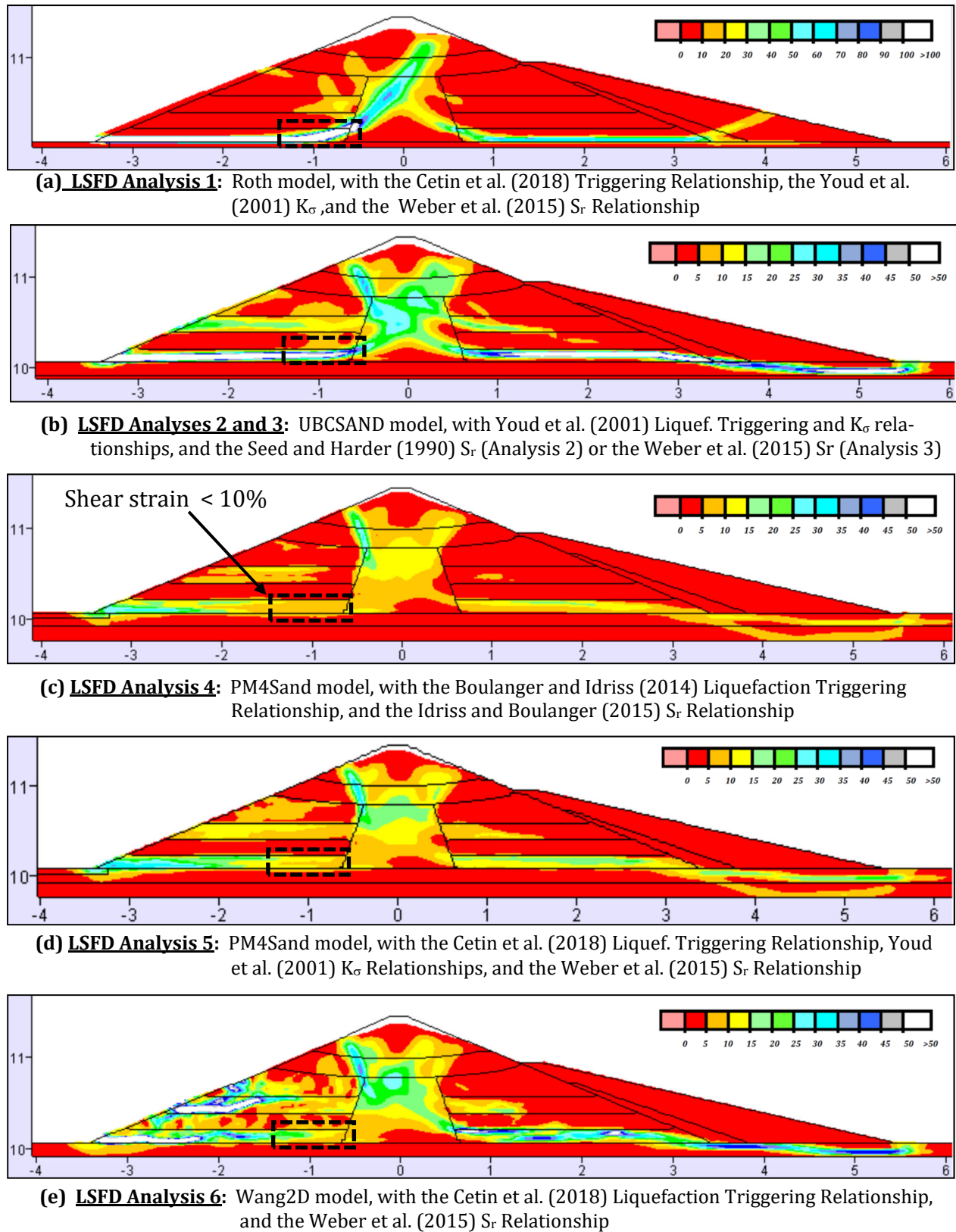
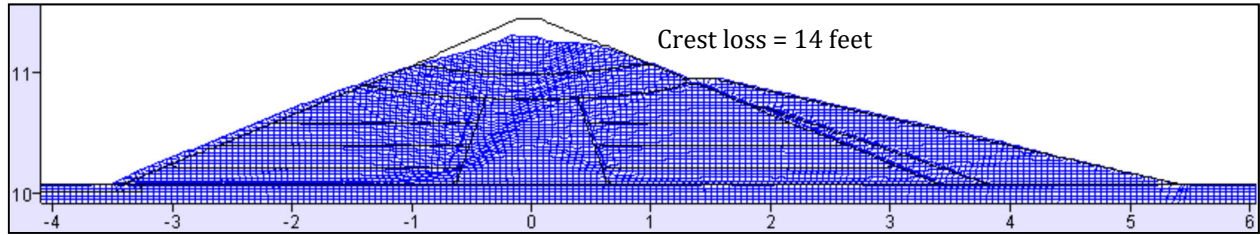
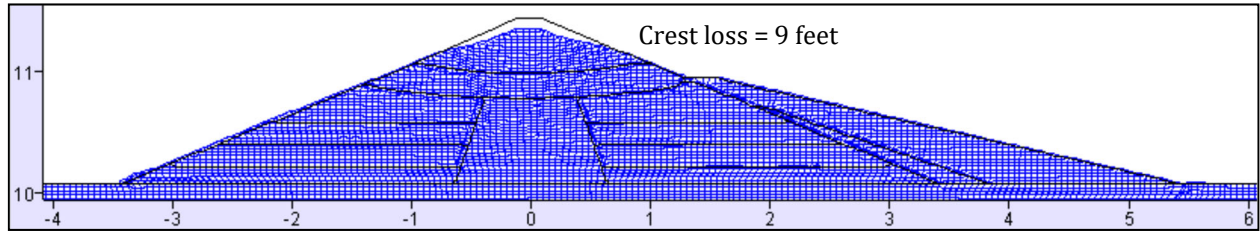


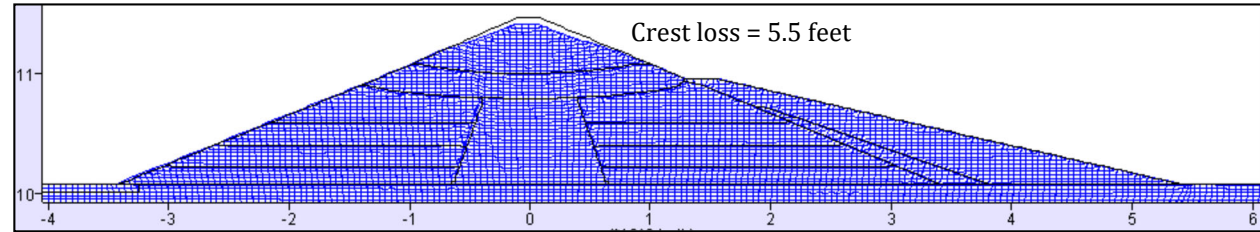
Figure 6-2: Shear strains at the end of shaking (max. scale = 50%, except Analysis 1)



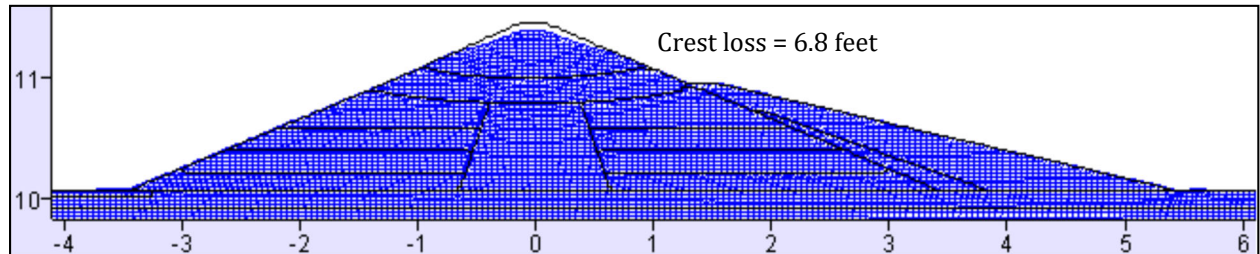
(a) LSF Analysis 1: Roth model, with the Cetin et al. (2018) Triggering Relationship, the Youd et al. (2001) K_σ , and the Weber et al. (2015) S_r Relationship



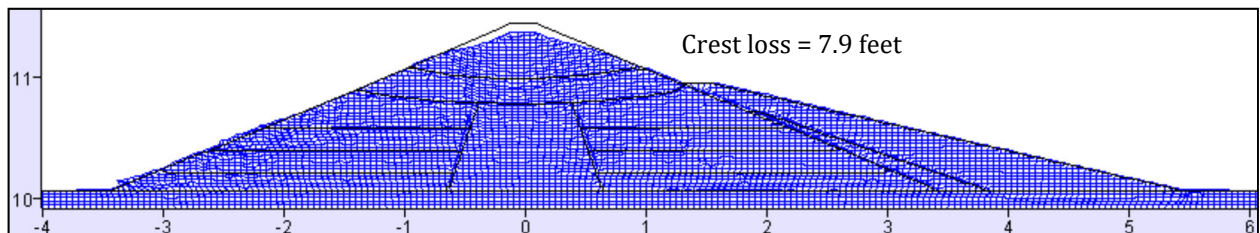
(b) LSF Analyses 2 and 3: UBCSAND model, with Youd et al. (2001) Liquef. Triggering and K_σ relationships, and the Seed and Harder (1990) S_r (Analysis 2) or the Weber et al. (2015) S_r (Analysis 3)



(c) LSF Analysis 4: PM4Sand model, with the Boulanger and Idriss (2014) Liquefaction Triggering Relationship, and the Idriss and Boulanger (2015) S_r Relationship



(d) LSF Analysis 5: PM4Sand model, with the Cetin et al. (2018) Liquef. Triggering Relationship, Youd et al. (2001) K_σ Relationship, and the Weber et al. (2015) S_r Relationship



(e) LSF Analysis 6: Wang2D model, with the Cetin et al. (2018) Liquefaction Triggering Relationship, and the Weber et al. (2015) S_r Relationship

Figure 6-3: Deformed mesh in LSF Analyses 1 through 6 at the end of shaking

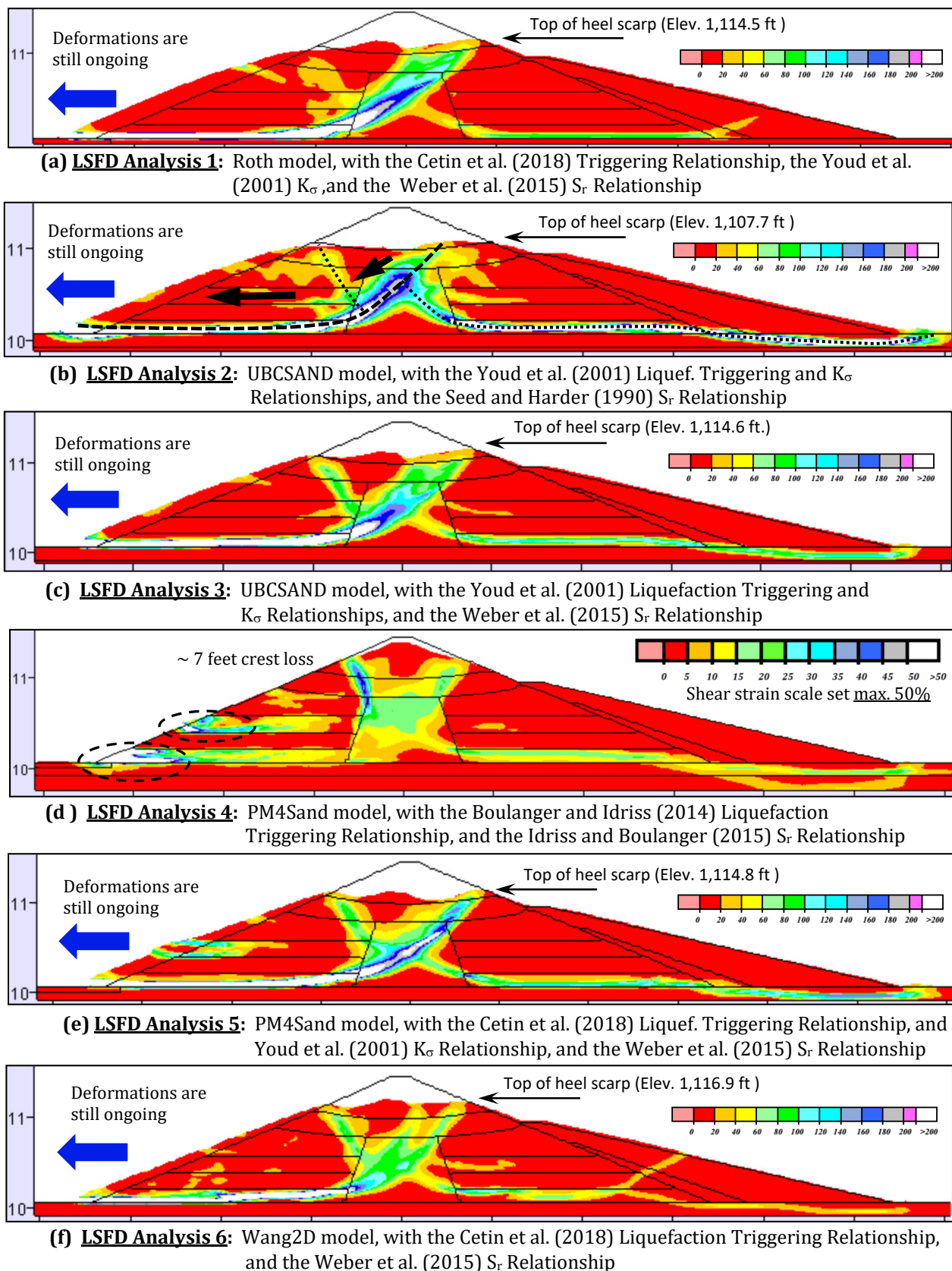


Figure 6-4: Shear strains of LSFD Analyses 1 through 6 at the end of analysis

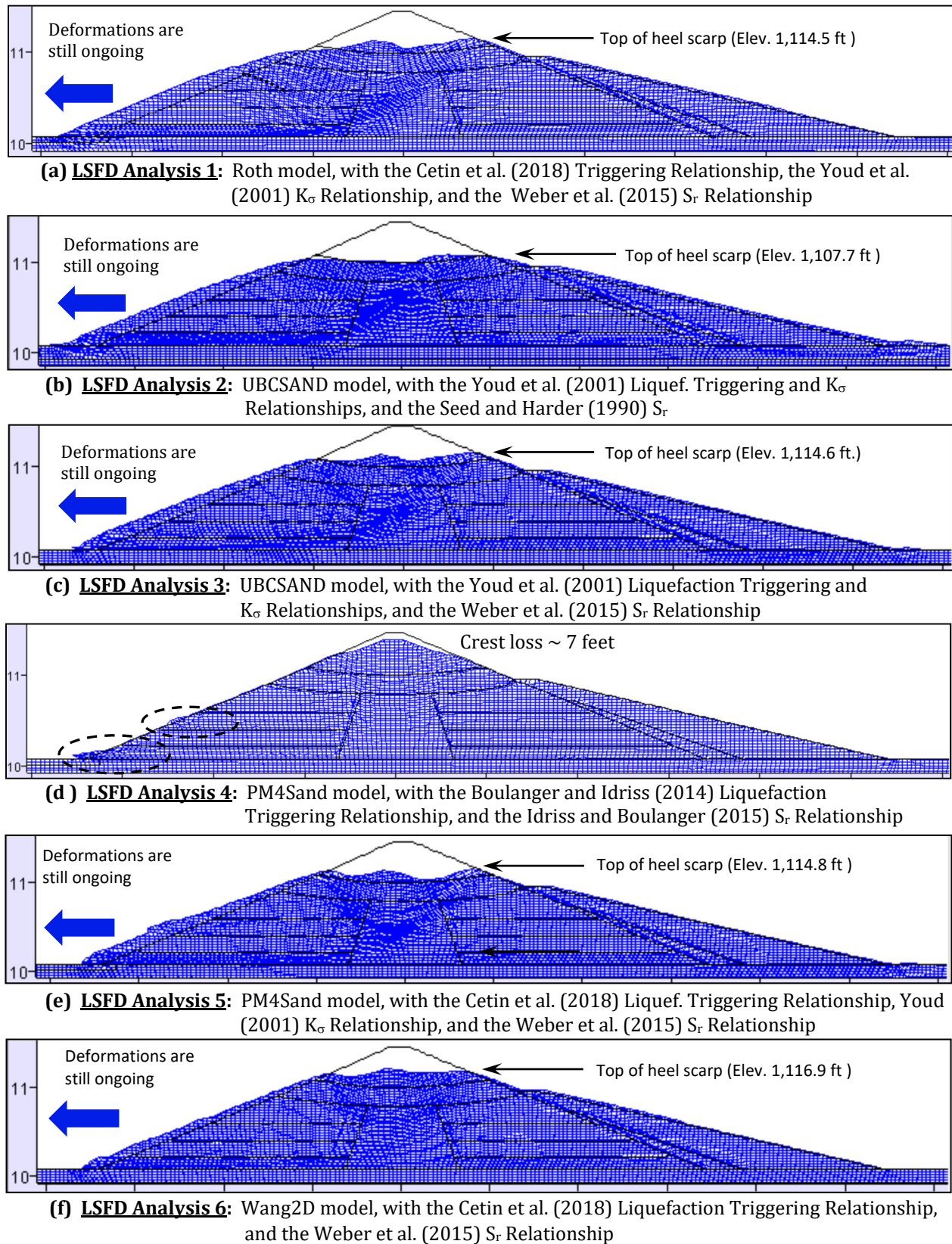


Figure 6-5: Deformed shape of LSFD Analyses 1 through 6 at the end of analysis

In the four successful analyses (LSFD Analyses 1, 3, 5, and 6), the upstream side feature continued to develop, and became an uncontrolled upstream slope stability failure (flow failure), and the downstream side incipient or potential shear stability feature did not develop; the downstream side deformations and displacements remained small, and the downstream side of the embankment was stable at the end of analysis. This matched well with the actual observed behavior.

As shown in the figures, as well as in Table 6-1, the analytical match with observed field performance was also very good in these four analyses with regard to their predictions of the elevation of the “lip” of the upstream slide heel scarp feature that would control effective crest elevation (and freeboard) in the immediate aftermath of the earthquake. All four of these analyses predicted the elevation of the top of this “lip” feature with an accuracy of +/- 1.5 feet or better. That is important, as it was the crest of this “lip” of the slide scarp that controlled (with suitable allowance for transverse cracking) the useful or effective crest height, and freeboard, in the immediate aftermath of the 1971 earthquake.

Lesson 6.2: These types of nonlinear seismic deformation analyses can predict very useful, and even accurate, engineering results.

LSFD Analysis 4 was unsuccessful. This analysis employed the PM4Sand model, calibrated with the Boulanger and Idriss (2014) liquefaction triggering relationship with regard to cyclic pore pressure generation behavior, and it used the Idriss and Boulanger post-liquefaction residual strength (S_r) relationship. Analysis 4 did not predict the occurrence of an upstream flow slide; the upstream side of the embankment remained stable.

The inability to successfully predict the occurrence of the upstream flow failure (which actually occurred in the field) was mainly due to the lack of pore pressure generation in the lowest level of the upstream hydraulic fill “shell” zone at locations adjacent and near to the central clay core; as shown in Figure 6-1(c). The dashed box in this figure indicates a zone in which most of the material fails to meet either of the two criteria for transition to post-liquefaction strength. In these current studies, for all models except the Roth model, potentially liquefiable soil elements transition to post-liquefaction strength (S_r) if they meet either of two criteria: (1) achievement $R_{u, seismic} \geq 0.7$ at any time during shaking, or (2) achievement of shear strain of $\gamma \geq 10\%$. [The Roth model transitions to S_r during shaking, when $Strength \leq S_r$.] As shown in the box in Figure 6-1(c), nearly all of the upstream shell materials within the dashed box had achieved maximum values of $R_{u, seismic}$ of less than 0.7 during shaking. Similarly, as shown by the same dashed box in Figure 6-2(c), nearly all of these soil elements had also failed to achieve shear strains of greater than 10% during shaking. This left a zone of higher strength soils adjacent at the upstream base of the core to “buttress” the core and prevent the full development of the upstream flow failure that had been actually observed in the field.

As discussed in Chapter 2, Section 2.3, this liquefaction triggering relationship is the least conservative of the three triggering relationships used in these current studies; it has three known errors in its derivation that produce unconservative bias, and it also employs

the least conservative K_σ relationship, further adding to the likely unconservative bias for soils at depth (e.g. at the base of the upstream shell, near the core).

Analysis 5 exactly repeats Analysis 4, but this time employing the liquefaction triggering relationship of Cetin et al. (2018), along with the K_σ relationship of Youd et al. (2001) which is the relationship recommended for use with Cetin et al. This produced higher cyclically-induced pore pressures in the zone adjacent to the upstream side of the clay core, at the base of the hydraulic fill, as indicated by the dashed box in Figure 6-1(d). More than 75% of the soils in this dashed box achieved $R_{u, seismic} \geq 0.7$ at some point during shaking, and there is a “path” laterally across this dashed box along which nearly all of the materials have met this criterion. Similarly, the soils within the dashed box in Figure 6-2(d) have nearly all met the second criterion of shear strain greater than 10%. That can be difficult to see at 100% scale, but readers accessing this dissertation on a screen can enlarge the view and see that a majority of the materials in this dashed box are the darker “mustard” color of yellow (indicating shear strains of greater than 10%), rather than the lighter yellow color (as with most of the materials in the dashed box of Figure 6-2(c)) indicating shear strains of between 5% to 10%. The higher cyclically induced pore pressures due to the switch to the triggering relationship thus caused nearly all of the soils in this dashed box to transition to post-liquefaction S_r (and by both of the two criteria in most cases).

This eliminated the buttressing effect of Analysis 4, and Analysis 5 successfully predicted the upstream side flow failure. This demonstrated that the PM4Sand model can successfully predict this failure, but not with the Idriss and Boulanger (2015) liquefaction triggering relationship.

Lesson 6.3: These types of nonlinear seismic deformation analyses can also produce very poor results if not suitably calibrated, and if the analytical models, and the engineering relationships (including the triggering relationship, and the post-liquefaction residual strength S_r relationship) are not suitable for the problem being analyzed.

The analysis that was only largely successful was LSFD Analysis 2. This analysis successfully predicted the upstream flow failure, but it also predicted the inception and partial development of a second, downstream side slope instability feature (which was not observed in the 1971 earthquake). This was due to the use of the Seed and Harder (1990) S_r relationship, which predicts S_r as a function of only $N_{1,60,CS}$ (rather than as a function of both $N_{1,60,CS}$ and also initial vertical effective stress, $\sigma'_{v,i}$). Due to the failure to also account for $\sigma'_{v,i}$, this relationship tends to under-predict S_r at high initial effective overburden stresses (e.g. at the base of the downstream hydraulic fill shell zone, especially near the core), and the result was the inception of a downstream side instability feature in addition to the upstream side stability that was also initiated.

As shown in Figures 6-4 (b) and 6-5 (b), the upstream slide progressed more rapidly, and it eventually “cut the top” off of the downstream slide feature by transporting the dam’s upper crest section laterally upstream towards the reservoir. The dashed lines added to Figure 6-4(b) indicated the shear surfaces of both the upstream and downstream slide features. The removal of the driving mass of the top crest section from the upper heel of the

downstream slide feature eventually limited the downstream side movements, and the downstream side became stable. The partial development of the downstream slippage feature did, however, produce settlements of the “lip” of the upstream slide feature, which is located in what had also been the heel area of the downstream slide feature, and as a result this is the analysis that shows the lowest predicted final elevation of this important lip feature (Elev. 1107.7 ft. vs. Elev. 1,114 ft. observed), as shown in Figures 6-4(b) and 6-(c). The partial development of a downstream slide feature in LSFD Analysis 2 also resulted in the prediction of larger lateral displacements at the downstream slope (~21.6 feet) than were observed (~1 foot) in the field after the earthquake.

As a test of this hypothesis that the S_r relationship of Seed and Harder (1990) was principally responsible for the poor results of LSFD Analysis 2, Analysis 3 exactly reproduced Analysis 2, but this time employed the S_r relationship of Weber et al. (2015) which predicts S_r as a function of both $N_{1,60,CS}$ and also initial vertical effective stress, $\sigma'_{v,i}$. This analysis was fully successful, and provided a good match with observed field performance with regard to both mechanisms and magnitudes of deformations and displacements.

Lesson 6.4: The lesson here is that the post-liquefaction residual strength relationship employed can be of essentially co-equal importance with (1) the analytical model used, and (2) the liquefaction triggering relationship used. All three must be suitable in order to reliably achieve good result.

Lesson 6.5: Current constitutive models, including critical state models, cannot predict post-liquefaction strengths (S_r) because they cannot account for localized changes in void ratio (sometimes even involving creation of water blisters at the tops of confined sub-strata in layered systems). At present, the best predictive relationships for evaluation of likely post-liquefaction strengths are those based on back-analyses of field liquefaction failure case histories. Some of the nonlinear seismic deformations of both the Lower San Fernando Dam, and the Upper San Fernando Dam, were unsuccessful primarily due to short-comings in the S_r relationships employed. It appears preferable to employ S_r relationships that predict S_r as a function of both $N_{1,60,CS}$ and $\sigma'_{v,i}$.

Lesson 6.6: A suitable algorithm must be employed to transition any given soil element to S_r . In these current studies, for analyses performed with the UBCSAND, PM4Sand and Wang2D models, post-liquefaction residual strengths are assigned to potentially liquefiable soils that satisfy either of two criteria: (1) occurrence of $R_{u,seis} \geq 0.7$ at any stage during shaking ($R_{u,seis,max} \geq 0.7$) or (2) development of a peak shear strain of $\gamma \geq 10\%$ at the end of shaking in saturated materials. In the Roth model, elements transition to post-liquefaction strengths during shaking if and when their shear strength drops to $Strength \leq S_r$.

LSFD Analysis 6 is used here as an example to summarize the mechanisms observed in the four successful LSFD Analyses (1, 3, 5, and 6), but any of the other three successful analyses listed here would serve similarly well as an example to describe the procedures and observations regarding the main failure mechanism of the LSFD, the mechanisms observed, and comparisons between the analytical results and the observed field performance.

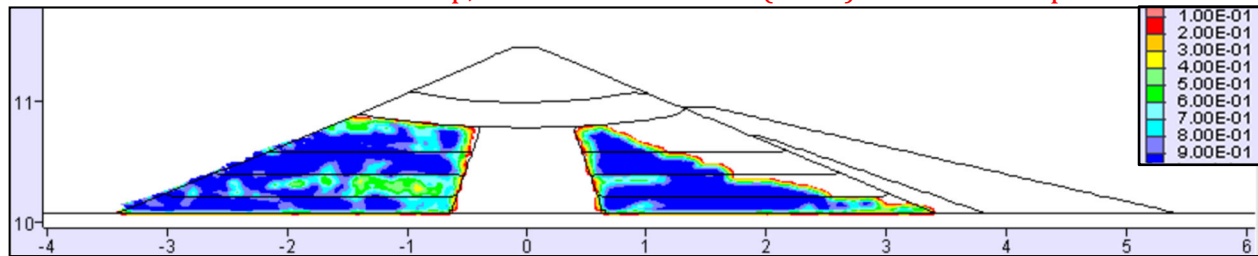
In LSFD Analysis 6, the Wang2D model is used in potentially liquefiable soils (which are the saturated semi-hydraulic fill shell zones). Non-liquefiable soils (the central clayey core, the upper rolled fill, and the upper and lower alluvium) were modeled using the FLAC Mohr-Coulomb model. The non-liquefiable layers were modeled with Mohr-Coulomb parameters. Shear strength of the puddled central clay core was modeled as $S_u/\sigma'_{vi} = 0.192$ during shaking in LSFD Analysis 6, which assumes approximately a 20% reduction of undrained shear strength (from peak static, or monotonic, shear strength of $S_u/\sigma'_{vi} = 0.24$) for the normally consolidated clayey core to account for both (a) cyclic softening and (b) strain softening.

Figure 6-6 presents the results of nonlinear seismic deformation analyses performed with the combinations of models and relationships of LSFD Analysis 6 [with the Wang2D model, the Cetin et al. (2018) liquefaction triggering relationship, and the Weber et al. (2015) S_r relationship] at the end of shaking analysis. As shown on Figure 6-6(a): LSFD Analysis 6 generated significant excess cyclic pore pressure ratios, $R_{u,seis}$ (shown as the maximum cyclic pore pressure ratio experienced at any time during earthquake analysis). High cyclic pore pressures developed in the lowest zones of both the upstream and downstream hydraulic fill shell materials (HFU-4 and HFD-4). Figure 6-6(b) shows contours of shear strain at the end of shaking. These usefully show that two deep-seated incipient potential failure surfaces had developed by the end of shaking; one towards upstream side, and the other towards the downstream side, but neither had yet progressed to produce very large displacements. It would not be possible in a forward analysis to reliably ascertain at this stage whether or not each of these two features (or even both of them) would progress and develop into full failures.

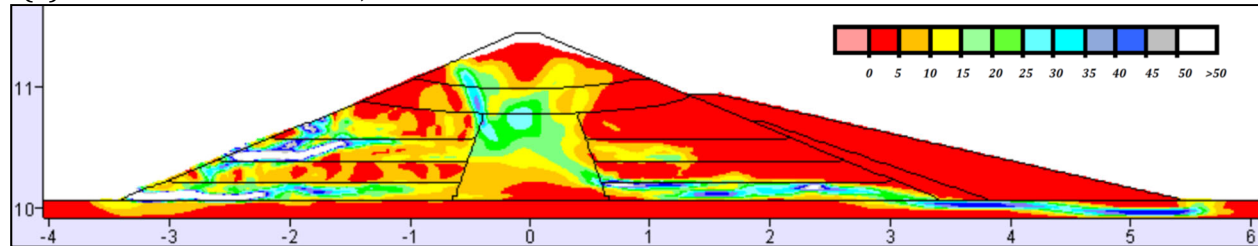
Many nonlinear deformation analyses stop at the end of shaking stage. As shown in Figures 6-6(a) through (c), to stop at that point would be to completely miss the ensuing upstream catastrophic full flow slide failure that actually occurred during the 1971 earthquake. At the end of earthquake shaking, the analytical results show only moderate deformations, with a vertical crest loss of 7.9 feet (Figure 6-6(c)). Shear strains are significant, but do not necessarily indicate that a full slope instability failure is underway. Conventional static stability analyses, if performed with end of shaking pore pressures, would suggest that the slopes are likely stable. It is relatively common practice to halt at this juncture, and take the end of earthquake deformed shape (and stability analysis) as final. To do so, would be to miss the ensuing upstream flow failure.

In these current studies, the protocol is that after the end of shaking elements are transitioned to post-liquefaction residual strengths (S_r) if they meet either of two criteria. After the end of shaking, S_r is applied within potentially liquefiable soil elements that satisfy

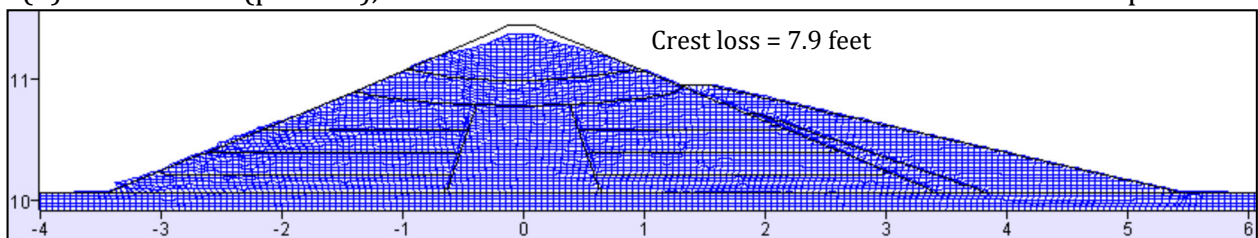
LSFD Analysis 6: Wang2D model, with the Cetin et al. (2018) Liquefaction Triggering Relationship, and the Weber et al. (2015) S_r Relationship



(a) Maximum value of $R_{u, \text{seismic}}$ recorded in each element

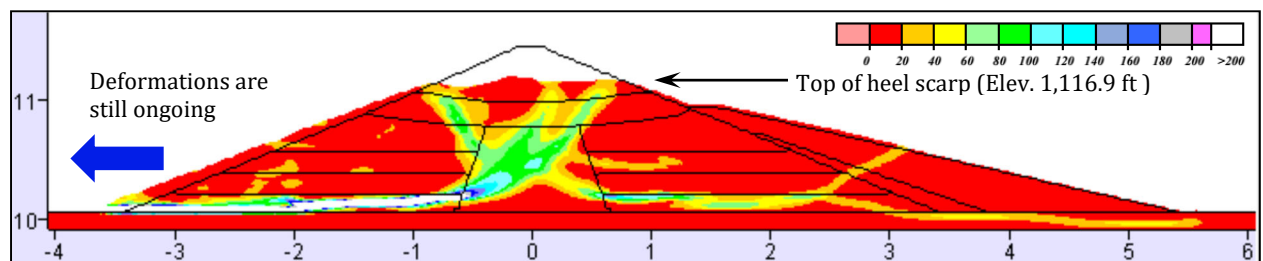


(b) Shear strain (percent), with the inset shear strain scale set to maximum of 50 percent

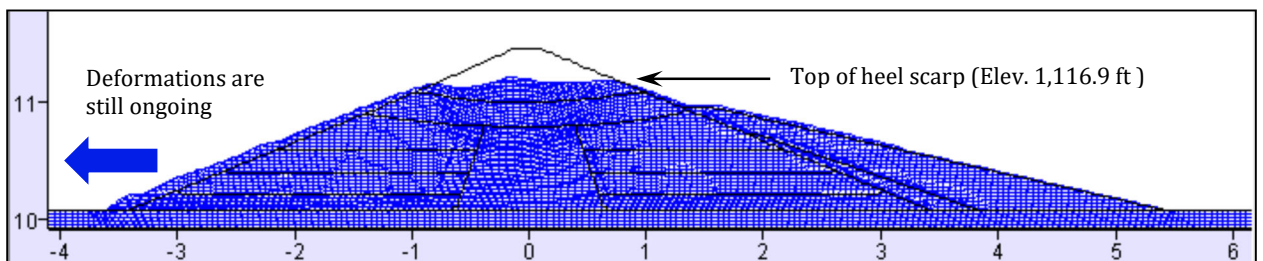


(c) Deformed mesh

Figure 6-6: Results of LSFD Analysis 6 at the end of shaking



(a) Shear strain (percent), with the inset shear strain scale set to maximum of 200 percent



(b) Deformed mesh

Figure 6-7: Results of LSFD Analysis 6 at the end of analysis

either of two criteria: (1) occurrence of $R_{u,seis} \geq 0.7$ at any stage during shaking ($R_{u,seis,max} \geq 0.7$) or (2) development of a peak shear strain of $\gamma \geq 10\%$ at the end of shaking in saturated elements. The protocol is then to continue the nonlinear deformation analysis after the end of shaking until either (1) deformations and displacements have ceased to occur, as the embankment is in a stable condition, or (2) mesh distortions are resulting in a need to perform significant (and time-consuming) re-meshing to continue the nonlinear deformation analysis, and the results at termination have become sufficient for purposes of engineering interpretation and decision-making, with recognition that deformations and displacements are still ongoing.

Also, at the end of shaking, shear strains across the core zone were examined, and in those analyses where the development of very large shear strains and deformations across the core zone warranted, the shear strength of the central core zone was then further reduced to a value intermediate between (1) the already 20% reduced value of $S_u/\sigma'_{v,i} = 0.192$ used during shaking to account for both cyclic softening and some strain softening, and (2) the fully residual strength of $S_{u,residual}/\sigma'_{v,i} = 0.08$. The intermediate reduced clay strength was therefore $S_u/\sigma'_{v,i} = (0.5) (0.192 + 0.08) = 0.136$. If shear strains in clay core continued to develop and become very large, the analysis was again halted, and clay strengths were further reduced to a fully residual value of $S_{u,residual}/\sigma'_{v,i} \approx 0.08$, and the analysis was again continued forward in time beyond the end of shaking unless and until either (1) deformations and displacements have ceased to occur, as the embankment is in a stable condition, or (2) mesh distortions are resulting in a need to perform significant (and time-consuming) re-meshing to continue the NDA deformation analysis, and the results at termination have become sufficient for purposes of engineering interpretation and decision-making, with recognition that deformations and displacements are still ongoing.

In LSFD Analysis 6 (also in LSFD Analyses 1, 3, 5), with (1) the transition to S_r in liquefied elements, and (2) the transition to $S_u/\sigma'_{v,i} = 0.136$ in the clayey central core materials, the embankment continued to deform and shear strains (and the shear displacement offsets across the narrowly banded shearing zones) in the clay core continued to increase. These eventually warranted further reduction to fully residual strengths of $S_{u,residual}/\sigma'_{v,i} \approx 0.08$. The analysis was again halted, and fully residual strength of $S_{u,residual}/\sigma'_{v,i} = 0.08$ was applied in the central clay core, and then the analysis was again re-started. The upstream side potential (or incipient) failure surface continued to develop, and an upstream flow failure occurred.

Figures 6-7(a) and (b) show conditions at the end of analysis. The analysis was terminated at this juncture because re-meshing was becoming less effective, and the engineering interpretation was already clear. The blue arrows in Figure 6-7 again indicate that deformations and displacements were still ongoing when the analysis was terminated.

LSFD Analysis 6 correctly predicts the apparent mechanisms of distress and upstream failure, in good agreement with Analyses 1, 3, and 5, and in good agreement with observed field performance during the 1971 San Fernando earthquake. As shown in Figure

6-6(b), two incipient (potential) failure surfaces begin to form; one towards the upstream side, and one towards the downstream side.

As shown in Figures 6-7(a) and (b), the upstream side stability failure continues to develop, and becomes an uncontrolled upstream flow failure. This upstream side failure begins at the base of the upstream toe, traverses laterally across the base of the upstream hydraulic fill shell zone, then arcs upwards across the puddled central clay core to exit high on the upper portion of the downstream face.

The location and elevation of the “lip” of the upstream slide heel scarp feature is again very well predicted; it occurs at an elevation of 1,116.9 feet (vs. 1,114 feet actually observed in the field in the immediate aftermath of the 1971 earthquake). This “lip”, with appropriate considerations for likely transverse cracking, controlled the effective (useful) crest elevation and freeboard immediately after the earthquake.

Lesson 6.7: It can be potentially dangerously unconservative to halt a nonlinear seismic deformation analysis at the end of shaking. Implementation of post-liquefaction residual strengths S_r (as warranted), and implementation of potential reductions in the strengths of strain sensitive cohesive soils, and continuation of the analysis after the end of shaking until an engineering result has been achieved can be important.

Lesson 6.8: Engineers engaged in analyses of challenging situations involving potentially liquefiable soils must also remember to devote similar attention to non-liquefiable soils (e.g. potentially strain sensitive cohesive soils, etc.).

Most of the LSFD analyses (Analysis 1, 2, 3, 5, and 6) accurately predicted the inception of large deformations or “flow failure” conditions of the upstream slope. However, a close comparison of a deformed mesh from end of analysis (e.g. LSFD Analysis 1) and the reconstructed geometry of the failure masses as determined in the field by Seed et al. (1973), as shown in Figure 6-8, serves to illustrate both strengths and potential weakness of continuum analyses; including both finite element analyses as well as finite difference analyses (e.g. FLAC).

The actual upstream failure mass of the Lower San Fernando Dam flow slide, as documented by Seed et al. (1973) included a number of massive, blocky pieces of the embankment that disaggregated (separated) due to tensile and/or shear cracking, and then were borne upstream into the reservoir atop the underlying liquefied materials. The upstream toe of the flow failure travelled approximately 140 feet back into the reservoir. Four of the nonlinear seismic deformation analyses correctly showed the inception of this upstream flow failure, but none of them could usefully predict the final resting geometry due to an inability to model bifurcation (localized shear or tensile offsets rather than shear or tensile strains.) This is the essence of what constitutes a “continuum” analysis.

Analytical developments are underway to transcend this limitation of continuum analyses, but for now these are research efforts and not yet fully reliable engineering tools.

There are two additional mechanisms that are not yet tractable to reliable engineering analyses that also likely occurred during the flow slide of the upstream face of the Lower San Fernando dam. These are hydroplaning, as the increasingly rapidly moving toe of the slide mass entered the reservoir and likely rode over and entrapped reservoir water beneath it, and plowing as the toe of the failure plowed over and through very soft and weak reservoir sediments. Neither hydroplaning, nor plowing, are generally addressed in most current seismic dam engineering practice; though they are sometimes addressed in the field of coastal and offshore engineering. It is not necessary to deal explicitly with these two issues in this current case; it is enough to recognize that they can further exacerbate expected deformations and displacements.

These limitations are not necessarily a major problem, however. Instead it is the view of the analysis team that the continuum-based nonlinear seismic deformation analyses performed were well able to provide the information and results needed for engineering evaluation of existing risk exposure, and for design of engineered mitigation. That does, however, require that engineers understand the intrinsic limitations of these type of analyses (including inability to bifurcate, numerical mesh lock) which can incorrectly limit otherwise ongoing deformations, and limitations in the ability to maintain useful analytical accuracy when performing re-meshing to continue analyses forward in the face of very large mesh deformations and resulting mesh lock.

All four of the successful analyses of the Lower San Fernando Dam succeeded in showing that an upstream side flow failure had initiated and was underway. It next requires engineering judgment, and an understanding of the limitations of current continuum analysis capabilities in common practice, to interpret these results and see that the failure will propagate and move considerably further back into the reservoir. Also that the final movements are likely to become very large, and cannot be predicted with good accuracy. That level of information, and the determination of the likely elevation of the lip of the upstream slide scarp that will (with suitable allowance for likely transvers cracking) control both effective reservoir crest height and freeboard in the immediate aftermath of a major earthquake, are excellent engineering findings. And they well suffice, if interpreted with suitable engineering judgment.

Lesson 6.9: Engineers must understand the current intrinsic limitations of these types of nonlinear seismic deformation analyses, and they must interpret these types of analytical results with good engineering judgment. These can be valuable analytical and engineering tools if that is done.

In Figure 6-8, the final deformed mesh from LSFD Analysis 1 (shown here as another example of the four analyses that correctly predicted large deformations) shows large deformations initiated by a deep basal shear surface propagating through the lower-most hydraulic fill layer, HFU-4, and diagonally crossing the soft clay core and reaching the heel scarp almost at the identical location as was actually observed in the immediate aftermath of the earthquake. The shape and location of the deep basal shear surface, as well as the elevation of the top lip of the remaining heel scarp that (with allowances for likely transverse cracking) controlled the remaining effective crest height (and freeboard) in the

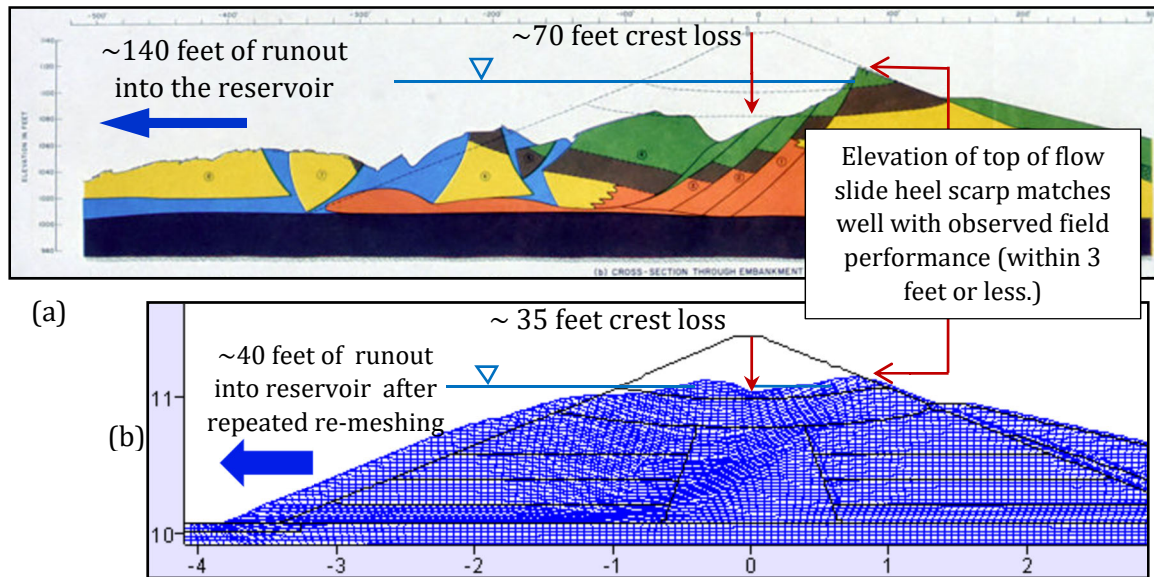


Figure 6-8: Comparison between (a) the observed deformed geometry of the Lower San Fernando Dam after the 1971 San Fernando earthquake (Seed et al., 1973) vs. (b) the final deformed shape from the current FLAC analyses (LSFD Analysis 1).

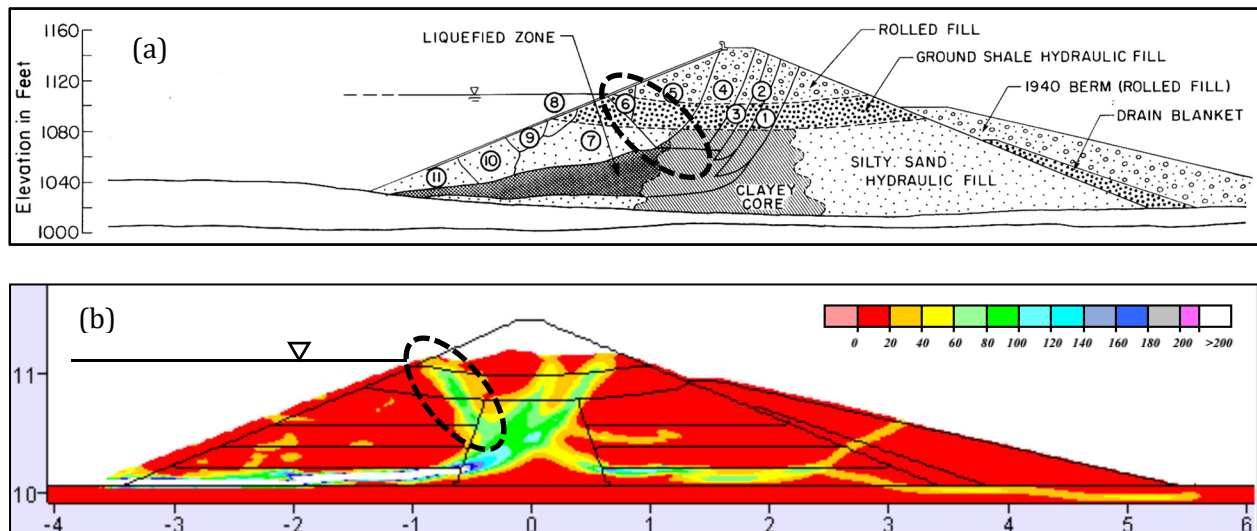


Figure 6-9: Comparison between (a) the location of a downslope transverse crack from the re-constructed geometry of the failure mass (Castro et al, 1992, based on Seed et al, 1973) vs. (b) the shear strains and strain concentrations at the end of analysis (LSFD Analysis 6) showing downslope transverse crack.

immediate aftermath of the 1971 earthquake, were both very accurately predicted by the FLAC models in LSFD Analyses 1, 2 to 3, 5, and 6.

These four analyses also revealed some interesting details regarding the internal geometry of the evolving failure mechanics. As shown in Figure 6-9, the nonlinear seismic deformation analyses showed the development of an incipient or partially developed downstream slide feature, with a rear scarp located as shown by the dashed oval of Figure 6-9(b). This corresponds well with the location of a similar feature observed in the post-earthquake investigations, as shown in Figure 6-9(a). It appears that the partially developed heel scarp of the incipient downstream slide feature represented a demarcation between the upper portion of the controlling downstream flow failure above which the blocky disaggregation of the slide mass had a very different character, and the geometry of Slide Block #5 in Figure 6-9(b) may have been partially controlled by this incipient slide scarp.

Lesson 6.10: One of the pleasant surprises in these current studies was the level of detailed insight that can be provided by these types of nonlinear seismic deformation analyses; in this case revealing a mechanism detail that had not previously been noted.

Lesson 6.11: That success cannot be allowed, however, to seduce engineers and analysts into excessive belief in these types of analyses; there is still the need to recognize that the analyses cannot model the full runout, and that the results of these types of analyses must be evaluated with an understanding of both the strengths and the weaknesses of this analytical approach, and they must be interpreted with suitable engineering judgment.

6.4 LESSONS LEARNED FROM BACK-ANALYSES OF THE UPPER SAN FERNANDO DAM DURING THE 1971 SAN FERNANDO EARTHQUAKE

6.4.1 Overview and Lessons Learned

Seismic deformation analyses for the USFD were performed with combinations of four constitutive models for potentially liquefiable soils, three liquefaction triggering relationships, and three post-liquefaction strength relationships.

Chapter 5 presents details of these analyses. Table 5-30 presented an overview of the nine analysis combinations used; detailing (1) the analytical model, (2) the triggering relationship, and (3) the post-liquefaction residual strength (S_r) relationship employed in each of the nine analyses.

As shown in Figure 6-10, a potential deep-seated basal shear surface can be inferred from the upstream face damage and offset near the crest, passing diagonally across the main dam embankment, and then forming a basal shear surface that extends laterally to exit at the downstream toe. The upstream face damage would then represent the top of a heel scarp, and the scarp would delineate the back heel of a massive lateral translational movement of

Table 6-2: Summary comparison between selected analytical results and observed field performance of the USFD

Analysis ID No. and Model	Liquefaction Triggering Relationship	Post-Liquefaction Residual Strength (S_r) Relationship	Maximum crest loss	Maximum crest lateral translation to D/S	Maximum lateral translation of the D/S slope face	Maximum lateral translation of the D/S toe
Observed Performance	-	-	2.5 to 3.0 feet	4.9 to 6.0 feet	7.2 to 8.7 feet	3.6 to 5.3 feet
1 Roth	Youd et al. (2001)	Seed and Harder (1990)	7.0 to 7.7 feet	3.4 feet	11.7 feet	7.3 feet
2 Roth	Boulanger and Idriss (2014)	Idriss & Boulanger (2015)	> 13.0 feet (and ongoing)	> 4.7 feet (and ongoing)	> 45.0 feet (and ongoing)	> 36.0 feet (and ongoing)
3 Roth	Cetin et al. (2018)	Weber et al. (2015)	6.3 to 7.3 feet	1.1 feet	9.7 feet	6.0 feet
4 UBCSAND	Youd et al. (2001)	Seed and Harder (1990)	6.4 to 7.2 feet	3.3 feet	10.1 feet	4.1 feet
5 UBCSAND	Youd et al. (2001)	Idriss & Boulanger (2015)	> 14.0 feet (and ongoing)	> 8.2 feet (and ongoing)	> 70.0 feet (and ongoing)	> 50.0 feet (and ongoing)
6 UBCSAND	Youd et al. (2001)	Weber et al. (2015)	5.1 to 5.6 feet	1.7 feet	7.3 feet	3.6 feet
7 PM4SAND	Boulanger and Idriss (2014)	Idriss & Boulanger (2015)	1.3 to 1.4 feet (and ongoing)	1.2 feet (and ongoing)	> 46.0 feet (and ongoing)	> 28.0 feet (and ongoing)
8 PM4SAND	Cetin et al. (2018)	Weber et al. (2015)	1.7 to 1.8 feet	1.0 feet	7.2 feet	3.3 feet
9 WANG2D	Cetin et al. (2018)	Weber et al. (2015)	1.9 to 2.0 feet	1.0 feet	6.3 feet	3.4 feet

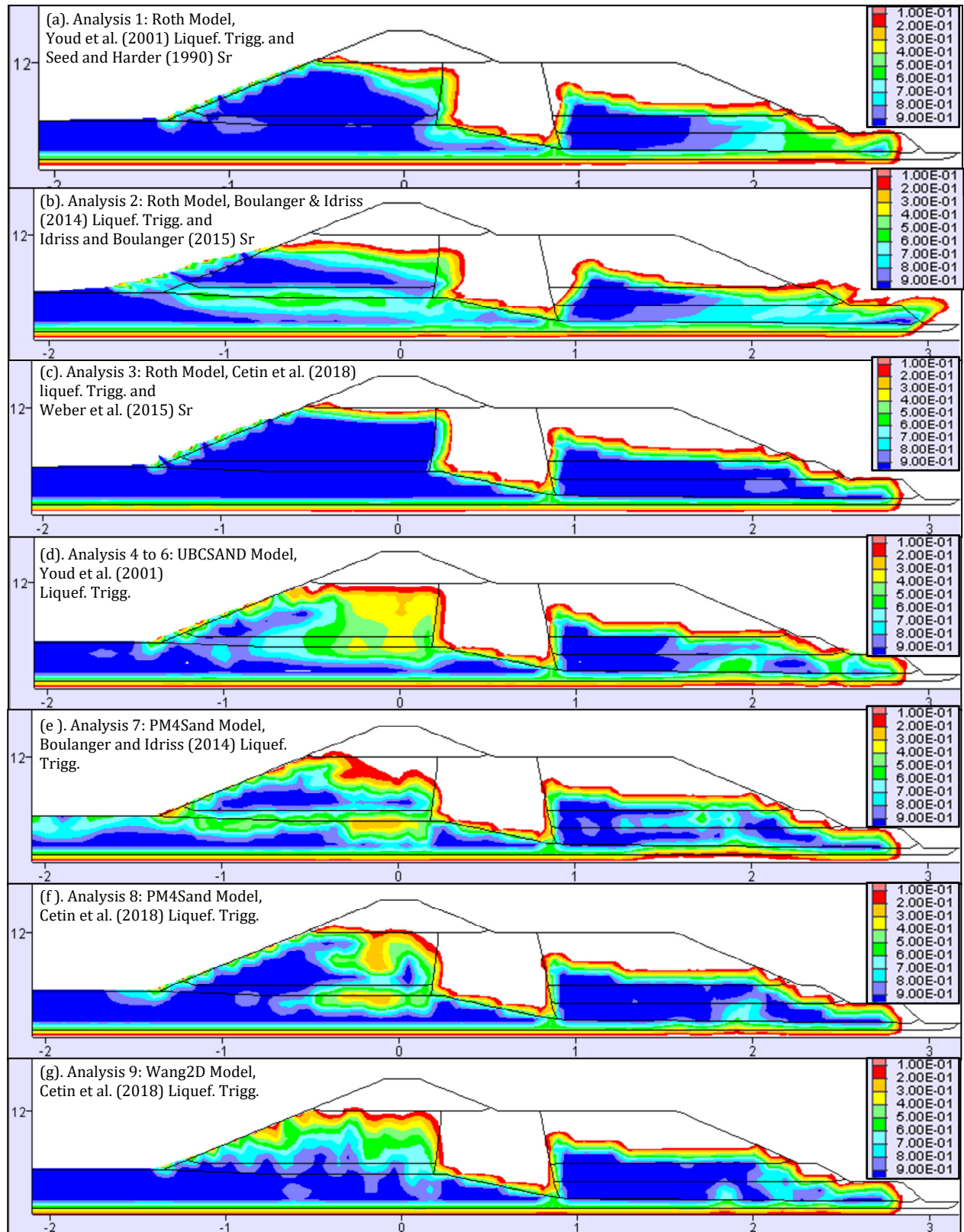


Figure 6-11: Excess Pore Pressure Ratio (Max. $R_{u, seismic}$) recorded anytime during shaking in USFD Analyses 1 to 9

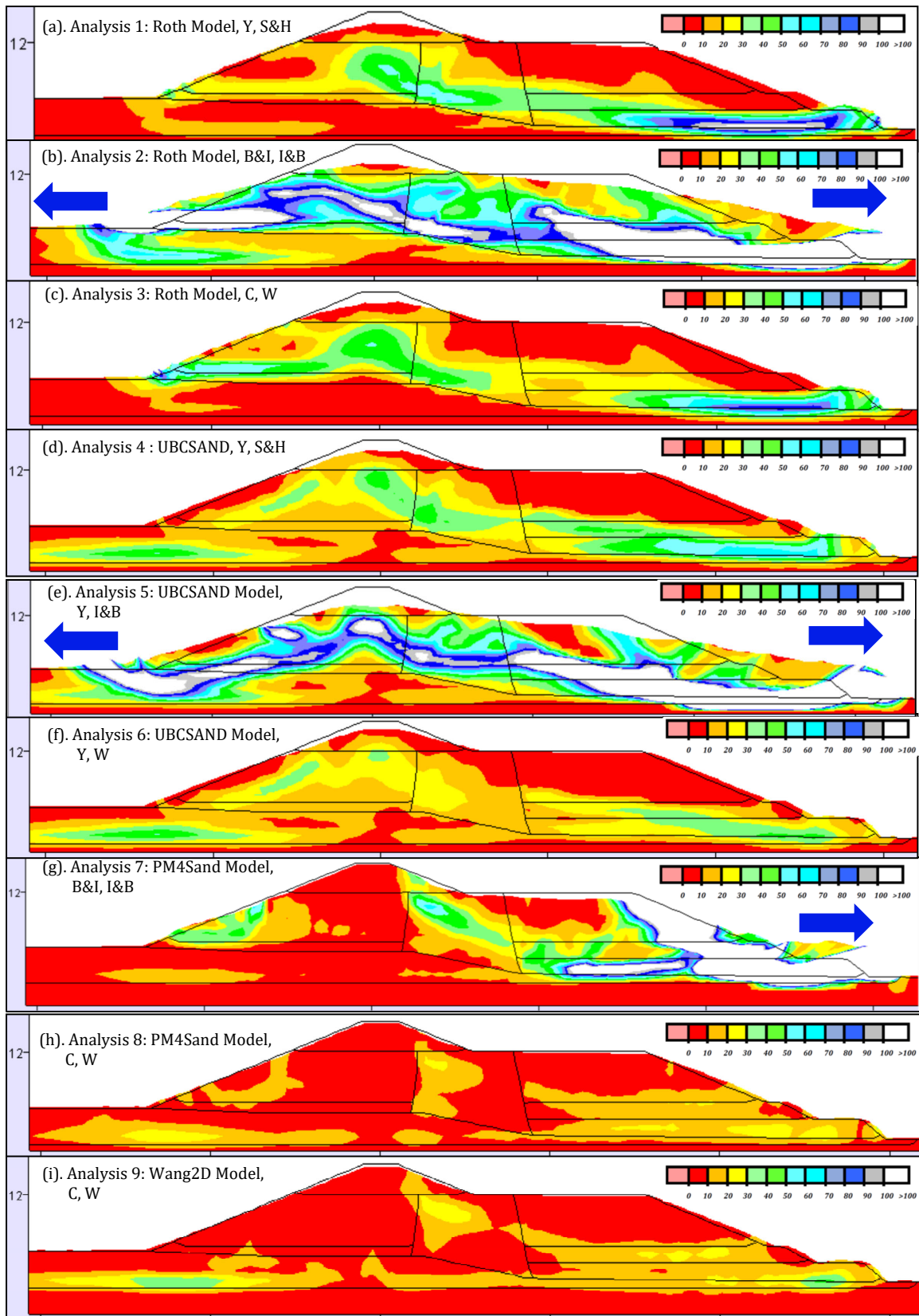


Figure 6-12: Shear strains (percent) of USFD Analyses 1 to 9 at the end of analysis

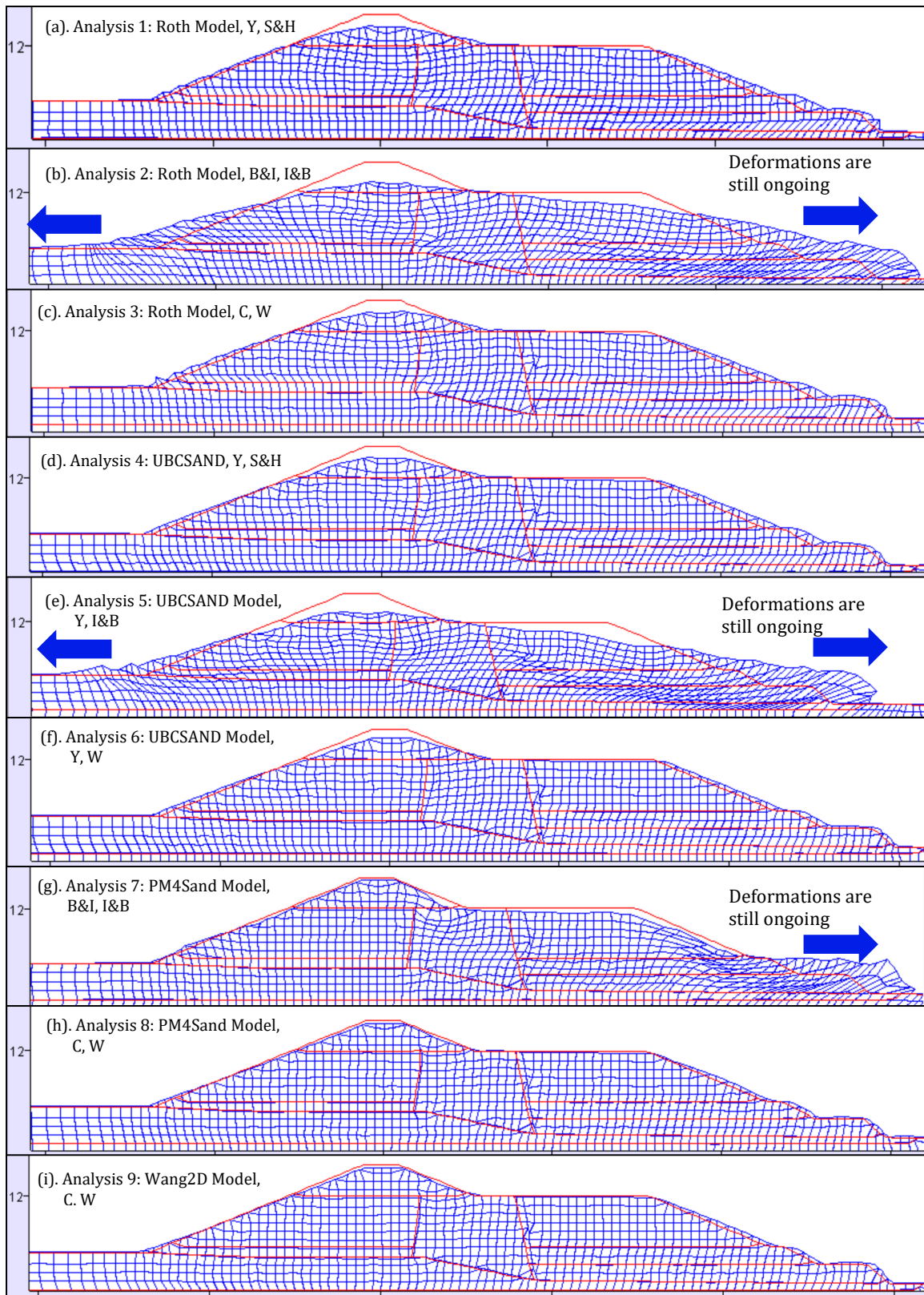


Figure 6-13: Deformed meshes of USFD Analyses 1 to 9 at the end of analysis

(Figure 6-10) been postulated by Weber et al. (2015) based on the post-earthquake investigations and cross-sections, but it took these types of more advanced nonlinear seismic deformation analyses (NDA) to analytically demonstrate the feasibility and likelihood of this mechanism.

Figures 6-11 through 6-13 present the results of nonlinear seismic deformation analyses performed with the combinations of models and relationships of USFD 1 through 9 at the end of analyses. As shown in Figure 6-11, significant maximum cyclic pore pressure ratios developed in all nine analyses. Figure 6-12 presents shear strains (in percent) in USFD Analyses 1 to 9 at the end of analyses. Figure 6-13 presents the final deformed meshes of USFD Analyses 1 to 9 at the end of analyses

All six successful analyses (USFD Analyses 1, 3, 4, 6, 8, and 9) have cause to claim success; and there was no clear overall “winner”. Each of the four analytical models showed itself well able to produce useful and accurate engineering “predictions”, so long as it was calibrated and used in conjunction with (1) a suitable liquefaction triggering relationship, and (2) a suitable post-liquefaction S_r relationship.

Neglecting the three analyses that were unsuccessful due to the incorrect prediction of flow failures due to the use of an un-suitable post-liquefaction S_r relationship (USFD Analyses 2, 5 and 7), and then considering the remaining six “successful” analysis results:

1. The Roth model is the oldest, and the simplest of the four analytical models employed. It did the best job (in both Analyses 1 and 3) of predicting the observed exit location of the heel scarp (high on the upstream face) of the massive downstream side slippage feature; very closely matching the observed heel scarp location. It provided predictions of lateral displacements of the downstream slope face, and of the downstream toe, that were all within a factor of 1.34 or less relative to the displacements observed. But it conservatively over-predicted the observed crest loss, by factors of approximately $7.7 \text{ ft} / 3.0 \text{ ft} = 2.57$ and $7.3 \text{ ft} / 3.0 \text{ ft} = 2.43$ in these two analyses. Conservative prediction of crest loss is currently targeted in the Roth model, to compensate for the current lack of a well-vetted approach to analysis of post-earthquake reconsolidation settlements.
2. The UBCSAND model represents a mid-level range of complexity between that of the Roth model, and the two higher-order plasticity models (PM4Sand and Wang2D). In USFD Analyses 4 and 6, the UBCSAND model predicted the exit point of the heel scarp of the deep-seated downstream side deep-seated displacement feature to occur at the very top of the upstream face of the dam; essentially at the heel point where the upstream face meets the horizontal crest deck. The actually observed exit location of the heel scarp was a bit lower (still near the top of the upstream face); this represented a good (and useful) prediction. The UBCSAND model conservatively slightly over-predicted the observed crest loss, by factors of approximately $7.2 \text{ ft} / 3.0 \text{ ft} = 2.0$, and $5.6 \text{ ft} / 3.0 \text{ ft} = 1.87$, in these two analyses. It provided predictions of lateral displacements of the downstream slope face, and of the downstream toe, that were also all within a factor of 1.16 or less relative to the displacements observed. These were also good engineering results.

3. The PM4Sand model is one of the two higher-order plasticity models employed. In USFD Analysis 8, this model predicted an exit location of the heel scarp of the downstream side deep-seated displacement feature high on the downstream side face near the lip of the upper crest section (deck) of the dam. This was the least successful prediction of this heel scarp location. But it should also be noted that in a forward engineering analysis this exiting feature would likely still have been of some concern. The PM4Sand model under-predicted crest loss by a factor of $1.8 \text{ ft.} / 3.0 \text{ ft.} = 0.60$, and it under-predicted lateral translation of the downstream face of the dam, and of the downstream toe, by factors of $7.2 \text{ ft.} / 8.7 \text{ ft.} = 0.82$ and $3.3 \text{ ft.} / 5.3 \text{ ft.} = 0.62$, respectively. These were all unconservative results, but they were only slightly unconservative, and were within factors of less than 1.5 of the observed movements; representing good engineering accuracy for a complex problem involving interactions between cyclic pore pressure generation, resulting strength reduction and softening, and large seismic inertial lurching forces.
4. The Wang2D model is the other higher-order plasticity model employed. In USFD Analysis 9, this model predicted an exit location of the heel scarp of the downstream side deep-seated displacement feature on the top deck of the crest, near the downstream end of the deck. This was a somewhat better prediction than the PM4Sand Analysis 8, but it was not as good as any of the four successful Roth and UBCSAND analyses. The Wang2D Analysis 9 provided the closest predictions of (1) crest loss (2.0 feet vs. 3.0 feet observed), and close predictions of (2) maximum lateral translation of the downstream face (6.3 ft. calculated vs. 8.7 ft. observed) and (3) lateral translation of the downstream toe (3.4 ft. vs. 5.3 ft. observed).

Lesson 6.12: With suitable diligence on the part of the engineering team, it appears that these types of analyses can suitably identify potentially critical deformation and/or failure mechanisms, and that they can also provide engineering predictions of expected magnitudes of deformations and displacements within a factor of approximately 2 or better. That was a somewhat surprising and positive outcome of these back-analyses of a challenging case history involving “moderate” seismically induced deformations, with challenging geometry, strong near-field seismic motions, and significant occurrence of soil liquefaction; producing a very challenging combination of (a) seismic pore pressure generation, (b) resulting strength loss and softening, and (c) strong seismic inertial “lurching” forces.

In the six successful USFD back-analyses (USFD Analyses 1, 3, 4, 6, 8, and 9), a recurring theme is that the analyses show significant seismic (cyclic) pore pressure generation in the saturated portions of the upstream and downstream hydraulic fill shell zones, as well as in the upper alluvium, as shown in Figure 6-11, but the post-liquefaction residual strengths are sufficient to maintain overall stability of the embankment.

The USFD was subjected to significant near source effects of ground motions due to close proximity to the hypocenters of the San Madre and San Fernando faults. Based on an evaluation of the seismology of the site, the near source directivity pulse and fling effects likely exerted a greater push towards downstream slope, which resulted in deformations in crest and downstream slope and toe area directed towards downslope. Even with development of liquefied conditions due to higher excess pore pressures in most of the

hydraulic fill and UA layers, the USFD Analyses 1, 3, 4, 6, 8, and 9 did not show excessive deformations and the moderate deformations at the end of analyses in these analyses have shown good match with deformations observed in downstream toe and slope area.

Lesson 6.13: The “moderate” deformations observed in the performance of the USFD during the 1971 San Fernando Earthquake were not due to lack of liquefaction, but rather due to adequate post-liquefaction strengths, S_r , in the downstream hydraulic fill which prevented a full failure of the embankment. It is important to suitably assess and implement post-liquefaction residual strengths in these types of analyses.

Three of the nine USFD back-analyses were unsuccessful (USFD Analyses 2, 5, and 7); incorrectly predicting the occurrence of liquefaction-induced full flow failures towards the downstream side of the dam that were not observed in the field. Two of these analyses also incorrectly predicted upstream side flow failures, and the third incorrectly predicted a significant slump or localized failure on the central upstream face.

The two analyses that incorrectly predicted flow failures towards both the upstream and downstream sides of the embankment were USFD Analyses 2, and 5, and it was Analysis 7 that incorrectly predicted a downstream flow slide with upstream side localized slumping. As shown in Table 5-30, each of these three analyses employed a different analytical or constitutive model (Roth, PM4Sand, and UBCSAND, respectively), and they employed two different triggering relationships (the Boulanger and Idriss, 2015 triggering relationship for Analyses 2 and 7, and the Youd et al., 2001 triggering relationship for Analysis 5). All three of these analyses employed the same post-liquefaction residual strength relationship; the Idriss and Boulanger (2015) S_r relationship. As discussed in Section 2.4, that relationship predicts the ratio of $S_r/\sigma'_{v,i}$ as a function of only $N_{1,60,CS}$, rather than as a function of both $N_{1,60,CS}$ and $\sigma'_{v,i}$, and as a result it under-predicts S_r for low to moderate initial effective overburden stresses. The analytically predicted flow failures in these three analyses all initiated at and near the toes of the embankment, where effective overburden stresses ($\sigma'_{v,i}$) are small.

This appears to serve to further emphasize Lesson 6-10 above.

USFD 3 repeats Analysis 2, except that they substitute the Cetin et al. (2018) liquefaction triggering and the Weber et al. (2015) S_r relationships for the Boulanger and Idriss (2014) liquefaction triggering and Idriss and Boulanger S_r relationships. USFD Analysis 6 exactly repeats Analysis 5, except that they substitute the Weber et al. (2015) S_r relationship for the Idriss and Boulanger S_r relationship. USFD Analysis 6 produces very good results. Similarly, Analysis 8 largely repeats Analysis 7, except that it employs an even more conservative triggering relationship (Cetin et al., 2018) which results in prediction of even higher seismic (cyclic) pore pressure generation, but it also employs the Weber et al. (2015) S_r relationship in place of the Idriss and Boulanger (2015) S_r relationship, and the post-liquefaction strengths are again sufficient to maintain post-shaking stability and Analysis 8 also produces very good predictive results.

There is an important lesson here, and that is the largely co-equal importance of employing a suitable post-liquefaction S_r relationship as well as a suitable liquefaction triggering relationship. Engineers to date have often tended to be more focused on the liquefaction triggering relationship; neglect of the S_r relationship can produce very poor analytical results in these types of nonlinear seismic deformation analyses.

The Upper San Fernando Dam case history is arguably the more challenging of the two case histories because it is more difficult to accurately predict “limited” deformations and displacements than the “on/off” nature of the occurrence or non-occurrence of an uncontrolled liquefaction-induced flow slide in the Lower San Fernando Dam. The accuracy of many of the predictions produced was a pleasant surprise. This is important, as it is cases of expected limited to moderate deformations that are often the most challenging in forward engineering analyses, especially with regard to assessment of resulting risk and hazard exposure.

Lesson 6.14: The observed levels of accuracy and usefulness of the analytical results of the six successful USFD analyses (vs. the actual observed seismic performance of the USFD during the earthquake) were encouraging.

6.5 ADDITIONAL LESSONS LEARNED FROM BACK-ANALYSES OF BOTH THE LSFD AND USFD DURING THE 1971 SAN FERNANDO EARTHQUAKE

6.5.1 Overview and Lessons Learned

There are a number of additional, over-arching lessons learned which were developed from evaluations of both the LSFD and USFD analyses, and also based on evaluation of the current State of Practice in seismic dam engineering. These are as follow:

Lesson 6.15: Potential strain softening of strain sensitive cohesive soils can be important.

Both cyclic softening and strain softening of the puddled central clay core materials were important in the back-analyses of both the USFD and the LSFD. Engineers engaged in analyses of a “liquefaction problem” can sometimes tend to neglect these issues. The cohesive soils warrant the same levels of engineering attention as are typically granted to the potentially liquefiable soils. The levels of success achieved in the back-analyses of both dams would not have occurred without careful consideration, and engineering treatment and modeling, of strain softening effects on cohesive soils.

Lesson 6.16: It can be dangerously unconservative to stop the analysis at the end of shaking.

The current State of Practice, as outlined in many regulatory or owner Agency guidelines, allow use of post-earthquake (identified as post-shaking) limit equilibrium static stability analyses to evaluate the post-earthquake stability conditions. A relatively low Factor of Safety such as $FOS = 1.0$ to 1.3 is often allowed as an acceptable FOS for post-earthquake stability. However, based on an evaluation of the results of LSFD and USFD deformation analyses, the following discussions describe the limitations of this Factor Safety approach to evaluate post-earthquake deformation conditions:

A post-earthquake limit equilibrium analyses may assist in evaluating the stability conditions, but it does not show the deformations (magnitude or shape). As most of the constitutive models (such as the UBCSAND, PM4Sand, and Wang2D models) do not transition to post-liquefaction strengths during shaking analyses, the deformed shape at the end of shaking can be quite different from the actual expected deformations if post-liquefaction residual strengths (and also strain softening of cohesive soils) are implemented and the nonlinear deformation analyses are then continued forward.

Potential development of tension cracks can be an important characteristic of response of an embankment dam during earthquake. These cracks may develop in both the longitudinal and transverse directions due to weak tensile strengths in soils. And they can be exacerbated by combined tensile and shear loadings. Many post-earthquake static limit equilibrium analyses unconservatively neglect tensile cracking,

In post-earthquake stability analyses, it is fairly common to use (1) peak drained strengths or (2) peak or slightly reduced undrained strengths (up to 20 percent) for non-liquefiable layers. The strengths of the non-liquefiable layers should incorporate the cyclic and strain softening effects. The strengths of clay layers for the post-shaking analysis should be estimated based on an evaluation of the strains developed in these layers at the end of shaking analysis.

“Static” limit equilibrium analyses performed at the end of shaking neglect momentum of embankment soil masses that are actually in motion. Force must be applied to these masses to reduce their momentum back to inertia. That additional force is not generally included in post-earthquake “static” limit equilibrium analyses, and that can produce unconservative analytical results.

Factors of Safety that represent acceptable levels of risk should be carefully considered.

Lesson 6.17: Simply multiplying “End of Shaking” deformations by a factor of “Two” does not suitably predict large deformations, nor does it rule out the possibility that large deformations may occur.

It is not uncommon to (1) perform an analysis up to “end of shaking” conditions (also known as “end of earthquake”), and then (2) halt the analysis, and then (3) assume that the

eventual/overall final deformations would be within a range of ± 2 of the end of shaking deformations and displacements. End of shaking displacements of the upstream toe of the Lower San Fernando Dam were typically less than 10 feet in the analyses performed in these current studies; the observed runout of the flow failure that occurred traveled 140 feet into the reservoir. The multiplier here would have been significantly higher than a factor of 2 (approximately a factor of 70 or so).

Lesson 6.18: Allowing excessive negative pore pressures in nonlinear seismic deformation analyses can be unconservative.

Modern constitutive models employed in these types of analyses often correctly model both cyclic compression and cyclic dilation during seismic loading. It is important not to allow excessively negative pore pressures to occur during cyclic dilation. Water “cavitates” (spontaneously vaporizes) at a gauge pressure of approximately -1 atmosphere (varies slightly with elevation, and thus local atmospheric pressure). Unfortunately, it is not uncommon to model tensile strength of water at high enough levels that cavitation does not occur in nonlinear seismic deformation analyses. That produces excessively negative pore pressures that are physically impossible, and these produce shear strengths and stiffnesses (by virtue of the principle of effective stress) that are also not physically possible. In these current studies, attention was paid (unless established model-specific procedures and/or examples address this differently) to the tensile strength of water to ensure that cavitation would correctly limit negative pore pressures to not less than -1 atmosphere.

Lesson 6.19: Appropriate combinations of models, liquefaction triggering and residual strength relationships, and analysis procedures can predict both (1) small to moderate deformations, and (2) large deformations with the same engineering protocols.

One of the basic tenets of these current studies was to utilize the same protocols for both USFD (a low to moderate deformation case history) and LSFD (a large deformation or “flow failure” case history) case histories. Another was to perform all of the analyses as if the answers were not already known. These are also good ideas for performance of actual “forward” engineering analyses of real projects. The forward analyses should not be performed with a pre-determined anticipation of deformations; instead an effort should be made to perform a complete analytical scheme with a good understanding and proper implementation of concepts, models, and relationships. As shown in this dissertation, the same engineering protocols have resulted in good matches with observed field behavior for both low to moderate deformations (USFD) and for large deformations and “flow failure” (LSFD) case histories. *Using the same analytical approaches, and protocols allows the analyses to determine the nature of the performance that is likely to occur, instead of biasing the analyses with a priori assumptions and risking missing something that is potentially important.*

Lesson 6.20: The most important lesson from these studies is that these types of nonlinear seismic deformation analyses can produce useful engineering results. These back-analyses

demonstrated an ability to produce very good engineering “predictions” of both observed mechanisms of displacements and distress, as well as magnitudes of deformations and displacements.

Accomplishing this appears to require the following:

1. Suitable analytical or constitutive models.
2. Calibration of these models with respect to cyclic (seismic) pore pressure generation with suitable liquefaction triggering relationships, including both K_α and K_σ relationships.
3. Use of suitable post-liquefaction residual strength (S_r) relationships.
4. Suitable procedures and protocols for transition to S_r behaviors in potentially liquefiable soils.
5. Suitable treatment of potential cyclic softening, and strain softening, behaviors in sensitive clayey soils.
6. Suitable characterization of geometry and stratigraphy, and suitable evaluation of material properties and behaviors.
7. Suitable development and application of appropriate seismic “input” motions.
8. Appropriate evaluation and interpretation of the analysis results, with an understanding of the models and relationships employed, and also the intrinsic limitations of the continuum analysis methods employed with regard to accurate analyses of very large deformations and displacements.
9. And engineering judgment.

Further Work:

This concludes this dissertation. The overall research effort will continue, however, and the remaining research tasks will include: (1) performance of additional one-dimensional nonlinear seismic deformation (and site response) back-analyses of the Port Island Array site response in order to more fully assess the seismic site response capabilities of all four analytical models studied here, (2) nonlinear seismic deformation back-analyses of both the USFD and the LSFD employing input motions scaled to $a_{\max} = 0.65g$ (represented the estimated likely near lower bound of motions that may have occurred during the 1971 San Fernando earthquake), (3) additional nonlinear seismic deformation analyses of both the USFD and the LSFD employing model combinations shown to be effective for each, and employing synthetic motions generated by the SCEC BBP simulations as a test of the ability of these types of synthetically generated motions to produce useful engineering results for this challenging case involving complicated near-field source mechanisms, and (4) implement a practical approach to compute volumetric recompression-induced settlement as part of post-earthquake analyses. An over-arching U.C. Berkeley Geotechnical Research Report will present the full set of final overall studies and findings.

References

- Abrahamson, N. A. (2018). Class notes of Seismic Hazard Analysis and Design Ground Motions, Spring, 2018.
- Abrahamson, N. A. and Silva, W. J. (1997). "Empirical response spectral attenuation relations for shallow crustal earthquakes." *Seismological Research Letters*, Volume 68, Number 1, January/February.
- Abrahamson, N. A., Silva, W., and Kamai, R. (2014). "Update of the AS08 ground motion prediction equations based on the NGA-West2 dataset." PEER Report 2013/04, Pacific Earthquake Engineering Research Center, University of California, Berkeley.
- Akai, K., Kamon, M., Sano, I., and Soga, K. (1991). "Long-Term Consolidation Characteristic of Diluvial Clay in Osaka Bay." *Soils and Foundations* Vol. 31, No. 4, 61-74, Dec.1991. Japanese Society of Soil Mechanics and Foundation Engineering.
- Aki, K. (1967). "Scaling law of seismic spectrum." *Journal of Geophysical Research*, Volume 72, Number 4.
- Allen, C.R., Hanks, T.C., and Whitcomb (1975). *Seismological Studies of the San Fernando Earthquake and Their Tectonic Implications*. Chapter 20 of Bulletin 196, California Division of Mines and Geology, Sacramento, CA.
- Anderson, J. (2015). "The composite source model for broadband simulations of strong ground motions." *Seismological Research Letters*, Volume 86, Number 1, January/February 2015. Doi: 10.1785/0220140098.
- Ansari, M.A., Yamazaki, F., and Katayama, T. (1997). "Analysis of Ground Motions at a Reclaimed Site During the 1995 Great Hansin Earthquake". *Journal of Civil Engineering*, The institution of Engineers, Bangladesh; Vol. CE25, No. 1, 1997.
- Atkinson, G. M., and Assatourians, K. (2015). "Implementation and validation of EXSIM (a stochastic finite-fault ground-motion simulation algorithm)." *Seismological Research Letters*, Volume 86, Number 1. Doi: 10.1785/0220140097.
- Baise (2000). "Investigations in Site Response from Ground Motion Observations in Vertical Arrays." A dissertation submitted in partial satisfaction of the requirements for the degree of Doctor of Philosophy in Engineering – Civil and Environmental Engineering in the Graduate Division of the University of California, Berkeley; Fall, 2000.
- Beaty, M.H. (2001). *A Synthesized Approach for Estimating Liquefaction-Induced Displacements of Geotechnical Structures*. A thesis submitted in partial fulfillment of the requirements for the degree of Doctor of Philosophy, The University of British Columbia (Vancouver), Canada.
- Beaty, M.H. and Byrne, P.M. (2011). *Documentation Report: UBCSAND Constitutive Model*. Available on Itasca UDM Website; February. <http://www.itasca-udm.com/>
- Berckhemer, H. (1962). "Die Ausdehnung der Bruchfläche im Erdbeben Herd und ihr Einfluss auf das seismische Wellen Spektrum." *Gerlands. Beitr. Geophys.*, 71, 5-26.
- Bolton, M. D. (1986). "The strength and dilatancy of sands." *Geotechnique* 36, No. 1, 65-78.

- Boore, D. (2009). "Comparing stochastic point-source and finite-source ground motion simulations: SMSIM and EXSIM." *Bulletin of Seismological Society of America*, 99, 3202-3216.
- Boore, D. M., (1983). "Stochastic simulation of high-frequency ground motions based on seismological models of the radiated spectra." *Bulletin of Seismological Society of America*, 73, 1865-1894.
- Boore, D. M., Stewart, J. P., Seyhan, E., and Atkinson, G. M (2013) "NGA-West2 equations for predicting response spectral accelerations for shallow crustal earthquakes." PEER Report 2013/05, Pacific Earthquake Engineering Research Center, University of California, Berkeley.
- Boore, D.M. (2010). "Orientation-independent, nongeometric-mean measures of seismic intensity from two horizontal components of motion." *Bulletin of Seismological Society of America*, 100, 1830-1835.
- Boore, DM (1999). "Effect of baseline corrections on response spectra for two recordings of the 1999 Chi-Chi, Taiwan, Earthquake." USGS Open-File Report 99-545, version 1.0.
- Boore, DM (2001). "Effect of baseline corrections on displacements response spectra for several recordings of the 1999 Chi-Chi, Taiwan, earthquake." *Bulletin of the Seismological Society of America* 2001; 91(5): 1199-1211.
- Boulanger, R. W. (2003). "Relating K_a to relative state parameter index." *ASCE. Journal of Geotechnical and Geoenvironmental Engineering*, 129(8), 770-73.
- Boulanger, R.W. and Idriss, I.M. (2014). "CPT and SPT based liquefaction triggering procedures." Report No. UCD/CGM-14/01, Center for Geotechnical Modeling, Department of Civil and Environmental Engineering, College of Engineering, University of California, Davis.
- Boulanger, R.W. and Ziotopoulou, K. (2015). PM4SAND (Version 3): A Sand Plasticity Model for Earthquake Engineering Applications. Report No. UCD/CGM-15/01, U.C. Davis.
- Bray, J.D., and Rodriguez-Marek, A., (2004) "Characterization of forward-directivity ground motions in the near-fault region." *Soil Dynamics and Earthquake Engineering*, 24, 815-828.
- Brune, J. N. (1970). "Tectonic stress and the spectra of seismic shear waves from earthquakes." *Journal of Geophysical Research*.
- Bureau, G., Inel, S., Davis, C. A., and Roth, W.H. (1996). "Seismic response of Los Angeles Dam, CA during the 1994 Northridge earthquake." *Proceedings of USCOLD 1996 Annual Meeting*, Los Angeles, California, 281-295.
- Byrne, P.M., Cheung, H., and Yan, L. (1987). *Soil Parameters for Deformation Analysis of Soil Masses*. Canadian Geotechnical Journal.
- Campbell, K.W. and Bozorgnia, Y. (2014). "NGA_West2 ground motion model for the average horizontal components of PGA, PGV, and 5% damped linear acceleration response spectra." *Earthquake Spectra*, Volume 30, No. 3, pages 1087-1115, August 2014. Earthquake Research Institute.

- Castro, G., Keller, T.O., and Boynton, S.S. (1989). "Re-Evaluation of the Lower San Fernando Dam, An Investigation of the February 9, 1971 Slide", Report 1 of USACE Contract Report GL-89-2, Prepared for USACE Waterways Experiment Station (WES).
- Castro, G., Seed, R.B., Keller, T.O., Seed, H.B. (1992). Steady-State Strength Analysis of Lower San Fernando Dam Slide. *Journal of Geotechnical Engineering*, Volume 118, No. 3, March.
- Cetin, K. O., Bilge, H. T., Wu., J., Kammerer, A. M., and Seed, R. B. (2009). "Probabilistic model for the assessment of cyclically induced reconsolidation (volumetric) settlements." *Journal of Geotechnical and Geoenvironmental Engineering*, Volume 135, No. 3. Doi: 10.1061/(ASCE) 1090-0241(2009)135:3(387)
- Cetin, K. O., Seed, R. B., Kayen, R. E., Moss, R. E. S., Bilge, H. T.; Ilgac, M., and Chowdhury, K. (2018). "The use of the SPT-based seismic soil liquefaction triggering evaluation methodology in engineering hazard assessments." *Method Article Methods X* 5(2018) 1556-1575, Elsevier. <https://doi.org/10.1016/j.mex.2018.11.016>
- Cetin, K. O., Seed, R. B., Kayen, R. E., Moss, R. E. S., Bilge, H. T.; Ilgac, M., and Chowdhury, K. (2018). "Dataset on SPT-based seismic soil liquefaction." *Data article, Data in Brief* 20 (2018) 544-548, Elsevier. <http://dx.doi.org/10.1016/j.dib.2018.08.043>.
- Cetin, K. O., Seed, R. B., Kayen, R. E., Moss, R. E. S., Bilge, H. T.; Ilgac, M., and Chowdhury, K. (2018). "Examination of differences between three SPT-based seismic soil liquefaction triggering relationships." *Soil Dynamics and Earthquake Engineering*, Elsevier. <https://doi.org/10.1016/j.soildyn.2018.03.013>.
- Cetin, K. O., Seed, R. B., Kayen, R. E., Moss, R. E. S., Bilge, H. T.; Ilgac, M., and Chowdhury, K. (2018). "SPT-based probabilistic and deterministic assessment of seismic soil liquefaction triggering hazard." *Soil Dynamics and Earthquake Engineering*, Elsevier. <https://doi.org/10.1016/j.soildyn.2018.09.012>.
- Cetin, K.O., and Seed, R. B. (2004). "Nonlinear shear mass participation factor (rd) for cyclic shear stress ratio evaluation." *Soil Dynamics and Earthquake Engineering* 24 (2004) 103-113. Doi: 10.1016/j.soildyn.2003.10.008
- Cetin, K.O., Seed, R.B., Kiureghian, A. D., Tokimatsu, K., Harder, L.F., Kayen, R. E., and Moss, R.E.S. (2004). Standard Penetration Test-Based Probabilistic and Deterministic Assessment of Seismic Soil Liquefaction Potential. *Journal of Geotechnical and Geoenvironmental Engineering*, ASCE.
- Chiou, B. S. J. and Youngs, R. R. (2013). "Update of the Chiou and Youngs NGA ground motion model for average horizontal component of peak ground motion and response spectra." PEER Report 2013/07, Pacific Earthquake Engineering Research Center, University of California, Berkeley.
- Chowdhury, K., Perlea, V., Seed, R. B., Beaty, M., Dawson, E., and Hu, G. (2017). A Case History Evaluation of State of Practice for Seismic Deformation Modeling of Earthen Dams. USSD Annual Meeting and Conference, Anaheim, CA, April, 2017.
- Chowdhury, K., Seed, R.B., Dreger, D., Perlea, V., Ma, F., and Beaty, M. (2018). Re-Evaluation of the Performance of the Upper San Fernando Dam: A Liquefaction-Induced

- Moderate Deformation Case History. Proc., Geotechnical Earthquake Engineering and Soil Dynamics (GEESD), Austin, Texas, ASCE, June.
- Chowdhury, K., Seed, R.B., Dreger, D., Perlea, V., Ma, F., and Beaty, M. (2018). Re-Evaluation of the Performance of the Lower San Fernando Dam: A Seismic Performance Case History Involving Liquefaction Flow Failure Conditions. Proc., Geotechnical Earthquake Engineering and Soil Dynamics (GEESD), Austin, Texas, ASCE, June.
- Crempien, J. and Archuleta, R. (2015). "UCSB method for broadband ground motion from kinematic simulations of earthquakes." *Seismological Research Letters*, Volume 86, Number 1. Doi: 10.1785/0220140103.
- Cubrinovski, M. and Ishihara, K. (1999). Empirical Correlation Between SPT-N Value and Relative Density for Sandy Soils. *Soils and Foundations*, Japanese Geotechnical Society, Volume 39, No. 5, pp 61-71, October.
- Cubrinovski, M., Ishihara, K., and Furukawazono, K. (2000). "Analysis of two case histories on liquefaction of reclaimed deposits." 12th World Conference on Earthquake Engineering, Auckland, New Zealand, 2000.
- Dafalias, Y., F., and Manzari, M. (2004). "Simple plasticity sand model accounting for fabric change effects." *ASCE, Journal of Engineering Mechanics*, Vol. 130, No. 6. Doi: 10.1061/(ASCE)0733-9399(2004)130:6(622)
- Dames and Moore (1985). "Evaluations of earthquake-induced deformations of Pleasant Valley Dam." Report to City of Los Angeles, Dept. of Water and Power, May 24.
- Darendeli, M. (2001). "Development of a new family of normalized modulus reduction and material damping curves." Ph.D. dissertation, Dept. of Civil Engineering, University of Texas, Austin.
- Darragh, B., Silva, W., and Gregor, N. (2011). "Strong motion record processing for the PEER center." Pacific Engineering, El Cerrito, California.
- Dawson, E.M. and Mejia, L.H. (2012). Updates to a Practice-Oriented Liquefaction Model. Geo-Congress 2012, Geo-Institute, ASCE, Oakland, California.
- Dawson, E.M., Roth, W.H., Nesarajah, Bureau, G., and Davis, C.A. (2001). A Practice Oriented Pore-Pressure Generation Model. Proceedings, 2nd International FLAC Symposium, Lyon, France, October.
- Department of Water Resources (1989). The August 1, 1975 Oroville Earthquake Investigation, Supplement to Bulletin 203-78.
- Dreger, D., Beroza, G.C., Day, S.M., Goulet, C.A., Jordan, T.H., Spudich, P.A., and Stewart, J.P. (2015). Validation of the SCEC Broadband Platform V14.2 Simulation Methods Using Pseudospectral Acceleration Data. *Seismological Research Letters*, Volume 86, Number 1.
- Dreger, D., G. Hurtado, A. Chopra, and S. Larsen (2011). Near-Field Across-Fault Seismic Ground Motions, *Bull. Seism. Soc. Am.* v. 101; no. 1; p. 202-221; DOI: 10.1785/0120090271
- Duke, C. M., Johnson, K. E., Larson, L. E., and Egman, D. C. (1972). "Effects of site classification and distance on instrumental indices in the San Fernando earthquake." Report UCLA Eng. 7247, School of Engineering, UCLA.

- Duncan, J. M., and Chang, C. Y. (1970). "Nonlinear analysis of stress and strain in soils." ASCE, Journal of the Soil Mechanics and Foundation Division, 96(5), 1629-1653.
- Duncan, J.M. and Wright, S.G. (2005). "Soil Strength and Slope Stability." ISBN 0-471-69163-1. John Wiley & Sons, Inc. Hoboken, New Jersey.
- Elgamal, A-W., Zeghal, M., and Parra, E., et al. (1996). "Liquefaction of Reclaimed Island in Kobe, Japan." Journal of Geotechnical Engineering, Vol. 122, No. 1, January 1996. ASCE, ISSN 0733-9410/96/0001-0039-0049.
- GeoPentech (2015). "Southwestern United States ground motion characterization SSHAC Level 3." Technical Report, Revision 2, March 2015. Prepared for Arizona Public Service Company and Pacific Gas and Electric Company.
- Gingery, J. R. (2014). "Effects of Liquefaction on Earthquake Ground Motions." A dissertation submitted in partial satisfaction of the requirements for the degree of Doctor of Philosophy in Structural Engineering in University of California, San Diego.
- Golesorkhi, R. (1989) "Factors influencing the computational determination of earthquake-induced shear stresses in sandy soils." Dissertation submitted in partial fulfillment of the requirements for the degree of Doctor of Philosophy, University of California, Berkeley.
- Goulet, C. A., Abrahamson N.A., Somerville, P.G., and Wooddell, K.E. (2015). "The SCEC broadband platform validation exercise: methodology for code validation in the context of seismic-hazard analyses." Seismological Research Letters, Volume 86, Number 1, January/February 2015. Doi: 10.1785/0220140104.
- Graves, R. and Pitarka, A. (2015). "Refinements to the Graves and Pitarka (2010) broadband ground-motion simulation method." Seismological Research Letters, Volume 86, Number 1, January/February 2015. Doi: 10.1785/0220140101.
- Graves, R. W. (2004). "Processing issues for near source strong motion recordings." Proceedings of invited workshop on strong-motion record processing, COSMOS Publication No. CP-2004/02.
- Grazier, V. M. (1979). "Determination of the true displacement by using strong ground motion records." Phys. Solid Earth, Izvestiya Academy of Science, USSR, English published by AGU, 15:875-885.
- Hardin, B. O. (1978). "The nature of stress-strain behavior of soils." Proceedings of the ASCE Geotechnical Engineering Division Specialty Conference, Pasadena, California. Volume 1 of Earthquake Engineering and Soil Dynamics.
- Hatanaka, M. and Uchida, A. (1996). Empirical Correlation Between Penetration Resistance and Internal Friction Angle of Sandy Soils. Soils and Foundations, Japanese Geotechnical Society, Volume 36, No. 4, pp 1-9.
- Heaton, T.H. (1982). The 1971 San Fernando Earthquake: A Double Event? Bulletin of the Seismological Society of America, Volume 72, No. 6, pp 2037-2062.
<https://apps.peer.berkeley.edu/ngawest2/final-products/>
- Hudson, D. E, Editor (1971). "Strong motion instrumental data on the San Fernando earthquake of February 9 1971." Earthquake engineering research laboratory,

- California Institute of Technology and Seism. Field Survey, NOAA, US Department of Commerce, September.
- Idriss, I. M., and Boulanger, R. W. (2015). "2nd Ishihara Lecture: SPT- and CPT-based relationships for the residual shear strength of liquefied soil." *Soil Dynamics and Earthquake Engineering*, 68, 57-68, 10.1016/j.soildyn.2014.09.010.
- Idriss, I.M. and Boulanger, R.W. (2003). "Estimating $K\alpha$ for use in evaluating cyclic resistance of sloping ground." *Proceedings in 8th US-Japan workshop on earthquake resistant design of lifeline facilities and countermeasures against liquefaction*, Hamada, O'Rourke, and Bardet, eds., Report MCEER-03-0003, MCEER, SUNY Buffalo, NY, pp 449-468.
- Idriss, I.M., (1999). "An update to the Seed-Idriss simplified procedure for evaluating liquefaction potential." In *proceedings, TRB Workshop on New Approaches to Liquefaction*, Publication No. FHWA-RD-99-165, Federal Highway Administration.
- Inel, S., Roth, W.H., and De Rubertis (1993). *Non-Linear Dynamic Effective Stress Analysis of Two Case Histories*. *Proceedings of the Third International Conference on Case Histories in Geotechnical Engineering*. St. Louis, Missouri.
- Inel, S., Roth, W.H., and Rubertis, C. de (1993). "Nonlinear dynamic effective-stress analysis of two case histories." *Third international conference on case histories in geotechnical engineering*, St. Louis, Missouri, June 1-4, 1993, Paper NO. 14.14.
- Ishihara, K. (1996). "Soil behavior in earthquake geotechnics." Clarendon Press, Oxford. ISBN 019 856224 1
- Ishihara, K., and Yoshimine, M. (1992). "Evaluation of settlements in sand deposits following liquefaction during earthquakes." *Soils and Foundations*, 32(1), 173-188.
- Ishihara, K., and Yoshimine, M., (1992). "Evaluation of settlements in sand deposits following liquefaction during earthquakes." *Soils and Foundations* 32(1), 173-88, Japanese Geotechnical Society.
- Ishihara, K., Yasuda, S., and Nagase, H. (1996). "Soil characteristics and ground damage." *Special issue of Soils and Foundations*, 109-118, Jan. 1996. Japanese Geotechnical Society.
- Iwasaki, Y. and Tai, M. (1996). "Strong Motion Records at Kobe Port Island." *Special issue of Soils and Foundations*, 29-40, January 1996. Japanese Geotechnical Society.
- Jang, W., Y. and Mimura, M. (2005). "Effect of permeability and compressibility of sandwiched gravelly sand layers on subsequent settlement of pleistocene deposits." *Soils and Foundations*, Volume 45, No. 6, 111-119. Japanese Geotechnical Society.
- Kramer, S. L. (1996). "Geotechnical earthquake engineering." Prentice Hall, Upper Saddle River, New Jersey. ISBN 0-13-374943-6.
- Kuhlemeyer, R.L. and Lysmer. J. (1973) *Finite Element Method Accuracy for Wave Propagation Problems*. *Journal of the Soil Mechanics and Foundations Division*, 1973, Vol. 99, Issue 5, Pg. 421-427.
- Ladd. C. C., and Foott, R. (1974). "New design procedure for stability of soft clays." *ASCE Journal of Geotechnical Engineering*, 100(7), 763-786.

- Langston, C. A. (1978). "The February 9, 1971 San Fernando earthquake: a study of source finiteness in teleseismic body waves." *Bulletin of the Seismological Society of America*, Volume 68, February 1978, No. 1.
- Lasley, S. J., Green R. A., Rodriguez-Marek, A. (2016). "New stress reduction coefficient relationship for liquefaction triggering analyses." *Journal of Geotechnical and Geoenvironmental Engineering*, ASCE. Doi: 10.1061/(ASCE)GT.1943-5606.0001530
- Lay, T. and Wallace, T. C. (1995). "Modern global seismology." *International geophysics series: Volume 58*. ISBN-13: 978-0-12-732870-6, Academic Press.
- Leonard, M. (2010). "Earthquake fault scaling: self-consistent relating of rupture length, width, average displacement, and moment release." *Bulletin of Seismological Society of America*, Vol. 100, No. 5A, pp 1971-1988, October 2010. Doi: 10.1785/0120090189
- Li, X.-S., Wang, Z.-L., and Shen, C.K. (1992). "SUMDES, a nonlinear procedure for response analysis of horizontally layered sites subjected to multidirectional earthquake loading." Report to Department of Civil Engineering, University of California, Davis.
- Li, Y.-G., Aki, K., Vidale, J.E., Alvarez, M.G. (1998). "A Delineation of the Nojima Fault in the M7.2 Kobe, Japan, Earthquake of 1995 Using Fault Zone Trapped Waves." *Journal of Geophysical Research*, Vol. 103, No. B4, Pages 7247-7263, April 10. Paper No. 98JB00166.
- Maechling, P.J., Silva, F., Callaghan, S., and Jordan, T.H. SCEC Broadband Platform: System Architecture and Software Implementation. *Seismological Research Letters*, Volume 86, Number 1, January/February 2015.
- Manzari, M.T. and Dafalias, Y.F. (1997). A Critical State Two-Surface Plasticity Model for Sands. *Geotechnique* 42(2): 255-272.
- Matsuoka, H., and Nakai, T. (1977). "Stress-strain relationship of soil based on the SMP." In *Proceedings of the Specialty Session 9, 9th International Conference on Soil Mechanics and Foundation Engineering*, pp. 153-162.
- Mejia, L. H. and Dawson, E. M. (2006). "Earthquake deconvolution for FLAC." 4th International FLAC Symposium on Numerical Modeling in Geomechanics – 2006 – Hart and Varona (eds.). Paper: 04-10. Itasca Consulting Group, Inc. Minneapolis, ISBN 0-9767577-0-2.
- Mesri, G. and Funk, J.R. (2015). "Settlement of the Kansai International Airport Islands." *Journal of Geotechnical and Geoenvironmental Engineering*. DOI: 10.1061/(ASCE)GT.1943-5606.0001224.
- Mimura, M. and Jang, W., Y. (2004). "Description of time-dependent behavior of quasi-overconsolidated Osaka pleistocene clays using elasto-viscoplastic finite element analyses." *Soils and Foundations*, Volume 44, No. 4., 41-52. Japanese Geotechnical Society.
- Mimura, M., Takeda, K., Yamamoto, K., Fujiwara, T., and Jang, W-Y. (2003). "Long-term settlement of the reclaimed quasi-overconsolidated pleistocene clay deposits in Osaka Bay." *Soils and Foundations*, Volume 43, No. 6, 141-153, December. Japanese Geotechnical Society.

- Mitchell, J. K. and Soga, K. (2005). *Fundamentals of Soil Behavior*. ISBN: 978-0-471-46302-3. Wiley.
- Montgomery, J., Boulanger, R. W., and Harder, L. F. (2014). "Examination of the K_s overburden correction factor on liquefaction resistance." *Journal of Geotechnical and Geoenvironmental Engineering*.
- Moriwaki, Y., Beikae, M., and Idriss, I. M. (1988). "Nonlinear seismic analysis of the Upper San Fernando Dam under the 1971 San Fernando Earthquake." *Proceedings of Ninth World Conference on Earthquake Engineering*, August 2-9, 1988, Tokyo, Japan (Volume VIII).
- Morrill, B. J. (1972). "Seismoscope results – San Fernando earthquake of 9 February, 1971." Chapter 3 of California Institute of Technology Report EERL 72-02, pp. 72-124.
- Nakakita, Y. and Watanabe, Y. (1981). "Soil stabilization by preloading in Kobe Port Island." *Proceedings of 9th International Conference on Soil Mechanics and Foundation Engineering*, Japanese Society of Soil Mechanics and Foundation Engineering, Tokyo, Japan, pp 611-622.
- NCEER (1997). "Proceedings of the NCEER workshop on evaluation of liquefaction resistance of soils." Edited by Youd., T. L., and Idriss, I. M., Technical Report NCEER-97-0022. National Center for Earthquake Engineering Research.
- of the Performance of the Upper San Fernando Dam: A Liquefaction-Induced Moderate Deformation Case History. *Proc., Geotechnical Earthquake Engineering and Soil Dynamics(GEESD)- 2018*, ASCE, June.
- NRC (1985). "Liquefaction of soils during earthquakes." Committee on earthquake engineering commission on engineering and technical systems, National Research Council.
- Olsen, K. and Takedatsu, R. (2015). "The SDSU broadband ground-motion generation module BBtoolbox version 1.5." *Seismological Research Letters*, Volume 86, Number 1, January/February 2015. Doi: 10.1785/0220140102.
- Olson, S. M. (2001). "Liquefaction analysis of level and sloping ground using field case histories and penetration resistance." PhD thesis, University of Illinois at Urbana-Champaign, Urbana, Illinois.
- Olson, S. M., and Stark, T. D. (2002). "Liquefied strength ratio from liquefaction flow failure case histories." *Canadian Geotechnical Journal*, 39(5), 629-647.
- PEER (2013). *Pacific Earthquake Engineering Research Center*, Berkeley, CA. Published reports on NGA-West2.
- Perlea, V. G., and Beaty, M. H. (2010). "Corps of Engineers Practice in the Evaluation of Seismic Deformation of Embankment Dams." *Fifth International Conferences on Recent Advances in Geotechnical Earthquake Engineering and Soil Dynamics*.
- Roth, W. H., Bureau, G., and Brodt, G. (1991). "Pleasant Valley Dam: an approach to quantifying the effect of foundation liquefaction." *17th International Congress on Large Dams*, Vienna, 1199-1223.

- Rowe, P. W., (1962). "The stress-dilatancy relation for static equilibrium of an assembly of particles in contact." In Proceedings of the Royal Society of London, Mathematical and physical Science, Series A, 269: 500-557.
- Sato, K., Kokusho, T., Matsumoto, M., and Yamada, E. (1996). "Nonlinear Seismic Response and Soil Property During Strong Motion." Special issue of Soils and Foundations, 41-52, January 1996. Japanese Geotechnical Society.
- Schofield, A. N., and Wroth, C. P. (1968). "Critical state soil mechanics." McGraw Hill, London.
- Scott, R. F. (1973). "The calculation of horizontal accelerations from seismoscope records." Bulletin of the Seismology Society of America, Vol. 63, No. 5, pp 1637-1661. October, 1973.
- Seed, H. B., and Idriss, I. M. (1971). "Simplified procedure for evaluating soil liquefaction potential." Journal of the Soil Mechanics and Foundations Division, ASCE, Vol 107, No. SM9, pp. 1249-1274.
- Seed, H. B., Idriss, I. M., Makdisi, F., and Banerjee, N. (1975). "Representation of irregular stress time histories by equivalent uniform stress series in liquefaction analyses." EERC 75-29, Earthquake Engineering Research Center, University of California, Berkeley.
- Seed, H.B. (1987). "Design problems in soil liquefaction." Journal of Geotechnical Engineering, Vol. 113, No. 8, August, 1987. American Society of Civil Engineers. ISSN 0733-9410/87/0008-0827.
- Seed, H.B., and Idriss, I.M., (1970). "Soil moduli and damping factors for dynamic response analyses." Report No. EERC 70-10, Earthquake Engineering Research Center, University of California, Berkeley, California.
- Seed, H.B., Lee, K., Idriss, I.M., Makdisi, F. I. (1975). "The slides in the San Fernando dams during the earthquakes of February 9, 1971." Journal of the Geotechnical Engineering Division, ASCE, July.
- Seed, H.B., Lee, K.L., Idriss, I.M., and Makdisi, F. (1973). Analysis of the Slides in the San Fernando Dams During the Earthquake of Feb. 9, 1971. Report No. 73-2, June 1973, Earthquake Engineering Research Center, University of California, Berkeley.
- Seed, H.B., Seed, R.B., Harder, L.F., and Jong, H-L. (1989). Examination of the Post-Earthquake Slide of February 9, 1971. Report 2 of USACE Contract Report GL-89-2, Prepared for USACE Waterways Experiment Station (WES).
- Seed, H.B., Tokimatsu, K., Harder, L.H., and Chung, R.M. (1984). The Influence of SPT Procedures in Soil Liquefaction Resistance Evaluations. Report No. UCB/EERC-84/15, Earthquake Engineering Research Center, College of Engineering, University of California, Berkeley.
- Seed, H.B., Wong, R. T., Idriss, I.M., and Tokimatsu, K. (1986). "Moduli and Damping Factors for Dynamic Analyses of Cohesionless Soils." Journal of Geotechnical Engineering, Vol. 112, No. 11, November 1986. American Society of Civil Engineers.
- Seed, R.B. and Harder, L.F. (1990). SPT-Based Analysis of Cyclic Pore Pressure Generation and Undrained Residual Strength. Proc., H. Bolton Seed Memorial Symposium, University of California, Berkeley, Vol. 2. pp. 351-376.

- Seed, R.B., Cetin, K.O., Moss, R.E.S., Kammerer, A.M., Wu, J., Pestana, J.M., Riemer, M.F., Sancio, R.B., Kayen, R.E., and Faris, A. (2003). Recent Advances in Soil Liquefaction Engineering: A Unified and Consistent Framework. 26th Annual ASCE Los Angeles Geotechnical Spring Seminar, Keynote Presentation, H.M.S. Queen Mary, Long Beach, CA.
- Serff, N, J. (1976). Earthquake-Induced Deformations of Earth Dams. A dissertation submitted in partial satisfaction of the requirements for the degree of Doctor of Philosophy in Engineering – Civil and Environmental Engineering in the Graduate Division of the University of California, Berkeley.
- Shamoto, Y., Zhang, J. M., and Tokimatsu, K. (1998). “Methods for evaluating residual post-liquefaction ground settlement and horizontal displacement.” *Soils and Foundations*, 2(2), 69-83.
- Shibata, T., Oka, F., and Ozawa, Y. (1996). “Characteristics of Ground Deformation Due to Liquefaction.” *Special Issue of Soils and Foundations*, 65-79, January, Japanese Geotechnical Society.
- Sitar, N., ed. (1995). “Geotechnical Reconnaissance of the Effects of the January 17, 1995, Hyogoken-Nambu Earthquake, Japan.” Report No. UCB/EERC-95/01, Earthquake Engineering Research Center (EERC), University of California, Berkeley, California.
- Skempton, A.W. (1986). Standard Penetration Test Procedures and the Effects in Sands of Overburden Pressure, Relative Density, Particle Size, Ageing, and Overconsolidation. *Geotechnique* 36, No. 3, pp 425-447.
- Somerville, P.G., N.F. Smith, R.W. Graves, and N.A. Abrahamson (1997). Modification of empirical strong ground motion attenuation relations to include the amplitude and duration effects of rupture directivity. *Seismological Research Letters*, 68: 199-222.
- Stark, T. D. and Mesri, G. (1992). “Undrained shear strength of liquefied sands for stability analysis.” *Journal of Geotechnical Engineering, ASCE*, 118(11), 1727-1747.
- Terzaghi, K. and Peck, R. B. (1967). *Soil mechanics in engineering practice*. Wiley.
- Toki, K. (1995). Committee of Earthquake Observation and Research in the Kansai Area.
- Tokimatsu, K., and Seed, H. B. (1984). “Simplified procedures of the evaluation of settlements in clean sands.” Report No. UCB/GT-84/16, University of California, Berkeley, California.
- Trifunac, M. D., and Hudson, D. E. (1971). “Analysis of the Pacoima Dam accelerogram – San Fernando, California, earthquake of 1971.” *Bulletin of the Seismological Society of America*, Volume 61, No. 5, pp. 1393-1141.
- USBR (2015). “Seismic risks for embankments.” IV-6.
<https://www.usbr.gov/ssle/damsafety/risk/BestPractices/Presentations/IV-6-20150402-PP.pdf>
- USGS (2018). Quaternary faults and folds database of the United States.
<https://earthquake.usgs.gov/hazards/qfaults/>
- Verdugo, R. (1992). “Characterization of sandy soil behavior under large deformation.” Doctoral thesis, Department of Civil Engineering, University of Tokyo, Japan.

- Verdugo, R., and Ishihara, K. (1996). "The steady state of sandy soils." *Soils and Foundations*, Vol. 36, No. 2, 81-91. Japanese Geotechnical Society.
- Wald, D. (1996). "Slip History of the 1995 Kobe, Japan, Earthquake Determined from Strong Motion, Teleseismic, and Geodetic Data." *Journal of Physics, Earth*, 44, 489-503, 1996.
- Wang, Z.L. 1990. Bounding Surface Hypo-Plasticity Model for Granular Soils and Its Application. Ph.D. dissertation for the University of California at Davis.
- Wang, Z.-L., and Ma, F. (2018). "Wang2D: A plasticity sand model updated based on simple shear test data." <https://www.itascacg.com/udms/wang2d>
- Wang, Z.L., Dafalias, Y.F., Li, X, S., and Makdisi, F.I. (2002). State Parameter Index for Modeling Sand Behavior. *Journal of Geotechnical and Geoenvironmental Engineering*, June.
- Wang, Z-L, Chang, C.Y., and Mok, C, M. (2001). "Evaluation of Site Response Using Downhole Array Data from a Liquefied Site." *International Conferences in Geotechnical Earthquake Engineering and Soil Dynamics*. Paper 24.
<http://scholarsmine.mst.edu/icrageesd/session04/24>
- Wang, ZL., and Ma, F. (2018). WANG2D: A plasticity sand model updated based on simple shear test data (<https://www.itascacg.com/udms/wang2d>).
- Weber, J.P. (2015). "Engineering Evaluation of Post-Liquefaction Strength." A dissertation submitted in partial satisfaction of the requirements for the degree of Doctor of Philosophy in Engineering – Civil and Environmental Engineering in the Graduate Division of the University of California, Berkeley.
- Weber, J.P., Seed, R.B., Pestana, J.M., Moss, R.E.S., Nweke, C., Deger, T.T., and Chowdhury, K. (2015). "Engineering Evaluation of Post-Liquefaction Strength." Department of Civil and Environmental Engineering, University of California, Berkeley. Prepared for the U.S. Nuclear Regulatory Commission.
- Whitcomb, J. H., Allen, Clarence, R., Garmny, J D., Hileman, J. A. (1973). "San Fernando earthquake series, 1971: focal mechanisms and tectonics." *Reviews of Geophysics and Space Physics*, Volume 11, p 693. Doi: 10.1029/RG11i003p00693.
- Wong, K.S., and Duncan, J.M. (1974). "Hyperbolic Stress-Strain Parameters for Nonlinear Finite Element Analyses of Stresses and Movements in Soil Masses." *Geotechnical Engineering Report TE 74-3 to the National Science Foundation, Office of Research Services, University of California, Berkeley, California*.
- Wu, J., and Seed, R.B. (2004). "Estimating of liquefaction-induced ground settlement (case histories)." *Proceedings of 5th International Conference on Case Histories in Geotechnical Engineering*, Paper 3.09, New York.
- Wu, J., Seed, R.B., and Pestana, J.M. (2003). Liquefaction Triggering and Post Liquefaction Deformations of Monterey 0/30 Sand Under Uni-Directional Cyclic Simple Shear Loading. *Geotechnical Engineering Report No. UCB/GE-2003/01, U.C. Berkeley*.
- Yasuda, S., Ishihara, K., and Harada, K., and Shinkawa, N. (1996). "Effect of soil improvement on ground subsidence due to liquefaction." *Special issue of Soils and Foundations*, 99-107, Jan. 1996. Japanese Geotechnical Society.
- Yee, E., Stewart, J.P., and Tokimatsu, K. (2013). "Elastic and large-strain nonlinear seismic site response from analysis of vertical array recordings." *Journal of Geotechnical and*

- Geoenvironmental Engineering, Vol. 139, No. 10, October 1, 2013. DOI: 10.1061/(ASCE)GT.1943-5606.0000900. American Society of Civil Engineers.
- Yoshimine, M. and Ishihara, K. (1998). "Flow Potential of Sand During Liquefaction." *Soils and Foundations*, Vol. 38, No. 3, 189-198, September, Japanese Geotechnical Society.
- Youd, T.L., Idriss, I.M., Andrus, R.D., Arango, I., Castro, G., Christian, J.T., Dobry, R., Finn, W.D.L., Harder, L.F. Jr., Hynes, M.E., Ishihara, K., Koester, J.P., Liao, S. S. C., Marcuson III, W. F., Martin, J. R., Mitchell, J. K., Moriwaki, Y., Power, M.S., Robertson, P.K, Seed, R.B., and Stokoe II, K. H. (2001). "Liquefaction resistance of soils: summary report from the 1996 NCEER and 1998 NCEER/NSF workshops on evaluation of liquefaction resistance of soils." *Journal of Geotechnical and Geoenvironmental Engineering*, ASCE, Vol. 127, No.10, pp.817- 833, October, 2001.
- Ziotopoulou, A. (2010). "Evaluating model uncertainty against strong motion records at liquefiable sites." A dissertation submitted in partial satisfaction of the requirements for the degree of Master of Science in Civil and Environmental Engineering in the Office of Graduate Studies of the University of California, Davis. 2010.
- Ziotopoulou, K., Boulanger, R.W., and Kramer, S.L. (2012). "Site Response Analysis of Liquefying Sites." *GeoCongress 2012*. American Society of Civil Engineers.